Atomistic Simulation of Cementitious Systems

THÈSE N^{O} 5754 (2013)

PRÉSENTÉE LE 24 MAI 2013

À LA FACULTÉ DES SCIENCES ET TECHNIQUES DE L'INGÉNIEUR
LABORATOIRE DE TECHNOLOGIE DES POUDRES
PROGRAMME DOCTORAL EN SCIENCE ET GÉNIE DES MATÉRIAUX

ÉCOLE POLYTECHNIQUE FÉDÉRALE DE LAUSANNE

POUR L'OBTENTION DU GRADE DE DOCTEUR ÈS SCIENCES

PAR

Sandra Caroline GALMARINI

acceptée sur proposition du jury:

Prof. A. Mortensen, président du jury
Dr P. Bowen, directeur de thèse
Dr E. Gartner, rapporteur
Prof. N. Marzari, rapporteur
Prof. S. Parker, rapporteur

ÉCOLE POLYTECHNIQUE
FÉDÉRALE DE LAUSANNE
Suisse
2013

'Tis the note of the Jubjub! Keep count, I entreat;
You will find I have told it you twice.
'Tis the song of the Jubjub! The proof is complete,
If only I've stated it thrice.
— *Lewis Carroll, The Hunting of the Snark, An Agony in Eight Fits*

Acknowledgements

There are so many people, without whom this thesis would not have been possible. In fact so many people should be thanked here, I feel certain I will forget someone. If that is the case I would like to apologize sincerely.

The work was made possible by funding from nanocem, the industrial-academic research network on cement and concrete, for which I would like to thank them profoundly. I would also like to thank Dr. Paul Bowen, who gave me the opportunity to do this work and for his help and guidance throughout the project. I would like to thank him for his trust in me and the scientific liberty he accorded me. He also made it possible for me to travel and to meet and discuss with a great number of proficient scientists and profit from their knowledge.

Secondly I would like to thank Dr. Uli Aschauer for making my start at LTP as easy as possible and for his help and friendship throughout the project. He helped me setting up the computational tools in the beginning, with the metadynamics calculation and a lot more. Without his help, my work would have been a lot harder.

A very big thanks goes to Prof. Steve Parker for his help and for his contribution to the work as well as welcoming me to his computational solid state chemistry (CSSC) group at the university of Bath for several stays. He helped me amongst other things to get solid-water interface calculations and with the C-S-H defect calculations. His great knowledge and experience of atomistic simulations was invaluable. I would also like to thank the different members of the CSSC group for always making me feel welcome and for their help while I was visiting.

I would also like to thank Prof. Heinrich Hofmann for welcoming me to LTP and for always making me feel part of the group even though my research topic was somewhat apart from the main research interests at LTP.

I would also like to thank the students I was working with over the years, especially Nicolas Ruffray, Amirreza Kiani, Tina Saberi and Aslam Kunhi whose contributions can be found in this thesis, as well as my colleagues Anne Aimable, Marijana Mionic, Michael Stuer and Vianney Bernau who helped with the supervision of the student projects, with SEM imaging etc. and whose contributions can also be found in this thesis.

A big thanks also goes to my other colleagues at LTP, past and present, for all their help and companionship. A special thank goes to Lionel Maurizi, Usawadee (June) Sakulkhu and Marie-Gabrielle Ollivier-Beuzelin for their friendship and helping me out during the rather tedious writing phase at the end of the thesis. And of course Ruth Gacoin, for making the

administrative tasks as easy as possible, for always keeping her calm in the face of e.g. expired deadlines and for always having a friendly word.

I would also like to thank Prof. Karen Scrivener for taking an interest in my work and including me in the activities of LMC as well as the members of LMC past and present, especially Elise Berodier, Arnaud Muller and Berta Mottet, for always making me feel welcome and for interesting scientific discussions.

Furthermore I would like to thank Dr. Barbara Lothenbach for helping me with GEMS for the thermodynamic modeling and Dr. Ellis Gartner, Dr. Patrick Juilland and Prof. Robert Flatt for taking their time to get involved in the project and for their stimulating scientific discussions.

My work was greatly influenced by nanocem and I would like to thank all the members. The inclusion in the nanocem network was very helpful and made it easy to discuss with both experienced researches and with fellow PhD students as well as to get the industrial viewpoint, which was very enriching. The level of collaboration that has been achieved by the members of nanocem is impressive and an inspiration. One of the persons making this possible is Marie-Alix Dalang-Secrétan, whom I would like to thank for always being there for any questions and making sure the project was running smoothly on the administative level as well.

Last but not least I would like to thank the members of the jury, for taking the time to evaluate the thesis and for their helpful remarks and interesting discussions during the thesis exam.

And what would life be without friends. During the four years of my thesis I had many a splendid evening or week-end with friends, in different parts of Switzerland, which made me approach work with renewed energy the day after. Thank you all and I am looking forward to the next beer or the next meal or ...

Finally none of this would have been possible without my family. Most of all I would like to thank my parents for always being there when I needed them, for teaching me to think for myself, for expecting something from me while trusting me to make my own decisions and for their unwavering support. I would also like my brother and my sisters for being the best of companions and friends and for always helping me out when I needed help. And thanks to the next generation, my niece, my nephews and my godsons, for many a nice hour during which they did not allow me to think about anything but the present.

Lausanne, 3 Mars 2013 S. G.

Abstract

The objective of the current thesis is to apply atomistic simulation techniques to further the current knowledge of cementitious systems. Hydrated cement is a part of concrete which is one of the most widely used materials in the world. As such the production of cement is responsible for about 5-8% of global CO_2 emissions. The optimization of the mechanical properties and durability of concrete can therefore aid in the reduction of CO_2 emissions. However hydrated cementitious materials are complex systems with many components: different hydrated phases, possibly unreacted cement grains of different composition and pore solution, possibly with organic additives.

The aim of this thesis was to identify areas where classical atomistic simulation can be used to further our knowledge of cementitious systems. The focus was on the two main hydration products, portlandite and calcium-silicate-hydrate.

For portlandite the atomistic mechanisms of growth from solution and the influences on the final morphology were studied. In addition to the interactions between the portlandite surfaces and water, the influence of different ionic species on portlandite growth has been considered. The influence of different ionic species present in the solution on the growth and final morphology of portlandite in cementitious systems has been observed previously. These phenomena are important to understand as portlandite growth influences the hydration kinetics of cementitious systems. Consequently a better understanding of the mechanisms governing the growth of portlandite might lead to a better control of the hydration kinetics. The final morphology of portlandite on the other hand will influence the final properties of cement, such as the mechanical strength or the diffusion of different ionic species in the cement microstructure.

Our results indicate that water noticeably influences the relative interfacial energies and hence the equilibrium morphology of portlandite. Whereas the equilibrium morphology of portlandite in a weakly interacting environment is expected to be hexagonal platelets, in water the equilibrium morphology becomes equiaxed.

Metropolis Monte Carlo calculations of the electrical double layer at the [00.1] portlandite surface indicate that the positive zeta potential measured experimentally in quasi pure portlandite-water systems may arise from the adsorption of Ca^{2+} ions at what can be considered the outer Hemholtz plane, due to favorable interactions between the solvation shell of the calcium ions and the structured water region above the portlandite surface. The different origin of the charge at the interface leads to differences of the structural details of the diffuse

layer from the classical Gouy-Chapman picture.

Silicates appear to have an important influence on the growth and final morphology of portlandite. Atomistic simulations indicate that this might be due to the preferential adsorption of neutral $CaSiO_2(OH)_2$ complexes, the stability of which has been confirmed by metadynamics. These complexes appear to retain a certain amount of mobility at the portlandite surfaces, performing a sort of walking movement by consecutively breaking and reforming one of two hydroxyl bonds donated to the portlandite surface hydroxyl groups. This might result in the poisoning of portlandite growth by silicates and explain the large influence of silicates on portlandite morhpology.

The addition of sulfates has been observed to promote a hexagonal platelet morphology of portlandite. This might be partially due to the formation of a calcium-sulfate complex which leads to an increase of the pH and a decrease of the calcium to hydroxide concentration ratio in the solution. As at the [00.1] surface the dehydration of the Ca^{2+} ions is likely to be the rate limiting step, a reduction of the Ca^{2+} concentration in the solution might lower the growth rate in [00.1] direction. It was also observed, that the precipitation of gypsum in these systems was retarded and indications of the existence of metastable calcium-sulfate nuclei, on which the portlandite particles precipitate, was found.

For the second hydrate studied here, calcium-silicate-hydrate, the most abundant hydrate in conventional cementitious systems, the exact atomic structure is still not fully known. However the atomistic structure is a key feature to better understand the C-S-H nanostructure and its thermodynamic and mechanical properties.

Our results indicate that 14 Å tobermorite is good model structure for C-S-H. Both the precipitation enthalpies and general structural features of the calcium to silicon ratio increasing defects studied were in reasonable agreement with experimental results. Although further work will be needed to understand e.g. the interaction of defects with other defects and with tobermorite/pore solution interfaces, the current approach seems to be promising to develop a model of the atomistic structure of C-S-H.

The atomistic simulation results also indicate that the tobermorite/water interfacial energy of tobermorite surfaces that are parallel to the linear silicate chains, is very small and may even be slightly negative. A slightly negative surface energy would indicate that there is a optimal size of the tobermorite particles in water and the particles do not grow larger than that size. The reason for a slightly negative surface energy might e.g. be internal stresses in the crystal structure.

Keywords: cement, portlandite, crystal growth, atomistic simulation, C-S-H, surface interactions

Résumé

L'objectif de cette thèse était l'étude de système cimentaire par l'application de différentes techniques de simulation atomistique. Le ciment hydraté est une composante majeure du béton qui est un des matériaux les plus utilisés au monde. En conséquence la production de ciment est responsable d'environ 5.8 % des émissions globales de CO_2. Les systèmes cimentaires sont très complexes. La mircrostructure du ciment hydraté est composé d'un grand nombre de différentes composantes (différents hydrates, éventuellement des grains de ciment non dissous et la solution aqueuse présente dans les pores probablement avec des additifs organiques ou autre).

Le but de ce travail était donc d'identifier des questions concrètes ou l'application de différentes méthode de simulations atomistique peuvent mener à une augmentation de la connaissance des systèmes cimentaires. Les deux phases hydratés principales, la portlandite et C-S-H, ont été au centre de la recherche menée.

Dans le cas de la portlandite, la croissance de la phase solide à partir d'une solution aqueuse et la morphologie finale des particules ont été étudiées. L'influence de l'eau et des espèces ioniques en solution a été considéré. Il est connu que les espèces ioniques ont une grande influence sur la morphologie finale des particules de portlandite. Il est donc important de comprendre ces phénomènes car la croissance de la portlandite peut avoir une influence sur la cinétique de l'hydratation du ciment. C'est pourquoi une meilleure compréhension de la croissance de la portlandite peut mener à un meilleur contrôle de la cinétique de l'hydratation du béton. De plus, la morphologie finale du béton va avoir une influence sur ces propriétés finales, comme par exemple les propriétés mécaniques et le transport d'eau au sein du béton.

Nos résultats indiquent que la présence d'eau a une grande influence sur la morphologie d'équilibre de la portlandite. Dans des environnements qui n'interagissent pas avec les surfaces de portlandite on attend des particules cristallisées en forme de plaquettes hexagonal. En présence d'eau par contre la morphologie de la portlandite devient équiaxe. Ceci est probablement dû à la formation d'un réseau de molécules d'eau fortement liées aux surfaces de haute énergie, ce qui les stabilise par rapport aux surfaces de plus basse énergie.

Des calculs de Metropolis Monte Carlo de la double couche électrique en contact avec la surface [00.1] de portlandite indique que l'adsorption des ions Ca^{2+} à ce qui peut être considéré comme le plan Helmholtz extérieur, causé par une interaction favorable entre la couche de solvatation des ions et la région d'eau structurée à la surface, peut être à l'origine du potentiel Zêta légèrement positif, mesuré expérimentalement dans des système pure d'eau et de port-

landite. Une telle origine de la charge interfaciale n'est pas prise en compte par les théories classiques de la double couche, comme la théorie de Gouy-Chapman. En conséquence la structure de la couche diffuse diverge de la prédiction de Gouy-Chapman.

Les silicates ont apparemment une grande influence sur la croissance et la morphologie des particules de portlandite. Les résultats de simulations atomistiques indiquent que ceci peut être la conséquence de l'adsorption stable de $CaSiO_2(OH)_2$ aux surfaces de la portlandite. Ces espèces neutres retiennent une certaine mobilité une fois adsorbées. En fait, ils peuvent se propager le long de la surface en défaisant et reformant alternativement une de deux liaisons hydrogène avec la surface. Un tel comportement pourrait expliquer le ralentissement de la croissance de portlandite quand des silicates sont ajoutés.

L'addition de sulfates au système entraine un changement de la morphologie des particules de portlandite vers des plaquettes hexagonales. Une raison possible pour ce changement peut être la formation de complexes de silicates avec les ions Ca^{2+}. Ces complexes causent une augmentation du pH et une baisse de la concentration des ions Ca^{2+}. A la surface [00.1] de la portlandite, la déshydratation des ions Ca^{2+} est probablement l'étape déterminante pour la cinétique. En conséquence, une faible concentration de Ca^{2+} va probablement ralentir la croissance en direction [00.1]. Il a aussi été observé que la précipitation du gypse, dans le système portlandite contentant du sulfate, est retardée. De plus, selon nos observations, il est possible que les particules de portlandite croissent sur des germes de calcium-sulfate métastables.

Pour la phase principale du ciment hydraté, le C-S-H, la structure atomistique n'est toujours pas exactement connu. En revanche, connaître cette structure atomistique serait un point clé pour la compréhension de la nanostructure de C-S-H et ses propriétés mécaniques et thermodynamiques.

Les résultats obtenus dans le cadre de cette thèse renforcent la supposition que la tobermorite 14 Å est une bonne structure de modèle pour le C-S-H. Les calculs d'enthalpie de précipitation ainsi que des propriétés structurales des défauts possibles, pour augmenter le rapport calcium sur silicate, ont donné des résultats coïncidant avec les observations expérimentales. Par contre, plus d'études, notamment concernant l'interaction entre les différents défauts et l'interaction entre les défauts et les surfaces, devrons être réalisées pour clarifier ces résultats. Mains dans l'ensemble l'approche choisie pour le développement d'un modèle atomistique de C-S-H semble être prometteuse.

D'après les simulations atomistiques, l'énergie d'interface entre la portlandite et l'eau est très faible et pourrait même être négative. Une énergie de surface légèrement négative indiquerait une taille optimale des cristallites de portlandite. Ceci pourrait être expliqué, par exemple, par des contraintes internes dans la structure cristalline.

Mots clefs : ciment, portlandite, croissance cristalline, simulation atomistique, C-S-H, interactions de surface

Contents

List of Figures

List of Tables

1 Introduction

This chapter will set the present thesis into context. First the particularities of hydrated cementitious systems are discussed and areas of interest for atomistic modelling identified. Then important notions such as interfaces and interfacial energies, the precipitation of solids from solution, the equilibrium distribution of ions in solution close to a solid-liquid interface and defective crystalline structures are discussed. The chapter then ends with the motivation, goals and structure of the thesis.

1.1 Cementitious Materials

Hydrated cement is a part of concrete which is one of the most widely used materials in the world. As such the production of cement is responsible for about 5-8% of global CO_2 emissions. The optimisation of the mechanical properties and durability of concrete can therefore aid in the reduction of CO_2 emissions. However hydrated cementitious materials are complex systems with many components (different hydrated phases, possibly unreacted cement grains of different composition and pore solution, possibly with organic additives). A cement microstructure from K. Scrivener [Scr04], showing the typical components of a hydrated cement mortar can be seen in figure 1.1.

It is also known that hydrated cement contains a complex multi-scale pore structure with pores ranging from nanometric to macroscopic. This means that the specific interface area is very high. The significant role of the different types of interfaces, which ultimately control the properties of cements and concretes, from the early stages of hydration to the final microstructure, demands a deep knowledge of the processes taking place at the interfaces at an atomistic level. The nature of the solid-liquid interfaces where dissolution of the anhydrous phase, adsorption of cement admixtures and growth of new crystalline phases take place are however very difficult to access experimentally. This makes the optimisation of the material very complex.

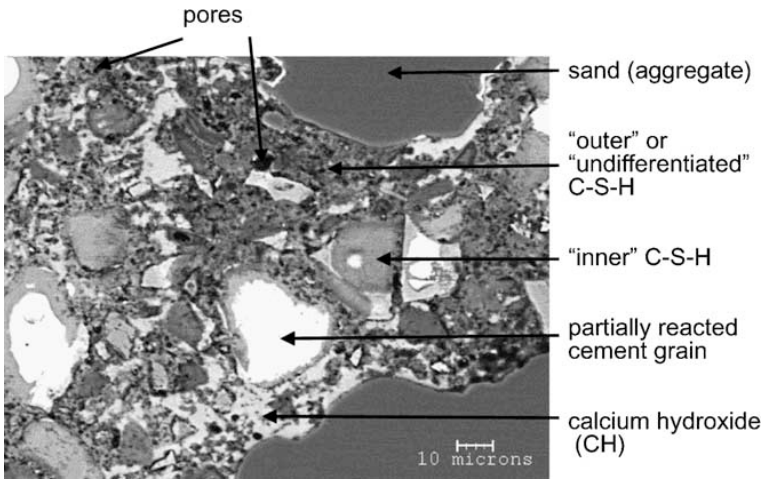

Figure 1.1: Typical microstructure of hydrated cement. Taken from [Scr04]

It has for instance been shown, that the final morphology of the second most abundant hydrate, portlandite, is notably influenced by the composition of the cement and thus the composition of the pore solution during hydration [GS07]. If the cement mixture contains both sulfates and aluminates, portlandite is observed as individual particles of a size of about 10 μm distributed throughout the material. If either aluminates, sulfates or both of them are absent in the original cement mixture, large, irregularly shaped portlandite agglomerates with a size of 50-70 μm are observed [GS07]. These changes in morphology are not yet understood and their working mechanisms are difficult to access experimentally.

Another example of the complexity of cement is the hydration behavior (see e.g. [SN11, BJL$^+$11]). When ordinary portland cement is mixed with water, after a short initial reaction, which corresponds mostly to the initial dissolution of a small part of the cement grains, the reaction slows down and little change is observed for a few hours. This period of slow reaction is often called the dormant or the induction period. Over approximately the next day after the induction period, the reaction accelerates and then decelerates again (the aptly named acceleration and deceleration periods). Finally the deceleration period is superseded by a period of continued slow hydration. The origin of the induction period and the following acceleration as well as of the deceleration period is still not entirely understood. There are several coexisting and debated theories explaining the observed hydration behaviour, the evidence presented for each theory is often indirect and sometimes contradictory. Consequently the role of the two main hydration products, calcium-silicate-hydrate (C-S-H) and portlandite, during these periods is not entirely clear either.

Let us for example look at the role of portlandite. After the initial dissolution of the anhydrates, little changes in the compositon of the pore solution during the induction period. During this period the pore solution is supersaturated with respect to portlandite [LW06]. It has been shown early that, during the hydration of alite (Ca_3SiO_5) the supersaturation increases slightly during the induction period [YTB77]. Then, at the end of the induction and the beginning

of the acceleration period, portlandite nucleates and, slightly delayed with respect to the observed portlandite nucleation [YTB77], the portlandite supersaturation in the solution decreases again. At the same time C-S-H starts precipitating in large quantities. The induction period can be slightly reduced and the subsequent reactions accelerated by adding $CaCl_2$ to the system.This will lead to higher initial supersaturations with respect to portlandite and a critical supersaturation at which portlandite precipitates is reached earlier. The apparent link between portlandite precipitation and the start of the acceleration period lead Young et al. [YTB77] to initally propose that it might be the precipitation of portlandite that causes the end of the induction period.

However subsequent experiments did not unequivocally support that hypothesis. Several authors [BHP86, WY84] replaced the water in the cement mix by a saturated lime solution with the hope of accelerating the precipitation of portlandite, but no reduction of the induction time was observed. At the same time the authors of both articles also observed that, contrary to when calcium cloride is added, the calcium concentration and the portlandite supersaturation follow a similar profile as when pure water is used. The similar portlandite supersaturation profile explains why no acceleration of the hydration was observed. The conclusion drawn by the authors of both papers was that the initally higher calcium concentrations lowers the dissolution rate of the anhydrates, making the overall supersaturation profile similar to the hydration with pure water. This is in accordance with more recent results by Juilland et al. [JGFS10] which indicate that the induction period might be at least partially due to a decrease of the dissolution rate of the anhydrates due to the decrease of the undersaturation of the solution with respect to the anhydrates.

Odler and Dörr tried a different approach to decrease the induction time by accelerating portlandite precipitation [OD79]: They added a relatively high surface area (7.8 $\frac{m^2}{g}$ as measured by nitrogen adsorption) crystalline portlandite to the cement mix with the idea to eliminate the supersaturation necessary for nucleation and thus both increase the dissolution rate of the anhydrate phase and speed up the portlandite precipitation. However calcium concentration measurements indicated that, after an initial short decrease the calcium concentration raises again and reaches similar values as in the absence of added portlandite at the end of the induction period. Only then, in the acceleration period, was a slight acceleration of the hydration observed. The authors stated that a possible explanation of the observed evolution might be the poisoning of the growth of the portlandite particles by silicates. This would be in agreement with results from Tadros et al. [TSK76] that show that silicates do slow down the growth of portlandite. Additionally it would explain why the portlandite supersaturation still increases after the nucleation of portlandite [YTB77] and indeed indicate that the acceleration period coincides with the accelerated growth of portlandite rather than portlandite nucleation. Evidence of portlandite precipitation already during the induction period was also reported by Makar and Chan [MC08]. This indicates that portlandite precipitation is not the cause of the end of the induction period but that the accelerated portlandite growth is a contributing factor. These results are also confirmed by experiments where an acceleration period was observed even though portlandite precipitation was retarded or altogether suppressed (by keeping the

calcium concentrations in the solution below portlandite saturation) [GGN99, DNB90]. In other words an acceleration can be observed independent of the precipitation of portlandite.

The evidence as to whether or not the addition of crystalline portlandite to the cement mix will increase the acceleration following the induction period is ambiguous. Whereas Odler and Dörr observed such an effect [OD79], Leture et al. did find little or no effect of the addition of crystalline portlandite [LCL98]. Nicoleau recently even published results indicating that the addition portlandite leads to a reduction of the induction period but leads to a subsequent slowing down of the hydration [Nic11], which goes in the opposite direction of the evidence presented above.

Another complication to understand cementitious systems is that the exact atomistic and nanoscale structure of the main hydration product, calcium silicate hydrate (C-S-H), is not yet fully known. C-S-H is nearly x-ray amorphous, indicating the absence of long-range three dimensional order. The fact that C-S-H contains water and the structure will be changed upon drying means, that the range of applicable experimental methods is limited. Transmission electron microscopy (TEM) images of carefully dried samples show different morphologies of C-S-H, often with a pronounced texture, with the smallest characteristic dimension of the structure being of the order of 3 nm [Ric04]. TEM images with an even higher resolution have even revealed layering of the material with an approximate interlayer distance of ~ 12-14 Å [PKS$^+$09]. These observations along with NMR ^{29}Si spectroscopy measurements (e.g. [AJS04]) have led to the conclusion that C-S-H is probably composed of particles of defective nano-crystalline tobermorite, possibly intermixed with other phases such as jennite or portlandite. In neat C_3S pastes local energy dispersive X-ray analysis (EDS) have shown that, while the average calcium to silica ratio $\langle\frac{Ca}{Si}\rangle$ is 1.75, on a scale of 100 nm, the ratio varies between 1.2 and 2.1 [RG93]. The stoichiometry of the tobermorite (14 Å tobermorite) with the highest $\langle\frac{Ca}{Si}\rangle$ on the other hand is $Ca_{2.5}Si_3O_8(OH)\cdot 3.5H_2O$, leading to a $\langle\frac{Ca}{Si}\rangle$ of 0.83, which is much lower than observed for C-S-H. This indicates that the structure of C-S-H is defective compared to tobermorite, the more so the higher the $\langle\frac{Ca}{Si}\rangle$ ratio. This is confirmed by NMR ^{29}Si spectroscopy [BBC$^+$04] and Rietveld analyses [RRL$^+$09a]. The nano-crystalline nature of the material means that interfaces play an important role in the overall structure. Therefore, to further understand C-S-H, the properties of the interfaces in C-S-H as well as the defects present in the crystals need to be further studied. Again these are systems that are difficult to access experimentally.

The use of atomistic modeling has made great progress over recent years in many different fields such as properties of interfaces, crystal growth and self-assembly [AGM$^+$09, SBP08, SDMW02]. This progress has made it possible to simulate different phases of hydrated cement, namely portlandite and tobermorite as a C-S-H model structure, their interfaces with the pore solution and possible defects. While some work in that direction has already been done [KK02, KWK07, Chu09, ADC$^+$07, PKS$^+$09, DGH07] a systematic study of the hydrate - pore solution interfaces and their structure and properties is still missing. The objective of this PhD thesis is therefore to elucidate areas of research where classical atomistic modeling can

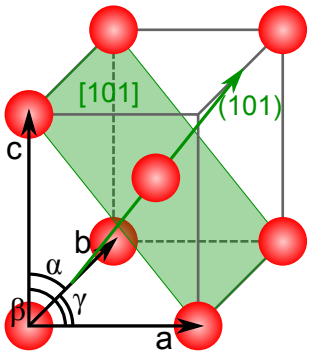

Figure 1.2: Schematic illustration of the cell parameters a, b, c and α, β, γ. Also shown is the [101] surface with the surface normal (101).

be used to further the knowledge of hydrated cementitious systems. Also the choice and development of different atomistic simulation methods that are applicable for the study of the different phenomena taking place in cement hydration, e.g. dissolution, adsorption, growth and structural disorder. The main focus was put on the two main hydration products, portlandite and C-S-H. According to the observations above, different topics were studied for portlandite and C-S-H. First the influence of species in solution on the growth and final morphology of portlandite was investigated, in particular with the aim of clarifying the role different species present in the pore solution can have on the growth. Secondly the energetics of different types of defects in 14 Å Tobermorite (a crystalline model for C-S-H) affecting the Ca/Si ratio were studied.

1.2 Interfaces of Inorganic Solids

Since cementitious systems are multiphase materials, interfaces are very important and abundant. Interfaces are the consequence of the fact that in reality systems and phases are finite. Where one domain of compositional and structural coherence terminates and an other begins, and interface is formed. Close to an interface the equilibrium arrangement of atoms forming the domain is perturbed and thus interfaces cost energy. In the case of inorganic solids there can be several types of interfaces present:

- Interfaces between regions with different compositions.
- Interfaces between regions with same or similar composition but different thermodynamic state (e.g. solid - melt interface).
- Interfaces between solid, crystalline regions with the same composition and thermodynamic state but different orientation of the crystalline lattice (Grain Boundaries).

The most important type of interface for cementitious systems are interfaces between regions of different composition. Due to the multiscale, porous nature of cement, the pore solution -

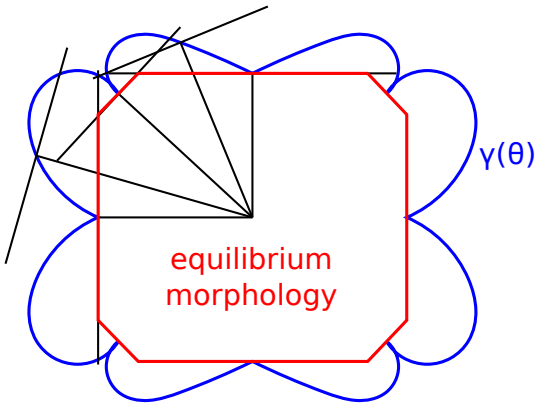

Figure 1.3: Schematic illustration of the Wulff construction in 2D. The interfacial energy curve is shown in blue, the tangents used for the Wulff construction in black and the resulting equilibrium morphology in red.

hydrate interfaces are probably the most abundant and very important for the study of the hydration process and the final properties.

For the crystalline phases the energy of an interface depends on the orientation with respect to the crystalline lattice. The reason for this is that the orientation of the interface will determine which "bonds" of the original crystal structure will be cut. Additionally, for more complex crystals, the crystal might be cut at different depths, exposing different atomic planes. This would in theory lead to different possible interfacial energies for a single interface orientation (see section 2.3.2). However usually only the cut depth with the lowest resulting interfacial energy is considered to be physically relevant.

The dependence of the interfacial energy on the interface orientation with respect to the crystal lattice means that the shape, minimizing the total interfacial energy of a finite sized crystal, is no longer a sphere. G. Wulff [Wul01] developed a general method to predict the equilibrium morphology of a finite sized crystal based on the interfacial energy $\gamma(\phi,\theta)$ as a function of the orientation. In fact Wulff showed that, in order to minimize the overall interfacial energy, the distance of an interface from the center of mass should be proportional to $\gamma(\phi,\theta)$ (see image 1.3). This means that one can construct the equilibrium or Wulff shape by drawing $\gamma(\phi,\theta)$ as a distance from the origin. In the next step all the possible interfaces for each orientation at that distance equal to the energy are drawn (i.e. the perpendicular plane to the vector from the origin to the value of $\gamma(\phi,\theta)$). The minimum energy morphology will then be the inner envelope of all the drawn interfaces.

The Wulff construction demands a knowledge of the interfacial energy with respect to the interface orientation. However $\gamma(\phi,\theta)$ is not easily accessible with experimental methods. In the case of ionic crystals, the low energy interfaces are usually parallel to a crystal plane [h k l]. h, k and l are the miller indices of the plane, giving the direction of the surface normal in the $\vec{a}$, $\vec{b}$, $\vec{c}$ coordinate system (see figure 1.2). For a crystalline plane h, k and l are

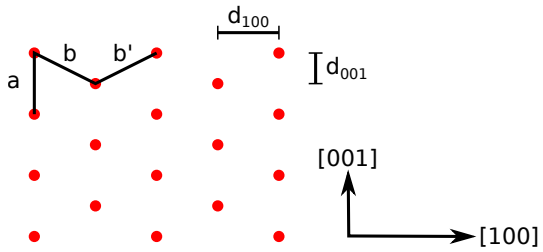

Figure 1.4: Schematic illustration of the BFDH and the PBC theory. In the BFDH theory, both the relative surface energy and the relative growth rate are approximated by the inverse of the interlayer distance d_{hkl}. The periodic bond chain (PBC) theory is based on the construction of chains of nearest neighbor bonds. If two such periodic bond chains with all bonds parallel to the surface can be constructed, the surface is flat. If there is only one such chain, the surface is stepped and if no such chain exists, the surface is kinked. In the image above, if there is a PBC with bonds parallel to [010], the [100] is a flat and the [001] is a stepped surface. Otherwise [100] is a stepped and [001] a kinked surface.

the smallest integers describing the surface normal. The continuous function $\gamma(\phi,\theta)$ can thus be reduced to a certain number of surface energies of different crystallographic planes $\gamma_{h,k,l}$. Taking this into account, a simplistic model to predict the surface energy for different orientations from the crystal structure has been developed by Bravais, Friedel, Donney and Harker (BFDH theory) ([Mye05] and references therein). In the BFDH theory, the surface energy $\gamma_{h,k,l}$ is approximated by the inverse of the distance between the interatomic planes $d_{h,k,l}$ (see figure 1.4). The reasoning behind the theory is that the adjacent atoms of closely spaced crystallographic planes are likely to be connected by strong bonds and thus the surface energy can be expected to be higher.

The BFDH can be useful to estimate which surfaces are likely to be important for the crystal morphology. However for a final morphology prediction, the BFDH theory is usually not accurate enough. There are several sources of inaccuracy. Firstly the BFDH theory does not take into account any details of the bonding within the crystal, the distance between the atomic planes is not the only property determining the strength of a bond. Secondly the atomic positions at the interfaces are likely to relax from the bulk positions to reduce the surface energy. This surface relaxation might be more important for some planes than for others, thus changing the relative interfacial energies $\frac{\gamma_{h_1,k_1,l_1}}{\gamma_{h_2,k_2,l_2}}$ and consequently the equilibrium morphology. Thirdly the theory does not take into account the interaction of the crystal interfaces with the surrounding phase. If we are for instance interested in the morphology of a crystal in solution, the solvent will interact with the surfaces. Since the interaction is likely to depend on the interface orientation, the relative surface energies and thus the equilibrium morphologies are likely to change with the presence of a solvent phase. Finally the method does not take into account the surface entropy. However this last point is probably of less importance for crystals with strong ionic character, where the effect of the surface entropy at room temperature generally plays a secondary role [TSB+99, Jur54].

This means that for more accurate surface energy predictions, other methods are needed. Here classical atomistic simulation can be useful (see e.g. [KPH03, MP04]).

1.3 Precipitation of Inorganic Solids from Solution

The precipitation of solids from the solution generally happens in two steps: nucleation and growth. Nucleation is a statistical process, controlled by the solid-solution interfacial energy. In fact the free energy of formation of a solid particle from solution is the sum of the bulk free energy of formation ΔF_{bulk} plus the total interfacial energy ΔF_{surf}. Let us consider a solid with composition $s_1 As_2 B...$ (where s_i are the stoichiometric factors and $A, B...$ are the different components of the solid). Let us further assume that the solid has an isotropic surface energy γ. For such a system the total free energy change of the formation of a solid particle with a size d can be further expressed in terms of the chemical potential of component i in the solution μ_i^l and in the solid μ_i^s (eq. 1.1). V_m is the volume of a stoichiometric unit $s_1 As_2 B...$ in the solid phase and β_{surf} and β_{vol} are shape dependent factors determining the surface and the volume of the particle (e.g. for a spherical particle the factors are π and $\pi/6$ respectively). If the system is in equilibrium, the chemical potentials are the same in the liquid and in the solid phase. This means that there is an equilibrium concentration c_i^{eq} where $\mu_i^l(c_i^{eq}) = \mu_i^s$. Consequently ΔF_{bulk} can also be described as the difference of the chemical potential at the current and the equilibrium concentration (eq. 1.1).

$$\begin{aligned}\Delta F_{tot}(d) = \Delta F_{bulk} + \Delta F_{surf} &= \beta_{surf} d^2 \gamma + \frac{\beta_{vol} d^3}{V_m} \sum_i s_i \cdot \left(\mu_i^s - \mu_i^l(c_i)\right) \\ &= \beta_{surf} d^2 \gamma + \frac{\beta_{vol} d^3}{V_m} \sum_i s_i \cdot \left(\mu_i^l(c_i^{eq}) - \mu_i^l(c_i)\right)\end{aligned} \tag{1.1}$$

In addition, if we consider an ideal solution, where the chemical potential of component i in the solution can be described as $\mu_i^l(c_i) = \mu_i^{l*} + k_b T \ln(c_i)$, the total energy gain $\Delta F_{tot}(d)$ can be further simplified and no longer explicitly depends on the chemical potentials (eq. 1.2).

$$\Delta F_{tot}(d) = \beta_{surf} d^2 \gamma - \frac{\beta_{vol} d^3}{V_m} k_b T \ln \prod_i \left(\frac{c_i}{c_i^{eq}}\right)^{s_i} = \beta_{surf} d^2 \gamma - \frac{\beta_{vol} d^3}{V_m} k_b T \ln S \tag{1.2}$$

Since the positive surface term varies with d^2, whereas the negative volume term varies with d^3, for small particle sizes the surface term is dominant and the energy will increase with increasing particle size, until an energy maximum ΔF_{tot}^{max} at a critical particle size d_{crit} is reached. The critical size can be determined from the derivative of $\Delta F_{tot}(d)$ with respect to the particle size (equation 1.3). The period of time where the kinetics are determined by

the rate, at which stable particles (i.e. nuclei) with a size bigger than d_{crit} are formed, is called the nucleation period. The ratio of the concentrations with respect to the equilibrium concentrations raised to the power of the stoichiometric coefficent is often called the total saturation index S and the logarithm $\ln S$ is often called the total relative supersaturation [JGFS10].

$$\begin{aligned} &\frac{\partial \Delta F_{tot}}{\partial d} = 2 \cdot \gamma \beta_{surf} \cdot d - \frac{3\beta_{vol} \cdot d^2}{V_m} k_b T \ln S \overset{\Delta F_{tot}^{max}}{=} 0 \\ &\longrightarrow d_{crit} = \frac{2\gamma \beta_{surf} V_m}{3\beta_{vol} k_b T \ln S} \end{aligned} \tag{1.3}$$

The nucleation rate Υ will depend on the activation energy i.e. on ΔF_{tot}^{max} and can be given as an Arrhenius type of equation. This means that variations of the nucleation rates with the supersaturation or the temperature can be used to determine ΔF_{tot}^{max} and consequently the interfacial energy γ.

$$\Upsilon = \Upsilon^0 e^{-\frac{\Delta F_{tot}^{max}}{k_b T}} \tag{1.4}$$

The matter is further complicated if the solution is not ideal, and consequently the concentrations in equation 1.2 are replaced by the activity coefficients, or by an anisotropic surface energy which would have to be taken into account by equations 1.1 and 1.2).

The homogeneous nucleation process described above will influence the size of the final particles that are produced. If the number of nuclei created increases, the size of the final particles decreases. This is generally done by increasing the supersaturation and thus increasing the importance of the energy gain from the particle volume ΔF_{bulk} as compared to the energy coming from the creation of the surface ΔF_{surf} and thus decreasing the critical nuclei size d_{crit}.

The theory developed above does not take into account any external surfaces such as the walls of a beaker where the solution is contained or, as in the case of cementitious systems, other solid phases (e.g. the anhydrates) present in the system. These surfaces often provide a preferential point of nucleation since the already existing surface generally lowers the total energy of the surface that has to be created for a stable nuclei. The process of creating nuclei at external surfaces is called heterogeneous nucleation in contrast to the above described homogeneous nucleation. Additionally the already formed nuclei or subsequent growing surfaces can serve as secondary nucleation sites (so called secondary nucleation).

Both heterogeneous nucleation and secondary nucleation can have drastic effects on the morphology of the precipitated particles. Heterogeneous nucleation will limit the possible

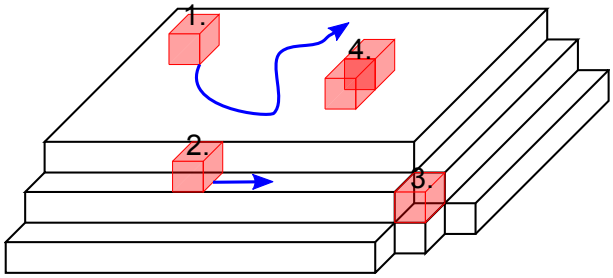

Figure 1.5: Schematic illustration of different processes happening at the surfaces of crystals. Species form the solution can adsorb to and desorb from different surface sites. There are three different types of surface sites: flat surface sites (1.), step sites (2.) and kink sites (3.). Whereas species at kink sites can only move when they desorb, surface diffusion is possible for the other two sites. At flat surfaces 2D surface diffusion is possible whereas at step sites diffusion is only possible in one dimension. Two or more adsorbed species can form surface complexes (4.) and can thus eventually serve as sites for nucleation of another crystal layer at flat surfaces or another step at step sites.

growth directions, thus growth directions away from the original nucleation site are favored. Also heterogeneous nucleation often results in agglomerated rather than separated particles.

Once nuclei have been formed they start to grow, leading to the second stage of precipitation, the growth period, which is controlled by the kinetics of all possible processes happening at the solid - solution interface. In order for the crystal to grow, the atoms have to move first from the bulk solution to the interfaces. In doing so they will have to move through the electrical double layer (see section 1.4) and through the structured water layers that can generally be found close to inorganic surfaces [SCKP06, AGM$^+$09] and where the diffusion coefficient is usually reduced. The properties of both the electrical double layer and the structured water region depend on the orientation of the interface with respect to the crystalline lattice which will determine the type and density of the surface groups.

An atom that is close to the surface can then adsorb on it by loosing part of its hydration shell and forming bonds with the surface. Of course the inverse desorption process will also happen. Schematically one can imagine different types of surfaces for which the adsorption process can be different: atomically flat surfaces which run parallel to a certain crystal plane, stepped surfaces which only one direction in common with a crystal plane and finally kinked surfaces that have no direction in common with any crystalline plane (see figure 1.5). An atom that adsorbs at a kink site will immediately become part of the crystal and indistinguishable from other surface sites.

An atom that adsobes at a step site still retains a certain mobility in one direction, due to the reduced number of bonds formed with the surface compared with a kink site. In order to definitely become part of the crystal it would have to associate with one or more other atoms, forming a one dimensional nucleus, terminated on both ends by a kink site that can then grow easily. Alternatively an atom adsorbed at a step site can move along the step until it finds and

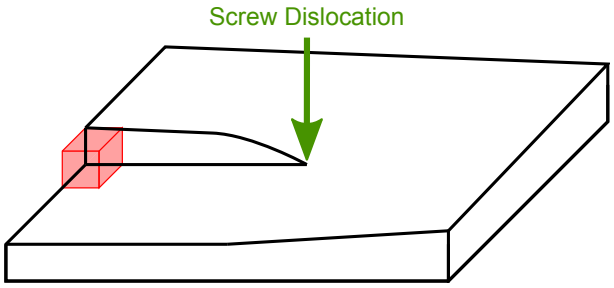

Figure 1.6: Schematic illustration of growth at screw dislocation sites. The screw dislocation can grow continuously, making step or layer nucleation unnecessary.

kink site where it can be integrated into the crystal.

An atom adsorbed at a flat surface is even less strongly bound to the surface and even more mobile. It can undergo two dimensional surface diffusion until it either encounters a step or a kink site or another surface atom. If it encounters another surface atom, a surface complex can be formed. Such a surface complex has to reach a certain size, similar to the case of homogeneous nucleation described above but in two dimensions, in order to become a stable layer nucleus. Such a nucleus will then be surrounded by step and kink sites that can grow more easily.

The nucleation of layers and kinks can be expected to be slower than the adsorption and desorption at different sites, since it is dependent on a statistical process of complex formation by two or more atoms that have to randomly encounter each other.

The growth can further be aided by the presence of defects, namely screw dislocations, at a surface. A screw dislocation is a line defect where, at a certain line in the crystal, part of the planes are shifted by an interatomic distance parallel to the defect line. If the screw dislocation reaches a surface, step sites will be created over part of the crystal (see figure 1.6). This step can now grow in a spiral fashion without ever reaching the edge of the surface and being annihilated. This means that due to the presence of screw dislocations, a flat surface oriented parallel to an atomic plane can grow continuously without needing to periodically go through a layer nucleation step.

Any of the above processes can determine the growth rate, models for the kinetics of diffusion controlled, layer nucleation controlled and defect controlled growth can be found in literature (see e.g. [Mye05] and references therein). The morphology of the precipitated particles will depend on the relative growth rates of the different surfaces, until, when equilibrium conditions are reached, the morphology will theoretically approach the equilibrium or Wulff morphology described in the previous section. However the driving force for the morphology to reach equilibrium is often much smaller than for the original precipitation. This means that the precipitation time scale is often much shorter than the equilibration time scale. In other words particles precipitated from solution often show a growth rather than an equilibrium morphology.

If the growth rate as a function of the surface orientation is known, the growth morphology can be predicted with a construction essentially similar to the Wulff construction (see figure 1.3) but where the surface energy is replaced by the growth rate. In other words the distance of a facet from the center of a particle is proportional to the growth rate.

Several theories to predict the growth rate have been developed. The main question is what is determining the relative growth rates of the surfaces. A number of theories suppose that the different attachment energies H_{attach} of a growth unit at the different surfaces are the rate determining properties. The higher the attachment energy, the faster the growth perpendicular to that surface and consequently the smaller the corresponding facets in the growth morphology. The simplest theory approximates the strength of the bond between a growth unit and a surface by the inverse of the distance d_{hkl} between crystal layers perpendicular to the surface ($H_{att} \sim d_{hkl}^{-1}$). This leads to the Bravais - Friedel - Donney - Harker theory described in the previous section. In fact, due to the simplistic view of the crystal, the BFDH theory is at once a prediction of the equilibrium and the growth morphology.

The idea of the attachment energies being the rate determining property, along with a more complex theory, the so called periodic bond chain (PBC) theory, to predict them, was originally developed by Hartman and Perdok (see [Mye05] and references therein). As for the BFDH theory, the interactions in the crystal are essentially reduced to nearest neighbor bonds. A periodic bond chain is then a certain number of these bonds that span the crystalline unit cell, and, due to the lattice periodicity, continue ad infinitum in an infinite crystal. Based on these periodic bond chains the possible surfaces are divided into three categories (see figure 1.4):

- Flat Surfaces: for flat surfaces two different periodic bond chains can be identified for which all bonds are parallel to the surface.
- Stepped Surfaces: for stepped surfaces only one peridic bond chain has all bonds parallel to the surface.
- Kinked Surfaces: for kinked surfaces no periodic bond chain can be constructed with bonds parallel to the surface.

Flat surfaces are expected to grow with a two dimensional layer nucleation, stepped surfaces with a one dimensional step nucleation and kinked surfaces with nucleation free mechanism, as described above. Since, as a general rule, nucleation is a slow process, more so the higher the dimensionality, kinked surfaces are supposed to grow the fastest, followed by stepped surfaces and finally the flat surfaces are expected to have the slowest growth rate. Consequently according to the PBC theory, generally only flat surfaces are expected to be present in the growth morphology.

The attachment energy then depends on the weakest bond energy of periodic bond chains that run perpendicular to the surface. A crystal slice parallel to the surface is constructed,

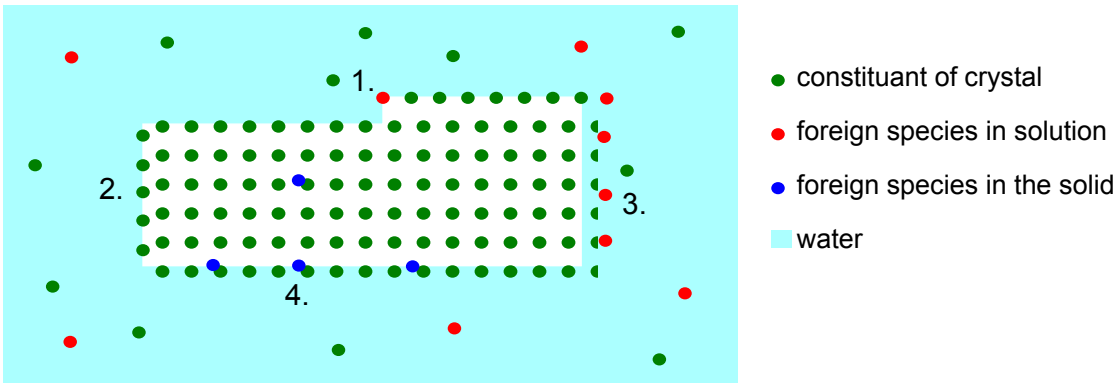

Figure 1.7: Schematic illustration of different mechanisms which influence the relative surface energies and/or the relative growth rates. 1.) Solute or solvant molecules can strongly adsorb onto growth feature (e.g. steps and kink sites) thus hindering growth. 2.) The atomic positions at the surfaces can relax from bulk position to minimize the surface energy. 3.) Solute or solvant molecules can interact with the surface, changing its energy. Additionally this can have an effect on the distribution of the dissolved crystal ions and their diffusion towards the crystal surface. 4.) Point defects in the crystal, such as impurities, can segregate to the surfaces, influencing the relative energy and the growth rate.

delineated on all sides by periodic bond chains. Perpendicular to the surface, the stronger bonds are within the slice whereas the weakest bonds separate two identical slices. The slice has to be stoichiometric and the growth of the crystal has to be possible by the addition of subsequent, identical slices.

The crystalline lattice or bulk energy H_{bulk} can then be divided into a slice energy, which is the energy to form an isolated crystal slice, and the attachment energy, which is the energy of attaching the slice to the crystal (eq. 1.5). The latter is then assumed to determine the growth rate. The exact rules of how to construct the periodic bond chains and the slices are quite complicated and are explained in detail in e.g. [Mye05]. In addition there is generally a separate treatment for the long range coulombic interactions. However the underlying assumptions, i.e. that the characteristic property, governing the relative growth rate, is the attachment energy, and that this property can be determined based on the bulk structure of the crystal, do not change.

$$H_{bulk} = H_{slice} + H_{attach} \tag{1.5}$$

Both the BFDH theory and the PBC theory have been successfully used for the prediction of the morphology namely for molecular crystals (see e.g. [Str01, DCRB91]). For ionic, inorganic crystals the theory has been less successful. There are several reasons for this:

- **Neglected rate determining mechanisms:** In both the BFDH and the PBC theory, the

attachment of a growth unit to the surface is considered to be the only property influencing the relative growth rate. However other processes, such as the diffusion of ions towards the surface and/or surface diffusion can influence the relative growth rates as well (see e.g. [vdV90]). Additionally an underlying assumption is that only flat surfaces are present in the growth morphology since they grow by a slow layer-nucleation mechanism. However the presence of e.g. screw dislocations can change the growth mechanism. The concentration of screw dislocations perpendicular to the surface is likely to depend on the surface orientation and can thus influence the relative growth rates. Finally, if solutes other than the crystal components are present in the solution, these can strongly adsorb to surfaces, steps and kink sites. The desorption of those adsorbed molecules, especially from growth features such as steps and kink sites, can then become the rate determining step [Roh03] (figure 1.7). In some cases these strongly adsorbed molecules can also be solvent molecules [vdV90].

- **Growth unit:** Contrary to molecular crystals, the growth unit of ionic crystals is often poorly defined or unknown. The growth of the crystal might either happen by subsequent incorporation of the different ions or by the incorporation of previously formed ionic complexes from the solution. The concentration of ionic species close to the surface are likely dependent on specific adsorption terms and on the exact structure of the electrical double layer (see section 1.4). The concentration of the different ionic species close to the surface can influence which attachment energy is determining the growth rate. Considering for example calcium hydroxide, if the concentration of hydroxyls is higher close to the surface, the attachment energy determining the relative growth rate is likely to be the one of the calcium ion rather then the attachment energy of a hydroxyl ion. Additionally, depending on the chemical composition, the supersaturation can be different for the different ions, which again can change the rate determining step.

- **Surface relaxation:** The above described theories extrapolate the properties of the surface from the properties of the bulk crystal. However it has been shown that, especially for inorganic ionic crystals, the positions of the atoms at the surface relax to minimize the surface energy [MDBD87, dLP99, dLP98b, Sto81] (see figure 1.7). This will influence the relative surface energies and hence the equilibrium morphology. The kinetics and the growth speed of the surfaces will also be influenced by the surface relaxation. Due to the difference between the bulk and the surface properties, the definitions of slice and attachment energy (equation 1.5) become ill defined at the surface. This means that, although some effort has been done to include at least surface restructuration or roughening [GMB$^+$98, DCRB91], surface relaxation is difficult to account for with the BFDH and the PBC theory.

- **Solvent - surface interactions:** The molecules of the solvent will interact with the surfaces of the crystal. For ionic crystals, the strength of the interactions with the solvent molecules has been shown to depend on the surface orientation [DCRB91, dLP99, dLP98b, vdV90] (see figure 1.7). Again this will influence both the relative surface energies and the relative growth rates, even if the rate determining step does not necessarily

change. This effect can be included in the BFDH or the PBC theory but can not be predicted by it. To reliably estimate the interaction of solvents with the different surfaces, atomistic simulations are needed, preferably simulations including dynamic effects [DLP98a, DHAB12], although for ionic crystals, static calculations can give good results as well [dLP99, dLP98b]. Interactions of the surface with other species present in the solution can have a similar effect.

- **Point defect segregation:** Crystals often contain defects. These defects can, amongst other factors, be controlled by the composition of the solution. For example an other solute molecule can be incorporated into the crystal as a substitutional or interstitial defect (e.g. incorporation of aluminium ions into C-S-H [Ric04]) or intrinsic defects can form, e.g. when the supersaturation with respect to one crystal component A is much higher than with respect to the an other component B and hence A/B ratio increasing defects are created (e.g. Ca/Si ratio increasing defects in C-S-H [Ric08, AJS04]). The energy of such defects is often lower at the surfaces and consequently they segregate to the surfaces [BHJP02, MT89] (see figure 1.7). This will influence both the surface energies and the growth rates.

Due to these limitations of the PBC theory, surface energy calculations with classical atomistic methods, taking into account surface relaxation [MDBD87, dLP99, dLP98b, DHAB12], solvant-surface [DLP98a, dLP99, dLP98b, DHAB12] and solute-surface [dLPSN00, AJR$^+$08] interactions as well as the segregation of point defects to surfaces [BHJP02, CRP04] have often been more reliable than the PBC (or the BFDH) theory for predicting the morphology of ionic crystals produced from solution and to understand the important influences on the morphology. Often these calculations are restricted to the enthalpic portion of the surface energy, which is generally considered to be more important than the surface entropy at room temperature in the case of ionic crystals [TSB$^+$99, Jur54].

1.4 Distribution and Adsorption of Solutes at Inorganic-Water Interfaces

The distribution of the ions is influenced by the presence of a surface. Different factors are at the root of this influence. One of the factors can be a charge developing at the surface. The origin of this surface charge can for example be a surface reaction i.e. a deprotonation or protonation of the surface. Another influence can be the specific interaction and adsorption of ions at the surface. As the adsorbtion / interaction energies can differ for the differently charged ions, a net charge can develop. The charge developed at and close to the surface is then compensated in the so called diffuse layer. The two surface regions, the adsorption and the diffuse layer, where the distribution of the ions differs form the bulk solution, are often referred to as the electrical double layer. The characteristics of the double layer can influence both the crystal growth and the collidal stability of the particles.

1.4.1 Surface Charge

The surface charge is often thought to develop as a result of an acid-base reaction of surface groups of the form of equation 1.6 or 1.7. However other types of reactions, such as the selective desorption of a negative or a positive ion from the surface may occur as well (eq. 1.8 and 1.9, where dangling "−" indicate a bond to the solid).

$$-B + \left[H^+\right]_{aq} \rightarrow -BH^+ \tag{1.6}$$

$$-A - OH \rightarrow -A - O^- + \left[H^+\right]_{aq} \tag{1.7}$$

$$-AB \rightarrow -A^+ + [B^-]_{aq} \tag{1.8}$$

$$-BA \rightarrow -B^- + \left[A^+\right]_{aq} \tag{1.9}$$

Let us consider a generic reaction (equation 1.10). We can define a reaction constant K_S which defines the relative concentrations of the reactants and the products, similar to standard bulk reactions (equation 1.11). The activity coefficient $a_X(s)$ is the activity of species X at the surface and not in the bulk solution. The surface activity however will depend on the properties of the specific adsorption region and the diffuse layer which in turn depend on the surface charge. This interdependency can be solved analytically only if one neglects any specific adsorption and ion-ion correlation effects, which means that the system can be accurately described by an average linear charge density $\rho(x)$, where x is the distance from the surface [HW78]. For such a system, the potential at the surface can be described as a function of the surface charge ($\sigma_S = \frac{c^{gc}(-S^{\pm})^{gc}}{\rho_S}$, where ρ_S is the surface area per $-SX$ group, c is the concentration of charged sites and gc is used to indicate the Gouy-Chapman theory) according to the Gouy-Chapman theory (eq. 1.12 and 1.13 [HW78], where n_b is the bulk concentration of the solution and z^i the valence of the ions, ϵ is the dielectric constant and q_e is the charge of an electron).

$$-SX \rightarrow -S^{\pm} + \left[X^{\mp}\right]_{aq} \tag{1.10}$$

$$K_S = \frac{c(-S^{\pm}) \cdot a_{X^{\mp}}(s)}{c(-SX)} \tag{1.11}$$

$$\frac{c^{gc}(S^{\pm})}{\rho_S} = \sigma_S^{gc} = \sqrt{4\epsilon k_b T n_b} \cdot \sinh\left(\frac{z^i q_e \psi_0}{2k_b T}\right) \overset{Debye-Hückel}{\approx} \sqrt{\frac{2\epsilon q_e^2 \sum_i n_b^i z^i 2}{k_b T}} \psi_0 \tag{1.12}$$

$$a_{X^{\mp}}^{gc}(s) = e^{\pm \frac{q_e \psi_0}{k_b T}} \tag{1.13}$$

The issue is further complicated by the fact that the discrete charges created at the surface interact with each other. In fact locally, close to a ionized site $-S^{\pm}$, the surface potential ψ_s can be much higher than ψ_0, which is the electrostatic potential at the surface according to the Gouy-Chapman theory. In theory this makes the equilibrium constant K_S dependent on the concentration of charges at the surface $c(-S^{\pm})$. The strenght of the interactions between the charges will depend on the spacial distribution of the ionizable surface groups $-SX$ at the surface and on the ionic strength $I_c^s = \sum_i n_s^i$ of the solution at the surface which again depends on the surface charge. For low surface charges Levine and Smith [LS71] developed a correction term for the formalism described above to take into account the discrete nature of the surface charges. The surface potential ψ_s is corrected by adding a so called micropotential $\phi_s(\sigma_S)$ to the Gouy-Chapman surface potential ψ_0 (eq. 1.14). This will lead to a corrected reaction constant K_a^{lev} that contains a surface charge dependent term [HW78] (eq. 1.15). For high surface charge concentrations the full complexity of the interdependencies is difficult to tackle analytically. Here Metropolis Monte Carlo calculations [LJP+06] or other simulation techniques [JA12] can be useful.

$$\psi_s^{lev}(\sigma_S^{lev}) = \psi_0^{gc}(\sigma_S^{lev}) + \phi_s(\sigma_S^{lev}) \tag{1.14}$$

$$K_s^{lev} = K_s e^{\mp \frac{q_e \phi_s(\sigma_S^{lev})}{k_b T}} \tag{1.15}$$

Experimentally the surface charge is usually measured by a surface titration [LJP+06, Son96]. A surface titration experiment allows the determination of the total amount of hydroxyl and/or protons that interact with the particle surfaces. This is done by controlling the total amount of the hydroxyl ions in the system and comparing it to the measured pH in the bulk solution. The

same can be done for other ionic species if their activity in the bulk solution can be measured. Generally the total amount of ions interacting with the surface is assumed to have participated in a surface reaction and the amount is directly converted into a surface charge, neglecting an eventual change of concentration in the electrical double layer, which might contribute to changes of the bulk activity. Finally by observing the change of the surface charge with e.g. varying pH, the reaction constant K_S^{gc} or K_s^{lev} can be calculated, depending on the model assumptions.

1.4.2 Specific Adsorption / Compact Layer

It has been known for a long time that close to the surface, non-continuum effects have a large impact. An obvious way to see this was that, for high surface charges, a continuum description according to Gouy-Chapman (see next section) would lead to an unphysically high ion density in the solution in immediate proximity of the surface. For high surface potentials, the ion density according to Gouy-Chapman can exceed an atomic monolayer. The basic concepts to better describe this region close to the surface has been developed by Stern [Ste24] and later slightly adapted by Grahame [Gra47]. The theory takes into account the fact that both the ions in solution and at the surface are surrounded by solvent molecules, forming the solvation shell (see figure 1.8). This can be described by a effective diameter of the solvated ions d^i_{solv}. The solvated ions can not move closer than $x^{H_{out}} = 0.5 \cdot d^i_{solv}$ to the surface. That distance is the definition of the outer Helmholtz plane, named after Helmholtz who did some of the first work on electrical interfaces [Hel79]. To move closer to the surface the ion has to loose its solvation shell, which will result in a certain change of the chemical free energy ΔF^i_{ads}. For convenience we define a pseudo-potential $\phi^i_H = \frac{\Delta F^i_{ads}}{\epsilon \cdot z^i}$, where z^i is the valence of the ion. These adsorbed ions will then be situated at the distance of half the diameter of the unsolvated ion d^i. This distance $x^{H_{in}} = 0.5 \cdot d^i$ from the surface is the definition of the inner Helmholtz plane (see figure 1.8). The region up to the outer Helmholtz plane is named the compact or Stern layer. For distances larger than the outer Helmholtz plane, the so called diffuse layer, the solution is assumed to behave approximately like a continuum.

The work $w_i^{H_{in}}$ done by bringing an ion i from the bulk solution at x_∞ to the inner Helmholtz plane is then defined by equation 1.16, where $\psi^{H_{in}}$ is the electrostatic potential at the inner Helmholtz plane. The distinction between the electrostatic and chemical work implied is not always clear. For instance the dielectric constant of the solvent can change close to the surface, due to the alignment of the dipoles of the solvent molecules with the electrostatic field. The number of ions adsorbed per surface area n_s^i depends not only on the work $w_i^{H_{in}}$ but also on the number of ions per volume in the bulk solution n_b^i and the maximum possible surface $n^i_{s,max}$ and volume $n^i_{b,max}$ concentrations at the surface and in the bulk solution respectively. $\frac{n_s^i}{n_b^i}$ can then be described by the ratio of the number of free sites at the surface and in the bulk phase times the Boltzmann factor (eq. 1.17). If the number of free sites is much higher than the number of occupied sites, the expression can be further simplified. The charge at the inner

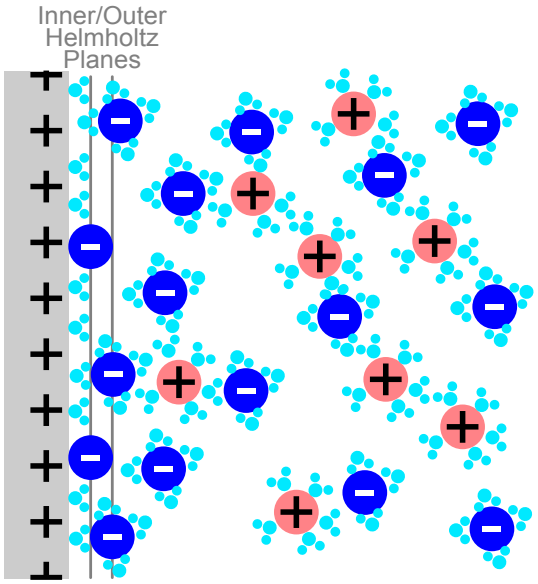

Figure 1.8: Schematic illustration of the double layer. The distance of the inner Helmholtz plane from the surface is equal to the minimum approach distance of the unhydrated ions. for the outer Helmholtz plane the distance is equal to the minimum approach distance of the hydrated ion. Water molecules that are not directly interacting with either the surface or the ions are not shown.

Helmholtz layer can then be approximated by $\sigma_H = \sum_i z^i \cdot n_s^i$.

$$w_i^{H_{in}} = z^i q_e \cdot \left(\psi^{H_{in}} + \phi_H^i\right) \tag{1.16}$$

$$\frac{n_s^i}{n_b^i} = \frac{(n_s^i - n_s^{i,max})}{(n_b^i - n_b^{i,max})} \cdot e^{-\frac{w_i^{H_{in}}}{k_b T}} \overset{n^i \ll n^{i,max}}{\approx} \frac{n_s^{i,max}}{n_b^{i,max}} \cdot e^{-\frac{w_i^{H_{in}}}{k_b T}} \tag{1.17}$$

Between the surface and the inner Helmholtz plane as well as between the inner Helmholtz plane and the outer Helmholtz plane, the charge density is zero and accordingly the electrostatic potential in these two regions is linear with a slope of $-\frac{\sigma_s}{\epsilon_s}$ and $-\frac{\sigma_s+\sigma_H}{\epsilon_s}$ respectively (see figure 1.9).

The theory for the compact layer is not entirely rigorous. The main problem lies within the definition of $n^{i,max}$, as in theory these quantities would also depend on the concentration of all other species j in the system. This is not taken into account by equation 1.17. In practice the assumption is often that only one species (the counter ion with respect to the surface charge) adsorbs at the surface. This makes the definition of $n_s^{i,max}$ better defined. For $n_b^{i,max}$

one can assume that the available space can be occupied by the ions according to the bulk ratio in the solid, but the definition remains somewhat sketchy. However the Stern theory has been able to explain the upper limit of the double layer capacity and, to some extent, specific adsorption, at least qualitatively.

The model for the Stern layer has been developed mostly phenomenologically, with a general idea that the surface and the ions are covered by a solvation shell the size of one solvent molecule. Consequently the position of the inner Helmholtz layer has generally been considered to be around 2 Å and the outer around 3 Å. However in recent years, atomistic simulations have shown that the interface seems to be more complicated, with multiple solvent layers [AGM$^+$09, KP04, KK02, KCSP05, SCKP06, RSS$^+$13]. The solvent structure close to the surface will, to a large extent, determine the behavior of the ions close to the surface [SCKP06, KCSP05, KK02, KP04, KCMP05, ZKR10, RSS$^+$13]. Again instead of one well defined adsorption plane, the inner Helmholtz plane, there seem to be several modulations of the different ionic densities. This restructuring of the solution close to the surface seems to be influenced only to some extent by the surface charge [KCMP05]. Also the extent of the region where important non-continuums effects persist is 10-15 Å, much larger than the typical size of a hydrated ion (3 Å). These general trends of the different atomistic simulations have recently been substantiated by experimental evidence from atomic force microscopy [RSS$^+$13].

The properties of the compact region will have an impact on the surface charge. The influence comes mainly from the concentration of the reactive species a_i close to the surface, which will influence the surface charge (eq. 1.11). The surface charge in turn influences the exact distribution of the ions in the compact layer.

1.4.3 Diffuse Layer

The last part of the model for the electrical double layer is the diffuse layer furthest from the surface. In the diffuse layer any charge built up at the surface and in the compact layer is compensated.

The underlying model for the classical treatment of the diffuse electrical double layer is the ideal polarized electrode, i.e. an electrode which behaves like an electrical capacitor without leakage. In other words charges may approach or recede from the interface but cannot cross it. In the conventional electrical double layer theory this is expressed by putting the outer Helmholtz layer at the minimum approach distance of the solvated ions. This means that the ions can approach the outer Helmholtz plane but can not cross it. Gouy [Gou10] and Chapman [Cha13] derived an expression to describe the diffuse double layer, based on the ideal polarized electrode. The Gouy-Chapman theory is derived from three different equations [Gra47]:

- The 1D Poisson equation, describing the variation of the electrical potential as a function of the volumetric charge density $\rho_q(x)$, for a semi-infinite system, where the electrical

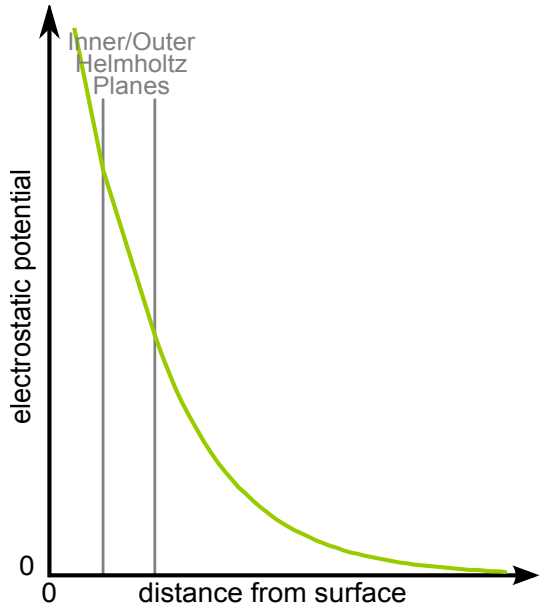

Figure 1.9: Schematic illustration of the surface potential of the double layer. The charge density in the surface region up to the inner Helmholtz plane (minimum approach distance of the unhydrated ions) is zero and consequently the electrostatic potential is linear with a slope of $-\frac{\sigma_s}{\epsilon_s}$. At the inner Helmholtz plane ions can adsorb with an additional chemical adsorption potential ϕ_H^i leading to a Helmholtz plane charge σ_H. Up to the outer Helmholtz plane the charge density is again zero and the potential linear with a slope of $-\frac{\sigma_s+\sigma_H}{\epsilon_s}$. For distances larger than the outer Helmholtz plane, the solvated ions can move freely and the potential is described by the Gouy-Chapman model.

potential $\psi(x)$ and $\rho_q(x)$ vary in x direction only:

$$\frac{d^2\psi}{dx^2} = -\frac{\rho_q(x)}{\epsilon} \tag{1.18}$$

- The Boltzmann equation describing the variation of the ionic density with the work required to move the ion from the bulk solution:

$$n^i(x) = n_b^i e^{-\frac{w_i(x)}{k_b T}} \tag{1.19}$$

- An expression for the work needed to bring an ion of type i from the interior of the solution to the point in question:

$$w_i(x) = z_i q_e \psi(x) \tag{1.20}$$

There are several assumptions contained in these three equations. In fact in order to arrive at the third of the above equations, one has to suppose that the ions are point charges, interacting only with the overall electrostatic potential. This means that the following contributions have

been neglected:

- The work involved in displacing the solvent molecules from the point in question to the bulk.
- The explicit ion-ion interactions within the double layer, both electrostatically (ion-ion correlation effects) and through short range forces (e.g. excluded volume effects, complex formation).
- Changes in the solvation shell of the ion with changing electrostatic field.
- Specific interactions of the ions with the species in the compact layer.
- Changes of the dielectric constant ϵ of the solvent is constant over the domain of the diffuse layer, due to the alignment of the solvent dipoles with the electrical field. Such changes would lead to a different strength of ion-ion interactions at the surface compared to the bulk solution.

The first, third and fifth assumption, involving the solvent molecules, are likely to become more important with higher surface charges and the ensuing higher field strengths close to the surface.The second and forth assumption are likely to become more important with higher ionic concentrations, either in the bulk solution or close to the surface due to a high surface charge and the ensuing high surface potential. All in all therefore Gouy-Chapman can only be expected to be valid for diluted solutions and low surface charges.

The charge density ρ_q can be expressed in terms of the density of the individual ions $n^i(x)$ and their valence z^i (eq. 1.21). Thus equations 1.18 to 1.20 can be combined to the final second order differential equation for the electrostatic potential (equation 1.22).

$$\rho_q = \sum_i n^i(x) z_i q_e = \sum_i n_b^i z_i q_e e^{-\frac{z_i q_e \Psi}{k_b T}} \tag{1.21}$$

$$\frac{d^2\psi}{dx^2} = \frac{d\psi}{dx}\frac{d}{d\psi}\left(\frac{d\psi}{dx}\right) = \frac{1}{2}\frac{d}{d\psi}\left(\frac{d\psi}{dx}\right)^2 = -\frac{1}{\epsilon}\sum_i n_b^i z_i q_e e^{-\frac{z_i q_e \psi}{k_b T}} \tag{1.22}$$

By integrating over ψ one can get a first order differential equation (equation 1.23). The integration constant can be determined by taking into consideration that the electrostatic potential in the bulk solution is constant: $\lim_{x\to\infty}\frac{d\psi}{dx} = 0$. Finally for the total charge per surface area in the double layer up to x ($\sigma_{tot}(x_q > x) = \int_x^\infty \rho_q(x_q)dx_q$), we can develop an expression by combining equation 1.23 and 1.18 (eq. 1.24). At the outer Helmholtz plane we can calculate the total excess charge of the diffuse layer per surface area $\sigma_{tot}(x_q > x^{H_{out}})$.

Since overall the system is neutral, $\sigma_{tot}(x_q > x^{H_{out}})$ corresponds to the sum of the surface charge and the charge at the inner Helmholtz plane $\sigma_{tot}(x_q > x^{H_{out}}) = \sigma_s + \sigma_H$.

$$\left(\frac{d\psi}{dx}\right)^2 = \frac{2k_bT}{\epsilon}\sum_i n_b^i \cdot \left(e^{-\frac{z^i q_e \psi}{k_b T}} - 1\right) \tag{1.23}$$

$$\sigma_{tot}(x_q > x) = \pm\sqrt{2\epsilon k_b T \sum_i n_b^i \left(e^{-\frac{z^i q_e \psi}{k_b T}} - 1\right)} \tag{1.24}$$

Let us now look at a simplified system with only two types of atoms with opposite valences $z^1 = -z^2 = z$. For such a system the bulk concentrations of both ions have to be the same $n_b^1 = n_b^2 = n_b$, due to charge neutrality. The expression for the total charge can thus be simplified to equation 1.25. With the help of this simplification, equation 1.24 can be further integrated and a final expression for the electrostatic potential can be given (eq. 1.26 [Gra47]), where x_∞ comes from the integration constant and is the position of a theoretical plane (i.e. outside of the diffuse layer domain) with an inifinite potential.

$$\begin{aligned}
\sigma_{tot}(x_q > x) &= \pm\sqrt{2\epsilon k_b T n_b \left(e^{\frac{zq_e\psi}{k_bT}} + e^{-\frac{zq_e\psi}{k_bT}} - 2\right)} \\
&= \pm\sqrt{2\epsilon k_b T n_b}\left(e^{\frac{zq_e\psi}{2k_bT}} + e^{-\frac{zq_e\psi}{2k_bT}}\right) \\
&= \pm\sqrt{4\epsilon k_b T n_b}\sinh\left(\frac{zq_e\psi}{2k_bT}\right)
\end{aligned} \tag{1.25}$$

$$\psi(x) = \pm\frac{4k_bT}{zq_e}\tanh^{-1} e^{-\sqrt{\frac{2z^2q_e^2n}{\epsilon k_bT}}(x-x_\infty)} \tag{1.26}$$

An expression for a general electrolyte can be derived under the Debye - Hückel approximation. This approximation is valid for low field strengths $z^i q_e\psi \ll k_bT$ where e^{-a} in equation 1.22 can be approximated by a (eq. 1.27). κ defined in equation 1.27 is called the inverse Debye length, κ^{-1} being the characteristic length of the diffuse layer. The general solution for the simplified differential equation is shown in equations 1.28 and 1.29. $\psi^{H_{out}}$ can be determined via the overall neutrality condition i.e. $-\sigma^{dl} = \sigma_s + \sigma_H$ (equation 1.30).

$$\frac{d^2\psi}{dx^2} \overset{Debye-Hückel}{\approx} \frac{q_e^2\psi}{\epsilon k_bT}\sum_i n_b^i z^{i2} \doteq \kappa^2\psi \tag{1.27}$$

$$\psi^{DH} = A \cdot e^{-\kappa x} + B \cdot e^{\kappa x} \tag{1.28}$$

$$\psi^{dl,DH} = \psi^{H_{out}} e^{-\kappa(x - x^{H_{out}})} \tag{1.29}$$

$$\sigma_{dl}^{DH} = -\epsilon \left(\frac{d\psi^{dl,DH}}{dx} \right)_{x=x^{H_{out}}} = \epsilon \kappa \psi^{H_{out}} = \sigma_s + \sigma_H \tag{1.30}$$

Under ambient conditions, the Debye-Hückel approximation has been shown to be very good if the outer Helmholtz potential $\psi^{H_{out}}$ does not exceed ~ 25 mV and still OK for potentials up to 75-100 mV [HHF66, VO99].

The effect of the different neglected contributions to the work of approaching an ion from the bulk solution to the surface (equation 1.20) has been investigated by many authors (see e.g. [OBL80, TV80, LOB81, TV82, FJWW97, QPMMHA04, JA12]). In general the Gouy-Chapman theory is found to be valid only for low surface charge, low ionc strengths and a low valence of the ions. Of the different factors, the ion-ion correlation is often found to be one of the most important factors, more important than the excluded volume effect [TV82].

The Gouy-Chapman theory described here is only strictly valid for infinite planar surfaces. However the theory can serve as a reasonable approximation for any surface for which the radius of curvature R^S is much larger that the double layer ($R^S \gg \kappa^{-1}$). That the results for infinite planes can not be valid for small radii of curvature can be demonstrated by a simple argument. Let us imagine a simplified system of a spherical particle with a radius of $R^S = \chi \cdot \kappa^{-1}$. Let us also simplify the diffuse layer as a region with a uniform charge density of $\rho_q = \frac{\sigma_S + \sigma_H}{\kappa^{-1}}$ within a region from $R^S + x^{H_{out}}$ to $R^S + x^{H_{out}} + \kappa^{-1}$. One can easily see that, for an infinite plate such a system would be globally charge neutral. For a sphere, the surface charge is overcompensated due to the higher surface area of the spherical shells in the double layer compared to the surface of the particle. The ratio of the surface charge that is overcompensated σ^{over} can be calculated by equation 1.31. The function does not explicitly depend on the surface charge but only on the ratio of the surface charge that is compensated at the inner Helmholtz plane $\left(\frac{\sigma_H}{\sigma_S}\right)$. Additionally, if we suppose the compact layer to be much smaller than the particle radius and the diffuse layer, the ratio of the overcompensated charge becomes independent of the value for κ^{-1}, $x^{H_{in}}$ and $x^{H_{out}}$. If we plot the function (see figure 1.10) we can see that the solution for the infinite plane can not be assumed to be valid if the radius of

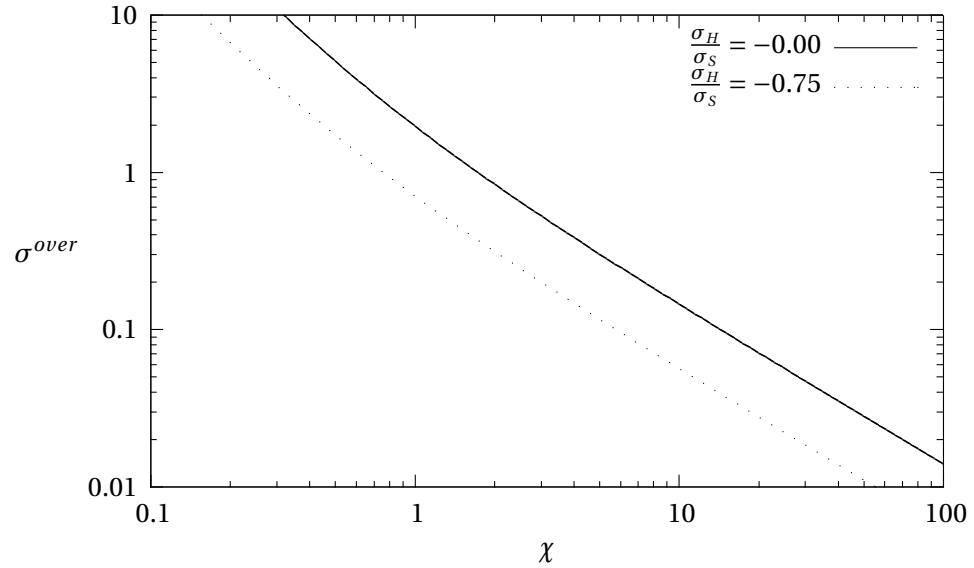

Figure 1.10: Overcompensation of the surface charge in the double layer as a function of the ratio χ between the curvature radius of the surface R^S and the Debye length κ^{-1} for different values of $\frac{\sigma_H}{\sigma_S}$. Typical values of for $x^{H_{in}} = 2$ Å, $x^{H_{out}} = 3$ Åand $\kappa^{-1} = 15$ Å have been chosen for the plot, however the shape of the curve is almost independent of these exact values (eq. 1.31).

curvature is smaller that at least ten times the Debye length ($\chi > 10$).

$$\begin{aligned}\sigma^{over} &= -\left(1+\frac{\sigma_H}{\sigma_S}\left(1+\frac{x^{H_{in}}}{\chi\cdot\kappa^{-1}}\right)^2 - \frac{1+\frac{\sigma_H}{\sigma_S}}{3\chi^2\kappa^{-3}}\left[\left((\chi+1)\cdot\kappa^{-1}+x^{H_{out}}\right)^3 - \left(\chi\cdot\kappa^{-1}+x^{H_{out}}\right)^3\right]\right) \\ &\overset{x^H \ll \kappa^{-1}}{\approx} -\left(1+\frac{\sigma_H}{\sigma_S} - \left(1+\frac{\sigma_H}{\sigma_S}\right)\frac{(\chi+1)^3-\chi^3}{3\cdot\chi^2}\right)\end{aligned} \tag{1.31}$$

Consequently some work to investigate the diffuse layer for non-planar geometries, especially for spheres, can be found in literature. No analytical solution can be found for the electrical double layer of a spherical particle. However a number of authors used numerical integration [LOWK61, OHW82, LGARH07] or Monte Carlo techniques [GGGTCP09] to get an idea of the diffuse layer around a spherical particle. Disk shaped particles have been investigated as well [CS96].

Experimentally, to determine the properties of the double layer, zeta potential measurements are most widely used. Zeta potential measurements consist of measuring the velocity v_p of particles in a constant electric field $\vec{E}$. The ratio between the particle velocity and the electric field is called the electrophoretic mobility $\mu_e = \frac{v_p}{\vec{E}}$. The electrophoretic mobility will depend on the potential of the accelerated particle with respect to the bulk fluid. The accelerated particle consist not only the solid particle itself but also includes part of the electric double layer. The distance from the particle surface up to which the double layer is moving with the

particle is called zeta or shear plane. The exact location of the zeta plane is not known. In literature, different assumptions for the zeta plane position can be found. Values range from at the surface (no solvent is moving with the particle) to 6 Å above the surface.

Another not altogether known factor is how the measured electrophoretic mobility can be converted to a zeta potential measured at the zeta plane. A very simple expression has been developed by Smoluchowski [Smo03] (see figure 1.32, where η is the dynamic viscosity of the solvent). However this formula is only valid for hard spheres with $\chi > 50$ [WLO66]. Other, more complicated, expressions have been developed by e.g. Henry [AHRS31] or by Wiersema et al. [WLO66]. These more complicated expressions take into account different factors, such as the exact shape of the particle and/or the rearrangement of the double layer up to the shear plane due to the movement of the particle (relaxation effect).

$$\zeta = \frac{\mu_e \eta}{\epsilon} \tag{1.32}$$

Some more exact experimental methods, capable of probing the double layer with more detail have been developed in recent years as well [PMB10, RSS+13].

1.4.4 Influence of the Ionic Distribution on Colloidal Stability

According to the Derjaguin-Landau-Verwey-Overbeek (DLVO) theory, the interaction $V^{h,k}$ between two particles h and k is in general described as the sum of two types of interactions: dispersive, for identical particles always attractive, London - van der Waals interactions V^{disp} and generally repulsive electrostatic interactions V^{el} coming from the interaction of the electric double layers (eq. 1.33). There can also be other contributions, such as steric interactions V^{steric} coming from adsorbed polymers at the surface, which will not allow the particles to move closer than a certain distance, or magnetic interactions V^{mag}.

$$V^{p,p} = V^{disp} + V^{el} + \left[V^{steric} + V^{mag} + ... \right] \tag{1.33}$$

The most widely used expression for the dispersion forces has been developed by Hamaker [Ham37]. Between two atoms i and j the London - van der Waals interactions $V_{at}^{i,j,dip}$, coming from the interaction of weak, induced dipoles, can be described with the atom dependent London - van der Waals constant $\lambda_{at}^{i,j,vdW}$: $V_{at}^{i,j,disp} = \frac{\lambda_{at}^{i,j,vdW}}{r^{i,j^6}}$. In order to go from the discrete atom-atom to an average particle-particle interaction we introduce the volumetric atom density ρ_{at}^{k} in material k and replace the atom-atom van der Waals constant by a material dependent one $\lambda^{h,k,vdW}$. This means that we can calculate the total interaction of two particles in vacuum by integrating the interactions over the particle volumes (eq. 1.34). In the case

of two spherical particles with radius R^k the integration can be solved analytically (eq. 1.34, where r_0^k is the position of the center of the particle). One can see that the final equation can be divided into a material dependent term $A^{h,k}$, generally called the Hamaker constant, and a geometry dependent term E^{geom}, depending on the shape of the two particles only.

$$\begin{aligned} V_{vac}^{disp} &= -\int_{V_h}\int_{V_k} \frac{\rho_{at}^h \rho_{at}^k \lambda^{h,k,vdW}}{\left(\vec{r}^h - \vec{r}^k\right)^6} d\vec{r}^h d\vec{r}^k \\ &= -\frac{\pi^2 \rho_{at}^h \rho_{at}^k}{6} \cdot \left[\frac{2R^h R^k}{\left(\vec{r}_0^h - \vec{r}_0^k\right)^2 - \left(R^h + R^k\right)^2} + \frac{2R^h R^k}{\left(\vec{r}_0^h - \vec{r}_0^k\right)|^2 - \left(R^h - R^k\right)^2} + \ln \frac{\left(\vec{r}_0^h - \vec{r}_0^k\right)^2 - \left(R^h + R^k\right)^2}{\left(\vec{r}_0^h - \vec{r}_0^k\right)^2 - \left(R^h - R^k\right)^2} \right] \\ &= -A^{h.k} \cdot E^{geom} \end{aligned} \tag{1.34}$$

If we are interested in the interaction of two particles in a solvent, we have to consider the solvent-solvent and solvent-particle interactions as well. In fact if the particles are infinitely far apart, compared to the particles at finite distances, each particle will interact with an additional volume of solvent with the same geometry as the other particle. On the other hand if the particles are brought close together, there is an additional solvent - solvent volume interaction, again of the same geometry as the particles. This means that in the solvent the dispersive interparticle interaction energy is described by equation 1.35 where the index l indicates the solvent. There is a distance dependent effect, the so called retardation effect, coming from a slight time delay in dipole-dipole coupling at large distances, that is not taken into account by the Hamaker formula described here. Corrections for the retardation effect have been developed by different authors (see [ABMMB11] and references therein).

$$V_{solv}^{disp} = -\left(A^{h,k} + A^{l,l} - A^{h,l} - A^{k,l}\right) E^{geom} \tag{1.35}$$

The attractive London-van der Waals interactions are counterbalanced by the generally repulsive electrostatic interactions. An expression for the electrostatic interaction of particles was developed by Hogg et al. [HHF66]. The starting point of the derivation is the interaction between the diffuse layers of two parallel infinite plates according to the Debye - Hückel approximation. In fact, in the case of two parallel plates, the general Debye - Hückel solution (eq. 1.29) becomes equation 1.36, where $\Delta x^{H_{out}} = x_k^{H_{out}} - x_h^{H_{out}}$.

$$\psi = \psi_h^{H_{out}} \cosh\kappa\left(x - x_h^{H_{out}}\right) + \frac{\psi_h^{H_{out}} - \psi_k^{H_{out}} \cosh\kappa \cdot \Delta x^{H_{out}}}{\sinh\kappa \cdot \Delta x^{H_{out}}} \sinh\kappa\left(x - x_h^{H_{out}}\right) \tag{1.36}$$

Verwey and Overbeek [VO99] have shown that the total energy of a planar diffuse electric layer can be expressed by equation 1.37. We can use this property to calculate the interaction of two double layers by comparing their energy at finite and infinite separation distances (eq. 1.38).

$$G = -\frac{\epsilon}{2}\left[\frac{d\psi}{dx}\right]_{x=x^{H_{out}}} \psi^{H_{out}} = -\frac{\epsilon}{2}\dot{\psi}^{H_{out}}\psi^{H_{out}} \tag{1.37}$$

$$\begin{aligned} V_{plate}^{el}\left(\Delta x^{H_{out}}\right) &= -\frac{\epsilon}{2}(\dot{\psi}_h^{H_{out}}\psi_h^{H_{out}} + \dot{\psi}_k^{H_{out}}\psi_k^{H_{out}}) + \lim_{\Delta x^{H_{out}}\to\infty}\left[\frac{\epsilon}{2}(\dot{\psi}_h^{H_{out}}\psi_h^{H_{out}} + \dot{\psi}_k^{H_{out}}\psi_k^{H_{out}})\right] \\ &= \frac{\epsilon\kappa}{2}\left[\left({\psi_h^{H_{out}}}^2 + {\psi_k^{H_{out}}}^2\right)\left(1-\coth\left(\kappa\Delta x^{H_{out}}\right)\right) + 2\psi_h^{H_{out}}\psi_k^{H_{out}}\operatorname{cosech}\left(\kappa\Delta x^{H_{out}}\right)\right] \end{aligned} \tag{1.38}$$

Derjaguin [Der54] developed a method to use the expression for infinite plates as an approximate solution for spherical particles. In order to be able to use the solution for plates, Derjaguin approximated the sphere by a series of parallel rings (eq. 1.39). This method underestimates the surface of the sphere. In fact if one integrates over the parallel rings, to get an approximation of half the surface of the sphere one gets $2\cdot\int_0^R 2\pi h dh = 2\cdot\pi h^2|_0^R = 2\cdot\pi R^2$, this means that the surface of the sphere is underestimated by a factor of two. In other words Derjaguins approximation is only accurate, if the main contribution to the particle - particle interaction comes from a limited region of small h. For that region the Derjaguin approximation is more accurate. According to Hogg et al., the Derjaguin approximation is valid for $\chi > 10$. Since for smaller χ the approximation of the parallel plates is anyway expected to be inaccurate (see previous section), the DLVO theory is expected to be invalid for values of $\chi < 10$.

$$\begin{aligned} V_{sph}^{el}\left(\left|\vec{r}_0^{\,h} - \vec{r}_0^{\,k}\right|\right) &= \int_0^{\min(R^h,R^k)} 2\pi h V_{plate}^{el}\left(\left|\vec{r}_0^{\,h} - \vec{r}_0^{\,k}\right| - \sqrt{R^{h2}-h^2} - \sqrt{R^{k2}-h^2}\right) dh \\ &= \frac{2\pi\epsilon R^h R^k\left({\psi_h^{H_{out}}}^2 + {\psi_k^{H_{out}}}^2\right)}{\left(R^h+R^k\right)}\left[\frac{2\psi_h^{H_{out}}\psi_k^{H_{out}}}{{\psi_h^{H_{out}}}^2 + {\psi_k^{H_{out}}}^2}\ln\left(\frac{1+e^{-\kappa\left(\left|\vec{r}_0^{\,h}-\vec{r}_0^{\,k}\right|-R^h-R^k\right)}}{1-e^{-\kappa\left(\left|\vec{r}_0^{\,h}-\vec{r}_0^{\,k}\right|-R^h-R^k\right)}}\right) + \ldots\right. \\ &\quad \left. \ldots + \ln\left(1-e^{-2\kappa\left(\left|\vec{r}_0^{\,h}-\vec{r}_0^{\,k}\right|-R^h-R^k\right)}\right)\right] \end{aligned} \tag{1.39}$$

For particles where the DLVO theory is supposed to be valid, it can be used to estimate the colloidal stability. The determining quantity is the maximum of the interaction $V_{max}^{h,k}$ with respect to the particle distance. This energy maximum has to be passed in order for particles

to agglomerate, in other words $V_{max}^{h.k}$ is the activation energy for agglomeration. This means that the agglomeration rate v^{agg} can be expressed as the product of the collision rate f_{coll}, which depends on the average particle velocity and interparticle distance, and the exponential of the activation energy divided by $k_b T$ (eq. 1.40) [ABMMB11]. If the energy maximum is zero, the agglomeration rate is equal to the collision rate.

$$v^{agg} = f_{coll} \cdot e^{\frac{V_{max}^{h.k}}{k_b T}} \tag{1.40}$$

1.5 Goals and Organisation of the Thesis

The aim of this thesis is to identify areas where classical atomistic simulation can be used to further our knowledge of cementitious systems. Different classical atomistic simulation methods are then applied to those areas and the results discussed. The focus is on the two main hydration products, portlandite and calcium-silicate-hydrate. The questions of interest are quite different for the two different products. For portlandite the open question is how the different dissolution products of cement influence the growth and final morphology of portlandite, which in turn can affect the kinetics of C-S-H formation and eventually the hardening of cement. For calcium-silicate-hydrate the exact atomic structure is still not fully known, and is a key feature to better undertsand the C-S-H nanostructure, its solution thermodynamics and its mechanical properties. For the study of both hydrates, using classical atomistic scale methods such as molecular dynamics, a force field capable of dealing reliably with calcium, silicate, hydroxide and water structures has to be chosen and validated.

This thesis has been written with a disparate audience in mind (modelers, cement chemist, powder technologist). The methodology used is described in some detail. There are different reasons for this:

- A goal of this thesis was to establish how and in which areas classical atomistic simulations can be used to further the understanding of cementitious systems. Consequently the necessary theoretical background for the appropriate choice of method and to understand the subsequent discussion of the limitations of the methods was included for the interested reader.
- Part of the methodology, such as the long range description of electrostatic forces used for coarse grained Monte Carlo calculations or the force field error estimation, are new and have been developed in house, therefore they form an integral part of the thesis.

Consequently, depending on the reader, parts of the thesis will be of lesser interest. The experienced modeler might treat the first part of chapter 2 in a cursory fashion and be more interested in the second part as well as in chapter 3, where some novel approaches are described. For the reader interested in the choice of methods and approaches useful for

cementitious systems on the other hand, the entirety of chapter 2 and 3 might be of interest. And finally for the reader interested in the results on cementitious systems only, the chapters on the computational methods and force fields used (chps. 2 and 3) can to some degree be treated as annexes and be read in an overview fashion.

The thesis is structured as follows:

- **Chp 1. Introduction:** This chapter introduces the topic of the thesis, putting it into context and summarizes the main theoretical notions concerning interfaces in cementitious systems, the growth of solids from solution and the electrical double layer around solids

- **Chp 2. Computational Method:** This chapter summarizes the computational methods used for the rest of the work (energy minimization, molecular dynamics, metadynamics, Monte Carlo) as well as their advantages and limitations. The way in which long range eletrostatic forces are treated in the Monte Carlo calculation of the electrical double layer, represents a further development of the method originally employed by Torrie and Valleau [TV80] and is hence treated in some detail.

- **Chp 3. Force Fields:** In this chapter the choice and enhancement of the force field used for the rest of the work is described. Additionally a methodology is developed, allowing the estimation of the errors on the physical parameters resulting form simulations using the force field (such as distances, surface energies, enthalpy of hydration, ...).

- **Chp 4. State of the Art Portlandite:** This chapter summarizes what is known about portlandite and the influences on its growth and morphology both from pure systems and from portland cement systems.

- **Chp 5. Experiments on Model Portlandite Systems:** In this chapter the results of some experimental work on model portlandite systems are summarized. To directly link the "clean" atomistic simulations to the complicated pore solution found in portland cement is very difficult without an intermediate step. Here the key species in the pore solution were identified and their effect on portlandite precipitation investigated without the competing complexity of anhydrous phase dissolution and concurrent C-S-H precipitation and growth. The influence of silicates, sulfates and aluminates on the growth and morphology of portlandite was looked at. The influence of each species was first studied separately before possible synergies were considered. Contrary to current opinion, the morphology of portlandite in the pure water system was found to be equiaxed and not hexagonal platelets. If silicates are added to the system, portlandite seemed to precipitate as irregularly shaped agglomerates and not individual particles. If sulfates are added, the morphology of the portlandite particles changed to hexagonal platelets. Gypsum precipitation was retarded in these systems and the possibility of a metastable calcium-sulfate phase that served as nuclei for the portlandite particles

is discussed. The addition of aluminates lead to portlandite particles with similar morphology but increased particle size.

- **Chp 6. Speciation of Model and Cementitious Systems:** The speciation in solution for the different model portlandite precipitation experiments is important for two reasons: changes in the calcium - hydroxyl speciation can in itself change the growth morphology if e.g. the incorporation of the Ca^{2+} ion is the rate determining step for one and the OH^- incorporation for another facet. Additionally it is important which silicate, sulfate and aluminate species are present in the solution and therefore likely to interact with the growing portlandite particles. Consequently changes in the speciation of the solutions for the different model systems as well as for typical cementitious systems were looked at in this chapter. This was done by thermodynamic modeling using the geochemical thermodynamic package GEMS v2 [KW09, WKHD12, KWD$^+$12] with the CEMDATA database [KK01, LW06]. Silicates were shown to have little effect on the calcium-hydroxide speciation and the predominant silicate species was found to be the $CaSiO_2(OH)_2$ complex, the existence of which has been confirmed by classical atomistic metadynamics calculations. Sulfates seem to reduce the Ca^{2+} and increase the OH^- concentration by the formation of a $CaSO_4$ complex. The predominant sulfate species is the SO_4^{2-} ion. Aluminates do not form any complex with the calcium ions and the predominant species seems to be the $Al(OH)_4^-$ ion. The conditions in the coprecipitation experiments most closely resemble those at the beginning of the hydration of ordinary portland cement (w/c 0.5) although the concentration of silicates, sulfates and aluminates are all lower in the coprecipitation experiments. As the hydration in the OPC system progresses, the concentration of the calcium, sulfates and aluminates decreases whereas the pH and the concentration of silicates increases.

- **Chp 7. Portlandite Surfaces:** Different influences on surface energies and the equilibrium morphology of portlandite are studied in this chapter: surface relaxation, solvent-surface interactions and solute-surface interactions were looked at. According to atomistic simulations, portlandite-water interactions seem to stabilize high energy interfaces both energetically and kinetically. A stable network of strongly bound surface water forms at most of the higher energy surfaces. At the [00.1] surface neither the adsorption of Ca^{2+} or OH^- at the inner Helmholtz plane is energetically favorable. However while Ca^{2+} adsorbs at the outer Helmholtz plane and further approaching the surface is clearly energetically unfavorable, the OH^- ion can move relatively freely between the inner and the outer Helmholtz plane. This lead to the assumption that it is the adsorption of the Ca^{2+} ion that might be the rate determining step for portlandite growth in [00.1] direction. Indications have been found that for other surfaces, namely the [10.1] surface, the situation might be inverse. Consequently changes in the relative concentrations of Ca^{2+} and OH^- might already influence the morphology of portlandite. Finally the $CaSiO_2(OH)_2$ complex was found to interact more strongly with the portlandite surfaces than the $SiO_2(OH)_2$ ion. The silicate species seem to adsorb to the flat portlandite surfaces by retaining a certain mobility. At the [00.1] surface the $CaSiO_2(OH)_2$ adsorp-

tion appears to be energetically favorable, in contrast to the adsorption of both OH^- and Ca^{2+}. At edge like sites the silicate species seem to loose their mobility. Consequently a theory was put forward, according to which the silicate species might poison the growth of portlandite by adsorbing preferentially to the surfaces, diffusing along them until being immobilized at a step or other growth feature.

- **Chp 8. Electrical Double Layer at Portlandite Surfaces:** In this chapter the equilibrium distribution of ions (i.e. the electrical double layer) at portlandite surfaces was studied with Monte Carlo techniques. Results from the previous chapter were used as input. First results for a concentrated $Ca(OH)_2$ system are compared to results for molecular dynamics simulations to verify the accuracy of the Monte Carlo calculations in describing the molecular dynamics system. The Monte Carlo calculations were found to reproduce the important features of the molecular dynamics system, although the accuracy could be improved by including a more accurate description of the short range Ca^{2+} - OH^- interactions. The results for a less concentrated system, corresponding to a pure portlandite water system at equilibrium, are then presented. The calculated zeta potential (6.9-8.9 mV) is in good agreement with experimental measurements (7.35 ± 3.96 mV [PRM$^+$06]). Although the charge density of the diffuse layer can be fitted to the classical Gouy-Chapman theory, the details of the electrical "double layer" differ. The implications of the results for cementitious systems and colloidal systems in general is then discussed.

- **Chp 9. Summary of Portlandite Work:** This chapter summarizes the work done on portlandite and discusses the implication of the results for the growth and morphology of portlandite. The still open questions are considered as well as the possible ways to elucidate them further in future work, both experimentally and with further theoretical calculations.

- **Chp 10. State of the Art Calcium-Silicate-Hydrate:** In this chapter the current knowledge of the atomistic structure of C-S-H is summarized and the different atomistic and mictrostructural models for C-S-H reported in literature are discussed. Additionally previous atomistic simulations done for C-S-H are reviewed. The full atomistic model structures based on atomistic simulations are discussed and their weak points, where further work is necessary, elucidated.

- **Chp 11. Atomistic Structure of Calcium-Silicate-Hydrate:** In this chapter atomistic simulation work on possible C-S-H structures is summarized. Different possible, isolated defects, ranging in calcium to silicon ratio from 0.83 to 2.5, in 14 Å tobermorite were studied and their energies compared. The resulting precipitation enthalpies agreed well with data from the CEMDATA thermodynamic database for C-S-H with calcium to silicon ratios above 0.83 [LMMG08], indicating that 14 Å tobermorite might be a good C-S-H model structure, even for high calcium to silicon ratios. The structural properties of the simulated defect structures also agreed well with experiment, however more work on structures with higher defect concentrations would be needed to confirm

these results. The 14 Å tobermorite / water interfacial energy was estimated for two different surface orientations. For both surfaces a slightly negative interfacial energy was found, although a zero or even a small positive surface energy would also be within the expected error interval. A slightly negative surface energy might explain why the crystallite size of C-S-H particles does not grow even after prolonged aging.

- **Chp 12. Summary of Calcium-Silicate-Hydrate Work:** In this chapter the work on calcium-silicate-hydrates is summarized, the implications of the results as well as the still open questions are elucidated and possible ways for further work discussed.
- **Chp 13. Final Conclusions:** In this chapter the entirety of work done to explore the possibilities of classical atomistic simulation techniques for the study of cementitious systems is summarized. The implications of the results for the knowledge and engineering of cementitious systems is discussed as well as possible future areas, where classical atomistic simulations can be used for the study of cementitious systems.

2 Computational Methods

In this chapter the computational methods employed (i.e. energy minimisation, molecular dynamics and Monte Carlo calculations) are described and their strengths and limitations are discussed. All methods used for the presented work are based on a classical description of interatomic forces and energies via empirically determined analytical functions. This way of describing atomic structures will be further elucidated and the consequences of such a description discussed. This will be followed by a brief discussion of the spatial boundaries in atomistic simulations and a description of all the individual methods used.

2.1 Classical Description of the Energy of Atomic Structures

In the classical atomistic description of matter, the atoms or ions in the system are described as positions in space. The forces and interactions between the atoms are then described by a set of analytical functions depending on the relative positions of the atoms in the system.

Typically the interaction between ionic species is described by pairwise interactions V^{pair} composed of long range coulombic interactions V^{coul} and short range van der Waals type interactions $V^{vdWaals}$ (see equation 2.1). The form of the coulombic interactions is well defined and depends only on the respective charge q of the ions i and j and the distance between them $r_{i,j}$. For the van der Waals interactions on the other hand there exist several functional forms that are typically used, with the set of parameters $c^n_{i,j}$ being determined empirically.

$$V^{pair}_{i,j} = V^{coul}_{i,j} + V^{vdWaals}_{i,j} = \frac{q_i \cdot q_j}{4\pi\epsilon \cdot r_{i,j}} + 4c^1_{i,j}\left[\left(\frac{c^2_{i,j}}{r_{i,j}}\right)^{12} - 2\left(\frac{c^2_{i,j}}{r_{i,j}}\right)^{6}\right] \tag{2.1}$$

In addition to ionic interactions there may also be covalent bond interactions in a system.

Bonded interactions are often described by a bond distance dependent term $V_{i,j}^{bond}$ and/or by an angle dependent term $V_{i,j,k}^{ang}$ between two covalent bonds. The first involves only two atoms where the second is a three body potential. Again there are several functional forms to describe the bonded interactions. Another possibility to deal with covalent bond interactions is to keep some distances and angles fixed throughout the simulation.

Independent of the functional form, there are several empirical parameters that have to be fitted to either experimental data (such as atomistic structures and thermodynamic properties) or to the results of ab initio methods, such as density functional theory (DFT). The fitting is very time consuming. Fortunately a lot of the work to fit these parameters for different functional forms has already been done and can be found in literature [AV05, LC85, FHC+07, KPH03, PCPJ92, CLK04]. A collection of consistently fitted parameters and functions is called a force field (FF) or a potential set. However there is no universally valid force field and therefore the force field employed has to be carefully chosen, its validity for the system of interest assessed and the force field adapted if necessary. Consequently the choice, enhancement and validation of the force field employed for the present calculations will be described in detail in the chapter 3.

2.2 Spatial Boundaries of Atomic Structures in Simulations

Depending on the type of force field (pair potentials, three body forces ...) as well as the implementation of the code, the scaling of the computational cost with the number of atoms in the system is quite unfavourable. If we consider a system which can be described with pair-wise interactions only, we would have to calculate $\frac{1}{2}N^2$ interactions, where N is the number of atoms. Thus we would expect the computational cost to scale as $O(N^2)$ with the number of atoms. Since in general the pair interactions are much stronger at small distances than at large distances, often only pairs within a certain cutoff distance r_c are considered explicitly. The interactions of pairs outside the cutoff distance are either approximated by separate methods or neglected altogether. Thus the scaling of the computational cost with the number of atoms can be brought down to $O(N \cdot log(N))$. This means that the size of the systems we are able to look at is limited to generally in the order of tens of thousands of atoms, although calculations of up to a million of atoms have been reported in literature [SCGT07]. Of course the maximum size of the system will also depend on the force field and the calculation method employed as well as the resources available. However in reality the system of interest usually contain much more atoms and hence only a portion of the system can be modeled. For example portlandite contains about 90 atoms per nm^3 which means that even a crystal in the μm range contains about 9e10 atoms. This means that we have to find a way to describe how the portion of the system we consider explicitly interacts with the rest of the system, i.e. we have to impose boundary conditions. There are many different types of boundary conditions but only four different types were employed in the context of this thesis.

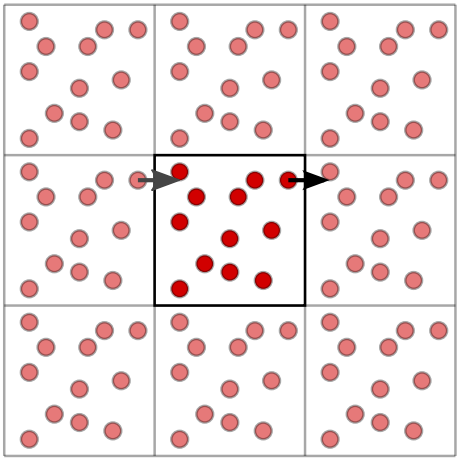

Figure 2.1: Schematic illustration of periodic boundary conditions.

2.2.1 Periodic Boundary and Ewald Sum

The most frequently employed type of boundary in atomistic simulations is periodic boundaries. This type of boundary is very useful for the simulation of bulk structures. If we simulate a representative part of the bulk structure, the surrounding structure should be similar to the simulated part. This property is exploited with periodic boundaries by supposing that the simulated structure interacts with images of itself. In other words the right boundary of the simulation box encompassing the simulated part is equivalent to the left boundary of an image of this box. Thus an atom exiting the simulation box at the right boundary can be considered to re-enter it at the left boundary (see figure 2.1). This is equivalent of replicating the simulated atoms on a infinite periodic lattice (or wrapping space into a 4 dimensional torus). Consequently an atom would theoretically not only interact with the other atoms in the simulation box but with an infinite number of periodic images $\vec{n}_{im}$. The distance of an image from the original cell box is $\vec{n}_{im} \cdot \overline{C}$, where $\overline{C}$ is the matrix of the cell vectors of the simulation box and $\vec{n}_{im}$ is an integer vector indicating how many cell vectors away the image is. The energy of such a system would be impossible to calculate as one would have to sum over an infinite number of interactions. However, as mentioned previously, a cutoff radius r_c is often employed to reduce the calculation cost. Only interactions of pairs closer than the cutoff radius are calculated explicilty. Interactions of pairs outside the cutoff are either neglected altogether or approximated with a different method. In the case of periodic boundaries the Ewald summation [Ewa21] is often used to approximate interactions outside the cutoff radius.

If we look at the typical pair potential function (equation 2.1) the van der Waals interactions are short range (depending typically on $r_{i,j}^{-6}$ plus a term describing the short range repulsion) and thus the error introduced by the cutoff radius is generally small. The range of the Coulombic interactions ($\propto r_{i,j}^{-1}$) is larger and hence the error introduced by the cutoff is dominated by the Coulombic part of the pair potential. Ewald summation therefore deals with the coulombic part of the pair potentials only. The idea behind Ewald summation consists of subtracting a

Gaussian charge distribution ($q_i \cdot G_\sigma = \frac{q_i}{(2\pi\sigma^2)^{\frac{3}{2}}} exp^{-\frac{r^2}{2\sigma 2}}$ where σ determines the width of the Gaussian) from the short range coulombic term of each pair (equation 2.2).

$$\begin{aligned} V_{tot}^{coul} &= -\frac{1}{4\pi\epsilon} \sum_{\vec{n}_{im}} \sum_{\substack{i,j \\ i\neq j}} \frac{q_i \cdot q_j}{\cdot|\vec{r}_{i,j} + \vec{n}_{im}\overline{C}|} \\ &= -\frac{1}{4\pi\epsilon} \left(\sum_{\vec{n}_{im}} \sum_{\substack{i,j \\ i\neq j}} q_j \cdot \left(\frac{q_i}{|\vec{r}_{i,j} + \vec{n}_{im}\overline{C}|)} - q_i \int \frac{G_\sigma(\vec{r} - \vec{r}_j)}{\cdot|\vec{r}_i - \vec{r} + \vec{n}_{im}\overline{C}|} dr^3 \right) + \sum_{\vec{n}_{im}} \sum_{\substack{i,j \\ i\neq j}} q_j \cdot q_i \int \frac{G_\sigma(\vec{r} - \vec{r}_j)}{\cdot|\vec{r}_i - \vec{r} + \vec{n}_{im}\overline{C}|} dr^3 \right) \\ &= -\frac{1}{4\pi\epsilon} \left(\sum_{\vec{n}_{im}} \sum_{\substack{i,j \\ i\neq j}} \frac{q_i \cdot q_j}{|\vec{r}_{i,j} + \vec{n}_{im}\overline{C}|} \left(1 - erf \frac{|\vec{r}_{i,j} + \vec{n}_{im}\overline{C}|}{\sqrt{2}\sigma} \right) + \sum_{\vec{n}_{im}} \sum_{\substack{i,j \\ i\neq j}} \frac{q_i \cdot q_j}{|\vec{r}_{i,j} + \vec{n}_{im}\overline{C}|} erf \frac{|\vec{r}_{i,j} + \vec{n}_{im}\overline{C}|}{\sqrt{2}\sigma} \right) \\ &= V_S^{coul} + V_L^{coul} \end{aligned} \tag{2.2}$$

This will result in a $(1 - erf(r/(\sqrt{2}\sigma)))$ correction factor, which will attenuate the short range potential V_S^{coul} at long distances and thus reduces the cutoff error (see equation 2.3).

$$\begin{aligned} V_S^{coul} &\doteq -\frac{1}{4\pi\epsilon} \sum_{\vec{n}_{im}, i, j; i\neq j} \frac{q_i \cdot q_j}{|\vec{r}_{i,j} + \vec{n}_{im}\overline{C}|} \left(1 - erf \frac{|\vec{r}_{i,j} + \vec{n}_{im}\overline{C}|}{\sqrt{2}\sigma} \right) \\ &\approx -\frac{1}{4\pi\epsilon} \sum_{\vec{n}_{im}, i, j; i\neq j; |\vec{r}_{i,j} + \vec{n}_{im}\overline{C}| < r_c} \frac{q_i \cdot q_j}{|\vec{r}_{i,j} + \vec{n}_{im}\overline{C}|} \left(1 - erf \frac{|\vec{r}_{i,j} + \vec{n}_{im}\overline{C}|}{\sqrt{2}\sigma} \right) \end{aligned} \tag{2.3}$$

However we now have to add the Gaussian charge distribution again or the total error will not really have changed (see equation 2.2). The sum over these long range interactions V_L^{coul} is then done in the reciprocal space. Since we have a periodic structure the summation over a limited range of $\vec{k}$ values should be sufficient to get a good approximation of the long range term of the coulombic interactions (see equation 2.4).

$$\begin{aligned} V_L^{coul} &\doteq -\frac{1}{4\pi\epsilon} \sum_{\vec{n}_{im}, i, j; i\neq j} \frac{q_i \cdot q_j}{|\vec{r}_{i,j} + \vec{n}_{im}\overline{C}|} erf \frac{|\vec{r}_{i,j} + \vec{n}_{im}\overline{C}|}{\sqrt{2}\sigma} \\ &= \frac{1}{2V_{cell}\epsilon} \sum_{\vec{k}, i, j, k\neq 0} \frac{q_i q_j}{k^2} e^{i\vec{k}(\vec{r}_i - \vec{r}_j)} e^{\sigma^2 k^2/2} - \frac{1}{2\left(\sqrt{2\pi}\right)^3 \epsilon\sigma} \sum_i q_i^2 \end{aligned} \tag{2.4}$$

Boundaries other than periodic grain boundaries also exist. However for molecular dynamics calculations only periodic boundaries were employed.

2.2.2 Other Types of Spatial Boundaries

For some of the Monte Carlo calculations a much simpler hard wall boundary was employed. This type of boundary adds a infinite or very high energy if an atom goes outside a certain region (i.e. the simulation cell). This means that the system is essentially interacting with a hard wall and the only interaction with the surrounding structure is via a spacial restriction, hence the namie of this type of boundary. Hard wall boundaries usually only makes sense for coarse grained systems, where the details of the interactions with the environment can be simplified. For molecular dynamics or energy minimisation this type of boundary would introduce significant errors.

The third type of spacial boundary conditions was only used for energy minimisation. It consists of simply neglecting any interactions of the simulated part with the rest of the system. These so called vacuum boundary conditions only make sense for ionic or covalent crystals with a large lattice energy, where the strong interactions ensure cohesion of the structure and evaporation is expected to be a very slow process. For energy minimisation this boundary can be employed for a much larger range of systems since only a local energy minimum is searched for and no entropic effects or time evolution is considered i.e. evaporation does not pose a problem. Additionally this type of boundary is generally only applied to crystal - vapor surfaces where the vapor - surface interactions are expected to be minimal and can therefore be neglected.

For the last type of boundary employed, the simulated structure is in contact with a region where the atomic positions are fixed. This type of boundary is sometimes referred to as extended wall boundary conditions. It is generally used to calculate the relaxation of a defective structure which is in contact with an intact region, where the properties of the latter are well known. An example is a surface, where surface relaxation is expected, which is in contact with a bulk region, with atomic positions corresponding to that of a perfect infinite crystal. Again the use of this type of boundary for molecular dynamics poses problems, as the movement of the atoms close to the boundary is very restricted. For energy minimisation on the other hand this type of boundary can in general be used without reservation.

2.3 Energy Minimisation

Energy minimisation calculations consist of finding a minimum in the energy landscape with respect to the atomic positions. In other words the aim of energy minimistion is to find the position the system would relax to at 0 ° K. These calculations are very fast compared to other methods such as molecular dynamics, but the temperature and the dynamics of the system are not taken into account. Consequently the method can only be used as a starting point for the characterization of systems such as water, where the structure is strongly dependent on the temperature. To fully characterize these systems, other methods such as molecular dynamics or Monte Carlo are needed. For other systems, such as ionic crystals, where the temperature has only a minimal effect on structural properties, energy minimisation can be

used directly to calculate bulk as well as interfacial properties.

The code used here was METADISE [WKdL+96] which was developed by the computational solid state chemistry group of Prof. S.C. Parker at the University of Bath. The techniques employed by METADISE to find an energy minimum are mostly based on the Newton-Raphson method [Ypm95]. The Newton-Raphson method locally approximates the energy landscape by the gradient vector ($\vec{g}(\vec{r})$) and the second derivative or Hessian matrix ($\overline{H}(\vec{r})$). The atomic positions ($\vec{r}$) are then adjusted towards the minimum of the local approximation of the surface (see equation 2.5, where α is a factor between 0 and 1 and k denotes the minimization step). At the new position, the energy landscape is again locally approximated and the position of the atoms adjusted and thus a minimum of the true energy landscape is approached iteratively. The iterative process is terminated when the gradient vector is below a certain threshold value or the maximum number of iterations has been reached.

$$\vec{r}_{k+1} = \vec{r}_k - \alpha \cdot \overline{H}(\vec{r}_k)^{-1} \cdot \vec{g}(\vec{r}_k) \tag{2.5}$$

While in the optimal case, the Newton-Raphson method converges quadratically to a minimum, the method does not always converge. Additionally the calculation and the inversion of the Hessian matrix at each step is very time consuming. Therefore other minimisation methods that are more stable and do not demand the calculation of the Hessian matrix at each step (such as Broyden-Fletcher-Goldfarb-Shanno (BFGS) [HZ85] or conjugate gradient [HS52]) are often used initially for a certain number of iterations followed by a certain number of the faster convergent newton-raphson algorithm.

It should be mentioned that the minimum found by energy minimisation is a local rather than a global minimum. This can be an advantage, as metastable structures can be studied, and a disadvantage, as the result depends greatly on the initial configuration of the atoms. To be able to find the most stable structure, the number of initial configurations to be tested can be quite high. Especially to look for low energy permutations of e.g. defects, the number of permutations to test can quickly exceed what is computationally feasible. However for some systems the number of permutations are still feasible with energy minimisation while other methods such as molecular dynamics would be too computationally intensive. As an example, let us imagine we want to construct a C-S-H model from 14 Å tobermorite by removing 4 bridging Si tetrahedra and replace 2 further bridging tetrahedra by a Ca atom in a 14 Å supercell containing a total of 8 Si trimers (or "dreierketten"). This would lead to a final compound with a Ca/Si ratio of 1.6. Since the defects are likely to interact, the exact configuration of the defects will influence the energy and the properties of the final structure. The total number of possible permutations would be $\binom{4}{8} \cdot \binom{2}{4} = 420$. To calculate the energy of each possible defect configuration with molecular dynamics would require a relatively large amount of CPU time (e.g. if we suppose that one calculation takes three hours on 2 processors i.e. 6 hours of CPU time we would need a total of 2'520 hours or 105 days of CPU time). To estimate the

energy of each configuration with energy minimisation on the other hand can be easily done without having to have access to large CPU resources (if we suppose a calculation would take 10 minutes on one processor we would have to use 70 hours or 3 days of CPU time).

2.3.1 Bulk Calculations

To calculate the properties of bulk crystals with energy minimisation, periodic boundary conditions in all three dimensions were used. The simulation cell was typically equal to the crystalline unit cell. In addition to the atomic positions, both the dimensions and the angles of the simulation cell were relaxed. A short range cutoff of r_c^{em} = 15 Å was used for all energy minimisation calculations. The long range interactions $r_{i,j} > 15$ Å were neglected.

2.3.2 Surface Calculations

A surface disrupts the periodicity of the crystal in the direction of the surface normal. Therefore, while periodic boundaries are applied in the two dimensions parallel to the surface, a different setup is chosen in the direction of the surface normal. To be able to do so, the simulation cell has first to be reoriented in such a way that two cell vectors are parallel to the surface (see figure 2.2). The thus constructed surface cell is then repeated a certain number of times perpendicular to the surface to construct a super cell. This super cell is then divided into a region (reg_{free}) adjacent to the surface where the atom positions are relaxed during the energy minimisation and second region (reg_{fixed}) further away from the surface where atom positions are held fixed at the previously determined bulk positions (see figure 2.2). The free region (reg_{free}) has to be larger than the pair potential cutoff r_c^{em} perpendicular to the surface. In practice the size of reg_{free} is chosen to be greater than $1.3 \cdot r_c^{em}$. The size of the second region. where atom positions are held fixed (reg_{fixed}), is chosen about five times larger than the size of the free region. In other words perpendicular to the surface the simulation cell has a vacuum boundary (no constraints) on one side and an extended wall boundary (region of fixed atomix positions) on the other.

The surface or cleavage enthalpy γ_{sv} can be calculated as the total energy of the free region (V_{free}) minus the interaction energy between the two different regions ($V_{free-fixed}$) minus the energy of a bulk containing the same number N of atoms as reg_{free} ($V_{bulk,N}$) divided by the surface area of the slab (A_{slab}) (see equation 2.6).

$$\gamma_{sv} = \frac{\delta V}{\delta A} = \frac{\Delta V_{slab}}{A_{slab}} = \frac{V_{free} - V_{free-fixed} - V_{bulk,N}}{A_{slab}} \tag{2.6}$$

Several slabs per surface were considered. The different slabs were produced by a cutting the crystal unit cell at different depths, exposing different atomic planes. Only cuts leading to unpolar surfaces were considered. The surface enthalpy of each of these slabs is then

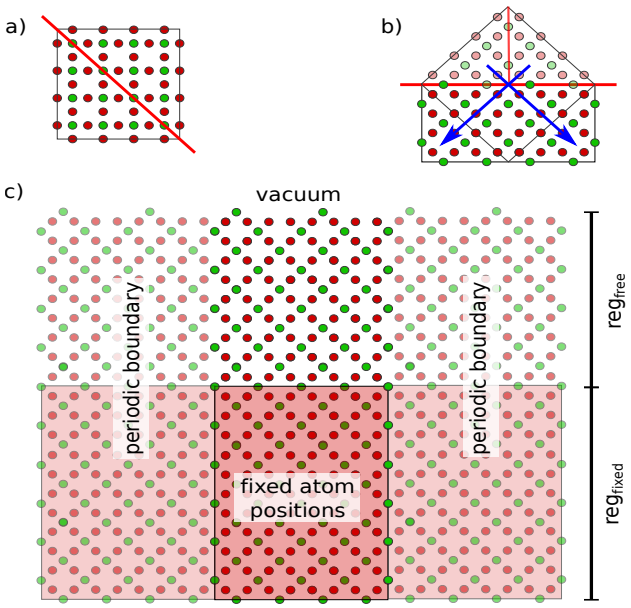

Figure 2.2: Schematic illustration of the surface cell construction: a) initial unit cell with cut plane indicated in red. b) rotation of unit cell and reconstruction of surface cell with two cell vectors parallel and one cell vector perpendicular to the surface cell. c) final surface slab with central simulation cell (reg_{free}) which is in contact with vacuum (vacuum boundary condition) on one side and a region (reg_{fixed}) with fixed atom position (extended wall boundary condition) on the other side. Parallel to the surface periodic boundary conditions are applied.

calculated with energy minmisation. The surface slab with the lowest energy is likely to be the physically relevant surface structure and the corresponding surface enthalpy was retained.

2.4 Molecular Dynamics

Molecular dynamics consists of simulating the evolution in time of a system by using Newtons law of motion [New14] (equation 2.7). A great number of available molecular dynamics codes exist. Two different ones were used for the current work, mostly DL_POLY 2.20 [SF96] was used but for a few of the calculations (notably for changing temperature conditions during the simulation) LAMMPS was used [Pli95]. The forces $\vec{F}_i$ acting on atom i of mass m_i can be calculated as the gradiant of the interatomic potential $V_i = \sum_j V_{i,j}^{pair} + \sum_j V_{i,j}^{bond} + \sum_{j,k} V_{i,j,k}^{ang}$ of the atom (see section 2.1).

$$\frac{d^2\vec{r_i}}{dt^2} = \vec{a_i} = \frac{1}{m_i} \cdot \vec{F_i} = \frac{1}{m_i} \cdot \frac{\partial V_i}{\partial \vec{r_i}} \tag{2.7}$$

The time integration to get the evolution of the atomic positions r_i with time has to be done numerically. Several different methods for the numerical integration exist [AT90]. The one

generally used for this thesis is called leap frog algoritm. The leap frog algorithm is based on a second order Taylor expansion of both the positions (equation 2.8) and the velocities $\frac{d\vec{r_i}}{dt} = \vec{v_i}$ (equation 2.9).

$$\vec{r_i}(t'+dt) = \vec{r_i}(t') + \vec{v_i}(t') \cdot dt + \frac{1}{2}\vec{a_i}(t') \cdot dt^2 + O(dt^3) \tag{2.8}$$

$$\vec{v_i}(t+dt) = \vec{v_i}(t) + \vec{a_i}(t) \cdot dt + \frac{1}{2} \cdot \frac{d\vec{a_i}(t)}{dt} \cdot dt^2 + O(dt^3) \tag{2.9}$$

If we subtract the value for $dt = -\frac{1}{2} \cdot \Delta t$ from the value for $dt = +\frac{1}{2} \cdot \Delta t$ for both the positions and the velocities and set $t' = t + \frac{1}{2} \cdot \Delta t$ we finally get the algorithm used for the leap frog integration (equations 2.10 and 2.11).

$$\vec{r_i}(t+\Delta t) = \vec{r_i}(t) + \vec{v_i}(t+\frac{1}{2}\Delta t) \cdot \Delta t + O(\Delta t^3) \tag{2.10}$$

$$\vec{v_i}(t+\frac{1}{2}\Delta t) = \vec{v_i}(t-\frac{1}{2}\Delta t) + \vec{a_i}(t) \cdot \Delta t + O(\Delta t^3) \tag{2.11}$$

The thus developed leap frog algorithm is third order accurate, time reversible and simple. The positions are calculated for time t whereas the velocities are calculated for $t + \frac{1}{2} \cdot \Delta t$ (hence the name of the algorithm). Consequently, to know the velocities at the same time as the positions, they have to be interpolated between different timesteps.

The timestep Δt has to be chosen small enough to correctly sample the movement of the atoms. A reasonable assumption for a good sampling of the movement of the atoms is to consider that an atom with mass m_i, with an average velocity according to the thermal excitation $< v_i > \approx \sqrt{\frac{3k_bT}{m_i}}$ should not move further than $\frac{1}{50}$ of an typical interatomic distance d_{ia} within a timestep [AB08] (see equation 2.12). This means that generally the lightest atom of the system with the fastest movement determines the maximum timestep possible. For cementitious systems the lightest atom is typically the hydrogen with a mass of 1 u and a typical interatomic distance is the oxygen-hydrogen distance of 1 Å and thus at a simulation temperature of 300 ° K a good timestep would be in the order of 0.7 fs. These are indeed the conditions chosen for the simulations, unless otherwise specified. The cutoff chosen was 8.5 Å with Ewald summation

for the long range coulombic part.

$$\Delta t^{est} = \frac{\frac{1}{50} \cdot d_{ia}}{< v_i >} \tag{2.12}$$

Since the Newton equation, on which molecular dynamics is based, is energy conserving and the boundary conditions will keep the number of atoms and the volume constant, the molecular dynamics algorithm described above will perform a simulation in the microcanonical ensemble (NVE ensemble). Additional methods are required for other themodynamic ensembles, such as a thermostat for the canonical ensemble (constant number of particles, volume and temperature, NVT) or a barostat and thermostat for the grand-canonical ensemble (constant number of particles, pressure and temperature, NPT).

2.4.1 Thermostat

In order to keep the temperature of the simulation constant, the velocities of the atoms have to be controlled. There are several methods to do so [AT90], however the one employed in this work is the Nosé-Hoover thermostat [Hoo85] implemented in DL_Poly. In the Nosé-Hoover thermostat the temperatures are controlled by a time dependent friction coefficient χ (see equation 2.13).

$$\frac{d\vec{v_i}(t)}{dt} = \vec{a_i}(t) - \chi(t)\vec{v_i}(t) \tag{2.13}$$

The variation of the friction coefficient is dependent on the diffference of the target (i.e external) temperature T_{ext} and the instantaneous temperature $\mathscr{T}$ at time t (equation 2.14, where τ_T is a specified time constant). In other words, the more the system diverges from the target temperature, the faster the friction coefficient will increase to push the system back to the target value. τ_T will determine how fast the system will be pushed back to the target temperature, in the current work τ_T was chosen to be 0.5 ps if nothing else is specified.

$$\frac{d\chi(t)}{dt} = \frac{1}{T_{ext}\tau_T^2}(\mathscr{T}(t) - T_{ext}) \tag{2.14}$$

The details of the implementation in DL_POLY are not given here. They can be found in the DL_POLY manual [Smi12]. If nothing else is specified simulations reported here were done for an external temperature $T_{ext} = 300°$ C

2.4.2 Barostat

To keep both the temperature and the pressure constant during the simulation, not only the velocities have to be controlled but also the dimensions or the volume of the simulation cell V and consequently the position of the atoms. Again there are several methods to do so [AT90] but the one used for this work is the Melchionna modification of the Hoover algorithm [MCLH93] implemented in DL_POLY. Compared to the Nosé-Hoover thermostat, in addition to the time dependent friction coefficient for the temperature $\chi(t)$ we now also have a time dependent friction coefficient for the pressure $\eta(t)$ which is acting on the positions, the velocities and the volume of the simulation cell (equation 2.15-2.17, where $\vec{r}_0$ is the center of mass of the system).

$$\frac{d\vec{r}_i(t)}{dt} = \vec{v}_i + \eta(t) \cdot (\vec{r}_i(t) - \vec{r}_0(t)) \tag{2.15}$$

$$\frac{dV(t)}{dt} = (3 \cdot \eta(t)) \cdot V(t) \tag{2.16}$$

$$\frac{d\vec{v}_i}{dt} = \vec{a}_i - \big(\chi(t) + \eta(t)\big) \cdot \vec{v}_i(t) \tag{2.17}$$

The variations of the two friction coeficients χ and η now depend on the difference between the target temperature T_{ext} and the instantaneous temperature $\mathscr{T}(t)$ and on the difference between the target pressure P_{ext} and the instantaneous pressure $\mathscr{P}(t)$ respectively. In addition, since temperature and pressure can not be varied independently, the variations of the two friction coefficients are coupled (see equations 2.18 and 2.19 where N_f is the number of degrees of freedom of the system). The two specified time constants τ_T and τ_P determine how fast the system is driven towards the target temperature and pressure respectively. In the current work a value of 0.5 ps was chosen for both constants if nothing else is specified.

$$\frac{d\chi(t)}{dt} = \frac{1}{T_{ext}\tau_T^2}(\mathscr{T}(t) - T_{ext}) + \frac{1}{\tau_T^2} \cdot \left(\tau_P^2 \eta(t)^2 - \frac{1}{N_f}\right) \tag{2.18}$$

$$\frac{d\eta(t)}{dt} = \frac{3 \cdot V(t)}{N_f k_b T_{ext} \tau_P^2}(\mathscr{P}(t) - P_{ext}) - \chi(t) \cdot \eta(t) \tag{2.19}$$

The barostat descibed above only takes into account the isotropic part of the pressure tensor and the volume of the simultation cell. In some situations (namely for the simulation of crystals) it is useful to control the different components of the pressure tensor seperatly. This can be done by replacing the friction coefficient $\eta(t)$ by a friction tensor $\overline{\eta}(t)$. Further information and the details of the implementation in DL_POLY can be found in the DL_POLY manual [Smi12].

For the calculations done in the context of this work, generally no external pressure was applied ($P_{ext} = 0$ atm). For e.g. an equilibrium simulation of water at 300 ° K (see section 3.1.5) for different force fields the resulting average pressure is in the order of $< \mathscr{P}(t) >=$ 0.6-0.9 atm while the root mean squared variations of the pressure were $\left\langle (\mathscr{P}(t) - < \mathscr{P}(t) >)^2 \right\rangle$ =300-900 atm. This means that the effect of the external atmospheric pressure of about 1 atm is negligible, hence the choice of $P_{ext} = 0$ atm.

2.4.3 Rigid Bodies

In some of the simulations reported here, part of the system was described by rigid molecules. For the type of small planar rigid molecules (i.e. TIP4P/2005 water molecules, see chapter 3 for more details) the easiest way to deal with them in a molecular dynamics simulation is to consider them as rigid bodies. The rigid body M is then described by a translational velocity $\vec{v}_M$ and an angular momentum $\vec{j}_M$. Instead of considering the equation of motion for each individual atom one can therefore consider two different equations of motion for the entire rigid body, one for the translational movement (equation 2.20, where $\vec{F}_M$ is the total translational force acting on the molecule) and one for the angular momentum (equation 2.21, where $\vec{\tau}_M$ is the torque acting on the molecule).

$$\frac{d\vec{v}_M}{dt} = \frac{1}{\sum_{i,i\in M} m_i} \cdot \vec{F}_M \tag{2.20}$$

$$\frac{d\vec{j}_M}{dt} = \tau_M \tag{2.21}$$

The translational velocity is defined as the mass weighted sum of the velocities of the individual atoms constituting the molecule (see equation 2.22). Similarly the translational force acting on the rigid body is equal to the sum of the forces on the individual atoms (equation 2.23).

$$\vec{v}_M = \frac{1}{\sum_{i,i\in M} m_i} \sum_{i,i\in M} m_i \vec{v}_i \tag{2.22}$$

$$\vec{F}_M = \sum_{i,i\in M} \vec{F}_i \tag{2.23}$$

For the angular momentum and the torque, the distance of each atom from the center of mass $\vec{r}_M = \frac{1}{\sum_{i,i\in M} m_i} \sum_{i,i\in M} m_i \vec{r}_i$ has to be calculated. The angular momentum can then be defined according to equation 2.24 and the torque according to equation 2.25.

$$\vec{j}_M = \sum_{i,i\in M} m_i \cdot (\vec{r}_i - \vec{r}_M) \times \vec{v}_i \tag{2.24}$$

$$\vec{\tau}_M = \sum_{i,i\in M} (\vec{r}_i - \vec{r}_M) \times \vec{F}_i \tag{2.25}$$

Further details and the exact implementation can be found in the DL_POLY manual [Smi12].

2.5 Metadynamics / Local Elevation

Usually in molecular dynamics the system is trapped in a local minimum of the energy landscape. According to the harmonic transition state theory [Vin57, Vot07], the rate k_e at which the system escapes from such a minimum is approximately exponentially dependent on the depth of the free energy well ΔF_e (see equation 2.26, where $\tilde{\nu}$ is the effective attempt frequency to move out of the minima and t_c is the characteristic timescale of the process). In oxides, for processes such as the jump of a vacancy, a typical value for the attempt frequency is $\tilde{\nu}$ = 6.2e12 Hz [Vot07] and the maximum timescale that is accessible with brute force molecular dynamics is $t_{max} \sim 1$ ns (for a total simulation time of several nanoseconds). This means that, according to equation 2.27, we can simulate systems with energy differences up to $\Delta F_{max} \sim 0.23$ eV. For diffusive systems, where the attempt frequency $\tilde{\nu}$ is expected to be smaller, the range of accessible energy differences is even smaller. For systems with a larger characteristic time, so called rare events, additional methods are needed. Several methods to simulate rare events exist, the one chosen for a number of simulations in the present work is called Metadynamics [HTG94, LG08] (also sometimes referred to as local elevation method).

$$k_e = \frac{1}{t_c} = \tilde{\nu} e^{-\frac{\Delta F_e}{k_b T}} \tag{2.26}$$

$$\Delta F_{max} = k_b T \ln(\tilde{\nu} t_{max}) \tag{2.27}$$

The first step of metadynamics is to look at the energy landscape with respect to a limited number d of properties of the system, so called collective variables $s_{\alpha,\alpha\in(1,d)}$. The collective variables have to be explicit functions $S_\alpha(\vec{r})$ of the position of the atoms. A collective variable can e.g. be an angle between two bonds or a distance between two atoms or groups of atoms. The probability distribution $P_b(\vec{s})$ of the system state with respect to the vector of collective variables $\vec{s} = (s_1, s_2, ..., s_d)$ depends only on the total free energy of the system $F(\vec{s})$ (see equation 2.28). The initial free energy of the system $F_{sys}(\vec{s})$ can be found by integrating over the partition function of the energy of all the states with the same value for $\vec{s}$ (see equation 2.29).

$$P_b(\vec{s}) = \frac{e^{-\frac{F(\vec{s})}{T}}}{\int e^{-\frac{F(\vec{s})}{T}} d\vec{s}} \tag{2.28}$$

$$F_{sys}(\vec{s}) = -T \ln\left(\int e^{-\frac{V_{sys}(\vec{r})}{T}} \delta(\vec{s} - \vec{S}(\vec{r})) d\vec{r}\right) \tag{2.29}$$

As discussed above, the system will initially stay preferentially in the potential wells. The idea of metadynamics is now to add a small repulsive Gaussian bias potential to the system potential $V_{sys}(\vec{r})$ at times $n \cdot \tau_G, n \in (1, 2, 3, ...)$. The total metadynamics bias potential $V_G(\vec{s}, t)$ at time t is then given by equation 2.30, where σ_α is the width of the Gaussians in the direction of s_α and ω is their height. Consequently the free energy $F(\vec{s}, t)$, which determines the probabilty distribution $P_b(\vec{s}, t)$ is now time dependent, with $V_G(\vec{s}, t)$ being added to the initial free energy $F_{sys}(\vec{s})$ (see equation 2.31).

$$V_G(\vec{S}(\vec{r}), t) = w \sum_{n, n\cdot\tau_G < t} e^{-\sum_\alpha \frac{(S_\alpha(\vec{r}) - s_\alpha(n\cdot\tau_G))^2}{2\sigma_\alpha^2}} \tag{2.30}$$

$$\begin{aligned} F(\vec{s}, t) &= -T \ln\left(\int e^{-\frac{V_G(\vec{s},t) + V_{sys}(\vec{r})}{T}} \delta(\vec{s} - \vec{S}(\vec{r})) d\vec{r}\right) \\ &= -T \ln e^{-\frac{V_G(\vec{s},t)}{T}} - \ln\left(\int e^{\frac{-V_{sys}(\vec{r})}{T}} \delta(\vec{s} - \vec{S}(\vec{r})) d\vec{r}\right) \\ &= V_G(\vec{s}, t) + F_{sys}(\vec{s}) \end{aligned} \tag{2.31}$$

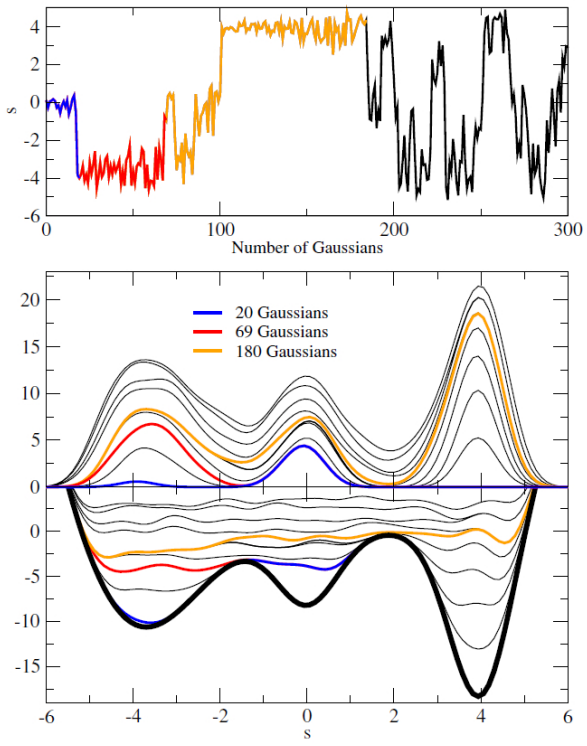

Figure 2.3: Trajectory of the collective variable s for a one-dimensional system during a metadynamics simulation on the 3-minima potential represented in the lower panel. The parameters for the metadynamics are $\delta s = 0.4$, $w = 0.3$ and $\tau_G = 300$. Middle panel: time evolution of the metadynamics bias potential V_G. Blue line: V_G at the time when the first minimum is filled and the system 'escapes' to the second minimum; red line: V_G at the time when the second minimum is filled as well; orange line: V_G at the time when the entire profile is filled. Lower panel: time evolution of the sum of the metadynamics potential V_G and the intrinsic potential of the system V_{sys}. V_{sys} is represented by a thick black line. Figure taken from [LG08].

Since in the beginning the system will be preferentially at the bottom of an energy well, that is where the repulsive bias potentials will be put. This will gradually fill up the well which allows the system to escape to the next energy well. After that the next well will be filled and so on and so forth (see figure 2.3) until at some time t_{fill} all the potential wells have been filled. At that point the free energy $F(\vec{s}, t_{fill}) = F_{sys}(\vec{s}) + V_G(\vec{s}, t_{fill})$ will essentially be costant for all values of $\vec{s}$ and the system will diffuse freely within the whole energy landscape, i.e. the probability distribution $P_b(\vec{s}, t)|_{t>t_{fill}} \approx \frac{1}{\int d\vec{s}}$ will essentially be constant. This means that for $t > t_{fill}$ the additional Gaussians will be evenly distributed within the whole energy landscape and $V(\vec{s}, t)$ will increase evenly independent of $\vec{s}$. In other words the bias potential $V_G(\vec{s}, t)$ becomes equal to the free energy of the system plus a time dependent shift (see equation 2.32,

where k_{fill} is the filling rate).

$$V_G(\vec{s},t)|_{t>t_{fill}} \approx -F_{sys}(\vec{s}) + k_{fill} \cdot (t - t_{fill}) \tag{2.32}$$

This means that the bias potential can be used as an estimate of the free energy landscape. For all metadynamics calculations done within this thesis the PLUMED plugin [BBB$^+$09] was used.

2.5.1 Choice of collective variables and parameters

The most important choice for a metadynamics calculation is that of the collective variables [LG08]. A bad choice of the collective variables can lead to a hysteretic behaviour of the energy landscape and hence a lack of convergence. Additionally the type of behaviour and the relevance of the result will depend on the choice of the collective variables. The set of characteristics that an ideal choice of collective variables should fulfill are:

- **They should provide a good description of the system properties of interest.** The collective variables should have some physical relevance for the system of interest. Specifically the set of collective variables should be able to distinguish between the initial state, the final state and all the intermediate states of interest [LG08]. E.g. the collective variables to study a liquid-solid phase transition could be something like an order parameter, on the other hand to study the complex formation of two ions in solution an interatomic distance would be more adapted.
- **The set of collective variables should describe all slow modes relevant to the system** [LG08]. If one of the slow modes of the system is neglected the system might not proceed from the initial to the final state of interest or greatly overestimate the barrier for the transition. To illustrate this point let us imagine a system of heavy polyions in solution that rotate very slowly. We now want to study the complex formation of two of those slowly rotating ions. To do this we only take into account the distance between the atoms. Let us further imagine that the complex formation is only energetically favorable for a specific relative orientation of the two ions. Since we are not taking into account the relative orientation, the metadynamics simulation will just push the two ions together irrespecive of their orientation. This means we have to add much more energy to overcome the unfavorable energy barrier for misoriented complex formation. Such a simulation will not only fail to give an accurate energy prediction but will also push the system towards physically irrelevant configurations.
- **The different collective variables should be independent of each other.** If the chosen collective variables are not independent of each other, we might have spurious variations in the energy profile. As an example let us imagine we want to describe the adsorption

of an ion onto a surface. We choose two collective variables: the distance between the surface and the ionic species (s_1) as well as the localised electrostatic potential (s_2) which takes into account the electrostatic interaction of the ion with the portion of the surface within a certain cutoff r_{s2}. If the ion is close to the surface the local electrostatic potential of the ion with the surface depends on the exact location and, if we are considering a polyion, on the orientation of the ion with respect to the surface. With increasing distance from the surface however s_2 will decrease until, at a distance greater than r_{s2}, s_2 will be zero independent of the orientation and location of the ion. In other words the available s phase space close to the surface is much larger that further away. This might be good to explore possible positions of the ion at the surface but will overestimate the adsorption energies.

- **The total number of collective variables d should remain small** [LG08]. If the number of collective variables becomes too big, the number of steps required to explore the whole phase space becomes much too large and hence convergence will be very slow.

The above stated conditions can serve as guidelines to a good choice of collective variables, however they do not provide a recipe. A good choice of collective variables is often not unique and sometimes a choice fulfilling all the conditions above might not be possible, for instance when the number of slow modes is relatively large and would require a number of collective variables too large to still be able to reach convergence within a reasonable time frame. Additionally the choice of the collective variables depends on the objective of the metadynamics calculations. If for instance the objective is to explore the phase space rather than to get an accurate prediction of the free energy profile, some of the conditions above can be relaxed.

The other parameters to choose are the hight of the Gaussian repulsive potentials ω, their width in the direction of the different collective variables ($\sigma_1, \sigma_2, ..., \sigma_d$) and the frequency of their addition τ_G. Laio et al. did an extensive study to find the optimal conditions for the estimation of a free energy profile with a maximum depth ΔF_e and a phase space extent of $\Delta s_{\alpha,max}$ in direction of the different collective variables s_α [LG08]. For the width of the Gaussians they found that for small values of σ_α the error decreased with increasing σ_α. Up to the point where σ_α reached a critical value of about a tenth of the characteristic lengthscale $\Delta s_{\alpha,ch}$ of the energy landscape, after which the error increases again. In other words a value of about $\sigma_\alpha \sim 0.1 \cdot \Delta s_{\alpha,ch}$ seems to be ideal. Laio et al. found that the error did not explicitly depend on ω but on the ratio $\frac{\omega}{\tau_G}$. However the height of the Gaussians ω should be smaller than the characteristic height of the energy profile ΔF_{ch}. Generally within this work, a value of $w = 0.05 \cdot \Delta F_{ch}$ was chosen. Finally τ_G has to be chosen to ensure the complete filling of the energy profile within the total simulation time t_{sim} (see equation 2.33).

$$\tau_G = t_{sim} \cdot \frac{\omega}{\Delta F_e} \prod_\alpha \frac{\sigma_\alpha}{\Delta s_{\alpha,max}} \tag{2.33}$$

2.5.2 Error Estimation

Laio et al. [LG08] developed an apriori estimate for the error ϵ_{meta} on the metadynamics approximation of the free energy. The estimate was developed for a symmetric system with $\sigma_\alpha = \sigma$ (equation 2.34). The error estimate depends on the diffusion coefficient D_α^{meta} of the collective variable α, which is not always well known. The authors showed that this expression seems to be valid for small enough values of $\frac{\sigma}{\Delta s_{ch}}$. However the error of the metadynamics approach can be further reduced by using the arithmetic average over a number of profiles instead of just the last.

$$\bar{\epsilon}^2_{prior} = \frac{\Delta s^2_{max} \Delta F_e T (2\pi)^{\frac{2}{\pi}}}{D_\alpha^{meta} t_{sim}} \sum_{\vec{k}, k_\alpha \in (0,1,2,\ldots), \vec{k}^2 \neq 0} \frac{1}{\vec{k}^2 \pi^2} e^{-\frac{\vec{k}^2 \pi^2 \sigma^2}{2\Delta s^2_{ch}}} \tag{2.34}$$

Additionally Laio et al. showed that the error was mostly constant over the whole domain (only close to the boundaries the error is a bit larger) which makes it possible to estimate the error *a posteriori* by averaging over the whole domain. This of course supposes that the error at any point of the domain can be estimated e.g. by comparing the result between two methods.

2.5.3 Well-Tempered Metadynamics

Well-tempered metadynamics is a variant of metadynamics developed by Barducci et al. [BBP08]. The bias potential $V_G^{wt}(\vec{s}, t)$ for well-tempered metadynamics is defined by equation 2.35, where w and ΔT are parameters with energy and temperature units respectively. By looking at the time derivative of $V_G^{wt}(\vec{s}, t)$ one can see that, since the $N(\vec{s}, t) \propto t$ grows linearly with t, the derivative will tend to zero as $\frac{1}{t}$ for $t \to \infty$ (see equation 2.36). In other words for large t the bias potential $\lim_{t\to\infty} V_G^{wt}(\vec{s}, t) = V_G^{wt}(\vec{s})$ is constant. This means that $\delta(\vec{s} - \vec{s}(t))$ in equation 2.36 can be replaced by the probability distribution $P_b(\vec{s}, t)$ (see equation 2.37). This in turn means that for $t \to \infty$ the free energy can be approximated by $F(\vec{s}) \approx -\frac{T+\Delta T}{\Delta T} V_G^{wt}(\vec{s}) + f(t)$. This convergence behaviour is now independent of the initial parameter w and ΔT. With the well-tempered metadynamics algorithm the energy landscape is only filled up to a certain height, states with a higher energy will not be accessed. The filling height depends on ΔT.

$$\begin{aligned} V_G^{wt}(\vec{s}, t) &= \Delta T \ln\left(1 + \frac{w N(\vec{s}, t)}{\Delta T}\right) \\ N(\vec{s}, t) &= \int_0^t \delta(\vec{s} - s(\vec{t'}))\, dt' \end{aligned} \tag{2.35}$$

$$\frac{\partial V_G^{wt}(\vec{s},t)}{\partial t} = \frac{w\Delta T\delta(\vec{s}-\vec{s}(t))}{\Delta T + wN(\vec{s},t)} = w\cdot e^{-\frac{V_G^{wt}(\vec{s},t)}{\Delta T}}\delta(\vec{s}-\vec{s}(t)) \tag{2.36}$$

$$\begin{aligned}\lim_{t\to\infty}\frac{\partial V_G^{wt}(\vec{s},t)}{\partial t} &= w\cdot e^{-\frac{V_G^{wt}(\vec{s},t)}{\Delta T}}P_b(\vec{s},t) = w\cdot e^{-\frac{V_G^{wt}(\vec{s},t)}{\Delta T}}\frac{e^{-\frac{F_{sys}(\vec{s})+V_G^{wt}(\vec{s},t)}{T}}}{\int e^{-\frac{F_{sys}(\vec{s})+V_G^{wt}(\vec{s},t)}{T}}d\vec{s}} = \frac{1}{t}\\ \lim_{t\to\infty}\left((T+\Delta T)\cdot V_G^{wt}(\vec{s},t)+\Delta T\cdot F_{sys}(\vec{s})\right) &= \ln\left(\frac{w\cdot t}{\int e^{-\frac{F_{sys}(\vec{s})+V_G^{wt}(\vec{s},t)}{T}}d\vec{s}}\right) = f(t)\end{aligned} \tag{2.37}$$

To compute the full histogram $N(\vec{s},t)$ would be computationally expensive. However from equation 2.35 we can see that to add the bias potential $V_G^{wt}(\vec{s},t)$ is essentially equivalent to do a metadynamics simulation with a variable hight of the Gaussians as defined by equation 2.38. The big advantage of the well-tempered metadynamics algorithm is that the convergence is much less dependent on the choice of the initial parameters σ_α, ω and τ_G. Additionally the exploration of the phase space can be restricted to physically relevant configurations by choosing the value of ΔT.

$$\omega = we^{-\frac{V_G(\vec{s},t)}{\Delta T}}\tau_G \tag{2.38}$$

2.6 Metropolis Monte Carlo

The term Monte Carlo is used to designate a range of numerical integration methods that use random numbers. Although some similar algorithms already existed before, the first intensive use of Monte Carlo methods as well as the name is usually traced back to John von Neumann, Stanislaw Ulam and Nicholas Metropolis [MU49]. A variant of the Monte Carlo methods is to evaluate the function $f(\vec{x})$ for a certain number n of random samples $\vec{x}_i$ according to a certain probability distribution $\vec{x}_i \propto P_s(\vec{x})$. The integral of the function can then be approximated by averaging over the evaluated value of the fuction divided by the value of the sample probability distribution (see equation 2.39). The method converges with $n^{-\frac{1}{2}}$. If one compares the convergence behavior of Monte Carlo to more conventional methods such as the trapezoidal rule (convergenc with $n^{-\frac{2}{d}}$ where d is the dimensionality of the vector $\vec{x}$) one can see that the method is especially interesting for high dimensional systems as the

convergence behavior is independent of the dimensionality of the system.

$$\int f(\vec{x})d\vec{x} = \int \frac{f(\vec{x})}{P_s(\vec{x})} P_s(\vec{x})d\vec{x} = \lim_{n\to\infty} \left\langle \frac{f(\vec{x}_i)}{P_s(\vec{x}_i)} \right\rangle \tag{2.39}$$

The accuracy of the method can be further improved if $P_s(\vec{x})$ is approximately following the function $|f(\vec{x})|$. This is because if $P_s(\vec{x})$ is large in the areas where $|f(\vec{x})|$ is large, there are more samples in the regions that contribute more to the integral and consequently the areas that are more important for the integal are better approximated. This is called importance sampling [AT90].

A typical problem within statistical mechanics is the evaluation of a given property $A(\vec{r})$ of a system that follows the Boltzmann distribution (i.e. Boltzmann integrals, see equation 2.40). For the majority of problems in statistical mechanics the integral $\int A(\vec{r})P_b(\vec{r})d\vec{r}$ is dominated by the Boltzmann distribution (an exception is e.g. the Ising spin model where the phase space is much larger for higher energies). In other words low energy regions which have low energy (and are therefore much more populated) are more important for the evaluation of the integral than high energy regions. This means that if we perform a Monte Carlo integration with the configuration samples $\vec{r}_i$ following the Boltzmann distribution we should get a good approximation of the property $\langle A(\vec{r})\rangle$ of interest (see equation 2.41).

$$\langle A(\vec{r})\rangle = \frac{\int A(\vec{r}) e^{-\frac{F(\vec{r})}{k_b T}} d\vec{r}}{\int e^{-\frac{F(\vec{r})}{k_b T}} d\vec{r}} = \int A(\vec{r})P_b(\vec{r})d\vec{r} \tag{2.40}$$

$$\langle A(\vec{r})\rangle \overset{\vec{r}_i \propto P_b(\vec{r})}{=} \lim_{n\to\infty} \left\langle \frac{A(\vec{r}_i)P_b(\vec{r}_i)}{P_b(\vec{r}_i)} \right\rangle = \lim_{n\to\infty} \langle A(\vec{r}_i)\rangle \tag{2.41}$$

The problem is that the Boltzmann distribution is not a trivial function of $\vec{r}$ and therefore we need an additional method to generate samples $\vec{r}_i$ according to $P_b(\vec{r}_i)$. In the Metropolis Monte Carlo method (sometimes also called Markov chain Monte Carlo) Markov chains are used for the sample generation [AT90, Fre04]. Markov chains are stochastic series of states $\vec{x}_m$ of a system where the probability of state $P(\vec{x}_m = \vec{x}^i) = P_m(\vec{x}^i)$ only depends only on the previous state $\vec{x}_{m-1}$ (equation 2.42). Such a process can be constructed by defining the m independent transition probabilities $p^{\vec{x}^i \to \vec{x}^j}$ for the system to go from state $\vec{x}^i$ to state $\vec{x}^j$. The Markov chain will then obey the master equation (equation 2.43).

$$P_m(\vec{x}^i|\vec{x}_{m-1}, \vec{x}_{m-2}, ..., \vec{x}_0) = P(\vec{x}_m = \vec{x}^i|\vec{x}_{m-1}) \tag{2.42}$$

$$\frac{\partial P_m(\vec{x}^i)}{\partial m} = \int \left(p^{\vec{x}^j \to \vec{x}^i} \cdot P_m(\vec{x}^j) - p^{\vec{x}^i \to \vec{x}^j} \cdot P_m(\vec{x}^i) \right) d\vec{x}^j \tag{2.43}$$

If we construct the system such that any state x^i can be reached from any other state x^j (ergodicity), we can use the Markov chain to sample according to a desired sample distribution $P_s(\vec{x}^i)$ by forcing $P_m(\vec{x}^i)$ to relax to the sample distribution ($\lim_{m\to\infty} P_m(\vec{x}^i) = P_s(\vec{x}^i)$). This is possible by ensuring that the derivative with respect to m becomes zero for $P_s(\vec{x}^i)$ (equation 2.44). The easiest way to do so is to ensure that the integrand is zero (so called detailed balance, equation 2.45).

$$\int \left(p^{\vec{x}^j \to \vec{x}^i} \cdot P_s(\vec{x}^j) - p^{\vec{x}^i \to \vec{x}^j} \cdot P_s(\vec{x}^i) \right) d\vec{x}^j = 0 \tag{2.44}$$

$$\begin{aligned} & p^{\vec{x}^j \to \vec{x}^i} \cdot P_s(\vec{x}^j) - p^{\vec{x}^i \to \vec{x}^j} \cdot P_s(\vec{x}^i) \equiv 0 \\ & \frac{p^{\vec{x}^j \to \vec{x}^i}}{p^{\vec{x}^i \to \vec{x}^j}} = \frac{P_s(\vec{x}^i)}{P_s(\vec{x}^j)} \end{aligned} \tag{2.45}$$

In practice it would often be difficult to directly sample from transitions according to equation 2.45. Consequently a random transition is chosen with a trial probability $tr^{x^i \to x^j}$ and then the move is accepted or rejected according to the acceptance probability $acc^{x^i \to x^j}$. The transition probability is then the product of the trial probability and the acceptance probability ($p^{\vec{x}^i \to \vec{x}^j} = tr^{x^i \to x^j} \cdot acc^{x^i \to x^j}$).

If we go back to the statistical mechanics problem (equation 2.40), the first thing to do for any Metropolis Monte Carlo calculation is to select a set of transitions of the system which allow access to the complete phase space to satisfy ergodicity. Consequently, as the Markov chains created are in any case not equivalent to a time evolution of the system, the chosen transitions do not have to be physically possible or have any physical meaning. In fact for fast convergence unphysical movements are often better. We now have to ensure that the Markov chain relaxes to the Boltzmann distribution. This means that the transitions probabilities have to satisfy equation 2.46. In practice we chose equal trial probability for all moves $tr^{\vec{x}^i \to \vec{x}^j} = tr^{\vec{x}^j \to \vec{x}^i}$ and acceptance probabilities according to equation 2.47.

$$\frac{p^{\vec{r}^j \to \vec{r}^i}}{p^{\vec{r}^i \to \vec{r}^j}} = \frac{tr^{x^j \to x^i} \cdot acc^{x^j \to x^i}}{tr^{x^i \to x^j} \cdot acc^{x^i \to x^j}} = \frac{P_b(\vec{r}^i)}{P_b(\vec{r}^j)} = e^{-\frac{F(\vec{r}^i) - F(\vec{r}^j)}{k_b T}} \tag{2.46}$$

$$acc^{x^i \to x^j} = min\left(1; e^{-\frac{F(\vec{r}^i)-F(\vec{r}^j)}{k_b T}}\right) \tag{2.47}$$

A Metropolis Monte Carlo scheme according to the description above was implemented into LAMMPS [Pli95] within the framework of this thesis. The details and the validation of the Monte Carlo implementation can be found in appendix A.

2.6.1 Long Range Potential for a Linear Charge Distribuion

Within the framework of this thesis Metropolis Monte Carlo calculations were used to calculate the electrostatic arrangement of ions close to a planar surface (electrostatic double layer). The long-range electrostatic forces are very important for a correct description of the double layer. However the previously described Ewald summation (see section 2.2) is not well suited for the description of the electrostatic double layer for two reasons. Firstly Ewald summation can only be employed for a system, with periodic boundary conditions in all directions. This will introduce an artificial periodicity perpendicular to the surface and consequently any charge fluctuations in the box will actually be replicated on the periodicity lattice. This will artificially increase the total coulombic energy of charge fluctuations and lead to an undesired smoothening of the charge distribution [TV80]. Secondly, since the number of charges to consider in the system is quite high and the charge distribution does not follow any particular periodicity, either the short range cutoff has to be chosen quite large, which will increase the computational cost for the short range interactions, or the Ewald summation has to be done over a wide range of $\vec{k}$ values, which will increase the computational cost for the long range part of the potential. This means that for the calculation of the electrostatic double layer, Ewald summation is computationally not very efficient.

However an other method to account for the long range electrostatic interactions for a linear charge distribution $\rho_q(\vec{r}) = \rho_q(x)$ has been developed by Torrie and Valleau [TV80]. Torrie and Valleau did some Metropolis Monte Carlo calculations of the electrical double layer at a charged plate. They used a rectangular simulation box with periodic boundaries parallel and hard wall boundaries perpendicular to the plate. Within the central simulation box they calculated the Coulombic interaction V^{pair} of each ion with the nearest periodic image of each other ion explicitly. To take into account the long range electrostatic interaction V_{tv}^{lr}, they approximated the linear charge distribution by a series of infinite plates $p \in (1,2,...,n_p)$ that are placed a distance $\Delta_p x$ apart. The charge of each plate was approximated by the average charge density in the region $(p-1)\cdot\Delta_p x < x \leq p\cdot\Delta_p x$ times $\Delta_p x$. However since within the central simulation box the electrostatic interactions are already calculated explicitly, they had to subtract the interaction of that region (short range cutoff interactions, V_{tv}^{co}) from the long range interactions. The total interaction considered by Torrie and Valleau can thus be described by equation 2.48,where ϕ^j is the potential of a point charge, ϕ^d is the potential of

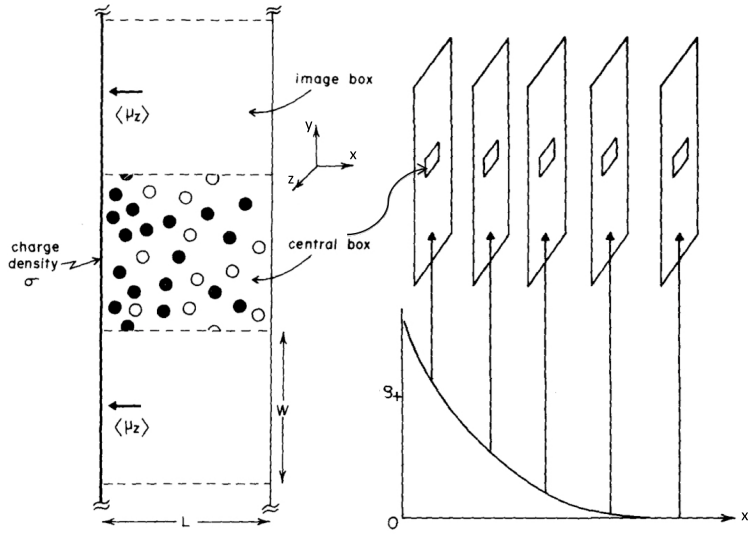

Figure 2.4: Illustration of the long range electrostatic interactions calculation scheme employed by Torrie and Valleau [TV80]. To the right: illustration of the central simulation box containing the ions with the boundary conditions. To the left: schematic view or the series of plates used for the long range interactions with the area overlapping with the central box that has to be subtracted. Illustration taken from [TV80].

an infinite plate and ϕ^r is the potential of a charged rectangle.

$$V(\vec{r}) = V^{pair}(\vec{r}) + V_{tv}^{lr}(\vec{r}) - V_{tv}^{co}(\vec{r}) = \sum_{i,j>i} \phi^j(\vec{r}_i) \cdot q_i + \sum_{i,p} \phi^d(x_i) \cdot q_i - \sum_{i,r} \phi^r(x_i) \cdot q_i \quad (2.48)$$

A long range potential scheme similar to the one developed by Torrie and Valleau was implemented in LAMMPS [Pli95] within the framework of this thesis. There were two main differences between the original algorithm developed by Torrie and Valleau and the one used for the current work:

- The charge distribution was not explicitly divided into infinite charged plates. Instead the long range potential was developed by considering the one dimensional Poisson equation (see section 2.6.1). This means that the sum over i and p for the long range ($V^{lr}(\vec{r})$) and the short range cutoff interactions ($V^{co}(\vec{r})$) reduces to a sum over i.
- The ion-ion interactions were only considered explicitly within a certain cutoff r_c. This means that instead of subtracting a rectangular region from each plate we now have to subtract a spherical region with a linear charge distribution (see section 2.6.1)

The exact expression used for the long range potential $\phi^{lr}(x)$ and for the short range cutoff potential $\phi^{co}(x)$ will be developed in the following sections. For more implementation details

and the validation of the method please see appendix B.

Long Range Potential

We know that a charge distribution that develops because of a charged plate, should conserve the linearity i.e. $\phi^{lr}(\vec{r}) = \phi^{lr}(x)$. Hence we can use the one dimensional Poisson equation (equations 2.49 and 2.50, where $Q_{tot}(x_q < x)$ is the sum of the charges in the system with a position x_q lower than x. L_y and L_z are the simulation box lengths in y and z direction).

$$\frac{d^2\phi^{lr}(x)}{dx^2} = -\frac{\rho_q(x)}{\epsilon} \tag{2.49}$$

$$\phi^{lr}(x) = -\int\int \frac{\rho_q(x)}{\epsilon} dxdx = -\int \left[\frac{Q_{tot}(x_q < x)}{\epsilon L_y L_z} + C_1\right] dx \tag{2.50}$$

The potential should be independent on the definition of the integration variable i.e. we should be able to redefine $x' = -x$ and get the same potential (equation 2.51 and 2.52, where Q_{tot} is the total charge in the system).

$$\frac{d\phi^{lr}(x)}{dx} = -\frac{Q_{tot}(x_q < x)}{\epsilon L_y L_z} - C_1 \tag{2.51}$$

$$\frac{d\phi^{lr}(x')}{dx'} = \frac{d\phi^{lr}(x)}{dx}\frac{dx}{dx'} = -\frac{d\phi^{lr}(x)}{dx} = -\frac{Q_{tot}(x'_q < x')}{\epsilon L_y L_z} - C_1 = -\frac{Q_{tot} - Q_{tot}(x_q < x)}{\epsilon L_y L_z} - C_1 \tag{2.52}$$

Consequently we can determine the first integration constant C_1 (see equation 2.54). And we can develop the final expression for the long range potential (equation 2.55, where $I(x)$ is the integral of $Q_{tot}(x_q < x)$). The integration constant C_2 will only cause a shift of the whole potential. If we apply the developed long range potential over the whole domain we can choose C_2 arbitrarily since it will not influence the behaviour or the system. We therefore chose to set C_2 to zero.

$$\frac{Q_{tot}(x_q < x)}{\epsilon L_y L_z} + C_1 = -\frac{Q_{tot}}{\epsilon L_y L_z} + \frac{Q_{tot}(x_q < x)}{\epsilon L_y L_z} - C_1 \tag{2.53}$$

$$C_1 = -\frac{Q_{tot}}{2\epsilon L_y L_z} \tag{2.54}$$

$$\begin{aligned}\phi^{lr}(x) &= -\int \left[\frac{Q_{tot}(x_q < x)}{\epsilon L_y L_z} - \frac{Q_{tot}}{2\epsilon L_y L_z} \right] dx \\ &= -\int \frac{Q_{tot}(x_q < x)}{\epsilon L_y L_z} dx + \frac{Q_{tot}}{2\epsilon L_y L_z} x + C_2 \\ &= -\frac{I(x)}{\epsilon L_y L_z} + \frac{Q_{tot}}{2\epsilon L_y L_z} x + C_2\end{aligned} \tag{2.55}$$

This means that if we have a charge distribution that is non-zero only in a certain region, the potential behaves like the potential of an infinite charged plate with a surface charge of $Q_{tot} \cdot L_y^{-1} \cdot L_z^{-1}$ outside of that region.

Examples To understand what equation 2.54 means it is useful to look at a couple of examples.

Charged Plate If we consider a charged plate, $Q_{tot}(x_q < x)$ is actually a step function which is 0 for $x < x_{plate}$ and $\sigma \cdot L_y \cdot L_z$ for $x > x_{plate}$. Consequently for $x < x_{plate}$ the electrostatic potential is described by equation 2.56 and for $x > x_{plate}$ by equation 2.57. If we redefine $C_2 = C_2' - 0.5 \cdot \sigma \cdot x_{plate}/\epsilon$ we recover the text book formula for an infinite charged plate.

$$\phi^{lr}(x) = \frac{Q_{tot}}{2\epsilon L_y L_z} x + C_2 = \frac{\sigma}{2\epsilon} x + C_2 \tag{2.56}$$

$$\phi^{lr}(x) = -\frac{Q_{tot}}{\epsilon L_y L_z}(x - x_{plate}) + \frac{Q_{tot}}{2\epsilon L_y L_z} x + C_2 = -\frac{\sigma}{2\epsilon} x + \frac{\sigma}{\epsilon} x_{plate} + C_2 \tag{2.57}$$

Region of Uniform Charge Distribution Let us consider a region of uniform charge distribution within a certain region (e.g $\rho_q(x) = 1$ for $0 < x < 5$). As mentioned above for $x < 0$ and $x > 5$ we have the same potential as that of an infinite charged plate with a charge of $\sigma = Q_{tot}/(L_x \cdot L_y)$. In the charged region equation 2.55 becomes 2.58. Thus the overall electrostatic potential behaves like a charged plate outside of the charged region and is smooth within the charged region (see figure 2.6).

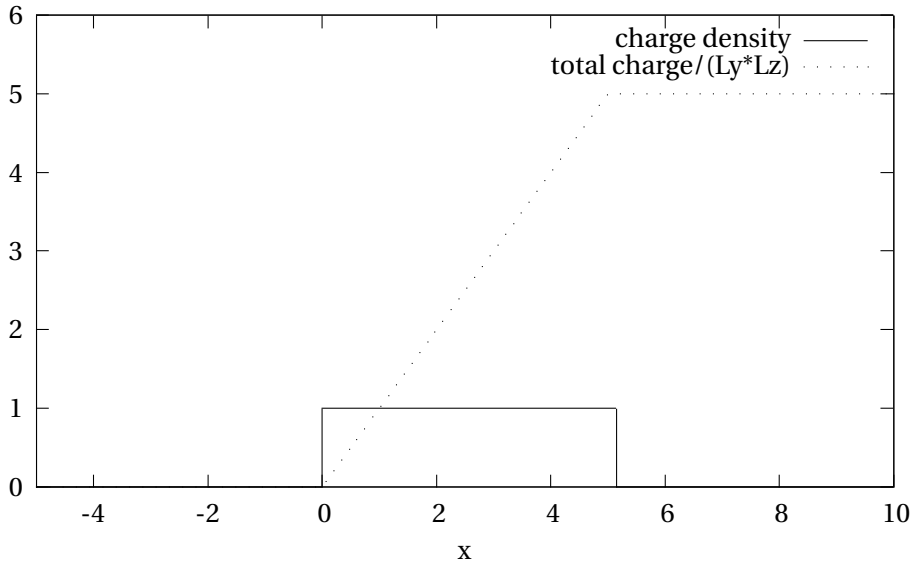

Figure 2.5: Example of a uniform charge distribution within a certain region ($\rho_q(x) = 1$ for $0 < x < 5$) and the corresponding total charge $Q_{tot} \cdot L_y^{-1} \cdot L_z^{-1}$.

$$\phi^{lr}(x) = \frac{Q_{tot}}{2\epsilon L_y L_z} x - \frac{\rho}{2\epsilon L_y L_z} x^2 + C_2 = \frac{Q_{tot}}{2\epsilon L_y L_z}(x - x_p) - \frac{Q_{tot}}{2\epsilon L_z L_y L_x} x^2 + C_2' \tag{2.58}$$

Short Range Cutoff Potential

For the short range cutoff potential ($\phi^{co}(x)$), that has to be subtracted from the long range potential, we are interested in the potential at the center of a sphere with a charge density varying in x only (see figure 2.7). To calculate the potential, we have to integrate the charge density $\rho_q(x)$ over the volume of the sphere (equation 2.59). By using the cylindrical coordinates x, r_{yz} and θ we get equation 2.60. And finally, by using partial integration for the second and third term, we get to the final expression for the short rage cutoff (equation 2.61).

$$\phi^{co}(\vec{r}_i) = -\int_{sphere} \frac{\rho_q(x)}{4\pi|\vec{r}_i - \vec{r}|} d\vec{r} \tag{2.59}$$

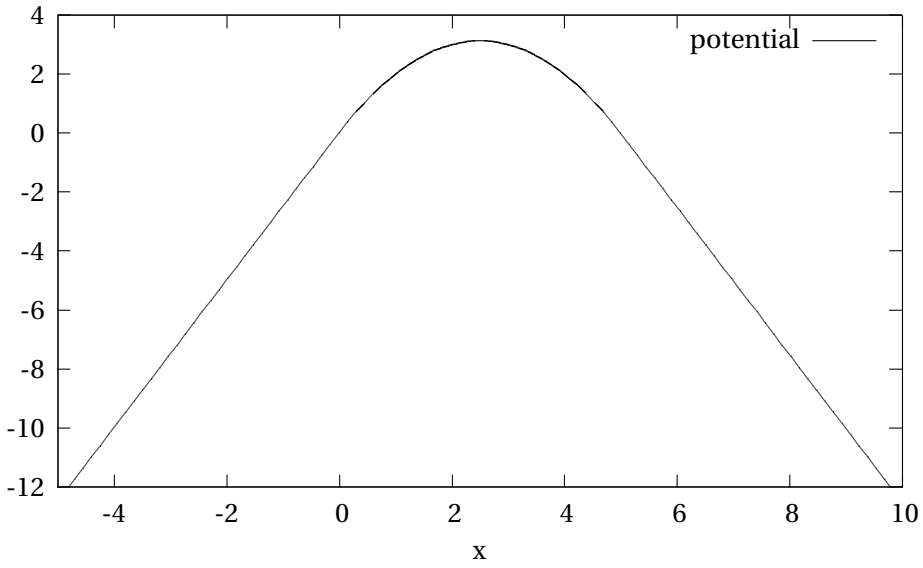

Figure 2.6: Electrostatic potential of a uniform charge distribution within a certain region ($\rho_q(x) = 1$ for $0 < x < 5$) according to equation 2.55.

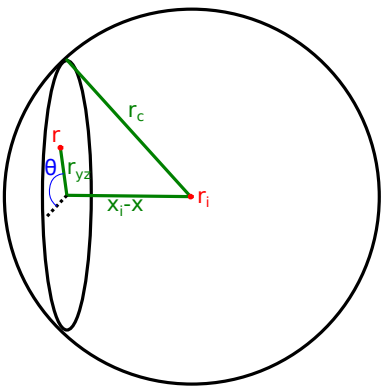

Figure 2.7: Schematic view of the short range cutoff for the electrostatic potential of a linear charge distribution.

$$
\begin{aligned}
\phi^{co}(\vec{r}_i) &= -\frac{1}{4\pi\epsilon}\int_{-r_c}^{r_c}\int_{0}^{2\pi}\int_{0}^{\sqrt{r_c^2-(x-x_i)^2}} \frac{\rho_q(x)}{\sqrt{r_{yz}^2+(x-x_i)^2}} r_{yz}\,dr_{yz}\,d\theta\,dx \\
&= -\frac{1}{2\epsilon}\int_{-r_c}^{r_c}\int_{0}^{\sqrt{r_c^2-(x-x_i)^2}} \frac{\rho_q(x)}{\sqrt{r_{yz}^2+(x-x_i)^2}} r_{yz}\,dr_{yz}\,dx \\
&= -\frac{1}{2\epsilon}\int_{-r_c}^{r_c} \rho_q(x)\left[\sqrt{r_{yz}^2+(x-x_i)^2}\right]_0^{\sqrt{r_c^2-(x-x_i)^2}} dx \\
&= -\frac{1}{2\epsilon}\int_{-r_c}^{r_c} \rho_q(x)\left(r_c+|x-x_i|\right) dx \\
&= -\frac{1}{2\epsilon}\left(\int_{x_i-r_c}^{x_i} \rho_q(x)(r_c-x_i)dx + \int_{x_i-r_c}^{x_i} \rho_q(x)x\,dx + \int_{x_i}^{x_i+r_c} \rho_q(x)(r_c+x_i)dx - \int_{x_i}^{x_i+r_c} \rho_q(x)x\,dx\right)
\end{aligned}
\tag{2.60}
$$

$$
\begin{aligned}
\phi^{co}(x_i) &= -\frac{1}{2\epsilon L_y L_z}\Bigg([Q_{tot}(x_c<x)(r_c-x_i)]_{x_i-r_c}^{x_i} + [Q_{tot}(x_c<x)x]_{x_i-r_c}^{x_i} + \int_{x_i-r_c}^{x_i} Q_{tot}(x_c<x)dx \\
&\quad + [Q_{tot}(x_c<x)(r_c+x_i)]_{x_i}^{x_i+r_c} - [Q_{tot}(x_c<x)x]_{x_i}^{x_i+r_c} - \int_{x_i}^{x_i+r_c} Q_{tot}(x_c<x)dx\Bigg) \\
&= -\frac{1}{2\epsilon L_y L_z}\left(\int_{x_i-r_c}^{x_i} Q_{tot}(x_c<x)dx - \int_{x_i}^{x_i+r_c} Q_{tot}(x_c<x)dx\right) \\
&= \frac{1}{2\epsilon L_y L_z}\left(I(x_i-r_c)+I(x_i+r_c)-2I(x_i)\right)
\end{aligned}
\tag{2.61}
$$

Example Again to get an idea of what equation 2.61 means, we look at an example. If we consider an infinite plate at a position $x_i-\Delta x$, $Q_{tot}(x_{charge}<x)$ is actually a step function which is 0 for $x<x_i-\Delta x$ and $\sigma\cdot L_y\cdot L_z$ for $x>x_i-\Delta x$. This means that equation 2.61 becomes equation 2.62.

$$
\phi^{co}(x_i) = -\frac{\sigma}{2\epsilon}(\Delta x - r_c) \tag{2.62}
$$

The derived expression should be equal to the text book potential of a charged disk. For a charged disc the electric field as a function of the distance (Δx) from the center is expressed by equation 2.63, where a is the radius of the charged disc. If we integrate this with respect to Δx and multiply by -1 to finally get the potential for a charged disk (equation 2.64). Since in our case $a^2 + \Delta x^2 = r_c^2$ the two expressions (equation 2.62 and equation 2.65) are equivalent.

$$E(\Delta x) = \frac{\sigma}{2\epsilon}\left(1 - \frac{\Delta x^2}{\sqrt{a^2 + \Delta x^2}}\right) \tag{2.63}$$

$$\phi^{disk}(\Delta x) = -\frac{\sigma}{2\epsilon}\left(\Delta x - \sqrt{a^2 + \Delta x^2}\right) \tag{2.64}$$

$$\phi^{disk}(\Delta r) = -\frac{\sigma}{2\epsilon}(\Delta x - r_c) \tag{2.65}$$

2.7 Summary

In this chapter the different methods and concepts used for the theoretical calculations were described. First general concepts, such as how the interactions between atoms are described within the context of this work, were introduced. Then the spacial boundary between the simulated system and the surrounding environment was developed. Finally the different calculation methods were described. The following methods were described:

- Energy Minimization: Energy minimization is a method that relaxes the atomic structure towards a local energy minimum. The method can be used to estimate structural properties namely of crystalline solids. Energy minimization results are reported in chapter 3. In addition energy minimization was often used as a pre-equilibration method for molecular dynamics simulations.

- Molecular Dynamics: Molecular dynamics simulates the evolution of an atomic structure in time. It is used for systems where the dynamic properties are important (e.g. for water containing systems) and is the most used method in this thesis. Molecular dynamics results can be found in chapters 3, 6, 7, 8 and 11.

- Metadynamics: Metadynamics is a method which is used in combination with e.g. molecular dynamics. It allows the exploration and estimation of the energy landscape as a function of certain properties of the system, so called collective variables, and can be used to speed up rare events. It is used in chapters 6 and 7.

- Metropolis Monte Carlo: Metropolis Monte Carlo is a method, which can be used to estimate properties of a thermodynamic ensemble in equilibrium. It is used here to estimate the properties of the equilibrium distribution of ions ("double layer") at portlandite surfaces in chapter 8. The development of the method, used for the long range interactions for the linear charge distribution developing at the double layer, is described in detail in this chapter.

3 Force Fields

In this section the choice and validation of the force field employed for the atomistic simulations will be described. First the three force fields originally considered and their performance for different systems (portlandite, tobermorite, water) are discussed. Based on these results, the choice of the finally employed force field is elucidated. Then the enhancements of the original force field are explained and discussed. The chapter ends by an estimation of the force field error on energies, distances and angles.

3.1 Choice of Force Field

Three different force fields were originally considered and compared. Two of the force fields had previously been employed for the description of cementitious systems and the third is known to give a very good description of water. The performance of the three force fields was tested for portlandite, water, $[Ca^{2+}]_{aq}$ and $[OH^{-}]_{aq}$ ions in water as well as for 9 Å tobermorite.

3.1.1 FF1: CLAYFF

The first force field tested was the CLAYFF force field [CLK04]. The CLAYFF force field is a partial charge model which means that the ions in the solid phases have charges which are only a fraction of their formal charge. The partial charges of the ions in the solid phase were assigned according to the Mulliken charge [Mul55] of electronic densities calculated by density functional theory (DFT). A partial charge description has been shown to give very good results for bulk structures of e.g. clays [HS04] or titanium oxide [SG00]. The problem with the partial charge model is, that the partial charges are dependent on the local atomic structure. This means that the partial charges are likely to change at structural defects, such as vacancies, substitutional defects or at surfaces and interfaces. CLAYFF has different partial charges for different atomic coordinations, but does not implement any variable partial charge which automatically adapts to the local structure (c.f. [SG00]). This might lead to problems for the

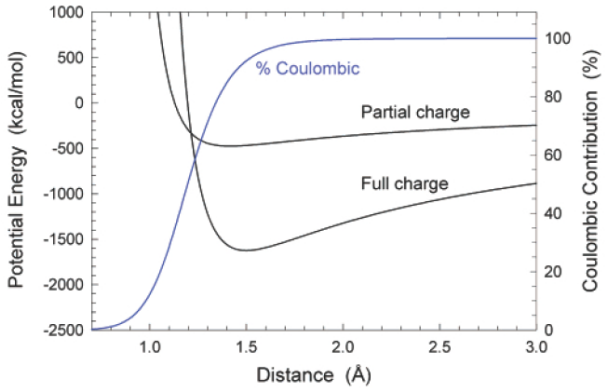

Figure 3.1: Interaction energy between a tetrahedrally coordinated silica and a bridging oxygen as a function of the distance between them for CLAYFF (partial charge) compared to a similar full charge force field. Shown as well is the percentage of the Coulombic interaction for the full charged force field. Figure taken from [CLK04].

description of defective structures.

Usually the covalent part of the bond, which is responsible for the reduction of the effective charge, is taken into account with separate bonded interactions [HS04, SG00]. CLAYFF however only takes into account bonded interactions for the hydroxyl groups. The uncompensated partial charges lead to relatively shallow ion-ion energy minimas (see figure 3.1). For surface calculations the CLAYFF force field includes additional angle dependent terms for the cation - hydroxyl angles. These angle dependent terms for the hydroxyls are however generally not used for bulk structures.

The water potential used by the CLAYFF force field is the flexible variant of the SPC [BPVGH81] model developed by Teleman et al. [TJE87]. CLAYFF has been developed for clays and has already been used for simulations of cementitious systems [KK02, KWK07, PXW10]. While the original CLAYFF force field contains a description of $[Ca^{2+}]_{aq}$ in solution, no corresponding model for the $[OH^{-}]_{aq}$ group exists. Therefore the description of $[OH^{-}]_{aq}$ has been taken from [BJR96]. The complete force field parameters used in this work can be seen in appendix C.1.

3.1.2 FF2: Lewis and Catlow, Kerisit, De Leeuw

The second force field is based on a force field by Lewis and Catlow [LC85], with further developments by various authors [KPH03, DLP98a, SSL^{+}92, dLWP95, dLPCP00]. The Lewis and Catlow force field is a full charge force field. This means that structural defects can be simulated without special care, but that the bulk properties might be slightly less well described (see section 3.1.1). The big advantage of this force field is that it allows the oxygen polarization to change with the changing local environment. This is achieved with the core-shell model of Dick and Overhauser [DO58], which divides the oxygen ions into a positively charged core and

a negatively charged shell. The oxygen core and shell are linked by a harmonic spring [LC85], the spring constant of which controls the polarizability of the oxygen. The short range van der Waals interactions are located at the position of the shell rather than of the core of the oxygen. The shell is usually considered to be quasi massless. In practice this is achieved by assigning a very small mass (i.e. 0.4 u) to the oxygen shells. Because of the faster movement of lighter particles, this has consequences on the maximum possible timestep (see section 2.4). In other words the timestep used for this force field was 0.2 fs instead of the 0.7 fs used for the rest of this work. The Lewis and Catlow force field has been shown to give good results for a wide range of inorganic bulk [KPH03, PCPW96, PCPJ92] as well as surface and interface structures [KPH03, KP04, AGM$^+$09, ASBP10, AMP12].

The water model has been developed by de Leeuw and Parker specifically for the use with the Lewis and Catlow force field [dLP98b]. The biggest limitation of this force field is the relatively high density of the water compared to experiment [dLP98b].

A version of this force field has already been used for simulations of cementitious systems by Pellenq et al. [PKS$^+$09]. In general the parameters used here are the same as the ones employed by Pellenq et al., except for the water. As the parameters reported for water reported by Pellenq et al. give unphysical results (see section 3.1.5) the original de Leeuw and Parker water model was used [DLP98a]. The attractive part of the short range interaction term for the hydrogen of the hydroxyl group with the water oxygen has been reduced with respect to the original force field. This was done to avoid stability issues when simulating an aqueous hydroxyl ion ($[OH^-]_{aq}$). The complete force field parameteres used in this work can be seen in appendix C.2.

3.1.3 FF3: TIP4P/2005 - Freeman

The third force field is an adaptation of FF2 by Freeman et al. The adaptation was made to be able to use the force field in combination with rigid molecule water force fields of the TIP familiy [FHC$^+$07]. Again this is a full charge force field with the associated advantages and disadvantages. The oxygen polarizability has been removed from the FF2 force field, which might result in less accurate results for the description of the solids, but is more consistent with the rigid molecule water model. Additionally the absence of shells in this force field allows for a larger timestep (0.7 fs).

For water the rigid molecule TIP4P/2005 model, developed by Abascal and Vega [AV05], was used. The TIP4P/2005 water model is based on four sites. Two sites represent the hydrogen atoms and two sites represent the oxygen atom. One of the oxygen sites carries no charge but is the site of the short range van der Waals or Lennard-Jones interactions. The second sites carries no mass but carries a charge. All the sites are contained within one plane and the distances and angles between them are kept fixed. This type of rigid water molecules has been shown to give very good results for water, especially the TIP4P/2005 force field [AV05, BRBK09] which is able to reproduce the phase diagram of water with a much better accuracy than other

force fields. The complete force field parameters used in this work can be seen in appendix C.3.

3.1.4 Results for Portlandite

The difference between the calculated and the experimentally observed [Pet61] portlandite lattice parameters were within less than +/- 10 % for FF1 (e.g. $\frac{|c(MD)^{FF1}-c^{exp}|}{c^{exp}}$ = 6.9 %) and within less than +/- 5 % for FF2 and FF3 (see table 3.1). This means that all force fields seem to be able to reproduce the portlandite structure with good accuracy (see table 3.1) with both energy minimization and molecular dynamics.

In addition to the structural details, the Voigt and the Reuss bounds of the bulk and shear modulus were calculated according to Monteiro and Chang [MC95] from the elastic tensor calculated by energy minimization. Here there are some differences between the force fields: FF1 seems to describe the Reuss bounds better than the Voigt bounds, which are underestimated by up to 12 GPa. FF2 and FF3 on the other hand underestimate the Reuss bound by up to 14 GPa while describing the Voigt bounds with good accuracy. The overall accuracy for describing the elastic properties of the material seems to be fair but not great for all tested force fields.

The surface enthalpy of 12 different surfaces has been calculated for each force field with energy minimisation (see section 2.3.2). The calculated surface enthalpies correspond to portlandite-vacuum surface enthalpies. Portlandite - vacuum surface enthalpies should essentially reflect the interface energies for portlandite in any gaseous phase, as long as the number of adsorbed molecules and e.g. the interaction with the gas phase is negligible. As such the calculated portlandite-vacuum surface enthalpies should reflect such properties as cleavage planes or low energy planes, found in the crystal habit of naturally occurring minerals. For portlandite, mineralogical literature values describe the [00.1] surface as a perfect cleavage plane indicating a low [00.1] surface energy [ABBN97]. The reported naturally occurring crystal habit is hexagonal plates [ABBN97]. Indeed these observations are consistent with the surface enthalpies calculated with FF2 and FF3. For those two force fields the enthalpy of the [00.1] surface was below 0.1 $\frac{J}{m^2}$, over 7 times lower then the enthalpy of the [10.0] surface which had the next lowest energy according to both force fields (see table 3.2). The equilibrium morphology according to the Wulff construction (see section 1.2) is that of hexagonal platelets for both force fields (see figure 3.2). Again this is consistent with experimental findings.

The values for the surface enthalpies for FF2 and FF3 can be compared to the experimentally determined surface enthalpy of portlandite in ambient conditions reported by Brunauer et al. [BKW56]. They estimated an overall surface enthalpy of 1.118 $\frac{J}{m^2}$ however it is not known what was the morphology of the portlandite crystals. Additionally the result might have been influenced by impurities present in the studied portlandite samples. Here the calculated surface enthalpies vary from 0.1 to 1.9 $\frac{J}{m^2}$ for FF2 and from 0.1 to 0.84 $\frac{J}{m^2}$ for FF3. Thus the values for FF2 are in slightly better agreement with the experimental values then the ones for

Table 3.1: Portlandite cell parameters calculated by energy minimization (EM) and molecular dynamics (MD) respectively and Voigt and Reuss bounds for the bulk elastic modulus (K) and shear modulus (G). Results for FF1, FF2 and FF3 compared to experimental results [Pet61, DGC+93, MC95].

	a (EM) [Å]	c (EM) [Å]	a (MD) [Å]	c (MD) [Å]	K_{voigt} [GPa]	K_{reuss} [GPa]	G_{voigt} [GPa]	G_{reuss} [GPa]
FF1	3.56	4.91	3.65	4.57	34.58	32.57	12.69	11.65
FF2	3.66	4.82	3.62	5.14	40.01	18.67	22.98	7.12
FF3	3.67	4.90	3.68	5.00	40.08	19.70	23.04	5.29
Exp	3.59	4.91	3.59	4.91	46.93	32.39	19.29	13.39

FF3, which are slightly lower. However taken into account the experimental uncertainties, the results for both force fields seem to be in fair agreement with the experimental results.

In contrast to FF2 and FF3, FF1 does not seem to capture the particularities of portlandite according to experimental observations. For the calculation of the surface enthalpies the additional angle dependent three body terms for surfaces have been employed according to Cygan et al. [CLK04]. If these angle terms are not included, the presence of the surface will lead to structural changes over the whole surface cell (see section 2.3.2) which leads to unrealistic surface energies. Even with the additional angle terms FF1 seems to miss important features of portlandite. While the surface enthalpies calculated with FF2 and FF3 vary by more than an order of magnitude depending on the surface orientation, the different surface enthalpies calculated with FF1 vary by no more than a factor of ~ 3. This means that FF1 fails to predict the perfect cleavage of the [00.1] plane, in fact according to FF1 the [00.1] surface has the same energy as the [10.2] surface. Additionally the predicted equilibrium morphology is rather equiaxed with large [10.2] facets, which is at variance with the hexagonal plate morphology reported experimentally. The average surface enthalpy calculated over all surfaces is about half the enthalpy calculated with FF2 and FF3. In other words the difference between the surface enthalpy reported by Brunauer et al. (1.118 $\frac{J}{m^2}$ [BKW56]) and the surface enthalpies calculated with FF1 (0.21-0.69 $\frac{J}{m^2}$) is quite big.

A possible reason for the difference between FF1 and the other force fields might be the much more shallow minima in the energy in function of the ion-ion distance due to the partial charge description (see section 3.1.1). Shallower energy minima can be expected to lead to lower defect energies for perturbations of the crystal structure and might thus be the cause of the lower interfacial energies and the smaller interfacial anisotropy observed with FF1. Since the aim of the current thesis is the study of solid - aqueous solution interfaces, the failure of FF1 to correctly describe the cleavage energies of portlandite seems worrying. It seems that both FF2 and FF3 would be better suited for our purpose.

Table 3.2: Portlandite-vacuum interfacial energies (i.e. cleavage energies) for different surface families. Results for FF1, FF2 and FF3.

surface hk.l	FF1 $[\frac{J}{m^2}]$	FF2 $[\frac{J}{m^2}]$	FF3 $[\frac{J}{m^2}]$
00.1	0.21	0.08	0.07
10.0	0.40	0.59	0.55
10.1	0.52	0.71	0.83
10.2	0.21	0.74	0.70
11.0	0.42	0.75	0.84
11.1	0.33	0.83	0.80
$1\bar{1}.\bar{1}$	0.69	0.71	0.83
11.2	0.29	0.60	0.62
11.3	0.33	0.66	0.60
$1\bar{2}.0$	0.38	0.73	0.84
20.1	0.36	1.92	0.74
22.3	0.43	1.16	0.80
average	0.38	0.79	0.69

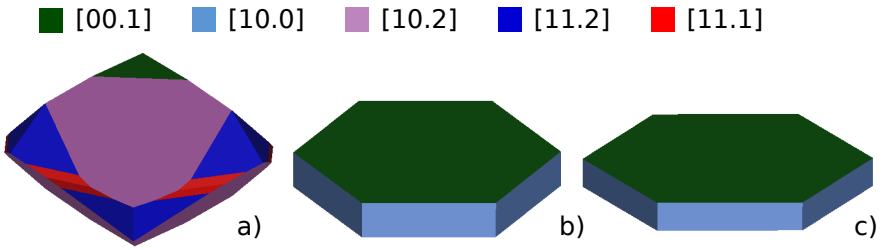

Figure 3.2: Calculated equilibrium morphology of portlandite in vacuum calculated with FF1 (a), FF2 (b) and FF3 (c).

3.1.5 Results for Water

Since water is an integral part of hydrated cementitious systems and very important for the study of interfaces, the performance of the different force fields for the description of water has been evaluated in some detail. To compare the structural details, the density of water (see table 3.3) and the oxygen-oxygen radial distribution function (RDF, see figure 3.4) at 300 ° K were calculated for a previously equilibrated box with 2048 water molecules during a NPT simulation over 30 ps. The results were then compared to experimental findings. The results for FF3 are almost indistinguishable from the experimental results. FF1 also gives very good results. FF2 on the other hand overestimates the density of the water by almost 30 %. Additionally the structuring of the water seems to be overestimated, which means that one observes higher peaks and lower minima in the RDF and the position of the peaks are shifted to larger distances. In other words there are clearly some issues with FF2 for the description of water. Pellenq et al. report a slightly different variant of FF2 in the supplementary materials

Table 3.3: Heat of vaporization (H_{vap}), specific heat capacity at constant pressure (C_p), self diffusion coefficient (D) and density (ρ) of water. Results for FF1, FF2 and FF3 compared to experimental results ([AV05]).

	H_{vap} $[\frac{kcal}{mol}]$	C_p $[\frac{kJ}{mol \cdot K}]$	D $[10^{-9}\ \frac{m^2}{s}]$	ρ $[\frac{g}{cm^3}]$
FF1	~8.83	~113.6	1.8 - 1.9	1.0
FF2	~11.20	~121.2	1.0 - 1.1	1.3
FF3	~11.30	~85.1	2.3	1.0
Exp	10.52	75.6	2.3	1.0

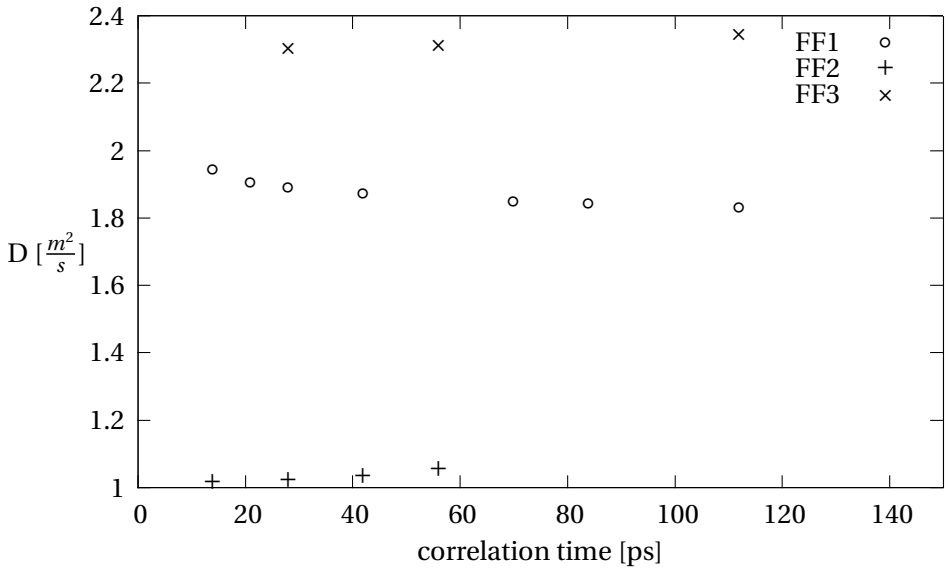

Figure 3.3: Dependence of the diffusion coefficient on the correlation time used for the calculation of the mean squared displacement for the different force field.

[PKS+09] with a changed short range interaction term between the oxygen and hydrogen of water. However, according to our calculations, this changed interaction term leads to an underestimated water desity (0.8 $\frac{g}{cm^2}$) and an self diffusion coefficient which is overestimated by an order of magnitude (~$14.3 \cdot 10^{-9}\ \frac{m^2}{s}$). Consequently we used the original parameters reported by de Leeuw and Parker [DLP98a].

To estimate the description of the thermodynamic properties, the enthalpy of vaporization ΔH_{vap} as well as the specific heat capacity at constant pressure C_p was estimated for the different force fields (see table 3.3). The heat of vaporization was estimated from the configurational energy of a NVT water simulation as compared to the configurational energy of a single water molecule. To estimate C_p, NPT simulations of a box with 256 water molecules were carried out, where the target temperature of the thermostat (T_{ext}, see section 2.4.1) varied during the simulations. T_{ext} was varied from 300 ° K to 500 ° K during 0.2 ns, then

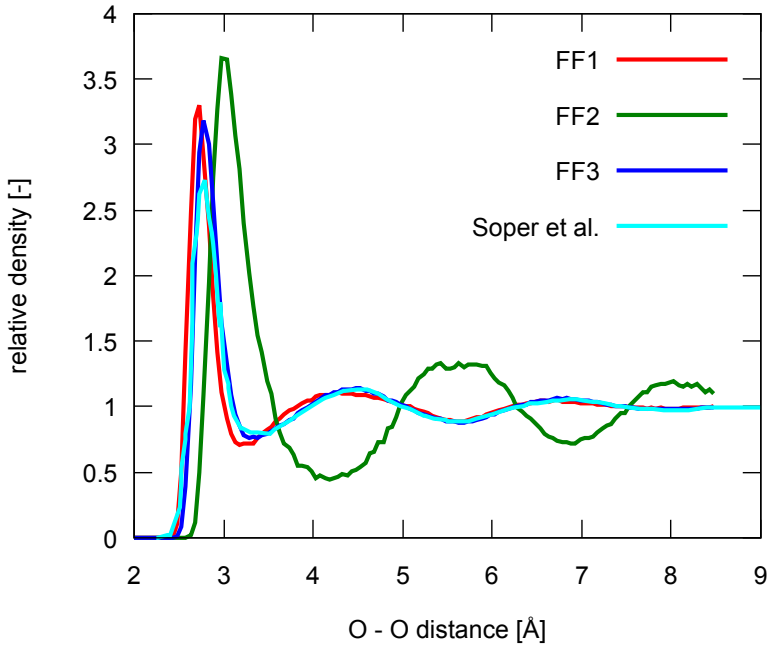

Figure 3.4: Calculated oxygen-oxygen radial distribution function for bulk water at 300 ° K for the different force fields as compared to the experimental result reported by A.K. Soper [Sop00].

decreased to 250 ° K during 0.3 ns. The calculations were carried out with LAMMPS [Pli95]. The specific heat capacity was then estimated as the slope of the configurational energy with respect to the temperature. The values for ΔH_{vap} and C_p are only approximate and self energy correction terms have been neglected. For FF3 these corrections lead to changes of about 10 % [AV05]. These missing correction terms taken into consideration the agreement between the calculated and the experimental value for ΔH_{vap} is fair for all considered force fields. For C_p on the other hand, FF3 seems to give a significantly better accuracy than the other force fields, which seem to overestimate the specific heat capacity.

Another interesting property is the self diffusion coefficient D of water. The self diffusion coefficient can be calculated according to the Einstein equation (equation 3.1, where $\vec{r}_i(t)$ is the position of water molecule i at time t). In practice the diffusion coefficient is estimated by calculating the mean squared displacement $MSD = \left\langle (\vec{r}_i(t) - \vec{r}_i(t_0))^2 \right\rangle$ over a certain correlation time from which the diffusion coefficient is extracted as the slope of the MSD as a function of time. However, since the diffusion coefficient is the limit of the slope for $t \to \infty$, the diffusion coefficient only converges for sufficiently large correlation times. On the other hand, as Mark and Nielsson have shown [MN01], often better statistics and hence a smaller variance of the estimated diffusion coefficent can be reached for smaller correlation times. To check whether convergence has been reached and to estimate its variance, the diffusion coefficient was estimated for different correlation times for NPT calculations of a water box with 2048 water molecules. The total simulation time was 245 ps for FF1 and FF3. For FF2 the total simulation

Table 3.4: 9 Å tobermorite cell parameters calculated by molecular dynamics. Results for FF1, FF2 and FF3 compared to experimental results [MBA99].

	a [Å]	b [Å]	c [Å]	α [°]	β [°]	δ [°]
FF1	11.63	7.34	9.83	98	89	89
FF2	11.25	7.34	10.07	97	89	89
FF3	11.37	7.24	12.53	98	80	90
Exp	11.16	7.30	9.57	101	93	90

time was only 150 ps, due to the higher computational cost. The values for the diffusion coefficient seem to be reasonably well converged, but some variation can be seen (see figure 3.3).

$$6Dt = \lim_{t\to\infty} \left\langle (\vec{r}_i(t) - \vec{r}_i(t_0))^2 \right\rangle \tag{3.1}$$

The spread of the diffusion coefficients for the different force fields are reported in table 3.3. Again FF3 gives the best estimate. FF1 slightly underestimates the diffusion coefficient but the calculated value is still within +/- 20 % of the experimental value. FF2 gives a significantly lower diffusion coefficient than experimentally observed. This is probably a consequence of the higher density and the stronger structuration of the FF2 water compared to experimental values.

3.1.6 Results for Tobermorite

Another component of importance for cementitious systems are silicates. In order to estimate the performance of the different force fields, to describe not only calcium but also calcium silicate systems, NPT simulations of 9 Å tobermorite have been performed for the different force fields (see table 3.4). For FF1 the maximum error on the cell parameters a, b and c is +/- 4.2 %, for FF2 it is +/- 5.2 %. All the differences between the calculated and the experimental angles of the crystal cell are less than +/- 5 degrees. For FF3 the errors are somewhat larger. The difference between c^{FF3} and c^{exp} is about 30 % of c^{exp} and the maximum error on the angles is 13 degrees. This indicates that the silicates are less well described by FF3 than by the other force fields. The reason for this might be, that the silicate parameters for FF3 are essentially the same as for FF2. However, due to the absence of the shells, the Si - O - Si and the Si - O - H bond angles are likely to be straightened out compared to FF2. This might be corrected with additional angle parameters.

3.1.7 Results for Portlandite-Water Interactions

As important as the description of the solid cementitious phases and water, is the description of water-solid phase interactions. With this in mind molecular dynamics calculations of a $[Ca^{2+}]_{aq}$ and two $[OH^{-}]_{aq}$ in a water box with 2045 water molecules were done. To estimate the solvation structure of the ions, the calcium (Ca) - water oxygen (O^{H_2O}), the hydroxyl oxygen (O^{OH}) - water hydrogen (H^{H_2O}) and the hydroxyl hydrogen (H^{OH}) - water oxygen (O^{H_2O}) nearest neighbor distances as well as the number of water molecules in the first solvation shell (coordination number CN) have been estimated form the radial distribution functions and compared to experimental values (see table 3.5). It has to be said that, while the first peak position in the radial distribution function and thus the nearest neighbor distance is well defined, the same can not always be said for the first minima. This means that, depending on the details of the radial distribution functions, the error on the coordination numbers can be as high as +/- 0.5.

The structure of the solvation shell of the calcium ion seems to be well described by all force fields. The nearest neighbor distances are within +/- 5 % and the coordination number within +/- 10 % of the results reported by Fulton et al. [FHBS03]. For the hydroxyl ion, the H^{OH} - water environment seems to be well described by FF1 and FF3, with similar errors for the calcium ion solvation shell. FF2 on the other hand seems to overestimate the number of water molecules in the hydration shell around the hydroxyl hydrogen by almost 15 %. Both the $O^{OH} - H^{H_2O}$ nearest neighbor distance and the number of water molecules in the first solvation shell around O^{OH} seems to be overestimated by all three force fields. However DFT Car-Parinello molecular dynamics simulations by Chen et al. [CIP+02] showed that the experimentally observed first neighbor peak is likely to be a mixture of different possible hydroxyl - water clusters. The one with the lowest $O^{OH} - H^{H_2O}$ distance and the lowest O^{OH} - water coordination number is a cluster where a hydrogen is being transfered from a water molecule to the hydroxyl group. This is a process that can not be described by any of the tested force fields, as the water molecules are predefined and can not change during the simulation. This would explain why the simulated distances and coordination numbers for the hydroxyl hydrogen are slightly larger than experimentally observed.

The coordination numbers calculated for FF2 are consistently higher than for both the other two force fields and the experimental results, especially for the hydroxyl ion. This is probably a consequence of the previously discussed higher density and stronger structuration of the FF2 water compared to reality (see section 3.1.5). The hydroxyl hydrogen - water oxygen distance might have been changed slightly compared to the original force field by the downscaling of the attractive part of the interatomic potential due to stability issues (see section 3.1.2), however the distance agrees well with the experimentally observed value.

In addition to the structural details, the dissolution enthalpy ΔH of portlandite according to the reaction below (equation 3.2) will give an indication of how well the portlandite-water interactions are described. Consequently the enthalpy (i.e. the total energy minus the pressure

Table 3.5: Heat of dissolution (ΔH) and nearest neighbor water distance ($X - O^{H_2O}$ for positively and $X - H^{H_2O}$ for negatively charged ions) as well as the number of water molecules in the first solvation shell (CN) for $[Ca^{2+}]_{aq}$ and $[OH^-]_{aq}$. Results for FF1, FF2 and FF3 compared to experimental results [BBI+03, FHBS03, LW06].

	ΔH [eV]	$Ca - O^{H_2O}$ [Å]	CN Ca [-]	$O^{OH} - H^{H_2O}$ [Å]	CN O^{OH} [-]	$H^{OH} - O^{H_2O}$ [Å]	CN H^{OH} [-]
FF1	-18.43	2.5	7.8	1.5	5.4	2.7	5.9
FF2	2.13	2.5	7.9	1.9	7.8	2.6	7.2
FF3	0.13	2.4	7.6	1.6	5.4	2.7	5.7
Exp	-0.19	2.4	7.2	1.4	3.7	2.6	6.3

times the volume, for more details see the DL_POLY manual [Smi12]) of the simulation box containing the calcium and the two hydroxyl ions was compared to the enthalpy of 2045 water molecules of pure water and a stoichiometric unit of portlandite. The results have been compared to the dissolution enthalpy of the reaction described in equation 3.2 according to the CEMDATA thermodynamic database [LW06]. The results can be seen in table 3.5.

$$Ca(OH)_2 \longrightarrow \left[Ca^{2+}\right]_{aq} + 2 \cdot [OH^-]_{aq} \tag{3.2}$$

By far the best result for the dissolution energy is given by FF3. For FF3 the stability of the aqueous ions seems to be underestimated by about 0.3 eV. A reason for this might be the previously discussed proton exchange event for the hydroxyl ion, which can not be described by the type of force field used here. However both the calculated and the experimental energies are very small, indicating a reasonable accuracy of FF3 to describe the portlandite - water interactions.

In accordance with the larger deviations in the solvation structures, the underestimation of the stability of the aqueous species by FF2 seems to be more important than for FF3. Their stability is underestimated by 2.3 eV. This difference starts to be rather important, however it is not unexpected due to the previously discussed problems of FF2 to accurately describe water.

Finally, despite the good description of the structure of the solvation shell, FF1 overestimates the stability of the aqueous species compared to portlandite by two orders of magnitude. This is a further indication that, due to the uncompensated partial charge description of the pair interactions in the solid, the energy minimas for portlandite are too shallow and thus the energy of the portlandite phase is underestimated.

3.1.8 Comparison with Results from Literature

In addition to the force field, the exact method employed will also determine the results. Therefore in this section current results are compared to previously reported results found in literature. There are several possible differences between the methods used by different authors, which might lead to slightly different results. For energy minimization the possible differences lay in the Ewald summation employed and/or the cutoff, the initial configuration of the atoms as well as the minimization algorithm employed. For molecular dynamics calculations possible differences lie in the Ewald summation employed and/or the cutoff, the time integration algorithm, the size of the simulation box, the thermostat and barostat employed as well as their relaxation times.

Radial distribution functions for FF1, FF2 and FF3 water can be found in [DLP98a] and [AV05, BRBK09] respectively. The radial distribution functions and densities for water reported here are essentially indistinguishable from results reported in literature.

As Mark and Nielsen showed, the calculated diffusion coefficient can vary substantially (up to +/- 7 %) with the number of water molecules in the simulation box, the correlation time over which the diffusion coefficient is calculated, the treatment of the long range interactions and whether or not and which thermostat is used [MN01]. The use of a barostat can have an even greater effect [DLP98a]. The diffusion coeffiecients reported here have been calculated for NPT calculations. Similar calculations were only reported by De Leeuw and Parker for FF2 [DLP98a]. Their calculated diffusion coefficient of $1.15 \cdot 10^{-9} \frac{m^2}{s}$ agrees well with our results. For FF1 Abascal and Vega calculated a diffusion coefficient of $2.08 \cdot 10^{-9} \frac{m^2}{s}$ for a NVT calculation[AV05]. Again, considering the influence the use of a barostat can have, the diffusion coefficients are in good agreement with results reported here. Finally Kalinichev et al. reported a value of $2.3 \cdot 10^{-9} \frac{m^2}{s}$ for bulk water FF1, however without giving any details of how this value was calculated [KWK07]. Our results lie about 17 % below that value. Given the possible variability of the diffusion coefficient whith the exact method employed, the observed difference does not seem to indicate any inconsistency, however more details about the calculation of the result by Kalinichev et al. would have to be known to draw any definite conclusions.

The heat of vaporization of water ΔH_{vap} reported here was roughly estimated for the NVT ensemble. For FF3 the value can be compared to the uncorrected value (11.99 $\frac{kcal}{mol}$) reported by Abascal and Vega also for the NVT ensemble [AV05]. This value and the value for the current calculations seem to be in good agreement, the difference between them being less than 6 %. For FF2 a value of 10.20 $\frac{kcal}{mol}$ for ΔH_{vap} has been reported by de Leeuw and Parker for the NPT ensemble [DLP98a]. Considering the different ensemble used, the values are again in good agreement, with a difference of less than 10 %.

The estimates reported here for the specific heat capacity at constant pressure C_p have not been checked for convergence. In order to check the convergence, a second series of calculations with a different rate for the temperature variation should be done. However the aim of the calculations was a rough estimate rather than an exact result. Thus no convergence check

was done. In the literature values for C_p have been reported for FF3 (uncorrected value: 88.2 $\frac{kJ}{mol}$) by Abascal and Vega [AV05] and for FF2 (98.2 $\frac{kJ}{mol}$) by de Leeuw and Parker [DLP98a]. The value reported for FF1 was calulated from a series of calculations at different temperatures. The difference between the value reported by Abascal and Vega and the value reported here is less than 5 %. For FF2 the C_p has been calculated form the fluctuation of one single molecular dynamics calculation. Here the difference between the results is more imoportant, being in the order of 20 %. As mentioned before, some more work would have to be done here to get a clear picture of the convergence of the different methods.

Results for portlandite bulk calculations have been reported by several authors [KPH03, KK02, CLK04]. The energy minimization results for FF1 reported by Kalinichev et al. [KK02] and for FF2 and FF3 reported by Kerisit et al. [KPH03] are all within 1% of the current results. The results for FF1 reported by Kerisit et al. differ slightly from current results (especially the values for the elastic constants); it is possible that Kerisit et al. used a slightly different version of the CLAYFF force field which does contain angle dependent terms for Ca-O-H [CLK04].

For FF1 results of portlandite molecular dynamics calculations were reported by Cygan et al. [CLK04]. Their results for the unit cell parameters (a,b: 3.69 Å, c: 4.80 Å, α: 82 °, β: 98 °, γ: 122 °) are not in very good agreement with our results (a,b: 3.65 Å, c: 4.57 Å, α: 87 °, β: 90 °, γ: 120 °). For both the calculations reported by Cygan et al. and our results, the difference between the cell parameters calculated with energy minimization and by molecular dynamics is relatively big. The direction of the changes is the same for both calculations as well: a and b increase, c and α decrease. However for the results reported by Cygan et al., the angles relax much more than the distances, i.e. in addition to α, which decreases by 8 °, β (increase by 8 °) and γ (increase by 2 °) change as well. For the results reported here the changes of the angles are maximum 3 ° but the change of the c parameter is more important (0.34 Å compared to 0.11 Å). The difference between the different results can also bee seen from the root mean squared fluctuations of the cell parameters. Cygan et al. report fluctuations in the order of +/- 0.06 Å for the length parameters and in the order of +/- 1.3 ° for the angles. For our results the fluctuations of the length parameters were higher (in the order of +/- 1.3 Å) whereas the fluctuations of the angles were smaller (in the order of +/- 0.4 °). These changes between the parameters reported by Cygan et al. and our calculations might be a consequence of a different barostat that was employed. In our calculations we used the Melchionna modification of the Hoover barostat ([MCLH93] see section 2.4.2) whereas Cygan et al. used the Parinello-Rahman method [PR81]. Additionally the relaxation time of the barostat might have been different as well. A contributing factor to the observed changes with changed calculation method of maximum +/- 5 % on lengths and maximum +/- 8 ° on angles might be the previously discussed shallow energy minimas for FF1 (see sections 3.1.2 and 3.1.4). These shallow minimas, allowing a greater structural flexibility, might lead to bigger changes with changing simulation method.

In summary the energies calculated within the context of this work were within +/- 6 % of results reported in literature employing similar methods. If different methods or different

thermodynamic ensembles were employed, the differences on energetic properties could be up to +/- 20 %. For energy minimization the lengths and angles were in very good agreement with other results reported in literature, with differences on distances of less than +/- 1 % and less than 1 ° on angles. The maximum differences between results for molecular dynamics results were +/- 5 % on lengths and +/- 8 ° on angles.

3.1.9 Final Choice of Force Field

The three different force fields showed different strengths and weaknesses for describing different systems. For FF1 the main disadvantage is that the force field seems to have too weak energy minimas in the ion-ion interactions. Despite a probably better description of the long range coulombic interactions, due to the partial charge description, the shallower minimas in the short range ion-ion interactions seem to lead to a too large structural flexibility and a too low lattice energy of the solid phases. Accordingly the cleavage energies of the different surface orientations and the equilibrium morphology in vacuum do not seem to be consistent with experimental observations and the dissolution energy of portlandite is overestimated by two orders of magnitude. Additionally the charges for the ions (e.g. Ca^{2+}) have been optimized for the bulk solid phases and for aqueous solutes separately. However for ions at surfaces the charge is likely to be somewhere in between, an effect that is not taken into account by the force field. This might potentially lead to problems for surface calculations. The way forward to alleviate these short comings would seem to be the inclusion of covalent bond interactions for the solid phase and possibly a variable description of the partial charge depending on the local structural environment (see e.g. [SG00]). However this development would be very time consuming and would therefore be outside the frame of the current thesis. Accordingly FF1 was not used for further calculations.

FF2 on the other hand, while giving a good description of the solid phases and the cleavage energies, leads to a water model with a too high density and an overestimated structuring. This in turn seems to lead to an error of the dissolution energy of portlandite of about 2.3 eV. This is likely to influence the solid - water interface as well as adsorption energies. A way to enhance the performance of this force field would be to reparametrize the water. However, since water is notoriously difficult to parametrize, this would probably be very time consuming. Additionally, due to the presence of oxygen shells for a varying oxygen polarizability, the maximum timestep to employ with this force field is more than three times lower than the time step possible with the other force fields. This would increase the computational cost of all the calculations reported here. Consequently FF2 was also not chosen for further calculations.

This leaves FF3. FF3 gave the best description of the properties of water, the best estimation of the dissolution energy as well as a good description of portlandite and portlandite cleavage energies. However the results for the cell parameters of 9Å tobermorite differed from the experimental results by about +/- 30 % for the cell lengths and by more than 10 ° for the angles. This needed to be rectified before the force field could be used for cementitious systems. One

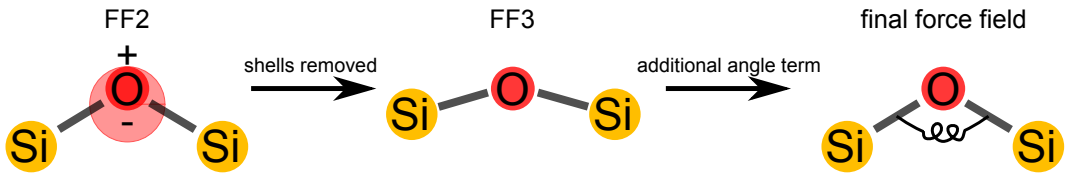

Figure 3.5: Schematic illustration of the effect of the removal of the oxygen from FF2 and the subsequent angle correction to get a correct $Si - O^{OX} - Si$ angle.

possible cause for the poor description of silicates is the removal of the shells from FF2 for the derivation of FF3. The removal of the shells is likely to straighten out the X-O-X bond angles. Thus the inclusion of X-O-X angle terms might lead to a better description of the silicate phases. This seemed to be a more feasible approach and less time consuming than to try to enhance FF1 or FF2. Therefore FF3 was chosen for further calculations.

3.2 Enhancement of Force Field

As mentioned previously, the originally chosen force field, FF3, did not describe silicate containing systems very well. Therefore some enhancements of the force field were necessary. The first step was to replace all oxygen - oxygen interactions with those developed for silicate systems by de Leuuw and Parker [dLPCP00]. This lead to a better description of the silicate phases while the description of the pure calcium phases remained good (see tables 3.7 and 3.8, portlandite cell parameters calculated with the original force field: a = b = 3.68, c = 5.00, α = β = 90 °, γ = 120 °).

The parameters for the solid structures of the original force field was derived from FF2 by removing the oxygen shells to be compatible with the TIP4P/2005 rigid molecule water model. If we consider a $Si - O - Si$ group, for FF2 the negatively charged shell of the oxygen is pulled towards the two Si ions and away from the positively charged core. This will bring the two Si ions closer together and decreases the $Si - O - Si$ angle. This means that if the oxygen shells are removed, the $Si - O - Si$ angle are straightened out (see figure 3.5). In order to counter this effect, new harmonic angle potentials were introduced to correct the angle. The parameters for the $Si - O - Si$ angle term were chosen such, as to fit the $Si - O - Si$ angle in quartz to the experimentally observed value. In addition to the $Si - O - Si$ angle, a term for the $Si - O - H$ angle was also added to FF3. The final angle parameters can be seen in table 3.6. The complete parameter set of the final force field can be found in annex C.4.

The final set of parameters was tested for a series of 6 different calcium and silicate structures (see table 3.7). The structures seem to be well described with the length parameters deviating by no more than +/- 4 % and the angles by no more than 8 ° from the experimental results (see table 3.7).

Table 3.6: Additional angle terms for the Si-O-Si bond angles and the Si-O-H angles for the final force field employed for this thesis.

Three-body potential $k \cdot (\theta - \theta_0)^2$	k $[\frac{eV}{rad^2}]$	θ_0 [°]
$Si - O^{OX} - Si$	2.1	132.0
$Si - O^{OH} - H^{OH}$	2.1	141.5

Table 3.7: Lattice parameters calculated by molecular dynamics of different crystals for the final force field employed for this thesis compared to experimental values reported in literature.

	a [Å]	b [Å]	c [Å]	α [°]	β [°]	γ [°]
caluclated values						
lime	4.82	4.82	4.82	90	90	90
portlandite	3.67	3.67	4.81	90	90	120
alite T_3	11.94	14.36	14.00	105	94	90
quartz	4.99	4.99	5.50	90	90	120
14 Å tobermorite	6.85	7.26	27.95	90	93	123
9 Å tobermorite	11.61	7.27	9.96	98	85	89
experimental values						
lime [PKW48]	4.80	4.80	4.80	90	90	90
portlandite [DGC$^+$93, Pet61]	3.59	3.59	4.91	90	90	120
alite T_3 [DlTDVCA08]	11.64	14.17	13.64	105	95	90
quartz [LPW80]	4.92	4.92	5.41	90	90	120
14 Å tobermorite [BMK05]	6.74	7.43	27.99	90	90	123
9 Å tobermorite [MBA99]	11.16	7.30	9.57	101	93	90

3.3 Error Estimation

In order to correctly interpret results, it is important to have an idea of the error on them. As for experiments, the error on simulations is usually composed of two parts, an error coming from random fluctuations and a systematic error coming from the theory and the method used. Let us for example consider experimental zeta potential measurements (see section 1.4.3). What is really measured experimentally is an average velocity of particles in a field. The exact velocity measured will vary depending on the browninan motion of the particles in the measuring volume, their size, the temperature etc. This will lead to random fluctuations of the value around a certain average value. Consequently this average value can only be determined with a certain error. Many statistical tools have been developed to deal with this error and to determine whether a result is statistically relevant (see section 5.3.2). Consequently an estimation of this error is usually given for experimental results. The measured average velocity measured by the zeta potential measurement is then, in general, converted to an

Table 3.8: Portlandite-vacuum interfacial energies (i.e. cleavage energies) γ for different surfaces and Voigt and Reuss bounds for the bulk elastic modulus (K) and shear modulus (G) calculated with energy minimization for the original and the final, enhanced force field employed for this thesis. Errors indicated are ϵ_{est}^{FF} (see equation 3.5) on the portion of the surface with relaxations ≥ 0.1 Å.

		original	final	
$\gamma^{[00.1]}$	$[\frac{J}{m^2}]$	0.073	0.096	± 0.019
$\gamma^{[10.0]}$	$[\frac{J}{m^2}]$	0.551	0.597	± 0.064
$\gamma^{[10.1]}$	$[\frac{J}{m^2}]$	0.833	0.737	± 0.097
$\gamma^{[20.3]}$	$[\frac{J}{m^2}]$	0.916	0.797	± 0.123
K_{voigt}	[GPa]	40.08	42.37	-
K_{reuss}	[GPa]	19.70	21.92	-
G_{voigt}	[GPa]	23.04	22.86	-
G_{reuss}	[GPa]	5.29	5.03	-

estimated electrostatic potential and sometimes even to a surface charge. To be able to do this conversion, certain theories are applied and certain approximations are done (e.g. particles are assumed to be spherical, a diffuse layer is assumed to follow the Gouy-Chapman theory ... see section 1.4.3). This will lead to a systematical error, the size of which depends e.g. on the shape and the size of the particles in question etc. An estimate of this type of error is rarely given for experimental results, as the systematical error is usually assumed to be much smaller than the error coming from the random fluctuations, although this might not always be the case.

For simulations the situation is quite different. Although there often are random fluctuations e.g. due to the temperature fluctuations in molecular dynamics that are controlled by the thermostat (see section 2.4.1) the generally much larger amount of data that is collected from the simulation means that the resulting error on the calculated average properties is very small. In fact when checking for convergence of the simulations, it is often made certain that the variation of the average quantities becomes very small. This means that, contrary to experimental measurements, the error of simulations is usually dominated by the systematical error. Therefore, in order to avoid their erroneous interpretation as an error estimate, no standard deviations are usually given for molecular dynamics result. If they are specified they are usually called root mean squared fluctuations.

Contrary to the random fluctuations no generalized methods exist to estimate the systematical errors. For some numerical methods an analytically developed error estimate is possible (see e.g. section 2.5.2), however this is not possible for an estimation introduced by approximating the forces between the atoms by the empirical force field employed. In order to get an idea of the magnitude of this force field error, what is generally done is, that the result of a certain number of properties for similar systems as the one of interest are compared to experimental results. However it is often difficult to asses what this means for the other results. Therefore

an effort was done within this thesis to develop a quantitative, empirical error estimate on energies and distances, based on calculations of experimentally well known properties, that can then be used as an error estimate of the classical atomistic results presented in this thesis. Such an approach has, to our knowlege, not been attempted before.

The errors on distances and angles can be estimated from calculations done with the final force field for solid structures (see table 3.7), water (see figure 3.4) and $\left[Ca^{2+}\right]_{aq}$ and $[OH^{-}]_{aq}$ aqueous species (see table 3.5). All errors on distances were smaller than +/- 5 % with the largest error of + 4.1 % being observed for the *c* parameter of the crystal cell of 9 Å tobermorite. In general distances are overestimated rather than underestimated, however underestimations are observed as well e.g. - 2.3 % for the b parameter of crystal cell of 14 Å tobermorite. This means that our estimated error on distance $\epsilon_{est}^{d,FF}$ is +/- 5 %.

The only distance that deviates by more than +/- 5 % is the $O^{OH}-H^{H_2O}$ distance of the aqueous hydroxyl ion $[OH^{-}]_{aq}$. This distance is overestimated by 14 %. As discussed in section 3.1.7, the origin of this larger error is likely to be the inability of the classically derived force field to describe proton exchange reactions.There are few structures where the proton exchange can be expected to have such a large effect on the structural environment as for the aqueous hydroxyl ion. However if any structure is simulated with the current force field where proton exchanges are expected to play an important part, the results should be treated with more caution and larger errors on distances (up to +/- 15 %) should be expected.

Angles were only calculated for the solid phases (see table 3.7). The maximum error of - 8 ° on angles was observed for the β angle of the crystal cell of 9 Å tobermorite. Generally the errors on angles were smaller, between 0 and 3 °. However to be on the safe side we estimate the error on angles to be $\epsilon_{est}^{a,FF}$ = +/- 10 °.

For both the distances and the angles the estimated error was similar to the maximum difference observed between current results and results reported in literature using similar conditions (see section 3.1.8). Although the highest differences between current results and the literature were observed for FF1, which seemed to show larger variations with the method employed than FF3, this indicates that part of the estimated errors on distances and angles might be from the method employed for the NPT molecular dynamic calculations rather than from the force field itself.

The final missing piece is the error estimation on the energies. To estimate the error on the energies, the reaction enthalpy of a series of reactions were estimated (see table 3.9). For a standard reaction (see equation 3.3) where a number of reactants R_i with stoichiometry s_i^R are transformed to a number of products P_j with stoichiometry s_j^P, the reaction enthalpy ΔH can be calculated from the enthalpy of the different reactants H_i^R and the enthalpy of the different products H_j^P according to equation 3.4. The different enthalpies were calculated from separate molecular dynamics calculations for each reactant and product. For aqueous solute species, their enthalpy could not be calculated directly. Instead the enthalpy of a water box containing the solutes was considered, this meant however that the enthalpy of the water box without the

solute species had to be added to the other side of the reaction. The thus calculated reaction enthalpies were then compared to experimental results based on the enthalpies reported in the CEMDATA thermodynamic database [LW06]. The agreement between calculated and experimental results is good (see table 3.9). The reaction with the highest relative error is the dissolution reaction of portlandite. Here one of the products for that reaction is the aqueous hydroxyl ion. As discussed previously, a limitation for the description of the aqueous hydroxyl ion is the inability of the classically derived force field to describe proton exchange. Consequently the error for that reaction can be expected to be a bit higher.

$$s_1^R \cdot R_1 + s_2^R \cdot R_2 + ... \longrightarrow s_1^P \cdot P_1 + s_2^P \cdot P_2 + ... \tag{3.3}$$

$$\Delta H = \sum_j s_j^P H_j^P - \sum_i s_i^R H_i^R \tag{3.4}$$

In the previous section differences between energies calculated here and energies reported in literature for the same force field and using a similar method were estimated to +/- 6 % (see section 3.1.8). For the current results we therefore consider that we have an error from the employed method of +/- 6.5 % on ΔH. In addition we have an error from the force field. This error will be on the individual enthalpies of the reactants H_i^R and the products H_j^P rather than on the reaction enthalpy ΔH. Based on the reactions in table 3.9 the force field error was estimated to be +/- 0.022 %. Together this leads to a final error estimation ϵ_{est}^{FF} according to equation 3.5. The final error estimates ϵ_{est}^{FF} for the different reaction enthalpies can be seen in table 3.9. The calculated enthalpies are all within the estimated error interval when compared to experimental data, even for the dissolution reaction of portlandite.

$$\epsilon_{est}^{FF} = 0.065 \cdot \Delta H + 0.00022 \cdot \left(\sum_j s_j^P \left| H_j^P \right| + \sum_i s_i^R \left| H_i^R \right| \right) \tag{3.5}$$

The error estimate was then tested on a final set of reactions (see table 3.10). These reactions were not included in the original set because they involve the dissociation of water i.e. the conversion of water molecules into hydroxyl groups. Since for the employed force field water molecules (rigid molecules) are described very differently from hydroxyl ions (morse bond between the oxygen and the hydrogen) there is a correction that has to be applied for each stochiometic water that is transformed into hydroxyl groups. Based on this second series of reactions, the correction factor per $H_2O + O \rightarrow 2 \cdot OH$ was estimated to be 3.45 eV with a standard error of 0.22 eV. The standard error of the correction factor was added to the error estimate. Again the error estimate encompasses all the differences between calculation and

Table 3.9: Calculated and experimentally determined (according to [LW06]) enthalpy of reaction ΔH for different reactions.

reaction	ΔH [eV]	ΔH_{exp} [eV]	ϵ_{est}^{FF} [eV]
$3 \cdot CaO + SiO_2 \longrightarrow C_3S$	-1.28	-1.20	0.19
$Ca(OH)_2 \longrightarrow \left[(Ca^{2+}) + 2 \cdot (OH^-)\right]_{aq}$	0.23	-0.19	0.42
$Ca(OH)_2 + SiO_2 \longrightarrow [CaSiO_4H_2]_{aq}$	2.31	2.46	0.61
$2 \cdot Ca(OH)_2 + SiO_2 \longrightarrow [Si(OH)_4]_{aq} + 2 \cdot CaO$	8.55	7.60	1.03

Table 3.10: Calculated and experimentally determined enthalpy of reaction ΔH for different reactions involving the dissociation of water. The reaction energies have been corrected for the different description of the hydroxyl groups as compared to water (correction of 3.46 +/- 0.22 eV per H_2O).

reaction	ΔH [eV]	ΔH_{exp} [eV]	ϵ_{est}^{FF} [eV]
$CaO + H_2O \longrightarrow Ca(OH)_2$	-1.08	-0.66	0.53
$2 \cdot H_2O + SiO_2 \longrightarrow [H_4SiO_4]_{aq}$	6.40	6.27	0.91
$\left[(Ca^{2+}) + 2 \cdot (OH^-) + (H_4SiO_4)\right]_{aq} \longrightarrow [CaSiO_4H_2]_{aq} + 2 \cdot H_2O$	-4.32	-3.62	1.44

results based on CEMDATA [LW06] (see table 3.10), serving as a certain validation of the developed error estimate (equation 3.5).

3.4 Summary

Three different force fields (FF1, FF2 and FF3) were tested for their description of portlandite, water, aqueous $\left[Ca^{2+}\right]_{aq}$ and $[OH^-]_{aq}$ species and 9 Å tobermorite. FF1 seemed to have a too large structural flexibility of the solid phases whereas FF2 gave relatively large errors for the water phase and was computationally more expensive. Therefore FF3 was chosen for further developments. However the original FF3 described the silicate phases with relatively large errors. This was corrected with a further development of the force field by, amongst other things, introducing a $Si-O-Si$ angle potential. Additionally the error of the corrected force field for distances ($\epsilon_{est}^{d,FF}$ = +/- 5 %) and angles ($\epsilon_{est}^{a,FF}$ = +/- 10 °) was estimated. Last but not least an expression (equation 3.5) for the estimation of the force field error on energies was developed and tested for the first time. The results obtained here indicate that the methods employed are reliable and correlate well with experimental data within the estimated error. It is hoped that in the future the methodology developed here will help establish the reliability of classical atomistic simulations and help in the choice and comparison of different force fields. Although we fully aknowledge that further statistical treatment would be needed to ensure its efficiency, we think the current results can serve as a prove of concept and do believe that the methodology has great potential value.

4 State of the Art of Portlandite Growth and Morphology

In this chapter an overview of the state of the art knowledge about portlandite is given with a special focus on the growth and morphology of portlandite. First the role of portlandite in the cement microstructure is reviewed. Then experimental knowledge of surface energies as well as the growth and resulting morphology of portlandite in different chemical environments is outlined.Thirdly the colloidal stability of portlandite, being important to understand growth and morphology in different environments, is discussed. Finally the theoretical work on portlandite reported in the literature is summarized.

For portlandite (i.e. calcium hydroxide, $Ca(OH)_2$ or CH in cement notation) the crystal structure is well known and has been previously reported [Ric04, Pet61, DGC+93]. The crystal structure consists of calcium sheets, terminated on each side by hydroxyl groups, with the hydrogen pointing towards the interlayer space (see figure 4.1). The crystal lattice is trigonal and the calcium ions are octahedrally coordinated by the hydroxyl groups. The crystallographic plane parallel to the layers ([00.1]) is reported to be a perfect cleavage plane [ABBN97]. Additionally the vibrational and thermal movement of the atoms in the calcium hydroxide crystal has been studied by several authors [DGC+93, BCM63, AOT11, BLOD01].

4.1 Role of Portlandite in Cementitious Systems

Within ordinary portland cements (OPC) hydrated for 100 days, calcium hydroxide accounts for 15-25 % wt of the structure [Dia01]. Often CH particles are observed closely intermixed with C-S-H [Gro81, RG93, CSV+10]. Calcium hydroxide plays a crucial role in buffering the pH within the pore solution of cement paste, thus helping to protect concrete reinforcement from corrosion. On the other hand it is susceptible to leaching, more so than other hydrates, such as C-S-H [Gla01]. Despite the layer structure with relatively weak interlayer bonds, calcium hydroxide does not appear to be the weak link upon fracture of the cement paste. In fact both the strength and the elastic modulus of CH is comparable to that of hydrated cement paste [MC95, Min01]. Fracture analysis shows that in young concretes (< 1 month)

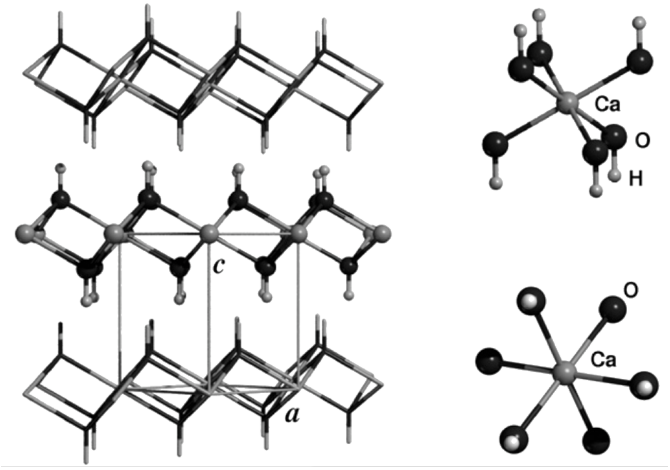

Figure 4.1: Crystal structure of portlandite, taken from [UZWTC09]

cracks will propagate preferentially in the C-S-H phase and around CH crystals and in some cases CH even seems to stop cracks. In older concretes most cracks will pass seemingly indiscriminately through both C-S-H regions and portlandite grains. Equally the interface between the CH grains and the C-S-H does not seem to be a weak link. In fact the majority of observed fractures were intragranular rather than along the interfaces indicating a strong CH - C-S-H interface [Ber72, Min01]. However in concrete, portlandite in the interfacial transition zone between aggregates and cement paste seems to be larger and preferentially orientated with the c-axis perpendicular (i.e. with the layer planes parallel) to the surface of the aggregates [Dia01, HAM$^+$03, DMWZ88, OMB95]. This seems to lead to a weakening of the interfacial transition zone for crack propagation to which other factors such as a higher porosity contribute as well [Min01, OMB95]. The thus observed trends seem to indicate that dispersed microcrystalline CH is not detrimental and may even be beneficial to the mechanical strength of hydrated cement paste [CSV$^+$10] whereas large oriented portlandite crystals or agglomerates seem to weaken the paste [Gro81, Min01]. However the effect of portlandite is often obscured by other convoluted factors. High strength concrete for example, which has a low water to cement ($\frac{w}{c}$) ratio, generally has the same amount of portlandite but the individual particles are smaller, which is probably contributing to the strength increase. At the same time the total porosity of the concrete decreases with decreasing $\frac{w}{c}$ ratio, which will also increase the strength. This makes the effect of portlandite morphology on cement strength difficult to quantify [Gla01].

4.2 Growth and Morphology of Portlandite

The growth mechanism of portlandite was studied in some detail by V.S. Harutyunyan et al. [HKM$^+$09]. Harutyunyan et al. observed the hydration of ASTM Type II Portland cement particles with the addition of 6 % $C_4A_3\overline{S}$ (in abreviated cement notation, full chemical formula: $4CaO \cdot 3Al_2O_3 \cdot SO_3$) in an aqueous solution saturated with respect to portlandite and gypsum

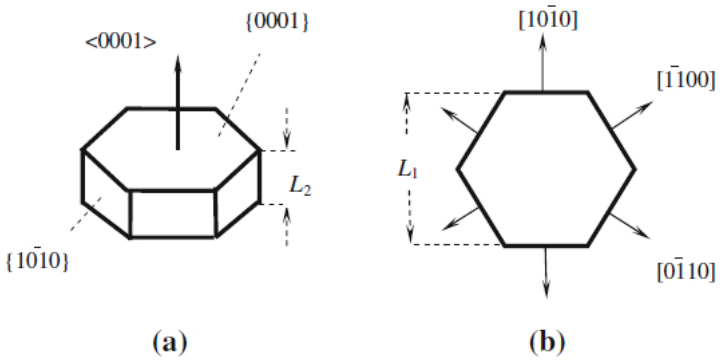

Figure 4.2: a: Hexagonal-prism shape of a portlandite crystallite with {00.1} basal and {10.0} lateral facets. b: View at a 0001 facet. Taken from [HKM+09]

(water to solid ratio: 50). They observed the growth of portlandite particles by soft X-ray transmission microscopy every 26.3 min on average for the first 118 min. The authors did not observe any portlandite crystals at times t < 15 min corresponding to the nucleation period. They supposed the growing nuclei to be quasi-spherical and estimate their growth rate (0.003 $\frac{\mu m}{min}$) and the nucleus-water interfacial energy (0.114 $\frac{J}{m^2}$). In the period following the nucleation (15 min < t < 25 min) the portlandite crystals begin to grow and start assuming the shape of hexagonal platelets with an maximum aspect ratio of $\frac{L_1}{L_2} = 2.7$ (def. L_1 and L_2 see figure 4.2). After that the aspect ratio slowly decreases again until a stable value of $\frac{L_1}{L_2} = 2.5$ is reached. During that period (15 min < t < 118 min) the mean growth speed was estimated to be $V_1 = 0.005\ \frac{\mu m}{min}$ in [00.1] direction and $V_2 = 0.014\ \frac{\mu m}{min}$ in [10.0] direction.

An earlier study of Klein and Smith [KS68] reports a lower CH-water interfacial energy of 0.065 J/m^2. Their estimation was based on the nucleation kinetics of CH particles precipitated from a sodium hydroxide solution to which a calcium nitrate solution is added. Likely causes for the different values, apart from experimental uncertainties, are the different nucleation theories taken into account (Harutyunyan et al. suppose a linear growth of all particles from t=0 whereas Klein and Smith use stochastic theory to describe the rate of nuclei formation) as well as the different composition of the solution from which the CH particles grow (in the work of Harutyunyan et al. silicates, sulfates and aluminates as well as other ions were present in the solution whereas the coprecipitation experiments of Klein and Smith contained only sodium and nitrate ions).

Both the CH-water interfacial energies estimated by Harutyunyan et al. and by Klein and Smith are about ten times lower than the value given in a earlier study by Brunauer et al. [BKW56] for the surface enthalpy of portlandite (1.118 $\frac{J}{m^2}$). Brunauer et al. estimated the surface enthalpy from the variation of solution enthalpies with varying surface area. This indicates that the presence of water significantly reduces the portlandite interfacial energy. However there are also other factors that might contribute to the difference between the estimated CH-water interfacial and CH surface energies. Firstly the chemistry of the sample studied by

Brunauer et al. was again slightly different from both the samples studied by Harutyunyan et al. and by Klein and Smith. The different portlandite samples studied by Brunauer et al. contained various amounts of sodium hydroxide, magnesium hydroxide, calcium carbonate and water. Although the authors did try to account for these impurities, the result might have been influenced if some of the impurities (namely the water) interacted strongly with the surfaces. Secondly both the particles observed by Harutyunyam et al. and by Klein and Smith were still growing and displayed a very distinct growth morphology whereas the morphology of the particles observed by Brunauer et al. was not reported and thus it is possible that the powders were far from equilibrium or growth morphology which might increase the surface energy. Finally while Brunauer et al. reported surface enthalpies, both Harutyunyan et al. and Klein and Smith reported surface free energies. However it is generally believed that the surface free energy of crystals with strog ionic character are dominated by the surface enthalpy and that the surface entropy plays a secondary role at room temparature [TSB+99, Jur54].

Growth over longer time scales was observed by Berger and McGregor [BM73]. They observed the influence of temperature and water to solid ratio on the growth of portlandite particles after mixing C_3S and water. One part of the mixture was placed between glass slides and observed periodically with an optical microscope, a second part was used for calorimetry measurements. Nucleation generally occurred after 1 to 6 hours, the nucleation slowing down with increasing water to solid ratio and with decreasing temperature. Nucleation was observed predominantly either at or near the C_3S particle surfaces, the resolution of the optical microscope being insufficient to distinguish between the two. Several minutes after the observation of the first crystals additional crystals were observed, the latter having either nucleated later or initially grown at a lower speed.

Berger et al. reported that after nucleation all mixtures with a water to solid ratio $\frac{w}{s} \geq 0.5$ showed initial rapid growth parallel to the c axis ([00.1] direction in figure 4.2) which subsequently slowed down or stopped and was followed by slower growth perpendicular to the c axis. For a water to solid ratio $\frac{w}{s} < 0.5$ initial growth in [00.1] direction was observed for some particles whereas others grew in all directions throughout the study. As probable causes for a change in the relative growth speed Berger and McGregor listed a change in the calcium hydroxide concentration in the solution and the adsorption of silicates at some surfaces, resulting in growth poisoning. They also observed protuberances perpendicular to the c axis developing towards the end of the growth. This observation was most marked for samples with a water to solid ratio of 1.0 and least for samples with a water to solid ratio of 0.3. As a possible reason spatial constraints on the growing portlandite particles due to undissolved C_3S particles was listed. In general the euhedral character of the portland grains increased with increasing water to solid ratio. Finally the portladite crystals formed at lower temperatures seemed to be more elongated parallel to the c axis than those formed at higher temperatures and the number of crystals per mm^2 decreased with decreasing temperature.

All in all the growth observed by Berger and McGregor does not seem to correspond to the observations made by Harutyunyan et al. who observed hexagonal platelets only and not the

Table 4.1: Influence of different admixtures on the morphology of portlandite formed upon hydration of C_3S after ref [BM72]

hexagonal				irregular
$\frac{L_1}{L_2} > 2$	$\frac{2}{3} < \frac{L_1}{L_2} < 2$		$\frac{L1}{L2} < \frac{2}{3}$	
$CuCl_2$	Control	CaF_2	$NaBr$	$Cu(N0_3)_2$
$LiOH$	$(NH_4)_2CO_3$	NaF	$BaCl_2$	$Pb(N0_3)_2$
$NaOH$	$CdNO_3 \cdot 4H_20$	Li_4SiO_4	$SnCl_2 \cdot 2H_20$	maleic acid
$Ca(OH)_2$	$(NH_4)_6Mo_70_{34} \cdot 4H_20$	$AgNO_3$	$NaNO_3$	Ca lignosulfate A
$MnSO_4$	ammonium oxalate	AlF_3	NH_4NO_3	glycolic acid
$CaSO_4 \cdot 2H_2O$	$MgSiF_6 \cdot 6H_20$	MgO	$Al(N0_3)_3$	mandelic acid
$CuSO_4 \cdot 5H_2O$	Ca formate	$Al(OH)_3$	$FeCl_3.6H20$	salicylic acid
$FeSO_4$	Ca stearate	MnO_2	$LiCl$	
ZnO	Ca lignosulfate B	CuO	$Fe(N0_3)_3$	
$(NH_4)_2SO_4$	Ca lignosulfate C		$CdSO_4 \cdot 8H_2O$	
$CaSO_4$			$CaCl_2$	
$CaSO_4 \cdot \frac{1}{2}H_2O$				
K_2SO_4				
$MgSO_4 \cdot 7H_2O$				
ariline green				
Ca acetate				

rather irregularly shaped particles Berger and McGregor observed. However there are many differences between the two studied systems. First of all the time scale and spatial resolution are different; Berger and Mc Gregor observed the first particles within 1 to 6 hours whereas Harutyunyan et al. did all their measurements at a time $t < 118$ min after mixing. The size of the particles observed by Harutyunyan et al. was up to $1\mu m$ whereas the ones observed by Berger and McGregor were more of the order of $100\mu m$. Finally the chemical environment of the growing particles was different. Harutyunyan et al. used Portland cement with 6 % $C_4A_3\overline{S}$ addition and hydration took place in a solution saturated with respect to portlandite and gypsum whereas Berger and McGregor used only C_2S and hydration took place in distilled water. This means that not only were there more different species in solution with the system studied by Harutyunyan et al. but the concentration gradients around the anhydrous particles was likely to be different as well.

4.3 Influence of Chemical Environment on the Growth and Morphology of Portlandite

The influence of the different chemical environments (i.e. different admixtures) on the morphology and number of portlandite particles formed upon hydration of C_3S was studied by Berger and McGregor [BM72]. The water to solid ratio of the mixtures was 1 and 1 % admixtures based on the weight of C_3S was added. Hydration took place in between glass slides and

Table 4.2: Influence of different admixtures on the number of portlandite particle number density formed upon hydration of C_3S after ref [BM72]

$1-5\frac{crystals}{mm^2}$	$6-15\frac{crystals}{mm^2}$		$16-30\frac{crystals}{mm^2}$	$>30\frac{crystals}{mm^2}$
$CuCl_2$	control	aniline green	$LiCl$	$Ca(OH)_2$
$FeCl_3 \cdot 6H_2O$	$(NH_4)_2CO_3$	Ca acetate	$BaCl_2$	$LiOH$
AlF_3	$Al(NO_3)_3$	Ca formate	NaF	$NaOH$
NH_4NO_3	$Cu(NO_3)_3$	glycolic acid	$Al(OH)_3$	Ca lignosulfonate C
$Fe(NO_3)_3$	$Pb(NO_3)_2$	mandelic acid	$Cd(NO_3)_2 \cdot 4H_2O$	
$AgNO_3$	Li_4SiO_4	salicylic acid	CuO	
$MgSiF_6 \cdot 6H_2O$	$(NH_4)_2SO_4$	$CaSO_4 \cdot \frac{1}{2}H_2O$	MgO	
ammonium oxalate	$NaBr$	$CuSO_4 \cdot 5H_2O$	$CaSO_4 \cdot 2H_2O$	
Ca lignosulfonate A	$CaCl_2$	$CdSO_4 \cdot 8H_2O$	$MgSO_4 \cdot 7H_2O$	
Ca lignosulfonate B	CaF_2	$SnCl_2 \cdot 2H_2O$	K_2SO_4	
maleic acid	$NaNO_3$	$CaSO_4$	Ca stearate	
	MnO_2	$FeSO_4$		
	ZnO	$MnSO_4$		
	$(NH_4)_6Mo_7O_34 \cdot 4H_2O$			

the resulting crystals had sizes from one to several hundred μm. The crystals were observed by optical microscopy and the $\frac{L_1}{L_2}$ ratio as well as the number of particles observed per mm^2 at approximately equal degrees of hydration was measured. The results can be seen in tables 4.1 and 4.2.

Depending on the admixture, the morphology can change from hexagonal platelets with a ration $\frac{L_1}{L_2} > 2$ to hexagonal rods with an aspect ration of $\frac{L_1}{L_2} < \frac{2}{3}$. With the addition of other admixtures the particles loose their euhedral character and the shape of the particles becomes irregular. Based on their results (table 4.1), Berger et al. concluded that sulfates and hydroxides seem to endorse platelet formation whereas the addition of chlorides and nitrates seemed to provoke the formation of rods. Finally with the addition of organic acids the formed portlandite particles adopt an irregular shape. There was no clear tendency observed for the influence of the addition of different cationic species. As for the number of particles formed per mm^2 at equal degrees of hydration (table 4.2), hydroxide and, to a lesser extent, sulfates seem to provoke the formation of smaller and more numerous particles whereas nitrates seem to have an inverse effect. However the tendencies are less clear than for the aspect ratio.

The influence of the chemical composition of the solution on the morphology of portlandite has also been studied by A. C. Gray in his doctoral thesis [Gra90]. The studied portlandite crystals were produced by mixing a $NaOH$ and a $CaCl_2$ solution. Gray found that the ratio of calcium to hydroxyl had a significant influence on the morphology of portlandite. If the calcium concentration with respect to the hydroxyl concentration is increased from 1:20 to 1:1, the morphology of the precipitated particles changes from equiaxed, facetted particles to elongated hexagonal prisms (see figure 4.3). The authors also found that the replacement of

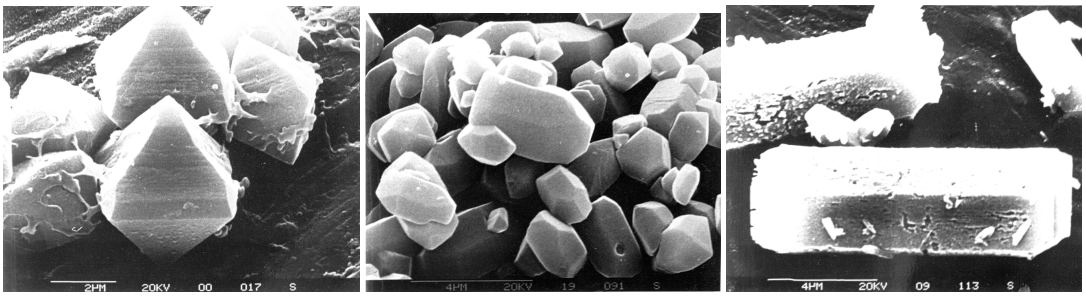

(a) (b) (c)

Figure 4.3: SEM images of portlandite particles produced by coprecipitation with different relative amounts of $NaOH$ and $CaCl_2$: $\frac{c^{NaOH}}{c^{CaCl_2}} = 20$ (a), $\frac{c^{NaOH}}{c^{CaCl_2}} = 2$ (b) and $\frac{c^{NaOH}}{c^{CaCl_2}} = 1$ (c). Images taken from [Gra90].

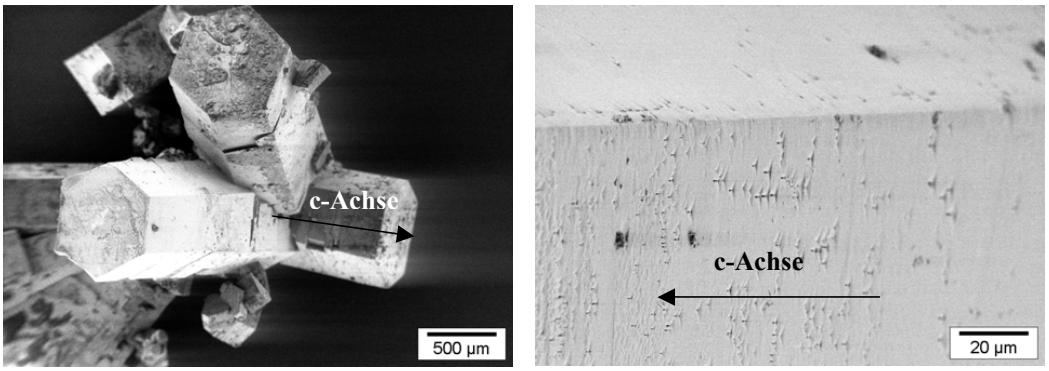

Figure 4.4: Morphology and surface quality of portlandite crystals produced by diffusion synthesis from KOH and $CaCl_2$ after 40 days of precipitation. Images taken from [Arn04].

water as the solvent by a water/ethanol mix, as well as the addition of acetate or propionate would change the morphology of the precipitated portlandite particles to hexagonal platelets.

The influence of different polymeric additives on the growth and morphology of portlandite was studied more recently by M. Arnold in his doctoral thesis [Arn04]. The studied portlandite particles were produced both by diffusion crystallization and by coprecipitation of a $CaCl_2$ and KOH solution. The morphology of the portlandite particles observed for the two precipitation methods was different (see figures 4.4 and 4.5). For the diffusion crystallization several crystals with differerent orientations seem to grow from the same initial nucleation point. The crystals seem to grow mainly in [00.1] direction leading to long hexagonal rods with smooth, well defined surfaces with some triagonal pits visible. The morphology of the portlandite particles produced by coprecipitation consists of isolated crystals with well defined facets. They are still slightly elongated in [00.1] direction, although less so than the crystals produced via diffusion precipitation. Three of the four studied additives (Bockcopolymer EA 3007, copolymer ZK 2247/144 1a (BASF AG) and citric acid) seem to be incorporated into the surface or even the interior of the crystals, only the addition of surface modified PS-latex does not seem to modify the surfaces. Generally the [00.1] surfaces seems to be less modified than the other

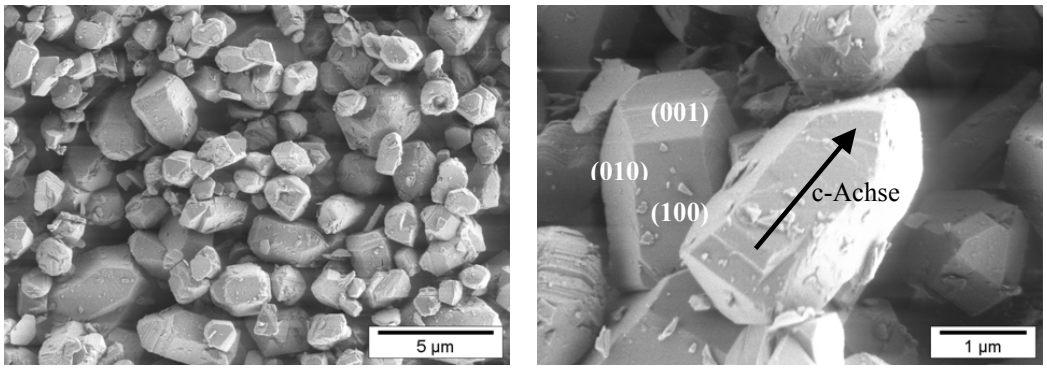

Figure 4.5: Morphology of portlandite crystals produced by coprecipitation of KOH and $CaCl_2$ after 4 minutes of precipitation. Images taken from [Arn04].

sufaces. Three of the four studied additives (Bockcopolymer EA 3007, surface modified PS-latex and citric acid) seem to lead to a reduction of the particle size whereas the addition of the copolymer ZK 2247/144 1a (BASF AG) seems to lead to larger particles.

A dependence of the morphology of portlandite crystals on the chemical composition of the surrounding solution can also be observed by comparing OPC systems with hydrated C_3S. C_3S is the main component of OPC, which also contains C_2S, several aluminate phases (C_4AF, C_3A), gypsum ($C\overline{S}$ or in full notation $CaSO_4 \cdot 2H_2O$) and others. Hydrated C_3S show few, large, irregularly shaped and randomly dispersed portlandite particles whereas the portlandite particles formed in OPC systems are smaller, more evenly dispersed and with more regular shape, some crystals even showing a hexagonal platelet morphology [GS07, KJ04]. To a certain extent these results are consistent with the results of Berger et al. [BM72] who observed that the addition of sulfates provoked the formation of more numerous and smaller particles, often with a reduced $L2$ dimension i.e. a hexagonal platelet morphology. E. Gallucci & K. Scrivener [GS07] tried to determine which components of OPC were responsible for the observed change in portlandite morphology. They studied C_3S systems with the addition of either C_3A or gypsum or both and compared the resulting portlandite morphology to that of pure C_3S and OPC systems. They observed that the addition of both C_3A and gypsum was necessary to observe potlandite morphology similar to that of OPC. Additionally the authors observed that nucleation seems to be favored in the neighborhood of gypsum.

4.4 Colloidal Stability of Portlandite

Another important mechanism to understand the nucleation and growth process of portlandite is the agglomeration of crystallites. Agglomeration of portlandite particles were studied by Rodrigez-Navarro et al. [RNRAOHH05] in dry and slaked lime putty (formed upon the hydration of CaO with stoichiometric water to CaO ratio and with an water excess respectively). The exact chemical composition of the limes was not given beyond the MgO content (0.2 - 0.6

wt %). For both systems the size of the crystallites was similar ($L_1 \cong 40-60$ nm and $L_2 \cong 10-30$ nm) and agglomeration was observed in both samples but the agglomeration factor of the dry lime putty ($F_{ag} = 4.03$) was almost double that of slaked lime putty ($F_{ag} = 2.29$). Most of the observed agglomeration was random but in both the dry lime putty and oven-dried slaked lime putty some oriented agglomeration was also observed through high resolution TEM and selected area electron diffraction (SAED). As redispersed oven-dried lime putty still retained a larger agglomeration factor than the original slaked lime putty, the authors concluded that the oriented part of the agglomeration is likely to be irreversible. This means that some of the non-euhedral particles described by Berger and McGregor might in fact be either oriented or random agglomerates rather than individual particles. In fact in hydrated OPC concretes only very few euhedral crystals can be observed [Dia01, SFM01]. Even at young ages the portlandite particles in hydrating OPC do not display a euhedral character and their shape becomes more and more irregular, probably because of the spacial constraint of the network of the simultaneously growing C-S-H [Dia01]. Whether these particles are random or oriented aggregates is difficult to assess, but at fracture surfaces oriented aggregates are often observed [SFM01]. However this might be a consequence of fractures preferentially going through large oriented aggregates of portlandite.

The agglomeration or aggregation behavior of portlandite will depend on the colloidal stability of the portlandite particles in solution. Traditionally the zeta potential is measured to get an idea about the colloidal stability and agglomeration behavior. The zeta potential is then linked to the colloidal stability via standard DLVO theory. There are several authors who did zeta potential measurements of portlandite [Arn04, PRM$^+$06, GDC$^+$02, ENK09]. The exact composition of the solution varied for the different measurements and consequently the values for the zeta potential varied from -14 to 34 mV (see table 4.3). Since the zeta potential depends on the exact composition of the solution, such variations are to be expected. However even the values reported for CH in water with only minimal additions varied from 7.35 to 34 mV, however the reliability of some of the values seem questionable either due to a lack of experimental conditions given or due to a reported pH that was not in agreement with equilibrium conditions. The remaining values are 7.35 mV for a system with minimal additions of about 0.01 mol/l KOH and 0.004 mol/l NaOH reported by Pointeau et al. [PRM$^+$06] and 23.5 mV for a system containing 2.9e-2 mol/l Lutensol AT 50 for colloidal stabilisation reported by Arnold et al. [Arn04]. To link the measured zeta potential to a colloidal stability according to conventional DLVO theory, two additional properties of the system have to be known: the shear plane distance d_s i.e. the distance form the particle surface at which the zeta potential is measured and the Hamaker constant of the portlandite - water system. Experimentally the shear plane distance can not be measured directly, which means that generally d_s is not really known. In cementitious systems the values assumed for d_s varies from 0 [PRM$^+$06] to 6 Å [LPJN11]. A value for the Hamaker constant of portlandite in water could not be found in literature. This means that it is difficult to give any definite indications on whether or not a portlandite solution is stable under any given conditions. The only information one can give is the energy barrier for agglomeration according to DLVO theory for different values of

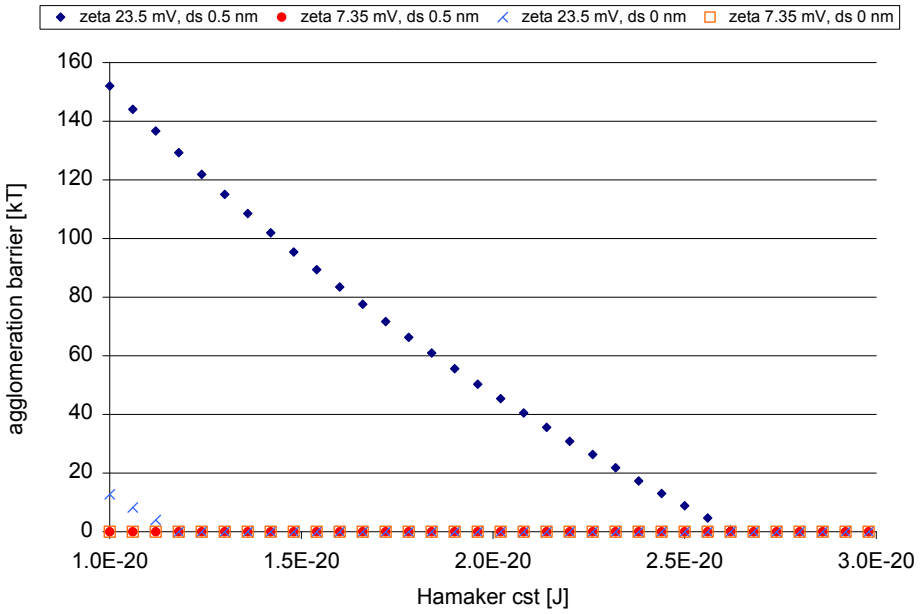

Figure 4.6: Energy barrier for agglomeration for zeta potential values reported in literature (see table 4.3) for different possible values of d_s and Hamaker constant.

d_s and the Hamaker constant and for the different values reported for portlandite in water (see figure 4.6). Only the higher zeta potential reported in literature for a d_s of 0 Å a non-zero energy barrier is predicted. This means that probably portlandite in pure water is not stable.

4.5 Theoretical Work on Portlandite

Not much theoretical or simulation work has been done on portlandite. Apart from the aforementioned studies of the vibrational properties of portlandite [DGC+93, BCM63, AOT11, BLOD01] there are a few studies looking at the importance of dispersion forces for the description of portlandite with computational quantum chemistry methods [UZWTC09]. Some work on portlandite-water interfaces has been done by Kalinichev et al. [KK02, KKY01]. The authors used molecular dynamics simulations to assess the chloride binding at portlandite surfaces. This issue is of interest as the binding of chloride and the accompanying reduction of cloride diffusion will slow down chloride penetration into reinforced concrete which might eventually attack the reinforcing steel. The authors simulated a slab of portlandite consisting of 8 x 8 x 4 crystallographic unit cells which were cleaved parallel to the Ca layers ([00.1] plane). Periodic boundary conditions were applied in all directions, long range coulombic interactions were calculated by Ewald summation and a gradual cutoff of 8.0 - 8.5 Å was applied to short range interactions. Between two periodic images of the portlandite slabs ~ 38 Å of water with four Cl^- ions and four counter ions (either Na^+ or Cs^+) were placed. The CLAYFF force field [CLK04] was used to describe atom interactions and the $Cerius^2$ simulation package was used for the simulations. The simulation cell was equilibrated for 80 ps and production run

was again 80 ps. The simulations were carried out at constant volume and temperature. All simulated ions adsorbed to the surface, the chloride ions forming hydrogen bonds with the hydroxyl groups of portlandite at the surface. The residence time of chloride ions at the surface was ~ 20 ps and their diffusion rate was 3.6e-6 $\frac{cm^2}{s}$ when they were directly absorbed at the surface (i.e. forming a inner-sphere surface complex), 1.5e-5 $\frac{cm^2}{s}$ when forming an outer sphere surface complex and 2.3e-5 $\frac{cm^2}{s}$ in bulk solution. About 65 % of the chloride ions were bound to the surface whereas 85 % of the Na^+ ions and 60 % of the Cs^+ were bound to the surface.

The calculations of Kalinichev et al. were essentially repeated by Pan et al. [PXW10]. Pan et al. also used CLAYFF. Essentially the only differences to the previous calculations were a slightly different force field for the solute species and a longer simulation time (200 ps equilibration + 200 ps production run). As one would expect for so similar simulations the reported results for the chloride binding were similar with 50 % of the chloride ions bound to the surface and diffusion rates of 3.7e-6 $\frac{cm^2}{s}$ for ions < 3 Å , 1.6e-5 $\frac{cm^2}{s}$ for ions at a distance of 3-10 Å and 2.3e-5 $\frac{cm^2}{s}$ for ions >10 Å from the surface. However for the counter-ions the results differ substantially, Pan et al. report only 25 % of the sodium ions to be bound to the surface which is in contrast to the 85 % reported by Kalinichev et al.

Kalinichev et al. also looked at the hydrogen bonding of water at the surface of portlandite and other hydrates using essentially the same simulation setup as described above [KWK07]. Kalinichev et al. report that according to their simulations the water molecules closest to the surface accept on average ~ 0.5 and donate ~ 1.0 hydrogen bonds to the surface OH groups. The total number of hydrogen bonds formed per water molecule increases from 3.5 in the bulk to 3.8 at the surface.

4.6 Summary

This chapter summarized current knowledge about the growth and morphology of portlandite. Most of the work done on the growth of portlandite was done for cementitious systems which means that composition as well as the water to solid ratio and hence the dissolution kinetics changed between the different studies reported in literature. Several authors [HKM$^+$09, KS68] tried to estimate the portlandite-water interfacial energy from the nucleation period. The estimated energies ranged form 0.065 to 0.114 $\frac{J}{m^2}$. These values are much smaller than the surface energy of portlandite in ambient condition estimated by Brunauer et al. (1.118 $\frac{J}{m^2}$) [BKW56].

In cementitious, sulfate containing systems, the initial growth morphology of portlandite seems to be hexagonal plates with a aspect ratio of $\frac{L_1}{L_2}$ = 2.5-2.7 [HKM$^+$09]. Over longer times scales the morphology of portlandite in cementitious systems does not seem to be so well defined [BM73]. Additionally the growth mecanism seems to change during the precipitation, possibly due to changes in hydroxide concentration or due to growth poisoning of portlandite by silicates[BM73].

The effect of the chemical composition of the solution from which portlandite is grown on its morphology was studied by several authors [GS07, BM72, Arn04]. In cementitious systems both sulfates and aluminates have to be present to change the morphology from large agglomerates to dispersed particles with sometimes hexagonal plate morphology [GS07]. In general sulfates seem to promote the formation of hexagonal platelets and smaller and more numerous portlandite particles in cementitious systems [BM72]. Chlorides and nitrates seem to elongate the portlandite particles in the [00.1] direction [BM72].

Based on results from literature the colloidal stability of portlandite can not be conclusively determined. Zeta potential measurements do exist in literature but they are not necessairily consistent (see table 4.3). However for slaked lime putty evidence for oriented irreversible agglomeration does exist [RNRAOHH05].

Finally the results of some atomistic simulation done on portlandite was summarized. Work has been done on the hydrogen bonding between the [00.1] surface and water as well as on the ability of portlandite surfaces to bind chlorides [KWK07, KK02, PXW10]. According to Kalinichev et al the portlandite surfaces seem to both donate to and accept hydrogen bonds from the water molecules [KWK07]. Both Kalinichev et al. and Pan et. al. showed that the diffusion coefficient of sodium, chloride and cesium ions is reduced by about an order of magnitude at the surface of portlandite. However there were some variations between the calculations with respect to the ability of portlandite surfaces to bind the different ionic species.

Table 4.3: Different values for zeta potential ζ measurements with error $\Delta\zeta$ reported in literature for portlandite in aqueous solutions with different compositions. The ionic strength I_c, the Debeye length κ^{-1} and the pH are shown as well. An estimated value for the surface charge (σ_{est}) for an supposed shear plane distance d_s equal to 0.5 nm according to Aschauer et al. [ABMMB11] has been estimated if enough experimental details were available. Values shown in italic are based on an ionic strengh estimated from the pH measurement ($I_c = 1.5 * 10^{pH-14}$).* the composition of the artificial pore solution (CPS) used in [PRM$^+$06] was: 3.2 g/l NaOH, 12.34 g/l KOH and 0.033 g/l CaO.

ref	details	I_c $[mol/l]$	pH	κ^{-1} $[nm]$	ζ $[mV]$	$\Delta\zeta$ $[mV]$	$\Psi_{0,est}$ $[mV]$ d_s=5Å	σ_{est} $[\frac{e}{nm^2}]$ d_s=5Å
[PRM$^+$06]	CH in water with 5.0 %^{vol} cement pore solution (CPS)*	0.083	12.65	1.07	7.35	3.96	11.73	0.048
	CH in water with 17.5 %^{vol} CPS*	0.107	12.82	0.94	-2.19	12.54	-3.73	-0.018
	CH in water with 34.2 %^{vol} CPS*	0.116	12.98	0.9	-8.79	5.35	-15.32	-0.075
	CH in water with 48.9 %^{vol} CPS*	0.189	13.1	0.71	-8.49	7.55	-17.17	-0.107
	CH in CPS*	0.257	13.36	0.61	-14.07	8.8	-31.94	-0.231
[ENK09]	CH in water, no more details	*0.005*	11.49	*4.36*	11.56	?	*12.96*	*0.013*
[GDC$^+$02]	CH in water, no more details	?	?	?	34	?	?	?
[Arn04].	CH in 2.9e-2 m Lutensol AT 50 1m solution.	*0.046*	12.48	*1.44*	23.5	?	*33.26*	*0.102*

5 Characterisation of Portlandite Morphology under Controlled Model Conditions

In this chapter some experimental work on portlandite precipitation in a model systems is presented. The objective was to find the close to equilibrium morphology of portlandite in a pure system and then to study the influence of the silicates, sulfates and aluminates separately. The portlandite particles were studied with scanning electron microscopy (SEM), thermogravimetric analysis (TGA) and particle size distribution measurements. Some X-ray diffraction (XRD) measurements were done as well to confirm the composition of the solid. In contrast to the work reported in literature [BM72, GS07], where changes of the portlandite morphology in cementitious systems were reported, the model systems used here allowed to clearly separate the effect of the different ionic additives. Possible synergies were then studied by adding different combinations of ionic additives.

The aim of the experimental work done in this chapter was to distinguish the effect of different additives, including silicates which are always present in cementitious systems, and aluminates and sulfates, which have been shown by different authors [GS07, BM72] to have an important effect upon the growth and morphology of portlandite. The data treated and discussed in this chapter were produced by Nicolas Ruffray [RBA10], Amirreza Kiani and Tina Saberi in the framework of semester and summer projects. SEM images were taken by Nicolas Ruffray, Michael Stuer and Marijana Mionic.

In the following sections the methods used to treat the collected data and to characterize the produced portlandite particles are described. Then results for the morphology of portlandite in pure calcium-hydroxide-water systems are presented, followed by results of morphological changes upon the addition of silicates, sulfates and aluminates. Lastly the influence of combinations of ions are discussed.

5.1 Methods for Morphology Characterization

For the three main methods (TGA, PSD and SEM) used to characterize the portlandite particles, the data was treated and, except for the SEM images, only the treated data will be discussed. Therefore in this section the protocol employed for the measurements as well as the methods used to treat the data are explained. More details can also be found in the appendix D.

5.1.1 Thermogravimetric Analysis

Thermogravimetric analysis consists of heating up a sample at a constant rate and observing changes of the total mass of the sample. This will show characteristic weight losses at decomposition temperatures of the different components. The thermogravimetric curves for the portlandite samples were collected with a Mettler TGA/DSC/TMA analyzer from room temperature to 800 ° C under flowing air at a heating rate of 10 ° C/min. The raw data that results form the measurement is the weight relative to the initial weight as a function of the temperature and the weight loss rate as a function of the temperature.

The quantities of interest are the characteristic temperatures at which weight losses occur and the amount of loss in a particular temperature range. A R [Tea10, WR09] script was used for the data treatment. The measured weight loss rates were first smoothed with a local polynomial nonparametric regression estimator in order to be able to correctly identify the peaks and valleys in the rate of weight loss curve. The peak locations were then considered to be the characteristic temperatures T^r of the weight loss. The total weight loss Δw^r for a characteristic temperature T^r was estimated from the weight loss between the two neighboring minimas of T^r (see figures 5.1 and 5.2, for more details see appendix D.1).

The weight loss peaks situated at 420 - 490 ° C were identified as portlandite decomposition peaks T^{CH} according to the reaction 5.1. This means that the initial weight percentage of portlandite w^{CH} can be estimated from the weight loss at the portlandite decomposition peak Δw^{CH} according to equation 5.2 where a^X is the atomic weight of element X.

$$Ca(OH)_2 \longrightarrow CaO + [H_2O]_{vap} \tag{5.1}$$

$$w^{CH} = \frac{\Delta w^{CH}}{a^O + 2 \cdot a^H} \cdot \left(a^{Ca} + 2 \cdot a^O + 2 \cdot a^H\right) \tag{5.2}$$

Another weight loss peak that could be identified was that of calcium carbonate $CaCO_3$ with decomposition peak positions at temperatures of 610-700 ° C. The decompositon reaction of calcium carbonate can be seen in equation 5.3. Again the total weight loss Δw^{CaCO_3} can be

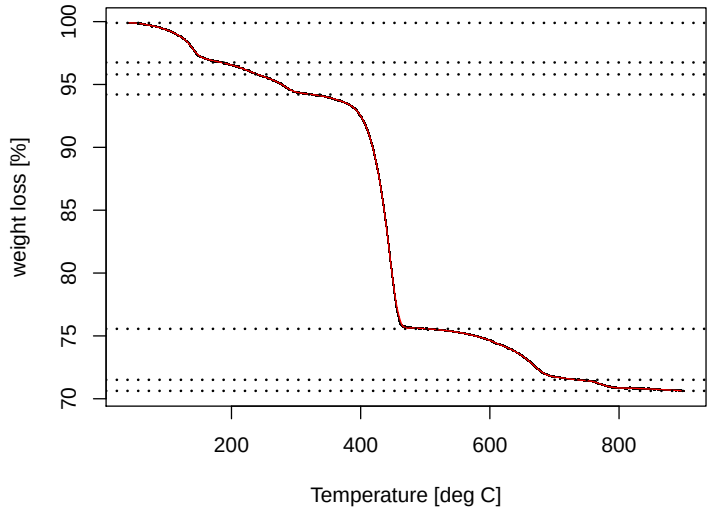

Figure 5.1: Weight loss measured by TGA. The weight loss per characteristic weight loss temperature T^r was estimated between the dotted lines. The black line represents the originally measured data, the red line represents the local polynomial nonparametric regression used to interpolate the weigth losses at the valley positions of the weight loss rate (dotted lines).

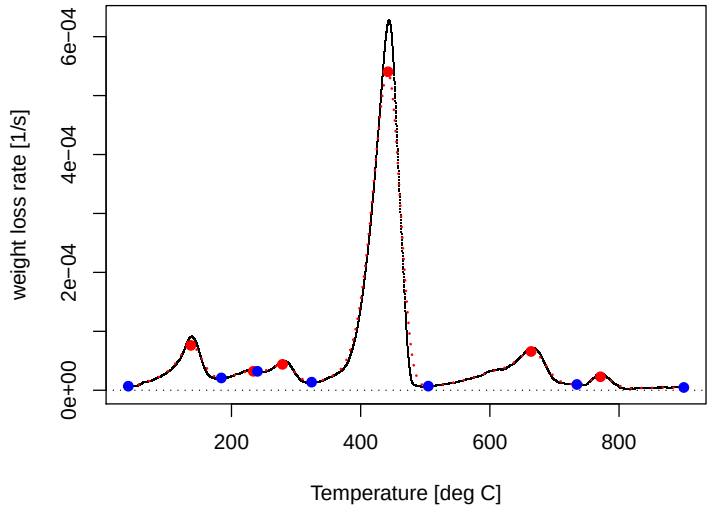

Figure 5.2: Weight loss rate measured by TGA (black line). The smoothed function used to identify the peaks and valleys (red dotted line) and the peak (red dots) and valley (blue dots) positions are shown as well.

used to determine the initial amount of calcium carbonate (see equation 5.4).

$$CaCO_3 \longrightarrow CaO + [CO_2]_{vap} \tag{5.3}$$

$$w^{CaCO_3} = \frac{\Delta w^{CaCO_3}}{a^C + 2 \cdot a^O} \cdot \left(a^{Ca} + a^C + 3 \cdot a^O\right) \tag{5.4}$$

The other weight loss peaks were often gradual with no clearly defined characteristic temperature and no peak other than the portlandite and calcium hydroxide peak could be clearly assigned to a known decomposition reaction.

5.1.2 Particle Size Distribution

A Malvern Mastersizer S was used for the particle size distribution measurements (PSD). The Mastersizer uses the change in the laser diffraction pattern with the size of the particles to estimate the particle size distribution. The Mie theory used for the conversion of the diffraction pattern to a particle size distribution has been developed for spherical particles and is more accurate for equiaxed particles than for particles which show a large deviation from the spherical shape. Care has to be taken to avoid the dissolution of the particles during the measurement. The exact protocol for the PSD measurements was as follows:

- A saturated solution of $Ca(OH)_2$ was prepared by measuring 4 g of commercial $Ca(OH)_2$ Fluka powder in a beaker and completing to 1 l with ultrapure water. The solution was put on a magnetic stirrer with a magnetic bar for one hour. Finally the solution was filtered at 0.2 μm.
- A suspension of the powder of interest was produced by dispersing 0.1 g of powder in 10 g of saturated $Ca(OH)_2$ solution. The suspension was then sonicated for 15 minutes with an ultrasonic horn (150 $Watt$, 20 kHz).
- 120 ml of saturated $Ca(OH)_2$ were put into the Malvern Mastersizer S, to avoid dissolution of the sample. A few droplets of the previously prepared powder suspension was then added.
- Finally the measurements were done using the following parameters:
  - analysis model : Polydisperse
  - active beam lenth : 2.4 mm
  - density : ρ =2.23 $\frac{g}{cm}$

- refractive index: 1.5295
- absorption : i =0.1000

Five consecutive measurements approximately 1-2 min apart were done to check for any time evolution phenomenon such as dissolution or agglomeration.

The measured particle size distribution is often multimodal which makes it more difficult to interpret. Therefore, to deconvolute the different modes, the data was treated with an R [Tea10, WR09] script. The script fitted a certain number of log-normal distributions to the measured particle size distribution. As a first step the first and second derivative of the particle size distribution is estimated by local polynomial nonparametric regression. The number and initial guesses for the median of the log-normal distributions fitted to the measured data is then determined from the valley positions of the second derivative. The initial guess for the width of the distribution is determined form the distance between the minimum and maximum in the first derivative. The medians, widths and weights of the different distributions are then fitted to the measured data (see figure 5.3). For more details see appendix D.2.

5.1.3 Treatment of SEM images: Relative Interfacial Energies

Most of the SEM images were used for the qualitative comparison of the different morphologies. However for some model experiments the particles were very regular with clearly defined facets. This allowed a quantitative analysis of the particle morphology. In fact, if we can determine the distance of each facet form the center, we can estimate the shape determining quantity, whether this is the relative surface energy (see section 1.2) or the relative growth rate (see section 1.3) or a combination of the two. For simplicity's sake, we will consider the relative surface energy to be the determining quantity for the description of the method. To determine the distance of each facet from the center, a new analysis tool was developed. The first step of the analysis was to digitalize the SEM projection of a portlandite particle by recording the positions of the corners of the shape. This was done manually. The corner coordinates were then read into an adapted version of the Wulffman program [RMC98]. Wulffman is capable of calculating the equilibrium morphology for a system with known crystallographic symmetry and relative surface energies which determine the distance of the corresponding facets from the centroid of the shape.

The Wulffman program was expanded as to be able to fit the projection angles and relative surface energies of the calculated to the experimentally observed particle shape. Since the overall size of the particle is unimportant for the determination of the shape, the calculated and the experimental projections were scaled to have the same total surface area. In order to compare the facets of the two shapes, they have to be sorted the same way to ensure the right facets are compared with each other. The first facet in the sorting order is the facet furthest away from the centroid of the total shape. The other facets are sorted in a clockwise manner. The accuracy of the fit between the calculated and the experimental shape has to be

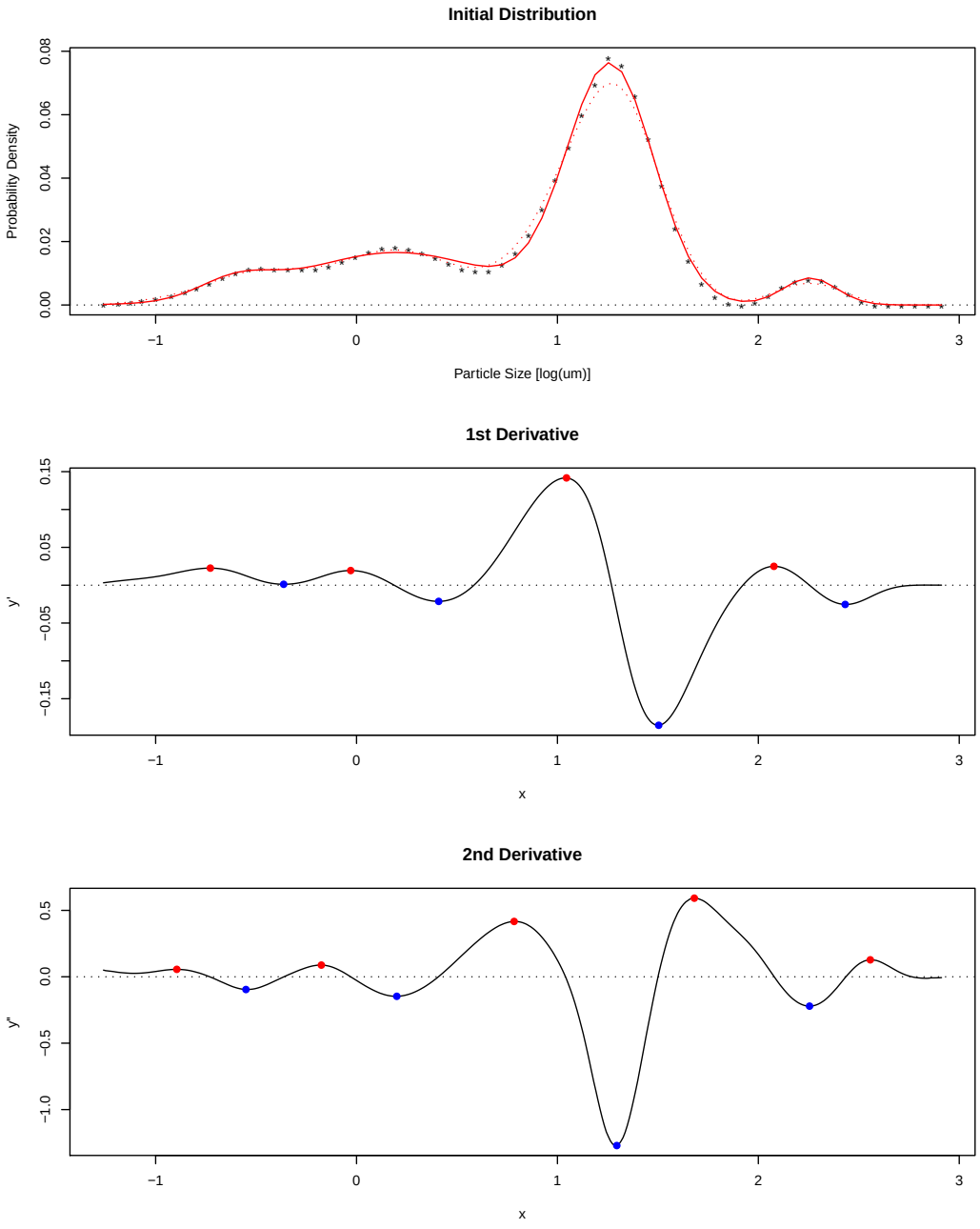

Figure 5.3: Illustration of the deconvolution procedure of the particle size distribution. On the topmost graph the original data (black points), the local polynomial approximation used for the estimation of the first and second derivative (red dotted line) and the final fit of the four log-normal distributions to the data points (red line) are shown. The second and third plot show the estimations of the first and second derivative as well as the peak positions used for the initial guess for the parameters of the log-normal distributions.

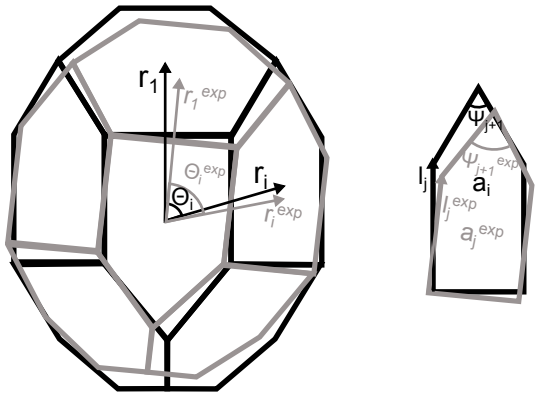

Figure 5.4: Schematic view of parameters used for the fitting between the calculated (black) and the experimentally observed (gray) shape.

quantified with a fitting function to allow a fitting procedure. This fitting function developed here takes into account the projection area a_i and the position $\vec{r}_i$ with respect to the centroid of the different facets as well as their shape F_i^{shape} and the angle between the positions of the different facets Θ_i (see equation 5.5 and figure 5.4). The shape of the facet is described by the angles between the edges Ψ_j^i and the length of the edges l_j^i (see equation 5.6).

$$F^{tot} = \frac{1}{N_{faces}} \sum_i^{N_{faces}} \left[\alpha \cdot \left(\Theta_i - \Theta_i^{exp}\right)^2 + \beta \cdot \left(\frac{r_i^2}{a_{tot}} - \frac{\left(r_i^{exp}\right)^2}{a_{tot}^{exp}} \right)^2 + \gamma \cdot \left(\frac{a_i}{a_{tot}} - \frac{a_i^{exp}}{a_{tot}^{exp}} \right)^2 + F_i^{shape} \right] \tag{5.5}$$

$$F_i^{shape} = \frac{1}{N_{corner}^i} \sum_i^{N_{corner}^i} \left[\kappa \cdot \left(\Psi_j^i - \Psi_j^{i,exp} \right)^2 + \lambda \cdot \left| \frac{\left(l_j^i\right)^2}{a_i} - \frac{\left(l_j^{i,exp}\right)^2}{a_i^{exp}} \right| \right] \tag{5.6}$$

In equations 5.5 and 5.6, N_{faces} is the number of facets of the shape, r_i is the position of the centroid of facet i relative to the centroid of the total shape, Θ_i is the angle between r_i and r_1, a_i is the area of facet i, a_{tot} is the total area N_{corner}^i is the number of corners of facet i, l_{ij} is edge j of facet i and ψ_{ij} is the angle between edge j and edge $j+1$ of facet i (see figure 5.4). α, β, γ, κ and λ are weighting parameters which were set to $\alpha = \beta = \gamma = 0.33$ and $\kappa = \lambda = 0.005$.

The parameters changed during the fitting are the relative surface energies, and the projection angles. The fitting was done via the simplex minimization method [NM65] of the GNU Scientific Library [Gal09]. For more information see appendix D.3.

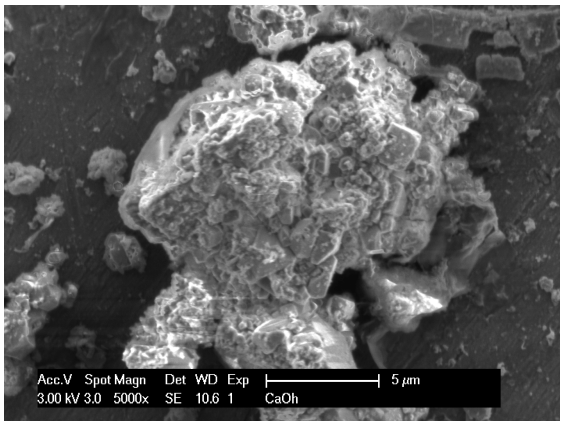

Figure 5.5: Portlandite morphology observed for hydrated CaO.

5.2 Thermal Precipitaion of Portlandite in Pure Ca-OH systems

The first step to understand the influence of different ionic additions on the growth and morphology of portlandite is to determine the morphology in the pure Ca - OH - water system. Coprecipitation from a calcium salt solution (e.g. $CaCl_2$) and a hydroxide solution (e.g. NaOH), which is an easy way to precipitate portlandite, can not be used for the study of the pure system, since there are always counter ions present. Therefore, to study pure Ca - OH - water systems, a different approach had to be used. A possibility to precipitate portlandite from a pure Ca - OH solution is to mix calcium oxide (CaO) with water, the calcium oxide will dissolve and calcium hydroxide will precipitate. Another method is to partially evaporate the solvent. Both methods were tested, but for both the conditions could not be well controlled. A reason for this might be that for both methods a second process is also influencing the $Ca(OH)_2$ concentration in solution. For the first method this second process is the continuous dissolution of the calcium hydroxide and for the second method the continuous evaporation of the solvent. This seems to lead to irregular microstructures, far from equilibrium (see figure 5.5).

A third method, allowing the study of portlandite morphology in pure systems, is thermal precipitation. Since the solubility of portlandite is higher at lower temperatures, portlandite can be precipitated by increasing the temperature of a saturated $Ca(OH)_2$ solution. However the possible relative supersaturation $\ln \frac{a_{Ca}^{max} \cdot a_{OH}^{max2}}{a_{Ca}^{min} \cdot a_{OH}^{min2}}$ that can be reached with this method is limited to less than 3 due to the limited range of possible temperatures (0 - 100 ° C) [CM04]. This means that the precipitation is a relatively slow process.

The effect of the precipitation time was studied with a series of experiments with precipitation times between 6.5 days and 11 weeks. The observed particle shape stays approximately the same for precipitation times of 23 days or longer (see figure 5.6). The only change observed if the precipitation time is increased from 23 days to 11 weeks is the appearance of some needle-like particles. Most likely these are carbonates, however no TGA or XRD measurements were done to confirm this. The final protocol for the precipitation of close to equilibrium

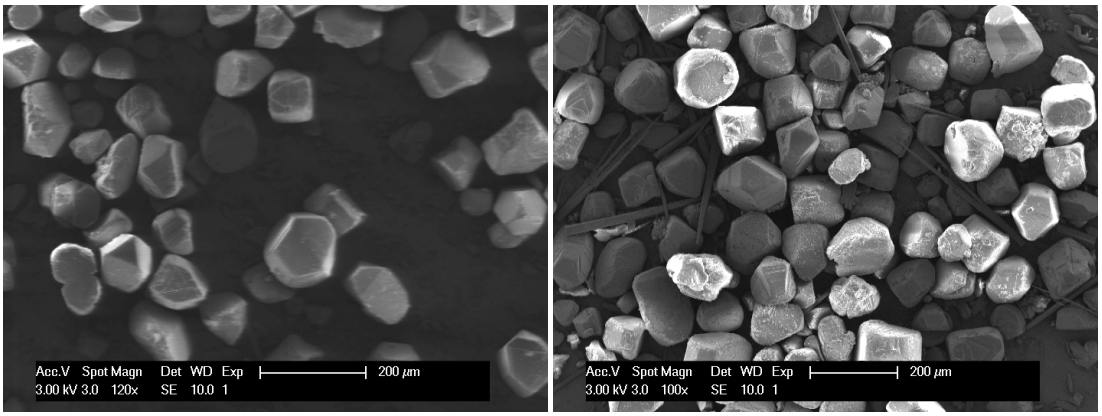

(a) (b)

Figure 5.6: SEM image of portlandite particles produced in pure Ca-OH-water system according to the protocol above with a precipitation time of 23 days (a) and ~ 11 weeks (b).

shaped particles was as follows:

- 4g of $Ca(OH)_2$ powder were mixed with 1 l of pure H_20 and stirred during 2 hours in an ice bath with an average temperature of 0 ° C.
- The resulting solution was conserved at 0 ° C until used.
- 40-50 g of the solution was then filtered at 0.22 μm and put into a closed container to avoid evaporation and carbonation.
- The samples were then put in an oven at 60 ° C for at least 23 days.

The thus produced particles were isolated, facetted crystals but quite irregularly shaped, indicating that the particles are close to but not completely equilibrium shaped (see figure 5.6). The size of the particles is approximatly 100 μm. The shape of particles seems very equiaxed with approximately three different families of facets that can be distinguished. Two of them are readily identified because of the trigonal symmetry of the portlandite particles:

- The equiaxed triangular facets that are observed on many particles are [00.1] facets.
- The facets that are perpendicular to the [00.1] surface are most likely [10.0] facets.

The rather equiaxed shape and absence of large [00.1] facets were unexpected since the [00.1] facet is a perfect cleavage plane i.e. a plane with low surface energy [ABBN97]. One could argue that the observed morphology is determined by the relative growth rates rather than by the relative interfacial energies, however attachment energy calculations (see chapter 7 or [Har12]) also predict a slow growth of the [00.1] surface and hence a hexagonal platelet morphology.

Another possible explanation for the observed equiaxed morphology are strong, anisotropic interactions of the surfaces with the solvent. In the literature a hexagonal equilibrium morphology of portlandite in aqueous systems is generally assumed [HKM$^+$09, Har12, BM73] and is often observed in cementitious systems [HKM$^+$09, RNRAOHH05, Dia01]. However these systems always contain other ionic additives and the morphology in pure systems has not, to our knowledge, been studied before. It therefore seems likely, that the assumption of a hexagonal platelet growth and equilibrium morphology of portlandite in pure aqueous systems may be erroneous.

No TGA or PSD measurements were done on the portlandite particles produced in the pure system, due to the very low yield of the experiments. According to thermodynamic calculation only about 0.45 g/l of portlandite is expected to precipitate (see chapter 6). In fact the particles observed by SEM were collected form the walls of the container used for the precipitation and the quantity was not enough for further analysis. Consequently, for the study of the influence of different ionic species on the morphology of portlandite, a different precipitation method i.e. coprecipitation, with a much higher yield, was used.

5.3 Coprecipitation of Portlandite

Copreciptation consists of mixing two stable solutions, one containing calcium, the other containing hydroxyls. If the concentrations of the initial solutions are high enough, the mixed solution will be supersaturated with respect to portlandite and portlandite will precipitate. The calcium solution can be produced by dissolving a calcium salt, such as calcium chloride ($CaCl_2$) or calcium nitrate ($Ca(NO_3)_2$), in water. The hydroxyl solution, i.e. a high pH solution, can be produced with any strong chemical base, such as sodium hydroxide ($NaOH$) or potassium hydroxide (KOH). This means that the exact chemical composition of the initial solutions can be varied but there will always be counterions present, in the same initial concentration as the calcium and the hydroxide respectively. This means that before the effect of other ionic additives can be studied, the effect of the counterions has to be elucidated. Other parameters, such as the precipitation time and the initial supersaturation, can be varied as well. Conditions under which portlandite particles show a well defined and controlled morphology have to be chosen in order to be able to study the effect of different ionic additives. Once the control experiment is well characterized the effect of different ionic additives can then be investigated.

The ionic additions looked at in this chapter correspond to the ionic species that have been shown [BM72, GS07] to have an influence on the final morphology of portlandite in cementitious systems: sulfates and aluminates (see section 4.3). Additionally the influence of silicates, which are always present in cementitious systems, is investigated as well. A further understanding of the influence of these ions on the growth and morphology of portlandite could lead to insights into the hydration process. Such insights might help understand how the initial properties, such as early strength, can be influenced and potentially allow a better

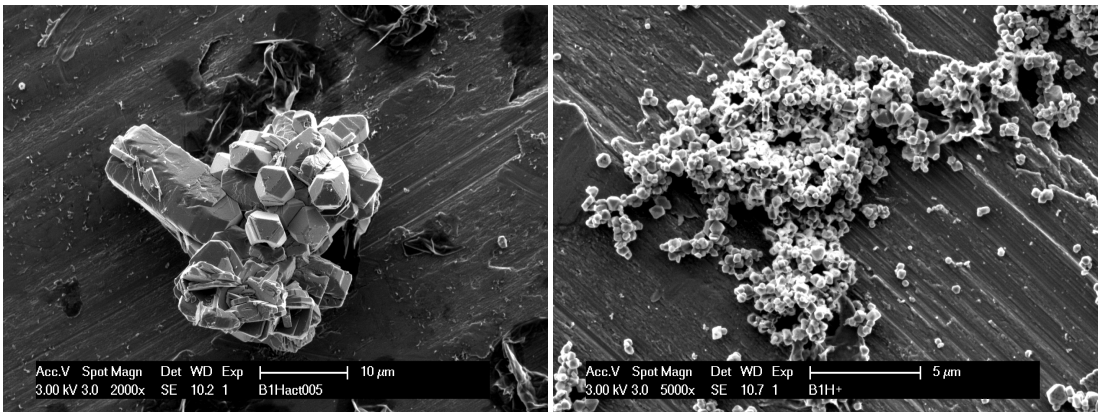

(a) (b)

Figure 5.7: Effect of supersaturation on the morphology of portlandite particles produced by corprecipitation with 1 hour precipitation time. SEM images for an initial concentration of 0.05 $\frac{mol}{l}$ $CaCl_2$ + 0.1 $\frac{mol}{l}$ $NaOH$ (a) and of 0.1 $\frac{mol}{l}$ $CaCl_2$ + 0.4 $\frac{mol}{l}$ $NaOH$ (b).

control of the final microstructure.

5.3.1 Control System

As an initial system chloride ($CaCl_2$) and sodium ($NaOH$) were chosen as the counter ions for the calcium and the hydroxyl ions respectively. Varying nominal supersaturations from initial concentrations of 0.05 $\frac{mol}{l}$ $CaCl_2$ + 0.1 $\frac{mol}{l}$ $NaOH$ (nominal relative supersaturation $\ln\left(\left(c_{Ca}^{init} \cdot c_{OH}^{init\,2}\right) / \left(a_{Ca}^{eq} \cdot a_{OH}^{eq\,2}\right)\right)$ of ~ 2.7) to 0.1 $\frac{mol}{l}$ $CaCl_2$ + 1.0 $\frac{mol}{l}$ $NaOH$ (nominal supersaturation of ~ 8.0) and were initially tested. A precipitation time of 1 hour was used for all experiments.

At low supersaturations large aggregates of relatively large primary particles are observed (see figure 5.7a). Growth directions away from the center of the aggregate seem to be preferred and some primary particles in the shape of elongated hexagonal rods can be found alongside the more frequent equiaxed morphology similar to the one observed in pure $Ca(OH)_2$ conditions.

At high supersaturation the size of the primary particles is reduced and nucleation seems to become homogeneous. However at very high supersaturations (nominal supersaturation of 6.2 and higher, see figure 5.7b) the primary particles become too small to be easily analyzed with SEM. Also the particles seem to have a tendency to form agglomerates due to their small size.

Consequently an initial concentration of 0.1 $\frac{mol}{l}$ $CaCl_2$ + 0.2 $\frac{mol}{l}$ $NaOH$, corresponding to an initial nominal supersaturation of 4.8, was used for the further study of portlandite morphology with coprecipitation. At that concentration the particles observed after 1 hour of precipitation are individual particles with very regular, equiaxed and facetted morphology (see figure 5.8a). The particle sizes range from 0.2 to 3 μm with a particle size median $d[v,50]$ of 0.74 μm (see

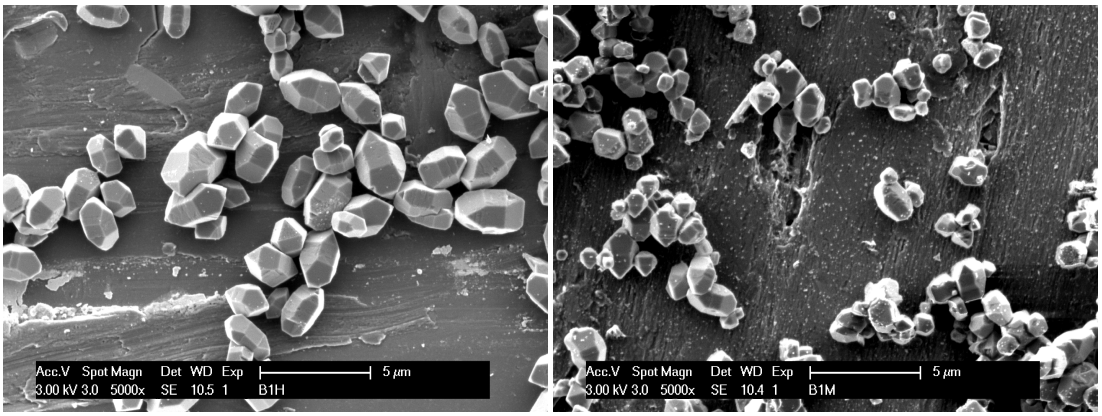

(a) (b)

Figure 5.8: SEM image of portlandite particles produced by coprecipitation of 0.1 $\frac{mol}{l}$ $CaCl_2$ + 0.2 $\frac{mol}{l}$ $NaOH$ after 1 hour (a) and after ~ 2 months (b) precipitation time. For sample (b) a Y-mixer was used to accelerate the complete mixing of the two fluids.

figures D.3a and 5.11a). The regularity of the particles makes it possible to determine the orientation of the facets [hk.l] and evaluate the morphology determining quantities $\frac{\gamma_{hk.l}}{\gamma_{00.1}}$ for the different facets with the previously described analysis tool. This is possible whether $\frac{\gamma_{hk.l}}{\gamma_{00.1}}$ corresponds to a relative interfacial energy, to a relative growth speed or to a mixture of the two. The results can be seen in table 5.1. The triangular cap surfaces correspond to [00.1] facets with the highest γ. The facets perpendicular to the [00.1] surfaces in the shape of elongated pentagons with two parallel sides are [10.0] facets. The relative γ of the [10.0] facet with respect to the [00.1] facet is estimated to be in the order of $\frac{\gamma_{10.0}}{\gamma_{00.1}}$ = 0.51 - 0.63. The third type of facet, shaped as irregular hexagons with two very small sides, are [10.1] facet with a $\frac{\gamma_{10.1}}{\gamma 00.1}$ of 0.56 - 0.72.

The observed portlandite morphology for the control system is similar to the portlandite morphology in pure systems discussed in the previous section. The particle size on the other hand (d(v,50) = 0.74 μm) is much smaller than the particle size of portlandite particles precipitated by thermal precipitation in pure systems (in the order of 100 μm). the supersaturation for the coprecipitation experiments (~ 4.8) is much larger compared to the thermal precipitation experiments (~ 2.1), this is consistent with the previously observed larger primary particle size with lower supersaturation. Additionally the particles are not quite as equiaxed as in the pure system but slightly elongated in the [00.1] direction. This is consistent with results of Berger and McGregor which indicate that the addition of chlorides or nitrates leads to an elongation of the particles in the [00.1] direction [BM72].

In order to get a better idea of the influence of the counter ion on the morphology, the concentration of counter ions was increased to 0.3 in one experiment and in an other $CaCl_2$ was replaced by $Ca(NO_3)_2$. For both experiments the general shape of the particles seems to be similar to the initial samples (see figure 5.9). The quantification of the morphologies

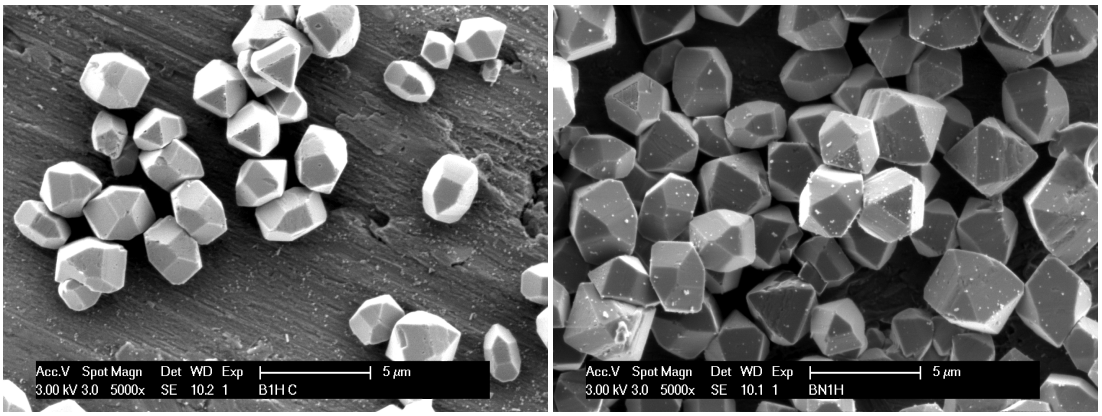

(a) (b)

Figure 5.9: SEM image of portlandite particles produced by coprecipitation with varying counterion type and concentration. The initial concentrations were 0.1 $\frac{mol}{l}$ $CaCl_2$ + 0.2 $\frac{mol}{l}$ $NaOH$ + 0.1 $\frac{mol}{l}$ $NaCl$ for (a) and 0.1 $\frac{mol}{l}$ $Ca(NO_3)_2$ + 0.2 $\frac{mol}{l}$ $NaOH$ for (b).

Table 5.1: Estimated relative interfacial energies of the different facets for different concentrations and combinations of counterions present under the coprecipitaion of portlandite. Also given is the total number of particles N_{part} analyzed.

		average		minimum		maximum	
initial concentrations	N_{part}	$\frac{\gamma_{10.0}}{\gamma_{00.1}}$	$\frac{\gamma_{10.1}}{\gamma_{00.1}}$	$\frac{\gamma_{10.0}}{\gamma_{00.1}}$	$\frac{\gamma_{10.1}}{\gamma_{00.1}}$	$\frac{\gamma_{10.0}}{\gamma_{00.1}}$	$\frac{\gamma_{10.1}}{\gamma_{00.1}}$
0.1 M $CaCl_2$ + 0.2 NaOH	10	0.58	0.65	0.51	0.56	0.63	0.72
0.1 M $CaCl_2$ + 0.2 NaOH + 0.1 M NaCl	10	0.68	0.73	0.51	0.63	0.79	0.79
0.1 M Ca(NO3)2 + 0.2 NaOH	9	0.75	0.73	0.61	0.66	0.96	0.88

(see table 5.1) indicate that the both $\frac{\gamma_{10.0}}{\gamma_{00.1}}$ and $\frac{\gamma_{10.1}}{\gamma_{00.1}}$ might increase slightly with increasing Cl^- concentration, $\frac{\gamma_{10.0}}{\gamma_{00.1}}$ more so than $\frac{\gamma_{10.1}}{\gamma_{00.1}}$. This would go against the previous observation of chloride elongating the particle shape slightly in the [00.1] direction, however the change is not very marked and within the spread of the data. Replacing the Cl^- ions by NO_3^- ions has a similar effect as increasing the chloride concentration i.e. both $\frac{\gamma_{10.0}}{\gamma_{00.1}}$ and $\frac{\gamma_{10.1}}{\gamma_{00.1}}$ increase slightly. The effect is more marked but still very limited. For both experiments the size of the particles, measured with laser diffraction, is slightly smaller than for the original experiment. The estimated median volume diameter $d[v,50]$ of the measured size distributions were 0.68 and 0.67 μm respectively (original experiment: $d[v,50]$ = 0.74 μm). The width of the distribution decreases slightly as well. The estimated standard deviation of the particle size for the original experiment was 1.1 μm whereas for the experiments with increased counterion concentration and with NO_3^- a standard deviation of 0.4 μm was estimated. However the observed changes are relatively small.

The final parameter that was looked at was the influence of the precipitation time. To this effect an experiment with a precipitation time of 2 months was done. The general shape and

morphology of the particles does not change with the increased precipitation time (see figure 5.8b). Additionally the size distribution with an estimated $d[v,50]$ of 0.76 μm is similar to the one measured after one hour of precipitation ($d[v,50]$: 0.74 μm). The fact that the morphology of the portlandite particles does not seem to change over a period of 2 months indicates that the morphology is already close to equilibrium and the driving force for further equilibration is small.

In addition the phase composition of the samples were studied by TGA to determine the amount of carbonates in the system. For the duration of the precipitation the solution was put into a polyethelene bottle to protect it from carbonation but during the initial mixing and during the subsequent washing and drying step the samples were unprotected from carbonation. The amount of carbonates determined by TGA for a precipitation time of 1 h was 11 % by weight. For a precipitation of 2 months a calcite amount of 5 % was estimated. This indicates that during the precipitation the samples are effectively shielded form carbonation and that the measured amounts of carbonate are either introduced during the initial preparation and mixing of the solutions or during the subsequent washing and drying steps.

Consequently the final protocol chosen to study the influence of different ionic additions on the growth and morphology of portlandite was as follows:

- Weigh 20 g of 1 $\frac{mol}{l}$ $CaCl_2$ solution into a 250 ml glass beaker. Add the desired amount of additives. Complete to 100 g with ultrapure water.
- Weigh 40 g of 1 $\frac{mol}{l}$ $NaOH$ solution into a second 250 ml glass beaker. Add the desired amount of additives. Complete to 100 g with utrapure water.
- Put a 500 ml glass beaker on a magnetic stirrer, with a magnetic bar inside. Simultaneously add the 2 solutions manually into this beaker.
- After 1 minute of stirring, measure the pH.
- Then put the mixture into a polyethelene bottle of 250 ml. Close it, and put it on rolling bars for 1 hour.
- Measure the pH.
- Transfer the mixture to a filter (0.45 μm).
- Add 100 ml of ultra pure water, and filter again (washing step).
- Transfer the filter into an oven at 60 ° C. Let it dry 24 to 72 hours (until no change of weight is observed).
- Take the powder out of the tube and store it in a closed, labeled bottle.

The results reported here for the protocol above are consistent with results reported by Arnold et al. [Arn04]. Arnold et al. did two series of experiments. One series of experiments consisted

of gradually adding a total amount of 20 ml 1 $\frac{mol}{l}$ KOH solution to 100 ml of 0.1 $\frac{mol}{l}$ $CaCl_2$ solution over a timespan of 4 minutes. There are small differences between their experiments and the ones reported here: Arnold et al. used potassium hydroxide instead of sodium hydroxid, had a slightly lower total nominal supersaturation ($\sim$ 4.3 instead of $\sim$ 4.8) and added the hydroxide gradually over the whole timespan of the precipitation instead of mixing at the beginning of the experiment. Also the total precipitation time was only 4 minutes and not one hour and the samples were protected from carbonation during the mixing and drying steps as well as during the precipitation step. Despite these differences the morphology of the particles observed by Arnold et al. (see figure 4.5) is very similar to the ones observed here with the three families of facets ([00.1], [10.0] and [10.1]) clearly discernible. The reported size of the particles (from a few 100 nm to $\sim$ 3.5 μm) is similar to the range reported here. The authors did not see any carbonates with TGA, indicating that the samples were protected effectively.

Arnold et al. [Arn04] also did so called diffusion precipitation experiments where a beaker with a saturated KOH solution and a beaker with a saturated $CaCl_2$ solution was put into the same container which was then carefully filled up with water. The diffusion of the hydroxyl towards the saturated $CaCl_2$ solution will then lead to the precipitation of portlandite in the vicinity of the $CaCl_2$ solution over a period of 40 days. The nucleation of the portlandite particles was clearly heterogeneous, the particles growing primarily at external surfaces of the system such as e.g. the wall of the beaker. The final morphology of the portlandite particles were long hexagonal rods in the mm range, protruding from the same initial nucleation point (see figure 4.4). Similar morphologies, although at much smaller scale, started being observed here at very low supersaturation (see figure 5.7a).

All in all the comparison between results for the control system and results for the pure system as well as for systems with different counter ions reported here and in literature [Arn04] indicate the the effect of the chosen counter ions (Na^+ and Cl^-) on portlandite morphology is limited. Additionally comparison with results reported by Arnold et al. for particles which were completely protected from carbonation indicate that the small amount of carbonates found in our systems does not significantly affect the morphology of the portlandite particles. This means that effects observed upon the addition of other ions can be assumed to be effects from the interaction with portlandite and Ca/OH species in solution rather than a competition effect between the counter ions and/or the carbonates and the additional ions.

Last but not least a control experiment was done where the time evolution of the calcium activity was measured during the precipitation using a calcium specific electrode (Orion 97-20 Ionplus, linked to Orion420). The aim of this experiment was to get an idea of the concentration of species interacting with the growing portlandite particles. The results show that, after an initial rapid change the Ca concentration in the first $\sim$ 75 seconds, the calcium activity values are only slightly higher than the equilibrium concentrations (see figure 5.10). This indicates that, after an initial nucleation and rapid growth period, a slower growth seems to take place which will in all probability be responsible for the final shape of the particles. In the slower growth period the concentrations are already close to the equilibrium

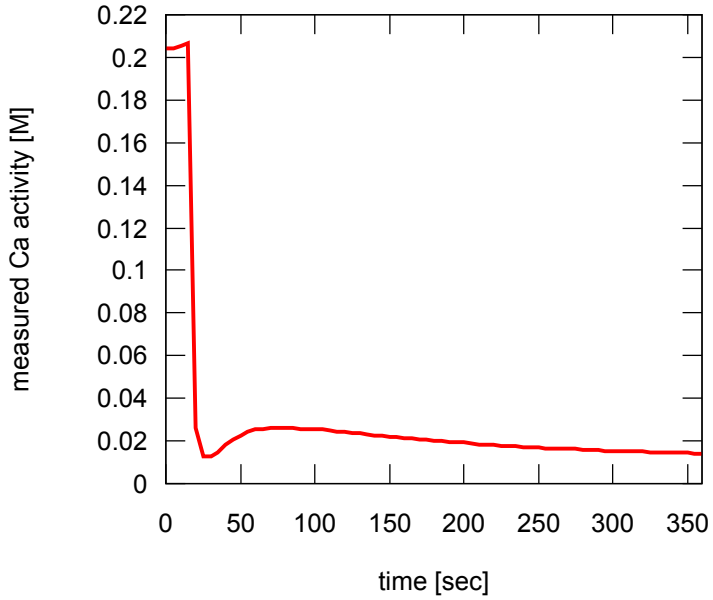

Figure 5.10: Ca activity measurement during the precipitation of portlandite particles produced by coprecipitation of 0.1 $\frac{mol}{l}\,CaCl_2 + 0.2\,\frac{mol}{l}\,NaOH$. One can distinguish two different periods, an initial nucleation and rapid growth period up to ~ 75 seconds with rapid changes of the concentration followed by a slower growth and equilibration period.

concentrations. Therefore thermodynamic calculations of the equilibrium concentration of different species in solution should give some indication as to which species are most likely to interact with the growing portlandite particles.

5.3.2 Reproducibility and Statistical Treatment of Data

In order to judge the reproducibillity of the results, the results of two series of experiments, done according to the same protocol but over a year apart and by different people, were compared. The first series of experiments (B1H series) was done by Nicolas Ruffray in 2010 and the second series (r series) was done by Amirreza Kiani in 2012. The series done by Amirreza Kiani was randomized to minimize the influence of parasitic effects. The reproducibility of the results appeared to be good (see appendix D.4).

The complete set of data from TGA and PSD measurements as well as from the $\frac{\gamma_{hk.l}}{\gamma_{00.1}}$ estimation form the SEM image analysis was treated with multiple linear regression using the least squares method to estimate the statistically relevant factors (for more details see appendix D.5).

For the particle size distribution the quantity considered for the linear regression was the logarithm of the median $d[v,50]$ of the main peak. A set of 11 predictors were initially considered: the sulfate S, silicate Si, aluminate Al concentration in mM, the chloride Cl and nitrate NO_3 concentration in M, the series, the precipitation time t in months, the sulfate concentration

Table 5.2: Estimated parameters β^{est} with their estimated standard error Δ and their P-value indicating their statistical relevance. Only the parameters which were estimated to be relevant and included in the final model are shown. Also shown are the estimated standard deviation of the random fluctuation σ^{est}, the estimated mean squared error of the predictions and the global P-value.

	$\gamma_{10.0}/\gamma_{00.1}$			$\gamma_{10.1}/\gamma_{00.1}$			$d[v,50]$			% other		
	β^{est}	Δ	P-val.	β^{est}	Δ	P-val.	β^{est}	Δ	P-val.	β^{est}	Δ	P-val.
S	0.02	1e-3	< 2e-16	0.02	9e-4	< 2e-16	-	-	-	-	-	-
Si	0.95	0.32	4.6e-3	0.81	0.26	4.1e-3	0.59	0.15	1e-3	4.92	1.72	0.01
Al	-0.62	0.18	3.7e-4	-0.52	0.13	3.1e-4	0.27	0.06	3e-4	4.18	0.87	4.5e-4
S*Al	-	-	-	-	-	-	-	-	-	0.12	0.02	1.9e-6
S*t	-	-	-	-	-	-	-	-	-	0.15	0.01	1.1e-7
	σ^{est}	R^2	P-val.	σ^{est}	R^2	P-val.	σ^{est}	R^2	P-val.	σ^{est}	R^2	P-val.
	0.29	0.94	< 2e-16	0.24	0.96	< 2e-16	0.28	0.75	1e-5	3.60	0.97	5e-10

times the time $S \cdot t$ as well as the different combination of ions: $Si \cdot S$, $Si \cdot Al$ and $S \cdot Al$. A set of 18 data points on 18 samples was used for the fitting (see appendix D.2). Only two parameters, the silicate and the aluminate concentration, were estimated to be statistically relevant for the size of the particles (see table 5.2). This to some extent confirms the previously discussed observations that the experiments were well reproducible (no statistically significant effect of the series) and that the influence of the type and concentration of the counter ions can be neglected (no statistically significant effect of Cl or NO_3). Additionally the results indicate that both silicates and aluminates increase the size of the precipitated particles whereas the sulfates do not seem to have a statistically significant effect within the range of concentrations studied here. However there appear to be significant violations of the assumptions of the linear model which means that the results have to be treated with care (see appendix D.5).The problems of the linear model can also be seen from the unrealistically high estimated standard deviation of the random fluctuations σ^{est} as well as the bad correspondence between model and measurements (see figure 5.11a). The overestimated σ^{est} might mask other statistically significant effects. However the most important influence on the particle size seems to come form the concentration of silicates and the concentration of aluminates.

The same set of 11 predictors was used to estimate the influence on the phase composition of the powder. The weight percentage of calcite as well as the weight percentage of phases other than portlandite and calcite, determined by TGA, was studied with least squares linear regression. Again the full data set of 19 measurements on 19 samples can be found in appendix D.1. The linear combinations of $S \cdot t$ was included since it has been observed that the precipitation of sulfate phases is retarded in the coprecipitation experiments (see section 5.3.4).

The statistically relevant factors for the weight percentage of other phases were the silicate and the aluminate concentration as well as the combined factors $S \cdot Al$ and $S \cdot t$ (see table 5.2). The experiments seem to be reproducible (i.e. the series has no statistically relevant effect)

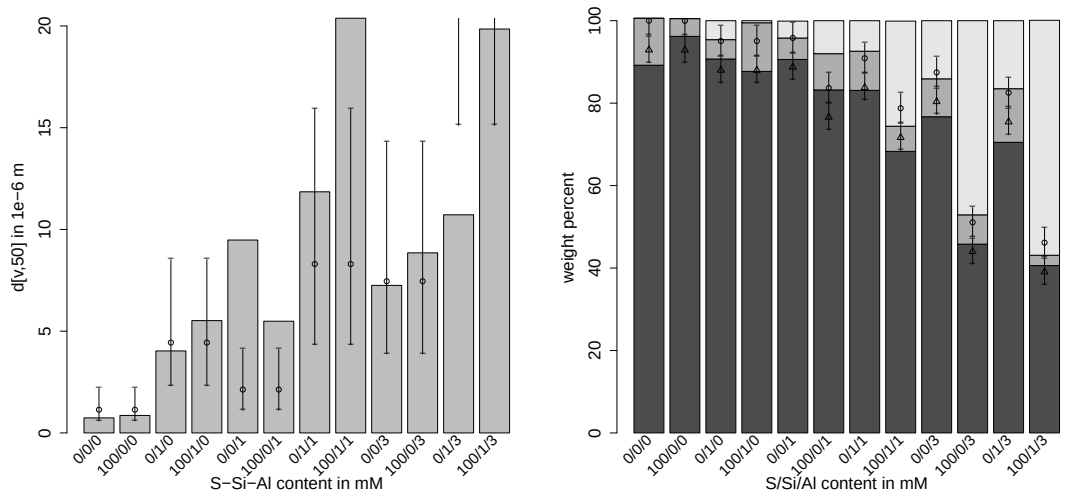

(a) (b)

Figure 5.11: Composition measured by TGA (a) (dark gray: portlandite, medium gray: calcite and light gray: other) and the main peak particle size median (d[v,50]) measured by laser diffraction (b) for powders produced by coprecipitation of 0.1 M $CaCl_2$ + 0.2 M $NaOH$ with different ionic additives. Except for the composition of sample 0/1/0, the results shown here are from the r series of experiments. The estimations from the linear model (points) and the estimated standard deviation (error bars) are shown as well.

and the estimated σ^{est} of 3.60 % is in the same range as the previously determined standard deviations. The model predictions are in good agreement with the measured data (see figure 5.11b).

None of the considered predictors seem to be relevant for the amount of calcite observed. The weight percent of calcite was on average 7.1 ± 0.8 % with an estimated standard deviation σ^{est} of 3.1 %. This seems to be sufficient to describe the amount of calcite and good agreement between predicted and measured values could be achieved (see figure 5.11b). The estimated standard deviation is similar to the one estimated for the amount of other phases. Since both quantities come from the same measurement technique, a similar standard deviation appears reasonable.

For the morphology determining quantities $\frac{\gamma_{10.0}}{\gamma_{00.1}}$ and $\frac{\gamma_{10.1}}{\gamma_{00.1}}$ a total of 45 measurements on 7 samples was used for the statistical analysis (see appendix D.3 for the full set of data). The reason for the limited amount of samples included was the fact that only regular, facetted particles with clearly defined edges could be included. Due to the reduced data set, only 5 predictors were initially included: the sulfate, silicate and aluminate concentration in mM as well as the chloride and nitrate concentrations in M. For the sulfate containing samples which had a hexagonal platelet morphology with only [10.0] and [00.1] facets, only a lower limit for $\frac{\gamma_{10.1}}{\gamma_{00.1}}$ could be determined, this means that results for the [10.1] surface have to be treated with

some care. For both the [10.0] and the [10.1] surface the statistically relevant factors seemed to be the sulfate, silicate and aluminate concentrations whereas the concentration and type of the counter ions did not seem to have a statistically significant effect (see table 5.2). However deviations from the model assumptions used for the least squares method were found (see appendix D.5). The model deviations might mask statistically significant influences of e.g. the counter ions. However the masked influences would have to be smaller than the influence of Si, S and Al in the range of concentrations studied.

In summary the experiments seem to be well reproducible. Although the employed least squares linear regression was not always ideal, statistically significant effects of different ionic additions could be observed. The effect of the counter-ions seem to be at the very least much smaller than, if not altogether negligible compared to, the effects of the other studied ionic additions. The overall effect of the different ionic additions on the growth and morphology of portlandite will be discussed in detail in the following sections.

5.3.3 Influence of Silicates

Silicates are always present in cementitious systems, therefore the study of the influence of silicates on portlandite growth and morphology is primordial in order to understand the morphological changes of portlandite in cementitious systems. However very little is known about the influence of silicates on the portlandite growth. Although most previous studies [BM72, GS07] have been done in cementitious systems, where silicates are always present, the effect of the silicates has, to our knowledge, so far not been specifically looked at.

The addition of 0.001 $\frac{mol}{l}$ Na_2SiO_3 is above the solubility limit of C-S-H (see chapter 6). Consequently a small amount of secondary phase precipitates. This can be seen both from the 4.6 % secondary phase that is estimated from TGA measurements (figure 5.11b) and from the positive β_{Si}^{est} for the amount of secondary phases estimated from the statistical analysis (table 5.2). The measured amount of secondary phase is in good agreement with the 5.2 % C-S-H predicted by thermodynamic calculations (see table 6.1).

The measured $d[v,50]$ of the main peak increases form 0.7 μm in the control system to 4.0 μm upon addition of 0.001 $\frac{mol}{l}$ Na_2SiO_3 (see figure 5.11a). This tendency is also confirmed by the positive β_{Si}^{est} for the $d[v,50]$ estimated by statistical analysis (see table 5.2). The size distibution also becomes multi-modal. Apart from the main peak which accounts for about 60 % of the particles by volume, a second peak of about 36 % at 0.8 μm and a third peak of about 0.4 % at 26 μm can be observed as well.

From SEM images (figure 5.12) one can see that the increase in size of the $d[v,50]$ comes from the aggregation of the particles rather than from an increase of the primary particle size. In fact the primary particle size of the agglomerates seems to be smaller then the particle size observed in the control system although some larger, slightly elongated particles can be seen as well. The shape of the primary particles observed is irregular and none of the three family

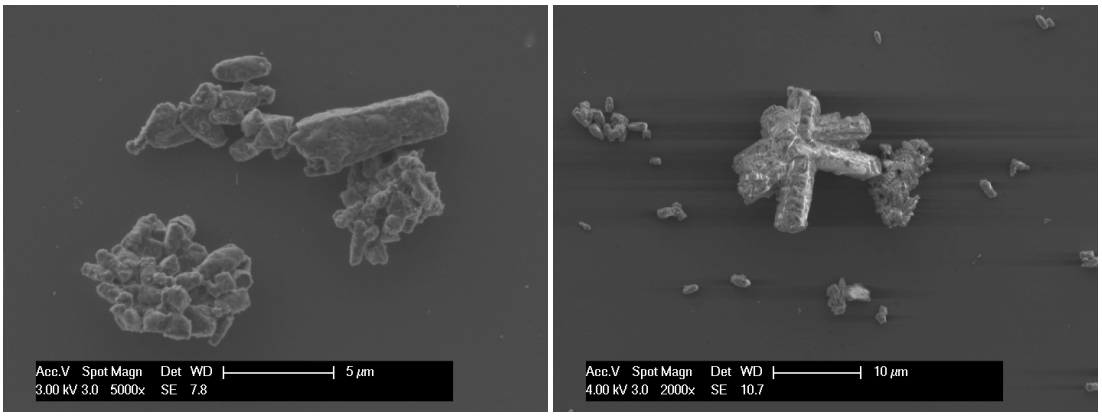

Figure 5.12: SEM images of portlandite particles produced by coprecipitation of 0.1 M $CaCl_2$ + 0.2 M $NaOH$ with the addition of 0.001 M Na_2SiO_3 after 1 hour precipitation time.

of facets, that can be observed int the control system, can be seen here. The second peak in the particle size distribution, at a similar size as the main peak of the control system, likely corresponds to the few individual particles or small agglomerates of ~ 2 particles that can also be observed.

Particles corresponding to the third peak in the particle size distribution can also be seen by SEM. These larger particles often show elongated hexagonal rods protruding from a central point. This morphology is similar to the one observed here (see figure 5.7a) and by Arnold et al. (see figure 4.4) for systems with lower supersaturations. The common feature of the particles observed at lower supersaturation with the current particles is the aggregation. The aggregation of the growing particles, either by heterogeneous or secondary nucleation or by some other mechanism is likely to promote growth directions away from the central point out into the solution. For a hexagonal system, the only one dimensional growth mode that can lead to particles growing out from the central point, without geometrical growth restraint from the other particles, is the [00.1] direction. Other growth directions, such as the [10.0] direction would lead to the formation of platelets which would quite soon intersect with each other. However the [00.1] growth mode seems to be infrequent and is only observed for few paricles. Maybe the particles are produced by different growth mechanism, such as defective growth, which can only be active if there is a suitable defect present at the [00.1] surface.

No particles which could clearly be identified as a secondary phase were observed. However the surface of the observed portlandite particles was often quite rough and the particles often appear to be linked by a secondary phase, indicating that the C-S-H phase might grow in between and at the surfaces of the portlandite particles.

In summary, the main effect of the silicates on the growth and morphology of portlandite appears to be the agglomeration of the particles. The shape of the particles becomes irregular and slow growth modes, usually only observed in systems with low supersaturation can be observed in silicate containing systems, although infrequently. Even though the concentration

of silicates was much lower than the concentrations of the counter-ions, the change in particle morphology is much more marked than for the other samples. This indicates that silicates have a great influence on portlandite morphology and growth. Since silicates are always present in cementitious systems this is of great importance when discussing changes in portlandite morphology in cementitious systems. The influences observed of some ions on the growth and morphology of portlandite in cementitious systems might come from the interaction with silicate ions rather than from the interaction with portlandite ions. To study such possible synergetic effects in more detail, the effect of the addition of different combinations of ions was also studied and will be discussed in section 5.3.6.

The observed effects might have further implications on the growth and morphology of both silicates and sulfates as well as on the induction period. According to our observations it seems likely that C-S-H forms at the portlandite surfaces leading to the agglomeration of the portlandite particles. This might also happen in cementitious systems, hindering the further growth of portlandite. In this type of situation, slower growth modes, perhaps depending on defect growth mechanisms, as are observed for systems with low supersaturation, might be activated. Such a scenario might contribute to the induction period by leading to a temporary deceleration of the growth even though nucleation has already taken place. Space resolved composition analysis techniques, such as energy-dispersive X-ray spectroscopy (EDS) could give more information on the intermixed growth of portlandite and C-S-H, however such measurements were not done in the framework of this thesis.

5.3.4 Influence of Sulfates

It has been observed by E. Gallucci & K. Scrivener [GS07] that the portlandite morphology in tricalcium silicate (C3S) systems changes with the content of gypsum and tricalcium aluminate (C3A). The authors studied C3S systems with the addition of either C3A or gypsum or both and compared the resulting portlandite morphology to that of pure C3S and to ordinary portland cement (OPC) systems. They observed that the addition of both C3A and gypsum was necessary to observe individual potlandite particles often of platelet shaped morphology similar to the portlandite morphology in OPC. Additionally the authors observed that nucleation seemed to be favored in the neighborhood of gypsum. To be able to understand the observed changes it is useful to study the influence of sulfates on the portlandite morphology in well controlled model systems.

The addition of 0.1 mol/l Na_2SO_4 to the coprecipitation experiments does neither have a statistically significant effect on the composition as measured by TGA (no phases other than portlandite and calcite observed, see figure 5.11b and table 5.2) nor on the particle size ($d[v,50]$ of $\sim 0.9\ \mu m$, see figure 5.11a and table 5.2). However the particle size distribution becomes multimodal with two equivalent peaks, one with a $d[v,50]$ of 0.35 μm and one with a $d[v,50]$ of 2.1 μm (see figure D.3b).

SEM images show that the morphology of the particles has changed to a hexagonal platelet

Table 5.3: Estimated relative interfacial energies of the different facets for particles precipitated from a 0.1 M $CaCl_2$ + 0.2 $NaOH$ solution with the addition of 0.1 M Na_2SO_4.

		average		min		max	
initial concentrations	no_{part}	$\frac{\gamma_{10.0}}{\gamma_{00.1}}$	$\frac{\gamma_{10.1}}{\gamma_{00.1}}$	$\frac{\gamma_{10.0}}{\gamma_{00.1}}$	$\frac{\gamma_{10.1}}{\gamma_{00.1}}$	$\frac{\gamma_{10.0}}{\gamma_{00.1}}$	$\frac{\gamma_{10.1}}{\gamma_{00.1}}$
0.1M $CaCl_2$ + 0.2M $NaOH$ + 0.1M Na_2SO_4	10	3.09	> 3.14	2.35	> 2.50	3.95	> 3.86

morphology (see figure 5.13a). No two separate particle populations, corresponding to the two peaks observed for the PSD measurement, can be distinguished by SEM. However the positions of the two peaks seem to correspond approximately to the hight and the width of the hexagonal platelets. Bi-modal distributions would be expected for random orientation in the laser diffraction measuring cell of such low aspect ratio platelets [KDS+06].

The portlandite morphology observed here is similar to the one observed by Harutyunyan et al. [HKM+09] for portlandite particles formed by hydration of ASTM Type II Portland cement with 6% C4A3$ admixture and in the presence of gypsum. The results are also consistent with results from Berger et al. [BM72] and Gallucci et al. [GS07] whose results indicate that the presence of sulfates promotes a hexagonal platelet morphology of the growing portlandite particles. Since a hexagonal platelet morphology means that the dimension of the particles in [00.1] direction is much smaller than in [10.0] direction, these results show that the relative growth speed and/or the relative interfacial energy in [00.1] is reduced by the presence of sulfate ions. This indicates that sulfates interact with the portlandite surfaces either by adsorbing onto specific surfaces and changing their relative interfacial energies or by adsorbing onto specific growth sites and changing their relative growth rate.

The statistically relevant increase of both $\frac{\gamma_{10.0}}{\gamma_{00.1}}$ and $\frac{\gamma_{10.1}}{\gamma_{00.1}}$ has been confirmed by the statistical analysis (see table 5.2) of the estimated relative interfacial energie from the SEM images (see table 5.3). The calculated $\gamma_{10.0}/\gamma_{00.1}$ for the sulfate containing system (3.09) was much higher than the value in the system without sulfates (0.58). The value is consistent with the value of > 2 reported by Berger and McGregor [BM72] for particles formed in the presence of sulfates. It is also mostly consistent with the value of 2.5 - 2.7 reported by Harutyunyan et al. for sulfate containing cementitious systems [HKM+09]. In fact the consistency of the experimental results of different authors with the current results is remarkable as the chemical compositions of the systems considered by Berger and McGregor as well as by Harutyunyan et al. were, apart from the sulfate content, quite different from the system considered here. It seems that the effect of the sulfate ions dominates the shape of the portlandite particles. Since the [10.1] surface does not appear in the morphology only a lower bound for its relative energy can be calculated. The relative surface energy of the [10.1] surface has to be higher than 3.14 for the facet not to appear in the morphology. This means that the relative energy or the relative growth rate of both the [10.0] and the [10.1] surfaces with respect to the [00.1] surface increase markedly with the addition of sulfates.

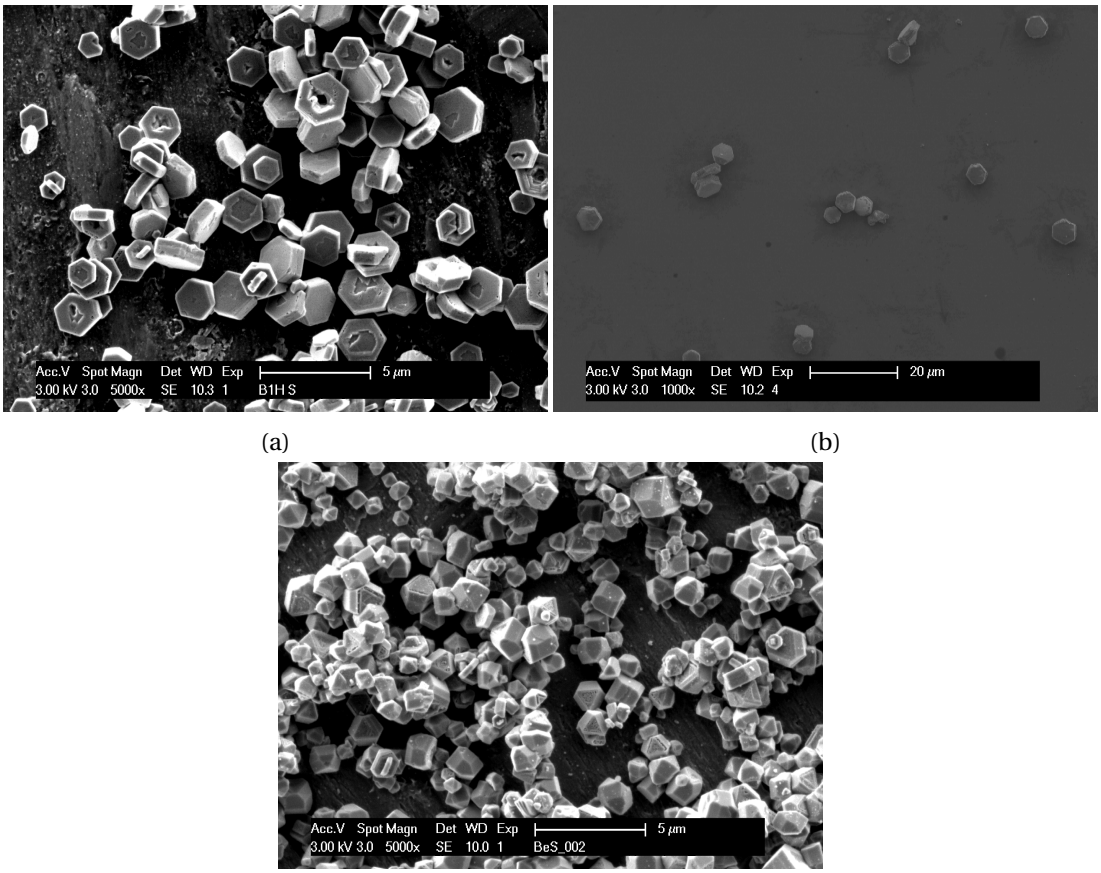

(a) (b)

(c)

Figure 5.13: SEM image of portlandite particles produced by coprecipitation of 0.1 M $CaCl_2$ + 0.2 M $NaOH$ with the addition of 0.1 M Na_2SO_4 (a) and (b) and with the addition of 0.02 M Na_2SO_4 (c) after 1 hour precipitation time. (a) and (c) have been washed with ultra pure water and (b) with a saturated $Ca(OH)_2$ solution. The contrast of image (c) has been enhanced for better visibility.

If the concentration of the sulfate ions is decreased to 0.02 $\frac{mol}{l}$ the shape of most particles shows again the three different families of facets observed for the control system (see figure 5.13c). However the particles are no longer elongated in [00.1] direction and some particles of almost hexagonal platelet morphology can also be observed, indicating a particle shape in between the ones observed for the control system and for system with a higher concentration of sulfates.

Secondary Precipitation of Gypsum

For an initial concentration of 0.1 M Na_2SO_4 thermodynamic calculations (see chapter 6) predict the formation of 45 % gypsum by weight under the conditions used for the coprecipitation experiments. The gypsum might transform to a hemihydrate phase during the

drying of the powder at 60 ° C during 24 to 72 hours. However for the original experiment with a precipitation time of 1 hour neither gypsum nor hemihydrate is observed with X-ray diffraction (XRD) (see figure 5.14a) or TGA (see figure 5.11b). With a precipitation time of 2 months however, peaks of a secondary phase can be observed with XRD (see figure 5.14b). The second phase XRD pattern shows similarities with the XRD pattern of gypsum. However the peaks seem to be slightly shifted to higher values and an additional peak at 11.8 ° is observed. TGA measurements indicate about 31 % secondary phases other than calcite. Additionally the TGA curve shows additional weight losses at 102 ° C and at 702 ° C. These temparatures are typical for the decomposition of gypsum. The peak at 101 ° C is approximately the temperature where gypsum looses its crystalline water and transforms to anhydrate (see equation 5.7). For gypsum n in equation 5.7 equals 2, however if the total weight loss at 102 ° C is used to calculate the amount of gypsum based on $n = 2$, only a percentage of 8 % of gypsum is estimated. If on the other hand one supposes that the initial phase is a hemihydrate with $n = 0.5$, 27.6 % weight of the initial sample are estimated to be hemihydrate. This is in good agreement with the 30 % secondary phase estimated from the amount of portlandite and the amount of calcite, indicating that the secondary phase might be, at least partially, hemihydrate instead of the thermodynamically predicted gypsum. However, as mentioned before, a conversion from gypsum to hemihydrate might also occurr during the drying step.

The fact that gypsum or hemihydrate are only observed after 2 months of precipiation indicates that the formation of gypsum is kinetically inhibited. Even after 2 months not the full 45 % predicted from thermodynamic calculations are observed. A possible reason for the absence of gypsum after 1 hour of precipitation can be seen from the SEM images. The SEM images of the powders after 1 hour of precipitation (see figure 5.13a) show defects or even holes in the middle of the portlandite crystals as if the central part of the particle had been dissolved during the washing step with 100 ml of ultrapure water. This lead us to the assumption that there might be a metastable calcium-sulfate phase forming initially and serving as nuclei for the portlandite particles.

$$CaSO_4 \cdot nH_2O \longrightarrow CaSO_4 + n \cdot [H_2O]_g \tag{5.7}$$

To confirm/disprove this theory an experiment was done with the same initial concentration of sulfates (0.1 M Na_2SO_4) and one hour of precipitation time. The resulting powder was then however not washed with ultrapure water but with a saturated $Ca(OH)_2$ solution. The SEM image for the sample washed with a saturated $Ca(OH)_2$ solution can be seen in figure 5.13b. Fewer defects at the center of the particles were observed. This indicates that the centers might indeed be preferentially dissolved during the washing step. The hypothesis of metastable calcium-sulfate nuclei would also be consistent with observations by Gallucci and Scrivener [GS07] of preferential portlandite nucleation in the neighborhood of gypsum grains. A space resolved composition analysis technique, e.g. EDS, of the particles washed

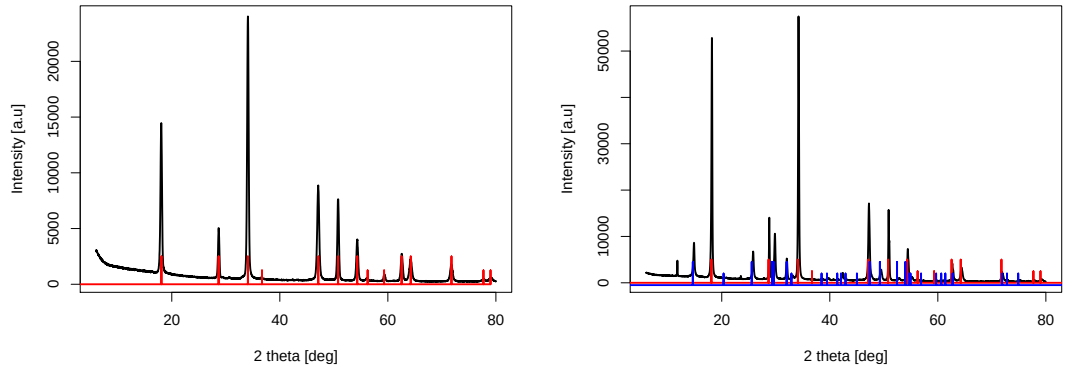

(a) (b)

Figure 5.14: XRD of portlandite particles produced by coprecipitation of 0.1 M $CaCl_2$ + 0.2 M $NaOH$ with the addition of 0.02 M Na_2SO_4 after 1 hour (a) and 2 months (b) precipitation time. The position of portlandite peaks is indicated in red and gypsum peaks in blue.

with a saturated $Ca(OH)_2$ solution would give further information on the composition of the central region of the portlandite platelets. However such measurements were not done in the framework of this thesis.

Due to the retardation of the precipitation of gypsum in the coprecipitation system, the predictor variable sulfate concentration times time ($S \cdot t$) has been included in the statistical analysis of the phase composition and the size of the particles. For the phase composition only this factor has been found to be statistically relevant and not the sulfate content itself (see table 5.2) reflecting the retardation effect.

In summary the main effect of sulfates on the growth and morphology of portlandite appears to be a change of morphology from an quasi equiaxed morphology to a hexagonal platelet morphology. This implies that the morphology determining quantities $\frac{\gamma_{1.00}}{\gamma_{00.1}}$ and $\frac{\gamma_{10.1}}{\gamma_{00.1}}$ are both significantly increased by the presence of sulfates. This could either be due to a preferentially adsorption of sulfates onto specific portlandite surfaces, most likely the [00.1] surface, lowering the relative interfacial energy of the [00.1] surface compared to the [10.0] and the [10.1] surfaces. It could also be due to the adsorption of the sulfates onto specific growth features thus slowing down the relative growth speed of the [00.1] surface compared to the [10.0] and the [10.1] surface. The observations are consistent with previously reported observations of a hexagonal platelet morphology of portlandite in the presence of sulfates [GS07, BM72, HKM$^+$09].

Another feature of the portlandite particles in the sulfate containing systems is the presence of defects or even holes at the center of the hexagonal platelets. This might indicate the presence of metastable sulfate containing nuclei on which the portlandite particles precipitate. This would also explain why the precipitation of gypsum is retarded in the coprecipitation systems as the concentration of sulfates in the solution would be lowered due to the presence of the

sulfate containing nuclei. Additionally it would be consistent with observations by Gallucci and Scrivener that portlandite preferentially precipitates in the neighborhood of gypsum. Future experiments with space resolved composition measurements, such as EDS, might give further insights. However the particles used in such experiments would have to be washed with a saturated $Ca(OH)_2$ solution so that the central region of the portlandite particles is not dissolved.

5.3.5 Influence of Aluminates

The second component, identified by Gallucci and Scrivener [GS07] as important for the change of the portlandite morphology from large agglomerates to individual platelets in C3S systems, are aluminates. In C3S systems the morphology of portlandite changed only if both sulfate and aluminates were present. Therefore, to study the influence of aluminates on the morphology of portlandite, coprecipitation experiments with the addition of 0.001 or 0.003 $\frac{mol}{l}$ $Al(NO_3)_3$ were done.

The concentration of aluminates had to be kept low to avoid precipitation of C3AH6 instead of portlandite. According to thermodynamic calculations only a small amount of aluminate phase (3.4 % by weight) is expected to precipitate according to thermodynamic calculations (see chapter 6) when 0.001 $\frac{mol}{l}$ $Al(NO_3)_3$ is added. TGA results confirm that the powder is mostly portlandite with an estimated 4.1 % of aluminate phase (see figure 5.11b). If the amount of aluminates is increased to 0.003 $\frac{mol}{l}$, the amount of aluminate phase estimated by TGA increases to 14.1 %. This is also reflected by the positive β_{Al}^{est} determined by the statistical analysis for the percentage of secondary phases other than calcite (see table 5.2).

The $d[v,50]$ of the main peak of the particle size distribution increases, statistically significantly (see table 5.2), upon the addition of 0.001 $\frac{mol}{l}$ $Al(NO_3)_3$ from 0.74 μm in the control to 9.48 μm in the aluminate containing system. Upon a further increase of the aluminate concentration to 0.003 $\frac{mol}{l}$ the size of the particles does not increase further but stays similar (main peak $d[v,50]$: 7.25 μm). This nonlinearity of the particle size with the aluminate concentration leads to the problems of the statistical analysis described earlier (see section 5.3.2). For both aluminate concentrations there is a secondary peak of about 14 and 24 % by volume with a $d[v,50]$ of 0.67 and 0.75 μm for the low and high aluminate concentration respectively.

From TGA and PSD results, the effect of aluminates on the growth and morphology of portlandite appears to be similar to the effect of silicates. The SEM images on the other hand (see figure 5.15) show that the effect is in reality quite different. Whereas the increase in the measured $d[v,50]$ for silicates was due to agglomeration, for aluminates the size increase seems to correspond to an increase of the primary particle size. For the sample containing 0.001 $\frac{mol}{l}$ $Al(NO_3)_3$ (see figure 5.15a), the general shape of the precipitated portlandite particles does not change markedly compared to the control system, the basic shape with three families of facets ([10.0], [10.1] and [00.1]) is conserved. However the observed shapes become more irregular. A reason for the observed irregularity of the particle shape might be

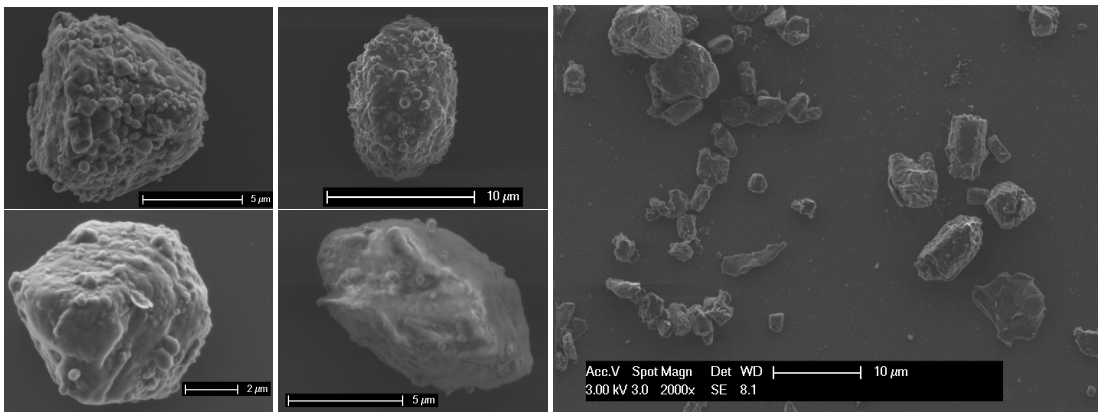

(a) (b)

Figure 5.15: SEM image of portlandite particles produced by coprecipitation of 0.1 M $CaCl_2$ + 0.2 M $NaOH$ with the addition of 0.001 M $Al(NO_3)_3$ (a) and with the addition of 0.003 M $Al(NO_3)_3$ (b) after 1 hour precipitation time. Contrast is enhanced.

the second phase that can be distinguished on the sufaces of the portlandite particles. This is possibly the secondary aluminate phase which is present in small amounts according to TGA measurements. Also the particles appear to be more elongated in [00.1] direction indicating a decrease of $\frac{\gamma_{10.0}}{\gamma_{00.1}}$ and $\frac{\gamma_{10.1}}{\gamma_{00.1}}$. This effect was also revealed by the statistical analysis (see table 5.2).

If the concentration is further increased to 0.003 $\frac{mol}{l}$ $Al(NO_3)_3$, the particle shape becomes even more irregular. Some facetted particles can still be observed but the shape of other particles has become random. A few very small particles, corresponding to the second peak in the particle size distribution, can be distinguished as well. Their shape is rather irregular and it is difficult to say whether they are primarily portlandite or primarily some other phase. Again compositional analysis, such as EDS, might be used here.

In summary the main effect of the addition of aluminates observed was the increase of the size of the primary particles. For constant nucleation and growth mechanisms, a change of the primary paricle size is usually caused by changes of the growth rate compared to the nucleation rate. To increase the size of the primary particles the growth rate has to be increased compared to the nucleation rate. It is difficult to see how the addition of aluminates could speed up the growth rate of the particles and therefore a more logial supposition is that the aluminates slow down the nucleation of portlandite to some extent. The effect is non linear, and an increase of the aluminate concentration from 0.001 to 0.003 $\frac{mol}{l}$ does not lead to a further increase in the particle size. Previous results reported by Berger and McGregor [BM72] were not so clear as to the effect of aluminates, whereas the addition of AlF_3 was observed to decrease the number of crystals formed per unit area, the addition of $Al(NO_3)_3$ had little effect and the addition of $Al(OH)_3$ even increased the number of portlandite particles per volume. However these previous observations were done by studing the effect of admixtures on the portlandite particles formed upon the hydration of $C3S$, which is a much more complex

system then the coprecipitation experiments used here. Consequently there are many possible indirect effects that may influence the result such as a change of the dissolution rate of the $C3S$ or changing spacial constraint due to influences on the morphology of the other hydrates.

Additionally a certain amount of secondary phase is observed at the surface of the portlandite particles, leading to more irregularities of the particle shape compared to the control system. The aluminates also lead to a slight increase in the growth rate or the surface energy of the [00.1] surface leading to more elongated particles. This is mostly consistent with previous observations by Berger and McGregor [BM72] where the addition of different aluminates was observed to have little effect or to decrease the aspect ratio of $\frac{L^{10.0}}{L^{00.1}}$ (see table 4.1).

5.3.6 Synergetic Effects

The effect of each ionic addition on the growth and morphology of portlandite has been discussed in some detail in the sections above. However in addition to the effect of individual ionic additions there might also be some synergetic effect upon the addition of different combinations of ions. As an example the change of the portlandite morphology in cementitious systems reported by Gallucci and Scrivener [GS07] was only observed if both aluminates and sulfates were added. Consequently a series of experiments with the addition of different combinations of ions was also done to study possible synergetic effects. The results for the different combinations of ions will be discussed in this section.

Silicate - Sulfate Synergy

TGA measurements of samples precipitated in systems with 0.001 M Na_2SiO_3 and 0.1 M Na_2SO_4 reveal similar phase compositions (0.5 % secondary phases by weight) as both the sample containing only silicates (4.6 % other phases) and the sample containing only sulfates (0 % other phases). The measured content of secondary phases is slighly lower than for the sample containing only silicates, however the difference can be explained by the estimated standard deviation of 3.6 % (see figure 5.11b). Consequently no statistically relevant synergetic effect on the phase composition could be found (see table 5.2).

PSD measurements paint a similar picture. The particle size distribution is similar to the sample with only silicates, with a slightly higher $d[v,50]$ of the main peak (5.5 μm compared to 4.0 μm for the sample containing only silicates, see figure 5.11a). Since the addition of sulfates has been found to have little effect on the particle size, this indicates that the effect of the silicates dominates the changes in the particle size distribution with no or little contribution of the sulfates. Consequently no statistically relevant synergetic effect of silicate and sulfate on the particle size could be found by statistical analysis (see table 5.2).

The additivity of the effects of the silicates and the sulfates can also be seen by looking at the SEM images (see figure 5.19). Previously it was found that the addition of silicates leads to the agglomeration of the portlandite particles whereas the addition of sulfates leads to a

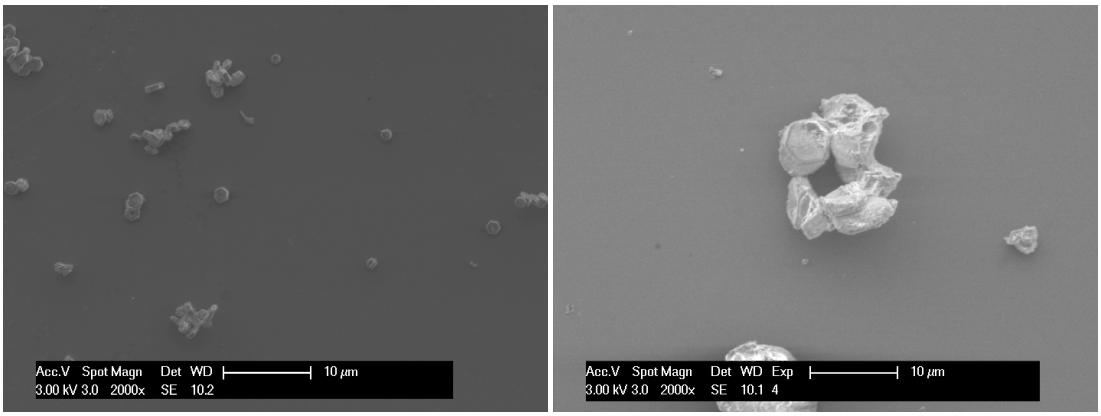

Figure 5.16: SEM image of portlandite particles produced by coprecipitation of 0.1 M $CaCl_2$ + 0.2 M $NaOH$ with the addition of 0.001 M Na_2SiO_3 and 0.1 M Na_2SO_4 after 1 hour precipitation time. The contrast of the left hand image was enhanced for better visibility.

change of the shape of the primary particles towards hexagonal platelets. The addition of both silicates and sulfates appears to lead to agglomerates of primary particles that have a hexagonal platelet shape.

Silicate - Aluminate Synergy

For a system with both 0.001 M Na_2SiO_3 and 0.001 M $Al(NO_3)_3$, an amount of 7.4 % by weight secondary phases have been estimated by TGA measurements. This is close to the sum of the amounts measured for the system with only silicates (4.6 %) and for the system with only aluminates (4.1 %). This indicates that there is no synergetic effect between silicates and aluminates on the amount of secondary phase precipitated, a hypothesis that is confirmed by the statistical analysis (see table 5.2).

A similar trend can be observed for the particle size distribution (see figure 5.11a). The $d[v,50]$ of the main peak of the particle size distribution at 11.9 μm is larger than observed for both the sample containing only silicates (4.03 μm) and for the sample containing only aluminates (9.9 μm). This is consistent with the previous observations that both silicates and aluminates increase the measured particle size. However the peak at larger particle sizes ($\sim$ 26 μm) observed for the system containing only silicates is absent in the aluminate - silicate system.

The shape of the particles observed by SEM (see figure 5.18) is very irregular. However, contrary to both the silicate and the silicate-sulfate system, there are no clearly distinguishable primary particles, making it difficult to say whether the observed particles are aggregates or individual primary particles. Sometimes large straight facet like features can be distinguished, however those features do not seem to be obeying the underlying crystal symmetry and thus they can not serve to distinguish reliably between aggregates and primary particles. There also appears to be some product at the surface of the particles as observed previously for both the silicate and the aluminate systems.

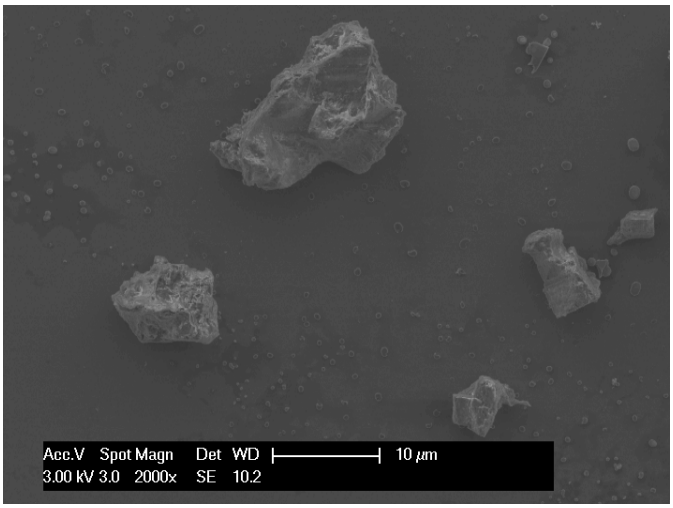

Figure 5.17: SEM images of portlandite particles produced by coprecipitation of 0.1 M $CaCl_2$ + 0.2 M $NaOH$ with the addition of 0.001 M $Al(NO_3)_3$ and 0.001 M Na_2SiO_3 after 1 hour precipitation time. Image contrast was enhanced.

Aluminate - Sulfate Synergy

If 0.001 M $Al(NO_3)_3$ and 0.1 M Na_2SO_4 are added to the system, the amount of secondary phases by weight estimated from TGA is 8.0 %. This is higher than both the amount of secondary phases estimated for the sulfate (0 %) and for the aluminate system (4.1 %). This indicates a synergetic effect since sulfate was previously estimated to have no effect on the amount of secondary phase precipitated after 1h. The amount of secondary phases is still low compared to the 50 % predicted by thermodynamic calculations. This synergetic effect is confirmed by the statistical analysis, predicting a positive $\beta^{est}_{S\cdot Al}$ (see table 5.2. The increase of secondary phases is probably due to the precipitation of aluminium sulfate minerals such as AFt phases (a family of calcium sulfoaluminate hydrates, the most common being ettrigite: $Ca_6Al_2(SO_4)_3(OH)_{12}\cdot 26H_2O$). Thermodynamic calculations predict the formation of 6.9 % AFt phases, which is in quite good agreement with the measured TGA results.

PSD measurements show a similar particle size distribution as for the aluminate samples, however the $d[v,50]$ of the main peak (5.5 μm) is lower than for the aluminate system (9.5 μm) but still significantly higher than for the sulfate sample (0.9 μm). As discussed above, sulfate does not appear to have a marked effect on the particle size and the size reduction compared to the system with only aluminates was not statistically significant according to the least squares linear regression used (see table 5.2).

The effect of the two ions seem to be remarkably additive. SEM images reveal that the morphology of the particles is that of hexagonal platelets (see figure 5.18). The change of the morphology to hexagonal platelets has previously been identified as the main effect of sulfate ions. The main effect of aluminates is a size increase of the particles and the particles precipitated in the presence of both sulfates and aluminates have a larger size than the particles

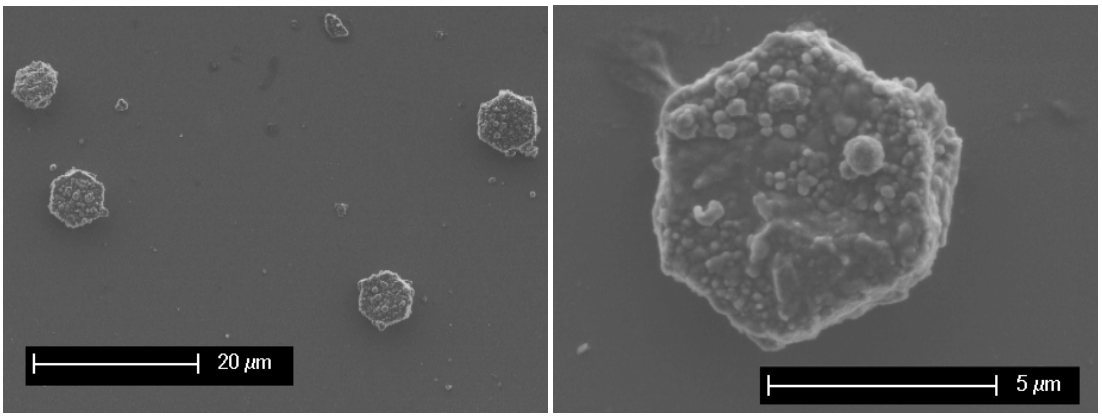

Figure 5.18: SEM images of portlandite particles produced by coprecipitation of 0.1 M $CaCl_2$ + 0.2 M $NaOH$ with the addition of 0.001 M $Al(NO_3)_3$ and 0.1 M Na_2SO_4 after 1 hour precipitation time. Image contrast was enhanced.

Table 5.4: Estimated relative interfacial energies of the different facets for particles precipitated from a 0.1 M $CaCl_2$ + 0.2 $NaOH$ solution with the addition of 0.001 M $Al(NO_3)_3$ and 0.1 M Na_2SO_4.

		average		min		max	
initial concentrations	no_{part}	$\frac{\gamma_{10.0}}{\gamma_{00.1}}$	$\frac{\gamma_{10.1}}{\gamma_{00.1}}$	$\frac{\gamma_{10.0}}{\gamma_{00.1}}$	$\frac{\gamma_{10.1}}{\gamma_{00.1}}$	$\frac{\gamma_{10.0}}{\gamma_{00.1}}$	$\frac{\gamma_{10.1}}{\gamma_{00.1}}$
0.1M $CaCl_2$ + 0.2M $NaOH$ + 0.1M Na_2SO_4	5	2.47	> 2.61	1.99	> 2.20	2.94	> 3.01

observed in systems containing only sulfates. A second product at the surface of the portlandite particles can be distinguished. The morphology of this product is similar to what is observed for systems with only aluminates however according to thermodynamic calculations and TGA measurements the amount and composition of the phase is probably different. TGA measurements showed a characteristic weight loss at 89.5 ° C, which would be consistent with AFt phases. EDS or XRD measurements might give further information but were not done in the context of this thesis.

Some particles with a regular shape and clearly defined edges could be found and analysed further to estimate the morphology controlling quantity $\frac{\gamma_{10.0}}{\gamma_{00.1}}$ and estimate a lower limit for $\frac{\gamma_{10.1}}{\gamma_{00.1}}$. The number of particles analyzed (5) was relatively low, as not all particles could be used for analysis. For example the height of particles perfectly oriented in such a way that only the hexagonal facet is visible can not be determined and thus those particles could not be used. However the estimated $\frac{\gamma_{10.0}}{\gamma_{00.1}}$ was lower than for the sulfate system. This effect was estimated to be statistically significant (see table 5.2) and is consistent with the fact that the particles observed in the sulfate system appeared to be slightly more elongated compared to the control system. Thus it can be concluded that aluminates appear to increase $\frac{\gamma_{10.0}}{\gamma_{00.1}}$ thus partially counteracting the effect of the sulfates. However the effect of the sulfates dominates.

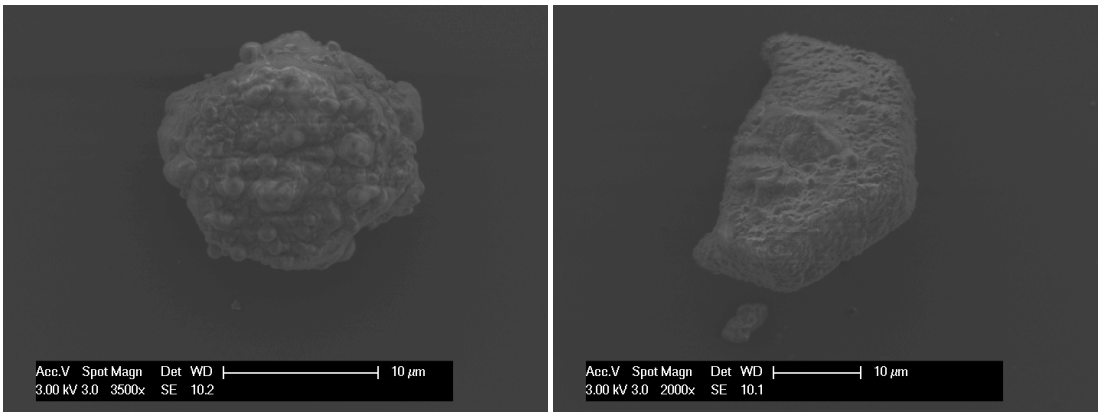

(a) (b)

Figure 5.19: SEM images of portlandite particles produced by coprecipitation of 0.1 M $CaCl_2$ + 0.2 M $NaOH$ with the addition of 0.001 M $Al(NO_3)_3$,0.001 M Na_2SiO_3 and 0.1 M Na_2SO_4 after 1 hours precipitation time. Image contrast was enhanced for better visibility.

A few of the particles observed had a defective region at the center of the particles which looked as if the central region had been partially dissolved or removed, similarly to what has been observed for the systems containing only sulfate. Indicating that a similar mechanism as observed for the sulfate system is still active, although no particles with complete holes at the center were observed.

Aluminate - Sulfate - Silicate Synergy

If all three studied ionic compounds, 0.001 M $Al(NO_3)_3$,0.001 M Na_2SiO_3 and 0.1 M Na_2SO_4, are added to the coprecipitation experiments, the amount of secondary phase observed with TGA (26 % by weight, see figure 5.11b) is more than double the amount of secondary phases observed in any of the above discussed systems. However the amount of secondary phases is still lower than the thermodynamic predictions of 51 %. On the other hand if gypsum is excluded, only 9 % of secondary phases are expected to precipitate, indicating that some gypsum might have precipitated. The only weight loss measured by TGA, apart form the portlandite and calcite signals, show a weight loss at a characteristic temperature of 111 ° C. This temperature could be consistent with the decomposition of gypsum but other phases, such as AFt and C-S-H also show characteristic weight losses in the same temperature range. The observed signal is probably a convolution of different signals. Consequently other methods, such as XRD, would be needed to conclusively study the composition of the precipitated powders.

The $d[v,50]$ of the main peak (18.0 μm) measured by TGA is also larger than that of any other sample discussed so far. However this effect is not taken into account by the statistical analysis which predicts the same size for the system containing both silicates and aluminates as for the system containing all three additions (see table 5.2).

The SEM images (see figure 5.19) show that the portlandite particles are shaped like large hexagonal plates. A second phase can be clearly distinguished at the surface of the particles. The sulfates and aluminates seem to have counteracted the agglomeration effect of the silicates. However the primary particle size has become much larger than for the previously discussed systems. The shape of the particles appear to be consistent with the hexagonal platelet morphology observed in cementitious systems with both aluminates and sulfates present [GS07, HKM$^+$09] but the size of our particles is significantly larger.

For one of the particles observed by SEM the edges were distinguishable clearly enough and the angle tilted enough to allow the estimation of $\frac{\gamma_{10.0}}{\gamma_{00.1}}$ (3.43) and the lower limit of $\frac{\gamma_{10.1}}{\gamma_{00.1}}$ (> 3.42). This result indicates that the aspect ratio is again higher than for the system with both sulfates and aluminates. This might indicate that the silicates have a tendency to increase $\frac{\gamma_{10.0}}{\gamma_{00.1}}$ (see table 5.2). However since the result is based on only one observed particle, it has to be treated with care.

5.4 Summary

In this chapter the precipitation, growth and final morphology of portlandite in model systems was studied experimentally. The first step was to determine the morphology of portlandite in a pure calcium-hydroxyde-water system. With thermal precipitation individual, facetted crystals could be obtained after 23 days of precipitation. The crystals were not completely regular, indicating a system close to but not completely at equilibrium. The observed crystal mophology in the pure system was equiaxed with three different families of facets. The fact that the morphology was equiaxed and not hexagonal with large [00.1] facets, as would be expected from the fact that the [00.1] facet is a perfect cleavage plane with low energy [ABBN97], indicates strong, anisotropic surface-solvant interactions.

The effect of different ionic additions on the growth and morphology of portlandite was then studied in a series of coprecipitation experiments. The coprecipitation experiments were faster and had a higher yield than thermal precipitation, which allowed further analysis of the precipitated powder (i.e. TGA and PSD measurements). The counter ions ($NaCl$) used for the coprecipiation experiment were shown to have no or a very limited effect on the growth and morphology of portlandite. Also the small amount of carbonates present in the coprecipitation systems was shown to have, in all probability, little effect on the growth and morphology of portlandite. The morphology observed for the control coprecipitation experiments was similar to the one observed in the pure system but the particle size was smaller and the particles were more regular. The three observed families of facets were identified to be [00.1], [10.0] and [10.1] facets and their morphology determining quantity (relative interfacial energy or growth speed) was estimated.

Silicates were then shown to have an important effect on the growth of portlandite. If silicates are added, the growing portlandite particles form agglomerates and the shape of the primary particles becomes irregular. Some primary particles with an elongated hexagonal rod mor-

phology, protruding from the center of an aggregate, could be observed in silicate containing systems. This morphology is otherwise characteristic for low supersaturations. A secondary phase could be distinguished at the surfaces and in between the primary particles of the aggregates. This secondary phase was in all likelihood C-S-H. The observations of the influence of silicates on the growth and morphology of portlandite could have some implications for cementitious systems. If the initial portlandite particles are covered with C-S-H, this could slow down the growth of portlandite, thus contributing to the induction period.

Sulfates were shown to promote a hexagonal platelet morphology of portlandite, indicating a decrease of the morphology determining quantity of the [00.1] surface with respect to the other surfaces. This is likely due to specific interaction of the sulfate species with the [00.1] surface which leads to a reduction of either the interfacial energy or the growth speed of the [00.1] surface or both. In addition the central region of the hexagonal portlandite platelets were found to be preferentially dissolved in ultrapure water, indicating that their composition might be different from the rest of the particle. Together with the fact that gypsum precipitation seemed to be retarded, this lead to the assumption that small metastable, sulfate containing precipitates serve as nuclei for the portlandite particles.

Aluminates were shown to increase the particle size of portlandite. This indicates that aluminates hinder the nucleation of portlandite particles. Additionally the addition of aluminates seems to lead to a slight elongation of the portlandite particles in [00.1] direction. This effect is opposite to the effect of sulfates, possibly indicating a specific interaction of the aluminates with the [10.0] surface.

Finally the effect of different combinations of ions on the morphology of portlandite has been studied. The effect of the different ions seems to be additive; the addition of silicates and sulfates leads to agglomerates of primary particles with hexagonal platelet shape whereas the addition of sulfates and aluminates leads to hexagonal platelet particles with an increased particle size. If silicates, sulfates and aluminates are added, huge hexagonal plates are formed. The particles seem to be well dispersed, indicating that the sulfates and the aluminates together counter the agglomerating effect of the silicates.

6 Species Present in Solution under Different Portlandite Precipitation Conditions

In this chapter the speciation of the solution for different precipitation conditions of calcium hydroxide is discussed. One of the aims was to estimate eventual changes in the calcium and hydroxide speciation upon the addition of aluminates, silicates and/or sulfates, which might influence the growth of portlandite. Another aim was to get an idea of what species are likely to interact with the growing portlandite particles. The speciation of the model experiments discussed in chapter 5 will be compared to the speciation in the pore solution of ordinary portland cements (OPC). Both thermodynamic calculations as well as metadynamics calculations were used to estimate the speciation.

In this chapter the species present in the solution under the different precipitation conditions will be discussed. The speciation of the solution surrounding the growing portlandite particles is important for two reasons. Firstly a change in the Ca and OH speciation might change the growth mechanism and the predominant growth unit. This will influence the growth and final morphology of portlandite particles. Secondly the predominant silicate, sulfate and aluminate species are most likely to interact with the growing portlandite particles and thus to be responsible for observed changes of portlandite growth and final morphology. According to previously discussed Ca activity measurements, the experimentally observed morphologies of portlandite produced by coprecipitation (see chapter 5) are formed in close to equilibrium conditions. Therefore thermodynamic calculations were done to estimate the equilibrium concentration, which were assumed to be a good approximation of the growth conditions. The results for the thermal and the coprecipitation experiments are compared to results for ordinary portland cements (OPC's). Finally further insight into the silicate speciation is gained with metadynamics calculations based on classical molecular dynamics.

6.1 Thermodynamic Calculations

The thermodynamic calculations were done with GEMS v2 [KW09, WKHD12, KWD$^+$12] with the thermodynamic database CEMDATA [KK01, LW06], which has been developed for cementitious systems, in combination with the Nagra / PSI chemical thermodynamic data base [HBC$^+$02]. The built in extended Debye-Hückel equation in Truesdell - Jones form with individual Kielland ionic radii a and a common third parameter $\beta_\gamma = 0.064$ has been chosen to calculate the activity coefficients. This model has been used before for cementitious systems [LW06] and should be accurate for ionic strengths up to 1-2 M [KW09].

If nothing else is specified, the thermodynamic calculations were performed for a temperature of 22 ° C and a pressure of 1 bar.

6.1.1 Results for Coprecipitation Experiments

Thermodynamic calculations for all the main coprecipitation experiments discussed in chapter 5 were done. This means that calculations were done for the control experiment, for the experiments with the single addition of sulfates, silicates or aluminates as well as for the experiments with the addition of different combinations of ions. Both the speciation and the amount of portlandite as well as the amount of secondary phases were looked at.

The thermodynamic calculations show that the concentration of the Ca and OH species for the coprecipitation experiments remain essentially unchanged upon the addition of silicates or aluminates (table 6.1). The thermodynamic calculations predict the predominant species to be Ca^{2+} and OH^- ions whose concentrations are 20 and 40 mM respectively. The concentration of a calcium hydroxyl complex, $CaOH^+$, is non negligible but 5 times lower than the concentration of Ca^{2+}.

Silicates

The main silicate species predicted by GEMS in the silicate containing systems is a neutral calcium silicate complex (see table 6.1). If 1 mM Na_2SiO_3 is added to the coprecipitation experiments, the predicted calcium - silicate complex concentration at equilibrium is 0.03 mM. This concentration is much smaller than the Ca^{2+} concentration and consequently the influence of the calcium-silicate complex formation on the calcium speciation is negligible. The predicted calcium-silicate complex is not included in all thermodynamic databases (e.g. PHREEQC [PA99]) and its existence is somewhat disputed. It is included in the GEMS Nagra /PSI chemical thermodynamic database [HBC$^+$02] based on work by Santschi and Schindler [SS74]. Santschi and Schindler did potentiometric titrations of H_4SiO_4 in the presence of Ca^{2+} from pH 3 to a maximum pH of 8.9. They estimated the amount of neutral complexes formed and calculated the corresponding equilibrium constants. However they could not distinguish between different types of neutral complexes. Consequently the authors calculated different

Table 6.1: Concentration of different species and precipitates expected at equilibrium for the different model systems (control system and experiments with single addition of silicates, sulfates or aluminates) according to thermodynamic calculations.

Initial conc. [mol/l]	pH	Ca^{2+} [mol/l]	$CaOH^{+}$ [mol/l]	OH^{-} [mol/l]	Other species [mol/l]	Solid phases [g/l]
0.1 $CaCl_2$ + 0.2 $NaOH$	12.6	0.02	0.004	0.04	0.2 Na^{+} + 0.2 Cl^{-}	5.6 g portlandite
0.1 $CaCl_2$ + 0.2 $NaOH$ + 0.001 Na_2SiO_3	12.7	0.02	0.004	0.04	0.2 Na^{+} + 0.2 Cl^{-} + 3e-5 $CaSiO_2(OH)_2$	5.6 g portlandite + 0.2 g C-S-H
0.1 $CaCl_2$ + 0.2 $NaOH$ + 0.1 Na_2SO_4	12.9	0.009	0.003	0.07	0.4 Na^{+} + 0.2 Cl^{-} + 0.005 $Ca(SO_4)$ + 0.02 $Na(SO_4)^{-}$ + 0.05 SO_4^{2-}	4.5 g portlandite + 3.7 g gypsum
0.1 $CaCl_2$ + 0.2 $NaOH$ + 0.001 $Al(NO_3)_3$	12.6	0.02	0.004	0.04	0.2 Na^{+} + 0.2 Cl^{-} + 0.003 $NaOH$ + 1e-4 $Al(OH)_4^{-}$	5.4 g portlandite + 0.2 g $C3AH6$

equilibrium constants for different hypothetical neutral complexes. However the authors do state that $CaSiO_2(OH)_2$ is the most probable neutral calcium-silicate complex. This lead Hummel et al. to include the calculated equilibrium constant for the $CaSiO_2(OH)_2$ complex in their database but they suggest further investigation if calcium-silicate complexes are found to be of importance [HBC+02].

The existence of stable calcium - silicate complexes in systems with a pH of 5-7 has since been confirmed by Tanaka and Takahashi [TT00, TT02] both by a measured increase of the amount of silicates dissolved in the presence of calcium and with the help of fast atom bombardment mass spectrometry (FAB-MS). However FAB-MS can only identify charged species. What is more, Tanaka and Takahashi only studied negatively charged species. In FAB-MS the characteristic ratio of the mass over the charge of the species is measured, allowing their identification. Takahashi identified a relatively large range of calcium - silicate complexes with both monomeric and polymeric silicate species. This reinforces the previous findings of stable calcium-silicate complexes by Santschi and Schindler. In other words it is very likely that calcium-silicate complexes exist in the portlandite coprecipitation systems studied here, as predicted by our thermodynamic calculations, however the type and exact nature of the species is somewhat uncertain. The uncertainty about the type of the calcium - silicate complexes in cementitious systems is enhaced by the fact that the studies by both Santschi and Schindler and Tanaka and Takahashi were done at lower pH, compared the systems studied here. At these lower pH the predominant non-complexed silicate species is $SiO(OH)_3^{-}$ and not $SiO_2(OH)_2$, which is favored at higher pH.

The addition of 0.001 M Na_2SiO_3 also leads to the precipitation of a small amount of C-S-H.

According to our calculations about 3 % by weight of the solid powder formed by coprecipitation is expected to be C-S-H. This is in good agreement with the phase composition measured by TGA (see chapter 5).

Aluminates

The main aluminate species present in the aluminate containing system is the $Al(OH)_4^-$ ion (see table 6.1). If 1 mM $Al(NO_3)_3$ is added to the coprecipitation experiments, the thermodynamic calculations predict a concentration of 0.1 mM $Al(OH)_4^-$ at equilibrium. Since no complex with Ca is formed, the addition of aluminates is predicted to have little effect on the calcium speciation. In fact aluminates are the only addition studied here where no complex formation was observed.

The addition of aluminates also leads to the precipitation of a small amount of C3AH6 (i.e. a hydrogarnet phase with exact stoichiometry $Ca_3Al_2(OH)_{12}$, also called tricalcium aluminate hydrate or katoite). When 0.001 M $Al(NO_3)_3$ is added to the coprecipitation, 4 % of the collected powder is expected to be C3AH6 according to the thermodynamic calculations. This agrees well with the TGA measurements discussed in chapter 5.

Sulfates

The main sulfate species in the coprecipitation systems according to the thermodynamic calculations are SO_4^{2-} and $NaSO_4^-$ ions. If 0.1 M Na_2SO_4 is added to the system, thermodynamic calculations predict 0.05 M SO_4^{2-} and 0.02 M $NaSO_4^-$ (see table 6.1).

In addition, if sulfates are added to the system a $Ca(SO_4)$ complex forms. For 0.1 M Na_2SO_4, 0.005 M $CaSO_4$ are expected. The existance of the calcium sulfate complex leads to a reduction of the Ca^{2+} (from 0.02 M in the pure to 0.009 M in the sulfate system) and the $CaOH^+$ concentration (0.004 M to 0.003 M) as well as a slight increase in pH (from 12.6 to 12.9). This means that the concentration of calcium ions, which can be readily incorporated into the portlandite crystal during its growth, decreases, whereas the amount of readily available hydoxyl ions increases. This is likely to increase the rate of hydroxyl incorporation and reduce the rate of calcium incorporation into the portlandite crystal. If the incorporation of calcium is the rate determining step, sulfates are thus likely to decrease the portlandite growth rate. If on the other hand the incorporation of hydroxyl is the rate determining step, sulfates are likely to increase the growth rate. The concentration of $CaOH^+$ complexes is slightly lowered as well. This means that if the $CaOH^+$ complex is the growth unit and their incorporation into the crystal is the rate determining step, sulfates can be expected to lower the growth rate slightly. If the rate determining step is different for the different surface orientations of the crystal, the change in concentration could have an effect on the final morphology of the portlandite particles. Also the changes in incorporation rates might actually change the rate determining step from hydroxyl incorporation towards calcium incorporation.

A decrease in the overall growth rate of the portlandite crystals would, if the nucleation rate is not changed, be likely to lead to a decrease of the final particle size. An increase on the other hand would lead to and increased particle size. However neither has been been observed experimentally. This indicates that either the nucleation rate changes as well, or that the growth rate changes differently for the different surfaces. Additionally it is possible, that the effect on the growth rate, for the coprecipitation systems studied here, was too small to have been statistically significant. As we discussed in the previous chapter, there seem to be some metastable initial precipitates that serve as nuclei for portlandite in the presence of sulfates. This indicates a change in nucleation rate which makes it difficult to judge the influence of sulfates on the growth rate.

Additionally gypsum is expected to precipitate in similar amounts as portlandite (~ 45 % gypsum by weight) in the sulfate containing system. However, as discussed in the previous chapter, it has been observed experimentally, that precipitation of gypsum is retarded (see section 5.3.4) and no evidence of gypsum could be found after 1 h of precipitation when portlandite precipitation was complete. This means that contrary to the pure system, where the ionic concentrations quickly change to values close to equilibrium, the solute concentrations in the sulfate containing system might be substantially different from the equilibrium concentrations during the entire growth period of the portlandite particles. Especially the concentration of the sulfate species is likely to be different from equilibrium. This indicates namely that the observed changes of the calcium speciation due to the presence of the sulfates - with all the ensuing effects on portlandite growth and morphology - might be more pronounced, as sulfate concentrations are likely to be higher during the growth of portlandite.

Interaction of Aluminates, Sulfates and Silicates

The biggest change observed if different combinations of ions are added compared to systems with single additions is the type of secondary phases that are expected to precipitate according to thermodynamic calculations (see table 6.2).

If silicates and aluminates are added (0.001 M Na_2SiO_3 + 0.001 M $Al(NO_3)_3$) the hydrogarnet precipitates take up part of the silicates. The stoichiometry of the hydrogarnet becomes $Ca_3Al_2(SiO_4)_{3-x}(OH)_{4x}$. This will decrease both the amount of C-S-H that precipitates (from 0.2 g/l in the silicate system to 0.1 g/l in the silicate-aluminate system) and the amount of aluminates in solution (from 0.1 mM in the aluminate to 2e-4 mM in the silicate-aluminate system).

If sulfates and aluminates are added (0.1 M Na_2SO_4 + 0.001 M $Al(NO_3)_3$), ettringite and other AFt phases precipitate instead of hydrogarnet. The AFt phases have a stoichiometry of $[Ca_3Al(OH)_6 \cdot 12H_2O]_2 \cdot X_3 \cdot nH_2O$, where X is a species with a valence of -2, in the case of the systems studies here, X corresponds pricipally to SO_4. The change from hydrogarnet to AFt phases leads to a reduction of the expected aluminate concentration in solution from 0.1 mM in the aluminate system to 1e-6 mM in the sulfate-aluminate system. Additionally the amount

Table 6.2: Concentration of different species and precipitates expected at equilibrium for the different model systems with the additions of different combinations of silicates, sulfates and aluminates according to thermodynamic calculations.

Initial conc. [mol/l]	pH	Ca^{2+} [mol/l]	$CaOH^{+}$ [mol/l]	OH^{-} [mol/l]	Other species [mol/l]	Solid phases [g/l]
0.1 $CaCl_2$ + 0.2 $NaOH$ + 0.001 Na_2SiO_3 + 0.1 Na_2SO_4	12.9	0.009	0.003	0.07	0.4 Na^+ + 0.2 Cl^- + 0.005 $Ca(SO_4)$ + 0.02 $Na(SO_4)^-$ + 0.05 SO_4^{2-} + 3e-5 $CaSiO_2(OH)_2$	4.5 g portlandite + 3.7 g gypsum + 0.2 g C-S-H
0.1 $CaCl_2$ + 0.2 $NaOH$ + 0.001 Na_2SiO_3 + 0.001 $Al(NO_3)_3$	12.6	0.02	0.004	0.04	0.2 Na^+ + 0.2 Cl^- + 3e-5 $CaSiO_2(OH)_2$ + 2e-7 $Al(OH)_4^-$	5.4 g portlandite + 0.1 g C-S-H + 0.2 g Si-hydrogarnet
0.1 $CaCl_2$ + 0.2 $NaOH$ + 0.1 Na_2SO_4 + 0.001 $Al(NO_3)_3$	12.9	0.009	0.003	0.07	0.4 Na^+ + 0.2 Cl^- + 0.005 $Ca(SO_4)$ + 0.02 $Na(SO_4)^-$ + 0.05 SO_4^{2-} + 9e-10 $Al(OH)_4^-$	4.3 g portlandite + 3.8 g gypsum + 0.6 g AFt + 0.001 g ettringite
0.1 $CaCl_2$ + 0.2 $NaOH$ + 0.001 Na_2SiO_3 + 0.1 Na_2SO_4 + 0.001 $Al(NO_3)_3$	12.9	0.009	0.002	0.07	0.4 Na^+ + 0.2 Cl^- + 0.005 $Ca(SO_4)$ + 0.02 $Na(SO_4)^-$ + 0.05 SO_4^{2-} + 3e-5 $CaSiO_2(OH)_2$ + 9e-10 $Al(OH)_4^-$	4.3 g portlandite + 3.6 g gypsum + 0.2 g C-S-H + 0.6 g AFt + 0.001 g ettringite

of secondary phases increases. In fact, in the systems containing both sulfates and aluminates, 51 % by weight of the precipitated powder is expected to be gypsum and AFt.

The combination of silicates and sulfates does not lead to any changes, as silicates and sulfates do not seem to interact according to the thermodynamic calculations.

If all three, silicates, sulfates and aluminates, are added, the interactions between aluminates and sulfates seem to dominate over the interaction between aluminates and silicates and AFt phases precipitate instead of hydrogarnet. This means that the amount of C-S-H expected to precipitate is similar to the amount in the systems with only silicates.

The speciation in the solution does not seem to be changed by combining different ionic additions. No complexes between aluminates, silicates and sulfates are expected to form.

Carbonation

TGA measurements did reveal between 4-13 % calcite by weight due to carbonation (see chapter 5). However it is not clear whether carbonation happens before or after precipitation

Table 6.3: Concentration of different species and precipitates expected at equilibrium for the different model systems according to thermodynamic calculations if carbonates are included by adding 400 g atmospheric air mixture per l of solution.

Initial conc. [mol/l]	pH	Ca^{2+} [mol/l]	$CaOH^{+}$ [mol/l]	OH^{-} [mol/l]	Other species [mol/l]	Solid phases [g/l]
0.1 $CaCl_2$ + 0.2 $NaOH$	12.6	0.02	0.004	0.04	0.2 Na^{+} + 0.2 Cl^{-} + 5.2e-6 $Ca(CO_3)$ + 2.5e-6 $Na(CO_3)^{-}$ + 2.1e-6 CO_3^{2-}	5.2 g portlandite + 0.5 g calcite
0.1 $CaCl_2$ + 0.2 $NaOH$ + 0.001 Na_2SiO_3	12.7	0.02	0.004	0.04	0.2 Na^{+} + 0.2 Cl^{-} + 3e-5 $CaSiO_2(OH)_2$ + 5.2e-6 $Ca(CO_3)$ + 2.6e-6 $Na(CO_3)^{-}$ + 2.1e-6 CO_3^{2-}	5.2 g portlandite + 0.5 g calcite + 0.2 g C-S-H
0.1 $CaCl_2$ + 0.2 $NaOH$ + 0.1 Na_2SO_4	12.9	0.009	0.003	0.07	0.4 Na^{+} + 0.2 Cl^{-} + 0.005 $Ca(SO_4)$ + 0.02 $Na(SO_4)^{-}$ + 0.05 SO_4^{2-} + 5.1e-6 $Ca(CO_3)$ + 1.2e-5 $Na(CO_3)^{-}$ + 6.3e-6 CO_3^{2-}	4.1 g portlandite + 3.8 g gypsum + 0.5 g calcite

or both. To estimate the effect that carbonates, if present, would have on the speciation in solution, thermodynamic calculations were done for the control system as well as for the silicate and the sulfate system including 400 g of the GEMS predefined atmospheric air mix per liter of solution. This lead to a calculated amount of 6-9 % of calcite by weight of the total amount of solid, which correspond approximately to the experimentally observed values.

The effect of the carbonates on the speciation was negligible. The total amount of carbonate species in solution is of the order of 1.2e-5 M. Some of the carbonate solution species seem to form complexes with the Ca^{2+} ions. However their concentration (5e-6 M) is much smaller than the Ca^{2+} concentration and thus the effect of the carbonate complex formation on the calcium speciation can be neglected.

These results are consistent with the experimental observations that the amount of carbonations did not seem to have a marked influence on the growth and morphology of portlandite (see section 5.3.1). Even if carbonates are introduced into the system prior to precipitation, they do not seem to have a marked influence on the speciation or the growth of portlandite.

Table 6.4: Concentration of different species and precipitates expected at equilibrium for the thermal precipitation model system at 60 ° C according to thermodynamic calculations.

Initial conc.	pH	Ca^{2+} [mol/l]	$CaOH^{+}$ [mol/l]	OH^{-} [mol/l]	Other species [mol/l]	Solid phases [g/l]
0.02 $Ca(OH)_2$ (60 °C)	11.4	0.01	0.006	0.02	-	0.45 g portlandite

6.1.2 Results for Thermal Precipitation

The results discussed so far were for the coprecipitation experiments. In order to estimate how the conditions and speciation of the thermal precipitation experiment, used to estimate the portlandite morphology in pure calcium-hydroxide systems (see section 5.2), differ from the conditions in the coprecipitation experiments, thermodynamic calculations for the thermal precipitation experiment were done (see table 6.4). Since the thermal precipitation experiment was a pure Ca-O-H system, no species other than calcium and hydroxide species are observed.

The pH (11.4) and consequently the concentration of the hydroxyl ions (0.02 M) is significantly lower than for the coprecipitation experiments. This is consistent with the higher temperature (60 ° C) used for the thermal precipitation experiment and the ensuing lower portlandite solubility.

The concentration of the Ca^{2+} ion (0.01 M) is smaller than for most coprecipitation experiments, except the coprecipitation experiments containing sulfates. Since, as previously discussed, the addition of sulfates lowers the concentration of Ca^{2+} ions, due to the formation of a calcium-sulfate complex, the expected Ca^{2+} concentration is lower in the sulfate containing experiments than in the thermal precipitation experiments, despite the higher portlandite solubility at lower temperatures. The ratio between the Ca^{2+} and the OH^{-} ions is the same as in the control coprecipitation experiment. This indicates that the incorporation of neither Ca^{2+} nor OH^{-} into the crystal during portlandite growth is favored, which means that from these variations no change in the growth morphology is expected but only a decrease of the overall growth rate. The decrease of the incorporation rate of both Ca^{2+} and OH^{-} might favor other growth mechanisms such as the defect growth mechanism. This would likely influence the growth morphology. However, in contrast to the coprecipitation experiments, the observed morphology for the thermal precipitation only develops after a prolonged precipitation time, indicating that the morphology might be closer to an equilibrium than to an growth morphology.

The predicted concentration of the $CaOH^{+}$ complex (0.006 M) is significantly higher for the thermal precipitation experiment than for all the coprecipitation experiments. If $CaOH^{+}$ would be the growth rate determining species, the growth rate would increase. The growth of precipitation of portlandite was however observed to be much slower in the thermal precipitation experiments compared to the coprecipitation experiments (see chapter 5), indicating a reduction rather than an increase of the the growth speed. Additionally the $CaOH^{+}$ con-

centration is still lower than that of the main calcium and hydroxide species present in the solution, i.e. the Ca^{2+} and the OH^{-} ion. This indicates that the Ca^{2+} ion is probably more important for the growth of portlandite. If the $CaOH^{+}$ species was important only for the growth of specific facets of portlandite, the growth morphology might be influenced by the increased relative concentration of the $CaOH^{+}$ ions compared to the Ca^{2+} and the OH ions. However, as discussed above, if the observed final morphology has been partially equilibrated such changes of the growth morphology might not be observed experimentally.

Due to the lower initial supersaturation less portlandite is expected to precipitate (only 0.45 g/l compared to 5.6 g/l for the control coprecipitation experiment). This was the main reason why coprecipitation was chosen to study the influence of different ions instead of thermal precipitation. The lower initial supersaturation will decrease the nucleation rate, contributing to the slower precipitation observed experimentally. Since the change in initial supersaturation is more pronounced than the change in the growth species concentrations, the nucleation rate is likely to be reduced relative to the growth rate. This supposition is confirmed by the much larger particle size observed for the thermal precipitation experiment compared to the coprecipitation experiments (see chapter 5). Also, as was observed experimentally, due to the lower initial supersaturation, the nucleation mechanism changes from homogeneous to heterogeneous (crystals forming at the wall of the container in the thermal precipitation experiment).

6.1.3 Comparison to Cementitious Systems

Since the aim of the current work was to better understand changes of the portlandite morphology in cementitious systems, the calculated speciation for the model portlandite systems was compared to the speciation of the pore solution in cementitious systems during cement hydration. In order to get an idea of the speciation in cementitious systems, solutions with compositions according to the measured values by Lothenbach et al. [LW06] for an ordinary portland cement (OPC) with a water to cement ratio of 0.5 at different hydration times were studied with GEMS.

In contrast to the coprecipitation experiments where the concentrations of the solution species quickly approach equilibrium concentrations (except possibly for the sulfate containing systems), the hydration of cement is a process happening at a longer time scale (days), with concentrations far from equilibrium for a prolonged period of time ($\sim$ 1 day). Therefore, in order to be able to calculate the speciation of the initially supersaturated solutions, the solid phases were excluded from the GEMS calculations. Thus the overall concentrations of the thermodynamic calculations were consistent with the concentrations measured by inductively coupled plasma optical emission spectrometry (ICP-OES) by Lothenbach et al. after 0.02, 7, 26 and 336 hours of hydration [LW06]. There were only two slight differences: due to a lack of thermodynamic data, we did not include any chromium in our caclulations and the calculated hydroxyl concentrations were consistently about 0.02-0.07 M (10 - 30 %) lower than measured

Table 6.5: Concentration of different species in the pore solution of ordinary portland cement with a water to cement ratio of 0.5 at different hydration times. Total concentrations are consistent with experimental measurements by Lothenbach et al. [LW06].

Time [h]	pH	Ca^{2+} [mol/l]	$CaOH^{+}$ [mol/l]	OH^{-} [mol/l]	Other species [mol/l]
"real" cement					
0.02	12.81	8.5e-3	2.2e-3	0.06	0.01 $Ca(SO_4)$ + 1.2e-4 $CaSiO_2(OH)_2$ + 7.9e-6 $SiO(OH)_3^-$ + 6.7e-6 $SiO_2(OH)_2^{2-}$ + 0.3 K^+ + 0.02 Na^+ + 0.05 KSO_4^- + 0.1 SO_4^{2-} + 4.0e-5 $Al(OH)_4^-$
7	13.07	8.4e-3	4.0e-3	0.11	8.8e-3 $Ca(SO_4)$ + 6.4e-5 $CaSiO_2(OH)_2$ + 2.3e-6 $SiO(OH)_3^-$ + 3.7e-6 $SiO_2(OH)_2^{2-}$ + 0.3 K^+ + 0.03 Na^+ + 0.05 KSO_4^- + 0.09 SO_4^{2-} + 3.0e-5 $Al(OH)_4^-$
26	13.49	1.5e-3	1.8e-3	0.29	7.9e-4 $Ca(SO_4)$ + 1.2e-4 $CaSiO_2(OH)_2$ + 9.4e-6 $SiO(OH)_3^-$ + 4.1e-5 $SiO_2(OH)_2^{2-}$ + 0.4 K^++ 0.02 KOH + 0.04 Na^+ + 0.03 KSO_4^- + 0.05 SO_4^{2-} + 7.0e-6 $Al(OH)_4^-$
336	13.73	5.7e-4	1.2e-3	0.50	2.9e-5 $Ca(SO_4)$ + 1.1e-4 $CaSiO_2(OH)_2$ + 1.4e-5 $SiO(OH)_3^-$ + 1.0e-4 $SiO_2(OH)_2^{2-}$ + 0.5 K^+ + 0.04 KOH + 0.05 Na^+ + 3.8e-3 KSO_4^- + 4.9e-3 SO_4^{2-} + 9.0e-5 $Al(OH)_4^-$

by Lothenbach et al. via a pH electrode. The calculated speciation for the different hydration times can be seen in table 6.5.

The initial concentrations (hydration time: 0.02 hours) of the pore solution of the OPC cement are quite similar to the coprecipitation system containing all three additions, silicates, sulfates and aluminates. The biggest differences, compared to the coprecipitation experiments, are the absence of chloride ions and the replacement of sodium ions with potassium ions as the main alkali in OPC. Additionally the concentrations of both silicates and sulfates are higher than the calculated equilibrium concentrations in the coprecipitation experiment. However, as discussed previously, the actual sulfate concentration in the coprecipitation experiment might exceed the calculated value due to the retardation of the gypsum precipitation. In the cement system, the concentration of aluminates is significantly higher in the coprecipitation system containing sulfates, silicates and aluminates but lower than in the system with only aluminates.

In the following induction period little changes, except the concentration of hydroxide, which increases to about double, and the silicate concentration, which decreases to about half the initial value after a period of 7 hours. This means that at the end of the induction period and the start of the acceleration period the pH is higher than in the coprecipitation systems while

the silicate concentration is similar.

As the hydration progresses, the pH increases even further to about 13.7 towards the end of the hydration. This is much higher than the pH in any of the coprecipitation experiments (12.6-12.9). The increase of the pH is caused by an increase of the alkali concentration both due to the further release of alkali by the slow dissolution of some anhydrate phases and due to the consumption of part of the water during cement hydration [LW06]. Due to the raise of the pH, in order to satisfy the portlandite dissolution product, the Ca^{2+} concentration decreases continually after the start of the acceleration period until the end of the hydration. The final concentration of the Ca^{2+} ion is 5.7e-4 M which is over ten times lower than the concentration in any of the coprecipitation experiments. The concentration of the $CaOH^{+}$ complex on the other hand seems to be similar to that of the coprecipitation experiments throughout the hydration. Only towards the end of the hydration does the $CaOH^{+}$ concentration become lower than at equilibrium in the silicate-sulfate-aluminate coprecipitation experiment (0.02 M), whereas at the end of the induction period it is higher.

The amount of aluminates, which decreases at the start of the acceleration period (from initially 4e-5 M to 7e-6 M) before increasing again (to 9e-5 towards the end of the hydration), is higher than in the silicate-sulfate-aluminate coprecipitation experiment (9e-10 M) during the entire OPC hydration. Towards the end the aluminate concentration is similar to the concentration observed in the coprecipitation experiment containing only aluminates (1e-4 M).

The sulfate concentration decreases after the induction period. The concentration of the main sulfate species, the SO_4^{2-} ion, drops from initially 0.1 M to 5e-3 towards the end of the hydration. However up to a hydration time of 26 hours the concentration is still greater than or equal to the equilibrium concentration in the coprecipitation experiments (0.05 M). Due to the decrease of the Ca^{2+} concentration, the amount of $CaSO_4$ complexes decreases more rapidly. However the concentration of $CaSO_4$ remains larger than or similar to the Ca^{2+} concentration up to a hydration time of ~ 26 hours. Indicating that the $CaSO_4$ complex may play an important role in how sulfates influence the growth and morphology of portlandite both in OPC cement and in our model portlandite systems.

Finally the concentration of silicates is higher throughout the hydration than in the coprecipitation experiments. This is consistent with the fact that the main phase precipitating upon hydration of OPC is C-S-H whereas the main phase in our system is portlandite. Also the pH in the cementitious system is higher, increasing the silicate solubility. The silicate concentration closest to the coprecipitation experiments is observed at the end of the induction period. The calcium silicate complex $CaSiO_2(OH)_2$ is the main silicate species throughout the hydration. Its concentration, after decreasing from 1.2e-4 M to 6.4e-5 M during the induction period, increases again to 1e-4 M during the acceleration period. Again the predominance of the $CaSiO_2(OH)_2$ silicate species is consistent with our coprecipitation experiments, although its influence on portlandite growth is likely to be more important for cementitious system

Table 6.6: Paramters used for the well-tempered and the non tempered metadynamics calculation of the $CaSiO_2(OH)_2$ complex formation as well as the apriori error estimate on the energy profile (shown are the width σ and the hight ω of the added Gaussians, the temperature parameter for the well-tempered simulation ΔT, the characteristic size Δs_{ch} and height ΔF_{ch}, the total size of the collective variable domain Δs_{max}, the filling height F_e, the filling frequency τ_G and the total simulation time t_{sim}, see section 2.5.2).

	ΔT [$^\circ K$]	D^{meta} [$10^{-9}\frac{m^2}{s}$]	Δs_{ch} [Å]	ΔF_{ch} [eV]	σ [Å]	ω [eV]	Δs_{max} [Å]	t_{sim} [ps]	F_e [eV]	τ_G [ps]
well-temp.	2700	-	-	-	0.2	0.010	-	-	-	0.0525
non temp.	-	1.2	2	0.1	0.2	0.005	12	1050	1	0.0875

than for the coprecipitations discussed in chapter 5. However, as discussed previously, the actual existence of that complex remains somewhat uncertain and warrants some further investigation.

6.2 Calcium - Silicate Complex Formation

For the further study of the interaction between silicate species with portlandite surfaces it is important to have an idea of the predominant silicate species. Consequently metadynamics calculations (see section 2.5) were done in order to eliminate some of the above discussed uncertainty as to the importance of the $CaSiO_2(OH)_2$ complex in cementitious systems (see section 6.1.1). More specifically the stability of the $CaSiO_2(OH)_2$ complex, predicted to be the predominant silicate species by the thermodynamic calculations, was studied by simulating a system of a $CaSiO_2(OH)_2$ complex in a periodic water box with 2047 water molecules. The chosen collective variable as a function of which the free energy profile was calculated was the distance between the Si^{4+} ion and the Ca^{2+} ion of the complex. If the complex is stable and likely to be important for cementitious systems, as predicted by the thermodynamic calculations, there should be a minimum in the free energy profile for a short distance between the Si^{4+} and the Ca^{2+}, reflecting the stable complex configuration. The energy of the complex compared to the energy at larger distances should correspond to the value of $\Delta G^{CaSiO_2(OH)_2}_{GEMS} = 0.27 \pm 0.01$ eV that is included in the Nagra / PSI chemical thermodynamic data base [HBC$^+$02] used for the thermodynamic calculations.

Two separate calculations were done to estimate the free energy profile of the complex formation: a well-tempered and a non tempered metadynamics calculation (see section 2.5). The well-tempered simulation was done first. The simulation was restricted to Ca^{2+}-Si^{4+} separation distances d^{Ca-Si} of less than 14 Å. This first simulation allowed a first estimate of the energy profile and its characteristics, such as the characteristic length scale Δs_{ch} and the characteristic well depth ΔF_{ch}.

The well-tempered was then followed by a non tempered metacynamics simulation. The

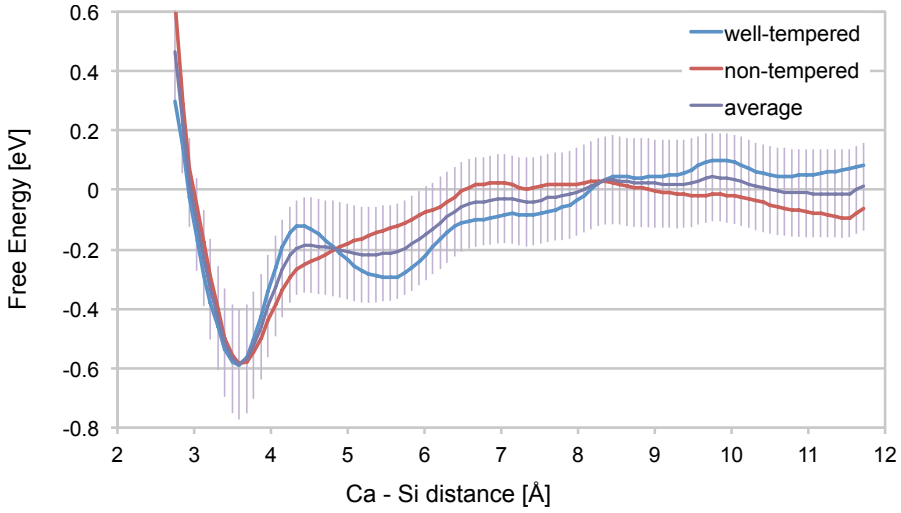

Figure 6.1: Estimated free energy of the $CaSiO_2(OH)_2$ complex as a function of the distance between the Ca^{2+} and the Si^{4+} ion.

parameters of the non tempered simulation were chosen based on the results of the well-tempered metadynamics calculation. The full set of parameters used for the calculation can be found in table 6.6. To reach a reasonable accuracy the Ca^{2+}-Si^{4+} separation distance was restricted to 2.75 Å $\leq d^{Ca-Si} \leq$ 12 Å. The final energy profile of the non-tempered metadynamics calculations has been averaged over a certain number of steps to reduce the error.

A priori the error of the non tempered simulation was estimated to be ϵ_{prior}^{meta} = 0.11 eV (see section 2.5.2). The diffusion coefficient D^{meta}, used for the a priori error estimation, was estimated by two separate simulations, one where the diffusion of the $CaSiO_2(OH)_2$ complex was estimated (1.5e-9 $\frac{m^2}{s}$) and one where the diffusion of the Ca^{2+} ion was estimated (1.2e-9 $\frac{m^2}{s}$). The lower of the two was used for the error calculations (see table 6.6).

After the completion of both calculations, the metadynamics error ϵ_{post}^{meta} on the energy profiles was estimated a posteriori as the standard deviation between the result for the non-tempered and the well-tempered calculation, averaged over the whole simulation domain, excluding the edges to avoid an influence of the boundaries (3.0 Å $\leq d^{Ca-Si} \leq$ 11.5 Å). The energy profiles from the different calculations are offset by a constant value. The offset was estimated by the average difference between the non tempered and the well-tempred free energy profile and taken into account for the error estimation. The thus estimated a posteriori error was ϵ_{post}^{meta} = 0.07 eV. The fact that the a posteriori error estimate ϵ_{post}^{meta} was lower than the a priori error estimate ϵ_{prior}^{meta} indicates that the collective variable for the metadynamics calculation was well chosen and no important system characteristics were neglected (see section 2.5). Finally the average over the two energy profiles was calculated. As we are interested in the energy of the complex relative to the energy of the separate species, the energy profile was shifted such that the average energy over distances of 10.0 Å $\leq d^{Ca-Si} \leq$ 11.5 Å is zero (see figure 6.1).

In addition to the metadynamics error we have the force field error. However the metadynam-

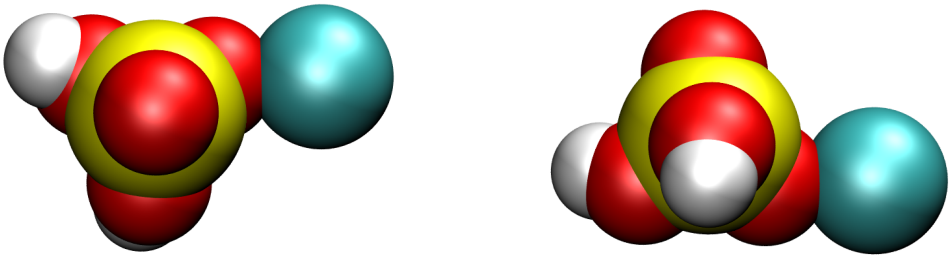

(a) (b)

Figure 6.2: Typical complex configuration at a $Ca^{2+} - Si^{4+}$ distance of 3.6 Å, view along the deprotonated oxygen-silicon bond (a) and along one of the hydroxyl oxygen-silicon bond (b). The size of the different spheres is according to the van der Waals radius of the ion, yellow: Si, red: O, white: H, turquoise: Ca

ics calculations only give us the relative free energy of the system as a function of the collective variables. In order to be able to apply equation 2.34 to estimate the force field error we need to know the energy of the part of the structure that is influenced by the collective variable. According to the Si-water and Ca-water radial distribution functions of seperate molecular dynamics calculations (of a $CaSiO_2(OH)_2$ complex in a box with 2047 water molecules and of a Ca^{2+} and two OH^- ions in a water box with 2045 water molecules respectively), about 71 water molecules are influenced by the presence of the $CaSiO_2(OH)_2$ species and about 48 water molecules by the presence of a Ca^{2+} ion in solution. Consequently, if we assume that 2047-119 = 1928 water molecules have exactly the same energy as in the bulk and that their energy is not relevant, the approximate energy of the Ca-Si species with the solvation shells is: H^{Ca-Si} = -215.60 eV. The estimated total error on the averaged free energy profile was the sum of the 95 % confidence interval ($\frac{1.96 \cdot \epsilon_{post}^{meta}}{\sqrt{2}}$) based on the a posteriori error estimate on the metadynamics calculations and the estimated force field error ϵ_{est}^{FF} (calculated according to eq. 3.5). This corresponds to the error bars shown in figure 6.1.

According to the metadynamics calculations, the $CaSiO_2(OH)_2$ complex is clearly stable, as can be seen from the free energy profile (figure 6.1). A well defined minimum is observed at a $Ca^{2+} - Si^{4+}$ distance of d^{Ca-Si} = 3.6 Å. This distance corresponds to a configuration where the calcium ion is associated with one of the deprotonated oxygens of the $SiO_2(OH)_2$ (see figure 6.2). The $O-Ca$ bond is tilted with respect to the $Si-O$ bond which seems to lead to a certain rotational entropy. For shorter $Ca-Si$ distances the Ca^{2+} ion moves to the mid-distance between the two deprotonated oxygen ions, thus loosing all rotational entropy. To our knowledge no data on the structure of the $CaSiO_2(OH)_2$ complex has been previously reported in the literature. However our results are in qualitative agreement with a previous Hartree-Fock study by Moravetski et al. [MHE+96] of the $KSiO(OH)_3$ complex structure and NMR shift where the K^+ was found to bind preferentially to the deprotonated oxygen.

The minimum energy is -0.59 ± 0.19 eV. If we add the error attached to the determination of the zero level, which is the force field error plus 95 % confidence interval on the determination

of the average energy for 10.0 Å ≤ d^{Ca-Si} ≤ 11.5 Å, corrected ad-hoc for the auto-correlation of the data points, we finally estimate the free energy of complex formation as -0.59 ± 0.30 eV. The complex formation energy is in reasonable agreement with the experimentally determined energy of -0.27 ± 0.01 eV, however the difference between the two energies is just outside the determined error estimate. This might be due to several reasons. One reason could be that the error estimate developed in section 3.3 has not yet been thoroughly tested and it is difficult to judge the probability of a calculation falling outside of the estimated error interval. Additionally there are possible error sources which are not included in the error estimate. One such contribution could be the cutoff of the electrostatic interactions, which might influence the final estimation of the complex formation energy. To check this hypothesis, the well-tempered calculation was repeated with a larger cutoff (14.5 Å) to estimate the influence of the cutoff on the results. The error between two well-tempered calculations with a different cutoff for the electrostatic forces was 0.08 eV and between the well-tempered calculation with a large cutoff and the non tempered calculation with a short cutoff was 0.10 eV. These errors are similar to the method error estimated originally (0.07 eV) and smaller than the a priori error estimate (0.11 eV), indicating that the cutoff has little influence.

Finally there might also be a larger error than the one indicated on the experimentally determined complex formation energy. A possible additional error source on the experimental data might for instance come from the approximations (e.g. that there are no polymeric silica species present in the solution), used by Santschi and Schindler [SS74] for the original calculation of the complex formation energy.

Irrespective of the slightly larger error than expected, the experimental and simulation results are in close enough agreement to indicate that the $CaSiO_2(OH)_2$ complex is stable and likely to play an important role in influencing the growth of portlandite. Consequently the complex was included for further calculations of the interaction between silicate species and portlandite surfaces.

6.3 Summary

In this chapter the calcium - hydroxide speciation of the solution surrounding growing portlandite particles was estimated with thermodynamic calculations for different model systems. In particular the influence of different ionic additions on the speciation was studied. Changes in the calcium-silicate speciation could, in theory, change the growth morphology of portlandite if the growth determining step is different for the different surfaces (i.e. the calcium incorporation is the rate determining step for one facet and the hydroxyl incorporation for another facet). Additionally the silicate, sulfate and aluminate species most likely to interact with the growing portlandite particles were determined.

The main species in all the model portlandite systems seem to be the Ca^{2+} and the OH^- ions, although a certain amount of $CaOH^-$ complexes exist as well. Their concentration is lower than the non-complexed ionic species although at higher temperatures (e.g. for the thermal

precipitation experiment) the relative concentration of the $CaOH^+$ complex increases.

Silicates were shown to have a negligible influence on the calcium - hydroxide speciation. Although calcium-silicate species are expected to form, their concentration is too small to have an effect on the Ca^{2+}, $CaOH^+$ and the OH^- concentrations. The species most likely to interact with growing portlandite particles is the neutral $CaSiO_2(OH)_2$ complex, the existence of which has been confirmed by metadynamics calculations.

At the concentrations used for the model experiments, sulfates seem to have the biggest influence on the calcium-hydroxide speciation. A neutral $CaSO_4$ complex is expected to form in sufficient concentration to decrease the Ca^{2+} concentration. Due to the common ion effect, the reduction of the Ca^{2+} is compensated by a higher pH. The predominant sulfate species in the coprecipitation experiments, according to the thermodynamic calculations, is the SO_4^{2-} ion. Due to the observed retardation of gypsum precipitation (see chapter 5), the influence of sulfates on the speciation in solution might be underestimated by the thermodynamic calculations.

Aluminate is the only addition that is not expected to form any complexes with calcium. Consequently its influence on the calcium-hydroxide speciation does seem to be negligible. The predominant aluminate species is the $Al(OH)_4^-$ ion.

The situation in cementitious systems is more complex than for the model systems. In an ordinary portland cement (w/c = 0.5) initially the concentration of the different species are similar to the coprecipitation experiment with all three additives. However there are some differences: the concentrations of silicates, sulfates and aluminates are slightly higher, there are no chlorides and sodium has been partially replaced by potassium. As the hydration progresses, calcium, sulfate and aluminate concentrations decrease whereas the silicate concentration increases. Additionally the pH increases to significantly higher values than observed for the coprecipitation systems.

7 Interaction between Solution Species and Portlandite Surfaces

In this chapter the interaction between portlandite surfaces and the surrounding environment is discussed. As growth happens at surfaces, the properties of portlandite surfaces and their interaction with the surrounding pore solution is important for the understanding of portlandite growth and morphology. Both the interaction with the solvent molecules (water in the case of cement) and any solute molecules present may influence the growing portlandite particles. Consequently the interaction of different portlandite surfaces with water as well as with Ca^{2+}, OH^{-}, $CaSiO_2(OH)_2$ and $SiO_2(OH)_2^{2-}$ solutes are studied in this chapter with classical atomistic modeling techniques.

The growth of a solid from a solution happens, as discussed in chapter 1, by the dynamical adsorption and desorption of different species at the surface. If the solution is supersaturated, some of these adsorbed species eventually become incorporated into the crystal and consequently the crystal grows. The interaction of the solute molecules with the surfaces may have an influence on the growth and morphology of portlandite (see section 1.3). This can happen via different mechanisms. Firstly the solvent molecules can interact more strongly with one family of facets than with another, thus lowering the relative interfacial energy of the former, which thus becomes more prominent in the equilibrium morphology. Secondly solvent molecules can bind strongly to growth sites, thus making their desorption the rate determining step. This can influence both the overall kinetics and the growth morphology. Consequently, in the first section of this chapter, the properties of different portlandite surfaces, as calculated with energy minimization techniques are discussed. This is then followed by a discussion of the interaction of portlandite surfaces with water, studied with classical atomistic molecular dynamics.

Additionally the interaction between portlandite-water interfaces and the most likely growth species, the Ca^{2+} and OH^{-} ion, is studied. This interaction will determine the distribution of those ions close to the surface and can consequently influence the growth kinetics. If for instance Ca^{2+} ions adsorb less easily at a surface than OH^{-}, it is likely that the incorporation

Table 7.1: Summary of different morphology determining quantities according to different theories (see chapter 1). Distance between interatomic planes ($d_{hk.l}$), attachment energies (H_{attach}), unrelaxed and relaxed surface energies ($\gamma_{hk.l}$) calculated with METADISE [WKdL$^+$96] as well as the portlandite-water interfacial energies ($\gamma_{hk.l}^{CH-H_2O}$) calculated with molecular dynamics for different surfaces.

hk.l	$d_{hk.l}$ [Å]	H_{attach} [eV]	$\gamma_{hk.l}^{unrelaxed}$ $[\frac{J}{m^2}]$	$\gamma_{hk.l}^{relaxed}$ $[\frac{J}{m^2}]$	$\gamma_{hk.l}^{CH-H_2O}$ $[\frac{J}{m^2}]$
00.1	9.5 ± 0.5	-0.07 ± 0.01	0.10 ± 0.03	0.10 ± 0.03	0.11 ± 0.06
10.0	6.3 ± 0.3	-0.99 ± 0.07	0.93 ± 0.06	0.60 ± 0.06	0.13 ± 0.06
10.1	5.3 ± 0.3	-3.25 ± 0.21	2.17 ± 0.14	0.74 ± 0.10	0.09 ± 0.06
20.3	2.2 ± 0.1	-24.87 ± 1.62	3.96 ± 0.26	0.80 ± 0.12	0.08 ± 0.07

of Ca^{2+} ions becomes the rate determining step and vice versa. However the distribution will, of course, also be influence by their overall concentration in the solution as discussed in chapter 6.

Finally the interaction between silicate species and portlandite surfaces will be estimated, to gain further knowledge about the mechanism by which silicates influence portlandite growth and morphology. According to the model systems studied here (see chapter 5) silicates seem to have a big influence on the growth and morphology of portlandite, without having a big effect on the calcium - hydroxide speciation (see chapter 6). This indicates that silicate species interact with the surfaces of the growing portlandite particles in some significant way. To better understand this interaction better, the adsorption of both the $CaSiO_2(OH)_2$ complex and the $SiO_2(OH)_2^{2-}$ ion at portlandite surfaces has been studied with classical atomistic simulations.

7.1 Portlandite surfaces

Before the interactions between portlandite surfaces and the surrounding solution can be studied, the structure and properties of portlandite surfaces in the absence of any interactions with the environment (i.e. portlandite in vacuum or in a non-interacting gas phase) have to be understood. As discussed in chapter 1, there have been many theories predicting the morphology of crystals, based on their crystalline structure. Four of the properties that are often used to predict morphologies, i.e. the distance between the interatomic planes ($d_{hk.l}$), the attachment energies (H_{attach}) and the unrelaxed as well as relaxed surface energies ($\gamma_{hk.l}$), have been calculated with energy minimization using METADISE [WKdL$^+$96] and will be discussed here. Four different families of facets were studied, three of the surfaces ([00.1], [10.0] and [10.1]) have been observed experimentally (see chapter 5) and the fourth was included as a more general, high energy surface.

The first property calculated was the distance between the interatomic planes $d_{hk.l}$. According

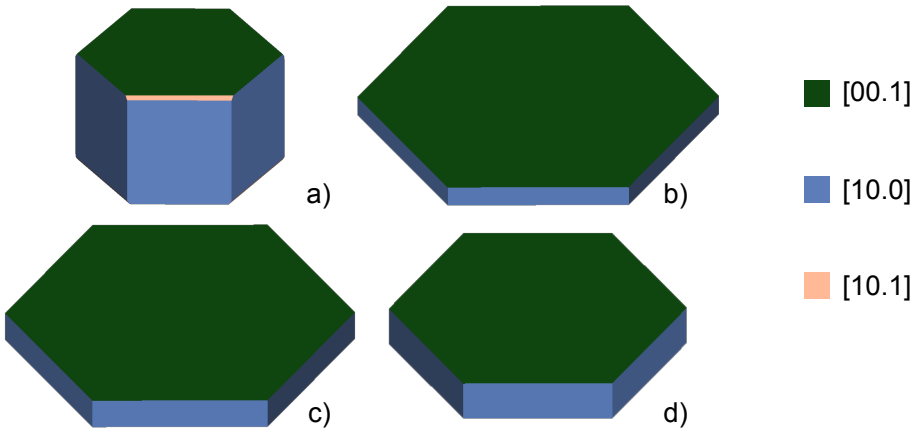

Figure 7.1: Calculated morphology of portlandite according to different theories BFDH (a), attachment energies (b), unrelaxed surface energies (c) and relaxed surface energies (d).

to the BFDH theory developed by Bravais, Friedel, Donnay and Harker (see [Mye05] and references therein), the importance of a surface for the crystal morphology can be approximated by the distance between the interatomic planes $d_{hk.l}$. The calculated $d_{hk.l}$ for the different surfaces can be seen in table 7.1. The distances have been determined according to the crystal structure previously relaxed with energy minimization. Consequently the error on the distances is equal to the force field error on distances $\epsilon_{est}^{d,FF}$ (see chapter 3). The thus predicted order of the surface energies is [00.1] < [10.0] < [10.1] < [20.3], where the differences between the different $d_{hk.l}$ are larger than the expected error. The ratio between the largest and the smallest distance is $\frac{d_{00.1}}{d_{20.3}} = 4.3$, and the ratio for surfaces [00.1] and [10.0] is $\frac{d_{00.1}}{d_{20.3}} = 1.5$.

The inverse of the distances can be compared to the attachment energy H_{attach} and to the unrelaxed surface energy $\gamma_{hk.l}^{unrelax}$. Both these quantities are derived from the bulk structure and were discussed in some detail by Hartman and Perdok in the periodic bond chain (PBC) theory (see e.g. [Mye05]). The unrelaxed surface energy is the energy that would be needed to separate two halves of a crystal, divided by the total surface area created, without allowing for any relaxation of the atomic positions at the surface and neglecting the surface entropy, which is expected to play a secondary role at room temperature [TSB+99, Jur54]. The attachment energy corresponds to the energy that is released per $Ca(OH)_2$ unit by attaching a parallel, unrelaxed crystal slice to the unrelaxed surface of a crystal, again neglecting any entropic effects.

The attachment energy can be calculated by subtracting the energy of an unrelaxed slice from the bulk energy of the crystal (see equation 1.5). The slice energy for different possible surface terminations were calculated and the one resulting in the lowest attachment energy was reported here. The results for both the unrelaxed surface energy and the attachment energies can be found in table 7.1. The error calculations are based on the force field error on energies ϵ_{est}^{FF}. According to the PBC theory the attachment energies can be used to approximate the relative growth kinetics. The underlying assumption is, that the crystal structure grows fastest

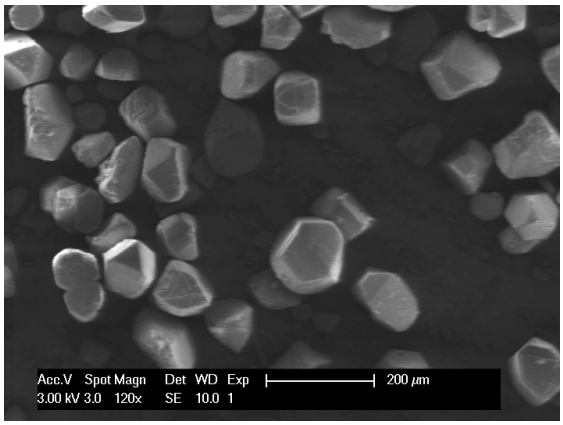

Figure 7.2: SEM image of portlandite particles produced in pure Ca-OH-water system by thermal precipitation (see chapter 5).

in the directions with the highest attachment energy, resulting in a morphology, where the importance of each facet is inversely proportional to the attachment energy.

The unrelaxed surface energies have been calculated similarly to the relaxed surface energies (see section 2.3.2), however without first minimizing the energy of the surface cell. For the unrelaxed surface the inclusion of the whole surface cell (see image 2.2) in the error estimation would be excessive, since the calculation is based entirely on the bulk structure. Consequently only the energy corresponding to one crystalline unit cell was used. The unrelaxed surface energy can, according to the PBC theory, be used as an approximation of the surface energy and hence the equilibrium morphology.

Due to the simplistic nature of the BFDH theory, the inverse of the distance between the interatomic planes $d_{hk.l}^{-1}$ can be viewed as an approximation of either or both the attachment energy and the unrelaxed surface energy. This is consistent with the fact that the order of the energies ([00.1] < [10.0] < [10.1] < [20.3]) is the same for all three methods. However the additional structural and interaction details included in both the attachment and the unrelaxed surface energy seem to emphasize the difference between the different surfaces. This is even more pronounced for the attachment energies, where the energies for the different surfaces vary by more than two orders of magnitude ($\frac{H_{attach}^{20.3}}{H_{attach}^{00.1}} = 355$, $\frac{H_{attach}^{10.0}}{H_{attach}^{00.1}} = 14$), than for the unrelaxed surface energies ($\frac{\gamma_{20.3}^{unrelax}}{\gamma_{00.1}^{unrelax}} = 40$, $\frac{\gamma_{10.0}^{unrelax}}{\gamma_{00.1}^{unrelax}} = 9$).

These different anisotropies can also be observed by looking at the corresponding calculated growth or equilibrium morphologies (see figure 7.1). The growth or equilibrium morphology calculated according to the BFDH theory is the most equiaxed whereas the growth morphology according to the attachment energies is the most anisotropic, showing a very thin hexagonal plate morphology. The equilibrium morphology according to the unrelaxed surface energies is somewhere in between, showing a hexagonal plate morphology though not as thin as for the attachment energies. This would indicate that the growth morphology might be slightly

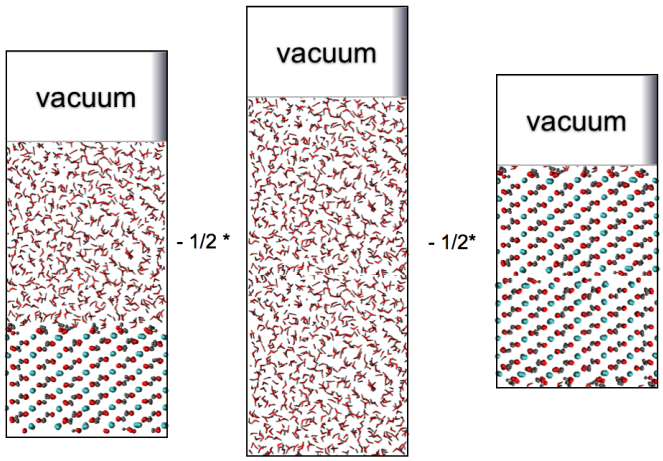

Figure 7.3: Schematic illustration of the calculation of portlandite-water interfacial energy.

more anisotropic than the equilibrium morphology.

However looking at the relaxed surface energies ($\gamma_{hk.l}^{relax}$, see table 7.1, errors have been calculated on the part of the surface cell with atom position relaxations of > 0.1 Å) one can see that surface relaxation, which has been neglected for both the attachment and the unrelaxed surface energies, plays a non-negligible role. As one would expect, surface relaxation is more pronounced for the higher energy surfaces. This reduces the differences between the surface energies ($\frac{\gamma_{20.3}^{relax}}{\gamma_{00.1}^{relax}} = 8$, $\frac{\gamma_{10.0}}{\gamma 00.1} = 6$). Consequently the resulting equilibrium morphology is less anisotropic than for the unrelaxed surface energies (see figure 7.1). As discussed in section 1.3, it is difficult to quantify the influence of the surface relaxation on the attachment energies, as the slice energies become ill defined. However it is likely that the anisotropy of the growth morphology is also reduced by the presence of surface relaxation.

The surface energies calculated here are in good agreement with the experimentally observed perfect cleavage plane in [00.1] direction [ABBN97] which indicates a low surface energy. The relaxed surface energies (or enthalpies as no entropic effects were included) of 0.10-0.80 $\frac{J}{m^2}$ are lower but still in reasonable agreement with the experimentally determined surface enthalpy of 1.1 $\frac{J}{m^2}$ reported by Brunauer et al. [BKW56], given the experimental uncertainties on the latter (such as impurities as well as types of interfaces present etc, see chapters 3 and 4). However the morphologies observed for particles produced by thermal precipitation in a pure calcium-hydroxide-water system by thermal precipitation (see figure 7.2) are quite different from any of the morphologies calculated for portlandite in a non-interacting environment. This indicates a strong influence of the water phase on the interfacial properties of portlandite.

7.2 Portlandite-Water interfaces

In order to estimate the interaction between water and different portlandite-water interfaces, the portlandite-water interfacial energies $\gamma_{hk.l}^{CH-H_2O}$ were calculated. Since dynamics is very important for water, molecular dynamics calculation with DL_POLY [SF96] and not energy minimization was used. The difficulty in simulating solid-water interfaces in molecular dynamics lies in the very different mechanical properties of the solid and the liquid. The different mechanical properties lead to very different pressure fluctuations in an NPT calculation (see section 2.4.2). For water the root mean squared pressure fluctuations are in the order of 0.2-0.5 katm whereas for portlandite the pressure fluctuations are more in the order of 1-3 katm. In separate simulations these differences would be taken into account by the barostat but in a mixed simulation both phases are treated equally. This leads to artificial stresses in the simulation. Anisotropic NPT is no solution to the problem for two reasons. Firstly, as for the simulations of a pure liquid phase, the angles are ill defined and will start to fluctuated in an uncontrolled manner. Secondly, parallel to the interface the solid and the liquid phase are still treated as one.

Consequently the setup chosen here was an NVT simulation of a portlandite-water slab, the periodic images of which were separated by a vacuum gap that lies parallel to the interface (see image 7.3). This means that perpendicular to the interface the volume of the liquid and of the portlandite slab can fluctuate independently whereas parallel to the interface no volume fluctuations are allowed. This alleviates the problem of artificial stresses but does not completely eliminate it. The interfacial energies are then calculated by comparing the configurational energy of the portlandite-water slab $E_{CH-H_2O}^{config}$ to half the energy of a slab with the same surface geometry but with no portlandite and twice as much water $E_{H_2O}^{config}$ and the energy of a slab with twice as much portlandite and no water E_{CH}^{config}, divided by the interface area A_{CH-H_2O} (see equation 7.1 and image 7.3). The artificial stresses developing in the different slabs should be similar and thus mostly cancel out. Again any entropic contribution was neglected under the assumption, that the interfacial energy is dominated by the surface enthalpy. However while this is often assumed in the case of ionic crystals [TSB+99, Jur54], there is some evidence that for solid-water interfaces [VTGN09], the entropy plays a slightly larger part. The dimensions of the surface portlandite-water cell were as follows: perpendicular to the surface the cell was composed of 20 Å portlandite, 50 Å water and 30 Å vacuum, with a surface area of approximately 20x25 Å. Of course the dimensions varied slightly for the different surfaces. In total there were between 190 - 240 $Ca(OH)_2$ and 900-1000 H_2O molecules in the portlandite-water simulation cell.

$$\gamma_{hk.l}^{CH-H_2O} = \frac{E_{CH-H_2O}^{config} - 0.5 \cdot E_{H_2O}^{config} - 0.5 \cdot E_{CH}^{config}}{A_{CH-H_2O}} \tag{7.1}$$

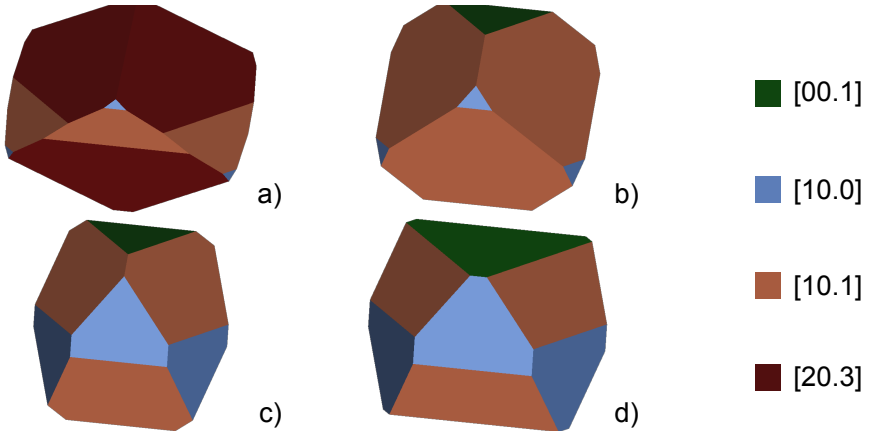

Figure 7.4: Different possible morphologies according to the calculated $\gamma_{hk.l}^{CH-H_2O}$. Original morphology (a) and other possible morphologies with $\gamma_{hk.l}^{CH-H_2O}$ differing by less than half the estimated error (0.3 $\frac{J}{m^2}$) from the original energies (b)-(d).

The resulting portlandite-water interfacial energies can be seen in table 7.1. Within the estimated error interval of about ± 0.06 $\frac{J}{m^2}$, which has been calculated based on the assumption that only half the slab is influenced by the presence of the interface, all the calculated interfacial energies are similar. The calculated interfacial energies of 0.08-0.13 ± 0.06 $\frac{J}{m^2}$ are in good agreement with the experimentally determined values of 0.065-0.114 $\frac{J}{m^2}$ reported by Harutyunyan et al. [HKM$^+$09] and by Klein and Smith [KS68]. This means that the water seems to stabilize the higher energy surfaces while interacting much less with the low energy surfaces. Consequently the equilibrium morphology of portlandite in water is expected to be equiaxed. Due to fact that the calculated energies are very similar for the different surfaces, the error can have a quite pronounced effect on the predicted morphology. To illustrate this, figure 7.4 does not only show the original morphology according to the calculated $\gamma_{hk.l}^{CH-H_2O}$, but also a range of possible morphologies calculated with energies that differ by no more than half the estimated error interval (i.e. ± 0.03 $\frac{J}{m^2}$) from the original ones. These morphologies are in good agreement with the morphologies observed in the pure portlandite-water system (see figure 7.2). These observations confirm the above formulated theory that water will strongly interact with the growing portlandite particles and is expected to influence their growth and final morphology.

The interaction between water and the portlandite surfaces depends on the surface orientation and hence on the surface structure. By looking at the structure of the [00.1] portlandite-water interface (figure 7.5a), one can see that the portlandite surface is terminated by a relatively high density of hydroxyl groups, oriented perpendicular to the surface. There seems to be little surface relaxation and atomic positions at the surface correspond approximately to bulk positions. Two types of surface bonded water sites can be distinguished. For one type of bound surface water both hydrogens are forming hydrogen bonds with surface oxygen atoms (b1 in figure 7.5a), for the other type only one of the hydrogen seems to form a bond (b2 in figure 7.5a). Qualitatively b2 seems to be more frequent than b1, although no detailed analysis was

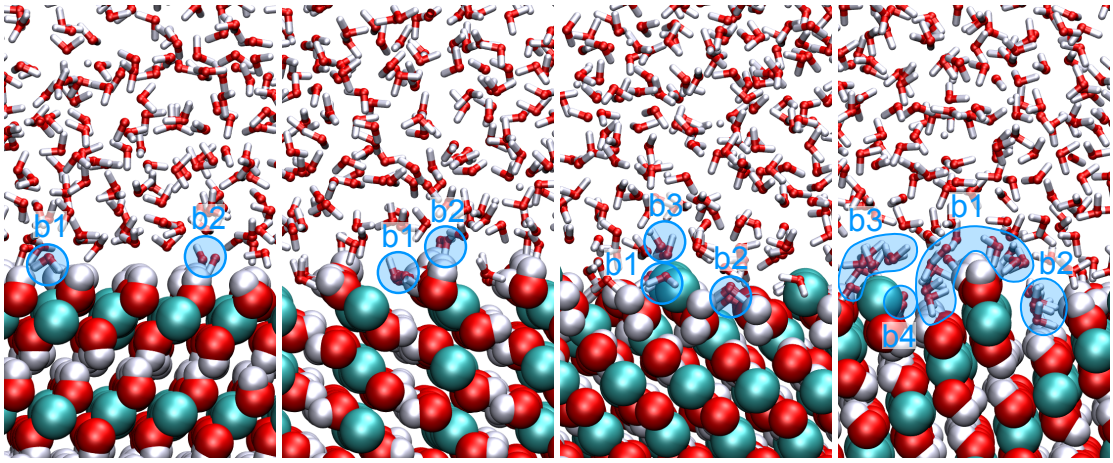

(a) (b) (c) (d)

Figure 7.5: Structure of different portlandite-water interfaces: [00.1] (a), [10.0] (b), [10.1] (c) and [20.3] (d). Ca: green, O: red, H: white

done. However the density of both types of surface bound water seems to be relatively low. The first peak in the water hydrogen number density profile perpendicular to the surface $\rho_n^{H_{water}}$ (see figure 7.6a), corresponding to the formation of the hydrogen bonding, is not very large. From the number density profiles for the different species one can calculate that about 34 % of the surface hydrogens have accepted a hydrogen bond. All in all the interaction between water and the [00.1] surface is rather weak, which is consistent with the essentially unchanged portlandite-water interfacial energy $\gamma_{00.1}^{CH-H_2O}$ compared to the relaxed surface energy $\gamma_{00.1}^{relax}$ (see table 7.1).

If we compare these results to the ones reported by Kalinichev et al. [KK02, KWK07] for calculations with FF1 (see chapter 3), we notice both similarities and differences. Both our results and results by Kanlinichev et al. indicate that the main interaction between water and the [00.1] portlandite surface comes from water donating a hydrogen bond to oxygens at the portlandite surface. The position of the first water hydrogen peak, which is indicative of these bonds, as well as the minimum approach distance of the water oxygens are consistent as well. However Kalinichev et al. predict a much higher density of these bonds. According to the density profile one can estimate that about 58 % of the surface hydroxyls accept a hydrogen bond, almost double as many as in our calculation. Probably as a result of the stronger hydrogen bonding of water with the portlandite surface, Kalinichev et al. report a stronger restructuring of the water close to the surface. Especially the first water oxygen peak is much higher and narrower than for our results, where the first water layer seems to be more disorganized.

Although Kalinichev et al. do not describe any water molecules that have formed two hydrogen bonds, such configurations can clearly be seen in the snapshot of the simulation supplied by the authors. However the authors describe another type of bonding where a water molecule

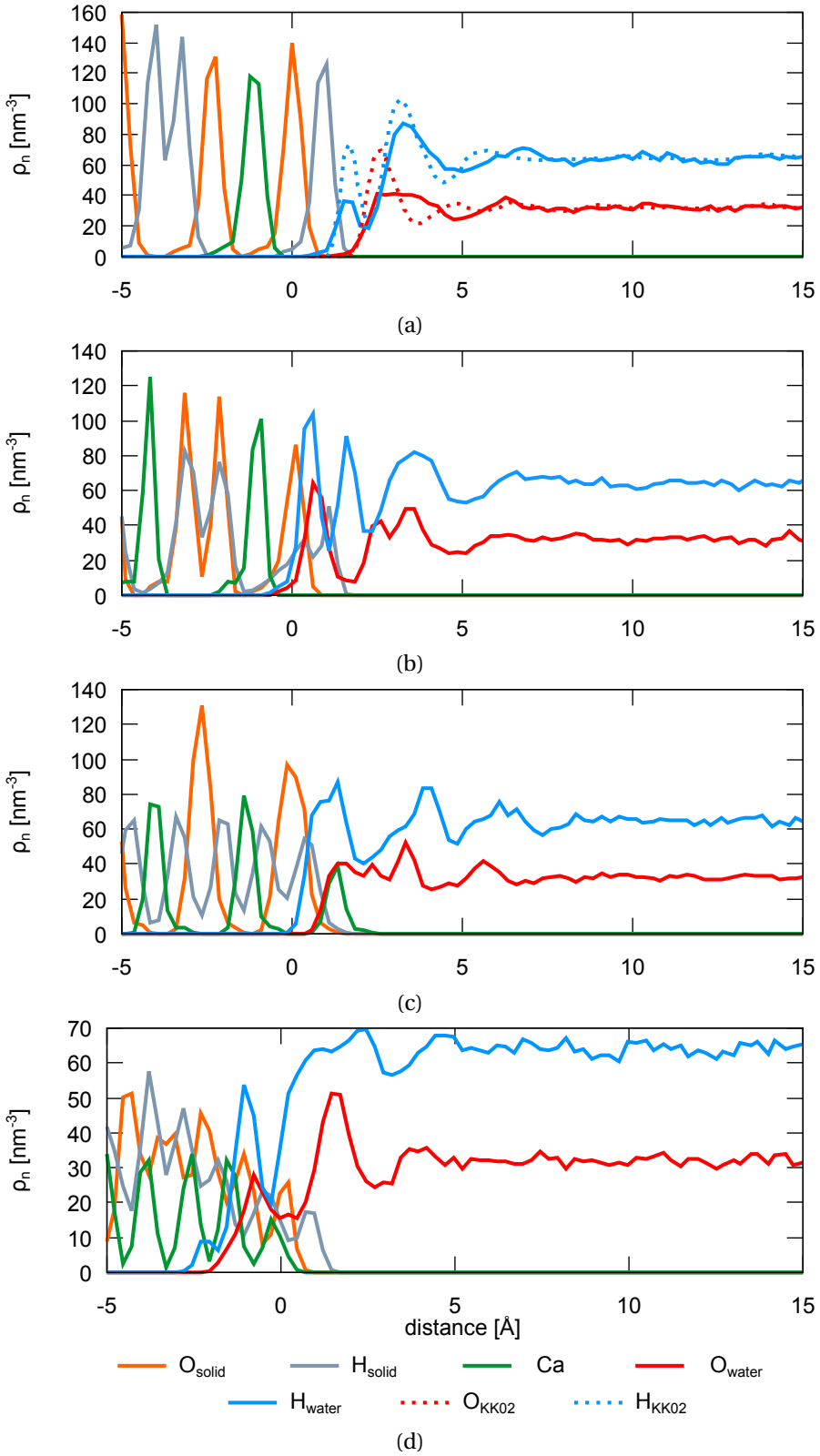

Figure 7.6: Number density of the different species as a function of the distance to the last oxygen layer of different portlandite surfaces: [00.1] (a), [10.0] (b), [10.1] (c) and [20.3] (d). For [00.1] the density profile reported for FF1 by Kalinichev and Kirkpatrik [KK02] is shown as well.

accepts a bond from a surface hydrogen with both water hydrogen pointing away from the surface. Considering the high percentage of hydroxyl groups accepting a hydrogen bond in their simulations, this second type of hydrogen bonding must be of less importance. The water-oxygen distance of water molecules accepting a hydrogen bond is reported to be about 0.3 Å further from the surface than for the water molecules donating hydrogen bonds to the surface. Surface water molecules with both hydrogens pointing away form the surface can be seen in the current simulation as well, however they seem to be further than 0.3 Å away from the b1 type of water molecules. This might cause the observed broader first water oxygen peak in our simulation. Further analysis would be necessary to determine whether these water molecules form hydrogen bonds with the surface. The stronger interaction between the portlandite [00.1] surface and water predicted by FF1, compared to the force field employed here, seems to be consistent with the force field comparison in chapter 3, where FF1 has been shown to overestimate the stability of the Ca^{2+} and OH^{-} species in solution compared to the stability of portlandite.

The [10.0] surface is also terminated by hydroxyl groups, but at a lower density than the [00.1] surface (see figures 7.5b and 7.6b). Compared to the bulk, where the hydroxyl groups are oriented parallel to the surface (hence the overlap of the portlandite oxygen and the portlandite hydrogen peaks in the density profile), at the surface about half of the hydroxyl groups have rotated and are pointing perpendicular to the surface. Two different types of bound water sites can be distinguished at the surface. The first type (b1 in figure 7.5b) are situated at about the position where the next hydroxyl layer of the portlandite structure would lay. This type is responsible for the first peak in the water oxygen density profile. These b1 water molecules donate one or two hydrogen bonds to the surface hydroxyl groups. Occasionally the b1 water molecules also accept a hydrogen bond from the surface hydroxyl sites. The b1 bonding site seems to be highly populated, according to the density profile about 94 % of the sites are occupied.

The second type of bound surface water site, b2, is similar to the predominant bonding at the [00.1] surface. The water at the b2 sites is situated directly above the surface hydroxyl groups, donating a hydrogen bond to the surface oxygen. The second hydrogen of the b2 bound water molecules is oriented away from the surface. The occupancy of the b2 sites is similar to the one of the [00.1] surface with about 30-35 % of the sites occupied.

All in all the interaction between the water and the [10.0] surface seems to be much stronger than between water and the [00.1] surface. This is consistent with the observation that the interfacial energy of the [10.0] surface is lowered by the presence of water whereas the energy of the [00.1] surface is practically unchanged (see table 7.1).

The [10.1] surface is terminated by alternating hydroxyl groups and calcium ions. While the surface calcium ions are above the surface hydroxyl layer, only every other calcium site at the surface is occupied, leaving the hydroxyl layer partly exposed (see figure 7.5c). The surface configuration of the atoms seems to be similar to the bulk positions. Three different bound

surface water sites can be distinguished. The first two (b1 and b2 in figure 7.5c) are both situated slightly above the middistance between two hydroxyl groups with the two hydrogens pointing towards the oxygens of the hydroxyl groups, forming hydrogen bonds. Whereas for the b1 sites the water molecules are situated between two occupied calcium sites, with the oxygen tilted towards the nearest calcium, probably forming a weak electrostatic bond, the b2 water molecules, which are situated slightly closer to the surface, are situated between two empty calcium sites and are oriented perpendicular to the surface with the oxygen pointing away from the surface. These two surface sites are responsible for the first peak in the water oxygen and the water hydrogen density (see figure 7.6c). The sites are fully occupied throughout the simulation with one adsorbed water molecule per two surface hydroxyls. This indicates a very strong interaction between the water molecules and the portlandite surface. Again this is consistent with the large difference between the relaxed surface energy $\gamma_{10.1}^{relax}$ and the portlandite-water interfacial energy $\gamma_{10.1}^{CH-H_2O}$ (see table 7.1). This difference is larger than for both the [00.1] and the [10.0] surface.

A third type of bonded water can also be distinguished at the [10.1] surface (b3 in figure 7.5c). For this site the water molecules sit above the surface calcium ions with the oxygen oriented towards the calcium, forming weak electrostatic bonds. This type of bond is responsible for the second peak in the water oxygen density profile and for the shoulder on the second peak of the water hydrogen density profile. Due to the convolution of the peaks with other peaks in the density profile it is difficult to determine the occupation of these surface water sites, however the bonding seems to be weaker than for the other two types of surface bonded water found at the [10.1] surface.

The last surface studied here, the [20.3] surface, is no longer quasi atomically flat but presents clear step-like features (see figure 7.5d). The steps are alternately terminated by calcium ions or hydroxyl groups. As was observed for the [10.0] surface, the topmost hydroxyl groups have partially rotated and some of the hydroxyl groups are now oriented perpendicular to the surface with the hydrogen pointing away from the surface.

Four different types of water sites are distinguishable at the [20.3] surface. The water molecules at the first bonding site (b1 in figure 7.5d) form a type of halo around the hydroxyl group of the hydroxyl terminated steps. One of the hydrogens of these water molecules point towards the oxygen of the surface hydroxyl groups, forming a hydrogen bond. The position of these water molecules is not clearly defined. The second type of bound surface water (b2) is located in the ridge after the hydroxyl terminated steps. One of the hydrogens of these water molecules is oriented towards the hydroxyl groups at the surface of the next step, forming a hydrogen bond. Essentially these water molecules seem to mimic the hydroxyls that would be positioned there in the bulk portlandite structure. However the sites seem to be much less well defined than for the [10.1] surface and the water molecules seem to be much less organized. The third type of bonded sites (b3) is situated above the exposed calcium sites with the oxygen pointing towards the calcium, forming a weak bond. Only the oxygen of the fourth type of bound water (b4) can be seen as these atoms seem to be very tightly bound to the portlandite. These water

molecules donate two hydrogen bonds to two neighboring surface hydroxyl groups of the second hydroxyl layer at the surface. The water atoms in these b4 sites seem to be very tightly bound, all the available b4 sites are occupied and no exchange of these water molecules was observed during the simulation whereas the water at the other sites seem to exchange quite frequently with the neighboring water layer (the least so for the b2 sites).

If we look at the density profile (see figure 7.6d), the second and fourth type of bonding (b2 & b4) as well as the first (b1) seem to be responsible for the first peak in the water oxygen density and the first and second peak in the water hydrogen density. The b1-type bonding is then likely responsible for the continuous density in the water oxygen profile and the shoulder in the water hydrogen density profile. The second peak in the water oxygen density profile is probably due to both b1 and b3 type bonding whereas the position of the maximum of the second peak of the water hydrogen density, at larger distances than the second maximum in the oxygen density, is probably due to the b3 type of bonding. All in all the interactions between water and the [20.3] surface is extensive, leading to the largest reduction of the interfacial energy observed for any of the surfaces studied here (see table 7.1), but rather disorganized.

Apart form the above described specific binding of water molecules, the presence of the portlandite surface also seems to lead to a diffuse layering of the surface up to about 8-10 Å from the surface (see figure 11.16). An exception is the [20.3] surface where the water seems to recover bulk properties already at a distance of about 5 Å from the surface. The reason for the fast recovery of bulk properties of water above the [20.3] surface is probably the above discussed disorganized nature of the bonding at that surface.

The strongly adsorbed water molecules at the [10.0] and the [10.1] surface are likely to influence the growth kinetics of those surfaces as well as the energetics. In order for growth to occur perpendicular to these surfaces, the adsorbed water molecules have to be desorbed first. This is likely to slow down the growth and makes it probable that the [10.0] and the [10.1] surface are stabilized energetically as well as kinetically, more so for the [10.1] surface where the surface water molecules seem to be adsorbed more strongly. The influence of the hydrogen bonding at the [20.3] surface on the growth kinetics might be less pronounced due to the mostly disorganized nature of the bonding.

7.3 Adsorption of Ca^{2+} and OH^{-}

In order to further understand the different portlandite surfaces and their growth, the adsorption of Ca^{2+} and OH^{-} at the different surfaces was studied by metadynamics. The first objective was to identify the adsorption sites at the different surfaces. For this purpose exploratory metadynamics calculations (see section 2.5) were done for both Ca^{2+} and OH^{-} at the [00.1], [10.0], [10.1] and [20.3] surfaces. The same simulation cells as for the surface energy calculations were used but three of the water molecules were replaced by a Ca^{2+} and two OH^{-} ions. The resulting $Ca(OH)_2$ concentration in the solution was in the order of 0.5-0.6 $\frac{mol}{l}$. Two

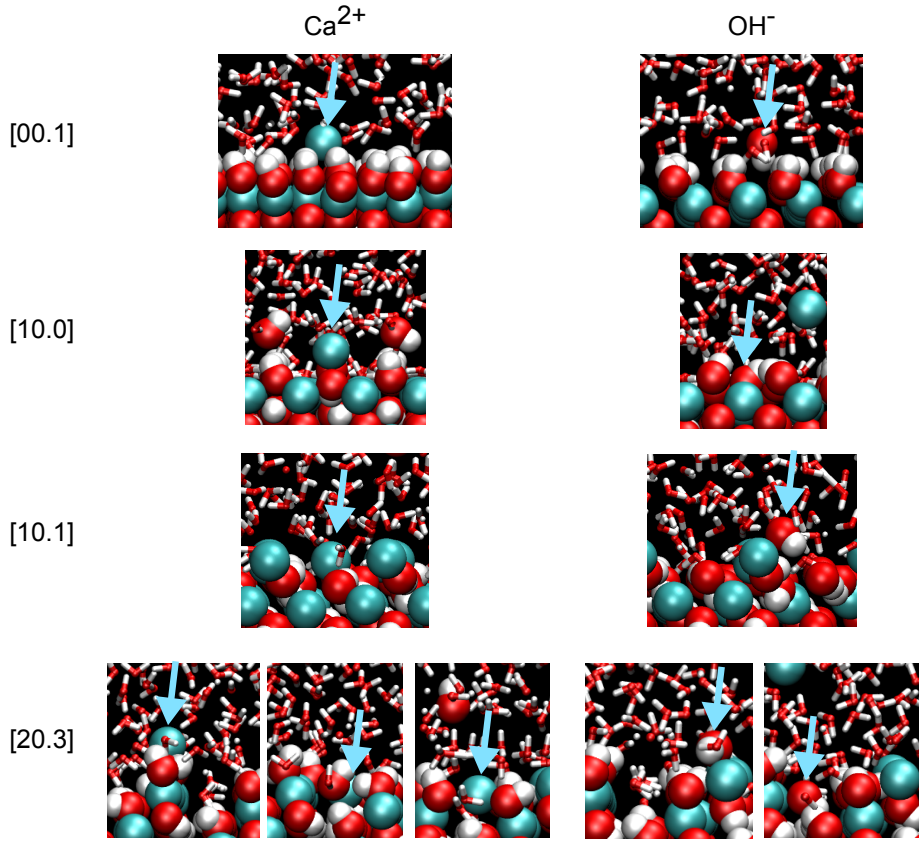

Figure 7.7: Adsorption sites for Ca^{2+} and OH^{-} ions at different portlandite surfaces identified by metadynamics calculations.

collective variables were used, the distance between the ion of interest and the portlandite slab as well as the energy of the local electrostatic interactions between the surface and the ion of interest within a gradual cutoff radius from 3.5 - 8.5 Å. The second collective variable was used to speed up the exploration of the surface and of different adsorption sites. The movement of the ion of interest was restricted to a region of about 15 Å from the surface. The total simulation time was 650 ps and the following parameters were used for the metadynamics simulation: σ_{CV1} = 0.2 Å, σ_{CV2} = 0.05 eV, ω = 0.02 eV and τ_G = 0.0525 ps. The identified adsorption sites can be seen in figure 7.7.

At the [00.1] surface the Ca^{2+} ion adsorbs between the surface hydroxyl groups. Qualitatively it can be observed that quite some energy seems to be required for the Ca^{2+} ion to adsorb, indicating that the adsorption might not be energetically favorable. The OH^{-} ion adsorbs with the hydrogen pointing towards the surface, forming a hydrogen bond with a surface oxygen. Contrary to the adsorbed Ca^{2+}, the position of the adsorbed hydrogen is essentially equivalent to the position a hydrogen would occupy in the next layer of portlandite, if the crystal were to grow. Based on these observations it is likely that, in order for the crystal to grow in [00.1] direction, the hydroxyl ions adsorb first, followed by the adsorption of the Ca^{2+} ions. Finally the adsorbed species would have to be incorporated into the crystal, in order to

form the next portlandite layer.

At the [10.0] surface the situation is somewhat similar. The Ca^{2+} ion does not seem to adsorb readily. Its position when adsorbed, in between two hydroxyl groups, does not corresponds to a prospective bulk position of a growing portlandite crystal. In addition the calcium ion seems to locally change the structure of the surface, both by adsorbing a hydroxyl from the solution and by moving one of the hydroxyl groups further into the solution. In fact, due to the temporary $CaOH^+$ complex formation just before adsorption, the process can be viewed as the adsorption of a $CaOH$ rather than a Ca^{2+} ion. The strongly bound water structure (b1 water, see figure 7.5b) seems to be locally perturbed by the presence of the adsorbed Ca^{2+} ion but no water molecules desorb.

The hydroxyl ion on the other hand seems to adsorb readily at the [10.0] surface. After briefly adopting a position similar to b2 water, with the hydrogen pointing towards the surface, forming a hydrogen bond with one of the surface oxygens, the hydroxyl eventually replaces one of the b1 surface bound water molecules and essentially adopts a position of a hydroxyl from the next portlandite layer. The hydroxyl seems to be very stably adsorbed at this adsorption site, donating alternately hydrogen bonds to one or the other of the neighboring surface hydroxyl groups and accepting a hydrogen bond from the other. These results seem to reinforce the above formulated assumption that the strongly adsorbed water molecules at the [10.0] surface are likely to slow down the growth of portlandite as first one of those water molecules has to desorb, before the hydroxyl group can adsorb. Secondly there are likely to be more adsorbed hydroxyls at the surface than Ca^{2+}. Also there might be some influence of the $Ca(OH)^+$ complex due to fact that the adsorption of the $Ca(OH)^+$ complex rather than of the Ca^{2+} ion was observed.

The case of the [10.1] surface is different. Here the Ca^{2+} ion seems to adsorb more readily than the OH^-. The Ca^{2+} seems to first replace one of the water molecules at a b2 bonding site. In this position the Ca^{2+} is slightly displaced from its theoretical bulk position in the next portlandite layer. After some time a second water molecule, this time from a b1 site, is desorbed as well and the Ca^{2+} moves to its theoretical bulk position. The adsorption of the Ca^{2+} ion seems to be quite stable at this position.

The OH^- adsorbs on top of a surface Ca^{2+} atom with the oxygen forming a weak bond with the Ca^{2+} atom. The hydrogen is oriented to one of the neighboring surface oxygens, forming a hydrogen bond. The adsorption of the OH^- atom does not seem to be very stable and the strongly adsorbed water molecules in the b1 and b2 sites are only slightly influenced by it. This seems to indicate that, contrary to the [00.1] and the [10.0] surface it is likely that the adsorption of the Ca^{2+} ions is the first step for the growth of a portlandite particle in [10.1] direction. The results also show that the desorption of the bound surface water is an important step in the adsorption process and likely to slow down the growth in [10.1] direction. If we compare to the [00.1] surface, two and not only one surface water molecule have to be desorbed for the adsorption of the first portlandite species. Therefore the Ca^{2+} and OH^-

Table 7.2: Paramters used for the non tempered metadynamics calculation of the adsorption free energy profile of different species at the [00.1] surface.

	D^{meta} $[10^{-9}\frac{m^2}{s}]$	Δs_{ch} [Å]	ΔF_{ch} [eV]	σ [Å]	ω [eV]	Δs_{max} [Å]	t_{sim} [ps]	F_e [eV]	τ_G [ps]
Ca^{2+}	1.200	2	0.1	0.2	0.005	9	2240	2.5	0.0996
OH^-	0.800	3	0.1	0.3	0.005	9	2240	1.5	0.2489
$CaSiO_2(OH)_2$	0.015	3	0.1	0.3	0.005	8	2240	0.5	0.8400
$SiO_2(OH)_2$	0.015	3	0.1	0.3	0.005	8	2240	0.5	0.8400

Table 7.3: A priori and a posteriori error estimate on the adsorption free energy profile as well as the parameters used for the force field error estimate.

	n_{H_2O} [-]	H^{est}_{tot} [eV]	ϵ^{meta}_{prior} [eV]	ϵ^{meta}_{post} [eV]
Ca^{2+}	48	-33.5	0.088	0.032
OH^-	39	-29.8	0.082	0.056
$CaSiO_2(OH)_2$	71	-195.6	0.097	0.045
$SiO_2(OH)_2$	71	-195.6	0.097	0.040

adsorption-desorption process at the [10.1] surface is likely to be slowed down more by the presence of water compared to the [00.1] surface.

At the [20.3] surface the adsorption of both the Ca^{2+} and the OH^- seems to happen via a two step process. The Ca^{2+} ion adsorbs first to the hydroxyl atoms at the hydroxyl terminated steps (b1 sites) and then moves further into the ridges between the steps, either the ridge after the hydrogen terminated ridge (b2 sites) or the ridge after the calcium terminated step (b1 sites). A similar process can be seen for OH^-. The hydroxyl first adsorbs onto the exposed Ca^{2+} ions (b3 site) then moves into the ridges after the hydroxyl terminated steps (b2 sites). The adsorption to the edge sites seems to be relatively easy for both species although the adsorption does not seem to be particularly strong and the species desorb again. The adsorption onto the ridge sites seems to require some energy for both the Ca^{2+} and the OH^- ion, possibly because of the desorption of the water molecules in the b1 and the b2 site respectively. However due to the disorganized nature of these sites no clear water desorption could be observed. The water bonded to the b4 sites does not seem to be perturbed. For the OH^- ions the adsorbtion to the b2 sites seem to be quite stable, more so than for the Ca^{2+} ions. All in all the adsorption at the [20.3] surface does seem to be quite complex, perhaps slightly favoring OH^- adsorption. The adsorbed water molecules at the b2 and partly at the b1 sites do seem to pose some hindrance for the adsorption of the different ions, however the tendency is not as clear as for the [10.0] and the [10.1] surfaces.

Although these exploratory metadynamics calculations did give some indication as to the adsorption sites and mechanisms, they could not be used to estimate the adsorption free

energy profile. Apart from the fact that they had not been optimized to minimize the error on the free energy profile, the two chosen collective variable were not independent of each other (see section 2.5). In fact the second collective variable, the local electrostatic potential, has only non-zero values for small values of the first collective variable, i.e. the distance between the surface and the ion. While this accelerates the adsorption of the ions and the exploration of the surface, it will influence the calculated free energy profile and make it difficult to interpret. Consequently the observations about adsorption strength above were only qualitative and based on the approximate total amount of energy that was put into the system before the adsorption and subsequent desorption occurred, i.e. the amount of simulation time spent close to the adsorption site before adsorption and the time spent at the adsorption site. To get a clearer and more reliable picture both a well-tempered and a non-tempered metadynamics simulation was done for the adsorption of Ca^{2+} and OH^{-} at the [00.1] surface to get the free energy profile. Only one collective variable, the distance between the ion of interest and the portlandite slab, was used for this simulation. The movement of the ion of interest was restricted to the surface region (up to ~ 10-14 Åfrom the surface) whereas the counter ions in solution were restricted the bulk region to avoid the influence of any complex formation on the adsorption free energy profile.

For the well-tempered metadynamics simulations the following parameters were used: ΔT = 2700 ° K, σ = 0.2 Å, ω = 0.005 eV and τ_G = 0.0525 ps. The parameters used for the tempered metadynamics simulations can be seen in table 7.2. The a priori and the a posteriori error estimations as well as the force field error were calculated according to the same method described in sections 2.5.2 and 6.2. The estimations as well as the estimated number of water molecules in the solvation shell and the total enthalpy used for the force field error estimation can be found in table 7.3. All a posteriori error estimates were smaller than the a priori error estimates which indicates that the conditions for the calculations were well chosen and that no slow mode was neglected. The final error on the adsorption free energy profiles was calculated as the sum of the standard error on the average energy profile from the metadynamics method plus the estimated force field error according to equation 3.5.

The final adsorption free energy profile can be seen in figure 7.8. For the Ca^{2+} ion there seems to be an adsorption minimum in the first diffuse water layer above the surface, at a distance of about 8 Å from the surface. To further approach the surface appears to be clearly energetically unfavorable. This might be caused by the loss of at least part of the solvation shell of the Ca^{2+} ion at closer distances from the surface. In fact, according to the radial distribution functions of water around a Ca^{2+} ion in solution, bulk water properties are recovered at a distance of about 6-7 Å from the Ca^{2+} ion. This is in quite good agreement with the position of the minimum in the adsorption free energy profile. It seems therefore likely that the minimum is caused by favorable interactions between the solvation shell of the Ca^{2+} ion and the structured water region above the surface and the subsequent increase in energy at smaller distance by the gradual loss of the hydration shell.

Globally this picture is partially consistent with the classical picture of the electrical double

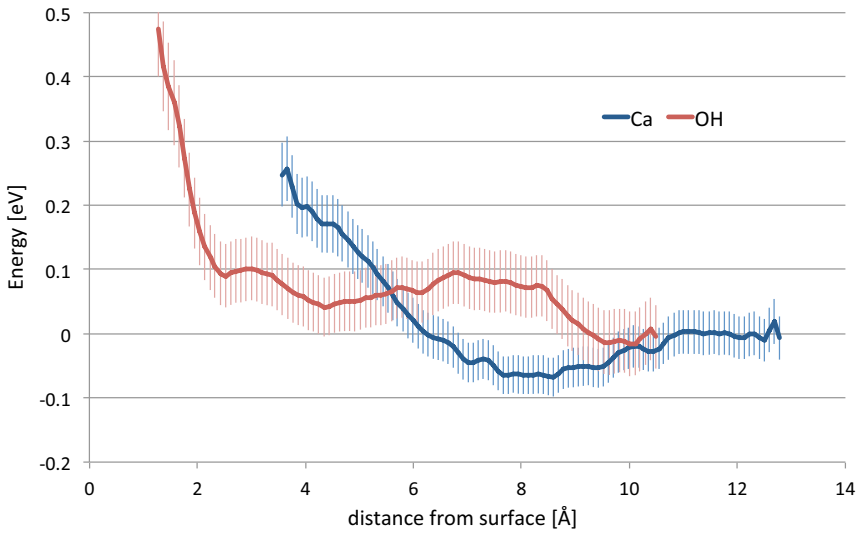

Figure 7.8: Adsorption energy profiles for Ca^{2+} and OH^- ions at [00.1] portlandite surface.

layer where the minimum approach distance of the ion at the surface for most ions is thought to be that of the hydrated ion (i.e. the outer Helmholtz plane, see section 1.4). There are however two differences from the classical electrical double layer picture and results obtained here. Firstly the minimum approach distance (~ 7 Å) is larger than the generally assumed typical distance of the outer Helmholtz plane (3 Å). Secondly there is an adsorption minimum at what can be assumed to be the outer Helmholtz plane for the Ca^{2+} ion. This minimum indicates that we have an additional specific adsorption of the Ca^{2+} ion at the outer Helmholtz plane which is not taken into account by the classical electrical double layer theory.

The adsorption free energy profile of the OH^- ion is quite different. The interaction between the hydration shell of the OH^- ion and the structured water region above the [00.1] portlandite surface does seem to be slightly unfavorable ($\leq$ 0.1 eV), however a further loss of part of the hydration shell does not seem to have an noticeable effect and the ion can approach the surface up to the inner Helmholtz plane at practically constant energy.

These observations are consistent with the above qualitative observations for the exploratory metadynamics calculations. Based on these result it seems probable that there are more hydroxyl at the surface and that the dehydration of the Ca^{2+} might be at least contributing to the rate determining step of portlandite growth in [00.1] direction. However it is impossible to predict the implications of the observed adsorption free energy profiles on the details of the ionic distribution at the surface and how the deviations from the assumptions of the classical electrical double layer theory might impact e.g. the colloidal stability and whether they are consistent with experimentally measured values such as zeta potentials (see section 4.4). To answer these questions the current results for the adsorption free energy profiles were used for Monte Carlo calculations of the ionic distribution, which will be discussed in chapter 8.

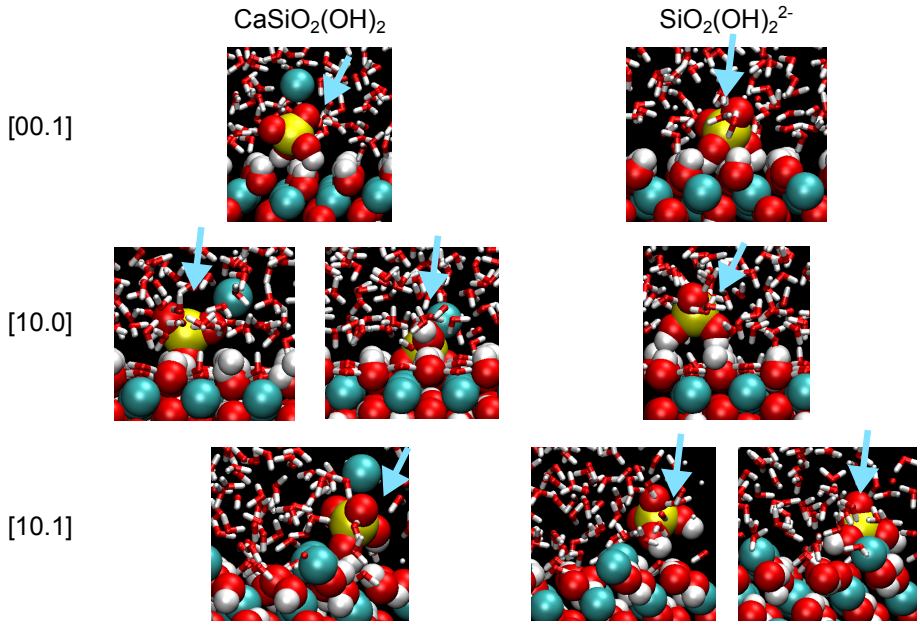

Figure 7.9: Adsorption sites for $CaSiO_2(OH)_2$ and $SiO_2(OH)_2^{2-}$ ions at different portlandite surfaces identified by metadynamics calculations.

7.3.1 A Note on the $CaOH^+$ Complex

Although the $CaOH^-$ complex has been calculated to be present in smaller but non-negligible quantities in our model system, it has not explicitly been included in the calculations presented above. In fact $CaOH^-$ complex formation could be observed in some of the simulations however the complex was generally observed to be quite transient, i.e. the life time of the complex is generally very short. A possible exception is the [10.0] surface where a $CaOH^+$ complex was observed over longer time scales and was found to adsorb at the surface. It seems therefore likely that it is not as much the adsorption behavior of the $CaOH^+$ complex as such that should be studied but the $CaOH^+$ formation and dissociation at the surface as compared to the bulk solution. This would allow the inclusion of the $CaOH^+$ complex in the discussion about portlandite growth. In the meantime, according to our results, the only surface for which any indication of the importance of the $CaOH^+$ ion was found is the [10.1] surface.

7.4 Adsorption of Silicate Species

To gain further insights into the influence of silicates on the growth and morphology of portlandite, the adsorption sites of both the $CaSiO_2(OH)_2$ complex and the $SiO_2(OH)_2^{2-}$ ion at the [00.1], [10.0] and [10.1] portlandite surfaces was studied with exploratory metadynamics calculations. The conditions were the same as for the adsorption site identification of Ca^{2+} and OH^- described above. The thus identified adsorption sites can be seen in figure 7.9.

For all surfaces, both the $CaSiO_2(OH)_2$ complex and the $SiO_2(OH)_2^{2-}$ ion adsorb with the

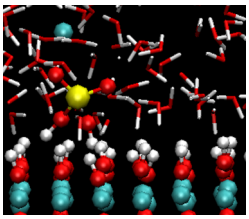
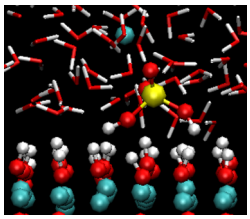

Figure 7.10: Consecutive snapshots of the $CaSiO_2(OH)_2$ complex adsobed at the [00.1] portlandite surface, illustrating the mobility of the complex at the surface.

hydroxyl groups oriented towards the surface where the hydrogen seems to form a hydrogen bond with a surface oxygen.

For the [00.1] surface the observed adsorption configuration of both the $CaSiO_2(OH)_2$ complex and the $SiO_2(OH)_2^{2-}$ ion is very similar. Both of the hydroxyl groups donate a hydrogen bond to surface oxygens. The $CaSiO_2(OH)_2$ complex however seems to adsorb slightly more readily and the adsorption slightly more stable than for the $SiO_2(OH)_2^{2-}$ ion but adsorption and desorption is quite rapid for both species. Interestingly both silicate species seem to retain a certain amount of mobility when adsorbed at the surface. The species seem to perform a type of walking movement with the two hydroxyl groups. The movement starts by the breaking of the hydrogen bond of one of the two hydroxyl groups. The silicate species is then free to rotate around the one remaining hydrogen group. This will make it possible for the free hydrogen group to reform a new hydrogen bond with another, neighboring surface oxygen. By alternate breaking and reforming of the two hydrogen bonds the silicate species can thus move along the surface, as illustrated in figure 7.10.

At the [10.0] surface the main adsorption site is again very similar for the two silicate species studied here. As for the [00.1] surface, both hydrogens form a bond with surface oxygens. The adsorption and desorption seems to be relatively easy and similar for both species. Again here the silicate species seem to retain a certain mobility at the surface by breaking and reforming alternately one of the hydrogen bonds with the surface, however the mobility seems to be slightly reduced compared to the [00.1] surface. This is probably due to the lower surface oxygen density at the [00.1] surface compared to the [10.0] surface (see figure 11.16). The configuration of the strongly adsorbed water molecules at the [10.0] surface (b1 site, see figure 7.5b) does not seem to be disturbed by the adsorption of the silicate species.

For the $CaSiO_2(OH)_2$ complex a second adsorption site at the [10.0] surface is observed. For this site two of the b1 bonded water molecules are desorbed, causing the calcium-silicate complex to be more strongly bound to the surface. The silicate moves closer to the surface and no mobility of the calcium-silicate complex was observed at this adsorption site. This adsorption configuration has not been observed for the $SiO_2(OH)_2^{2-}$ ion.

Finally at the [10.1] surface the adsorption of the $CaSiO_2(OH)_2$ complex seems to be easier and the adsorption more stable compared to the $SiO_2(OH)_2$ ion. The $CaSiO_2(OH)_2$ complex

adsorbs by forming a hydrogen bond between the hydrogen of one of the hydroxyl groups and a surface oxygen. The oxygen of the same hydrogen group seems to form a weak bond with a neighboring surface Ca^{2+} ion at the surface. No mobility was observed at this adsorption site. This appears to be logical as only one hydroxyl group has formed any bonds with the surface and consequently the above described mobility by breaking and reforming one of two hydrogen bonds is not possible. The configuration of the strongly bound water in the b1 and b2 sites (see figure 7.5a) was not changed by the adsorption of the calcium-silicate complex.

The same adsoption site as for the $CaSiO_2(OH)_2$ was observed as well for the $SiO_2(OH)_2^{2-}$ at the [10.1] surface. However a second adsorption site was also observed. This second adsorption site was only observed after desorption of both a strongly bound surface water and a surface hydroxyl group. For this site both hydroxyl groups donate hydrogen bonds to the surface while one of the deprotonated oxygens accepts a hydrogen bond from the surface. However this site is only observed towards the end of the simulation when a lot of energy was already added to the system. Consequently the observed adsorption site is probably not favorable energetically.

As for the Ca^{2+} and the OH^- adsorption, the above observations about the stability of different adsorption sites are only qualitative and approximate. Consequently well-tempered and non-tempered metadynamics simulations were done to calculate the adsorption free energy profile of $CaSiO_2(OH)_2$ and $SiO_2(OH)_2^{2-}$ at the [00.1] surface to get a better idea about the stability of the different adsorption site. The methodology used was the same as described above and the parameters used for the simulations and the error calculation can be seen in tables 7.2 and 7.3. For the choice of the parameters for the a priori error estimate a reduced diffusion rate was considered compared to what was estimated from a bulk solution simulation. This was done to allow for the rotation of the species as well as for the positional diffusion.

The final adsorption free energy profiles can be seen in figure 7.11. One can see that, despite the similarity of the adsorption sites the free energy curve is quite different for the $CaSiO_2(OH)_2$ complex than for the $SiO_2(OH)_2^{2-}$ ion. The energy profile for the calcium-silicate complex shows two minima, one at about 7 Å which, as discussed above, corresponds to the outer Helmholtz plane, and the second at about 4 Å from the surface (inner Helmholtz plane). The position of the inner Helmholtz plane is further away from the surface compared to what was observed for the OH^- ion (2 Å). This is consistent with the larger size of the $CaSiO_2(OH)_2$ complex compared to the hydroxyl ion.

The energy of the silicate ion on the other hand seems to continually increase as it approaches the [00.1] surface, with the possible exception of a slight minima at the outer Helmholtz plane which seems to have close to zero energy. Together with the above observations for the exploratory metadynamics simulations this indicates that, with the possible exception of the [10.0] surface, the calcium-silicate complex seems to interact more strongly with the portlandite-water interfaces than the silicate ion.

According to our calculations, the adsorption of the calcium-silicate complex at the inner

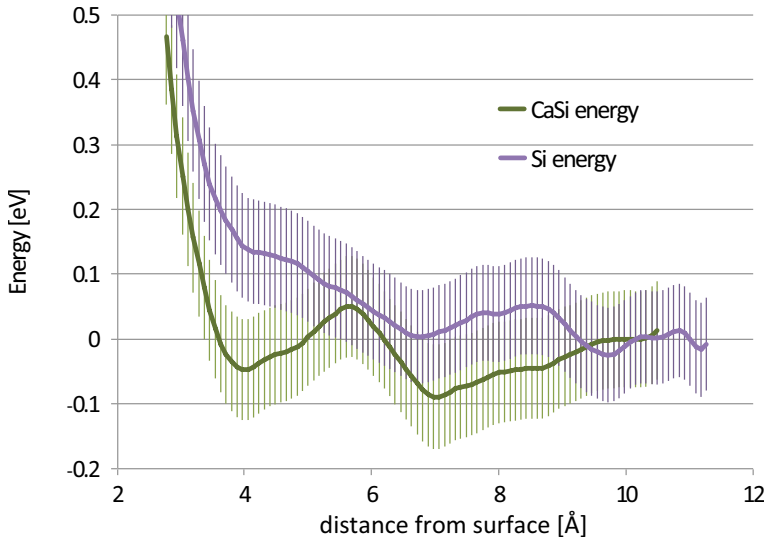

Figure 7.11: Adsorption energy profiles for $CaSiO_2(OH)_2$ and $SiO_2(OH)_2^{2-}$ ions at [00.1] portlandite surface.

Helmholtz plane of the [00.1] surface is energetically favorable, contrary to the adsorption of Ca^{2+} and OH^-. Additionally the calcium-silicate complex does seem to retain some mobility at the portlandite surfaces until such features as protruding surface calcium atoms are encountered. These protruding Ca^{2+} features at the [10.1] surface can be seen as step-like features. Indeed for the hydroxyl ion the adsorption onto the protruding calcium ion at the [10.1] surface was very similar to the adsorption onto the calcium terminated steps at the [20.3] surface (see figure 7.7). With these results it becomes easy to imagine how the calcium-silicate complex might adsorb at the flat surfaces, move around until they encounter an edge site where they will be immobilized.

Such a mechanism would certainly inhibit or even poison the growth of portlandite and indeed that is what is experimentally observed. Experiments by Tadros et al. have shown that the addition of silicates seems to notably slow down the growth of portlandite [TSK76]. The mechanism proposed here would help explain why this is the case. Such a growth inhibition by silicates would also help explain why no portlandite growth is observed in cementitious materials during the induction period, even though the solution is supersaturated with respect to portlandite. The poisoning of portlandite growth by silicates as a reason for the absence of portlandite growth during the induction period has been proposed before [YTB77, OD79] but a precise mechanism for the poisoning has not yet been put forward.

Additionally our results indicate that the portlandite surfaces could also serve as a template for C-S-H growth. In fact at the portlandite surfaces there seem to be mobile calcium-silicate species that all share the same orientation. If these species encounter each other they might form a calcium-silicate dimer which could be seen as a precursor for a tobermorite like structure.

These observations are also consistent with the previously discussed experimental observations for model systems (see section 5.3.3). Upon the addition of silicates, the primary particle size was reduced and agglomerates were formed. The agglomerates were probably formed by portlandite with a small amount of C-S-H at the surfaces and between the particles. According to the current results the reduction of the primary particle size can be caused by the portlandite growth poisioning due to the silicates. Additionally, as the portlandite surfaces might act as facilitators for the growth of C-S-H, this second phase forms preferentially at the portlandite surfaces and in between portlandite particles, forming the observed portlandite-C-S-H agglomerates.

7.5 Summary

In this chapters the properties of portlandite surfaces and their interaction with the surrounding solution was discussed. First the properties of portlandite surfaces in non-interacting environments were discussed.

The morphology of portlandite in a non-interacting environment is predicted to be that of a hexagonal platelet. It was found that surface relaxation slightly reduces the anisotropy of the hexagonal platelet. According to attachment energy calculations the growth morphology might be more anisotropic than the equilibrium morphology, however due to the presence of surface relaxation the results for attachment energies might not be reliable.

Water was found to markedly stabilize the higher energy surfaces. The surface energies of all the surfaces considered here were equal within the expected error. This indicates an equiaxed equilibrium morphology. At both the [00.1] and the [10.1] surface a regular network of strongly bound surface water was observed. This is likely to stabilize these surfaces kinetically, indicating that the growth as well as the equilibrium morphology is more equiaxed in water than in a non-interacting environment. This is consistent with the experimental results discussed in chapter 5. At the [20.3] surface, although extensive bonding between the water and the portlandite surface was found, only little systematic bonding was found. This indicates that this surface, while also stabilized energetically, might be less stabilized kinetically.

The simulation of the adsorption of Ca^{2+} and OH ions gave significantly different results for the different surfaces. At the [00.1] surface the hydroxyl ion seems to adsorb more easily than the Ca^{2+} ion. However the calculation of the adsorption free energy profile have shown that the adsorption of neither seems to be energetically favorable. For the Ca^{2+} ion on the other hand there seems to be an energy minimum further away from the surface, at what one can assume to be the outer Helmholtz plane. At the [10.0] surface the adsorption of the OH^- seems to be slightly favorable compared to the Ca^{2+} adsorption, although the exact adsorption energy profile has not been calculated. While the adsorption of the OH^- ion results in the desorption of one of the strongly bound surface water, the configuration of the strongly bound surface water is not perturbed by Ca^{2+} adsorption. Some indication for the importance

of the $CaOH^+$ complex at the [10.0] surface was found. The situation for the [10.1] surface is opposite. On that surface the adsorption of the Ca^{2+} seems to be easier than the OH^- surface. Also the adsorption of the Ca^{2+} ion desorbs two strongly adsorbed surface water molecules whereas the strongly bound surface water is undisturbed by the OH^- adsorption. At the [20.3] surface the behavior of Ca^{2+} and OH^- ions are quite similar. Due to the disorganized nature of the water bonding at this surface it is difficult to say how much the surface bound water is altered by the adsorption of the different species.

These result confirm the importance of surface bound water on the adsorption/desorption processes at the surface. The apparently different relative affinities for Ca^{2+} and OH^- for the different surfaces indicate that the species responsible for the rate limiting step during growth may differ for the different surfaces. For the [00.1] surface for instance the adsorption of the Ca^{2+} ion is likely to be the rate limiting step. For the [10.1] surface on the other hand, it looks as if it the adsorption of the hydroxyl could be the rate limiting step. This means that e.g. an increase in pH might kinetically stabilize the [10.0] surface compared to the [10.1] surface, thus changing the growth morphology.

Finally the adsorption behavior of two different silicate species, the $CaSiO_2(OH)_2$ complex and the $SiO_2(OH)_2^{2-}$ ion was looked at. Generally the $CaSiO_2(OH)_2$ complex seemed to interact more strongly with portlandite surfaces than the $SiO_2(OH)_2$ ion. Both species were found to adsorb with one or both of the hydroxyl groups donating hydrogen bond to the surface. At the atomically flat [00.1] and [10.0] surfaces the silicate species seemed to retain a certain amount of mobility at the surface, contrary to the [10.1] surface where the silicate species adsorb to the step-like exposed calcium ions. This lead to the theory that silicate species, or more specifically the $CaSiO_2(OH)_2$ complex, might poison growth by adsorbing to surfaces, migrate along them until a step like growth feature is encountered where they are immobilized. This theory seems to fit with experimental data obtained here (chapter 5 and elsewhere (see e.g. [TSK76]).

8 Equilibrium Distribution of Ions around a Portlandite Particle (Double Layer)

In this chapters the ionic distribution at a portlandite-solution interface in a pure $Ca(OH)_2$ - H_2O system is calculated by Metropolis Monte Carlo using the adsorption free energy profile obtained in the previous chapter. First results for a high $Ca(OH)_2$ concentration are discussed. For high concentrations, the results could be compared to molecular dynamics calculations to check whether the Monte Carlo system is a good approximation of the initial molecular dynamics system. These results are then followed by calculations corresponding to a $Ca(OH)_2$ - H_2O system at equilibrium. The results obtained here are compared to experimental measurements of the zeta potential and to the Gouy-Chapman theory. Finally the implications of the results for cementitious systems is discussed.

In this chapter the equilibrium distribution of Ca^{2+} and OH^- ions at the [00.1] surface are studied with Metropolis Monte Carlo calculations. The Monte Carlo calculations are based on the adsorption free energy profiles of the ions at that surface as calculated by metadynamics (see chapter 7). The motivation for calculating the ionic distribution was threefold.

Firstly the knowledge of the ionic distribution at the surface would allow for comparison with experiment via e.g. zeta potential measurements or surface titrations (see section 1.4). If calculations and experimental results are consistent, this would endorse the results on the adsorption of different species at different portlandite-water interfaces discussed in the previous chapter.

Secondly the knowledge of the ionic distribution close to the surface is the first step towards understanding the growth of portlandite. If for instance one of the growth species is not found close to the surface, it is possible that the dehydration and adsorption of that species at the surface might be the rate determining step. At the very least, if one would want to develop a full kinetic model for the growth of a portlandite particle, the distribution of the growth species close to the surface would have to be known.

Finally, there has been, over the recent years, more and more evidence, mostly based on atomistic simulations, that the classical picture of the electical double layer is oversimplified [AGM+09, KP04, KK02, KCSP05, SCKP06, KCMP05, ZKR10]. However there is still little known about how this influences the macroscopic system e.g. the colloidal stability and the interparticle forces. Partially this is due to the restrictions of molecular dynamics which only allow the study of small systems and consequently relatively concentrated solutions. Metropolis Monte Carlo on the other hand has already been shown to be a powerful tool for the study of the electrical double layer and interparticle forces [TV80, LOB81, TV82, FJWW97, QPMMHA04, JNL+05, LJP+06, LPJN11, PLVD08]. Consequently if one could succeed in correctly approximating the molecular dynamics model by Monte Carlo, valuable insight could be gained into how the deviations from the classical electrical double layer picture impact macroscopic properties such as interparticle forces and hence the role of aggregation in particle growth.

In the first section in this chapter the accuracy of the Metropolis Monte Carlo calculations in approximating the molecular dynamics system is assessed. This was done in a concentrated system to facilitate the molecular dynamics simulations. The calculations for a concentrated system where then followed by calculations for a system at equilibrium. Finally the implications of the results for cementitious systems and possible ways to gain further insight in future studies are discussed.

8.1 High Concentrations, Comparison to Molecular Dynamics

The system used for the high concentration was a box of size 15 x 10 x 10 nm with 343 Ca^{2+} and 686 OH^{-} ions. This means that the average concentration was 0.38 $\frac{mol}{l}$. Periodic boundaries were applied in the direction of the short dimensions of the box. In the direction of the longest dimension the system was terminated on both sides by a hard wall. At both hard walls the ions interact with the adsorption free energy profile calculated with metadynamics and discussed in the previous chapter (see figure 7.8). The adsorption free energy potentials act up to a distance of 9.4 and 11.7 Å for Ca^{2+} and OH^{-} respectively. This means that water was not considered explicitly, but is only considered implicitly via a relative permittivity ϵ_r of 80 and the adsorption free energy profiles. The long range potential for a linear charge distribution described in section 2.6.1 was used to approximate the long range electrostatic interactions. The short-range/long-range cutoff was chosen to be 50 Å. After an initial equilibration of 200000 steps the long range potential was reset (reinitiallization of the charge distribution calculations), the system equilibrated a further 500000 steps and finally data was collected over the next 2500000 steps (for more details see appendices A and B).

The final charge density profile and the number density profile of the different ionic species can be seen in figure 8.1. For the number density of the Ca^{2+} ions, one can clearly distinguish a peak at 6-9 Å, which corresponds to the minimum in the adsorption free energy profile. The adsorption of Ca^{2+} leads to a positive peak in the charge density. The positive charge developing in this region is properly speaking neither a surface charge σ_s, which is zero for our

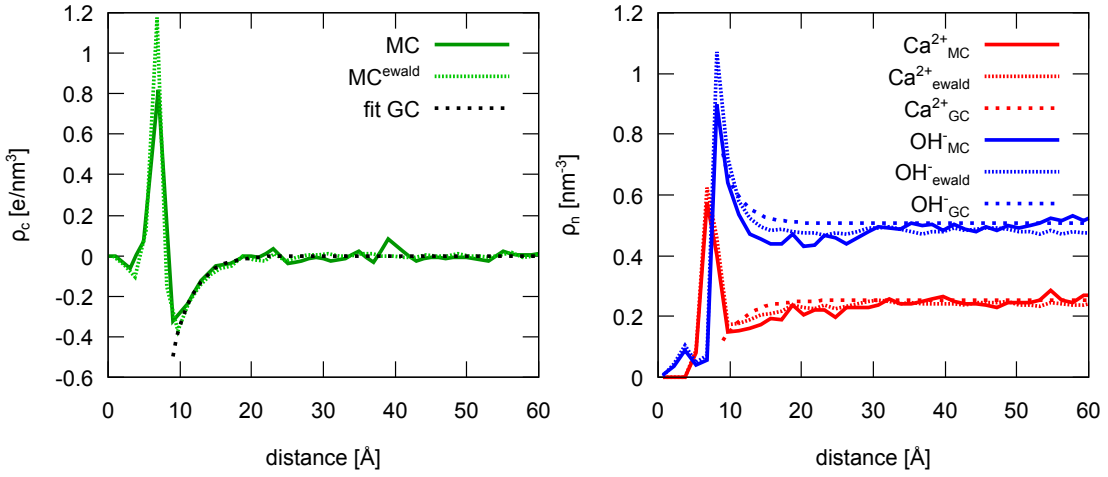

Figure 8.1: Charge distribution (a) and ionic distribution (b) perpendicular to the [00.1] portlandite-water interface according to Monte Carlo (MC, both with linear charge distribution or ewald summation (ewald)) simulations for a high concentration (0.42 $\frac{mol}{l}$ $Ca(OH)_2$). Results according to the Gouy-Chapman (GC) theory (using the Debye-Hückel approximation), fitted to the Monte Carlo charge density, are given as well.

calculations, nor the charge developed at the inner Helmholtz layer due to specific adsorption σ_H, which is slightly negative in our case (see first negative peak in the charge density and first peak in the OH^- number density profile if figure 8.1). We therefore call this charge outer Helmholtz charge $\sigma_{H^{out}}$.

From the charge density profile it looks as if the behavior of the diffuse layer after the $\sigma_{H^{out}}$ peak is consistent with the Gouy-Chapman theory. In fact for distances > 10 Å, the charge density can be accurately approximated by the Debye-Hückel approximation of the Gouy-Chapman theory (equation 1.36). In figure 8.1a, the Debye-Hückel solution for a bulk concentration of $c_b^{Ca^{2+}} = 0.42\ \frac{mol}{l}$, an equivalent interface charge density $-\sigma^{dl} = \sigma_s + \sigma_H + \sigma_{H^{out}} = 0.51\ \frac{e}{nm^2}$ or 25 $\frac{mC}{m^2}$ and a virtual diffuse layer minimal approach distance of $x_0^{dl} = 9.0$ Å is shown. The bulk concentration corresponds to the average concentration in the Monte Carlo system in the bulk region. The concentration is slightly higher than the overall concentration of 0.38 $\frac{mol}{l}$ and indicates a depletion of charges in the interface region, probably mostly due to the region at < 5 Å where the concentration of both Ca^{2+} and OH^- is very small. The minimal approach distance x_0^{dl} corresponds approximately to the distance at which the hydrated ions start interacting with the layered water region above the portlandite surface (see section 1.4.3). However, contrary to the underlying assumption of a ideal polarized electrode of the Gouy-Chapman theory, ions can pass this distance (i.e. there will be leakage of the charges at the interface). This, in addition to the other approximations contained in the Gouy-Chapman theory (e.g. no ion-ion correlations), might lead to deviations of the Monte Carlo results from the mean field Debye-Hückel approximation.

Indeed if one compares the ionic number density profiles one can see clear deviations of the Monte Carlo results form the Gouy-Chapman theory. For the OH^- profile we see two definite peaks, one small one at smaller distances than the Ca^{2+} peak and a more important one at larger distances. The second, more important peak is at a distance of about 8.3 Å and thus partially overlapping the Ca^{2+} peak. For the Gouy-Chapman theory the peak would partially result in a reduced σ^{dl}, as the estimated virtual minimal approach distance of 9.0 Å is larger than the peak position. At larger distances of ~ 10 Å, the solution is depleted of both Ca^{2+} and OH^- according to the Monte Carlo calculations. This is in contrast to the Gouy-Chapman theory which predicts an excess of OH^- ions in the diffuse layer. The depletion of Ca^{2+} ions in the diffuse layer is predicted by both Monte Carlo and Gouy-Chapman. However Monte Carlo predict a more important depletion than Gouy-Chapman. As both the OH^- and the Ca^{2+} concentration according to Monte Carlo lie below the Gouy-Chapman theory, the two charge density profiles for the two methods are similar.

In order to compare results to molecular dynamics simulations, five different Ca^{2+} and OH^- configurations for the molecular dynamics simulation cell with a water slab of approximately 21.8 x 25.3 x 57.2 Å was obtained from the end configurations of the Monte Carlo calculation. The molecular dynamics starting configurations were then corrected as to obtain charge neutrality for each cell. The histogram of the Ca^{2+} and OH^- ions over all 5 configurations was approximately following the ionic distribution according to the Monte Carlo calculations. The molecular dynamics starting configurations were then incorporated in 5 different instances of the preequilibrated portlandite-water slab described in section 7.2. The thus constructed slabs contained each between 5 and 7 $Ca(OH)_2$ in the solution. Each of the 5 slabs was equilibrated for 70 ps, followed by a production run over 1 ns. Although the total simulation time was insufficient to get the equilibrium distribution from one simulation, as evidenced by the different ion distributions for the different starting configurations (figure 8.3), the ionic distribution over all simulations should, it is hoped, be close to the equilibrium distribution of the ions according to the molecular dynamics distribution. What is more, since the original distribution corresponded approximately to the ionic distribution according to Monte Carlo, deviations from that distribution for molecular dynamics should start to show up.

The final charge density and ionic number density profiles averaged over the 5 molecular dynamics calculations can be seen in figure 8.2. The first Ca^{2+} peak as well as the general feature of the ionic distributions seem to be consistent between the Monte Carlo and the molecular dynamics calculations.

Closest to the surface there is a peak in the OH^- distribution which leads to a negative charge density close to the surface (up to 3-4 Å). This peak is difficult to quantify for the molecular dynamics calculations as the peak is convoluted with the much larger hydroxyl peak from the surface hydroxyl groups (see figure 7.6a). However there are some indications that this peak might be larger in the molecular dynamics simulation compared to the Monte Carlo simulations.

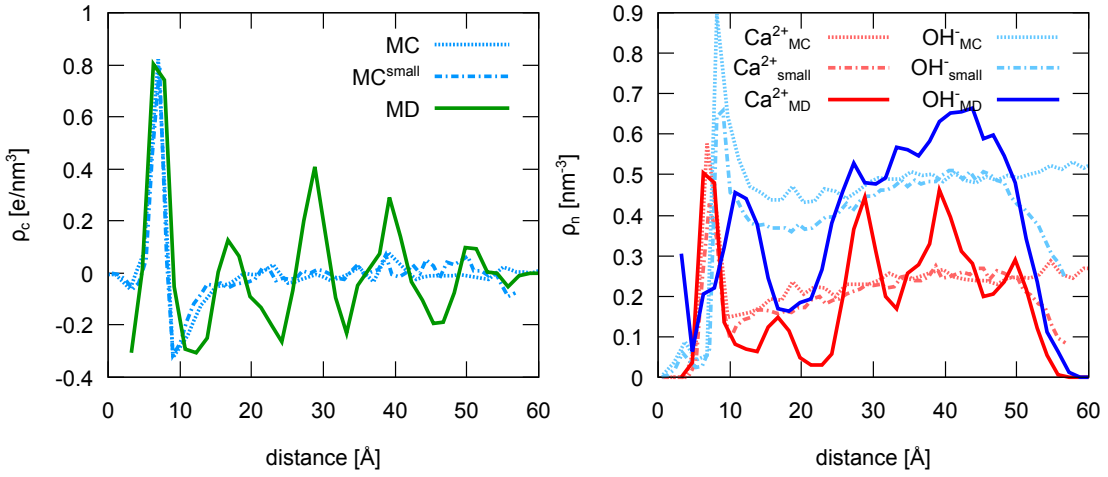

(a) (b)

Figure 8.2: Charge distribution (a) and ionic distribution (b) perpendicular to the [00.1] portlandite-water interface according to Monte Carlo (MC) simulations with a large and a small simulation box and according to molecular dynamics (MD) for a small simulation box. The bulk concentration was 0.42 $\frac{mol}{l}$ $Ca(OH)_2$.

After the first OH^- peak a peak in the Ca^{2+} number density can be observed, leading to a positive peak in the charge density profile. This peak, coming from the adsorption free energy profile of the Ca^{2+}, is almost identical for the Monte Carlo and the molecular dynamics simulations.

The Ca^{2+} peak is then followed by a second peak in the OH^- profile, which leads to a second negative peak in the charge density profile. This peak, although present in both the molecular dynamics and the Monte Carlo results, is less pronounced for the molecular dynamic simulations. Also this second OH^- peak seems to be at slightly larger distances for the molecular dynamics calculations compared to the Monte Carlo results.

After the second OH^- peak, a region can be distinguished where concentrations slowly approach the bulk values. This region can be considered to be equivalent to the diffuse region of the increasingly inaccurately named electrical "double layer". The diffuse region is characterized by a depletion in both the Ca^{2+} and the OH^- densities followed by a gradual recovery of bulk values. This is shown by a region of negative charge gradually approaching zero at large distances, compensating the charge from the first Ca^{2+} peak minus the charge already compensated in the first two OH^- peaks. There are two differences between the molecular dynamics and Monte Carlo results in the diffuse layer region. Firstly the depletion is more pronounced for the molecular dynamics than for the Monte Carlo calculations. Secondly the molecular dynamics results show pronounced oscillations throughout the whole simulation domain for both the ionic and the charge density profiles.

There are several possible reasons for the observed differences. First of all, not all the assumptions that are are underlying the Gouy-Chapman theory have been relaxed for the Monte Carlo

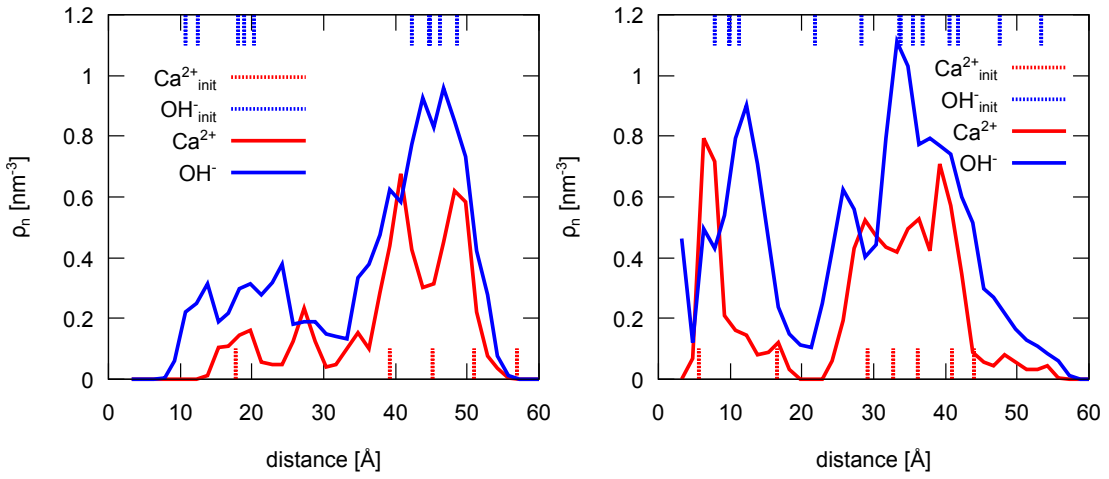

Figure 8.3: Ionic distributions perpendicular to the [00.1] portlandite-water interface according to molecular dynamics for two different starting configurations ((a) and (b)). The starting configuration of the ions is shown as dotted lines

calculations (see section 1.4.3). The work involved displacing the solvent molecules from the interface region to the bulk solution and the changes in the solvation shell when approaching the surface should both have been taken into account by the adsorption free energy profile. The ion-ion correlations have been taken into account by calculating the electrostatic ion-ion interactions explicitly within a certain cutoff radius. There are two more effects that have not been taken into account. One is a possible change of the dielectric constant of water at the surface due to the alignment of the water molecules and water density variations. This is an effect that is only expected within the region where water was observed to have non-bulk properties i.e. up to about 8-10 Å (see section 7.2). However most of the observed differences, apart from the possibly larger first hydroxyl peak, are outside this region. Consequently a change of the dielectric constant is probably not the main reason for the differences.

Finally the Monte Carlo calculations do not include any specific ion-ion interactions other than the electrostatic interactions and a very short range excluded volume repulsion in the order of 2.4-3.4 Å, depending on the species. This is an effect that could be active over the whole domain of the electrical "double layer". Further detail of the ion-ion interactions could be included by calculating the ion-ion free energy interaction profile with e.g. metadynamics and including it in the calculations.

The molecular dynamics simulations include all the above mentioned effects. However there are three other factors that might influence the results for the molecular dynamics calculations. First of all Ewald summation (see section 2.2) was used to include the long range electrostatic interactions. This means that the long range electrostatic interactions will actually be calculated for a infinite periodic array of interfaces. As Torrie and Valleau [TV80] pointed out, this is likely to lead to unphysical correlations of charge fluctuations and may

distort the observed density profiles. To estimate the influence of the Ewald summation on the observed density profile, the Monte Carlo calculations have been repeated using Ewald summation instead of the long range potential for linear charge distributions. As they are computationally more expensive, the calculations using Ewald sum take much longer than the ones using a linear charge distribution potential. The results for the Monte Carlo calculation using Ewald summation can be seen in figure 8.1. One can clearly see that both the charge and the ionic densities have been smoothed by the application of the Ewald sum. Additionally the magnitude of the first two peaks in the OH^- and the peak in the Ca^{2+} profile seem to be overestimated by the Ewald summation and the depletion in the diffuse layer underestimated. This leads to seemingly slightly lower bulk concentration values. However the effect is not pronounced and contrary to what is observed for the molecular dynamics simulation results, leading us to believe that the Ewald summation is not the major cause of the differences between molecular dynamics and Monte Carlo.

Secondly the simulation time for the molecular dynamics calculations might not have been sufficient to ensure that the final result is not influenced by the initial configuration of the ions. This can be seen by looking at the distribution for the separate simulations as compared to the initial configuration of the ions (figure 8.3). One can clearly see the influence of the initial configuration on the final profile, even though the ions also clearly diffuse over a large part of the system, causing a non-zero density in regions originally devoid of ions. This seems to justify the original assumption that the average density profiles is likely to have relaxed towards the equilibrium concentration for the molecular dynamics system even though there might still be some influence of the original ion configurations.

Last but not least, there might be an influence of the system size on the distribution. Due to the much higher computational cost of the molecular dynamics calculations the system was, of necessity, much smaller than the Monte Carlo system. Consequently there might be size effects. To have an idea on how the size of the system might influence the resulting density profile, Monte Carlo calculations were done for a system of similar dimensions as used for the molecular dynamics systems (21.8 x 25.3 x 57.2 Å) with only one portlandite surface and limited on the opposite end by a simple hard wall. The charge density profile for the small system is very similar to the one of the original system (figure 8.2a). The ionic densities on the other hand show significant changes (figure 8.2b). In fact in the small system the first peak in the Ca^{2+} profile as well as the second peak in the OH^- profile are less pronounced whereas the depletion in the diffuse layer is more pronounced. This is consistent with the observations for the molecular dynamics system where especially the second OH^- peak is significantly reduced and the depletion more pronounced than for the Monte Carlo calculations. In fact the size effect in the molecular dynamics system is likely to be more pronounced than for the small system Monte Carlo calculations as especially the Ca^{2+} ions prefer to stay some distance away from the water-vacuum interface, effectively reducing the size of the solution available for the ions. This also explains the slightly higher ionic densities in the region furthest away from the interface for the molecular dynamics system. The small system size is also likely to influence, to some extent, the observed fluctuations in both the charge and the ionic

densities. In a larger system the fluctuations would be expected to disappear towards the bulk solution, independent of their origin. However there is no clear indication of this for the molecular dynamics results. Although the last peak in both the charge and the Ca^{2+} density profile is a bit smaller, it is already in a region likely to be depleted of ions due to the closeness to the water-vacuum interface. Consequently, as the fluctuations persist through the whole simulation domain, the size of the system is likely to have some influence on the charge fluctuations.

All in all the results indicate that the Monte Carlo calculations are able to describe the original molecular dynamics system much better than the classical Gouy-Chapman theory which fails to describe both the second peak in the OH^- distribution and the ionic depletion in the first part of the diffuse layer. In fact the first peak in the Ca^{2+} density as well as the general features of the ionic distribution seem to be remarkably well described by the Monte Carlo calculations. It seems clear that Monte Carlo in combination with adsorption free energy profiles obtained with metadynamics is a powerful tool to link molecular dynamic results to macroscopic properties such as the zeta potential and interparticle forces. There are still some differences between the Monte Carlo and the molecular dynamics results. These are probably due to a simplistic description of the Ca^{2+}-OH^- short range interactions in the Monte Carlo simulations and due to size effects and incomplete equilibration in the molecular dynamics system. Here further insight and a better consistency between the two methods could be obtained by including a Ca^{2+}-OH^- interaction free energy profile obtained via metadynamics and by repeating the molecular dynamics calculations for larger systems and over longer time scales.

8.2 Ionic Distribution in pure $Ca(OH)_2$ - H_2O systems

As the Monte Carlo calculations have been shown to reproduce the important features of the molecular dynamics system, calculations were done for a less concentrated and physically more relevant system. The same basic setup as for the concentrated system was used but the dimensions of the system were 240 x 240 x 400 Å and the system contained 278 $Ca(OH)_2$. Additionally a larger short rage/long range cutoff (100 Å) was employed. The average concentration in the system was 20 $\frac{mmol}{l}$, which is consistent with a pure portlandite-water system at room temperature in equilibrium (see chapter 6).

The final results for the charge density and the ionic number density profiles can be seen in figure 8.4. The bulk concentration (20 $\frac{mmol}{l}$) is not noticeably changed by the presence of the electrical "double layer". As observed for the highly concentrated system, close to the surface the charge density is negative, however the effect is much smaller and no peak can be discerned for the lower concentration. This small region of negative charge density is followed by a positive peak corresponding to the Ca^{2+} adsorption at the outer Helmholtz plane. The Ca^{2+} peak is again followed by a diffuse layer. As for the concentrated system the charge density in the diffuse layer region can be fitted to a Gouy-Chapman like distribution. The fitted function

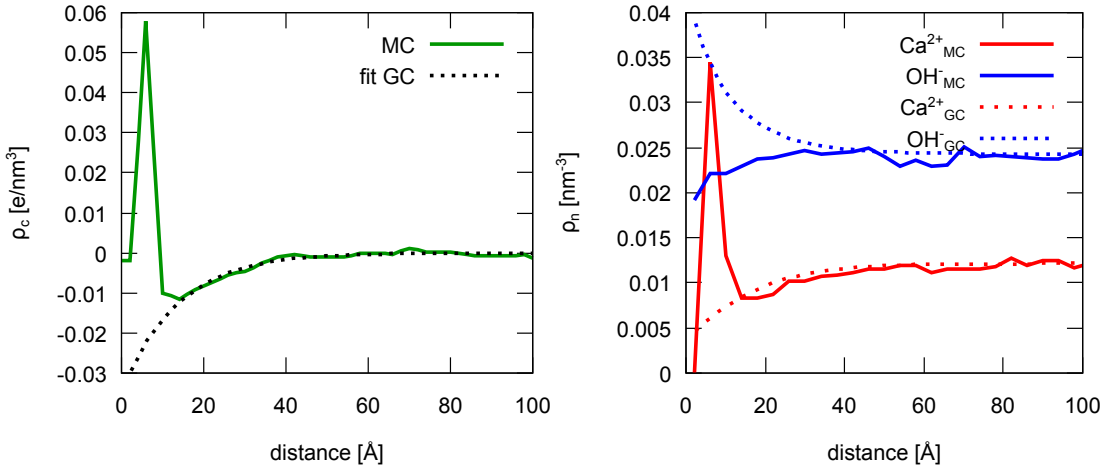

Figure 8.4: Charge distribution (a) and ionic distribution (b) perpendicular to the [00.1] portlandite-water interface according to Monte Carlo (MC) simulations. Results according to the Gouy-Chapman (GC) theory (using the Debye-Hückel approximation), fitted to the Monte Carlo charge density, are given as well.

can be seen in figure 8.4a. The parameters used for the fit were the equivalent interface charge $-\sigma^{dl} = \sigma_s + \sigma_H + \sigma_{H^{out}} = 0.04\ \frac{e}{nm^2}$ or $6.9\ \frac{mC}{m^2}$ and the virtual diffuse layer minimal approach distance $x_0^{dl} = 2.3$ Å. As one would expect, the equivalent interface charge is smaller than in the concentrated system. Additionally the virtual minimal approach distance is much smaller than in the concentrated system. In fact, contrary to the concentrated system, the distance is smaller than the Ca^{2+} peak position, making it devoid of any physical meaning. Another difference is the width of the Ca^{2+} peak. Whereas in the concentrated system the diffuse region seems to start at a distance of about 10 Å, the diffuse layer in the less concentrated system does not seem to start before a distance of about 20 Å.

The Ca^{2+} profile (figure 8.4b) looks similar to the concentrated case, with one peak followed by a depleted region which slowly regains bulk values at larger distances. As for the concentrated system, the depletion is slightly more pronounced for the Monte Carlo calculations than what is predicted by the Gouy-Chapman theory. The OH^- density profile on the other hand is quite different from the one observed for the concentrated system. No peak is observed for the OH^- density. Instead the density continually decreases towards the portlandite-water interface. Again this is in contrast to the Gouy-Chapman theory which predict an increase of the OH^- concentration for small distances from the surface. This means that while the Gouy-Chapman theory can be used to fit the charge density, the details of the ionic distribution may diverge significantly from the classical theory.

While deviations from the Gouy-Chapman theory have been observed by many authors, for low ionic concentrations and small surface charges the deviations are usually smaller (see [TV82]). This indicates that a large part of the deviation form the Gouy-Chapman theory

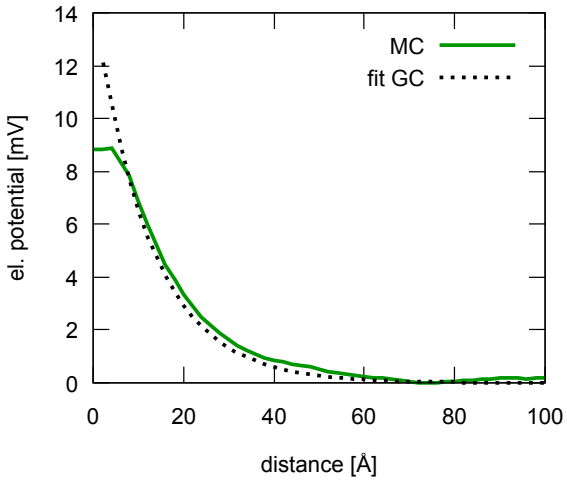

Figure 8.5: Evolution of the electrostatic potential perpendicular to the [00.1] portlandite-water interface according to Monte Carlo (MC) simulations for the equilibrium concentration ($0.02\ \frac{mol}{l}\ Ca(OH)_2$) in pure systems. Results according to the Gouy-Chapman (GC) theory (using the Debye-Hückel approximation), fitted to the Monte Carlo charge density, are given as well.

comes from the fact that, in the current calculation the origin of the equivalent interface charge σ^{dl} is not a hard wall carrying a certain surface charge, but the interaction between the ions in solution and the portlandite-water interface.

One of the aims of the calculations was to be able to compare results to experimental zeta potential measurements. To be able to do this, one has to look at the evolution of the electrostatic potential perpendicular to the surface. This can be seen in figure 8.5. As the potential depends only on the charge density profile, the electrostatic potential far from the surface resembles the fitted Gouy-Chapman potential closely, despite the above stated differences in the ionic distribution. However close to the surface (< 10 Å) the two electrostatic potentials diverge. While the Gouy-Chapman potential continues to increase, the potential according to the Monte Carlo calculations evens out close to the surface.

As discussed in sections 1.4.3 and 4.4, there is no general consensus as to how far from the surface the zeta potential is measured. Values from 0 to 6 Å from the surface can be found in literature. As the potential evens out at distances less than ~ 10 Å, the exact distance from the surface at which the zeta potential is measured does not make such a large difference. At distances from 0 to 10 Å, the electrostatic potential varies only between 6.9 and 8.9 mV. At a distance of 6 Å the zeta potential is 8.4 mV. There are no reliable values for the zeta potential in a pure portlandite-water system. The few values that could be found where either reported without any further experimental details [GDC+02] or for a pH value that is inconsistent with a pure portlandite-water system [ENK09] (see also table 4.3). The most reliable value (7.35 ± 3.96 mV) has been reported by Pointeau et al. [PRM+06] for a system with only minimal additions. Considering the differences and the uncertainty on the Monte Carlo measurements,

coming mostly from the error on the adsorption free energy profile, the agreement between experimental and simulated value is reasonable.

8.3 Implications for Cementitious Systems

The results discussed above have many implications for cementitious systems and colloidal systems in general. Some of them can already been seen quite clearly and for others further investigations will be necessary.

One important result of our calculations is that the structuring of water above the surfaces of inorganic crystals and the resulting adsorption free energy profile of the ions can have an important effect on the structure of the electrical "double layer". In fact the zeta potential developed in our calculations, which is consistent with experimental results, originates principally from the adsorption of Ca^{2+} ions at the outer Helmholtz plane, an effect that is generally not at all included in the classical electrical "double layer" theories. This effect is likely to be of more general relevance, as water structuring and ion adsorption free energy profiles, similar to the ones reported here, have been reported for interfaces of various inorganic materials other than portlandite [AGM$^+$09, KP04, KK02, KCSP05, SCKP06, KCMP05, ZKR10]. Additionally the different origin of the surface charge seems to have an impact on the whole electrical "double layer", leading to deviations of the ionic distribution from the conventional theory, not only in the "compact" layer but also in the diffuse layer (see section 1.4). Also the exact behavior might change substantially form surface to surface, as the structuring of the water is quite different for the different surface orientations (see section 7.2).

All in all our results seem to call for more caution in the interpretation of both experimental zeta potential measurements and surface titration experiments and especially in the conversion of these quantities to surfaces charges. In fact more studies would be desirable to further elucidate the structure of the electrical "double layer" and the exact definition of the experimentally measured quantities. A thorough study of a well characterized model system where the type of surfaces present are well known using both the theoretical approach combining molecular dynamics and Monte Carlo used here and experimental zeta potential measurements and surface titrations might shed more light on both the exact structure and origin of the electrical "double layer" in inorganic - water systems and their relation to the experimental results.

The exact structure of the electrical "double layer" will in turn influence the adsorption/desorption processes at the surface. Amongst other things this is important to understand the growth of portlandite. According to our results, the first 4-6 Å at the [00.1] portlandite - water interface are completely devoid of any Ca^{2+} ions. This makes it likely that the dehydration and adsorption of Ca^{2+} ions is at least a contributing factor to the growth of portlandite in [00.1] direction. This means that any reduction of the Ca^{2+} concentration is likely to slow down portlandite growth in that direction. As discussed in the previous chapter (see section 7.3), that the same might not be true for other portlandite surfaces. This indicates that changes

in the speciation might influence the growth and morphology of portlandite by reducing the growth speed of the [00.1] surface compared to other surfaces.

The ionic distribution will also influence adsorption/desorption phenomena other than the growth of portlandite. For instance the adsorption and desorption of different organic additives in the cement mix, such as superplastisizers, is certainly influenced by the electrical "double layer". Here the combination of atomistic simulations of the adsorption of different additives at the surface and the resulting free energy profile, similar to that done e.g. by Aschauer et al. on calcite [ASBP10], could be used in combination with the Monte Carlo approach used here to gain further insight into how the adsorption and desorption behavior of additives is influenced by the composition of the solution.

Finally the ionic distribution is also likely to influence interparticle forces and the colloidal stability of a system. How the observed deviations from the Gouy-Chapman theory influence interparticle forces is difficult to judge based on the current results. As the potential at large distances is similar to a Gouy-Chapman like potential it is possible that the interparticle forces in that range are still well described by classical models, such as the Hogg - Healy - Fürstenau (HHF) expression for the electrostatic interaction between particles (see section 1.4.4). However more information could be gained by a series of Monte Carlo calculations with decreasing distance between two interfaces (i.e. interparticle distance for infinitely large particles). By comparing the energy of the system for different interparticle distances, one could estimate the interparticle forces and compare them to the HHF theory.

8.4 Summary

In this chapter first Monte Carlo calculations were compared to molecular dynamics simulations. The important features of the ionic distribution seem to be well described by the Monte Carlo calculations, although their accuracy might be increased by adding a more accurate description of the short range Ca^{2+} - OH^{-} interactions.

The results of the Monte Carlo calculations for a pure portlandite - water system at equilibrium was compared to experimental zeta potential measurements. The consistency between the zeta potential estimated from Monte Carlo calculations (6.9-8.9 mV) and experimental results (7.35 ± 3.96 mV [PRM^{+}06]) was found to be very good, indicating that the adsorption free energy profile can not be neglected when trying to understand the electrical "double layer".

While the charge density profile can be fitted to a classical Gouy-Chapman like profile, the details of the ionic densities differ from the conventional continuum theory. The diffuse layer was found to be depleted of both Ca^{2+} and OH^{-} ions in contrast to the Gouy-Chapman theory which predicts a increased OH^{-} density in the diffuse layer. The main reason for the observed difference is thought to be the different origin of the equivalent interface charge which is compensated in the diffuse layer. While the Gouy-Chapman theory considers the charge to be located evenly at an impenetrable hard wall, for the current calculations the charge results

from Ca^{2+} adsorption in a region which is also accessible to the counterions.

Finally the implications of the results for cementitious systems were discussed. It was found that the deviation from Gouy-Chapman results should inspire caution in the conversion of zeta potential measurements and surface titration into surface charges for inorganic-water systems. Further studies of the electrical double layer and how it relates to experimental measurements of e.g. the zeta potential would be desirable. The method used here, combining molecular dynamics and Monte Carlo, is thought to be a powerful tool to gain further understanding of the electrical double layer.

The structure of the ionic double layer is also likely to influence the growth of portlandite. At the [00.1] surface the region up to 4-6 Å from the surface was found to be devoid of Ca^{2+} ions. This makes it likely that the adsorption of Ca^{2+} might be rate limiting for portlandite growth in that direction. Together with results from chapter 7, where evidence was presented that the situation might be different for other surfaces, this indicates that a change in calcium - hydroxide speciation, as discussed in chapter 6, might have an influence on the growth morphology of portlandite.

9 Summary and Conclusions about the Growth and Morphology of Portlandite

In this chapter the results concerning the growth and morphology of portlandite are summarized. The properties of portlandite-water interfaces in pure portlandite-water systems are discussed as well as the implications for portlandite growth and equilibrium morphology. This is followed by a summary of the results concerning the influence of silicates, sulfates and aluminates on the growth and morphology of portlandite. For each section an outlook is given as to how further insight into the growth and morphology of portlandite could be gained in the future based on the current work.

In the first section of this chapter the pure portlandite - water system is discussed in some detail. Results mainly concern the interactions of water with different portlandite surfaces as well as insights gained into the possible growth mechanisms. Also the probable structure of the electrical "double layer" at portlandite surfaces is described.

The discussion of the pure portlandite - water system is followed by a discussion of the influence of silicates on portlandite growth and morphology. As silicates are always present in conventional cementitous systems, their influence on the morphology and growth of portlandite is important to understand first, before investigating the influence of other species in the system. Experimental observations are compared to thermodynamic calculations and atomistic simulations. This made it possible to determine the effects of silicates as well as to get an idea of the possible atomistic mechanisms.

Sulfates were previously shown to have an important effect on the morphology of portlandite [GS07, BM72]. Further insights into why and how sulfates influence portlandite growth is presented here. Results from both experiments and thermodynamic calculations are discussed with respect to the insights gained for the properties of pure portlandite - water interfaces.

Finally the influence of aluminates is discussed. Aluminates are another class of additives that has been shown to influence the growth of portlandite [GS07]. Consequently results obtained

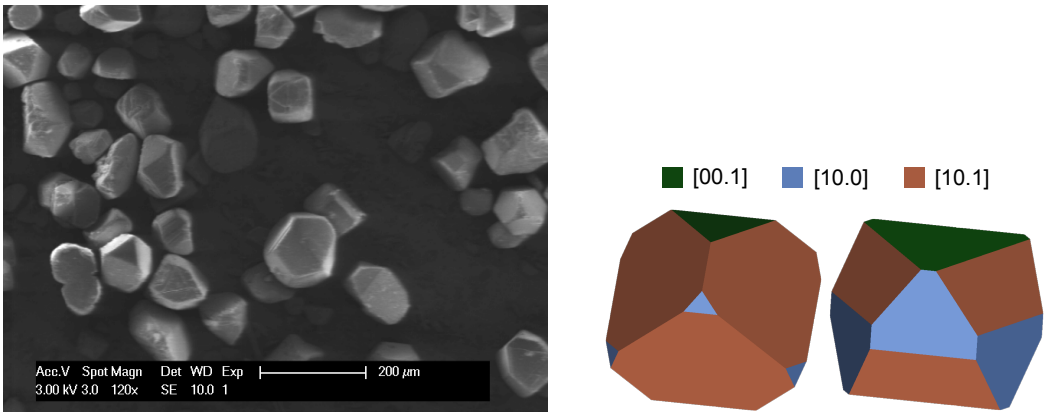

(a) (b)

Figure 9.1: Experimentally observed (a) and theoretically predicted (b) morphologies of portlandite in pure portlandite-water systems.

for the influence of aluminates on the growth of portlandite are summarized here and related to previous results.

9.1 Pure Portlandite - Water System

The morphology of portlandite in water was observed to be equiaxed (see figure 9.1a and chapter 5) despite the fact that the [00.1] plane is a perfect cleavage plane and consequently prominent in the morphology of portlandite in a non-interacting environment. Different theories (BFDH, attachment energies, surface energies and portlandite-water energies) to predict the morphology of crystals were compared to find the origin of the equiaxed morphology (see chapter 7). It was found that both surface relaxation and portlandite-water interaction have a tendency to make the morphology more equiaxed. However while relaxed surface energies still predict a hexagonal platelet morphology, water seems to noticeably stabilize the high energy surfaces and portlandite-water interactions seem to be the main cause of the observed equiaxed morphology. In fact the equilibrium morphologies predicted according to the portlandite-water interfacial energies calculated by molecular dynamics (see figure 9.1b) are in good agreement with experimental observations. Additionally the calculated interfacial energies (0.08-0.13 $\pm$ 0.06 $\frac{J}{m^2}$ are in good agreement with experimental values reported in literature (0.07-0.11 $\frac{J}{m^2}$ [HKM$^+$09, KS68]).

Closer inspection of the water structure at portlandite surfaces in the molecular dynamics simulations revealed that, at both the [10.0] and the [10.1] surface, a stable network of strongly bound surface water exists. This is in contrast to the [00.1] surface where only transient and less frequent hydrogen bonding was observed (see figure 9.2a). Due to the strongly bound nature of the surface water at both [10.0] and [10.1] surface, the desorption of the surface water might be, or contribute to, the rate limiting step of growth in both the [10.0] and the [10.1] direction. This would indicate that these surfaces are stabilized both energetically and

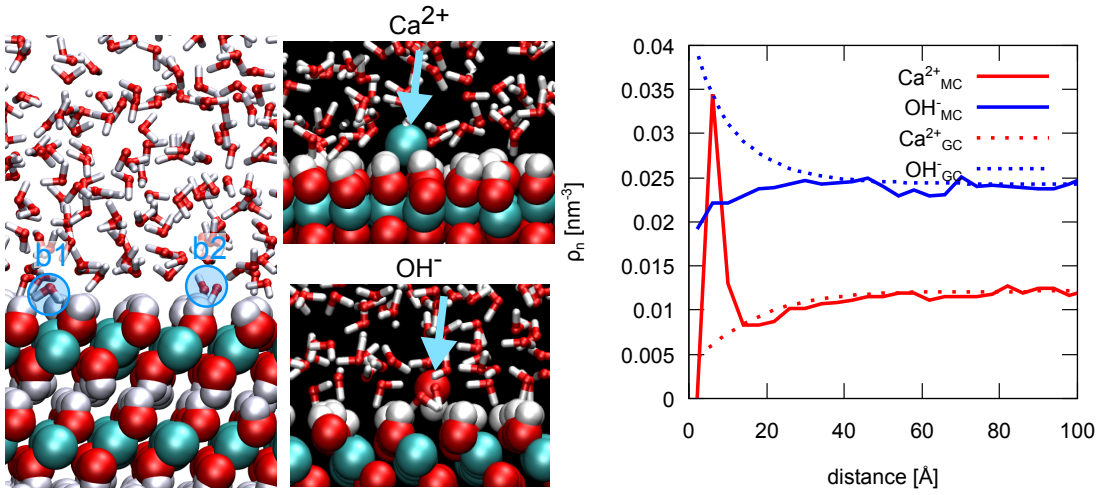

(a) (b) (c)

Figure 9.2: Different views of the [00.1] surface: Hydrogen bonding of water as observed with molecular dynamics (a), adsorption sites for Ca^{2+} and OH^{-} as observed with metadynamics (b) and the ionic distribution calculated with Metropolis Monte Carlo.

kinetically. The stepped [20.3] surface showed a slightly different behavior. Although hydrogen bonding at the [20.3] surface appeared to be extensive, most of the bonding seems to be rather disorganized and the surface bound water molecules are much more mobile. In turn this indicates that, even though the [20.3] surface was found to be stabilized more by the presence of water from an energetical point of view, kinetically the stabilization of the [10.0] and the [10.1] surface might be more important.

The observation that the morphology of portlandite in water is equiaxed rather than hexagonal platelet shaped is important, as generally the equilibrium morphology of portlandite in water is assumed to be hexagonal platelets. The fact that this does not seem to be the case will have an impact on the discussion of the effect of the different additives on portlandite morphology.

To gain further understanding about the growth mechanisms of portlandite, the adsorption of the main species in solution in the pure portlandite - water system, the Ca^{2+} and the OH^{-} ion, at different portlandite surfaces was studied with metadynamics. The adsorption of the $CaOH^{+}$ ion was not studied here although its concentration, according to thermodynamic calculations, is not negligible. The reason for this is that the $CaOH^{+}$ complex, although sometimes observed during the molecular dynamics simulations, was not found to be a stable species and its existence is transient. This means that the importance of the $CaOH^{+}$ complex is likely to come from different Ca^{2+} - OH^{-} interactions at the surface compared to the bulk solution rather than from the adsorption of the $CaOH^{+}$ species itself.

At the [00.1] surface, the hydroxyl adsobs at a positions which would be equivalent to the hydroxyl position in the next portlandite layer, with the oxygen oriented towards the solution and the hydrogen towards the surface, donating a hydrogen bond to a portlandite surface

oxygen (see figure 9.2b). The adsorption of the OH^- ion seemed to be more favorable than the adsorption of Ca^{2+}, which adsorbed in between the surface hydrogen groups. Consequently the Ca^{2+} adsorption site does not correspond to a bulk position. This quantitative observation was confirmed by the calculation of the adsorption free energy profile. According to the adsorption free energy profile, the energy of the OH^- ion increases slightly when the hydration shell of the hydroxyl group starts interacting with the structured water region close to the surface, but stays more or less constant at closer distances from the surface at which the hydroxyl starts loosing part of its hydration shell. The energy profile for the Ca^{2+} ion on the other hand shows a minimum at a distance of about 8 Å from the surface, indicating a favorable interaction between the hydration shell of the Ca^{2+} ion and the structured water region at the portlandite surface. The loss of part of the hydration shell however is energetically unfavorable, leading to an important increase in energy for a further approach of the surface.

Monte Carlo calculations were used to estimate the ionic distribution at the [00.1] surface, based on the adsorption free energy profiles (see chapter 8). According to the Monte Carlo calculations the OH^- concentration continually decreases towards the surface but is non-zero over the whole domain (see figure 9.2c). On the other hand the region up to 4-6 Å is completely devoid of Ca^{2+} ions. At larger distances on the other hand there is a peak in the Ca^{2+} density, followed by a Ca^{2+} depleted region that slowly recovers bulk properties at larger distances. The peak in the Ca^{2+} density corresponds to the minimum in the adsorption free energy profile coming from the favorable interaction between the Ca^{2+} solvation shell and the structured water region at the portlandite surface. These results indicate that for the [00.1] surface the rate limiting step might be the dehydration of the Ca^{2+} ions. This in turn would mean that any compositional change, increasing the pH and consequently reducing the Ca^{2+} concentration by the common ion effect is likely to slow down the growth of portlandite in [00.1] direction.

At the [10.0] surface, the Ca^{2+} ion does not seem to adsorb readily and, when adsorbed, does not disturb the structure of the network of strongly bound surface water. The OH^- ion on the other hand adsorbs more easily and replaces a strongly bound surface water when adsorbed. If we suppose that the desorption of the strongly bound surface water is the rate limiting step for portlandite growth in [10.0] direction, as according to our results the water desorption and the hydroxyl adsorption appear to be linked, the growth rate in [10.0] direction is likely to be influenced by the OH^- concentration. However, depending on the adsorption free energy profile, the dehydration of the Ca^{2+} ion might also be a contributing factor, and consequently the Ca^{2+} concentration might also have an influence.

The situation at the [10.1] surface is different from the other two surfaces. Here the Ca^{2+} ion adsorbs more readily and its adsorption causes the desorption of two strongly bound surface water. The adsorption of OH^- on the other hand seems to be more difficult and does not disturb the strongly bound surface water. Consequently, if the desorption of the strongly bound surface water is the rate limiting step, it is likely that the growth rate of portlandite in the [10.1] direction is influenced by the Ca^{2+} concentration. However the dehydration of the OH^- ion might be a contributing factor.

These results indicate that the calcium-hydroxide speciation of the solution might already influence the growth morphology of portlandite. Let us suppose for instance that the rate limiting step at the [10.0] surface and the [10.1] surface is the desorption of the strongly bound surface water, and at the [00.1] surface the dehydration of the Ca^{2+} ions. This would mean that an increase in pH and the corresponding decrease in the Ca^{2+} concentration, due to the common ion effect, would decrease the speed in the [00.1] and [10.1] direction and increase the speed in [10.0] direction. This means that the importance of the [00.1] and [10.1] surfaces compared to the [10.0] surface in the growth morphology would increase. This is to some extent consistent with results by Berger and McGregor. who found that the addition of hydroxides ($LiOH$ and $NaOH$) had a tendency to increase the aspect ratio $\frac{L^{10.0}}{L^{00.1}}$ [BM72] (see table 4.1). Additionally this would explain observations by Gray [Gra90], who found that decreasing the calcium to hydroxyl ratio would lead to more equiaxed particles, compared to the elongated hexagonal prism morphology, dominated by the [00.1] facet, observed at higher calcium concentrations (see figure 4.3).

In order to verify the accuracy of the ion distribution calculations, the zeta potential according to the Monte Carlo calculations for the [00.1] surface (6.9-8.9 mV) was compared to experimental results reported in literature (7.35 ± 3.95 mV). The consistency between theoretical and experimental results is reasonable good. However for our calculations the origin of the interfacial charge, giving rise to the calculated zeta potential, is different from the origins considered in conventional continuum theories (see section 1.4). Neither the surface of the solid, where ions can approach and recede but not pass through, nor the inner Helmholtz plane, where the ions have to lose part of the hydration shell and consequently the hydrated ions can only approach or recede but not pass through, is the origin of the charge. Instead the charge originates from an adsorption of the hydrated Ca^{2+} ion, coming from a favorable interaction between the hydration shell of the ion and the structured water region at the surface. Consequently the underlying assumption of an ideal polarized electrode used for the Gouy-Chapman theory, the most current theory to describe the diffuse part of the electrical "double layer", is not valid. This results in deviations of the ionic structure from the Gouy-Chapman theory. Indeed for a portlandite surface in contact with a 20 $\frac{mmol}{l}$ $Ca(OH)_2$ solution (equilibrium concentration), instead of an increase of the counter-ion concentration in the diffuse layer close to the surface, our calculations show a continuous decrease of the OH^- concentration (see figure 9.2b).

These results indicate that the water structure at the surface can have an important influence on the structure of the electrical double layer. As this is an effect not taken into account by most conventional continuum theories, these results should inspire some caution as to the interpretation of experimental measurements, such as the zeta potential and surface titration, especially when converting them to surface charges. The observed deviations from the classical mean field theories to describe the electrical "double layer" is likely to impact the adsorption and desorption processes at the surface, such as the adsorption of organic additives (e.g. superplasticizers in cement), and might also influence interparticle forces and consequently the colloidal stability.

The deviation of the structure of the diffuse part of the electrical double layer in cementitious systems has been investigated before by different authors [JNL+05, LJP+06, LPJN11, PLVD08], using similar Metropolis Monte Carlo calculations. These works show that the diffuse layer close to a highly negatively charged hard model C-S-H surface deviates significantly from the classical Gouy-Chapman deviation due mainly to ion-ion correlation effects. In fact the divalent Ca^{2+} ions overcompensate the surface charge and lead to an experimentally observed positive zeta potential. The difference between the previously reported and current results is the origin of the deviation. For the C-S-H surfaces, the high surface charges and the divalent calcium ions are at the origin of the divergence of the structure of the diffuse layer, the reason for the divergence in our case comes from the interaction potential of the ions with the surface calculated previously with metadynamics.

9.1.1 Outlook

More information about the growth of portlandite in a pure portlandite - water system could be gained by repeating the adsorption free energy profile calculations for Ca^{2+} and OH^- at other surfaces, namely the [10.0] and the [10.1] surface. The difficulty here lies within the fact that, according to preliminary calculations, a second collective variable would have to be used, describing the different adsorption positions at the surface. For the [10.0] surface some promising preliminary results were obtained by using the distance of the Ca^{2+} ion from the central oxygen column in the portlandite slab in [00.1] direction as the second collective variable. In order to take into account the fact that there exist many equivalent adsorption positions at the surface, the second collective variable was rendered periodic by converting it to a sawtooth wave with a periodicity of 4.8 Å (i.e. the portlandite cell parameter in [00.1] direction). The completion of these calculations for the [10.0] surface and with a similar setup for the [10.1] surface should lead to reliable adsorption free energy profiles for the Ca^{2+} and the OH^- ion at these surfaces.

The adsorption free energy profiles could then be used for Monte Carlo calculations of the ionic distribution at these different portlandite surfaces. The Monte Carlo calculations could, in addition, be improved by a more accurate description of the short range Ca^{2+}-OH^- interactions e.g. by using the result of metadynamics calculations. This would give a clearer image as to what is likely to be the rate determining growth step at the different surfaces. Such knowledge would in turn give some informations about the expected changes of growth morphology of portlandite solutions as a function of the pH. The predicted morphological changes could then be compared to experimental results where the relative concentration of Ca^{2+} with respect to the OH^- concentration is changed. Such experiments would be difficult in a pure system but could be done using coprecipitation experiments with weakly interacting counter ions (e.g. $NaCl$, KCl or KNO_3).

Another point of comparison between theoretical predictions and experiment could be a consistent series of zeta potential and surface titration experiments for portlandite in a pure

portlandite-water system. Due to the fact that the Gouy-Chapman theory might not be valid it would be important to compare primary experimental data (such as the zeta potential and the total excess or deficiency of hydroxyl ions at the portlandite surface) rather than converted quantities (such as surface charges). The study of the zeta potential of portlandite with different morphologies (e.g. equiaxed particles produced by thermal or coprecipitation and hexagonal platelets produced by coprecipitation in the presence of sulfates ...) would be interesting. According to our results different morphologies might lead to different zeta potentials. However such a study would to some extent be hampered by the uncertainty attached to the conversion of the electrophoretic mobility to a zeta potential (see section 1.4.3). The theory used would have to take into account the different geometries in order for the results to be reliable.

The Monte Carlo calculations could also be used to estimate interparticle forces. In fact the energy of two facing electrical double layers could be calculated as a function of the distance between the two by a series of calculations. The derivative of this function could then be used to estimate interparticle forces. Such an approach has been done before e.g. for cementitious systems [JNL$^+$05, PLVD08], however the novelty of the calculations proposed here would be the link to the molecular dynamic system with atomistic detail, due to the use of the adsorption free energy profile. This link to the details of the atomistic structure would also make it possible to compare the forces between different types of facets. This would e.g. give some indication whether oriented or random agglomeration is preferred (see e.g. [RNRAOHH05]) and under which conditions. The result could also be linked to the experimentally observed colloidal stability, however here more information about the Hamaker constant of portlandite in water would be needed as well (see sections 1.4.4 and 4.4).

If we project even further into the future, the incorporation of adsorbed Ca^{2+} and OH^- ions into the crystal surface could be studied i.e. with the help of metadynamics calculations using a order/disorder parameter as the collective variable. This could then lead to some informations about the energetics of both layer nucleation and step growth. Such an approach might eventually lead to a full kinetic model of the growth of portlandite from solution (using e.g. kinetic Monte Carlo).

Finally if results for the adsorption of organic additives at portlandite sufaces, using calculations similar to the ones done by e.g. Aschauer et al. [ASBP10], could be incorporated in the above described Monte Carlo results, further information about the adsorption of these additives under different conditions could be gained. Here special attention should be paid to the configurational entropy of the polymer (see e.g. [NA03]).

9.2 Influence of Silicates

The influence of silicates on the growth and morphology of portlandite has been studied both experimentally and theoretically. Experimentally it has been observed that the addition of silicates seemed to slightly reduce the primary particle size and promote the formation of

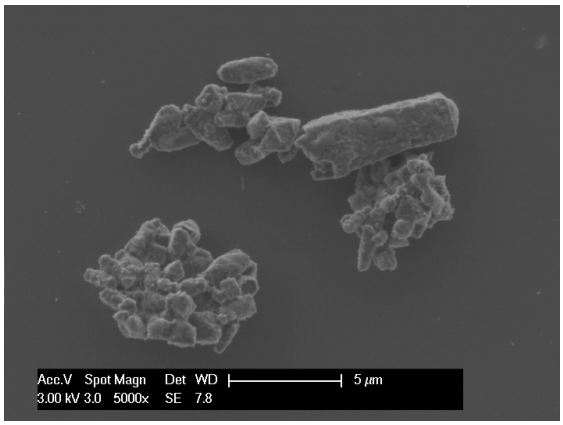

Figure 9.3: Experimentally observed portlandite morphology in the presence of silicates.

agglomerates (see figure 9.3). The primary particles loose their well defined shape and there appears to be a secondary phase at the surface of and in between the particles. This secondary phase was assumed to be C-S-H, which is the secondary phase expected to precipitate according to thermodynamic calculations.

The main silicate species present in the coprecipitation system, according to thermodynamic calculations, is the $CaSiO_2(OH)_2$ complex, the existence of which has been confirmed by metadynamics calculations (see chapter 6). However, due to the low overall silicate concentration, the concentration of the calcium silicate complex in the solution is too small to noticeably affect the calcium - hydroxide speciation and only causes a slight increase of the pH.

According to metadynamics calculations, both the $CaSiO_2(OH)_2$ complex and the less abundant $SiO_2(OH)^{2-}$ ion adsorb to portlandite surfaces with the hydroxyl groups oriented towards the surface, donating hydrogen bonds to the surface oxygens (see figure 9.4a). The $CaSiO_2(OH)_2$ complex seems to adsorb more readily than the $SiO_2(OH)_2^{2-}$ ion. For the [00.1] surface this was confirmed by the calculation of the adsorption free energy profile for the two silicate species. The adsorption free energy profiles indicate that, while the energy of the silicate ion increases more or less continually close to the surface, the adsorption of both the hydrated and the partially dehydrated calcium-silicate complex seems to be energetically favorable. Interestingly at the atomically flat [00.1] and [10.0] surfaces the silicate species seem to retain a relatively high degree of mobility, performing a sort of walking movement by breaking and reforming alternately one of two hydrogen bonds donated to the surface. On the [10.1] surface on the other hand the silicate species seem to adsorb onto the protruding, step like Ca^{2+} ions at the portlandite surface. The network of strongly bound surface water at the [10.0] and the [10.1] surface stays mostly unchanged by the adsorption of the silicate species.

This indicates that the calcium-silicate complex might inhibit the growth of portlandite by adsorbing preferentially to the portlandite surface, migrating along them until encountering a step or other growth feature, where they get immobilized. This would not only be consistent with the experimental observations for model systems reported here, where the size of the

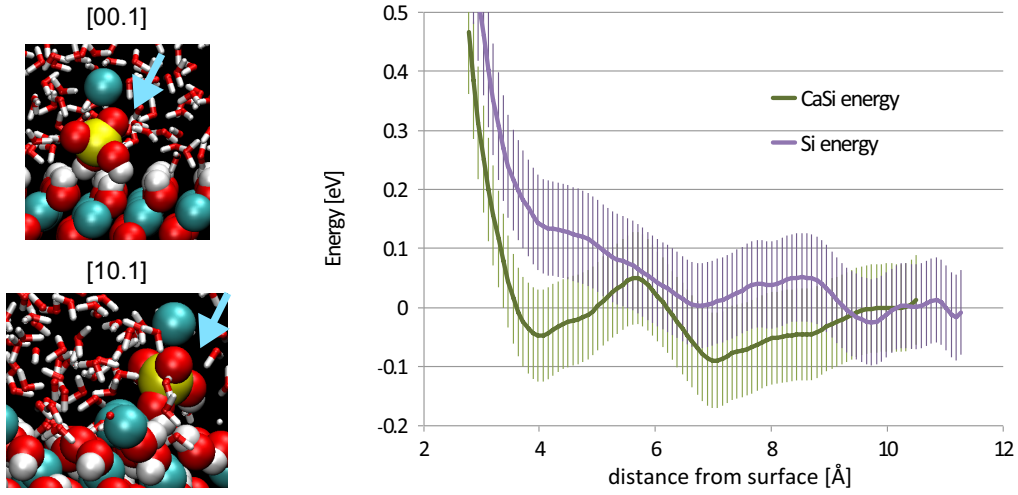

(a) (b)

Figure 9.4: Adsorption sites of the $CaSiO_2(OH)_2$ at the [00.1] and the [10.1] portlandite surface (a) as well as the adsorption free energy profile of $CaSiO_2(OH)_2$ and $SiO_2(OH)_2$ at the [0.01] surface (b).

primary particles is slightly decreased and the growth of portlandite less regular when adding silicates, but also with the fact that in cementitous systems no portlandite growth is observed during the induction period, despite the solution being oversaturated with respect to portandite. In fact the idea of growth poisoning of portlandite by silicates has been put forward as early as the 70's [TSK76, YTB77, OD79]. Our results seem to confirm that hypothesis and show a a possible atomistic mechanism for it. As it would be the growth and not the nucleation that is poisoned, it would also help explain why the increase of the Ca^{2+} concentration by adding e.g. $CaCl_2$ to the cement mix decreases the induction period but why the addition of crystalline portlandite seeds does not seem to have the same effect [YTB77, OD79].

Also, the fact that at the surfaces of portlandite there seem to be mobile, oriented, stably adsorbed calcium-silicate complexes might be seen as an indication that the portlandite surfaces promote the growth of C-S-H as the polymerisation of the calcium-silicate species might be easier at the portlandite surfaces. This would tie in with the fact that in our experiments a secondary phase, probably C-S-H, is observed at the surface of and in between the portlandite particles, apparently forming a surface layer and "gluing" the portlandite particles together. It would also be consistent with the fact that portlandite and C-S-H are often observed closely intermixed and that the acceleration of the growth of portlandite and C-S-H seems to be simultaneous (see section 1.1).

The statistical analysis of the experimental results revealed that the presence of silicates might increase the importance of the [00.1] surface in the portlandite morphology (see chapter 5). However, since the result is based on the characterization of a single particles for which the shape could be quantitatively analyzed, this result would need further confirmation.

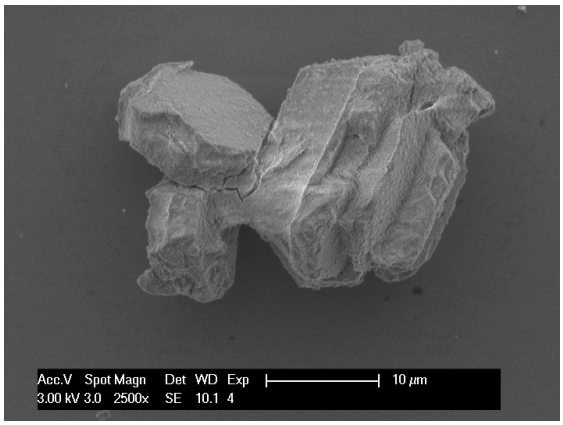

Figure 9.5: Example of unidentified phase in between portlandite particles. SEM image of a portlandite powder produced by coprecipitation in the presence of silicate, sulfates and aluminates.

9.2.1 Outlook

The knowledge about the influence of silicates on the growth and morphology of portlandite could be further improved in the future with the help of different calculations and experiments. Experimentally the use of spatially resolved composition analysis techniques (e.g. EDS) to analyze the composition of the particles produced by coprecipitation in the presence of silicates would help increase our understanding of the system. In fact on SEM images of powders precipitated in the presence of silicates, the portlandite particles often appear to be "glued together" by a secondary phase (see e.g. image 9.5). Based on the overall composition of the solution and thermodynamic calculations, it was assumed that this secondary phase is C-S-H. Spatially resolved compositional analyses could give some indication whether this assumption is justified. If this secondary phase is C-S-H, its growth morphology at the surface of portlandite particles is quite different from the one generally observed in cementitious systems. At the surface of the cement grains where C-S-H is often observed to form in a fibrillar fashion with the fibers oriented perpendicular to the original cement grain surface [GMS10, Ric04, JLM$^+$03]. The second phase observed in the coprecipitation experiments however seems to form a layer parallel to the portlandite surfaces as well as forming a link between the portlandite particles.

Additionally it might be interesting to look at coprecipitation experiments with a higher pH and a lower calcium to silicate ratio. This would more closely resemble conditions encountered during cement hydration. It would be interesting to see whether portlandite growth poisoning could be observed for high enough silicate ratios as well as to see the effect on portlandite morphology. If the growth of portlandite is decelerated by a high enough silicate concentration, the hypothesis of growth poisoning of portlandite by silicates could be confirmed.

From a theoretical standpoint further knowledge could be gained by repeating the silicate species adsorption free energy profile calculations that were done for the [00.1] surface for the

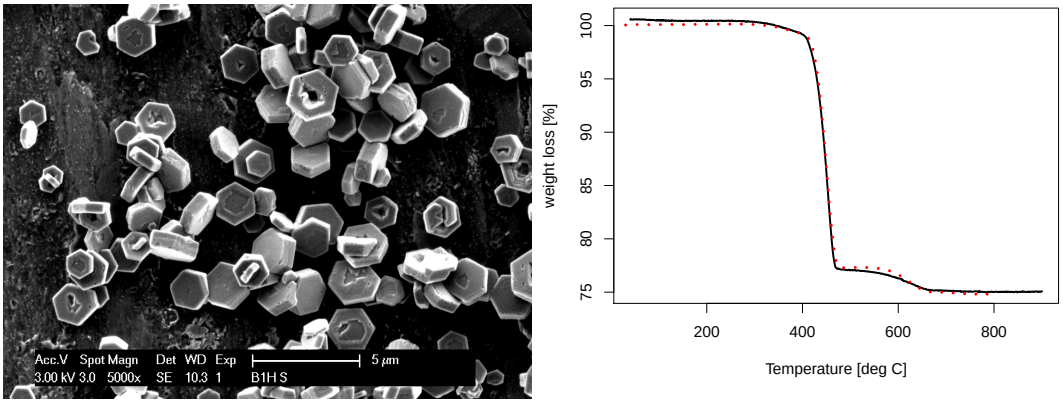

(a) (b)

Figure 9.6: Experimental morphology of portlandite in the presence of sulfates (a) and corresponding TGA results showing the absence of gypsum (b).

[10.0] and the [10.1] surface to see whether the adsorption of the calcium-silicate complex is stable at these other surfaces as well. As discussed in section 9.1.1, a slightly changed setup for the metadynamics calculations, with at least two collective variables, would have to be used for these calculations. Also the study of the adsorption of silicate species onto step-sites, such as are e.g. observed at the [20.3] surface, could be interesting and would give further insight into the influence of silicate species on the growth of portlandite.

Finally the obtained adsorption free energy profiles could be used for Monte Carlo calculations of the distribution of the different solutes close to the surface in the presence of silicates. This would lead to an estimation of the concentration of the calcium-silicate species adsorbed at the surfaces. Additionally it could be seen whether the presence of the silicate species is likely to change the structure of the electrical "double layer". This would give further insight into the extent and mechanisms of the influence of the silicate species on the growth of portlandite.

9.3 Influence of Sulfates

Experimental observations on model systems have shown that the main influence of sulfates on the growth and morphology of portlandite is to increase the importance of the [00.1] surface in the final morphology. In coprecipitation experiments (see chapter 5), the portlandite morphology changes from a quasi equiaxed morphology to a hexagonal platelet morphology if sulfates are added to the system (see figure 9.6a). Further analysis of the particle shapes showed that the morphology determining quantities $\frac{\gamma_{1.00}}{\gamma_{00.1}}$ and $\frac{\gamma_{10.1}}{\gamma_{00.1}}$ are both significantly increased by the presence of sulfates. These observations are consistent with previously reported observations of a hexagonal platelet morphology of portlandite in the presence of sulfates [GS07, BM72, HKM$^+$09].

According to thermodynamic calculations (see chapter 6), the dominant sulfate species in solution, and hence the species most likely to interact with the growing portlandite particles, is the SO_4^{2-} ion. These ions form a $CaSO_4$ complex with the calcium ions and, although the concentration of the calcium-sulfate complex is lower than that of the sulfate ions, the calcium-sulfate complex formation influences the calcium-hydroxide speciation. In fact the addition of sulfate leads to a reduction of the Ca^{2+} concentration and consequently, due to the common ion effect, to an increase of the pH. According to the results for the pure system discussed above (section 9.1), the observed increased importance of the [00.1] surface in the portlandite morphology could be partially due to the change in the calcium-hydroxide speciation. Whereas, according to atomistic simulations, the rate limiting step for growth in [00.1] direction is likely to be controlled by the Ca^{2+} concentration, there are some indications that the growth rate in [10.0] direction may be controlled by the OH^- concentration. This would mean that the decrease of the calcium to hydroxyl concentration ratio in the solution increases the importance of the [00.1] surface in the growth morphology of portlandite.

According to thermodynamic calculations, about 45 % of the precipitated powder in the coprecipitation experiment in the presence of sulfates should be gypsum. However after one hour of precipitation time, no gypsum was observed either by XRD or by TGA (see figure 9.6b). Only after a prolonged precipitation time (~ 2 months) can gypsum be observed in the system, even though according to the TGA measurements the amount is still less than 45 %. In other words gypsum precipitation seems to be retarded in the portlandite coprecipitation system. This is to some extent consistent with observations of ordinary Portland cement systems where gypsum does not precipitate during the induction period even though the solution is supersaturated with respect to gypsum (see e.g. [LW06]).

Another feature of portlandite particles precipitated in the presence of sulfates are defects, or even holes, at the center of the hexagonal platelets. This might indicate the presence of metastable sulfate containing nuclei on which the portlandite particles precipitate. These metastable nuclei might get dissolved during the washing step with ultrapure water, leaving the observed defects. This would also explain why the precipitation of gypsum is retarded in the coprecipitation systems as the concentration of sulfates in the solution would be lowered due to the presence of the sulfate containing nuclei. Additionally it would be consistent with observations by Gallucci and Scrivener that portlandite preferentially precipitates in the neighborhood of gypsum. It would also indicate that the absence of gypsum during the induction period of cementitous systems might be linked to similar metastable calcium-sulfate nuclei. However due to the possible growth poisoning of portlandite by silicates (see section 9.2), these nuclei would not grow and form portlandite particles during the induction period.

9.3.1 Outlook

One of the main avenues to pursue in the future, to continue the investigation of the influence of sulfates on portlandite, would be to verify the supposed existence of metastable calcium-

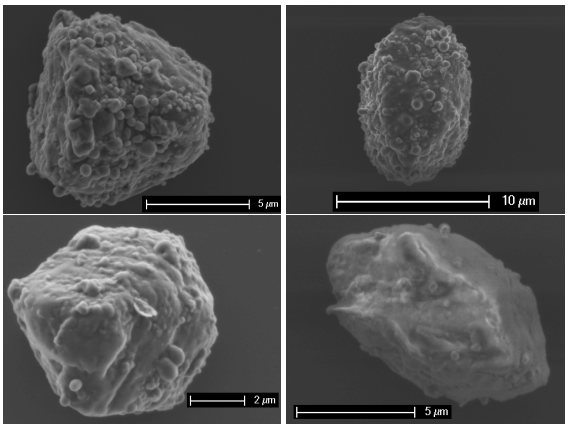

Figure 9.7: Experimentally observed portlandite morphology in the presence of aluminates.

sulfate nuclei. Here space resolved composition measurements, such as EDS, would be useful to see whether the central region of the portlandite particles does indeed contain sulfates. However, as the central region of the particles seems to get dissolved when washed with ultrapure water, the powder used for spatially resolved compositions analysis would have to be washed with a saturated $Ca(OH)_2$ solution, or maybe even a solution saturated with respect to both portlandite and gypsum, so that the central region of the portlandite particles is not dissolved.

In order to further study the influence of sulfates on the growth of portlandite, the interaction between sulfate species and different portlandite surfaces could be studied, similarly to that done here for silicates (see section 9.2). However in order to be able to do so the force field used for the current work (see chapter 3) would have to be extended to include sulfates. Different force field terms for sulfates, reported in literature for similar force fields as the one used here, could be used as a starting point [dLPSN00, ARG$^+$93, Ada03, GGLM08, MRA10]. This extension of the force field would then have to be tested similarly to that done for the calcium-silicate force field. Possible test structures would e.g. be gypsum, hemihydrate and anhydrate.

9.4 Influence of Aluminates

According to experimental observations in model systems, the main effect of the addition of aluminates on the growth and morphology of portlandite is to increase the particle size. This is usually an indication that either the nucleation rate is decreased or the growth rate increased. In the current context, as it is difficult to see how aluminates could increase the growth speed, a decrease of the nucleation rate appears more likely.

Previously reported results by Berger and McGregor [BM72] on the effect of aluminates on the morphology of portlandite formed when hydrating $C3S$ was not so clear. Different types of aluminate additives (AlF_3, $Al(NO_3)_3$ and $Al(OH)_3$ had different effects. This could be due

to possible indirect influences (e.g. changed $C3S$ dissolution rate) that might exist in the more complicated system studied by Berger and McGregor. This emphasizes the utility of experiments on model systems where conditions are well controlled.

Another effect of the addition of aluminates seems to be that the importance of the [00.1] surface in the final morphology decreases and the particles become more elongated. Indeed further analysis of the particle morphology in the systems containing aluminates showed that the morphology determining quantity $\frac{\gamma_{1.00}}{\gamma_{00.1}}$ is significantly increased when aluminates are added. This is mostly consistent with previously reported results by Berger and McGregor [BM72], where the addition of aluminates was found to have little effect or to decrease the aspect ratio $\frac{L^{10.0}}{L^{00.1}}$.

Finally the surface of the portlandite particles becomes irregular and small secondary phase particles seem to be observable at the surface of the portlandite particles.This is consistent with a small amount of aluminate phases (e.g. tricalcium aluminate hydrate), that is expected to precipitate in the aluminate containing system.

Thermodynamic calculations indicate that the aluminates, as the only additive studied here, do not form any complexes with the Ca^{2+} ion and have no other influence on the calcium-hydroxide speciation. This indicates that the interaction between the aluminates and the growing portlandite particles, rather than the interaction between aluminates and the calcium and hydroxide species in solution are causing the observed changes. The dominant aluminate species, and consequently the species that is most likely to interact, is predicted to be the $Al(OH)_4^-$ ion.

9.4.1 Outlook

From the results presented above it seems that the observed effects of the addition of aluminates are due to the interactions of the aluminate species in the solution with the surfaces of the growing portlandite particles, although the formation of secondary phases at the surface of the portlandite particles probably also plays a role. However the adsorption/desorption of aluminate species at the surface is difficult to access experimentally. One possiblility would be to study changes of the zeta-potential and/or do surface titrations for portlandite particles in the presence of aluminates and compare the results to those in the pure system. In order to see differences for the different surfaces, the same procedure might be repeated for different morphologies dominated by different facets (e.g. hexagonal platelets and equiaxed particles).

From a theoretical standpoint, one could hope further insight into the mechanisms, by which aluminates influence portlandite growth, by studying the adsorption of $Al(OH)_4^-$ at different portlandite surfaces. However, similarly to sulfates, the force field would first have to be expanded to include aluminates as well. Some initial work in that direction has already been done with force field terms previously reported in literature for similar potential [dLP99, HDLP02, SSL$^+$92] as a starting point. The different force fields were tested on alumina [LSF82],

gibbsite [SW74], tricalcium aluminate [MJ75], katoite [LVD96] and lawsonite [Bau78]. The results were not entirely satisfactory. Maybe $Al-O-H$ and $Al-O-Al$ angle term, similarly to the ones already developped for silicates, would increase the accuracy of the results.

9.5 Summary

Experimental as well as theoretical results showed that the morphology of portlandite in the pure portlandite-water system, in contrast to the morphology in a non-interacting environment which is dominated by the [00.1] surface, is equiaxed, the higher energy surfaces being stabilized by interactions with water. The stabilization seems to be due to extensive hydrogen bonding at the portlandite surface leading, at both the [10.0] and the [10.1] surface to a regular network of strongly bound surface water. At the [00.1] surface it is likely to be the dehydration of the Ca^{2+} ion that is the rate limiting growth step. At the [10.0] and the [10.1] surface on the other hand, theoretical results point towards the replacement of strongly bound surface water by a hydroxy group or by a Ca^{2+} ion respectively as the rate limiting step. This would indicate that a decrease of the calcium to hydroxide concentration ratio increases the importance of the [00.1] facet with respect to the [10.0] facet and vice versa.

Calculation of the structure of the electrical "double layer" with Metropolis Monte Carlo indicate, that a positive interfacial charge at the [00.1] portlandite surface, and the corresponding positive zeta potential measured experimentally, may originate from the adsorption of Ca^{2+} ions at the outer Helmholtz plane. The adsorption is due to positive interactions between the solvation shell of the calcium ions and the structured water layer close to the surface. An adsorption of ions at the outer Helmholtz plane is usually not considered in conventional continuum theories of the electrical "double layer" (e.g. the Gouy-Chapman theory). This leads to differences between the structure of the electrical "double layer" as predicted by Metropolis Monte Carlo and by conventional continuum theories. One can conclude that the restructuring of the water above the surface of crystalline oxides that is consistently predicted by molecular dynamics [AGM$^+$09, KP04, KK02, KCSP05, SCKP06, KCMP05, ZKR10], has an important influence on the structure of the electrical "double layer" and warrants further investigation.

Theoretical calculations indicate that the adsorption of calcium-silicate complexes (i.e. the $CaSiO_2(OH)_2$ complex), the stability of which has been confirmed by metadynamics calculations, is energetically favorable. The $CaSiO_2(OH)_2$ complex adsorbs with the hydroxyl groups oriented towards towards the surface, donating hydrogen bonds to surface oxygens. At the atomically flat surfaces the calcium-silicate complex retains a certain amount of mobility, contrary to step-like features where the calcium-silicate species seems to be immobilized. Such a behavior indicates that the addition of silicates might poison the growth of portlandite. This endorses earlier hypothesis by different authors as to the reason for the absence of portlandite growth during the induction period in cementitious systems [TSK76, YTB77, OD79] and is consistent with experimental results on model systems where the size of the primary

portlandite particles precipitated in the presence of silicates was reduced and their shape became irregular. The results also indicate that portlandite surfaces might facilitate the growth of C-S-H due to the presence of adsorbed, oriented, mobile species that might polymerize more easily. This would be consistent with observations in cementitious systems reported in literature where the growth of portlandite and C-S-H is often observed closely intermixed and the acceleration of portlandite and C-S-H growth is simultaneous. It might also help explain why the addition of silicates to the model experiments lead to the formation of aggregates where the portlandite particles appear to be linked with a secondary phase.

As observed previously by Berger and McGregor [BM72], the addition of sulfates to the model system lead to an increased importance of the [00.1] surface in the final morphology of the portlandite particles. This might be partially due to the formation of a calcium-sulfate complex which leads to an increase of the pH and a decrease of the calcium to hydroxide concentration ratio in the solution. Additionally the precipitation of gypsum in these systems was retarded and indications of the existence of metastable calcium-sulfate nuclei, on which the portlandite particles precipitate, was found. The existence of the metastable nuclei would explain the retardation of the precipitation of gypsum, which is also observed in cementitous systems, but has to be further confirmed experimentally.

Finally aluminates seem to cause an increase of the particle size, probably due to a decrease of the nucleation rate. The aluminates do not form any complexes with calcium and the calcium to hydroxyl concentration ration remains unchanged. Consequently the observed effect is likely to be due to the interaction of aluminates with the portlandite particles. Additionally the importance of the [00.1] is slightly reduced in the final portlandite morphology. While earlier results by Berger and McGregor [BM72] were inconclusive with respect to the influence on portlandite nucleation, their results concerning the decreased importance of the [00.1] surface seem to be consistent with ours.

10 State of the Art of Calcium-Silicate-Hydrate (C-S-H)

In this chapter an overview of the state of the art knowledge about C-S-H is given. First the experimental knowledge about the atomistic structure of C-S-H is reviewed. The different structural models for C-S-H (tobermorite/jennite, tobermorite/portlandite, highly defective tobermorite) reported in literature are summarized. This is then followed by a discussion of the microstructure and morphology as well as the different microstructural models reported in literature. The possible interplay between atomistic structure and the observed microstructure of C-S-H is examined. Finally the theoretical work, namely the classical and ab initio atomistic simulations, previously done on C-S-H is reviewed.

In this chapter the current knowledge about the C-S-H is summarized. In the first section experimental results on the atomistic structure of C-S-H are reviewed. Due to the lack of long range 3D order of C-S-H, the exact atomistic structure is inaccessible to conventional crystal structure and hence still unknown. However in recent years the knowledge about the structural features of C-S-H has been greatly improved, thanks to the application of different advanced measurement techniques. Different models, describing the atomistic structure of C-S-H, have been developed by different authors, based on the current experimental knowledge. These different models are discussed here, as well as the differences between them and which exterimental results supports which model.

The review of the state of the art knowledge of the atomistic structure is then followed by a summary of experimental observations concerning the microstructure and morphology of C-S-H. Again different microstructural models have been put forward by different authors. The differences and the similarities between the different models are discussed in some detail.

Finally the theoretical work on C-S-H is summarized. Quite a number of atomistic simulations on C-S-H model systems have been published in recent years. The results of these studies are summarized and the open questions to be studied discussed.

10.1 Atomistic Structure of C-S-H

Calcium silicate hydrate or C-S-H, the most abundant phase in hydrated cementitious systems, is nearly X-ray amorphous, in contrast to e.g. the previously discussed second most abundant phase, portlandite. The only two weak peaks that can be observed by X-ray diffraction (XRD) indicate repeat distances of about ~ 1.82 Å and ~ 3.05 Å [Gru84]. Similarly selected area electron diffraction show only a diffuse C-S-H ring ranging from 2.7 to 3.2 Å and a faint ring at about 1.83 Å [Ric04]. This implies that C-S-H does not have any 3D long range order. It also means that the exact atomistic structure of C-S-H can not be resolved by conventional XRD techniques.

A further complication is the varying chemical composition of C-S-H. The composition varies significantly not only between different samples but also within one and the same sample. In neat C_3S pastes local energy dispersive X-ray analysis (EDS) has shown that on a scale of 100 nm $\frac{Ca}{Si}$ varies between 1.2 and 2.1, with an average calcium to silica ratio $\langle\frac{Ca}{Si}\rangle$ of 1.75 [RG93]. At young age (hydration times of less than 1 year) the composition of the C-S-H phase in OPC systems is bimodal. With time the composition becomes more homogenous and after about 1 year the bimodality seems to disappear [RG93]. However composition still varies.

The first attempts to shed some lights on the atomistic structure of C-S-H, especially that of the Si groups, were done via trimethylsilylation followed by chromatography [MT82]. This technique revealed that the most abundant silicate species present in C-S-H are dimers which are essentially the only poly-Si-anions observed during the first few days of hydration. For longer hydration times of up to 6 months, longer Si polymers start to form, mainly pentamers but also octamers and even some longer polymers. Trimers and tetramers on the other hand are not observed. In C_3S pastes cured for 12 months, about 60 % of the silicate species are present as dimers and 40 % as longer chains. The distribution of chain lengths continues to change for many years, the mean chain length and the fraction of long polymers increases whereas the fraction of dimers decreases. In the C_3S pastes cured for 22 years or longer, Mohan and Taylor estimate about 40 % of the silicate species to form dimers and the remaining 60 % longer polymers [MT82].

In more recent years ^{29}Si NMR spectroscopy has been the method of choice to study of Si arrangement in C-S-H [SH08, BBC$^+$04, KJB$^+$00, BDRG94, CK96b]. ^{29}SI NMR spectroscopy easily distinguishes between Si monomers (Q^0) and Si connected to a number X of other Si species (Q^X, see also figure 10.1). In a review article I.G. Richardson summarizes the results of several authors as follows [Ric04]: In general no Si species with a higher connectivity than 2 are observed in C-S-H, indicating linear chains without any crosslinking. From the ratio between end chain Si (Q^1) and connecting Si (Q^2), the mean chain length (MCL) can be calculated. Consistent with the previously discussed results of Mohan and Taylor [MT82], in fresh cements no connectivity higher than Q^1 is observed by NMR and the calculated mean chain length is 2. Over the next 12 months of hydration the mean chain length increases from 2 to 3.3 in C_3S pastes and from 2 to 3.1 in OPC pastes. A few percent of monomers (~ 2 %) can still be

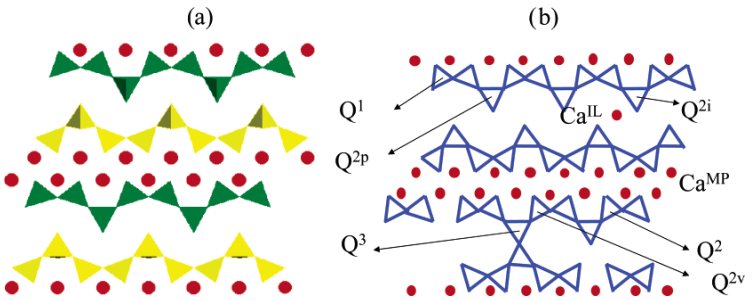

Figure 10.1: (a) The layered structure of tobermorite is composed of a calcium plane (red dots) bordered by two silicate planes (yellow and green chains) and separated by the interlayer space containing water molecules, hydroxyl groups and some calcium ions. (b) The silicate planes are composed of silicate chains with a specific three-unit repetition ("dreierketten"): two silicate tetrahedra, noted as Q^2, are coordinated by calcium planes (red dots) whereas the third silicate (called the bridging tetrahedron and noted as Q^{2p} or Q^{2i}) is not. The end-chain tetrahedra are noted Q^1. The tetrahedra linking two silicate chains in the interlayer space are noted Q^3 whereas the sites Q^2 next to Q^3 are named Q^{2v}. The calcium ions belonging to the main plane are noted Ca^{MP} whereas those in the interlayer are noted Ca^{IL}. Taken from [BBC+04].

observed even at high degrees of hydration. However these might be linked to C-S-H surfaces. The mean chain length continues to increase somewhat but even in 26 year old pastes the MCL is still less than 5.

The observation that the only silicate chain lengths present in C-S-H fit the formula $3 \cdot n - 1$, where n is an integer, leads to the assumption that the chains are formed of dimers which are linked with bridging Si tetrahedra (see figure 10.1). Such a "dreierketten" structure is similar to the structure observed in some naturally occurring hydrated calcium-silicate minerals. Different water containing calcium-silicate crystal structures containing linear "dreierketter" have been reported in literature. The ones most commonly compared to C-S-H are 14 Å tobermorite and jennite ($\frac{Ca}{Si}$ = 1.5, molar water content: 42 %). Both 14 Å tobermorite and jennite consist of calcium-silicate layers separated by an interlayer space containing both water and calcium. However whereas the calcium ions in the 14 Å tobermorite layers form a planar sheet (figure 10.2a), the calcium layer in the jennite structure is corrugated (figure 10.2b). For normal and anomalous 11 Å tobermorite ($\frac{Ca}{Si}$ = 0.75 and 0.67 respectively, interlayer distance 11 Å, molar water content: 34 - 38 %), 14 Å tobermorite ($\frac{Ca}{Si}$ = 0.83, interlayer distance 14 Å, molar water content: 42 %), although initially thought to be a calcium-silicate structure containing only linear chains [Ham81], the bridging tetrahedra of the "dreierketten" are linked [MBA01, KYM+97], leading to Q^3 sites which are inconsistent with observations in C-S-H. However the originally proposed 11 Å tobermorite structure proposed by S. Hamid [Ham81], lacking cross-linking of the silicate chains and with a calcium-silicate layer stacking much closer to the one of 14 Å tobermorite than to the one of 11 Å tobermorite, but an interlayer distance of 11 Å, is also sometimes used as a model structure for C-S-H.

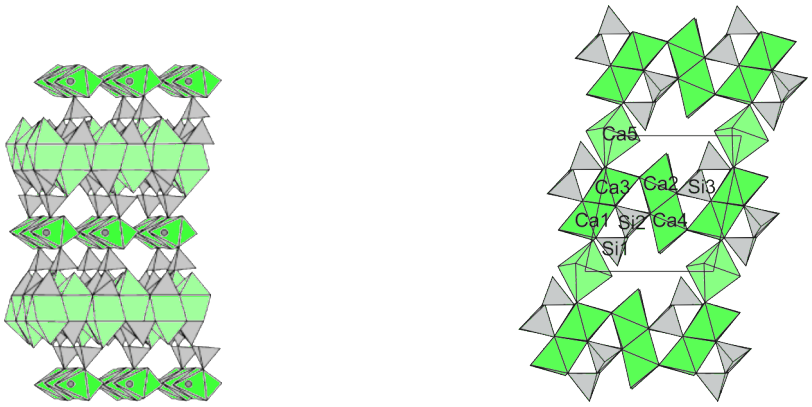

(a) (b)

Figure 10.2: Schematic illustration of the calcium-silicate structure of 14 Å tobermorite (a) and jennite (b). Calcium polyhedra are shown in green, silicate tetrahedra in gray. Images are adapted from [BMK05] and [BMT04] respectively.

Brunet et al. used more advanced NMR techniques, i.e. ^{29}Si MAS NMR, ^{29}Si homonuclear and $^{1}H-^{29}Si$ heteronuclear NMR correlation measurements, to further elucidate the atomistic structure of C-S-H [BBC+04]. For their studies the authors mixed SiO_2 with CaO in a water suspension with a water to solid ratio of 50. The mixture was kept at 40 °C for 4 weeks. The authors prepared three different mixtures with calcium to silicon ratios of 0.7, 0.9 and 1.5 respectively. For the lowest $\frac{Ca}{Si} = 0.7$ the resolution of the obtained spectra was very good. The authors observed end-chain tetrahedra Q^1, non bridging chain tetrahedra Q^2 and and bridging tetrahedra Q^{2p}, the ratio between the last two being 2:1 confirming a "dreierketten" structure. They also observed some Q^3-Q^3 correlations indicating occasional cross linking between the Si chains. On the other hand no Q^1-Q^1 correlations were observed indicating that the Q^1 signal comes from end-chain Si rather than from dimers. With increasing $\frac{Ca}{Si}$ the structure of the C-S-H becomes less ordered with less well defined peaks in the ^{29}Si MAS NMR spectra. The signal from the cross linking of Si chains (Q^3) vanishes and more end-chain Q^1 are observed. In addition the Q^1 chains begin to interact. Closer investigation of the $^{1}H-^{29}Si$ signal lead the authors to the conclusion that dimers are formed and that the mean chain length of the longer polymers decreases. The ratio between Q^2 and Q^{2p} on the other hand stays more or less equal to 2:1. Also $^{1}H-^{29}Si$ correlations indicate the existence of Ca-OH groups. At a calcium to silicon ratio of $\frac{Ca}{Si} = 0.9$ the protons from the Ca-OH groups seem to interact with the bridging tetrahedra only. Considering a tobermorite like structure, this would mean that the Ca-OH groups are present in the interlayer rather than within the Ca layer. At $\frac{Ca}{Si} = 1.5$ on the other hand all silicate species interact with the Ca-OH groups indicating that either the interlayer distance has shrunk or that the Ca-OH groups are present in the Ca layers themselves. Correlations between Si-OH groups and all other types of Si are observed for all studied $\frac{Ca}{Si}$ ratios. Similar NMR results have also been reported by other authors [CK96a, RZTHG93].

These NMR results are consistent with infrared spectroscopy measurements by Yu et al. [YKP+99]. Yu et al. observed that, although the general structural features of the silicate chains does not seem to change with increasing calcium to silicon ratio, detailed features, such as a broadening of the Si - O - Si bending peak, are consistent with a decreasing polymerization of the silicate chains. Additionally the number of observed Si - OH groups decreases and the number of Ca-OH groups increases with increasing calcium to silicon ratio. In fact no Si - OH groups were observed for calcium to silicon ratios larger than 1.2 and Ca - OH groups only appeared for ratios larger than 1.

Thomas et al. used inelastic neutron scattering to quantify the amount of Ca-OH bonds in C-S-H [TCJN03]. They found that while no Ca-OH bonds can be found at calcium to silicon ratios below 1, at a calcium to silicon ratio of 1.7 about 23 % of the charge of the Ca^{2+} ions in C-S-H are compensated by hydroxyl groups.

Garbev et al. used Raman spectroscopy to determine vibrational frequencies present in synthetic C-S-H samples with $\frac{Ca}{Si}$ ratios ranging from 0.2 to 1.5 [GSB+07]. $Si-O-Si$ symmetrical bending vibrational frequencies shifted to higher values (668-672 cm^{-1}) with increasing $\frac{Ca}{Si}$ ratios, indicating a narrowing of the $Si-O-Si$ angle and/or a decrease in polymerization. By comparing the frequency to several other minerals with a "dreierketten" Si chains (14 Å tobermorite, jennite, foshagite and wollastonite) the mean $Si-O-Si$ angle in C-S-H was estimated to be around 139.7-140.7 ° which was closest to the angle observed in 14 Å tobermorite (138.55 °). These results are consistent with other Raman spectroscopy studies found in literature [KYM+97, RRL+09a]. Kirkpatrick et al. found no evidence of structural similarities between C-S-H and jennite even at high calcium to silicon ratios, although for calcium to silicon ratios above ~ 1 an additional vibrational frequency appears, which probably corresponds to Ca - OH vibrations [KYM+97].

Renaudin et al. [RRL+09b] used Rietveld refinement to characterize the structure of synthetic C-S-H over a range of calcium to silicon ratios from 0.8 to ~1.59. Renaudin et al. showed that, while the interlayer distance decreases from 14 Å for a calcium to silicon ratio of 0.82 to 11 Å for calcium to silicon ratios larger than 1.1, it was possible to refine the whole series of structures with the Hamid 11 Å tobermorite structure [Ham81]. This indicates a structural continuity over the whole range of studied calcium to silicon ratios. The coherent size of the crystalline regions on the other hand was estimated to be very small, the crystallite size was estimated to be 90x85x40 Å for a calcium to silicon ratio of 0.8 and 130x65x55 Å for a calcium to silicon ratio of ~ 1.59 (in [100], [010] and [001] direction respectively). Other crystal structures (jennite, 11 Å normal and anomalous tobermorite and 14 Å tobermorite) were less successful in fitting the C-S-H XRD signal. The Hamid model used for the Rietveld refinement of the 11 Å tobermorite structure has a similar layer structure and stacking sequence as the 14 Å tobermorite structure later reported by Bonaccorsi et al [BMK05]. Contrary to the later structural refinements for 11 Å normal and anomalous tobermorite [MBA01] as well as the 14 Å tobermorite structure [BMK05], Hamid et al. did not especially take into account the order / disorder character of tobermorites nor their polymorphism. This might explain why the Hamid structure is better

adapted to fit to the overall XRD signal of C-S-H compared to the more refined structures [MBA01, BMK05]. The observed decrease of the interlayer distance upon an increase of the calcium to silicon ratio from 0.8 to 1.1 [RRL$^+$09b] is consistent with early XRD results reported by Cong et al. [CK96b] and more recent total x-ray scattering measurements by Soyer-Uzun et al. [SUCB$^+$12].

The nanocrystalline nature of C-S-H has been confirmed recently by total x-ray scattering measurements [SCB$^+$10, SUCB$^+$12, MBM11]. Contrary to e.g. amorphous silica glasses, the X-ray pair distribution function for C-S-H shows clear structural correlations up to ~ 35 Å, indicating crystalline regions of about that size [SCB$^+$10]. The radial distribution functions for different calcium to silicon ratios indicate that the nearest neighbor distances remain essentially unchanged with changing calcium content. The Ca-O coordination on the other hand decreases slightly from ~ 7 to ~ 6 when the calcium to silicon ratio is increased to 1.75 [SUCB$^+$12, MBM11].

Another not altogether clear question is the water content of C-S-H. Here the issue is complicated by the complex microstructure and the high specific C-S-H/pore solution interfacial area, which makes it difficult at times to clearly distinguish interlayer from surface and pore water. Early work by Cong et al. [CK96b], using X-ray fluorescence to determine the Si and Ca content and probably weight loss measurements (drying at 110 ° C followed by firing at 1000 ° C) to determine the amount of physically bound (weight loss at 110 °) and the amount of chemically bound water (weight loss at 1000 ° C), indicates that the molecular ratio of physically bound water in C-S-H decreases with increasing calcium to silicon ratio. The amount of chemically bound water and the total amount of water on the other hand increases. However the reported values appear somewhat questionable as for samples with a calcium to silicon ratio close to 0.83, where a C-S-H with essentially 14 Å tobermorite stoichiometry is expected, 20-24 % chemically bound and 20-27 % physically bound water was measured by Cong et al, while the overall water content is similar to one of 14 Å tobermorite (42 %), only 5 % of the water is chemically bound 37 % is physically bound in 14 Å tobermorite. In a very recent study by Muller et al. [MSGM13], using ^1H NMR relaxometry, the stoichiometry of C-S-H, excluding the surface bound water, was estimated to be approximately $Ca_{1.7}SiO_{3.7} \cdot 1.8H_2O$ (not including the aluminate content that is also considered by the authors) with a density of 2.65 $\frac{g}{cm^3}$. This leads to an estimated molar water content of 40 %, excluding surface water. As stated by the authors, due to the nanoparticulate nature of C-S-H, the exclusion of the surface water will have an impact on the results and has to be taken into account for further interpretations.

The experimental results obtained over time led to a large number of different structural models for C-S-H [Non04, CK96b, Gru99, Ric04]. A review of the different models and their differences and similarities can be found in [Ric08]. Because of the similarity of many of the experimentally observed features, most models are to some extent based on 14 Å tobermorite. 14 Å tobermorite, a rare mineral the structure of which has been described in detail by Bonaccorsi et al. [BMK05], is composed of Ca layers which are terminated on each side by

Si chains. The silicate chains are linear and have a "dreierketten" structure consistent with to the one observed in C-S-H (see figures 10.1 and 10.2a). The distance between the layers is 14 Å (hence the name). Other tobermorite structures with different interlayer distances (9 Å and 11 Å tobermorite) exist as well, with the same intralayer structure but different chemical composition of the interlayer as well as different distances between the layers (i.e. 9 and 11 Å respectively). In 14 Å tobermorite, both Ca ions and water can be found between the calcium-silicate layers. The problem with using tobermorite as a model structure for C-S-H is the differing calcium to silicon ratio. 14 Å tobermorite has a $\frac{Ca}{Si} = 0.83$ whereas the average calcium to silicon ratio of C-S-H in ordinary portland cement systems is generally about 1.75. This means that the calcium to silicon ratio of C-S-H in cementitious systems is generally higher than for 14 Å tobermorite. The different models proposed in literature use different possible mechanisms of increasing the calcium to silicon ratio. However the different mechanisms are more similar than at first apparent [Ric04]. The most obvious mechanism to increase the calcium to silicon ratio, based on the experimentally observed depolymerization of the silicate chains, is to eliminate some of the bridging tetrahedra originally present in 14 Å tobermorite (see figure 10.2a). This leads to the formation of dimers (figure 10.3a) and a distribution of polymers with lengths $3n-1$ (where n is a integer), consistent with the Si polymer population observed by trimethylsilylation and NMR measurements. Another way to increase the calcium content is to remove protons from the Si tetrahedra, converting neutral $Si-O-H$ groups into charged $Si-O^-$ groups. The thus created charge can then be compensated with additional Ca^{2+} ions each linked to 2 $Si-O^-$ groups (see figure 10.3b).

A defective 14 Å tobermorite structure which is fully depolymerized (i.e. containing no more bridging Si tetrahedra) and fully deprotonated has a calcium to silica ratio of 1.5. This is still lower than the typical ratio of ~ 1.75 observed in e.g. C_3S pastes. In addition NMR measurements [BBC$^+$04] show that both bridging Si tetrahedra and $Si-O-H$ groups are still present at $\frac{Ca}{Si} = 1.5$. This means additional defect mechanisms, raising the calcium content of the defective tobermorite structure, have to be taken into account. Here different models diverge considering essentially three different possible mechanisms [Ric04]:

- **Tobermorite/Portlandite (a) Model:** In this model, which is e.g. explained in [Non04], some of the charges created by the deprotonation of some of the $Si-O-H$ groups are compensated with a $Ca-O-H$ group instead of 0.5 Ca^{2+} ions. The additional calcium is thus accommodated in the interlayer space. According to the NMR measurements of Brunet et al. [BBC$^+$04] such a mechanism seems likely for moderate calcium to silicon ratios $\frac{Ca}{Si} < 1.5$ as the observed $Ca-O-H$ groups interact mainly with Si ions from bridging tetrahedra.

- **Tobermorite/Portlandite (b) Model:** Another way to include additional $Ca-O-H$ groups is to consider the inclusion of full or partial calcium hydroxide layers intermixed with the tobermorite like layers. In this model the additional $Ca-O-H$ groups are part of the calcium-silicate layers and not of the interlayer region. The idea of calcium hydroxide intermixed with a Si containing phase as a model for C-S-H was originally

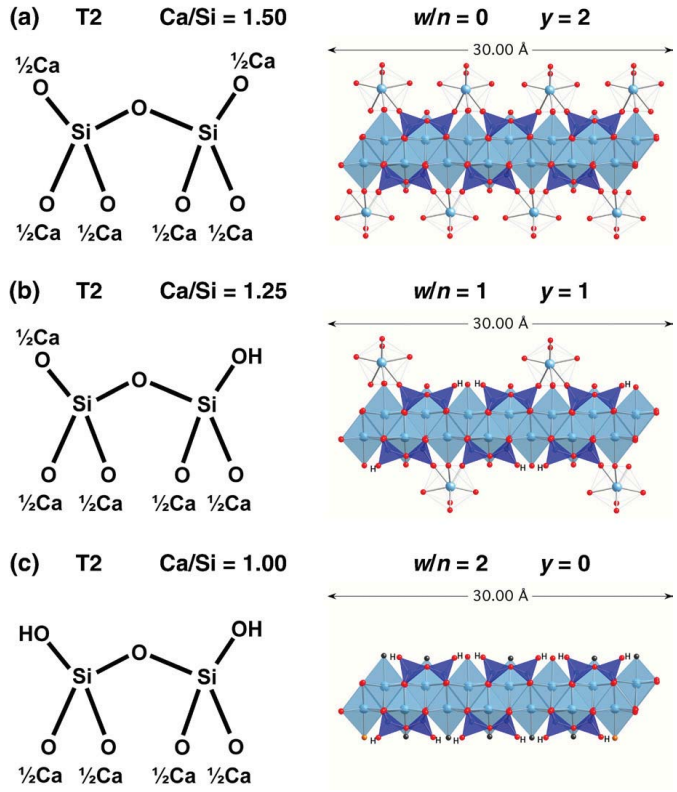

Figure 10.3: Diagrams illustrating tobermorite-based dimer (n=1) that has the minimum (a), intermediate (b), and maximum (c) degree of protonation of the silicate chains. The diagrams on the right-hand-side are more realistic structural representations that were derived from crystal-structure data for tobermorite [BMK05] (the silicate chains are aligned along the plane of the page). Taken from [Ric08].

put forward in the 1980's (e.g. [Gru84]).

- **Tobermorite/Jennite Model:** The third model, put forward for the first time by H.F.W. Taylor [Tay86], considers a mineral called jennite to be intermixed with tobermorite. Jennite has linear, infinite Si chains composed of "dreierketten" structures like tobermorite but the calcium layers are not planar like in tobermorite, instead the calcium layers are corrugated (figure 10.2b). The calcium to silica ratio of fully polymerized and protonated jennite is 1.5, but similar to tobermorite the calcium content can be raised by removing the bridging silicates from the "dreierketten" silicate chains. Consequently the calcium to silicon ratio of jennite can be raised to 2.25 by fully depolymerizing the silicate chains.

Linked to the different models described above is the question whether or not C-S-H at different compositions corresponds to a mixture of distinct structures or whether C-S-H

has the same underlying structure for all compositions with continuous structural changes introduced by an increasing number of defect due to the increasing calcium to silicon ratio. Chen et al. argued that there must exist a series of distinct structures based on a series of de- and recalcification experiments on C-S-H produced by different methods and with different initial calcium to silicon ratios [CTTJ04]. The different C-S-H structures followed different solubility curves, not only for the decalcification but also for the recalcification, exhibiting a structural memory effect that was interpreted by Chen et al. as evidence for the existence of a series of distinct C-S-H structures [CTTJ04]. Such a viewpoint would also indicate that the structure of synthetic C-S-H, produced e.g. by coprecipitation, is not necessarily consistent with the C-S-H structure observed in cementitious systems.

Results that can be interpreted to point in the same direction have been published by Klur et al. [KJB+00]. Klur et al. used $^1H-^{29}Si$ cross-polarization NMR measurements to get information about the proton environments of the different Si species present in C-S-H. The material used by the authors for their measurements was a synthetic C-S-H with a $\frac{Ca}{Si} = 1.05$. The authors used information about relaxation times and found that there are two different proton environments with which the silicate species in C-S-H interact. The ratio of Si within the two regions is about 1:10, and seems to be the same, within experimental error, for all different Si species. However the two different environments can correspond to two different distinct phases within the sample or they can reflect different environments within one and the same phase such as core and surface regions.

The observation of the structural features of C-S-H, where the changes seem to be continuous with increasing calcium to silicon ratio, point towards a common underlying structure [Non04, RRL+09b, KYM+97]. This would indicate that the observations by Chen et al. [CTTJ04] and Klur et al. [KJB+00] are e.g. due to the influence of the high interfacial area rather than due to different structures, a possiblity that was discussed by the authors of both papers. Chen et al however declared the influence of the specific interfacial area as unlikely, based on the fact that the interfacial area has been observed to be similar for different $C-S-H$ production methods [CTTJ04], however the referenced data is not or not readily publicly available and the specific surface area of the different samples used by Chen et al. has not been measured.

The specific surface area as well as the aspect ratio of cement has been observed to vary continuously with the calcium to silicon ratio [TCAJ04, RRL+09b]. This can be interpreted as an indication of interactions between the surfaces and structural defects introduced by the silicate deficiency. Another possible explanation would be microstructural strains developing due to the introduction of different defects, limiting the size of the crystalline domains (see e.g. the idea of a bending of the calcium-silicate layers due to a high concentration of defects developed by Gartner et al. [Gar97, GKM00]). Both the above explanations would indicate that different specific interfacial areas might lead to different solubility curves. Thus it appears likely that, due to the large surface area of C-S-H, the C-S-H / pore solution interfaces would have to be included in the discussion of the overall properties and the overall calcium to silicon ratio of the C-S-H phase. This has already been discussed by different authors [MSGM13, Ric04].

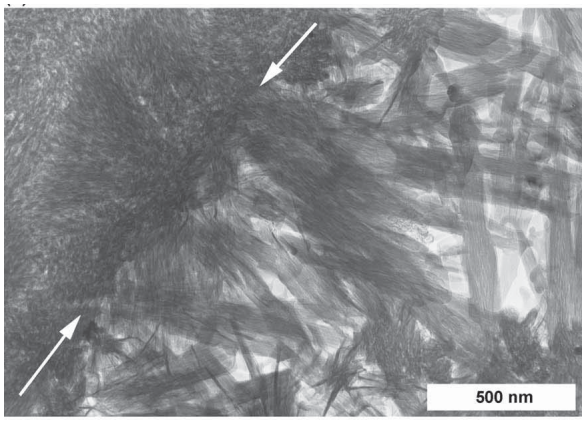

Figure 10.4: TEM micrograph showing Ip and Op C-S-H present in a hardened C3S paste with w/c = 0.4 hydrated at 20 °C for 8 years. White arrows indicate the Ip/Op boundary; the Ip is in the upper left of the micrograph. Taken from [Ric04].

10.2 Microstructure and Morphology of C-S-H

Two different kinds of C-S-H morphologies can be observed in hydrated cementitious systems. One type of morphology is usually observed in areas which correspond to pore spaces in the original unhydrated microstructure (see figure 10.4 [Ric04]). The second type of morphology is usually observed within the original volume of the unhydrated cement grains. Consequently the two different C-S-H morphologies are often termed outer product (Op) and inner product (Ip) C-S-H respectively [Ric04, Scr04, GMS10, Dia04].

The Op C-S-H displays a pronounced texture. TEM images from I.G. Richardson [Ric04] show that in fully hydrated OPC and C_3S pastes, Op C-S-H is composed of fibrils of up to ~ 100 nm in diameter. These fibrils can also be observed on fracture surfaces with environmental scanning electron microscopy (ESEM). In C_3S pastes with a water to solid ratio of 0.3 the fibres grow to a length of 1.5 μm after 600 days of hydration [SMW02]. The fibrils themselves appear to consist of long thin particles which are about 3 nm wide and up to several tens of nanometers long. The space between the fibrils forms a 3D interconnected capillary pore network [Ric04].

Ip C-S-H on the other hand is much more homogeneous and composed of less anisotropic particles with diameters of ~ 4 – 6 nm. The pores in Ip C-S-H are much smaller than in Op C-S-H (up to about 10 nm) and their appearance often presents a very fine scale texture, although more pronounced texture and directionality can also be observed [Ric04] (figure 10.4).

In backscattered scanning electron microscopy (SEM) the Op C-S-H appears darker than the Ip C-S-H, probably because of the lower density of Op C-S-H [Scr04, Dia04]. The boundary between Op and Ip C-S-H seems to follow the original boundary of the grains closely with a discrepancy of a few tens of a micron at most [Scr04]. In fact recent scanning TEM measure-

ments by Gallucci et al. [GMS10] on portland cement systems with a water to solid ratio of 0.35 show that a very fine layer of hydration product parallel to the grain surface develops after about 4 h of hydration. The position of this layer does not seem to move, even after continuing dissolution of the cement grains, and serves as support for growth of the initially fine fibrillar Ip as well as for the fibrillar Op C-S-H [GMS10].

According to I. Richardson, the morphology of Ip C-S-H seems to be largely unchanged with the addition of slag to OPC, which will decrease the average $\frac{Ca}{Si}$ ratio [Ric04]. The Op C-S-H on the other hand appears to change slightly in morphology: Instead of fibrils, foils are observed indicating a change from 1D to 2D growth. The foils however seem still to consist of elongated particles. Also the silicate mean chain length (MCL) observed by NMR increases, which is consistent with a decrease of the calcium to silicon ratio. The addition of alkali hydroxide (KOH or $NaOH$) can also enhance the structural order of the formed C-S-H. In fact XRD and SAED measurements on these systems both show diffraction characteristic for a layered structure with a interlayer distance of about 14 Å (a bit smaller for SAED measurements, probably due to drying) which confirms the 14 Å tobermorite based atomistic model. However neither the influence of the alkali on the $\frac{Ca}{Si}$ ratio nor on the Si chain lengths explains the enhanced structural order. In fact the $\frac{Ca}{Si}$ ratio seems to stay the same with the addition of alkali and the MCL of the Si chains decreases [Ric04].

Based on these experimental observations several microstructural models were developed. One of the first was developed by Feldman and Sereda [FS70]. It combined the knowledge of the layered atomistic structure of C-S-H with observation of hysteresis effects and irreversible behavior upon drying and rewetting. The authors concluded that the irreversible part of the drying was probably due to the elimination of water between different unconnected crystalline layers. This would bring the layers closer together and lead to the formation of crystalline bonds between the layers, which might not be broken again upon rewetting. Hysteresis was explained by the different way water would exit and enter the crystalline interlayer region: upon drying water would slowly exit at the edges, leaving a shrinking core region still containing water. This would mean that the distance between the layers will be smaller at the edges than in the core region until total drying occurs and interlayer distance is again uniform but smaller than initially. Upon rewetting water will start entering the interlayer space from the edges, leading to a slowly shrinking, dry core region with a smaller interlayer distance than at the edges. Consequently the authors developed a microstructural model composed of relatively long crystalline sheets which, in some regions, are bonded and stacked in an ordered fashion, forming nanocrystalline regions consisting of a few sheets. In other regions the layers are separated by pores (see figure 10.5).

Gartner et al. developed a very similar model based on the observation of exponentially increasing growth rates at the beginning of the acceleration and the end of the induction period as well as on soft X-ray microscopy of hydrating silica particles in a saturated lime solution [Gar97, GKM00]. The model considers layers with essentially two types of alternating regions: relatively defect-free linear regions and regions containing a large concentration of

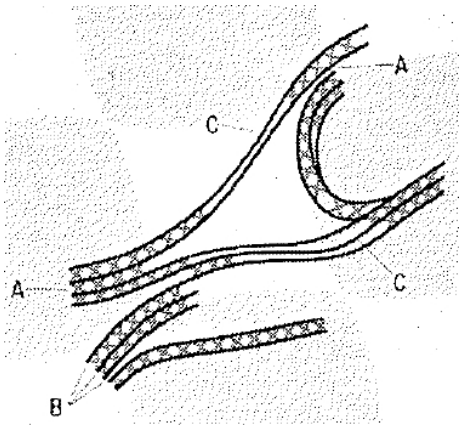

Figure 10.5: Microstructural C-S-H model from Feldman and Sereda. A - Intercrystallite bonds, B - Tobermorite sheets, C - Faults giving disordered layers, X - Interlayer water. Taken from [FS70].

defects, which will cause the sheets to curve. At the linear, relatively defect free regions, other sheets can nucleate on top of the original layer, allowing limited growth perpendicular to the sheets. At the next curved region however the sheets would separate and continue to grow independently. Thus the longer the chains get, the higher the number of nucleation points for new sheets. The new sheets then grow independently, creating additional nucleation sites for new sheets, explaining the acceleration of the growth rate at the end of the induction period. It might also explain the ”sheaf-of-wheat“ morphology of C-S-H formed at the surface of hydrating silica particles in a saturated lime solution. Initially there are a few ”needles“ or “fibrils” of C-S-H protruding from the surface of the silica particles. As hydration progresses, the growing C-S-H product fans out leading to “sheaf-of-wheat” morphologies. This might be explained by the curving of sheets away from the original growth direction and nucleation of new sheets on the individual, separated sheets of the original growing crystallite. The ensuing microstructure would probably be in agreement with Feldman and Sereda's model. This growth model seems to be much more adapted for the growth of the Op C-S-H than for the Ip C-S-H. However one could argue that, due to spacial restraints, the growth of C-S-H parallel to the calcium silicate layers is slowed down, forcing more growth perpendicular to the layers, thus forming a denser product with a more homogeneous appearance. This would be in quite good agreement with experimental observations [Ric04]. For the Op C-S-H, due to self similarity such a growth mechanism, one might expect a more dendritic growth and not the fibrillar final morphology observed in hydrated ordinary portland cement [Ric04]. However one could argue that, again due to spacial constraints, the growth of Op C-S-H changes from the initial growth, as described by Gartner et al., to a growth mode where the parallel growth of the calcium silicate layers is slowed down, again due to spacial restraints, and more perpendicular growth is observed, thus reinforcing the initial fibers without leading to additional branchings. This might lead to a morphology similar to the one observed experimentally and would be consistent with the microstructural "space filling" growth model

developed by Bishnoi and Scrivener [BS09] as well as with recent ^1H NMR relaxometry results by Muller et al. [MSGM13].

Jennings et al. [Jen00, ATJ07] developped a different microstructural model based on specific surface area measurements by different techniques. Jennings et al. observed of C-S-H with different densities and mechanical strength [CSV$^+$10]. With e.g. N_2 adsorption measurements only a part of the total porosity of C-S-H can be accessed, the remaining part being inacsessible to N_2. This lead the authors to develop a model consisting of spherical or ellipsoidal building blocks aggregating to form spherical “globules”. The “globules” themselves can then be packed either densely, to form so called high density (HD) C-S-H, or loosely, to form low density (LD) C-S-H. Because different densities are also observed for Ip and Op C-S-H the two designations might be roughly equivalent. If the globules are close packed, the internal porosity is not accessible to N_2 whereas the porosity of loosly packed LD C-S-H is. By combining this picture with small angle x-ray scattering (SAXS) and small angle neutron scattering (SANS) of OPC pastes, both in water and in d_3 methanol with different isotope exchanges, Allen et al. could estimate the size of the building blocks ($\sim$ 1.2 nm or if adjustments are made due to the underlying layer structure of C-S-H: $\sim$ 2.5 x 5 nm), their density (2.6 $\frac{g}{cm^3}$) and their approximate chemical formula: $(CaO)_{1.7}(SiO_2)(H_2O)_{1.8}$ [ATJ07]. The authors also found evidence for nanoscale portlandite particles contributing to the scattering. While the overall length scales and composition and C-S-H "crystalline" density are all consistent with recent ^1H NMR relaxometry results by Muller et al. [MSGM13], there is little evidence that a similar result could not be achieved with e.g. the Feldman Sereda model [FS70]. In fact while Muller et al. found porosity of the length scale of 10 nm, consistent with the porosity of the LD C-S-H considered by Jennings et al., Muller et al. did not associate this porosity with C-S-H as its total amount always decreased in volume when C-S-H grows [MSGM13].

With all the differences between the microstructural models, there is one thing all authors seem to agree upon: C-S-H includes a large quantity of nanometric pores and hence the specific interface area in C-S-H is very high. Apart from the previously discussed possible interactions between different defects and different interfaces which might limit the size of the crystalline regions, another reason for the high interfacial area might be a low C-S-H - water interfacial energy. Indeed nucleation studies of C-S-H done by Garrault-Gauffinet and Nonat [GGN99] indicated that the C-S-H - water interfacial energy is very low (0.012 $\frac{J}{mol}$). The high specific interfacial area means that surfaces and edges should be included in an atomistic model as the macroscopic composition and structural features observed experimentally will be largely influenced by the interfaces present in the microstructure [Ric04].

10.3 Theoretical Work on C-S-H

From the simulation perspective, the C-S-H phase has been studied by several groups. A few groups looked at the structural properties of different model minerals with Si “dreierketten” chains. Due to the structural similarity, observations on these systems might help understand

processes happening in C-S-H. Churakov et al. [Chu09, CM08, Chu08] used DFT methods to look at specific features of different tobermorite and related structures, such as the position of the water molecules and hydrogen bonds formed in the interlayer. Shahsavari et al. studied the elastic properties of different tobermorites and jennite, using density functional theory [SBPU09].

Faucon et al. [FDV$^+$97] looked at the differences between 11 Å tobermorite-like structures (using the Hamid tobermorite model [Ham81]) with and without Ca^{2+} in the interlayer as well as with aluminium substitutions. The authors used a reactive force field [SR78, FG90] and found that the introduction of interlayer calcium into the 11 Å Hamid tobermorite structure lead to the rupture of the silicate chains. This is inconsistent with experimental results [MBA01, KYM$^+$97], however it might be a consequence of the use of the metastable Hamid structure [MBA01].

Kalinichev et al. used classical molecular dynamics, using the CLAYFF force field (FF1 in chapter 3) to assess the chloride binding as well as the structure and properties of water at 9 Å tobermorite surfaces [KK02, KWK07, KMM$^+$07]. The method employed was the same as used for portlandite, described in section 4.5, the dimensions of the simulated slab of tobermorite were 2 x 4 x 2 crystallographic unit cells and the slab was cleaved parallel to the Ca layers ([001] plane). The simulations showed that Cl^- ions do not adsorb to 9 Å tobermorite surfaces whereas 25 % of the counterions (either Na^+ or Cs^+) did adsorb [KK02]. In summary within their simulations ions did not seem to interact strongly with the tobermorite surface, on the contrary some of the Ca ions initially at the surface moved into the solution during the simulation. The authors also looked at the diffusion coefficients of water at the 9 Å tobermorite surface. They distinguished between three types of water: water which is stongly adsorbed to the surface and is located between the bridging Si tetrahedra of the surface, water which is weakly absorbed and located at about the same hight as the hydroxyl groups of the surface bridging Si thetrahedron and bulk water. The calculated diffusion coefficients for the three types of water are 5.0e-11, 6.0e-10 and 2.3e-9 $\frac{m^2}{s}$ respectively. The diffusion coefficient of the Ca ions was calculated to be 3.0e-11 $\frac{m^2}{s}$ between the Si tetrahedron and 5.0e-11 $\frac{m^2}{s}$ above the surface [KWK07, Kal11].

The authors compared the calculated diffusion coefficients to the surface jump time estimated by proton field-cycling relaxometry on hydrated OPC pastes [KMM$^+$07, Kal11]. Based on a simulation with a total simulation time of 1 ns, the authors estimated an average surface jump time of $\tau_m \sim 0.8$ ns and a jump distance of a about $r_m = 5.5$ Å. This was seen by the authors as a consistency check between simulation and experiments as ^1H NMR relaxometry studies previously indicated an average surface diffusional jump time of 0.8-1.0 ns [Kal11]. There are some questions which might be asked about these results. First the reported ~ 0.8 ns for the average jump time seems to be quite large as, according to the Van Hove self-correlation functions for the surface molecules reported by the authors [Kal11], no molecules have jumped at 0.1 ns but all molecules have left the original surface site at 0.8 ns, indicating an average jump time of smaller than 0.8 ns (though higher than 0.1 ns). This would also explain why

the same diffusion coefficients were reported for a total simulation time of 1 ns [Kal11] and for a much smaller total simulation time (probably 0.2 ns, see [KMM+07, KWK07]). Secondly, as discussed by the authors, the similarity between a 9 Å tobermorite surface and the C-S-H surfaces in OPC pastes is not clear. The most common model structure for C-S-H is a highly defective tobermorite structure and defects at the surface, such as missing Si tetrahedra and changes in the protonation of the bridging Si tetrahedra at the surface, might be expected to change the behavior of both water and ions at the surface.

There is also a certain amount of work that can be found in the literature that tries to further elucidate the atomistic structure and the growth mechanisms of C-S-H with different atomistic simulation techniques.

Manzano et al. tried to identify the basic building blocks and the initial assembly mechanism for nucleation and growth of both tobermorite and jennite using Hartree-Fock calculations [MAD07]. The authors supposed two dimers linked by 4 "intralayer" Ca ions to be the initial growth unit. They then combined two of these units with one Ca ion, as well as with one Ca ion and four water molecules, to form tobermorite-like cluster without and with water in the interlayer and as well as linking two units with four Ca ions to form a jennite like cluster. Some of the hydrogen atoms were omitted from the initial structure to preserve charge neutrality. The first combination, which has a $\frac{Ca}{Si}$ ratio of 1.125 and no water, leads to a structure with 11 Å between the "layers" (i.e. the two initial growth units) after minimization. The partial charge of the Ca ion linking the two initial growth units is 1.39 and the dipole of the resulting structure is 3.8 Debyes. For the second combination ($\frac{Ca}{Si} = 1.125$, 4 H_2O) the "interlayer" distance is 12 Å, the partial charge of the central Ca ion 1.6 and the total dipole 1.6 Debyes. As the authors mention the interlayer distances of 11 and 12 Å have been found to be minimas by Gmira et al. [GZPVD04], however Gmira et al. considered Hamid's 11 Å tobermorite structure [Ham81] with $\frac{Ca}{Si} = 0.83$. The third combination leads to a structure which could be interpreted as part of a corrugated Si-Ca layer of a jennite structure with a charge of 1.6 on the central Ca ions and a dipole of > 25 Debyes [MAD07]. The authors concluded that the formation of tobermorite-like clusters is governed by the formation of bonds with partially covalent character, leading to a relatively low partial charge of the central Ca ion. The formation of jennite-like clusters on the other hand appears to be governed by dipole-dipole interactions.

Bhat and Debnath [BD11] used the precursor structure and one of the possible tobermorite growth unit structures reported by Manzano et al. [MAD07] for further density functional theory (DFT) calculations. Bhat and Debnath calculated the Fourier transform infrared (FTIR) spectra of both the precursor and the supposed growth unit and concluded that the infrared spectrum of these species is similar to the one of tobermorite structures and consequently it is possible that part of the FTIR spectra of hydrating cements at early ages comes from such species.

Two different groups tried to develop an atomistic model with a realistic $\frac{Ca}{Si}$ ratio with different classical atomistic methods. The first group, Dolado et al., used NVT molecular dynamics of

an initially oversaturated $Ca(OH)_2$ - $Si(OH)_4$ solution [DGH07] (in a periodic simulation box of 44x44x44 Å). Due to the use of an interatomic potential developed by Litton and Garofalini [LG01] the silicate species in the solution could polymerize, theoretically being able to form a C-S-H like structure. The cutoff distace of their simulations was 5 Å. Four systems with $\frac{Ca}{Si}$ ratios of 0.7, 1.0, 1.4 and 2.0 were simulated. The $Ca(OH)_2$, $Si(OH)_4$ and water molecules were randomly placed in the box in appropriate amounts. NVT molecular dynamics was performed initially at 300 K for 10 ps, then the temperature was raised to 1800 ° K during 90 ps. Simulated annealing at 1800 ° K was then carried out for 1500 ps followed by a decrease in temperature to 300 ° K over 500 ps and a final equilibration at 300 ° K for 100 ps. Simulated annealing, i.e. the increase of the temperature for part of the simulation, was done to speed up precipitation of "C-S-H" particles and decrease simulation time. After annealing the water and the $Ca(OH)_2$ and $Si(OH)_4$ had separated, forming a "C-S-H" particle. However the ensuing particle was amorphous, had a very low water content and a high percent of monomers (25 - 60 %) [DGH07], which is inconsistent with experimental observations [Ric04]. These important differences together with possible weaknesses of the employed computational method (very short cutoff distance, very high pressures and temperatures during annealing followed by a very short equilibration time) make the model unreliable as a model for C-S-H in cementitious systems. Despite these problems the original model was used for a further simulation in an effort to develop a microstructural model for C-S-H [DGHH11].

The second group used grand canonical Monte Carlo methods to develop an atomistic C-S-H model [PKS$^+$09]. The authors used a polarizable force field (FF2 in chapter 3[LC85, DLP98a, dLWP95, CC92]. All simulations were carried out using periodic boundary conditions and Ewald summation for the coulombic forces (cutoff distance for short range interactions: 12 Å). As a starting point the authors used the Hamid 11 Å tobermorite crystal structure [Ham81]. From this structure they removed all H_2O molecules and protons and compensated the ensuing charges with interlayer Ca ions. The authors then constructed a calculation cell of 4x2x1 crystallographic unit cells along the a, b and c axis respectively. The $\frac{Ca}{Si}$ ratio of the thus constructed starting structure was 1.0. From this structure the authors removed some Si tetrahedra until they got a calcium to silicon ratio of 1.65 and a silicate speciation of 13 % Q^0, 67 % Q^1 and 20 % Q^2. This structure was relaxed using energy minimization. Then grand canonical Monte Carlo sampling was used to introduce water into the structure, resulting in a final chemical composition of $(CaO)_{1.65}(SiO_2)(H_2O)_{1.75}$. The water molecules were not only introduced in the interlayer space but into one of the two defective tobermorite layers as well. The resulting structure was again relaxed with energy minimization, the final density being 2.45 $\frac{g}{cm^3}$. Additional NPT molecular dynamics simulations at room temperature gave the same result. The chemical composition and density were reported by the authors to be similar to the ones measured by Allen et al. ($(CaO)_{1.7}(SiO_2)(H_2O)_{1.8}$ with a density of 2.6 $\frac{g}{cm^3}$ [ATJ07]). X-ray diffraction pattern intensities, extended X-ray absorption fine structure (EXAFS) and indentation modulus considering a self-consistent scheme were then calculated for the final C-S-H model structure and were found by the authors to be in acceptable agreement with experimental results [PKS$^+$09].

Although these results look promising at a first glance, there are some important deviations of the model from experimental observations. The most obvious discrepancy between the model C-S-H structure and experimental observations is the absence of any Ca-OH groups. In fact the C-S-H model structure reported by Pellenq et al. [PKS$^+$09] does not contain any $O-H$ groups [PKS$^+$09] whereas both inelastic neutron scattering [TCJN03] and $^1H-^{29}Si$ heteronuclear NMR correlation measurements [BBC$^+$04] have shown that the $Ca-O-H$ content increases with increasing $\frac{Ca}{Si}$ ratio. In fact Thomas et al. estimated that in C-S-H with $\frac{Ca}{Si}$ = 1.7 approximately 23 % of the charge of the Ca atoms is compensated by hydroxyl groups [TCJN03]. Furthermore the silicate speciation is not in agreement with experimental observations. The structure published by Pellenq et al. contains 13 % of silicate monomers [PKS$^+$09] and 5 % trimers [Ric09] whereas experiments indicate a very low percent of silicate monomers in C-S-H (in the order of 2 % which are probably linked to C-S-H surfaces) and no trimers [Ric04]. Also the radial distribution functions reported by Pellenq et al. for their model [PKS$^+$09] show clearly glass-like character whereas recently published experimental pair distribution functions, determined by total x-ray scattering, indicate a much higher local order consistent with well defined nanocrystalline regions [SCB$^+$10, SUCB$^+$12, MBM11]. Finally the C-S-H model developped is a bulk model which does not consider any surfaces or surface effects whereas experiments on "real" C-S-H will be largely influenced by surfaces due to the nanoparticulate character of C-S-H.

Despite these shortcomings the model has been used in a number of subsequent studies [MMM$^+$12, MDGP$^+$12, VVPB$^+$12] without trying to address the above mentioned issues. Although in one of the studies [MMM$^+$12] Ca-OH groups were formed by dissociation of water due to the use of a reactive force field, the resulting single protons were converted to silanol groups (Si-OH), the concentration of which is known to be small or inexistent in C-S-H with a calcium to silicon ratio of 1.65. Thus one of the issues of the original model is replaced by another.

Finally Rejmak et al. used DFT to calculate the ^{29}Si shift of different possible defective 14 Å tobermorite and jennite structures [RDSA12]. The results were compared to previously reported experimental results for tobermorite, jennite and C-S-H [CK96b, MNSM03, KRFK87]. The best correspondence between the calculated and experimentally observed chemical shifts for C-S-H was found for model structures based on 14 Å tobermorite containing Ca-OH groups in the interlayer. Further distinction between more subtle structural differences were not possible [RDSA12]. The presence of Ca-OH groups in the interlayer is consistent with experimental results [TCJN03]. For model structures based on jennite the consistency between experiment and calculations was less good, indicating a tobermorite based underlying structure for C-S-H.

10.4 Summary

Due to the lack of three dimensional long range order, the atomistic structure of C-S-H is not yet well known. However over the last years the knowledge about the C-S-H structure has

been significantly improved, mostly due to advanced characterisation techniques. The current knowledge about C-S-H can be summarized as follows:

- The final microstructure of cement contains a very large specific interfacial C-S-H / pore solution area. This is due to the nanoparticulate character of C-S-H where the smallest dimension of structural coherence (e.g. the smallest dimension of the crystalline regions) is in the order of 3-6 nm [RRL$^+$09b, SCB$^+$10, MSGM13, Ric04, ATJ07]. Two different C-S-H morphologies with different densities are observed in cementitious systems. Although there exist different microstructural models explaining the different densities [FS70, Gar97, Jen00, ATJ07], the origin of the morphological differences are probably spatial constraints.

- Evidence for the interdependence between chemical composition (i.e. calcium to silicon ratio) and specific surface area has been presented by several authors using different measuring techniques [TCAJ04, RRL$^+$09b]. This indicates that, in order to correctly describe the macroscopic properties of C-S-H in cement, the properties of C-S-H / pore solution surfaces have to be taken into account when developing an atomistic C-S-H model [MSGM13, Ric04].

- The experimental evidence seems to point towards 14 Å tobermorite as the best model structure for C-S-H structures with low calcium to silicon ratios (< 1.5-1.6) [Ric04, GSB$^+$07, KYM$^+$97]. There is even some evidence pointing towards the validity of 14 Å tobermorite as a model structure for the complete range of C-S-H structures observed in tobermorite [Non04, RDSA12, KYM$^+$97] even though many authors consider a mixed tobermorite-jennite or tobermorite-portlandite model to be more valid for high calcium to silicon ratios (> 1.5-1.7) [CK96b, Ric08, Tay86].

- The following structural changes are observed with increasing calcium to silicon ratio compared to the structure with a calcium to silicon ratio of 0.83 (i.e. 14 Å tobermorite):

  - The interlayer distance between the calcium silicate layers decreases from 14 Å to 11 Å when the calcium to silicon ratio is increased 0.8 to 1.1. When the calcium to silicon ratio is increased further, the interlayer distance remains constant [RRL$^+$09b, CK96b, SUCB$^+$12].

  - The number of bridging silicon tetrahedra as well as the mean chain length of the silicate chains decreases, however some bridging silicon tetrahedra can still be observed even at high calcium to silicon ratios. Also the ratio of bridging to non-bridging Q^2 silicate species remains constant at 2:1 and the concentration of silicate monomers remains very low (~ 2 %), indicating that the sequence of possible silicate chain lengths (only species of length $3 \cdot n - 1$ are observed) does not change [MT82, SH08, BBC$^+$04, KJB$^+$00, BDRG94, CK96b, BBC$^+$04, CK96a, RZTHG93, YKP$^+$99, GSB$^+$07, RRL$^+$09b].

  - The number of protonated silanol groups (Si-OH) in the structure decreases [YKP+99], although a certain number of silanol groups is observed for all calcium to silicon ratios [BBC+04].
  - For calcium to silicon ratios larger than 0.9-1, an increasing amount of Ca-OH groups, absent for lower calcium to silicon ratios, can be observed [BBC+04, YKP+99, TCJN03, RDSA12]. In fact at a calcium to silicon ratio of 1.7 an estimated 23 % of the charge of the calcium species is compensated by hydroxyl groups. For calcium to silicon ratios between 0.9 - 1.5, the Ca-OH groups are only present in the interlayer region whereas for higher ratios their existence within the calcium-silicate layers is possible but not necessary [BBC+04].
  - Although in general the interatomic distances do not seem to change and the nanocrystalline character of C-S-H is conserved, the Ca - O coordination decreases from ~ 7 to ~ 6 when the calcium to silicon ratio is increased to 1.75 [SUCB+12, MBM11].

- The full atomistic models developed so far with atomistic modeling techniques [DGH07, PKS+09, MMM+12] were inconsistent with the above described, experimentally observed, structural features of C-S-H. Amongst other things both models contained a too large amount of silicate monomers and were too disordered with pronounced glass-like character.

11 Study of C-S-H structure with Atomistic simulations

In this chapter some initial results for the atomistic structure of C-S-H are presented. First the atomistic calculations on different 14 Å tobermorite polymorphs are presented. This is followed by a study of different possible bulk defects in 14 Å tobermorite that increase the calcium to silicon ratio, thus bringing the structure closer to C-S-H. Finally some initial simulations of 14 Å tobermorite surfaces are presented.

Many details about the atomistic structure of C-S-H are still unknown. There are many reasons for this. One of them is the fact that even the more crystalline model structure of C-S-H, such as 14 Å tobermorite, are polymorphic and have a pronounced order/disorder character. In the case of 14 Å tobermorite this means that, even though the structure of one polymorph (with B11b symmetry) has been fully characterized by Bonaccorsi et al. [BMK05], there are still unknown factors, such as the positions of the hydrogens, the exact nature and extent of the positional disorder in the interlayer as well as the structure of the other polymorphs present. Consequently in the first section of this chapter atomistic simulations of two different polymorphs of 14 Å tobermorite, as model structures of low calcium C-S-H, are presented.

It is well known that in ordinary portland cement systems, C-S-H has a higher Ca/Si ratio than the various model structures [Ric04]. Consequently in the second section results for different possible Ca/Si ratio increasing defects in bulk 14 Å tobermorite are discussed. Results are compared to experimental results to gain further insight into the validity of 14 Å tobermorite as a C-S-H model structure.

Finally the specific surface area of C-S-H is very high. In fact the smallest dimension of C-S-H crystallites is usually considered to be in the order of 3-6 nm. This means that the properties of C-S-H / pore solution interfaces are very important and will influence the overall microscopic properties of C-S-H as measured experimentally. Therefore, in the last part of this chapter, simulations of the [001] and the [010] /[$0\bar{1}0$] 14 Å tobermorite surfaces are discussed.

Table 11.1: Calculated dimensions of the crystalline unit cell of B11b 14 Å tobermorite. Values calculated with molecular dynamics (MD) and with DFT energy minimization (courtesy of Prof. Stephen Parker, CSSC group, University of Bath) as well as the experimental values according to Bonaccorsi et al. [BMK05].

	a [Å]		b [Å]		c [Å]		α [°]		β [°]		γ [°]	
MD	6.86	± 0.34	7.27	± 0.36	28.00	± 1.40	90	± 10	93	± 10	123	±10
DFT	6.68		7.39		28.76		89		91		122	
[BMK05]	6.74		7.43		27.99		90		90		123	

11.1 Bulk 14 Å Tobermorite

As discussed in section 10.1, according to experimental observations reported in literature, the best C-S-H model structure, at least for low calcium to silicon ratios, appears to be 14 Å tobermorite. Consequently 14 Å tobermorite was used as a starting structure for the current work aimed at gaining further insight into the atomistic structure of C-S-H. The structure of one of the polymorphs of 14 Å tobermorite, with B11b symmetry, was described by Bonaccorsi et al. [BMK05]. However, as Bonaccorsi et al pointed out, there exists at least one other polymorph, or more precisely a polytype, differing from the one described by Bonaccorsi et al. in the stacking of the calcium silicate layers. In addition to polytypism, Bonaccorsi et al. also state other probable sources of disorder, such as positional disorder of the interlayer and domains of different layer symmetry, which would account for limited accuracy of the final fit between the theoretical and the experimental X-ray diffraction data.

A supercell of 4x3x1 B11b 14 Å tobermorite unit cells [BMK05], was used to calculate the bulk properties of tobermorite. The bulk structure was simulated using anisotropic NPT molecular dynamics (see section 2.4). The system was relaxed for > 210 ps before the properties were calculated over the next 700 ps. The resulting structural properties were compared to both the XRD structure reported by Bonaccorsi et al. [BMK05] and to density functional theory (DFT) energy minimization calculations done by Prof. Stephen Parker from the Computational Solid State Chemistry group at the University of Bath.

The dimensions of the crystalline unit cell calculated by molecular dynamics (table 11.1) was found to be in very good agreement with the experimental values as well as with the DFT results, the difference between molecular dynamics results and the other two are all less than half of the estimated error.

To compare the structural details, the molecular dynamics structure was partially minimized (not until full convergence). This allowed a clearer distinction of the equilibrium position of the atoms and made the comparison to both the XRD structure [BMK05] and to the DFT structure easier. The result can be seen in figure 11.1. The DFT structure, for which a reduced unit cell (a: 6.74 Å, b: 7.43 Å, c: 14.39, α: 97.37 °, β: 76.47 ° and γ: 123.25 °) was used, is in

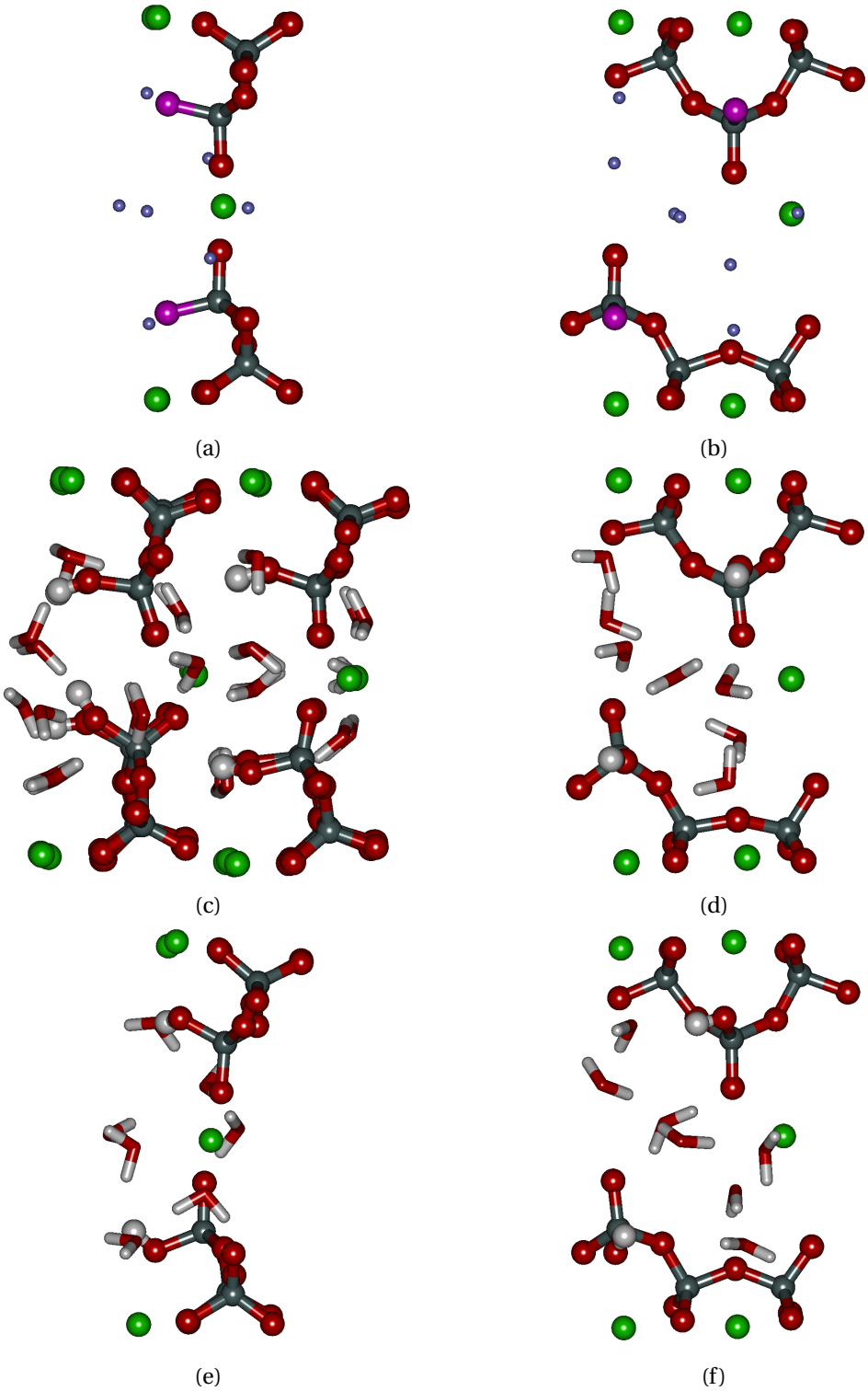

Figure 11.1: Structure of B11b 14 Å tobermorite. XRD [BMK05] structure ((a) and (b)), partially minimized snapshot of molecular dynamics calculations ((c) and (d)) as well as DFT structure courtesy of Prof. Stephen Parker, CSSC Group, University of Bath ((e) and (f)). Viewed along ((a), (c) and (e)) and perpedicular to ((b), (d) and (f)) the silicate chains. Ca: green, Si: gray, O: red, H: white. For the XRD structure: OH^-: purple, H_2O: blue.

very good agreement with the XRD structure, the biggest deviations being observed for the position and orientation of the water molecules in the interlayer.

The molecular dynamics calculations which, contrary to the DFT calculations, have not only been done for a larger supercell but also at 300 ° K, taking into account the vibrational movement of the atoms at room temperature, positional disorder, mainly of the interlayer, can be observed. Compared to the XRD structure, some of the bridging silicate tetrahedra in the structure rotate slightly, with the non-bridging oxygen and the hydroxyl group being observed at about the same distance from the calcium layers, contrary to the non-rotated bridging silicate tetrahedra where the hydroxyl group is closer to the calcium layer than the dangling oxygen (see figure 11.1c). In the vicinity of the rotated tetrahedra the position of the water molecules as well as the hydrogen bonding scheme is different from that close to non-rotated bridging silicate tetrahedra. The appearance of additional positional entropy is consistent with expectations based on the experimental observations [BMK05]. Overall however the structural features observed for the molecular dynamics calculations are consistent with both the experimental XRD structure and the DFT calculations. Again the largest differences are observed for the positions of the atoms in the interlayer.

Finally the precipitation enthalpy ΔH of B11m 14 Å tobermorite was calculated with both molecular dynamics and DFT. To this end the enthalpy of 14 Å tobermorite was compared to the energy of quartz, portlandite, lime and water (reaction 11.1). However the reaction enthalpy of reaction 11.1 is difficult to interpret. Consequently it was converted to an precipitation enthalpy according to reaction 11.3, with the help of the experimental reaction enthalpy of reaction 11.2 according to the CEMDATA thermodynamic database [LMMG08].

$$\begin{aligned} &2 \cdot CaO + 0.5 \cdot Ca(OH)_2 + 3 \cdot SiO_2 + 3.5 \cdot H_2O \longrightarrow \\ &[Ca_{2.5}Si_3O_8(OH) \cdot 3.5H_2O]^{0.83}_{tob} \end{aligned} \tag{11.1}$$

$$\begin{aligned} &2 \cdot CaO + 0.5 \cdot Ca(OH)_2 + 3 \cdot SiO_2 + 2.5 \cdot Ca^{2+} + 3 \cdot OH^- + 2 \cdot SiO(OH)_3^- \longrightarrow \\ &5 \cdot CaSiO_2(OH)_2 \end{aligned} \tag{11.2}$$

$$\begin{aligned} &5 \cdot CaSiO_2(OH)_2 + 3.5 \cdot H_2O \longrightarrow \\ &[Ca_{2.5}Si_3O_8(OH) \cdot 3.5H_2O]^{0.83}_{tob} + 2.5 \cdot Ca^{2+} + 3 \cdot OH^- + 2 \cdot SiO(OH)_3^- \end{aligned} \tag{11.3}$$

For the molecular dynamics calculations, the water molecule is described differently (rigid molecule) from the hydroxyl ion (harmonic bond). As a result the dissociation of water molecules leads to an additional source of error for the molecular dynamics results (see section 3.3). Consequently reactions 11.1 and 11.3 were defined in such a way that the dissociation of

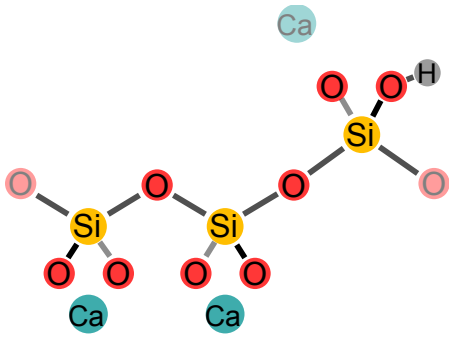

Figure 11.2: Schematic illustration of the structural unit of the calcium-silicate backbone of 14 Å tobermorite. Lighter colors are indicative of atoms shared between two units. The water molecules are not shown.

water molecules was avoided.

The definition of the precipitation reaction is not unique as different solute species could be considered for the reaction. This means that the defined precipitation enthalpy is not unique either. However the solution species were chosen to represent the most abundant species in cementitious systems (see chapter 6) and thus the precipitation enthalpy should give some indication of the stability of the solid with respect to the solution species. The reaction enthalpy is expressed for what is considered the structural unit of tobermorite (figure 11.2), composed of a silicate "dreierketten" unit with two intralayer and one interlayer calcium and 3.5 water molecules ($[Ca_{2.5}Si_3O_8(OH)\cdot 3.5H_2O]^{0.83}_{tob}$).

For the DFT calculations only the energy of quartz, portlandite and a water molecule were calculated. Consequently the energies of lime and bulk water were calculated using experimental data [LMMG08] for the dehydration of portlandite and the condensation of water respectively.

Although for the molecular dynamics calculations, the enthalpies of some solute species were calculated previously (see section 3.3), that data was not used for the calculation of the precipitation enthalpy. Instead the above described procedure was used. This was done to be consistent between the molecular dynamics and the DFT calculations as well as to avoid additional error sources, the error on the enthalpies of solids being generally smaller than the error on solute species (see chapter 3.3).

The results for the precipitation enthalpies can be seen in table 11.2 for both the molecular dynamics and the DFT calculations. The difference between the precipitation enthalpies according to molecular dynamics and DFT is 1.12 eV. The estimated error on the molecular dynamics calculations is only about ± 0.64 eV. However an error in the order of ± 0.5 eV on the DFT results does not seem unreasonable. In fact the DFT calculations reported here have not been corrected for dispersion forces. This is likely to lead to a certain error. Ugliengo et al. showed for instance that in the case of portlandite uncorrected DFT calculations underestimated the interlayer interactions by about 0.2 eV [UZWTC09]. If we consider

Table 11.2: Calculated precipitation enthalpies ΔH of the B11b 14 Å tobermorite [BMK05] and for a possible polymorph according to reaction 11.3. Results for both classical molecular dynamics (MD) and DFT energy minimization (courtesy of Prof. Stephen Parker, CSSC group, University of Bath) as well as the value according to the CEMDATA thermodynamic database [LW06] are shown.

Structure	ΔH^{MD} [eV]	ΔH^{DFT} [eV]	$\Delta H^{CEMDATA}$ [eV]
B11b	-6.58 ± 0.64	-7.70	-8.25
sy	-6.56 ± 0.64	-7.65	

a portlandite energy with an additional layer-interaction energy of -0.2 eV, the calculated precipitation enthalpy of tobermorite changes to -7.20 eV. However the uncorrected DFT calculations are also likely to underestimate the energy of tobermorite. If we consider that not only the portlandite interlayer energy has been underestimated by -0.2 eV but also the tobermorite interlayer energy by a somewhat ad hoc value of -0.4 eV, the precipitation enthalpy of tobermorite becomes -7.40 eV, which, although closer to the molecular dynamics result, is just outside the estimated error interval. In summary the molecular dynamics results and the DFT calculations appear to be consistent with an error interval of approximately ± 0.5 eV on the DFT calculations. However the error interval of the molecular dynamics results is probably slightly underestimated.

The precipitation enthalpies were also compared to the experimental value calculated according to the CEMDATA thermodynamic database [LMMG08]. The value included in CEMDATA was calculated by fitting the solubility data of a tobermorite/jennite solid solution model to the solubility of C-S-H at different calcium to silicon ratios. It is therefore not entirely clear how this value compares to the precipitation enthalpy of a single phase, single polymorph of 14 Å tobermorite. The experimental value is 0.56 eV lower than calculated by DFT and 1.67 eV lower than the molecular dynamics calculations. However the authors of the employed solid solution model [LMMG08, KK01] report large errors up to 20 entropy units for the energies normalized per silicate. This would lead to errors in the order of 0.8 eV on the experimental value of the precipitation enthalpy reported here. Together with the differences of the systems (bulk, single polymorph B11b 14 Å tobermorite for the theoretical calculations and nanocrystalline polymorphous C-S-H for the experimental data) leads us to conclude that both theoretical values are consistent with the experimentally determined value.

From the full comparison between the precipitation enthalpies calculated with different methods we can conclude that the molecular dynamics calculations probably underestimate the precipitation enthalpy of 14 Å tobermorite. Additionally there are some indications that the estimated error on the molecular dynamics energies is slightly optimistic. A ~ 20% larger error interval would probably be more accurate.The experimentally determined precipitation enthalpy on the other hand as well as probably the value according to the DFT calculation appear to be overestimated.

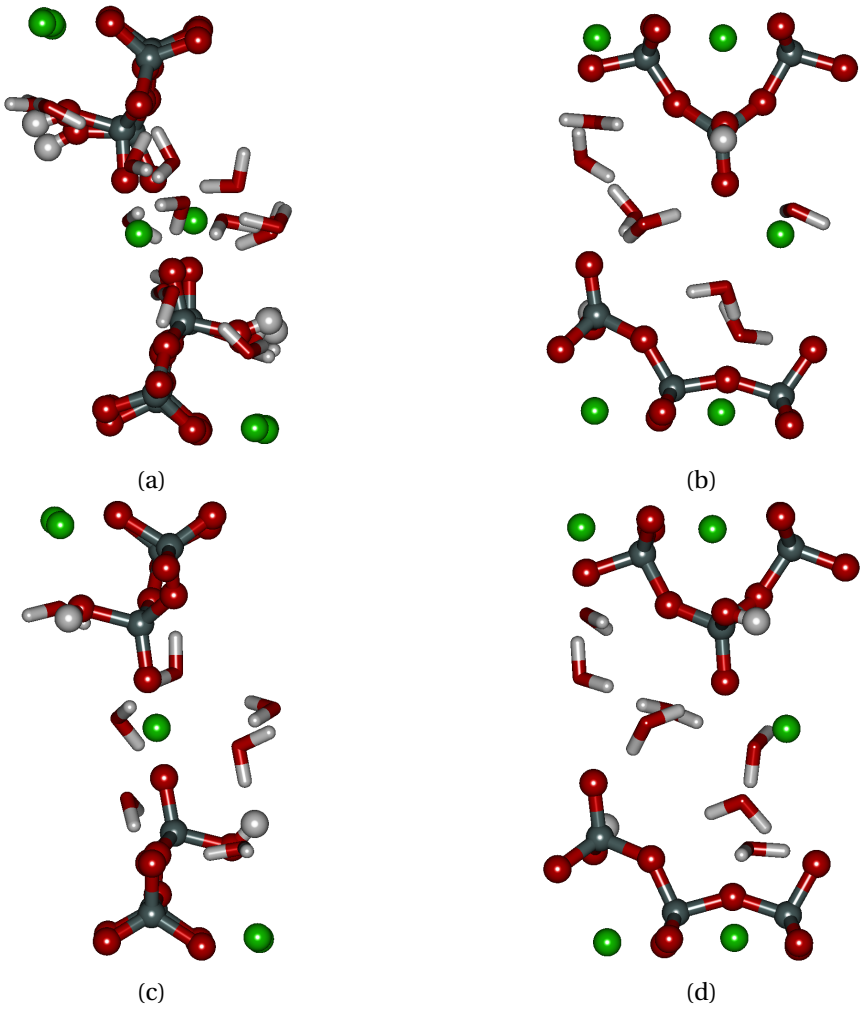

(a) (b) (c) (d)

Figure 11.3: Structure of a polymorph of 14 Å tobermorite. Partially minimized snapshot of molecular dynamics calculations ((a) and (b)) as well as DFT structure courtesy of Prof. Stephen Parker, CSSC Group, University of Bath ((c) and (d)). Viewed along ((a) and (c)) and perpedicular to ((b) and (d)) the silicate chains. Ca: green, Si: gray, O: red, H: white.

Table 11.3: Calculated dimensions of the crystalline unit cell of a possible 14 Å tobermorite polymorph. Values calculated with molecular dynamics (MD) and with DFT energy minimization (courtesy of Prof. Stephen Parker, CSSC group, University of Bath) are shown.

	a [Å]		b [Å]		c [Å]		α [°]		β [°]		γ [°]	
MD	6.86	± 0.34	7.28	± 0.36	28.71	± 1.44	91	± 10	87	± 10	123	±10
DFT	6.83		7.31		28.91		91		90		123	

To get a clearer idea of the influence of polymorphism, a possible 14 Å tobermorite polymorph was studied as well. The polymorph was chosen at random. The difference between the two polymorphs is seen most easily when looking along the silicate chains ([010] direction). By comparing e.g. images 11.1c and 11.3a one can see that the mirror symmetry situated at the center of the interlayer structure for the B11b structure has been transformed into a point symmetry for the polymorph. In other words whereas for the B11b structure the silanol groups point in the same direction for the silicate chains on either side of the interlayer, for the possible polymorph the silanol groups point in opposite directions.

The structures resulting from the molecular dynamics calculations (partially minimized to make the atomic positions more clearly defined) and from the DFT energy minimization are in good agreement (see figure 11.3 and table 11.3). Similarly to what was observed for the B11b structure, the molecular dynamics simulations show additional positional disorder compared to the DFT structure. However, contrary to the B11b structure, no bridging silicate thetrahedra are observed to rotate and the positional disorder appears to be restricted to the interlayer.

Both the molecular dynamics and the DFT calculations predict essentially identical energies for the two polymorphs (table 11.2), indicating that the randomly chosen polymorph structure might actually coexist with B11b 14 Å tobermorite in real structures.

11.2 Bulk Defects in 14 Å Tobermorite

One of the key challenges for the theoretical work on C-S-H so far, is the lack of knowledge about the different possible calcium to silicon ratio increasing defects in tobermorite. For the C-S-H model developed by Pellenq et al. [PKS$^+$09], random calcium to silicon ratio increasing defects were introduced into tobermorite. Apart from other deviations from the experimentally known structural details, as discussed in section 10.3, the final model had a strong amorphous, glass like character [PKS$^+$09] which is inconsistent with experimental observations [MBM11].

The idea behind the work presented here was therefore to study the different possible calcium to silicon ratio increasing defects in more detail. There have been a number of proposals for the different types of defects which can increase the calcium to silicon ratio, based on crystal chemistry considerations [Ric04, Non04]. These proposed defects have never been

Table 11.4: Calculated precipitation enthalpies of different defective 14 Å tobermorite units (calculated with molecular dynamics). Both for the B11b structrue [BMK05] and for a possible polymorph according to reaction 11.3. Results for DFT energy minimization (courtesy of Prof. Stephen Parker, CSSC group, University of Bath) are shown as well. Also indicated are the density ρ of the defective tobermorite unit in 14 Å tobermorite for the b11m structure reported by Bonaccorsi et al. [BMK05]. $c^{ch}_{H_2O}$ and $c^{p}_{H_2O}$ is the molar concentration of chemically and physically bound water respectively and $\frac{c_{OH}}{c_{Ca}}$ is the percentage of the charge of the calcium ions that is compensated by OH.

$\frac{Ca}{Si}$	Formula	$c^{ch}_{H_2O}$ [%]	$c^{p}_{H_2O}$ [%]	$\frac{c_{OH}}{c_{Ca}}$ [%]	ρ $[\frac{g}{cm^3}]$	ΔH_{b11m} [eV]	$\Delta H_{polym.}$ [eV]	ΔH_{DFT} [eV]
0.83	$Ca_{2.5}Si_3O_8(OH)\cdot 3.5H_2O$	5.3	36.8	0	2.22	-6.6 ± 0.6	-6.6 ± 0.6	-7.7
1	$Ca_3Si_3O_9\cdot 3.5H_2O$	0.0	36.8	0	2.34	-7.5 ± 0.9	-7.3 ± 0.9	-7.1
						-7.5 ± 0.9	-7.9 ± 0.9	-6.9
1.25	$Ca_{2.5}Si_2O_6(OH)\cdot 5.5H_2O$	4.8	52.4	0	2.10	-4.0 ± 0.7	-3.7 ± 0.7	
	$Ca_{2.5}Si_2O_5(OH)_3\cdot 4.5H_2O$	14.3	42.9	20	2.09	-1.2 ± 0.6		
1.5	$Ca_3Si_2O_7\cdot 5.5H_2O$	0.0	52.4	0	2.20	-4.0 ± 1.0		
	$Ca_3Si_2O_5(OH)_4\cdot 3.5H_2O$	19.0	33.3	33	2.20	-1.7 ± 0.8	-2.4 ± 0.9	-4.8
1.75	$Ca_{3.5}Si_2O_7(OH)\cdot 4.5H_2O$	4.8	42.9	14	2.31	-4.0 ± 0.7		-3.7
	$Ca_{3.5}Si_2O_6(OH)_3\cdot 3.5H_2O$	14.3	33.3	29	2.30	-2.5 ± 0.7		
2	$Ca_4Si_2O_7(OH)_2\cdot 3.5H_2O$	9.5	33.3	25	2.42	-5.0 ± 0.7	-4.2 ± 0.7	-3.4
2.5	$Ca_{2.5}Si_1O_{2.5}(OH)_2\cdot 7H_2O$	8.7	60.9	40	1.95	-1.6 ± 0.5		

identified or modeled and seem to hold the key to unraveling the structural complexities of C-S-H. This might help guide future atomistic simulations of defective tobermorite structures. By introducing a well chosen set of defects, rather than a random choice, it seems possible to obtain a less amorphous and more realistic model of C-S-H.

A total number of 11 different defects with calcium to silicon ratios ranging from 1.0 to 2.5 were considered (see table 11.4). For some of the defects the energy was calculated for both the B11b and the possible polymorph structure. For the molecular dynamics calculations an isolated defective unit in a supercell of 4x3x1 tobermorite unit cells was considered (resulting in a simulation cell of 27x18x28 Å). After pre-equilibration, the system was further equilibrated for 35 ps and then data was collected over a simulation period of 105 ps, using the anisotropic NPT ensemble. As only one isolated defect in a large bulk cell was considered, the defects can be considered as non interacting. For high defect concentrations the defects are likely to start interacting which will change their energy and probably influence their distribution in the structure. However defects having a low energy at low concentrations are also likely to be more important for higher concentrations, as has been shown for e.g. the sites occupied by dopants at alumina interfaces [TGSB12]. For some defects DFT calculations were done as well. The DFT calculations were done by Prof. Stephen Parker from the computational solid state chemistry group at the University of Bath. All DFT calculations were done for a reduced unit cell with half the volume of the original unit cell reported by Bonaccorsi et al. [BMK05]. This means that the defects are strongly interacting. Consequently the results of the DFT energy

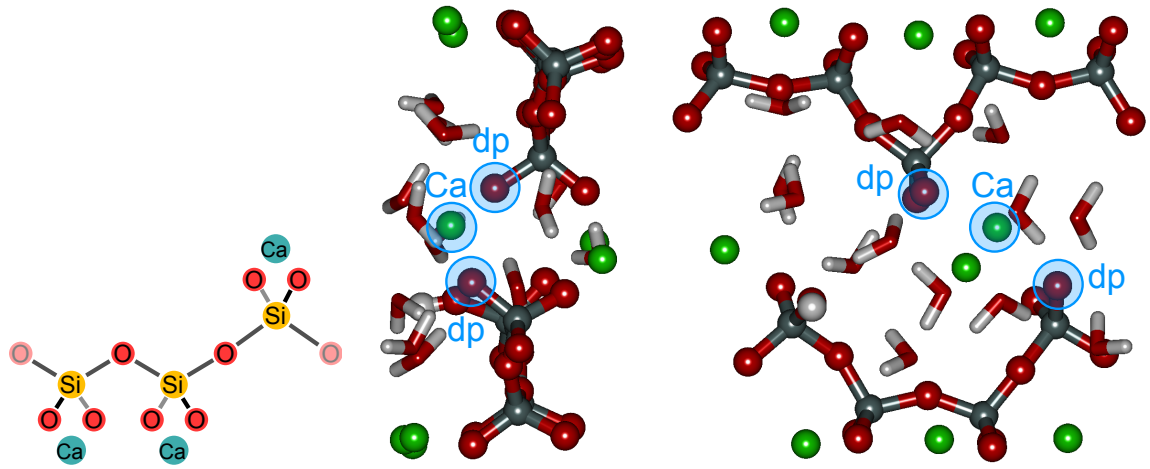

(a) (b) (c)

Figure 11.4: Structure of a 14 Å tobermorite defect increasing the Ca/Si ratio of two structural units to 1.0 by deprotonating two silanol groups (dp) and adding a calcium ion (Ca). Schematic view (a) and partially minimized snapshot of molecular dynamics calculations viewed along (b) and perpendicular to (c) the silicate chains. Ca: green, Si: gray, O: red, H: white. Labels: dp: deprotonated silanol group, Ca: additional calcium ion.

minimizations do not necessarily correspond to the molecular dynamics results. However, as for the bulk 14 Å tobermorite, the DFT and the molecular dynamics result were within the respective estimated error intervals of each other, the DFT calculations can also serve as an estimation of how important the defect interactions are.

In this work the water content was not varied for the different defects. In fact the total number of oxygens was held constant. This means that if e.g. a silicon tetrahedron (stoichiometry: SiO_2) was removed, the two oxygens were replaced by water molecules.

In the following section the results for the different calcium to silicon ratios will first be discussed separately, before the overall results are compared to experimental data.

11.2.1 Ca/Si Ratio of 1.0

The calcium to silicon ratio of a structural unit of 14 Å tobermorite can be increased from 0.83 to 1.00 by removing the protons of two neighboring silanol groups of two bridging silicate tetrahedra on either side of the interlayer (dp sites in figure 11.4a). The resulting charge is then compensated by an additional calcium in the interlayer (Ca site in figure 11.4a). There exist two different possible silanol group pairs that are about equidistant. Both possible arrangements were considered. Additionally the defect energy was calculated for both the original B11b and the possible polymorph structure.

The precipitation enthalpy ΔH was calculated according to reaction 11.4. The results for the

different defect configurations and for the different polymorphs can be seen in table 11.4. The differences between the precipitation enthalpies calculated by molecular dynamics for the different defect configurations for both tobermorite polymorphs were all less than half the estimated error interval, indicating that the different structures are equivalent and can probably be encountered in equal concentrations in real tobermorite or C-S-H structures.

$$\begin{aligned} &6 \cdot CaSiO_2(OH)_2 + 3.5 \cdot H_2O \longrightarrow \\ &[Ca_3Si_3O_9 \cdot 3.5H_2O]_{tob}^{1.0} + 3 \cdot Ca^{2+} + 3 \cdot OH^- + 3 \cdot SiO(OH)_3 \end{aligned} \tag{11.4}$$

For the $\frac{Ca}{Si}$ = 1.0 defect, DFT calculations were done as well. The calculated precipitation enthalpy of the defects (this time of the interacting defects due to the much smaller simulation cell used and the resulting high defect concentration) is very similar to the precipitation enthalpy calculated with molecular dynamics, the difference (maximum 1.0 eV) being smaller than the respective error intervals (see table 11.4). However the order of the energies are now inversed, with the molecular dynamics precipitation enthalpies being more negative than the ones calculated with DFT.

The calculated precipitation enthalpies are very similar to that of non-defective 14 Åtobermorite, the difference between them being within the estimated error interval for both molecular dynamics and DFT. This indicates that the defect is relatively stable.

If we look at the resulting structure of the B11b defect configuration with slightly lower energy (figure 11.4), we can see that both bridging silicate tetrahedra that were deprotonated (dp sites) have rotated compared to the initial bulk position and both the original and the additional (Ca site) interlayer calcium ions are shared between them, one on either side of the silicate chain. Locally the water positions appear to have changed somewhat, although the changes seem to be confined to the nearest neighbor waters. Qualitatively the interatomic distances do not appear to have changed much although further analysis would be necessary. The density of the structure is slightly increased from 2.22 to 2.34 $\frac{g}{cm^3}$ due to the replacement of two hydrogen (1.0 $\frac{g}{mol}$) with a calcium (40.1 $\frac{g}{mol}$) and the bound water content is decreased from 5.3 $\%_{mol}$ to 0 $\%_{mol}$ (table 11.4).

11.2.2 Ca/Si Ratio of 1.25

In order to raise the calcium to silicon ratio of a 14 Å unit from 0.83 to 1.25, one can remove a bridging silicate tetrahedron of a silicate dreierketten chain. From a stoichiometric point of view this is equivalent of removing SiO_2 from the structure. The hydrogen of the silanol group of the removed bridging silicate tetrahedron is transfered to one of the adjacent paired silicate tetrahedra (p site in figure 11.5a). Although there are in theory two possible choices for the position of the hydrogen, the hydroxyl group further away from the interlayer calcium appears the more logical choice, due to electrostatic considerations. The loss of the two oxygens can

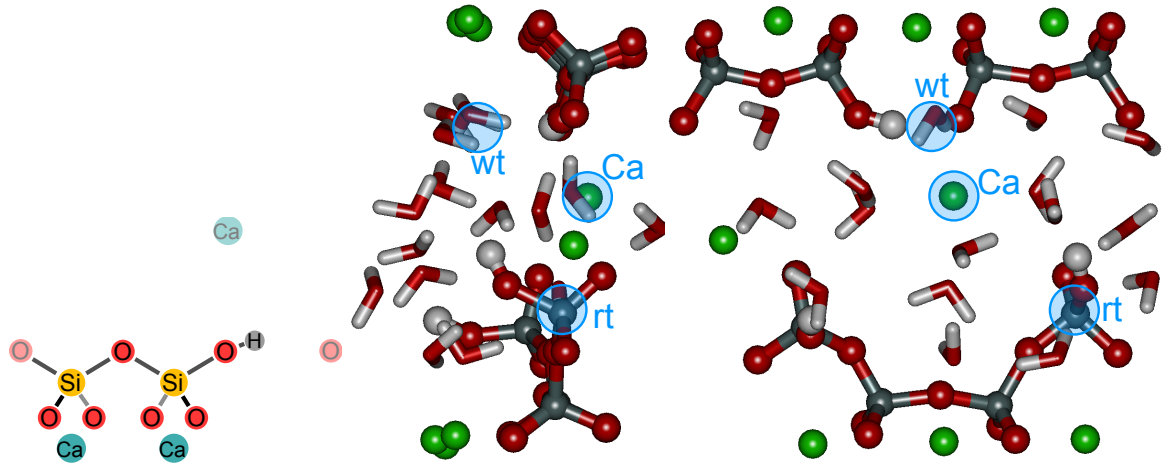

(a) (b) (c)

Figure 11.5: Structure of a 14 Å tobermorite defect increasing the Ca/Si ratio of one structural unit to 1.25 by removing a silicate tetrahedron and transferring the proton to a neighboring site (p). Schematic view (a) and partially minimized snapshot of molecular dynamics calculations viewed along (b) and perpedicular to (c) the silicate chains. Ca: green, Si: gray, O: red, H: white. Labels: wt: water site replacing the hydroxyl group of the original structure, Ca: interlayer calcium, rt: rotated silicate tetrahedron.

then be compensated by the addition of two water molecules.

The precipitation enthalpy of such a defective tobermorite unit can be calculated according to reaction 11.5. The precipitation enthalpy was calculated for both the B11b 14 Å tobermorite and for the possible polymorph structure (table 11.4). The difference between the precipitation enthalpies for the different structures is again small (0.3 eV), indicating that, as for the $\frac{Ca}{Si}$ = 1.0, polymorphism does not seem to play a major role for the $\frac{Ca}{Si}$ = 1.25 defect.

$$\begin{aligned} &4 \cdot CaSiO_2(OH)_2 + 5.5 \cdot H_2O \longrightarrow \\ &[Ca_{2.5}Si_2O_6(OH) \cdot 5.5H_2O]^{1.25}_{tob} + 1.5 \cdot Ca^{2+} + OH^- + 2 \cdot SiO(OH)_3 \end{aligned} \tag{11.5}$$

By looking at the structure (figure 11.5) one can see that one of the silicate tetrahedron adjacent to the defect, the one sharing the charge of the interlayer calcium with the defect site, has rotated compared to the bulk structure (rt site). The calcium ion has moved towards the original position of the removed silicate tetrahedron (Ca site). One of the additional water appears to occupy the original position of the hydroxyl group in the non-defective structure (wt site). The other additional water molecule does not appear to occupy a clearly defined site and causes a certain amount of positional disorder of the surrounding water molecules. The density of the defective unit (2.1 $\frac{g}{cm^3}$) is smaller than that of non-defective 14 Å tobermorite and the structure contains about the same amount of chemically bound water but significantly

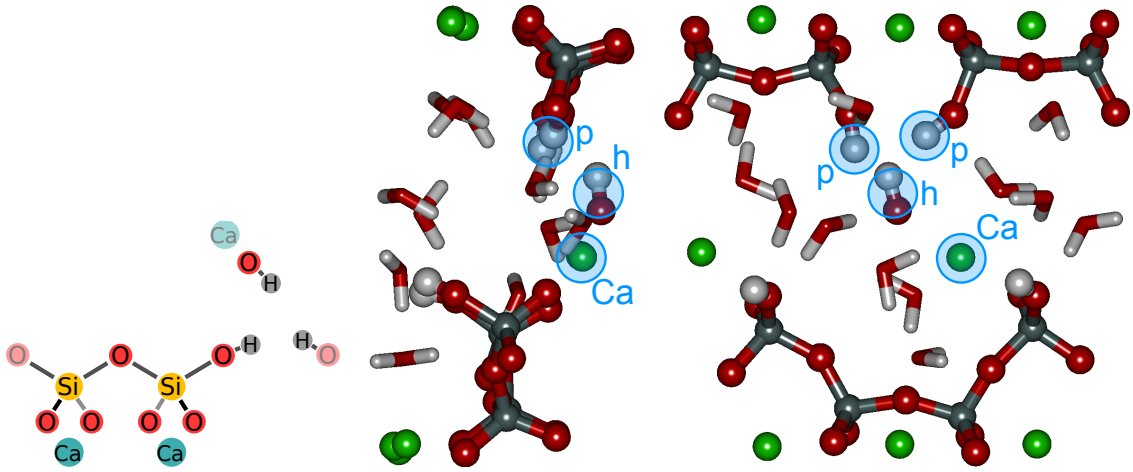

(a) (b) (c)

Figure 11.6: Structure of a 14 Å tobermorite defect increasing the Ca/Si ratio of one structural unit to 1.25. Schematic view (a) and partially minimized snapshot of molecular dynamics calculations viewed along (b) and perpedicular to (c) the silicate chains. Ca: green, Si: gray, O: red, H: white. Labels: p: protonated silanol groups, h: interlayer hydroxyl, Ca: interlayer calcium.

more physically bound water than the non defective structure (table 11.4).

There exists a second variant of the $\frac{Si}{Ca} = 1.25$ defect. For the second variant, the oxygens removed when removing the silicate tetrahedron are replaced with one water molecule and a hydroxyl group. The charge of the additional hydroxyl group is then compensated by protonating the dangling oxygen of the second paired silicate tetrahedron adjacent to the defect (figure 11.6a). Compared to the first variant of the defect the amount of chemically bound water is increased and the amount of physically bound water decreased, making the total water content constant. For this variant of the $\frac{Si}{Ca} = 1.25$ defect, 20 % of the charge of the calcium ions is compensated by hydroxyls of Ca-OH groups.

The structure of the second variant of the defect appears to be closer to the original 14 Å tobermorite structure than the first. The position of the interlayer calcium (Ca site) is essentially identical to the position in the non-defective bulk structure. The hydroxyl groups (h and p sites) are clustered around the vacated bridging silicate site and the positional disorder of the water structure is much less pronounced than in the first defect variant. Despite the smaller structural differences, the precipitation enthalpy, calculated according to reaction 11.6, is 2.8 eV smaller than for the first variant of the defect (table 11.4). The relatively large difference between the energies indicates that the first version of the defect is more stable.

$$\begin{aligned} &3 \cdot CaSiO_2(OH)_2 + 4.5 \cdot H_2O \longrightarrow \\ &[Ca_{2.5}Si_2O_5(OH)_3 \cdot 4.5H_2O]^{1.25v2}_{tob} + 0.5 \cdot Ca^{2+} + SiO(OH)^-_3 \end{aligned} \tag{11.6}$$

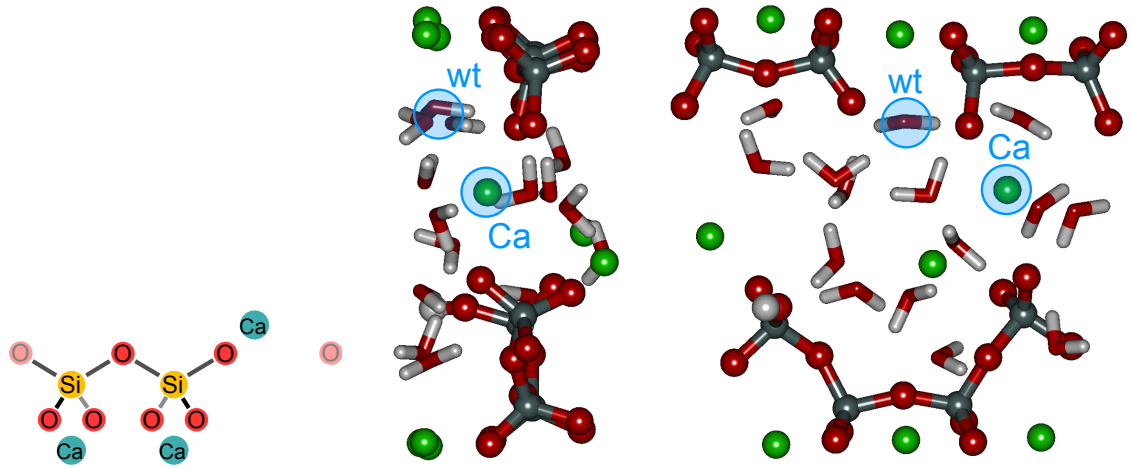

(a) (b) (c)

Figure 11.7: Structure of a 14 Å tobermorite defect increasing the Ca/Si ratio of one structural unit from 1.0 to 1.5. Schematic view (a) and partially minimized snapshot of molecular dynamics calculations viewed along (b) and perpedicular to (c) the silicate chains. Ca: green, Si: gray, O: red, H: white. Labels: wt: water with hydrogen bonds to dangling silicate oxygens, Ca: displaced calcium.

Compared to the $\frac{Ca}{Si}$ = 1.0 defect, the precipitation enthalpy for the $\frac{Ca}{Si}$ = 1.25 defect is significantly less favorable. Even the precipitation enthalpy calculated for the energetically more favorable first variant of the defect is about 3.5 eV above the $\frac{Ca}{Si}$ = 1.0 defect. This indicates that this defect is likely to be less frequent in defective tobermorite structures.

11.2.3 Ca/Si Ratio of 1.5

To increase the calcium to silicon ratio of a tobermorite unit to 1.5, one can start from the previously described $\frac{Ca}{Si}$ = 1.0 defect structure (section 11.2.1) and remove one of the bridging silicate tetrahedron, similar to how the calcium to silicon ratio can be raised from 0.83 to 1.25 (section 11.2.2). Stoichiometrically the removal of a silicate tetrahedron is equivalent to the removal of a SiO_2 group. Two water molecules are then added to the structure, to compensate the loss of the two oxygens of the removed silicate tetrahedron (figure 11.7a). The precipitation enthalpy of the described defective unit was calculated according to reaction 11.7 (see table 11.4).

$$\begin{aligned} &5 \cdot CaSiO_2(OH)_2 + 5.5 \cdot H_2O \longrightarrow \\ &[Ca_3Si_2O_7 \cdot 5.5H_2O]^{1.5}_{tob} + 2 \cdot Ca^{2+} + OH^- + 3 \cdot SiO(OH)_3^- \end{aligned} \tag{11.7}$$

By comparing the resulting $\frac{Ca}{Si}$ = 1.5 (figure 11.7) to the $\frac{Ca}{Si}$ = 1.0 defect structure (figure 11.4) one can see that the positional disorder in the interlayer has increased. One of the two

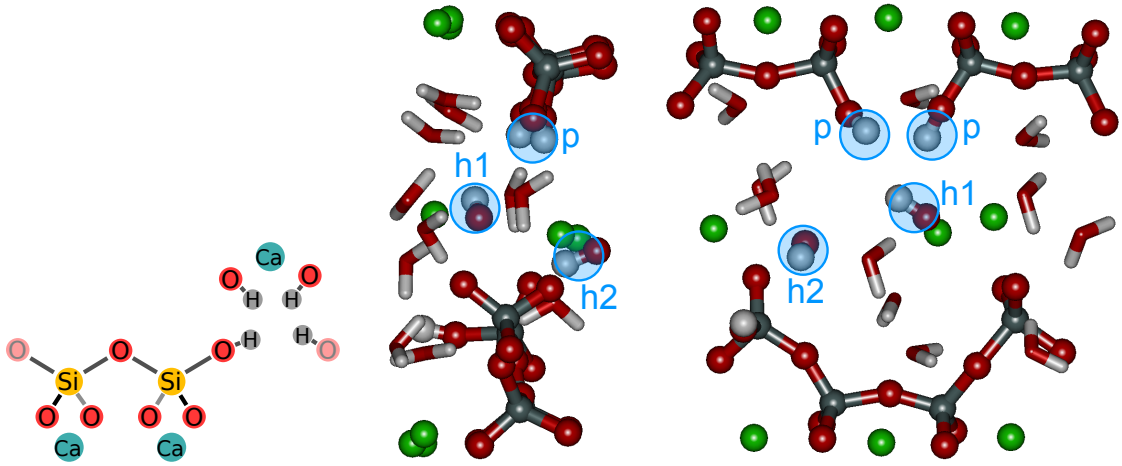

(a) (b) (c)

Figure 11.8: Structure of a 14 Å tobermorite defect increasing the Ca/Si ratio of one structural unit from 1.0 to 1.5. Schematic view (a) and partially minimized snapshot of molecular dynamics calculations viewed along (b) and perpedicular to (c) the silicate chains. Labels: Ca: green, Si: gray, O: red, H: white. Labels: p: protonated silanol groups, h1/h2: interlayer hydroxyl.

interlayer calcium (Ca site), that are shared between the defect site and the silicate chain on the other side of the interlayer, has move towards one of the dangling oxygens of the paired silicate tetrahedra adjacent to the defect structure. The position of the other calcium appears to be similar to the position in the $\frac{Ca}{Si}$ = 1.0 defect. One of the additional water molecules (wt site) is situated between the two dangling oxygen bonds adjacent to the defect site, donating a hydrogen bond to each of them. Otherwise the positions of the water molecules appear to have become quite ill defined.

The density of the defect (2.20 $\frac{g}{cm^3}$) is similar to that of non-defective tobermorite. The water content is very high (52 $\%_{mol}$) and none of the water is chemically bound. The precipitation enthalpy is almost identical to the $\frac{Ca}{Si}$ = 1.25 defect, indicating a similar stability.

As was the case for the $\frac{Ca}{Si}$ = 1.25 defect, there are different possible variants of the $\frac{Ca}{Si}$ = 1.5 defect. Instead of replacing the removed oxygens by two water molecules one can replace them by either one water molecule and a hydroxyl group, protonating one of the dangling oxygens, or by two hydroxyl groups, protonating the dangling oxygens of both of the paired silicate tetrahedra adjacent to the defect. Only the latter variant was considered here.

The precipitation enthalpy of the second variant of the defect was calculated according to reaction 11.8. Calculations were done for both tobermorite polymorphs (table 11.4). Compared to the first variant of the defect, this variant has a higher percentage of chemically bound water (19 $\%_{mol}$) and a smaller percentage of physically bound water (33 $\%_{mol}$) with an overall constant water content. Three of the four hydroxyl groups (p and h1 sites) are clustered around the defect position, the hydrogens more or less pointing towards the original position

of the removed silicon ion. The fourth hydroxyl (h2 site) has moved away from the original defect position (figure 11.8). The position of the two interlayer calcium atoms correspond approximately to the position in the $\frac{Ca}{Si}$ = 1.0 defect structure and the positions of the water molecules appear to be better defined than in the first version of the defect.

$$\begin{aligned} &3 \cdot CaSiO_2(OH)_2 + 3.5 \cdot H_2O + OH^- \longrightarrow \\ &[Ca_3Si_2O_5(OH)_4 \cdot 3.5H_2O]^{1.5b}_{tob} + SiO(OH)^-_3 \end{aligned} \tag{11.8}$$

Despite the apparently higher structural order, the precipitation enthalpy of the second version of the $\frac{Ca}{Si}$ = 1.5 defect differs from the first by +1.6-2.3 eV. In other words this version of the defect appears to be less energetically stable. However the energy difference between the different versions of the $\frac{Ca}{Si}$ = 1.5 defect is less pronounced than between the different versions of the $\frac{Ca}{Si}$ = 1.25 defect. The calculated precipitation enthalpies for the two different polymorph varied by less than the estimated error interval.

In addition to molecular dynamics, the precipitation enthalpy of the second version of this defect was also calculated with DFT. The result (for a small simulation cell containing interacting defects) is about 2.4 eV more negative than the molecular dynamics result. Although the difference corresponds approximately to the cumulated error intervals of the molecular dynamics and the DFT method, the difference between the two energies is quite large and could indicate a favorable interaction between the defects.

11.2.4 Ca/Si Ratio of 1.75

The calcium to silicon ratio of a tobermorite unit can be increased from the original 0.83 to 1.75 by replacing a bridging silicate tetrahedron by a calcium and a hydroxide ion. Stoichiometrically this means that we replace a SiO^{2+} unit by a Ca^{2+} ion (figure 11.9a). The removed oxygen is then replaced by a water molecule.

The precipitation enthalpy of this defect can be calculated according to reaction 11.9. The calculated precipitation enthalpy is similar to the one of both the $\frac{Ca}{Si}$ = 1.25 and the $\frac{Ca}{Si}$ = 1.5 defect, indicating a similar stability (table 11.4). In addition to the molecular dynamics calculations the precipitation enthalpy of the defect was also calculated by DFT. The DFT result, calculated for the small simulation cell and hence for interacting defects, differs by only 0.3 eV from the precipitation enthalpy calculated with molecular dynamics.

$$\begin{aligned} &5 \cdot CaSiO_2(OH)_2 + 4.5 \cdot H_2O \longrightarrow \\ &[Ca_{3.5}Si_2O_7(OH) \cdot 4.5H_2O]^{1.75}_{tob} + 1.5 \cdot Ca^{2+} + 3 \cdot SiO(OH)^-_3 \end{aligned} \tag{11.9}$$

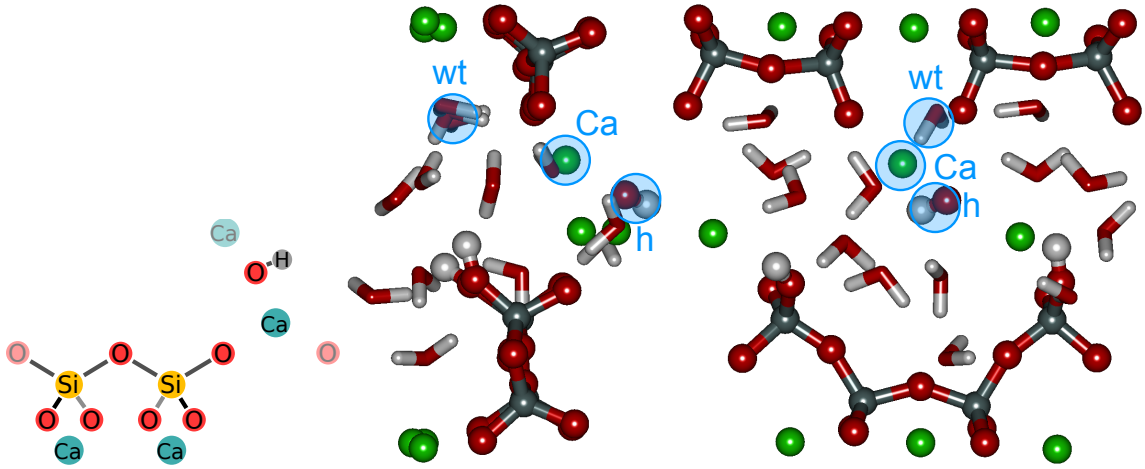

(a) (b) (c)

Figure 11.9: Structure of a 14 Å tobermorite defect increasing the Ca/Si ratio of one structural unit to 1.75. Schematic view (a) and partially minimized snapshot of molecular dynamics calculations viewed along (b) and perpedicular to (c) the silicate chains. Ca: green, Si: gray, O: red, H: white. Labels: wt: water site replacing the hydroxyl group of the original structure, Ca: additional interlayer calcium, h: additional interlayer hydroxyl.

The additional calcium ion (Ca site) adopts a similar position in the structure as the silicate tetrahedron it replaces (figure 11.10). However it is displaced towards the interlayer hydroxyl ion (h site) which is shared between the two interlayer calcium ions. The position of the second interlayer calcium is not much different from its position in the non-defective structure. Finally the additional water molecule (wt site) is adopting a position similar to the one occupied by the hydroxyl group of the bridging silicate tetrahedron in the original 14 Å tobermorite structure. The positional disorder of the other water molecules on the other hand seems to have significantly increased compared to the non defective structure.

Due to the additional calcium in the interlayer, the density of the structure (2.3 $\frac{g}{cm^3}$) has increased compared to non defective 14 Å tobermorite. The amount of chemically bound water is similar but the total amount of water in the structure has increased compared to the non defective tobermorite (table 11.4).

As is the case for most defects discussed so far, there exists another variant of the $\frac{Ca}{Si} = 1.75$ defect. In fact instead of adding a $Ca(OH)^+$ and a water molecule, one can add a $Ca(OH)_2$ group and protonate the dangling oxygen of one of the paired silicate tetrahedra adjacent to the defect (figure 11.10a). Compared to the first variant of the defect, this will increase the percentage of chemically bound and decrease the amount of physically bound water, keeping the total water content constant. In the resulting structure (figure 11.10), the additional calcium ion (Ca site) occupies more or less exactly the position of the removed silicon ion, only slightly displaced towards the center of the interlayer to accommodate the larger Ca-O nearest neighbor distance, compared to Si-O. One of the interlayer hydroxyl groups (h1 site) is shared

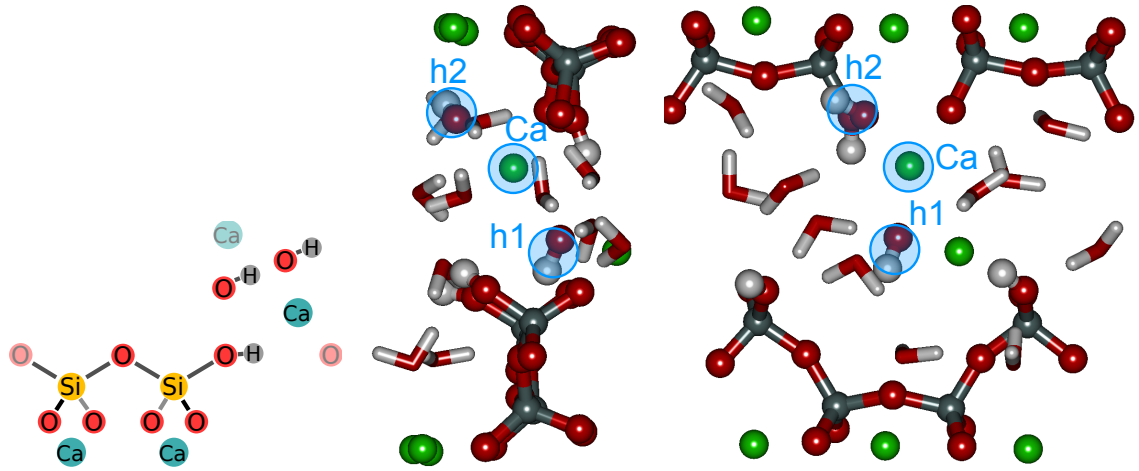

(a) (b) (c)

Figure 11.10: Structure of a 14 Å tobermorite defect increasing the Ca/Si ratio of one structural unit to 1.75. Schematic view (a) and partially minimized snapshot of molecular dynamics calculations viewed along (b) and perpedicular to (c) the silicate chains. Ca: green, Si: gray, O: red, H: white. Labels: Ca: additional interlayer site, h1/h2: additional interlayer hydroxyl.

between the two interlayer calcium ions whereas the second interlayer hydroxyl (h2 site) has moved towards the defective calcium silicate sheet and is occupying a position similar to that of the hydroxyl of the bridging silicate tetrahedron in the non defective structure. As observed for the other defects, the positional disorder of the interlayer water appears to be lower in the second version of the structure containing more chemically bound and less physically bound water.

Despite the apparently increased order of the structure, the precipitation enthalpy for the second variant of the $\frac{Ca}{Si}$ = 1.75 defect, calculated according to reaction 11.10, is less energetically favorable (by about 1.5 eV) compared to the first version. However the difference between the enthalpies for the different structures is less pronounced than for the lower calcium to silicon ratio defects.

$$\begin{aligned} &4 \cdot CaSiO_2(OH)_2 + OH^- + 3.5 \cdot H_2O \longrightarrow \\ &[Ca_{3.5}Si_2O_6(OH)_3 \cdot 3.5H_2O]_{tob}^{1.75b} + 0.5 \cdot Ca^{2+} + 2 \cdot SiO(OH)_3^- \end{aligned} \tag{11.10}$$

11.2.5 Ca/Si Ratio of 2.0

In a similar manner as described for $\frac{Ca}{Si}$ = 1.75, the calcium to silicon ratio of the $\frac{Ca}{Si}$ = 1.0 defect structure can be increased to 2.0 by replacing the bridging silicate tetrahedron with a calcium and two hydroxyl ions (figure 11.11a). Stoichiometrically this is equivalent to replacing SiO_2 by $Ca(OH)_2$. The $\frac{Ca}{Si}$ = 2.0 defect has been simulated with molecular dynamics for both 14 Å

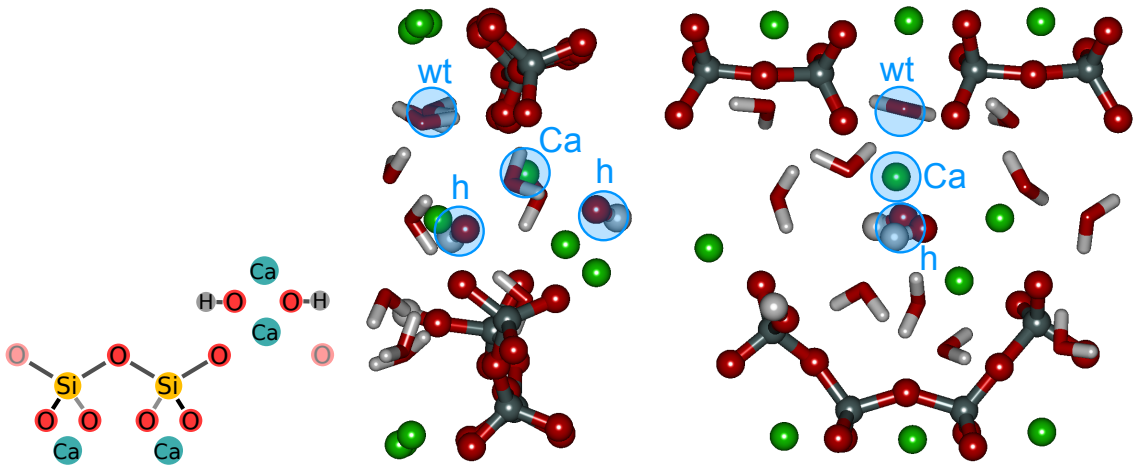

(a) (b) (c)

Figure 11.11: Structure of a 14 Å tobermorite defect increasing the Ca/Si ratio of one structural unit from 1.0 to 2.0. Schematic view (a) and partially minimized snapshot of molecular dynamics calculations viewed along (b) and perpedicular to (c) the silicate chains. Ca: green, Si: gray, O: red, H: white. Label: wt: water with hydrogen bonds to dangling silicate oxygens, Ca: additional interlayer calcium, h: interlayer hydroxyl

tobermorite polymorphs considered in this work. Additionally DFT calculations for this defect were available as well.

The precipitation enthalpy for the different polymorphs and methods was calculated according to reaction 11.11. The precipitation enthalpies calculated by molecular dynamics for the two 14 Å tobermorite polymorphs differed by 0.8 eV. This is the largest difference between the enthalpies calculated for the different polymorphs, although the difference is still significantly smaller than the sum of the respective estimated error intervals. For both polymorphs the precipitation enthalpy of the $\frac{Ca}{Si} = 2.0$ defect was the most energetically favorable of all calculated defects with a calcium to silicon ration of > 1.0. This indicates that the 2.0 defect appears to be more stable than other defects, at least at low defect concentrations.

$$\begin{aligned} &5 \cdot CaSiO_2(OH)_2 + OH^- + 3.5 \cdot H_2O \longrightarrow \\ &[Ca_4Si_2O_7(OH)_2 \cdot 3.5H_2O]^{2.0}_{tob} + Ca^{2+} + 3 \cdot SiO(OH)^-_3 \end{aligned} \tag{11.11}$$

The precipitation enthalpy according to the DFT calculations was significantly less favorable than the molecular dynamics results (difference of 0.8-1.6 eV). Due to the much larger defect concentration for the DFT calculation, this might indicate unfavorable defect interactions.

By looking at the resulting defect structure (figure 11.11), one can see that the additional interlayer calcium ion (Ca site) occupies a similar position as the silicon ion it replaces. The other two interlayer calcium ions have not significantly moved from the position they occupied

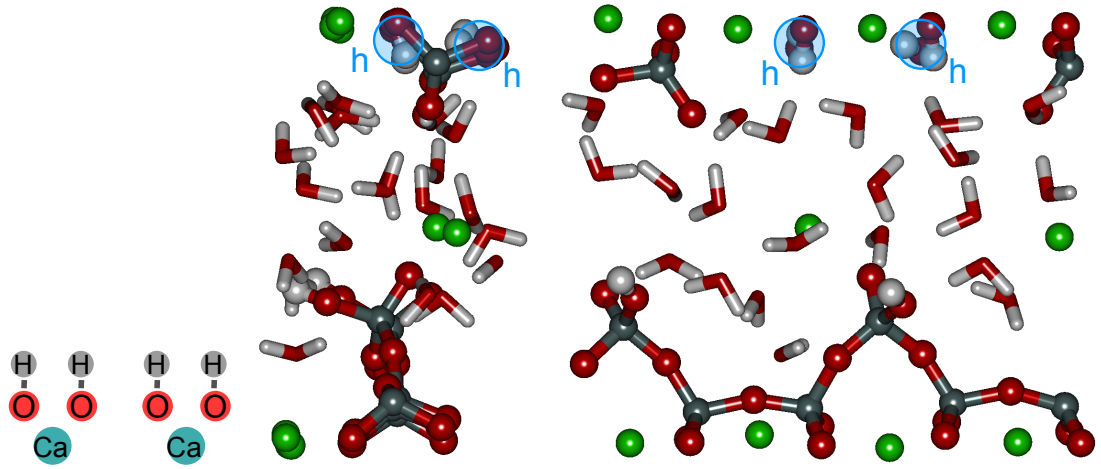

(a) (b) (c)

Figure 11.12: Structure of a 14 Å tobermorite defect increasing the Ca/Si ratio of two structural units to 2.5. Schematic view (a) and partially minimized snapshot of molecular dynamics calculations viewed along (b) and perpedicular to (c) the silicate chains. Ca: green, Si: gray, O: red, H: white. Labels: h: additional hydroxyl groups.

in the $\frac{Ca}{Si}$ = 1.0 defect structure. The two interlayer hydroxyl groups (h sites) are shared between the interlayer calcium ions and are positioned approximately in the middle of the interlayer. A water molecule (wt site) has positioned itself between the dangling oxygens of the paired silicate tetrahedra on either side of the defect site, donating a hydrogen bond to each of them. The positional disorder of the interlayer water has increased slightly compared to the $\frac{Ca}{Si}$ = 1.0 defect structure.

Due to the large concentration of interlayer calcium ions, the density of the $\frac{Ca}{Si}$ defect (2.4 $\frac{g}{cm^3}$) is relatively high and 25 % of the charge of the calcium ions in the structure is compensated by hydroxyl groups. However the amount of chemically bound water (9.5 $\%_{mol}$) is less than double that of the non defective structure. In contrast to the non defective structure, the hydroxyl groups in the $\frac{Ca}{Si}$ = 2.0 structure might retain a certain amount of mobility as they are part of the interlayer structure and not covalently bound to the calcium silicate layer.

11.2.6 Ca/Si Ratio of 2.5

The last defect studied here had a calcium to silicon ratio of 2.5. This quite high calcium to silicon ratio was achieved by removing two bridging and two paired silicate tetrahedra from two adjacent 14 Å tobermorite units. Stoichiometrically this is equivalent to removing $Si_4O_9(OH)_2^{4-}$. The resulting charge was compensated by adding 4 hydroxyl groups. Finally, to keep the total number of oxygens in the structure constant, 7 water molecules were added (figure 11.12).

The resulting structure, according to molecular dynamics, shows surprisingly little disorder.

The atomic positions in the calcium sheet do not appear to have changed and the added hydroxyl groups (h sites) remain stably bound to the calcium layer throughout the simulation. Additionally the position of the interlayer calcium do not change significantly compared to the non-defective structure. Due to the removal of a large number of silicates which are replaced by water, the density of the defective unit (2.0 $\frac{g}{cm^2}$) is very low and the water content (70 $\%_{mol}$) very high . Also 40 % of the charge of the calcium ions are compensated by hydroxyl groups. This time the hydroxyl groups are part of the calcium-silicate layer, though not present as silanol groups as in the non-defective structure.

The precipitation enthalpy of the $\frac{Ca}{Si}$ = 2.5 defect was calculated according to reaction 11.12. The resulting enthalpy was less favorable than the minimum enthalpy structure for any other calcium to silicon ratio considered here (see table 11.4), indicating that the defect is not very stable. Considering that a considerable part of the calcium silicate sheet was removed this does not seem to be surprising. However the precipitation enthalpy is not the least favorable of all defects. For both a calcium to silicon ratio of 1.25 and 1.5 for one of the defect versions the precipitation energy was less favorable than for the $\frac{Ca}{Si}$ = 2.5 defect, indicating that the defect can not be completely discarded as a possible defect in real structures.

$$\begin{aligned} &2.5 \cdot CaSiO_2(OH)_2 + 1.5 \cdot OH^- + 7 \cdot H_2O \longrightarrow \\ &[Ca_{2.5}SiO_{3.5}(OH)_2 \cdot 7H_2O]^{2.5}_{tob} + 1.5 \cdot SiO(OH)_3^- \end{aligned} \tag{11.12}$$

11.2.7 Comparison to Experimental Values from Literature

As mentioned before, the calculated precipitation enthalpies are not unique, in fact the exact order of stability of the different defects can depend on the definition of the precipitation reaction. To reliably calculate relative stabilities, a full thermodynamic model, taking into account all the possible solute species, would have to be used. However this was outside the scope of the current work. In order to get a clearer picture of the relative defect stabilities the enthalpy of the different defects were compared to the enthalpy of quartz, lime, portlandite and water (see e.g. reaction 11.1) and for a second variant of precipitation reactions defined by considering the $Si(OH)_4$ silicate solute species instead of $SiO(OH)_3$. Overall the enthalpies appear to have the following characteristics:

- Polymorphism has little effect on the defect energies.
- The molecular dynamics calculations of isolated defects predict little change of the defect stabilities for calcium to silicon ratios between 1.25 and 2.0. The DFT calculation on the other hand predict a slight, linear decrease of the strongly interacting defect energies over the same calcium to silicon range. This indicates that defect interactions might be more favorable for defects with low calcium to silicon ratios.
- The $\frac{Ca}{Si}$ = 1.0 defect is very stable.

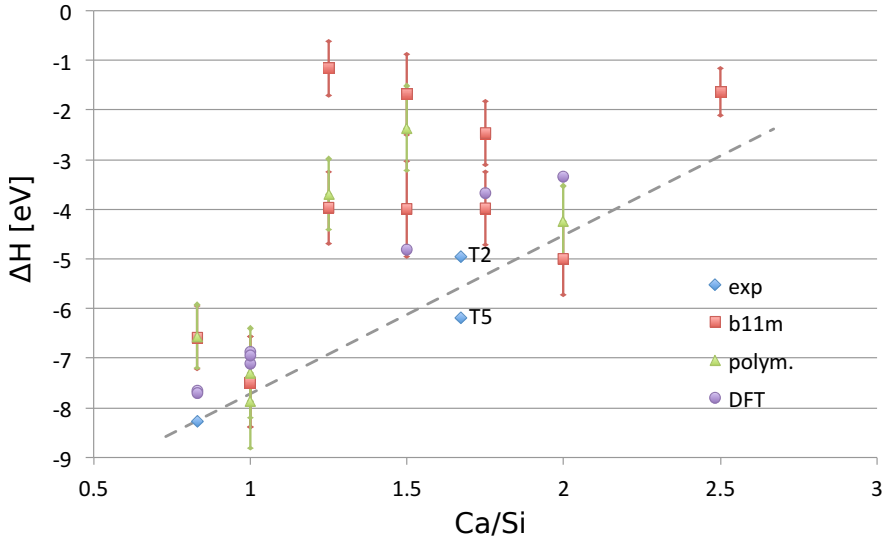

Figure 11.13: Variation of the calculated enthalpy of precipitation with the calcium to silicon ratio for the B11b 14 Å tobermorite model as well as for a possible 14 Å polymorph. Molecular dynamics calculations are shown as well as DFT calculations (courtesy of Prof. Stephen Parker, CSSC group, University of Bath) and experimental results according to the CEMDATA database [LMMG08].

- At low calcium to silicon ratios the defect variants containing a minimum amount of protonated silanol groups and interlayer hydroxyl groups appear to be more stable. At higher calcium to silicon ratios, this trend is less clear.

The general evolution of the calculated precipitation enthalpies with changing calcium to silicon ratio(for both polymorphs and calculated with molecular dynamics or with DFT) can be seen in figure 11.13). To estimate whether the calculated results are consistent with experiment, the evolution of the precipitation enthalpy according to the CEMDATA thermodynamic database [LMMG08] is shown as well. The CEMDATA database models the solubility of C-S-H, in the calcium to silicon range studied here, as a solid solution of two end members [LMMG08]. One of the end members is 14 Å tobermorite, as discussed previously (table 11.2). The other end member is a component (called jennite by Lothenbach et al.) with an overall stoichiometry of $Ca_{1.67}SiO_{5.8}H_{4.2}$. Thomas et al. reported that in C-S-H with a calcium to silicon ratio of 1.7, 23 % of the charge of the calcium ions is compensated by hydroxyl groups [TCJN03]. This means that the more exact stoichiometry of the second end member of the C-S-H model considered by CEMDATA is probably something like $Ca_{\frac{5}{3}}SiO_{\frac{10}{3}}(OH)_{\frac{2}{3}} \cdot 1.7\overline{6}H_2O$. Consequently one can calculate the precipitation enthalpy of the CEMDATA structure according to reaction

11.13, where n_{Si} is the number of silicates in the structural unit.

$$\begin{aligned}&\frac{7n_{Si}}{3}\cdot CaSiO_2(OH)_2 + 1.7\bar{6}n_{Si}\cdot H_2O \longrightarrow \\ &n_{Si}\cdot\left[Ca_{\frac{5}{3}}SiO_{\frac{10}{3}}(OH)_{\frac{2}{3}}\cdot 1.7\bar{6}H_2O\right]_{tob}^{1.67,exp} + \frac{2n_{Si}}{3}Ca^{2+} + \frac{4n_{Si}}{3}\cdot SiO(OH)_3^-\end{aligned} \tag{11.13}$$

The number of the silicates per unit depends on the silicate chain length and is not known exactly. Consequently the experimental precipitation enthalpy was calculated for two limiting chain lengths: dimers (T2) and pentamers (T5) for which n_{Si} is 2 and 2.5 respectively (figure 11.13). The real chain length lies somewhere between those values [Ric04].

The general trend of the experimental precipitation enthalpies and the molecular dynamics as well as the DFT calculations are in surprisingly good agreement. For the molecular dynamics results, a very similar energy evolution as experimentally observed could e.g. be reached by a statistical distribution of $\frac{Ca}{Si}$ = 1.0 and $\frac{Ca}{Si}$ = 2.0 defective tobermorite units. But given the uncertainties on both the experimental and the molecular dynamics results, a statistical distribution of a wider range of defects could also be expected to give results consistent with experimental observations.

For the DFT results, the energies lie approximately on a parallel line to the experimental trend, with a shift of about 0.5-1.5 eV. Again given the uncertainties on both experimental and theoretical results, the consistency between them is good.

Finally we can try to compare the structural details of our results to experimental observations reported in literature. The general trend of the structure for increasing calcium to silicon ratios, e.g. decrease of silicate chain length due to the removal of bridging silicate tetrahedra, enrichment of the interlayer with calcium and the appearance of Ca-OH groups is consistent with experimental observations [Ric04]. However this is not surprising given that the choice of possible calcium silicate increasing defects was guided by experimental observations reported in literature, e.g. the removal of a single paired silicate tetrahedron was never considered here.

The structural feature that can be discussed is the evolution of the number of protonated silanol groups with increasing calcium to silicon ratio. According to our results, the deprotonation of silanol groups appears to be especially favorable at low calcium to silicon ratios. At higher calcium to silicon ratios some of the dangling oxygen of the paired silicon tetrahedra might be protonated as the difference between the protonated and the deprotonated version of the high calcium to silicon ratio defects is smaller. However even at high calcium to silicon ratios, deprotonated silanol groups are still favorable. This appears to be globally consistent with experimental observations of an initially decreasing but non-zero number of protonated silanol groups for higher calcium to silicon ratios [Ric04]. However further information on the concentration of each defect at varying calcium to silicon ratios would have to be gained, e.g. by constructing a full thermodynamic model, to be able to further estimated the variation of

the number of protonated silanol groups with increasing calcium to silicon ratio.

Another point of comparison are the interatomic distances. Due to the small structural changes observed in the structures, mainly limited to an increased structural disorder of the interlayer, the increased calcium to silicon ratio is unlikely to change the nearest neighbor distances, which is again consistent with experiment. However further analysis, ideally the calculation of radial distribution functions of structures with higher defect concentrations should be done to confirm this point.

Due to the increase of the calcium concentration in the interlayer and the replacement of oxygens of the silicate tetrahedra with water, both the water content and the density of the considered defect structures increase with increasing calcium to silicon ratio, in agreement with experimental observations [ATJ07, MSGM13]. In fact let us consider a structure with an overall calcium to silicon ration of 1.7 composed of 26 % non-defective 14 Å tobermorite units and 74 % defective tobermorite units with a calcium to silicon ratio of 2.0. This makes it possible to compare our results to the results of e.g. Muller et al.[MSGM13]. The resulting structure would have an average density of 2.4 $\frac{g}{sm^3}$. The water content of 43 $\%_{mol}$ and 19 % of the charge of the calcium ions are compensated by hydroxyl groups. The overall water content is similar to what has been reported in literature for C-S-H (40-47$\%_{mol}$, depending on whether or not a correction for the surface water is applied [MSGM13]). The percentage of the calcium charge that is compensated by hydroxyl ions is a bit smaller the experimental value (23 %) determined by Thomas et al [TCJN03], however this could be compensated by the presence of a certain concentration of calcium to silicon ratio groups with e.g. a calcium to silicon ratio of 1.75 and 29 % of the calcium charge compensated by Ca-OH groups. Even the presence of some units with a calcium to silicon ratio of 2.5 could be imagined based on the calculated precipitation enthalpies. The overall density of the resulting structure is a bit lower than the density reported by Muller et al. (2.5-2.7 $\frac{g}{cm^3}$, depending on the correction to take into account the surface water). However the current results are for isolated defects in bulk tobermorite. Consequently some possible structural changes, such as a variation of the interlayer distance of the overall structure or the water content were not looked at. Consequently to get more accurate results, structures with higher defect concentrations and different defect configurations would have to be studied.

Additionally surfaces, which can make up over 50 % of the total amount of tobermorite, have not been considered in these results at all. For experimental results however the properties of surfaces are usually included. Consequently to be able to do a representative comparison between a model structure and experimental observations of structural features of C-S-H, surfaces should be studied as well.

11.3 Tobermorite Surfaces

Because C-S-H / pore solution interfaces are very important in cementitious systems, some work was done on B11b 14 Å tobermorite-water interfaces. Only tobermorite surfaces with

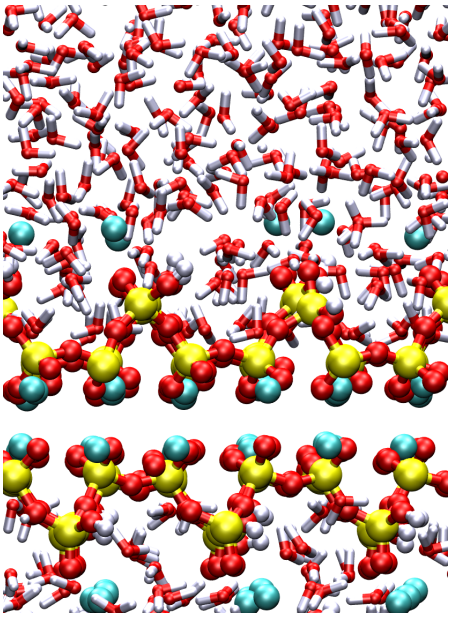

Figure 11.14: Structure of the 14 Å tobermorite [001] surface. Ca: green, Si: yellow, O: red, H: white.

infinite silicate chains i.e. where the silicate chains run parallel to the surface, were considered. There are two possible such surface directions: [001] and [010]. For the [001] surface the calcium silicate layers run parallel to the surface (figure 11.14) whereas for the surfaces perpendicular to the [010] direction the calcium to silicon layers are perpendicular to the surface (figure 11.15). Due to the space group of B11b 14 Å tobermorite, there are two different surfaces perpendicular to the [010] direction, the [010] and the $[0\bar{1}0]$ surfaces. The two surfaces differ in the orientation of the hydroxyl groups (h sites) of the bridging silicate tetrahedra. For the [00.1] surface no hydroxyls are directly at the surface and the hydrogen of the topmost hydroxyl groups point towards the interior of the crystal (figure 11.15a). For the $[0\bar{1}0]$ surface the hydroxyl are directly at the surface, with the hydrogens pointing towards the solution (figure 11.15b).

The method used to calculate the tobermorite-water interfacial energies was essentially the same as already described for portlandite-water interfaces (section 7.2). The energy of a tobermorite/water/vacuum slab was compared to half the sum of the energies of a pure water slab with twice as many water and the energy of a pure tobermorite slab with twice as much tobermorite, divided by the interface area. In the case of the [010] and $[0\bar{1}0]$ surfaces, the cleavage of the crystal will result in one [010] and one $[0\bar{1}0]$ interface. Consequently it is impossible to determine the energy of the two surfaces separately. Instead the average $[010]/[0\bar{1}0]$ interface energy was calculated by comparing the sum of the energies of the [010] and the $[0\bar{1}0]$ tobermorite/water/vacuum slab to the energy of the pure water/vacuum and the pure tobermorite/vacuum slabs. The results can be seen in table 11.5.

For both the [001] and the $[010]/[0\bar{1}0]$ surfaces a negative surface energy is calculated. For

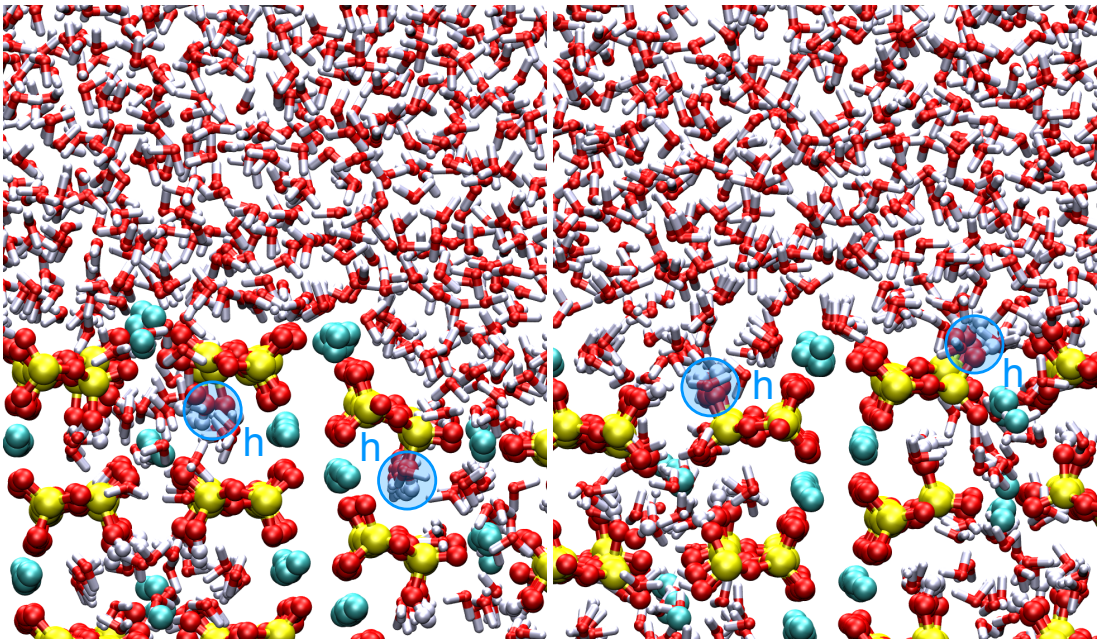

(a) (b)

Figure 11.15: Structure of the 14 Å tobermorite [010] (a) and [0$\bar{1}$0] (b) surface. Ca: green, Si: yellow, O: red, H: white. Label: h: surface hydroxyl groups.

the [00.1] surface, a zero energy would be within the estimated error interval, but not so for the [010]/[0$\bar{1}$0] surfaces. However there are several factors that are likely to increase the error. One additional error source comes from the fact that for the [001] and the [100] surface one or two water molecules respectively were observe to cross the vacuum gap and adsorb at the tobermorite/vacuum interface. For both surfaces the adsorption energy of a water molecule was estimated and a correction for the water adsorption applied, but this increases the error nonetheless. Additionally, as discussed in section 7.2, the energy estimation used to calculate the error intervals was developed for anisotropic NPT calculations. Due to the different mechanical properties of the solid and the solution on the other hand, NVT calculations had to be used to estimate the interfacial energies. This is likely to lead to internal stresses in

Table 11.5: Calculated tobermorite-water interfacial energies γ for two different tobermorite surface as well as an experimentally determined estimation of the overall tobermorite-water interfacial energy [GGN99].

surface	γ $[\frac{J}{m^2}]$
[00.1]	-0.17 ± 0.17
[010]/[0$\bar{1}$0]	-0.46 ± 0.30
exp C-S-H [GGN99]	0.01

the tobermorite slabs and is likely to lead to an additional error. Additionally any entropic contribution was neglected for the calculation of the surface energies, according to the general assumption, that the surface energy for these kinds of crystals is dominated by the enthalpy [TSB+99, Jur54]. There are however some indications that the surface entropy may in some cases play a role for solid-water interfaces [VTGN09]. The additional error sources mean that the experimentally determined value of 0.01 $\frac{J}{m^2}$ reported by Garrault-Gauffinet et al. [GGN99] is within the expected error of the calculated interfacial energies.

On the other hand a slightly negative tobermorite-water interfacial energy would not be completely inconsistent with experimental observations. In fact C-S-H is always observed to be nanocrystalline with the smallest dimension in the order of 4-6 nm, even after prolonged aging [Ric04]. This, along with the the very low tobermorite-solution interfacial energy estimated by Garrault-Gauffinet et al. with the help of C-S-H nucleation experiments [GGN99], suggests that the C-S-H/water and probably also the tobermorite/water interfacial energy is at the very least close to zero and could be negative. A negative interfacial energy would mean that the tobermorite particles in water would have an ideal size and would not grow larger than that.

Additionally a slightly negative tobermorite-water interfacial energy would reduce the difference between the experimental and the calculated precipitation enthalpies (see table 11.2), although the effect is relatively small. In fact if we consider an infinite tobermorite slab terminated on both sides by [001] surfaces, composed of four calcium silicate sheets and three interlayers, according to the molecular dynamics calculations the precipitation enthalpy of the structure is changed by -0.15 eV due to the presence of the surface.

Finally let us look at the structures of the different tobermorite / pore solution interfaces as calculated by molecular dynamics. At the [00.1] surface there appear to be well defined water sites, similar to the ones observed for the water in the interlayer but slightly more disordered. The surface calcium ions oscillate around their original position but stay adsorbed at the surface. The similarity between the interlayer water and the water at the tobermorite surface can also be seen from the surface density profile (figure 11.16a). The basic structure and the position of the density peaks are very similar for the interlayer and at the surface. However the water density appears to be higher at the surface than in the interlayer. Diffuse layering of the water at the surface can be clearly seen up to a distance of 1-1.2 nm from the surface, indicating a stronger water structuration than observed for the portlandite surfaces (see section 7.2).

The density profiles of the [010] and the [0$\bar{1}$0] surface are quite similar (see figures 11.16b and 11.16c). However by looking at the structures (figures 11.15a and 11.15b) some differences can be seen. Whereas the first water layer above the [010] surface, which does not have hydroxyl groups at the surface, appears to be mostly disordered, there are clearly discernible bound water sites at the [0$\bar{1}$0] surface. The [0$\bar{1}$0] surface contains hydroxyl groups oriented with the hydrogen towards pointing away from the surface. It appears that the hydrogen bonding of surface water with the surface hydroxyl groups increases the order of the first structured water layer. The diffuse structuration of the water above the [010] and the [0$\bar{1}$0] surface is similar

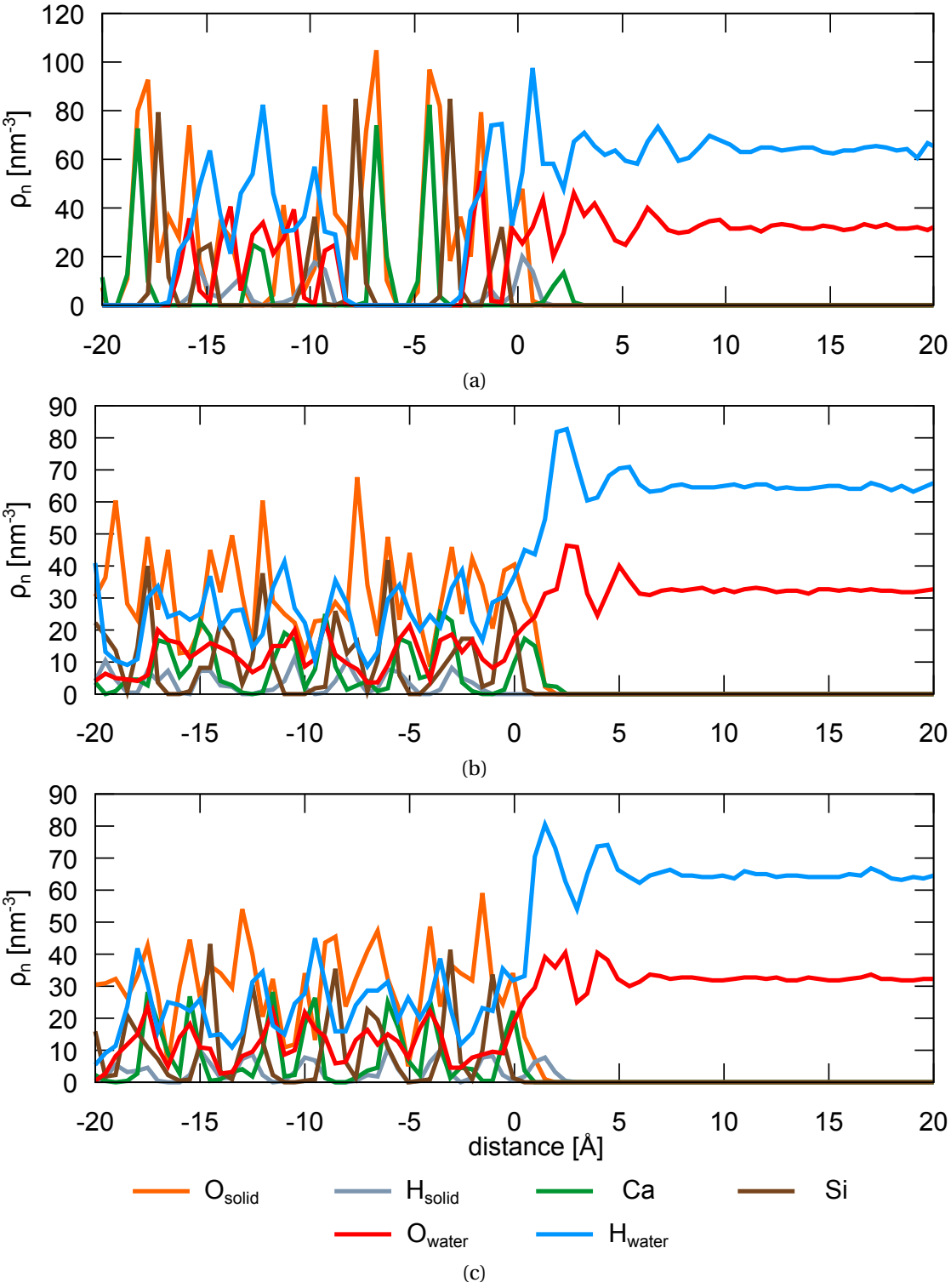

(a)

(b)

(c)

Figure 11.16: Number density of the different species as a function of the distance to the last oxygen layer of different tobermorite surfaces: [001] (a), [010] (b) and [0$\bar{1}$0] (c).

and less pronounced than for the [001] surface, showing layering up to a distance of about 7 Å.

11.4 Summary

In this section 14 Å tobermorite was studied as a model structure for C-S-H. Two different polymorphs were studied, one of them the B11b structure experimentally observed as being an existing polymorph of 14 Å tobermorite [BMK05]. According to both molecular dynamics and DFT calculations, the energy of the two polymorphs differed by no more than 0.05 eV, indicating that both polymorphs might actually be found in real structures.

The properties of different calcium to silicon ratio increasing 14 Å tobermorite defects were then studied. The calcium to silicon ratio of the defective tobermorite units varied from 1.0 to 2.5. The defects did not lead to large structural relaxations, the biggest difference being observed for the interlayer where the positional disorder increased with increasing calcium to silicon ratio. This appears to be in agreement with experimental observations reported in literature [RRL$^+$09b, MBM11].

The properties of some of the defects were studied for both 14 Å polymorphs. Polymorphism was found to play little role, the precipitation energy for the defects for different polymorphs not differing by more than 0.8 eV. However the difference between the largest differences were observed for large calcium to silicon ratios, indicating that polymorphism might be more important at higher calcium to silicon ratios.

The general trend of the variation of the precipitation enthalpies with increasing calcium to silicon ratio was found to be in good agreement with experimental results [LMMG08] for the calcium to silicon ratio range between 0.83 and 1.67. This adds to the increasing amount of evidence in the literature [Non04, RDSA12, KYM$^+$97] that 14 Å tobermorite is a good model structure for C-S-H even at high calcium to silicon ratios.

Finally tobermorite/water interfaces were looked at. Both the [001] and the [010]/[0$\bar{1}$0] surfaces were investigated. Due to the symmetry (or rather lack thereof) of the B11b 14 Å tobermorite structure used for the surface calculations, the [010] and the [0$\bar{1}$0] surfaces are not equivalent. Consequently only an average [010]/[0$\bar{1}$0] interfacial energy could be calculated, it being not possible to determine the two separately.

For both surfaces a slightly negative C-S-H / water interfacial energy was found, although a very small positive ($\leq 0.01\ \frac{J}{m^2}$) would be within the expected error. A slightly negative interfacial energy would not be inconsistent with experimental observations. A negative interfacial energy would indicate that the tobermorite crystallites in water have a preferred size and would not grow larger than that size. This is essentially what is observed for C-S-H where the crystallites remain nanometric even after a long period of aging [Ric04]. In natural tobermorite minerals the crystallite size can be larger, however both polymorphism and the conditions of growth and aging might have an influence on that. Natural tobermorite

minerals might have grown or aged over a long period of time in partially dry conditions. Consequently the observed crystallite size of naturally found minerals might be larger even if the tobermorite/water interfacial energy is negative.

At the [001] surface clear adsorbed water sites can be distinguished, the position of which is similar to the water sites in the interlayer. This indicates that the structure of the water at tobermorite surfaces is similar to interlayer water, however the density appears to be higher and the positional disorder more pronounced. Diffuse layering of the surface water can be observed up to the a distance of 10-12 Å from the surface.

The [010] and [$0\bar{1}0$] surfaces are similar but differ in the details of the first adsorbed water layer. Whereas the adsorbed water layer at the [001] is continuous and unstructured, specific adsorption sites can be distinguished at the [$0\bar{1}0$] surface. The larger structuration at the [$0\bar{1}0$] surface is probably due to hydrogen bonding with the surface hydroxyls, which are absent at the [010] surface. At both surfaces the diffuse layering of water above the surface is less pronounced than above the [001] surface, showing layers up to a distance of about 7 Å from the surface.

12 Summary and Conclusion about the Atomistic Structure of C-S-H

In this chapter the insights gained into the atomistic structure of C-S-H are summarized. The results are discussed in the context of previous work. What is known about the atomistic structure of C-S-H and what isn't as well as how the current work enhances our understanding of C-S-H and helps guide future work is elucidated. The chapter ends with a thorough outlook of directions future atomistic simulation work could take.

As discussed in the C-S-H state of the art chapter (chp. 10), the knowledge about the atomistic structure of C-S-H has increased significantly over the last couple of years, mainly due to more and more advanced measuring techniques. Based on these experimental observations, different phenomenological C-S-H models have been developed [Ric04]. These C-S-H models take into account the general structural features of C-S-H. All of them describe the structure on the basis of defective crystalline structures, usually either tobermorite or jennite or both. It is however difficult to distinguish between the different models to evaluate their accuracy and determine which one is closest to the real structure. Additionally these phenomenological models are not very detailed and consequently fail to explain some crucial questions regarding C-S-H, such as:

- How are the different defects in the C-S-H structure distributed?
- Why is the calcium to silicon ratio in C-S-H inhomogeneous?
- What is the interplay between C-S-H/pore solution interfaces and the atomistic structure of C-S-H? Why is no ripening of the structure observed even after prolonged aging?
- Why does the addition of alkali to the system increase the crystallinity of C-S-H?

Here atomistic simulation might be useful to develop a more detailed C-S-H model and to propose some answers to the questions above. However, although some progress has been

made to distinguish between the different phenomenological C-S-H models with the help of atomistic simulation techniques [RDSA12], a detailed, realistic C-S-H model has yet to be developed. Some work in that direction has been reported in literature [PKS+09, DGH07], however the C-S-H models developed so far are to a large extent inconsistent with experimental observations. The most publicized model, reported originally by Pellenq et al. [PKS+09], was constructed by introducing random defects into a dry 11 Å tobermorite structure, then adding water using grand canonical Monte Carlo. Amongst other inconsistencies, the final model had a clearly disordered, glass like character [PKS+09] that is contrary to experimental observations [MBM11, RRL+09b, Non04]. This was probably due to an unfortunate choice of calcium to silicon ratio increasing defects. Consequently, if we accept the viewpoint that tobermorite is the best suited model structure for C-S-H, an obstacle to the development of a realistic C-S-H model is the lack of knowledge about the different possible calcium to silicon increasing defects in tobermorite. Although the existence of some defects, such as the absence of only one paired silicon tetrahedron, have been excluded due to experimental observations, there is still a wide range of possible defects. Thus an increased knowledge about which defects are likely to be present in defective tobermorite would be desirable. Additionally, to answer the questions above, a C-S-H model would have to include C-S-H/water interfaces.

12.1 Current Insights into the Atomistic Structure of C-S-H

In the current thesis different defects with calcium to silicon ratios from 1.0 to 2.5 were studied for two different polymorphs of 14 Å tobermorite. For some defects density functional theory energy minimization by Prof. Steve Parker from the University of Bath were available in addition to the classical molecular dynamics calculations. The following conclusions could be drawn from the results.

Polymorphism seems to have little effect on defect energies, the same order of stability of the defects was found for two different polymorphs of 14 Å tobermorite. This indicates that future work on defective tobermorite structures can be confined to one polymorph and that results for different polymorphs should be comparable.

The calculated evolution of the defect energies with the calcium to silicon ratio is in reasonable agreement with thermodynamic data for C-S-H solids with a calcium to silicon ratio above 0.83. This is an indication that 14 Å tobermorite appears to be a good model structure for high calcium to silicon ratios as well as for low or intermediate calcium to silicon ratios, adding to earlier evidence which points into the same direction [Non04, RDSA12, KYM+97]. However it is in theory also possible that defect energies in jennite would follow a similar trend. A similar defect energy analysis for jennite would give a clearer picture here.

Although the molecular dynamics calculations of the defective tobermorites show an increase of the positional disorder in the interlayer, the structure of the calcium silicate layers appear to be little changed, except for the missing bridging silicate tetrahedra. This is consistent with experimental observation of nanocrystalline C-S-H with a much higher short range

order than what is e.g. observed in glasses but with pronounced disorder in the interlayer [MBM11, RRL$^+$09b, Non04].

In their article quantifying the amount of $Ca-OH$ bonding in C-S-H, Thomas et al. concluded that for high calcium to silicon ratios (~ 1.7), a jennite based structure is more likely due to the high concentration of $Ca-OH$ groups in the structure (23 % of the calcium charge is compensated by CaOH groups) [TCJN03]. Our results on the other hand indicate that the observed amount of calcium hydroxyl groups can also be reconciled with a tobermorite based structure viewpoint. In fact molecular dynamics calculations of isolated defects indicate that, at low defect concentrations, the replacement of a bridging silicate tetrahedron with a $Ca-OH$ group is at least as stable, if not more so, than the removal of a silicate tetrahedron without replacement of the silicon ion. This is likely to lead to an appreaciable amount of $Ca-OH$ in the interlayer, in the order of what has been observed by Thomas et al. [TCJN03].

The calculated defect structures can also be reconciled with other experimental observations such as the decreasing but never negligible number of protonated silanol groups and the increase of the density with increasing calcium to silicon ratio. Although none of the densities of the isolated defects ($\leq 2.42\ \frac{g}{cm^3}$) was quite as high as the density for C-S-H (2.47-2.70 $\frac{g}{cm^3}$) reported recently in literature by different authors [ATJ07, MSGM13], this could be explained by a decrease of the interlayer distance for higher calcium to silicon ratios. However this would have to be confirmed by simulations of tobermorite structures with high defect concentrations.

All in all our results indicate that 14 Å tobermorite is a good model structure for C-S-H for calcium to silicon ratios larger than 0.83 up to the highest calcium to silicon ratios of at least 1.7. Most of the results obtained here for structural properties as well as precipitation energies are consistent with experimental results obtained for C-S-H. However some structural features, such as the interlayer distance and the density, will need more investigation of structures with higher defect concentrations. C-S-H/water interfaces and the behavior and stability of the different defects at the interfaces would have to be studied as well.

Some work on tobermorite/water interfaces has been started. Our results indicate that the tobermorite/water interfacial energy for surfaces that are parallel to the silicate chains is very small or even slightly negative (~ -0.1/-0.46 ± 0.47 eV). A slightly negative interfacial energy would indicate that the particles have a preferred particle size and do not grow larger in aqueous conditions. This would be consistent with the fact that in C-S-H, the size of the crystallites does not exceed 3-4 nm in the smallest dimension, even after prolonged aging [Ric04]. Such a situation could e.g. arise from a slight mismatch of the ideal distances of the calcium sheet compared to the silicate sheet or by stresses in the calcium silicate sheet induced by the interlayer forces. This would mean that internal stresses are created in the structure which will increase with the size of the crystallites. In addition to a reduced crystallite size, such internal stresses could also be relaxed by the presence of defects and/or stacking faults and polymorphism.

The C-S-H/pore solution interfacial energy was estimated previously by Gaurrault-Gauffinet

et al. [GGN99], using classical nucleation theories (see section 1.3). The theory is based on the idea of a critical radius that has to be surpassed in order for a nucleus to become stable. The size of the critical radius is defined as the size of the particle at which the gain from the bulk energy surpasses the energy loss from the surface energies. Consequently the theory assumes a positive surface energy. The surface energy found with this method by Garrault-Gauffinet et al., was very low (0.012 $\frac{J}{m^2}$). The resulting critical radius for homogeneous precipitation conditions (total relative supersaturation $\ln(S) = 2.3$) is 5 Å, which is very small considering that the interlayer distance is around 11-14 Å. In other words the nucleation radius is smaller than the crystalline unit cell and represents a calcium-silicate cluster rather than a crystalline nucleus. Such a small critical radius could easily be reconciled with a slightly negative surface energy for C-S-H crystallites.

Finally for naturally occurring 14 Å tobermorite minerals, the crystallite size, though never macroscopic, can be several orders of magnitude larger than observed in C-S-H systems. There are several factors that might contribute to this. Firstly, as mentioned before, if internal stresses are at the origin of the negative surface energy, polymorphism and defects present in the structure might decrease the stresses and increase the interfacial energy. Secondly it is probable that the growth and aging of naturally found minerals has not always occurred under fully aqueous conditions. The tobermorite surface energy in a non or weakly interacting environment on the other hand is likely to be much larger than the tobermorite/water interfacial energy. Thus a partial drying of the structure is likely to increase the ideal particle size.

12.2 Outlook

Although the current work lead to some interesting conclusions, a lot of work still remains to be done to fully understand the atomistic structure of C-S-H. The current results might help guide future modeling work.

Firstly an important issue to study further is the interaction between the different calcium to silicon ratio increasing defects and the different tobermorite surfaces. It is possible that the stability of the defects at the surface is different from the bulk. This would have to be taken into account when developing a C-S-H model and when comparing to experimental observations. A study of defects at the tobermorite/water interfaces, similar to what has been done here for bulk defects, would give further insight. Additionally such a study, allowing the estimation of the interaction between defects and tobermorite/water interfaces, might shed further light on the variations of the specific surface area and aspect ratio of the particles with changing calcium to silicon ratio observed by different authors [RRL$^+$09b, TCAJ04].

Secondly the interaction between the defects at higher defect concentrations, which will influence the configuration of defects in the material and influence the precipitation enthalpies, would have to be studied to complete the knowledge about the atomistic structure of C-S-H. Calculations with higher defect concentrations would also allow a comparison between the molecular dynamics and density functional theory calculations. Also a better knowledge about

the interactions between the different defects might give some indications as to why in young cement pastes the calcium to silicon ratio shows a bimodal distribution [Ric04].

Thirdly the water content of the structure should be varied. So far the number of oxygens per tobermorite unit was kept constant. However this is not necessarily the case and therefore the water content should be varied to determine what the water content is likely to be for the different tobermorite defects.

Based on these calculations a full model of C-S-H should be possible, including C-S-H/water interfaces. The properties of such a model can then be compared to experimental data, such as pair distribution functions [MBM11], the silicate speciation and mean length of the silicate chains, the interlayer distance, the overall density of the structure and the XRD diffraction pattern. With more advanced modeling techniques, the NMR spectra for the different species could also be calculated and compared to experiment.

Additionally, based on the full set of data a thermodynamic model might be constructed and the effect of e.g. the calcium to silicon ratio, the temperature or the pH could be studied. In combination all these comparisons should give a very good idea of the accuracy of the developed model as well as allowing a good estimation of how the model can be improved.

12.3 Summary

The theoretical calculations presented here indicate that 14 Å tobermorite appears to be a good model structure for C-S-H. Both the precipitation enthalpies and general structural features of the calcium to silicon ratio increasing defects studied here were in reasonable agreement with experimental results. However there are several as yet unstudied points that still have to be clarified, such as the role of C-S-H/pore solution interfaces, the water content of the different calcium to silicon increasing defects and the interaction between the defects at higher defect concentration.

The atomistic simulation results also indicate that the tobermorite/water interfacial energy of tobermorite surfaces, at least those parallel to the silicate linear surface chains, is very small and may even be slightly negative. A slightly negative surface energy would indicate that there is a optimal size of the tobermorite crystallites in water and that crystallites do not grow larger than that size. The reason for a slightly negative surface energy might e.g. be internal stresses in the crystal structure.

13 Final Conclusions

In this chapter the results and achievements of all the different chapters are reviewed. Advances on methodology, the gained knowledge about the growth and morphology of portlandite as well as on the atomistic structure of C-S-H, discussed previously in more detail, are briefly summarized.

The aim of the current thesis was to elucidate how classical atomistic simulation techniques may be useful in the context of cementitious systems. Two areas of interest were identified, where the application of classical atomistic simulation could be useful:

- The growth and morphology of portlandite: The morphology of portlandite in cementitious systems changes, depending on the composition of the solution from which it grows. Classical atomistic simulation in combination with experiments on model systems and thermodynamic calculations was used to further the understanding of the growth of portlandite.
- The atomistic structure of C-S-H: Despite significant advances in the knowledge of the structure of C-S-H, due mainly to advanced experimental characterization techniques, the exact atomistic structure of C-S-H is still not fully understood. This is an other area where atomistic simulation techniques can be useful.

In addition to the areas mentioned above, some work was done to adapt existing methodologies to use for the study of cementitious systems. We will summarize here the methodological developments as well as the main results for the two aforementioned areas of interest: the growth and morphology of portlandite and the atomistic structure of C-S-H.

13.1 Methodology

A prerequisite for the simulation of cementitious systems is a good force field. Therefore some amount of work has been done to choose a suitable force field. A set of 3 force fields, that had

been previously used for similar simulations, has been tested. The finally chosen force field was based on work by Abascal and Vega [AV05] and Freeman et al. [FHC+07]. For the silicates, which were not part of the original force field, an additional angle potential was introduced for increased accuracy. The final force field was thoroughly tested and the error on angles and distances was estimated. Additionally an expression for the estimation of the error on enthalpies was developed. Although the expression will need further testing to estimated its accuracy and could very likely be improved, the approach proved very useful in the discussion of results, to see which trends were likely to be significant and which differences were smaller than the expected error interval.

In addition to the work concerning force fields, some work has also been done to develop a link between molecular dynamics and Monte Carlo calculations of inorganic/water interfaces. The aim was to estimate the influence of the structuration of water above a crystalline, inorganic surface, observed here as well as by many authors previously [AGM+09, KP04, KK02, KCSP05, SCKP06, KCMP05, ZKR10], on the structure of the diffuse part of the electrical double layer. The methodology consists of a combination of different metadynamics techniques with coarse grained Metropolis Monte Carlo calculations. The correspondence between molecular dynamics calculations and Metropolis Monte Carlo results was reasonable, although some further work would be needed to understand remaining differences. For the Metropolis Monte Carlo calculations a variant to the Torrie and Valleau approach [TV80], to describe the long range electrostatic forces, was developed. This new version could in theory also be used for molecular dynamics calculations and might allow the study of smaller ion concentrations with molecular dynamics.

The use of such methodology might help further elucidate the properties of the electrical double layer at inorganic surfaces. This is an important issue which would help understand different properties of colloidal systems, such as the growth of solids from solution or the colloidal stability of particles.

13.2 Growth and Morphology of Portlandite

Both atomistic simulations and experiment have shown that water noticeably influences the relative interfacial energies and hence the equilibrium morphology of portlandite. Whereas the equilibrium morphology of portlandite in a weakly interacting environment is expected to be hexagonal, in water the equilibrium morphology becomes equiaxed. The change in equilibrium morphology is probably due to a network of strongly bound surface water forming at the higher energy portlandite surfaces. The strong interaction with water lowers the energy of the high energy surfaces relative to the more stable ones.

Metropolis Monte Carlo calculations of the electrical double layer at the [00.1] portlandite surface showed that the positive zeta potential measured experimentally may arise from the adsorption of Ca^{2+} ions at what can be considered the outer Hemholtz plane, due to favorable interactions between the solvation shell of the calcium ions and the structured water region

above the portlandite surface. The different origin of the charge at the interface leads to differences of the structural details of the diffuse layer from the classical Gouy-Chapman picture. However the electrical potential at distances > 15 Å from the surface is similar to the one predicted by classical theories.

Experiments on model systems have shown that silicates have an important influence on the growth and final morphology of portlandite. Atomistic simulations indicate that this might be due to the preferential adsorption of neutral $CaSiO_2(OH)_2$ complexes, the stability of which has been confirmed by metadynamics. These complexes appear to retain a certain amount of mobility at the portlandite surfaces, performing a sort of walking movement by consecutively breaking and reforming one of two hydroxyl bonds donated to the portlandite surface hydroxyl groups. On step like sites on the other hand the calcium silicate complex becomes immobilized. This would indicate that the presence of calcium silicate complexes is likely to hinder or even poison the growth of portlandite. Additionally, due to the probable presence of stably adsorbed, oriented and mobile calcium-silicate complexes at the portlandite surfaces, one could readily imagine that portlandite surfaces might act as templates or catalysts for the growth of C-S-H, which is composed largely of calcium-silicate sheets.

Experimentally the addition of sulfates has been observed to lead to an increased importance of the [00.1] surface in the final portlandite morphology and hence promote a hexagonal platelet morphology. This might be partially due to the formation of a calcium-sulfate complex which leads to an increase of the pH and a decrease of the calcium to hydroxide concentration ratio in the solution. As at the [00.1] surface the dehydration of the Ca^{2+} ions is likely to be the rate limiting step, a reduction of the Ca^{2+} concentration in the solution might lower the growth rate in [00.1] direction. It was also observed, that the precipitation of gypsum in these systems was retarded and indications of the existence of metastable calcium-sulfate nuclei, on which the portlandite particles precipitate, was found. The existence of the metastable nuclei would explain the retardation of the precipitation of gypsum, which is also observed in cementitous systems.

Finally aluminates seem to cause an increase of the particle size, probably due to a decrease of the nucleation rate. The aluminates do not form any complexes with calcium and the calcium to hydroxyl concentration ration remains unchanged. Consequently the observed effect is likely due to the interaction of aluminates with the portlandite particles. Additionally the importance of the [00.1] facet is slightly reduced in the final portlandite morphology.

13.3 Atomistic Structure of C-S-H

Both molecular dynamics calculations and density functional theory energy minimization, courtesy of Prof. Stephen Parker from the University of Bath, indicate that 14 Å tobermorite appears to be a good model structure for C-S-H. Both the precipitation enthalpies and general structural features of the calcium to silicon ratio increasing defects studied were in reasonable agreement with experimental results. Although further work would be needed to understand

e.g. the interaction of defects with other defects and with tobermorite/pore solution interfaces, the current approach seems to be promising to develop a model of the atomistic structure of C-S-H, using defects with a calcium to silicon ratio varying from 0.83 to 2.5. Such a model might help understand e.g. the evolution of the specific interfacial area and the aspect ratio of C-S-H with changing calcium to silicon ratio.

The atomistic simulation results also indicate that the tobermorite/water interfacial energy of tobermorite surfaces that are parallel to the linear silicate chains, is very small and may even be slightly negative. A slightly negative surface energy would indicate that there is a optimal size of the tobermorite particles in water and the particles do not grow larger than that size. The reason for a slightly negative surface energy might e.g. be internal stresses in the crystal structure.

13.4 Outlook

The methodology used and partially developed in this thesis, could be used in the future to study different aspects of cementitious systems. For example the methodology used to study the portlandite-water interfaces could be used to study the effect of different additives, such as superplasticizers, on the hydration of cement and the colloidal behavior of cement. To understand how the different additives and components of cement influence the hydration and the colloidal behavior would allow a better control of the hydration process and the final properties of cement.

Additionally the study of the interaction between silicate species and different surfaces present in cementitious systems might help understand, which surfaces are more important for the nucleation and growth of C-S-H and what materials might consequently be suitable to use as seeds, to speed up the hydration process. This might e.g. allow a more extensive use of supplementary materials as one of the problems of their use is that they slow down the hydration.

A continuation of the started work on C-S-H might lead to a more complete understanding of the C-S-H structure. A good understanding of the atomistic C-S-H structure would mean that a better thermodynamic model could be developed, capable of predicting i.e. compositional changes of C-S-H with changing cement composition and temperature correctly. Additionally a better understanding of the role and properties C-S-H / pore solution interfaces might be possible.

13.5 Conclusion

In conclusion we can say that the application of atomistic simulation techniques to cementitious systems has been shown to be helpful in many areas. Although care has to be taken to validate simulations with experimental data wherever possible, simulation techniques can be

very helpful in developing and testing different theories to explain the atomistic mechanisms behind experimental observations. The current results both help explain previously observed experimental data, such as the poisoning of portlandite growth by silicates, and open up avenues for future research.

A Implementation Details and Validation of the Metropolis Monte Carlo Method

The Metropolis Monte Carlo method was implemented in the LAMMPS (version: 5 Dec 2010) code [Pli95]. Two additional classes were implemented. The first (*Metropolis_MC*) was subclass of *Integrate*, taking care of the actual Metropolis Monte Carlo routine, accepting and rejecting moves, using the Marsaglia random number integrator already implemented in LAMMPS. The input parameters of the *Metropolis_MC* class are the temperature and the random number seed.

The *Metropolis_MC* class does not actually change the configuration of the system. This is done by additional *Fix* classes. The one implemented here (*FixMcMove*) moves a certain number n_m of particles in the system in a random direction. The maximum size of the move can be chose for each direction (m_x^{max}, m_y^{max}, m_z^{max}) independently. Whether the moves are always the same size or randomly distributed between zero and the maximum move size can also be chosen. For increased accuracy, the random numbers for the *FixMcMove* class were produced by the *ranlxd2* random number generatro of the GNU scientific library [Gal09]. Good statistical properties for this random number generator have been reported in literature [SB98, MWKA07].

In theory any other moves, such as the creation and deletion of atoms for grand Canonical Monte Carlo calculations, can be added relatively easily by adding another *Fix* class.

The input format for the input parameters of the two additional LAMMPS classes is as follows:

```
#fix fix_name atom_group mc_move full/rand nm mx my mz seed
fix    mc_mov  all     mc_move  full 100 2e-2 2e-2 2e-2 1298

#run_style metropolis_mc temperature seed
run_style metropolis_mc 300 18905
```

The validity of the Monte Carlo was verified with the help of a test problem with a known

Table A.1: Total energy of the system E_{tot}, the ratio of particles in the potential well x_{well} and the minimum $min(x_{o_i})$ and maximum $max(x_{o_i})$ ratio of particles in the differnt octants.

	E_{tot} [eV]	x_{well} [-]	$min(x_{o_i})$ [-]	$max(x_{o_i})$ [-]
calculation	-11.96	0.666	0.124	0.127
expected	-11.95	0.667	0.125	0.125

solution. The test system was a spherical potential well with an energy of 1.79e-2 eV and a radius of 7.361 μm was placed in the middle of a cubic box, with a box length of 14.95 μm, containing 1000 non interacting particles. In other word the potential well occupied half the volume of the simulation box and at 300 ° K, the density of the particles inside the potential well should double the particle density outside the simulation box. This means that the total energy of the system should be -11.95 eV. Additionally, due to the symmetry of the system, the same number of particles should be found in each octant of the simulation box. All these properties were well reproduced by the Metropolis Monte Carlo calculations (table A.1).

B Implementation Details and Validation of the Long Range Potential for Linear Charge Distributions

The long range potential for linear charge distributions was implemented as a further extension of the LAMMPS (version: 5 Dec 2010) code [Pli95]. The long range potential was implemented as a subclass of *Fix*. There are a certain number of parameters that can be chosen:

- *frequency*: the frequency with which a new distribution profile is calculated (in number of steps). The frequency at which new distributions are calculated should be chosen such that the for each consecutive distribution profile is significantly different, otherwise the averaging is not very efficient. However a too large frequency means that the system has a large inertia as structural changes of the distribution will only be taken into account after a certain period.
- *n_dist*: the number of calculated distributions over which the final distribution is averaged. These first two parameters control the length of the "memory" of the system. In equilibrium the number of distributions over which to average can be chosen quite large. If however the system is still equilibrating this parameter should not be chosen too large.
- *dim*: The direction (x, y or z) in which the linear charge distribution is calculated.
- *lo, hi*: Lower and upper boundary between which the linear charge density is calculated.
- *n_bin*: The number of bins used for the calculation of the linear charge distribution. The higher this number, the finer the charge distribution but at the same time the larger the variance.
- *rc*: short range cutoff radius.
- *print*: An optional parameter that, if specified, controls the frequency with which the charge density, the total charge and the electrical potential are written to the standard output. If nothing is specified, nothing is written to the output.

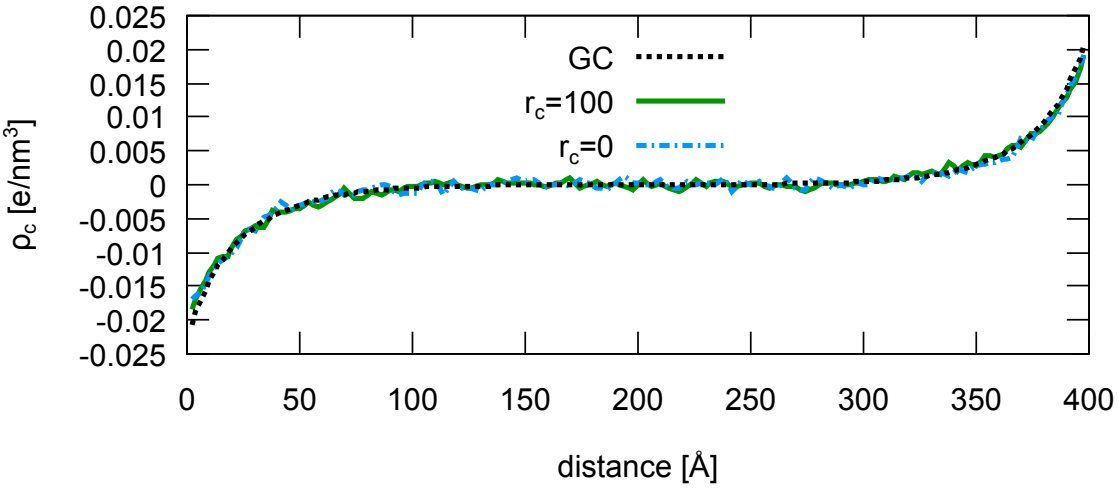

Figure B.1: Charge distribution for a test case according to the Gouy-Chapman (GC) theory and calculated with Metropolis Monte Carlo with a short range cutoff distance (r_c) of 100 Å and 0 Å respectively.

The input format for the input parameters of the long range potential for linear charge distributions is as follows:

```
#fix name group charge_lr_dist frequency n_dist dim lo hi n_bin rc [print]
fix long_range all charge_lr_dist 10000 100 x 0 400 100 100 100000
```

The validity of the long range potential for linear charge distributions was verified for a test case. The test system consisted of a 400x400x400 Å simulation box. The box contained 512 monovalent positive charges and 512 monovalent negative charges, in other words the concentration of both ions was 0.013 $\frac{mol}{l}$. Periodic boundary conditions were applied in y and z direction. In x direction the system was delimited on both sides by a hard wall. The wall on one side of the box carried a positive and on the other a negative surface charge of 0.05 $\frac{e}{nm^2}$. The ions in the system were essentially point ions, only interacting via coulomb forces.

For such a system the Gouy-Chapman mean field approximation should be valid [TV80]. This is indeed the case, the Metropolis Monte Carlo calculations reproducing both the charge density and the ionic densities with good accuracy (figures B.1 and B.2).

As the Gouy-Chapman theory is valid for the test case considered here, the choice of the short range cutoff should be unimportant. Indeed this is in agreement with our results as a short range cutoff 0 Å (no explicit ion-ion interactions) gave identical results to a cutoff radius of 100 Å (figures B.1 and B.2).

In summary the Metropolis Monte Carlo calculations for the chosen test case seem to confirm the validity of the implementation of the long range potential for linear charge distributions.

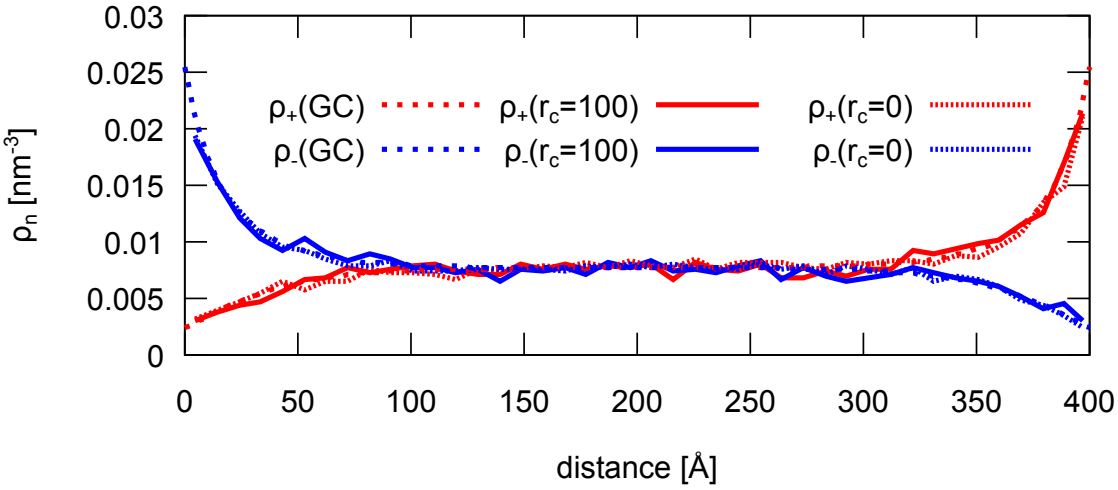

Figure B.2: Ionic distribution for a test case according to the Gouy-Chapman (GC) theory and calculated with Metropolis Monte Carlo with a short range cutoff distance (r_c) of 100 Å and 0 Å respectively.

C Parameters for the Different Force Fields

In the following appendix, the DL_POLY FIELD files with all force field parameters used for the different tested force fields are shown.

C.1 FF1: CLAYFF

```
UNITS eV
MOLECULES  5
O   CORE
NUMMOL      64
atoms       2
O            15.8000      -0.950    0    0    0
H             0.8000       0.425    0    0    0
bonds    1
harm 1 2 24.04831184 1.0
finish
CA  CORE
NUMMOL     160
atoms       1
CA           39.8800       1.050    0    0    0
finish
SI  CORE
NUMMOL     192
atoms       1
SI           27.9000       2.100    0    0    0
finish
OS  CORE
NUMMOL     512
atoms       1
OS           15.8000      -1.050    0    0    0
```

```
finish
WATER
NUMMOL      0
atoms       3
OW           15.8000       -0.820    0    0    0
HW            0.8000        0.410    0    0    0
HW            0.8000        0.410    0    0    0
bonds 2
harm 1 2 24.04831184 1.0
harm 1 3 24.04831184 1.0
angles 1
harm 2    1    3     1.986096767    109.47
finish
vdw      15
O       O       lj       6.7433e-3      3.165541
O       CA      lj       3.8364e-5      4.363622
O       SI      lj       2.3207e-5      3.233784
O       OS      lj       6.7433e-3      3.165541
O       OW      lj       6.7433e-3      3.165541
CA      CA      lj       2.1826e-7      5.561703
CA      SI      lj       1.3203e-7      4.431865
CA      OS      lj       3.8364e-5      4.363622
CA      OW      lj       3.8364e-5      4.363622
SI      SI      lj       7.9865e-8      3.302027
SI      OS      lj       2.3207e-5      3.233784
SI      OW      lj       2.3207e-5      3.233784
OS      OS      lj       6.7433e-3      3.165541
OS      OW      lj       6.7433e-3      3.165541
OW      OW      lj       6.7433e-3      3.165541
tbp       1
SI     O      H     shrm   0.176198166 109.4666667    2.5    2.5   4.0
CLOSE
```

C.2 FF2: Lewis and Catlow

```
UNITS eV
MOLECULES  5
O   CORE
NUMMOL      2
atoms       3
O            15.6000       0.800    0    0    0
```

```
O(S)          0.4000      -2.200
H             0.8000       0.400    0    0    0
shell         1   1
       1        2     74.9204
bonds         1
mors 2    3    7.0525    0.94285     3.1749
finish
CA  CORE
NUMMOL     1
atoms       1
CA           39.8800       2.000    0    0    0
finish
SI  CORE
NUMMOL     0
atoms       1
SI           27.9000       4.000    0    0    0
finish
OS  CORE
NUMMOL     0
atoms       2
OS           15.6000       0.86902    0    0    0
OS(S)         0.4000      -2.86902
shell         1   1
       1        2    74.92
finish
OW  CORE
NUMMOL      2045
atoms 4
   OW        15.8000       1.250
   OW(S)      0.2000      -2.050
   HW         1.0080       0.400
   HW         1.0080       0.400
shell    1    1
    1    2   209.4496
bonds         5
mors 2    3    6.203713 0.923670 2.220030
mors 2    4    6.203713 0.923670 2.220030
coul 2    3    0.5
coul 2    4    0.5
coul 3    4    0.5
angles   1
harm 3    2    4    4.19978   108.693195
```

```
finish
vdw      18
O(S)    O(S)    buck  22764.0000      0.1490     18.9700
O(S)    H       buck    436.7600      0.2500      2.5000
O(S)    CA      buck   2170.0000      0.2970      0.0000
O(S)    SI      buck    983.6000      0.3205     10.6600
O(S)    OS(S)   buck  22764.0000      0.1490     13.9400
O(S)    OW(S)   buck  22764.0000      0.1490     17.1400
O(S)    HW      buck    311.9700      0.2500      0.0000
H       OS(S)   buck    396.2700      0.2300      0.0000
CA      OS(S)   buck   1090.4000      0.3437      0.0000
CA      OW(S)   buck   1186.6000      0.2970      0.0000
SI      OS(S)   buck   1283.9000      0.3205     10.6616
OW(S)   SI      buck    983.5560      0.3205     10.6616
OS(S)   OS(S)   buck  22764.0000      0.1490     27.8790
OS(S)   OW(S)   buck  22764.0000      0.1490     28.9200
OS(S)   HW      buck    396.2700      0.2500      0.0000
OW(S)   OW(S)   12-6  39344.980000   42.150000 12.000000 6.000000
OW(S)   H       buck    396.2700      0.2500      0.0000
OW(S)   HW      buck    396.270000    0.250000   10.0000
tbp       3
O(S)   SI    O(S)    shrm   15.496300 109.4666667   1.8    1.8     3.2
OS(S)  SI    O(S)    shrm   15.496300 109.4666667   1.8    1.8     3.2
OS(S)  SI    OS(S)   shrm   15.496300 109.4666667   1.8    1.8     3.2
CLOSE
```

C.3 FF3: Freeman / TIP4P2005

```
UNITS eV
MOLECULES 8
HYDROXYL
NUMMOL     64
atoms 2
   O          16.000      -1.400
   H           1.008        .400
bonds     1
mors 1    2    7.052500    0.94290     3.174900
finish
CA  CORE
NUMMOL      160
atoms       1
```

```
CA           39.8800       2.000    0    0    0
finish
SI  CORE
NUMMOL      192
atoms 1
SI           28.0900       4.000    0    0    0
finish
OS  CORE
NUMMOL     512
atoms 1
OS           16.0000      -2.000    0    0    0
finish
MG  CORE
NUMMOL      0
atoms 1
MG           24.3050       2.000    0    0    0
finish
AL  CORE
NUMMOL       0
atoms 1
AL           26.9185       3.000    0    0    0
finish
K   CORE
NUMMOL        0
atoms 1
K            39.0983       1.000
finish
TIP4P/2005 water
NUMMOL      0
atoms 4
   OW       15.9996       0.0000     0    0    0
   OM       0.00000      -1.1128     0    0    0
   HW       1.00080       0.5564     0    0    0
   HW       1.00080       0.5564     0    0    0
rigid bodies 1
   4    1    2    3    4
FINISH
vdw      25
SI      OS      buck   1283.9073      0.3205     10.6616
OS      OS      buck  22764.0000      0.1490     27.8800
OS      MG      buck   1428.5000      0.2945      0.0000
SI      O       buck    983.5560      0.3205     10.6616
```

```
OS      O       buck  22764.0000      0.1490     13.9400
OS      OW      buck  22764.0000      0.1490     28.9200
MG      O       buck    941.5000      0.2945      0.0000
O       O       buck  16372.3300      0.2130      0.0000
O       OW      nm    0.0013000   9           6           4.63
O       H       nm    0.0073000   9           6           2.71
OS      H       nm    0.0073000   9           6           2.71
OS      HW      buck    396.2700      0.2500      0.0000
H       OW      nm    0.0555555   9           6           1.81712
OW      AL      buck    584.3000      0.2991      0.0000
O       AL      buck   1022.3000      0.2991      0.0000
OS      AL      buck   1460.3000      0.2991      0.0000
SI      OW      buck   1283.5560      0.3205     10.6616
MG      OW      buck    454.5000      0.2945      0.0000
OS      K       buck  65269.7100      0.2134      0.0000
O       K       buck  45688.8000      0.2134      0.0000
OW      K       buck  26107.9000      0.2134      0.0000
O       CA      buck   2251.0500      0.2970      0.0000
CA      OS      buck   1090.4000      0.3437      0.0000
CA      OW      buck   1186.6000      0.2970      0.0000
OW      OW      lj        0.0080314     3.1589
tbp       3
OS    SI    OS    shrm   15.496300 109.4666667    1.6    1.6    3.0
O     SI    OS    shrm   15.496300 109.4666667    1.6    1.6    3.0
O     SI    O     shrm   15.496300 109.4666667    1.6    1.6    3.0
CLOSE
```

C.4 Final Force Field

```
UNITS eV
MOLECULES 8
HYDROXYL
NUMMOL     36
atoms 2
   O          16.000      -1.400
   H           1.008        .400
bonds     1
mors 1    2    7.052500    0.94290     3.174900
finish
CA  CORE
NUMMOL      72
```

```
atoms       1
CA           39.8800       2.000    0    0    0
finish
SI  CORE
NUMMOL      108
atoms 1
SI           28.0900       4.000    0    0    0
finish
OS  CORE
NUMMOL     270
atoms 1
OS           16.0000      -2.000    0    0    0
finish
MG  CORE
NUMMOL      0
atoms 1
MG           24.3050       2.000    0    0    0
finish
AL  CORE
NUMMOL       0
atoms 1
AL           26.9185       3.000    0    0    0
finish
K   CORE
NUMMOL        0
atoms 1
K            39.0983       1.000
finish
TIP4P/2005 water
NUMMOL      90
atoms 4
   OW       15.9996      0.0000     0    0    0
   OM       0.00000     -1.1128     0    0    0
   HW       1.00080      0.5564     0    0    0
   HW       1.00080      0.5564     0    0    0
rigid bodies 1
   4    1    2    3    4
FINISH
vdw      25
SI      OS      buck   1283.9073      0.3205     10.6616
OS      OS      buck  22764.0000      0.1490     27.8800
OS      MG      buck   1428.5000      0.2945      0.0000
```

```
SI      O       buck    983.5560      0.3205     10.6616
OS      O       buck  22764.0000      0.1490     13.9400
OS      OW      buck  22764.0000      0.1490     28.9200
MG      O       buck    941.5000      0.2945      0.0000
O       O       buck  22764.0000      0.1490      6.9700
O       OW      nm    0.0013000   9           6           4.63
O       H       nm    0.0073000   9           6           2.71
OS      H       nm    0.0073000   9           6           2.71
OS      HW      buck    396.2700      0.2500      0.0000
H       OW      nm    0.0555555   9           6           1.81712
OW      AL      buck    584.3000      0.2991      0.0000
O       AL      buck   1022.3000      0.2991      0.0000
OS      AL      buck   1460.3000      0.2991      0.0000
SI      OW      buck   1283.5560      0.3205     10.6616
MG      OW      buck    454.5000      0.2945      0.0000
OS      K       buck  65269.7100      0.2134      0.0000
O       K       buck  45688.8000      0.2134      0.0000
OW      K       buck  26107.9000      0.2134      0.0000
O       CA      buck   2251.0500      0.2970      0.0000
CA      OS      buck   1090.4000      0.3437      0.0000
CA      OW      buck   1186.6000      0.2970      0.0000
OW      OW      lj        0.0080314     3.1589
tbp       5
OS    SI    OS    shrm   15.496300 109.4666667   1.6    1.6    3.0
O     SI    OS    shrm   15.496300 109.4666667   1.6    1.6    3.0
O     SI    O     shrm   15.496300 109.4666667   1.6    1.6    3.0
SI    OS    SI    shrm   15.496300 132.0000000   1.6    1.6    3.0
SI    O     H     shrm   15.496300 141.5000000   1.6    1.2    2.6
CLOSE
```

D Data Treatment Methods and Additional Data for the Portlandite Morphology Characterization

D.1 Thermogravimetric Analysis

The following R script was used for the treatment of the TGA data:

```
library(Hmisc)
library(KernSmooth)

bwd <- 10
sp <- 0.05
cutoff <- 0.5

weight <- read.table("tga/weight.txt", header=TRUE)
d <- read.table("tga/deriv.txt", header=TRUE)
x <- d$Ts
y <- -d$Value

approx<-loess(Value~Ts, weight, span=sp)
interp<-locpoly(x, y, bandwidth=bwd)

peak_pos   <- peaks( interp$y, span=3)
valley_pos <- peaks(-interp$y, span=3)
peaks.x <- interp$x[peak_pos]
peaks.y <- interp$y[peak_pos]
valleys.x <- interp$x[valley_pos]
valleys.y <- interp$y[valley_pos]

if(peaks.x[1] > valleys.x[1]){
  valleys.x <- valleys.x[-1]
```

```
  valleys.y <- valleys.y[-1]
}

if(peaks.x[length(peaks.x)] < valleys.x[length(valleys.x)]){
  valleys.x <- valleys.x[-length(valleys.x)]
  valleys.y <- valleys.y[-length(valleys.y)]
}

valleys.x <- c(x[1], valleys.x, x[length(x)])
valleys.y <- c(y[1], valleys.y, y[length(y)])

losses<- predict(approx, valleys.x[-length(valleys.x)])
  -predict(approx, valleys.x[-1])

peaks.x <- peaks.x[losses>cutoff]
valleys.x <- valleys.x[c(FALSE, losses>cutoff) | c(losses>cutoff, FALSE)]
peaks.y <- peaks.y[losses>cutoff]
valleys.y <- valleys.y[c(FALSE, losses>cutoff) | c(losses>cutoff, FALSE)]
losses <- losses[losses>cutoff]

res<-list()
res$temp<-peaks.x
res$loss<-losses

res
write.table(res, file="tga/out.txt", row.names=FALSE)

pdf("tga/TGA_losses.pdf", width=8.0, height=10.0)
par(mfrow=c(2,1))

plot(weight$Ts,weight$Value, lwd=1, pch=".",
  main="Weight",
  xlab="Temperature [deg C]", ylab="weight loss [%]")
lines(predict(approx, interp$x)~interp$x, col="red")
abline(h=predict(approx, valleys.x[1]), lty="dotted", lwd=2)
for(i in 2:length(valleys.x)){
   abline(h=predict(approx, valleys.x[i]), lty="dotted", lwd=2)
}

plot(x,y, lwd=1, pch=".",
  main="Weight loss rate",
  xlab="Temperature [deg C]", ylab="weight loss rate [1/s]")
```

```
abline(h=0, lty="dotted")
lines(interp$y~interp$x, col="red", lty="dotted", lwd=2)
points( peaks.x, peaks.y, pch=19, col="red")
points( valleys.x, valleys.y, pch=19, col="blue")

dev.off()
```

The *peaks* function was defined according to the fuction found on the R help pages:

```
# Find "peaks" in array.
# http://finzi.psych.upenn.edu/R/Rhelp02a/archive/33097.html
#
# peaks(c(1,4,4,1,6,1,5,1,1),3)
# [1] FALSE FALSE  TRUE FALSE  TRUE FALSE  TRUE

peaks <- function(series,span=3)
{
  z <- embed(series, span)
  s <- span%/%2
  v <- max.col(z, "first") == 1 + s   # take first if a tie
  result <- c(rep(FALSE,s),v)
  result <- result[1:(length(result)-s)]
  result
}
```

The full set of data used for the statistical analysis can be seen in table D.1.

D.2 Particle Size Distribution Measurement with Laser Diffraction

The following R script was used to treat the particle size distribution data, using the same *peaks* function as described above:

```
library(Hmisc)
library(KernSmooth)

bwd <- 0.1
cutoff <- 0.005
d <- read.table("deconv/in.txt", header=FALSE)

x <- log10(0.5*(d$V1 + d$V3))
```

Table D.1: Full set of data used for the statistical analysis of the thermogravimetric analysis.

Sample	S [mM]	Si [mM]	Al [mM]	series	t_{precip} [months]	Cl [M]	NO_3 [M]	$Ca(OH)_2$ [%]	$CaCO_3$ [%]	other [%]
r1	0	0	0	1	0.0013	0.2	0	89.2	11.4	0.0
r11	100	0	0	1	0.0013	0.2	0	96.2	4.3	0.0
r2	100	1	0	1	0.0013	0.2	0	87.7	11.8	0.5
r3	0	0	1	1	0.0013	0.2	0	90.6	5.2	4.1
r8	100	0	1	1	0.0013	0.2	0	83.2	8.8	8.0
r6	0	1	1	1	0.0013	0.2	0	83.1	9.5	7.4
r10	100	1	1	1	0.0013	0.2	0	68.3	6.1	25.5
r7	0	0	3	1	0.0013	0.2	0	76.7	9.2	14.1
r5	100	0	3	1	0.0013	0.2	0	45.8	7.1	47.1
r4	0	1	3	1	0.0013	0.2	0	70.5	13.0	16.5
r9	100	1	3	1	0.0013	0.2	0	40.6	2.5	57.0
b1h	0	0	0	0	0.0013	0.2	0	91.6	4.7	3.7
b1hs	100	0	0	0	0.0013	0.2	0	93.8	5.4	0.8
b2m	0	0	0	0	2	0.2	0	90.8	5.4	3.8
b2ms	100	0	0	0	2	0.2	0	64.9	4.4	30.7
b1hns00001	0	1	0	0	0.0013	0.2	0	90.7	4.7	4.6

```
y <- d$V2/100

interp<-locpoly(x, y, bandwidth=bwd)

derivative1 <- locpoly(x, y, bandwidth=bwd, drv=1)
derivative2 <- locpoly(x, y, bandwidth=bwd, drv=2)

##### 1st Derivative

peaks.Deriv1   <- peaks( derivative1$y, span=3)
valleys.Deriv1 <- peaks(-derivative1$y, span=3)
peaks.dv1x <- derivative1$x[peaks.Deriv1]
peaks.dv1y <- derivative1$y[peaks.Deriv1]
valleys.dv1x <- derivative1$x[valleys.Deriv1]
valleys.dv1y <- derivative1$y[valleys.Deriv1]

if(peaks.dv1x[1] > valleys.dv1x[1]){
  valleys.dv1x <- valleys.dv1x[-1]
  valleys.dv1y <- valleys.dv1y[-1]
}

if(peaks.dv1x[length(peaks.dv1x)] > valleys.dv1x[length(valleys.dv1x)]){
  peaks.dv1x <- peaks.dv1x[-length(peaks.dv1x)]
  peaks.dv1y <- peaks.dv1y[-length(peaks.dv1y)]
```

```
}

tmp <- (peaks.dv1y - valleys.dv1y) > cutoff

peaks.dv1y<-peaks.dv1y[tmp]
peaks.dv1x<-peaks.dv1x[tmp]
valleys.dv1y<-valleys.dv1y[tmp]
valleys.dv1x<-valleys.dv1x[tmp]

# Approximate location of peak and valley
peaks.dv1x
peaks.dv1y

s.approx <- (valleys.dv1x - peaks.dv1x)/2
# Approximate standard deviation
s.approx

##### 2nd Derivative

peaks.Deriv2   <- peaks( derivative2$y, span=3)
valleys.Deriv2 <- peaks(-derivative2$y, span=3)
peaks.dv2x <- derivative2$x[peaks.Deriv2]
peaks.dv2y <- derivative2$y[peaks.Deriv2]
valleys.dv2x <- derivative2$x[valleys.Deriv2]
valleys.dv2y <- derivative2$y[valleys.Deriv2]

if(peaks.dv2x[1] > valleys.dv2x[1]){
  valleys.dv2x <- valleys.dv2x[-1]
  valleys.dv2y <- valleys.dv2y[-1]
}

if(peaks.dv2x[length(peaks.dv2x)] < valleys.dv2x[length(valleys.dv2x)]){
  valleys.dv2x <- valleys.dv2x[-length(valleys.dv2x)]
  valleys.dv2y <- valleys.dv2y[-length(valleys.dv2y)]
}

tmp <- (peaks.dv2y[-1] - valleys.dv2y) > 10*cutoff &
   (peaks.dv2y[-length(peaks.dv2y)] - valleys.dv2y) > 10*cutoff
tmpv <- c(TRUE, (peaks.dv2y[-1] - valleys.dv2y) > 10*cutoff) &
   c((peaks.dv2y[-length(peaks.dv2y)] - valleys.dv2y) > 10*cutoff, TRUE)

if(sum(!tmp)==sum(!tmpv)){
```

```
peaks.dv2y<-peaks.dv2y[tmpv]
peaks.dv2x<-peaks.dv2x[tmpv]
valleys.dv2y<-valleys.dv2y[tmp]
valleys.dv2x<-valleys.dv2x[tmp]
}else{
tmp <- (peaks.dv2y[-1] - valleys.dv2y) > 10*cutoff
tmpv <- c(TRUE, (peaks.dv2y[-1] - valleys.dv2y) > 10*cutoff)
peaks.dv2y<-peaks.dv2y[tmpv]
peaks.dv2x<-peaks.dv2x[tmpv]
valleys.dv2y<-valleys.dv2y[tmp]
valleys.dv2x<-valleys.dv2x[tmp]
tmp <- (peaks.dv2y[-length(peaks.dv2y)] - valleys.dv2y) > 10*cutoff
tmpv <- c((peaks.dv2y[-length(peaks.dv2y)] - valleys.dv2y) > 10*cutoff,
            TRUE)
peaks.dv2y<-peaks.dv2y[tmpv]
peaks.dv2x<-peaks.dv2x[tmpv]
valleys.dv2y<-valleys.dv2y[tmp]
valleys.dv2x<-valleys.dv2x[tmp]
}

# Approximate location of mean of normal distribution:
mu.approx <-  valleys.dv2x
mu.approx

# Attempt non-linear curve fit to extract the parameters
fit_form <- "y ~ "
start_val <- list()

for(i in 1:(min(length(s.approx),length(mu.approx)-1))){
       fit_form <- paste(fit_form,
         "(w",i,"/s",i,")*exp(-(x-m",i,")^2/(2*s",i,"^2)) + ", sep="")
       start_val[[paste("w",i, sep="")]] <- (1/sqrt(2*pi)) / s.approx[i]
       start_val[[paste("s",i, sep="")]] <- s.approx[i]
       start_val[[paste("m",i, sep="")]] <- mu.approx[i]
}

i<-min(length(s.approx),length(mu.approx))
fit_form <- paste(fit_form,
  "(w",i,"/s",i,")*exp(-(x-m",i,")^2/(2*s",i,"^2))", sep="")
start_val[[paste("w",i, sep="")]] <- (1/sqrt(2*pi)) / s.approx[i]
start_val[[paste("s",i, sep="")]] <- s.approx[i]
start_val[[paste("m",i, sep="")]] <- mu.approx[i]
```

```
fit.dens <- nls(as.formula(fit_form),
                start=start_val,
        control=nls.control(tol=1E-5, minFactor=1/1024),
        trace=TRUE)

summary(fit.dens)

# Means (mu values)
tmp <- coef(fit.dens)[3*1:i]
10^tmp

#Output
pdf("deconv/Deconv.pdf", width=8.0, height=10.0)
par(mfrow=c(3,1))

plot(x,y, lwd=3, pch="*",
  main="Initial Distribution",
  xlab="Particle Size [log(um)]", ylab="Probability Density")
abline(h=0, lty="dotted")
lines(interp$y~interp$x, col="red", lty="dotted")
lines(predict(fit.dens)~x, col="red")

plot(derivative1$x,derivative1$y, type="l",
  main="1st Derivative", xlab="x", ylab="y'")
abline(h=0, lty="dotted")
points( peaks.dv1x, peaks.dv1y, pch=19, col="red")
points( valleys.dv1x, valleys.dv1y, pch=19, col="blue")

plot(derivative2$x,derivative2$y, type="l",
  main="2nd Derivative", xlab="x", ylab="y''")
abline(h=0, lty="dotted")
points( peaks.dv2x, peaks.dv2y, pch=19, col="red")
points( valleys.dv2x, valleys.dv2y, pch=19, col="blue")

sink("deconv/out.txt")
summary(fit.dens)
sink()

dev.off()
```

The full set of data used for the statistical analysis can be seen in table D.2.

Table D.2: Full set of data used for the statistical analysis of the particle size distribution measurements.

Sample	S [mM]	Si [mM]	Al [mM]	series	t_{precip} [months]	Cl [M]	NO_3 [M]	d[v,50] [μm]
r1	0	0	0	1	0.0013	0.2	0	0.74
r11	100	0	0	1	0.0013	0.2	0	0.86
r12	0	1	0	1	0.0013	0.2	0	4.03
r2	100	1	0	1	0.0013	0.2	0	5.52
r3	0	0	1	1	0.0013	0.2	0	9.48
r8	100	0	1	1	0.0013	0.2	0	5.49
r6	0	1	1	1	0.0013	0.2	0	11.85
r10	100	1	1	1	0.0013	0.2	0	20.38
r7	0	0	3	1	0.0013	0.2	0	7.25
r5	100	0	3	1	0.0013	0.2	0	8.85
r4	0	1	3	1	0.0013	0.2	0	10.72
r9	100	1	3	1	0.0013	0.2	0	19.85
b1h	0	0	0	0	0.0013	0.2	0	0.84
b1hs	100	0	0	0	0.0013	0.2	0	1.20
b1hc	0	0	0	0	0.0013	0.3	0	0.68
bn1h	0	0	0	0	0.0013	0	0.2	0.67
b2m	0	0	0	0	2	0.2	0	0.76
b2ms	100	0	0	0	2	0.2	0	0.98

D.3 Wulff Shape

To digitalize the observed morphology of a particle the visible edges of the particles were retraced on the image (image D.1). The corners of the particles, corresponding to the intersection of the traced edges, were then recorded. Based on the positions of the points an input file was then created which could be read into the modified version of the Wulffman program [RMC98]. The input file consisted of the number of corners on the first line, followed by the coordinates of each corner. This is then followed by the number of facets on the next line and the specification of each facet. For each facet first the number of corners is specified, followed by the index of each corner belonging to the facet:

```
10
4.955   5.596
9.27    0.876
16.146  2.461
18.303  9.169
17.831  10.416
13.449  15.135
6.236   13.551
4.315   7.382
```

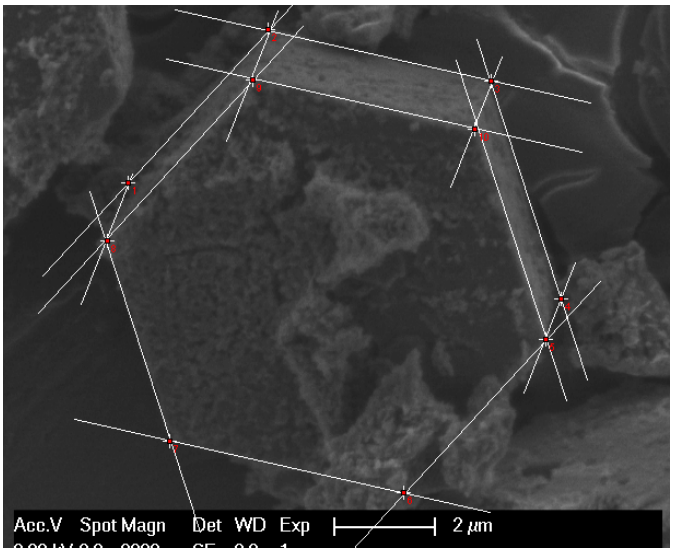

Figure D.1: SEM image of a particle (sample bsa1_1h) with retraced edges and corner positions used for the digitalization.

```
8.798    2.427
15.64    3.944
4
4 0 1 8 7
4 1 2 9 8
4 2 3 4 9
6 4 5 6 7 8 9
```

The complete set of particles thus analyzed as well as the results of the fit can be seen in table D.3

D.4 Reproducibility of Results

In order to judge the reproducibillity of the experimental coprecipitation results for portlandite, the results of two series of experiments, done according to the same protocol but over a year apart by different people, were compared. The first series of experiments (B1H series) was done by Nicolas Ruffray in 2010 and the second series (r series) was done by Amirreza Kiani in 2012. The series done by Amirreza Kiani was randomized to minimize the influence of parasitic effects. The results of two samples of each series, a control experiment and an experiment to which 0.1 $\frac{mol}{l}$ Na_2SO_4 was added, were compared to each other.

The SEM images for the sulfate containing experiment (figure D.2) reveal very similar morphologies for the two series of experiments. The SEM sample of the control experiment appeared to be contaminated as the observed particles did not correspond to the measured

Table D.3: Full set of data used for the statistical analysis of the relative interfacial energies.

sample	S [$\frac{mmol}{l}$]	Si [$\frac{mmol}{l}$]	Al [$\frac{mmol}{l}$]	Cl [$\frac{mol}{l}$]	NO3 [$\frac{mol}{l}$]	$\gamma^{rel}_{10.0}$	$\gamma^{rel}_{10.1}$
B1H	0	0	0	0.2	0	0.63	0.72
B1H	0	0	0	0.2	0	0.59	0.62
B1H	0	0	0	0.2	0	0.58	0.65
B1H	0	0	0	0.2	0	0.59	0.66
B1H	0	0	0	0.2	0	0.62	0.66
B1H	0	0	0	0.2	0	0.62	0.67
B1H	0	0	0	0.2	0	0.57	0.71
B1H	0	0	0	0.2	0	0.56	0.63
B1H	0	0	0	0.2	0	0.53	0.58
B1H	0	0	0	0.2	0	0.51	0.56
B1HC	0	0	0	0.30	0	0.77	0.79
B1HC	0	0	0	0.30	0	0.79	0.78
B1HC	0	0	0	0.30	0	0.75	0.76
B1HC	0	0	0	0.30	0	0.71	0.77
B1HC	0	0	0	0.30	0	0.73	0.79
B1HC	0	0	0	0.30	0	0.55	0.63
B1HC	0	0	0	0.30	0	0.72	0.73
B1HC	0	0	0	0.30	0	0.68	0.75
B1HC	0	0	0	0.30	0	0.51	0.64
B1HC	0	0	0	0.30	0	0.59	0.63
BN1H	0	0	0	0.00	0.2	0.75	0.75
BN1H	0	0	0	0.00	0.2	0.77	0.74
BN1H	0	0	0	0.00	0.2	0.65	0.67
BN1H	0	0	0	0.00	0.2	0.61	0.66
BN1H	0	0	0	0.00	0.2	0.81	0.75
BN1H	0	0	0	0.00	0.2	0.72	0.69
BN1H	0	0	0	0.00	0.2	0.96	0.83
BN1H	0	0	0	0.00	0.2	0.62	0.66
BN1H	0	0	0	0.00	0.2	0.83	0.88
B1HS	100	0	0	0.20	0	3.22	>3.3
B1HS	100	0	0	0.20	0	2.78	>2.9
B1HS	100	0	0	0.20	0	2.99	>3.0
B1HS	100	0	0	0.20	0	2.35	>2.5
B1HS	100	0	0	0.20	0	2.89	>3.0
B1HS	100	0	0	0.20	0	3.28	>3.3
B1HS	100	0	0	0.20	0	2.60	>2.7
B1HS	100	0	0	0.20	0	3.95	>3.9
B1HS	100	0	0	0.20	0	3.03	>3.1
B1HS	100	0	0	0.20	0	3.82	>3.8
bsa1_1h	100	0	1	0.20	0	1.99	>2.2
bsa1_1h	100	0	1	0.20	0	1.99	>2.2
bsa1_1h	100	0	1	0.20	0	2.56	>2.7
r8	100	0	1	0.20	0	2.87	>3.0
r8	100	0	1	0.20	0	2.94	>3.0
r10	100	1	1	0.20	0	3.43	>3.4

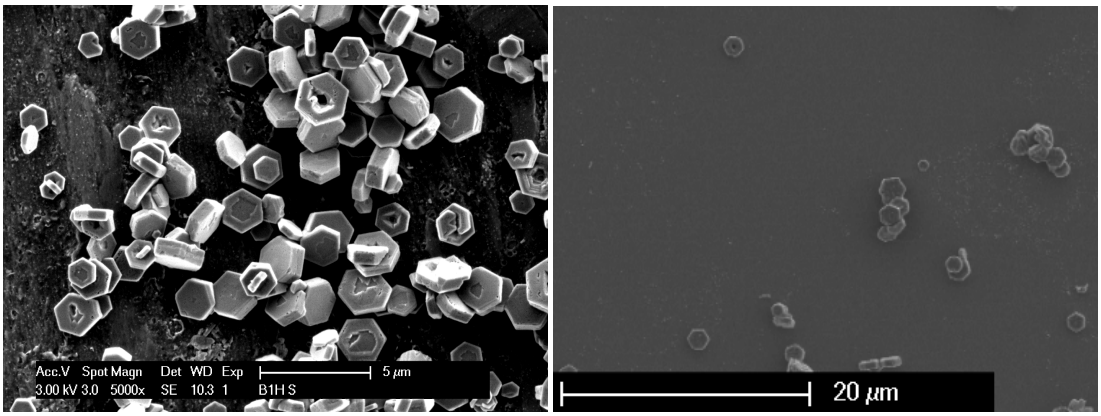

(a) (b)

Figure D.2: SEM image of two different samples of portlandite particles produced by coprecipitation according to the same protocol (initial concentration: 0.1 $\frac{mol}{l}$ $CaCl_2$ + 0.2 $\frac{mol}{l}$ $NaOH$ + 0.1 $\frac{mol}{l}$ Na_2SO_4, 1h precipitation time).

particle size distribution. However previous results indicate a good reproducibility of the particle shape of the control experiment as well 5.8b. To further quantify the reproducibility the more quantitative analysis methods, TGA and PSD, were compared.

For the measurements of the particle size distribution the exact protocol used varied slightly between the series. Nicolas Ruffray (B1H series) added polyacetic acid (PAA) to the powder suspension to sterically stabilize the particles. However later experiments revealed that the addition of PAA seemed to lead to a significant change of the opacity of the dispersion indicating some process, such as secondary precipitation of a polymer phase, was happening upon PAA addition. Therefore for the PSD measurement done by Amirreza Kiani (r series) no PAA was added. The secondary product formed when PAA is added can also be seen from the measured particle size distributions (see figure D.3). Compared to the r series, the B1H series of experiments contain an additional peak at around 4 μm. Consequently this additional peak for the PAA samples was excluded from analysis. For the sulfate containing experiments (see figure D.3b) the additional PAA peak is convoluted with a secondary peak form the portlandite particles. The two peaks could not be deconvoluted with our deconvolution method (see section 5.1.2). Due to a lack of alternatives the second portlandite peak was estimated as having the same weight as the first peak and the same median as the combined second portlandite and PAA peak. This leads to an additional error for the PSD measurements of the sulfate containing samples of the B1H series.

For the clearly defined portlandite peaks, the volumetric median was similar for the two series of experiments. For the control experiment the estimated $d[v,50]$ was 0.84 μm for the B1H series and 0.74 μm for the r series. For the first peak of the sulfate containing sample the estimated $d[v,50]$ was 0.35 μm for the B1H series and 0.44 μm for the r series. Since the size distribution is generally following a log-normal distribution rather than a normal, the standard

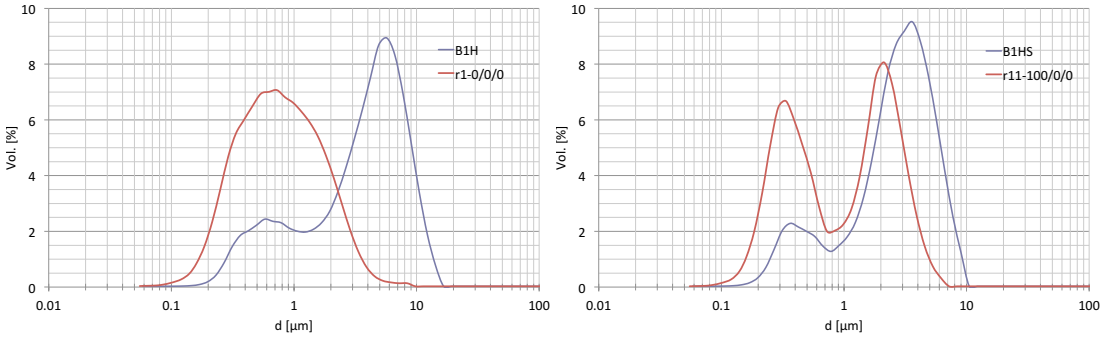

(a) (b)

Figure D.3: Reproducibility of particle size distribution measurement for the control experiments (0.1 $\frac{mol}{l}$ $CaCl_2$ + 0.2 $\frac{mol}{l}$ $NaOH$) (a) and the sulfate containing experiments (0.1 $\frac{mol}{l}$ $CaCl_2$ + 0.2 $\frac{mol}{l}$ $NaOH$ + 0.1 $\frac{mol}{l}$ Na_2SO_4) (b). The experiments were done over a year apart by different people. For the B1H series the portlandite powder was dispersed in a saturated $Ca(OH)_2$ solution and stabilized with polyacetic acid (PAA).

deviation was determined in the logarithmic scale. A standard deviation of 0.039 log(μm) and of 0.072 log(μm) was estimated for the unconvoluted peak of the control and the sulfate samples respectively.

The TGA weight loss curve for the four experiments can be seen in figure D.4. The measurement seem to be in relatively good agreement. The composition by weight of the control sample is estimated to be 91.5 % portlandite, 4.7 % calcite and 3.7 % other phases for the B1H series and 89.2 % portlandite, 11.4 % calcite and 0.0 % other phases for the r series of experiments. For the sulfate containing samples the composition is estimated to be 93.8 % portlandite, 5.4 % calcite and 0.8 % other phases for the B1H series and 96.2 % portlandite, 4.3 % calcite and 0.0 % other phases for the r series. This leads to estimated standard deviations in the region of 0.6-4.7 %.

D.5 Statistical Analysis of Results

The complete set of data from TGA and PSD measurements as well as from the $\frac{\gamma_{hk.l}}{\gamma_{00.1}}$ estimation form the SEM image analysis was treated with multiple linear regression using the least squares method to estimate the statistically relevant factors. The model formula for the linear model can be described by equation D.1 where $\vec{Y} = \{Y_i\}$ are the response variables i.e. the measured values of e.g. $d[v,50]$, $\bar{x} = \{x_{i,j}\}$ are the predictors i.e. the relevant states of the system such as the sulfate content, the aluminate content etc., $\vec{\epsilon} = \{\epsilon_i\}$ are random fluctuations and $\bar{\beta} = \{\beta_{i,j}\}$ are the unknown parameters that allow a prediction of the responses in function of the predictors. Both the parameters $\vec{\beta}$ and the random fluctuations $\vec{\epsilon}$ are a priori unknown. The parameters can be estimated by the least squares method (see equation D.2). Once the parameters are known, the standard deviation of the ϵ_i can be estimated as well (see equation

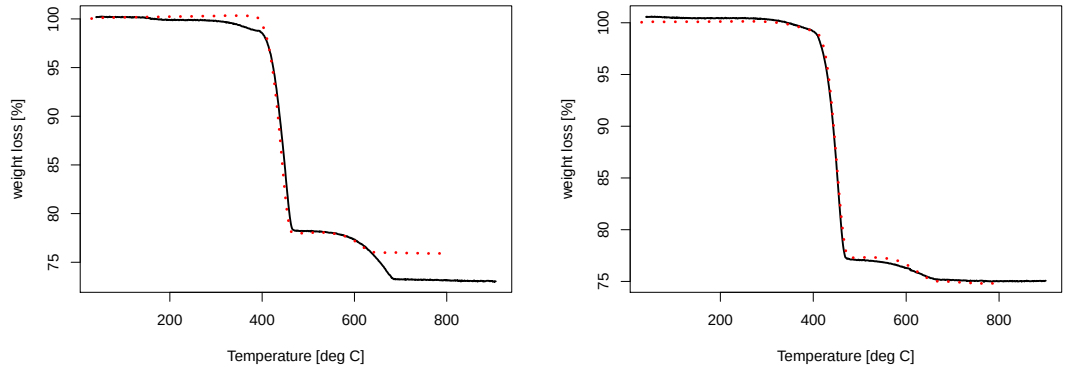

(a) (b)

Figure D.4: Reproducibility of TGA measurements for the control experiments (0.1 $\frac{mol}{l}$ $CaCl_2$ + 0.2 $\frac{mol}{l}$ $NaOH$, black line: sample r1_0-0-0, red dotted line sample b1h) (a) and the sulfate containing experiments (0.1 $\frac{mol}{l}$ $CaCl_2$ + 0.2 $\frac{mol}{l}$ $NaOH$ + 0.1 $\frac{mol}{l}$ Na_2SO_4, black line: sample r11_100-0-0, red dotted line sample b1hs) (b). The experiments were done over a year apart by different people.

D.3).

$$Y_i = \beta_1 \cdot x_{i,1} + \beta_2 \cdot x_{i,2} + \ldots + \beta_p \cdot x_{i,p} + \epsilon_i \tag{D.1}$$

$$\begin{aligned} \vec{\beta}^{est} &= \arg\min_{\vec{\beta}} \left\| \vec{Y} - \bar{x}\vec{\beta} \right\|^2 = \arg\min \left\| \vec{r}(\vec{\beta}) \right\|^2 \\ &= \left(\bar{x}^T \bar{x}\right)^{-1} \bar{x}^T \vec{Y} \end{aligned} \tag{D.2}$$

$$\sigma^{est} = \sqrt{\frac{1}{n-p} \sum_{i=1}^{n} r_i^2} \tag{D.3}$$

The statistical relevance of each predictor $\vec{x}_j$ (e.g. whether the precipitation time has an influence on the size of the particles) can then be calculated by estimating the probability (P-value) that the parameter β_j was estimated as β_j^{est} under the assumption that $\beta_j = 0$ (so called null-hypothesis). This is the so called t-test. Only predictors with a P-value of less than 0.05 (i.e. an estimated probability of less than 5 % for predicting β_j^{est} under the null-hypothesis) were considered to be statistically relevant. Additionally the most adapted subset of predictors

can be selected by estimating the mean square error on the predictions. The model with the smallest estimated mean squared error on the predictions, that only takes into account predictors with a P value of less than 0.05, was finally selected and is discussed here.

The underlying assumption for the use of the linear model are the following:

- The model used for the linear regression is correct. In other words the random fluctuations ϵ_i have an expected average value of 0 ($E[\epsilon_i] = 0$ for all i).
- All predictors $x_{i,j}$ are exact and could be measured exactly.
- The variance of the errors is constant ($Var(\epsilon_i) = \sigma^2$ for all i).
- The errors are uncorrelated.
- The errors ϵ_i are jointly normally distributed.

If any of these assumptions are significantly wrong the multiple linear regression can give erroneous results and other methods should be considered.

The second assumption is evidently always slightly violated but if the errors on the predictors x_i are much smaller than the error on the response variable Y_i, this should not introduce a big error. The assumption that the errors are uncorrelated is probably fulfilled. There might however be an effect of e.g. the changing ambient conditions with the weather which could lead to correlated errors. Such effects can sometimes be seen by looking at the residuals in function of the measuring date. The other model assumptions can be tested by looking at the calculated residuals and checking the normality of their distribution e.g. with the so called Q-Q plot or by looking at their distribution as a function of the different predictor variables to check for missing, non-linear terms and a non constant standard deviation.

For the particle size distribution the quantity considered for the linear regression was the logarithm of the median $d[v,50]$ of the main peak. As discussed previously, the additional peak coming from the PAA for the B1H series of experiments was not considered in the determination of the main peak. In general the main peak was clearly identifiable, except for the samples containing 100 mM of Na_2SO_4 as the only addition. Those samples showed a bimodal distribution with two equivalent peaks. Since the two peaks also had similar widths, the mid-distance between the two peaks in logarithmic scale was used for the statistical analysis instead of the $d[v,50]$ of one of the peaks.

The reason for using the logarithm of $d[v,50]$ was that the measured size distributions were log-normal rather than normal. Consequently the normality of the random fluctuations (one of the assumptions of the linear model) can only be assumed in the logarithmic scale.

A set of 11 predictors were initially considered: the sulfate S, silicate Si, aluminate Al concentration in mM, the chloride Cl and nitrate NO_3 concentration in M, the series, the precipitation

time t in months, the sulfate concentration times the time $S \cdot t$ as well as the different combination of ions: $Si \cdot S$, $Si \cdot Al$ and $S \cdot Al$. A set of 18 data points on 18 samples was used for the fitting (see appendix D.2). The results of the fit are discussed in sections 5.3.2. However there appear to be significant violations of the assumptions of the linear model which means that the results have to be treated with care. The biggest flaw of the model seems to be the assumption of linearity. We can see clearly from figure D.5b, showing the residuals in function of the aluminate concentration, that there are non-linear effects. However from the current set of data it is not possible to estimate the real functional form of the influence of aluminates on the particle size. The problems of the linear model can also be seen from the unrealistically high estimated standard deviation of the random fluctuations σ^{est} as well as the bad correspondence between model and measurements (see figure 5.11a). The overestimated σ^{est} might mask other statistically significant effects. However the most important influence on the particle size seems to come form the concentration of silicates and the concentration of aluminates.

The same set of 11 predictors was used to estimate the influence on the phase composition of the powder. The weight percentage of calcite as well as the weight percentage of phases other than portlandite and calcite, determined by TGA, was studied with least squares linear regression. Again the full data set of 19 measurements on 19 samples can be found in table D.1. The linear combinations of $S \cdot t$ was included since it has been observed that the precipitation of sulfate phases is retarded in the coprecipitation experiments (see section 5.3.4). No other phases than portlandite and calcite are expected for the control system. Therefore the intercept for the weight percentage of other phases was set to zero. The resulting fit seems to be valid and no violations of the liear model assumptions have been found when investigating the distribution of the residuals. The model predictions seem to be in good agreement with the measured data (see figure 5.11b). A full discussion of the results can be found in section 5.3.2.

For the morphology determining quantities $\frac{\gamma_{10.0}}{\gamma_{00.1}}$ and $\frac{\gamma_{10.1}}{\gamma_{00.1}}$ a total of 45 measurements on 7 samples was used for the statistical analysis (see appendix D.3 for the full set of data). The reason for the limited amount of samples included was the fact that only regular, facetted particles with clearly defined edges could be included. Additionally SEM images were not done for all samples. Due to a lack of data neither the influence of the precipitation time nor of the series was included. However since neither of these factors had an influence on the particle size one can assume that their influence on the particle shape might also be minimal. Consequently only 5 predictors were initially included: the sulfate, silicate and aluminate concentration in mM as well as the chloride and nitrate concentrations in M. For the sulfate containing samples which had a hexagonal platelet morphology with only [10.0] and [00.1] facets, only a lower limit for $\frac{\gamma_{10.1}}{\gamma_{00.1}}$ could be determined, this means that results for the [10.1] surface have to be treated with some care. Additionally the model assumption of a constant standard deviation of the random fluctuations is not valid as can be seen from the plot of the residuals in function of the sulfate concentration (figure D.5a). In fact the results for the sulfate containing samples show a much higher variance than the samples containing no sulfates. The reason for this is the change in morphology to hexagonal platelets with the

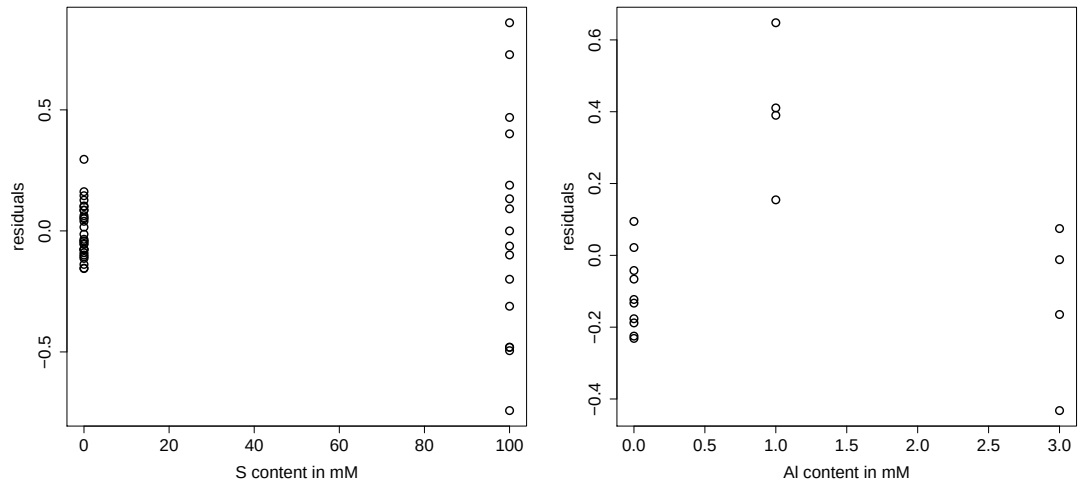

(a) (b)

Figure D.5: Illustration of the violations of the linear model assumptions for $\frac{\gamma_{10.0}}{\gamma_{00.1}}$ (a) and for the $d[\nu,50]$ of the particle size measurements (b). For $\frac{\gamma_{10.0}}{\gamma_{00.1}}$ the standard deviation of the random fluctuations is clearly higher for the sulfate containing samples. For the $d[\nu,50]$ the assumption of linearity is clearly not fulfilled.

addition of sulfates. For hexagonal platelets a change of the viewing angles often has a similar effect as a change of the hight of the particles. Due to this partially convoluted effect the morphology fitting procedure (see section 5.1.3) is often less precise for hexagonal platelets as for the more equiaxed morphology with three different types of facets observed for the other samples. Consequently the standard deviation is higher for the sulfate containing samples. The non-constant standard deviation might mask statistically significant influences of e.g. the counter ions. However the masked influences would have to be smaller than the influence of Si, S and Al in the range of concentrations studied.

Bibliography

[AB08] U. Aschauer and P. Bowen. *Atomistic simulation in powder technology: from growth control and dispersion stabilization to segregation at doped interfaces*. PhD thesis, EPFL, 2008.

[ABBN97] J. W. Anthony, R. A. Bideaux, K. W. Bladh, and M. C. Nichols. *Handbook of Mineralogy, Volume III, Halides, Hydroxides, Oxides*. Mineral data publishing, Tucson, AZ, USA, 1997.

[ABMMB11] Ulrich Aschauer, Olga Burgos-Montes, Rodrigo Moreno, and Paul Bowen. Hamaker 2: A toolkit for the calculation of particle interactions and suspension stability and its application to mullite synthesis by colloidal methods. *Journal of Dispersion Science and Technology*, 32(4):470, 2011.

[Ada03] Craig D Adam. Atomistic modelling of the hydration of CaSO4. *Journal of Solid State Chemistry*, 174(1):141–151, August 2003.

[ADC+07] A. Ayuela, J. S. Dolado, I. Campillo, Y. R. de Miguel, E. Erkizia, D. Sánchez-Portal, A. Rubio, A. Porro, and P. M. Echenique. Silicate chain formation in the nanostructure of cement-based materials. *The Journal of Chemical Physics*, 127:164710, 2007.

[AGM+09] J. P. Allen, W. Gren, M. Molinari, C. Arrouvel, F. Maglia, and S. C. Parker. Atomistic modelling of adsorption and segregation at inorganic solid interfaces. *Molecular Simulation*, 35(7):584–608, 2009.

[AHRS31] W. T. Astbury, D. C. Henry, E. K. Rideal, and R. K. Schofield. Colloid chemistry. *Annual Reports on the Progress of Chemistry*, 28:322–366, 1931.

[AJR+08] U. Aschauer, F. Jones, W.R. Richmond, P. Bowen, A.L. Rohl, G.M. Parkinson, and H. Hofmann. Growth modification of hematite by phosphonate additives. *Journal of Crystal Growth*, 310(3):688–698, February 2008.

[AJS04] M. D Andersen, H. J Jakobsen, and J. Skibsted. Characterization of white portland cement hydration and the CSH structure in the presence of sodium aluminate by 27Al and 29Si MAS NMR spectroscopy. *Cement and Concrete Research*, 34(5):857–868, 2004.

[AMP12] Jeremy P. Allen, Arnaud Marmier, and Stephen C. Parker. Atomistic simulation of surface selectivity on carbonate formation at calcium and magnesium oxide surfaces. *The Journal of Physical Chemistry C*, 116(24):13240–13251, June 2012.

[AOT11] Kisaburo Azuma, Takuji Oda, and Satoru Tanaka. Vibration analysis of O–H stretching mode in mg(OH)2, ca(OH)2, LiOH, and NaOH by plane-wave pseudopotential DFT calculation. *Computational and Theoretical Chemistry*, 963(1):215–220, January 2011.

[ARG+93] Neil L. Allan, Andrew L. Rohl, David H. Gay, C. Richard A. Catlow, Roger J. Davey, and William C. Mackrodt. Calculated bulk and surface properties of sulfates. *Faraday Discuss.*, 95:273–280, 1993.

[Arn04] M. Arnold. *Polymergesteuerte Kristallisation von Calciumhydroxid und Calciumsilicathydrat*. PhD thesis, Universitätsbibliothek, 2004.

[ASBP10] Ulrich Aschauer, Dino Spagnoli, Paul Bowen, and Stephen C. Parker. Growth modification of seeded calcite using carboxylic acids: Atomistic simulations. *Journal of Colloid and Interface Science*, 346(1):226–231, June 2010.

[AT90] M. P. Allen and D. J. Tildesley. *Computer Simulation of Liquids*. 1990.

[ATJ07] A. J Allen, J. J Thomas, and H. M Jennings. Composition and density of nanoscale calcium-silicate-hydrate in cement. *Nature Materials*, 6(4):311–316, 2007.

[AV05] J. L. F. Abascal and C. Vega. A general purpose model for the condensed phases of water: TIP4P/2005. *The Journal of Chemical Physics*, 123(23):234505–12, December 2005.

[Bau78] W. H. Baur. Crystal structure refinement of lawsonite. *American Mineralogist*, 63(3-4):311–315, 1978.

[BBB+09] Massimiliano Bonomi, Davide Branduardi, Giovanni Bussi, Carlo Camilloni, Davide Provasi, Paolo Raiteri, Davide Donadio, Fabrizio Marinelli, Fabio Pietrucci, Ricardo A. Broglia, and Michele Parrinello. PLUMED: a portable plugin for free-energy calculations with molecular dynamics. *Computer Physics Communications*, 180(10):1961–1972, October 2009.

[BBC+04] F. Brunet, Ph. Bertani, Th. Charpentier, A. Nonat, and J. Virlet. Application of 29Si homonuclear and 1H-29Si heteronuclear NMR correlation to structural studies of calcium silicate hydrates. *The Journal of Physical Chemistry B*, 108(40):15494–15502, October 2004.

[BBI+03] A. Botti, F. Bruni, S. Imberti, M. A. Ricci, and A. K. Soper. Solvation of hydroxyl ions in water. *The Journal of Chemical Physics*, 119(10):5001, 2003.

[BBP08] Alessandro Barducci, Giovanni Bussi, and Michele Parrinello. Well-tempered metadynamics: A smoothly converging and tunable free-energy method. *Physical Review Letters*, 100(2):020603, January 2008.

[BCM63] R. A. Buchanan, H. H. Caspers, and J. Murphy. Lattice vibration spectra of mg(OH)2 and ca(OH)2. *Applied Optics*, 2(11):1147–1150, November 1963.

[BD11] Priyanka A. Bhat and N.C. Debnath. Theoretical and experimental study of structures and properties of cement paste: The nanostructural aspects of C–S–H. *Journal of Physics and Chemistry of Solids*, 72(8):920–933, August 2011.

[BDRG94] A. R. Brough, C. M. Dobson, I. G. Richardson, and G. W. Groves. In situ solid-state NMR studies of Ca3SiO5: hydration at room temperature and at elevated temperatures using 29Si enrichment. *Journal of Materials Science*, 29(15):3926–3940, January 1994.

[Ber72] R. L. Berger. Calcium hydroxide: Its role in the fracture of tricalcium silicate paste. *Science*, 175(4022):626–629, 1972.

[BHJP02] A.L Braybrook, B.R Heywood, R.A Jackson, and K Pitt. Parallel computational and experimental studies of the morphological modification of calcium carbonate by cobalt. *Journal of Crystal Growth*, 243(2):336–344, August 2002.

[BHP86] Paul Wencil Brown, Caroline L. Harner, and Edward J. Prosen. The effect of inorganic salts on tricalcium silicate hydration. *Cement and Concrete Research*, 16(1):17–22, January 1986.

[BJL+11] Jeffrey W. Bullard, Hamlin M. Jennings, Richard A. Livingston, Andre Nonat, George W. Scherer, Jeffrey S. Schweitzer, Karen L. Scrivener, and Jeffrey J. Thomas. Mechanisms of cement hydration. *Cement and Concrete Research*, 41(12):1208–1223, December 2011.

[BJR96] P. B Balbuena, K. P Johnston, and P. J Rossky. Molecular dynamics simulation of electrolyte solutions in ambient and supercritical water. 1. ion solvation. *Journal of Physical Chemistry*, 100(7):2706–2715, 1996.

[BKW56] S. Brunauer, D. L. Kantro, and C. H. Weise. The surface energies of calcium oxide and calcium hydroxide. *Canadian Journal of Chemistry*, 34(6):729–742, 1956.

[BLOD01] P. Baranek, A. Lichanot, R. Orlando, and R. Dovesi. Structural and vibrational properties of solid mg (OH) 2 and ca (OH) 2–performances of various hamiltonians. *Chemical Physics Letters*, 340(3-4):362–369, 2001.

[BM72] R.L. Berger and J.D. McGregor. Influence of admixtures on the morphology of calcium hydroxide formed during tricalcium silicate hydration. *Cement and Concrete Research*, 2(1):43–55, January 1972.

[BM73] R. L. Berger and J. D. McGregor. Effect of temperature and water-solid ratio on growth of ca(OH)2 crystals formed during hydration of Ca3SiO5. *Journal of the American Ceramic Society*, 56(2):73–79, 1973.

[BMK05] Elena Bonaccorsi, Stefano Merlino, and Anthony R. Kampf. The crystal structure of tobermorite 14 a; (plombierite), a c-s-h phase. *Journal of the American Ceramic Society*, 88(3):505–512, 2005.

[BMT04] E. Bonaccorsi, S. Merlino, and H.F.W. Taylor. The crystal structure of jennite, Ca9Si6O18(OH)6·8H2O. *Cement and Concrete Research*, 34(9):1481–1488, September 2004.

[BPVGH81] H. J. C. Berendsen, J. P. M. Postma, W. F. Van Gunsteren, and J. Hermans. Interaction models for water in relation to protein hydration. *Intermolecular forces*, 331, 1981.

[BRBK09] B. R. Bickmore, K. M. Rosso, I. D. Brown, and S. Kerisit. Bond-valence constraints on liquid water structure. *The Journal of Physical Chemistry A*, 113(9):1847–1857, 2009.

[BS09] Shashank Bishnoi and Karen L. Scrivener. mic: A new platform for modelling the hydration of cements. *Cement and Concrete Research*, 39(4):266–274, April 2009.

[CC92] D. R. Collins and C. R. A. Catlow. Computer simulation of structures and cohesive properties of micas. *American Mineralogist*, 77(11-12):1172–1181, 1992.

[Cha13] David Leonard Chapman. A contribution to the theory of electrocapillarity. *Philosophical Magazine Series 6*, 25(148):475–481, 1913.

[Chu08] S. V Churakov. Hydrogen bond connectivity in jennite from ab initio simulations. *Cement and Concrete Research*, 38(12):1359–1364, 2008.

[Chu09] S. V Churakov. Structural position of H2O molecules and hydrogen bonding in anomalous 11 a tobermorite. *American Mineralogist*, 94(1):156, 2009.

[CIP+02] Bin Chen, Ivaylo Ivanov, Jung Mee Park, Michele Parrinello, and Michael L. Klein. Solvation structure and mobility mechanism of OH-: a car-parrinello molecular dynamics investigation of alkaline solutions. *The Journal of Physical Chemistry B*, 106(46):12006–12016, November 2002.

[CK96a] Xiandong Cong and R. James Kirkpatrick. 17O MAS NMR investigation of the structure of calcium silicate hydrate gel. *Journal of the American Ceramic Society*, 79(6):1585–1592, 1996.

[CK96b] Xiandong Cong and R. James Kirkpatrick. 29Si MAS NMR study of the structure of calcium silicate hydrate. *Advanced Cement Based Materials*, 3(3-4):144–156, 1996.

[CLK04] R. T. Cygan, J. J. Liang, and A. G. Kalinichev. Molecular models of hydroxide, oxyhydroxide, and clay phases and the development of a general force field. *Journal of Physical Chemistry B-Condensed Phase*, 108(4):1255–1266, 2004.

[CM04] Christomir Christov and Nancy Moller. A chemical equilibrium model of solution behavior and solubility in the h-na-k-ca-OH-Cl-HSO4-SO4-H2O system to high concentration and temperature. *Geochimica et Cosmochimica Acta*, 68(18):3717–3739, September 2004.

[CM08] S. V Churakov and P. Mandaliev. Structure of the hydrogen bonds and silica defects in the tetrahedral double chain of xonotlite. *Cement and Concrete Research*, 38(3):300–311, 2008.

[CRP04] D. J. Cooke, S. E. Redfern, and S. C. Parker. Atomistic simulation of the structure and segregation to the (0001) and surfaces of Fe2O3. *Physics and Chemistry of Minerals*, 31(8):507–517, October 2004.

[CS96] Fang-Ru Chou Chang and Garrison Sposito. The electrical double layer of a disk-shaped clay mineral particle: Effects of electrolyte properties and surface charge density. *Journal of Colloid and Interface Science*, 178(2):555–564, March 1996.

[CSV+10] Jeffrey J. Chen, Luca Sorelli, Matthieu Vandamme, Franz-Josef Ulm, and Gilles Chanvillard. A coupled Nanoindentation/SEM-EDS study on low Water/Cement ratio portland cement paste: Evidence for C–S–H/Ca(OH)2 nanocomposites. *Journal of the American Ceramic Society*, 93(5):1484–1493, 2010.

[CTTJ04] Jeffrey J. Chen, Jeffrey J. Thomas, Hal F. W. Taylor, and Hamlin M. Jennings. Solubility and structure of calcium silicate hydrate. *Cement and Concrete Research*, 34(9):1499–1519, September 2004.

[DCRB91] R. Docherty, G. Clydesdale, K. J. Roberts, and P. Bennema. Application of bravais-friedel-donnay-harker, attachment energy and ising models to predicting and understanding the morphology of molecular crystals. *Journal of Physics D: Applied Physics*, 24:89, 1991.

[Der54] B. V. Derjaguin. A theory of the heterocoagulation, interaction and adhesion of dissimilar particles in solutions of electrolytes. *Discussions of the Faraday Society*, 18:85, 1954.

[DGC+93] L. Desgranges, D. Grebille, G. Calvarin, G. Chevrier, N. Floquet, and J.-C. Niepce. Hydrogen thermal motion in calcium hydroxide: Ca(OH)2. *Acta Crystallographica Section B Structural Science*, 49(5):812–817, October 1993.

[DGH07] J. S Dolado, M. Griebel, and J. Hamaekers. A molecular dynamic study of cementitious calcium silicate hydrate (CSH) gels. *JOURNAL-AMERICAN CERAMIC SOCIETY*, 90(12):3938, 2007.

[DGHH11] Jorge S. Dolado, Michael Griebel, Jan Hamaekers, and Frederik Heber. The nano-branched structure of cementitious calcium–silicate–hydrate gel. *Journal of Materials Chemistry*, 21(12):4445, 2011.

[DHAB12] Ruslan L. Davidchack, Richard Handel, Jamshed Anwar, and Andrey V. Brukhno. Ice ih-water interfacial free energy of simple water models with full electrostatic interactions. *Journal of Chemical Theory and Computation*, 8(7):2383–2390, July 2012.

[Dia01] S. Diamond. Calcium hydroxide in cement paste and concrete- a microstructural appraisal. *Materials Science of Concrete Special*, page 37–58, 2001.

[Dia04] Sidney Diamond. The microstructure of cement paste and concrete–a visual primer. *Cement and Concrete Composites*, 26(8):919–933, November 2004.

[DLP98a] N. H. De Leeuw and S. C. Parker. Molecular-dynamics simulation of MgO surfaces in liquid water using a shell-model potential for water. *Physical Review B*, 58(20):13901–13908, 1998.

[dLP98b] Nora H. de Leeuw and Stephen C. Parker. Surface structure and morphology of calcium carbonate polymorphs calcite, aragonite, and vaterite: An atomistic approach. *The Journal of Physical Chemistry B*, 102(16):2914–2922, April 1998.

[dLP99] N. H. de Leeuw and S. C. Parker. Effect of chemisorption and physisorption of water on the surface structure and stability of alpha-alumina. *Journal of the American Ceramic Society*, 82(11), 1999.

[dLPCP00] N. H. de Leeuw, S. C. Parker, C. R. A. Catlow, and G. D. Price. Modelling the effect of water on the surface structure and stability of forsterite. *Physics and Chemistry of Minerals*, 27(5):332–341, May 2000.

[dLPSN00] N. H. de Leeuw, S. C. Parker, H. M. Sithole, and P. E. Ngoepe. Modeling the surface structure and reactivity of pyrite: Introducing a potential model for FeS2. *The Journal of Physical Chemistry B*, 104(33):7969–7976, 2000.

[DlTDVCA08] Ángeles G. De la Torre, Ruth N. De Vera, Antonio J.M. Cuberos, and Miguel. A.G. Aranda. Crystal structure of low magnesium-content alite: Application to rietveld quantitative phase analysis. *Cement and Concrete Research*, 38(11):1261–1269, November 2008.

[dLWP95] N. H. de Leeuw, G. W. Watson, and S. C. Parker. Atomistic simulation of the effect of dissociative adsorption of water on the surface structure and stability of calcium and magnesium oxide. *The Journal of Physical Chemistry*, 99(47):17219–17225, November 1995.

[DMWZ88] Rachel J. Detwiler, Paulo J.M. Monteiro, Hans-Rudolf Wenk, and Zengqiu Zhong. Texture of calcium hydroxide near the cement paste-aggregate interface. *Cement and Concrete Research*, 18(5):823–829, September 1988.

[DNB90] Denis Damidot, André Nonat, and Pierre Barret. Kinetics of tricalcium silicate hydration in diluted suspensions by microcalorimetric measurements. *Journal of the American Ceramic Society*, 73(11):3319–3322, 1990.

[DO58] B. G. Dick and A. W. Overhauser. Theory of the dielectric constants of alkali halide crystals. *Physical Review*, 112(1):90–103, 1958.

[ENK09] Y. Elakneswaran, T. Nawa, and K. Kurumisawa. Electrokinetic potential of hydrated cement in relation to adsorption of chlorides. *Cement and Concrete Research*, 39(4):340–344, April 2009.

[Ewa21] P. P. Ewald. Die berechnung optischer und elektrostatischer gitterpotentiale. *Annalen der Physik*, 369(3):253–287, 1921.

[FDV+97] P. Faucon, J. M. Delaye, J. Virlet, J. F. Jacquinot, and F. Adenot. Study of the structural properties of the c—s—h(i) BY molecular dynamics simulation. *Cement and Concrete Research*, 27(10):1581–1590, October 1997.

[FG90] B. P. Feuston and S. H. Garofalini. Oligomerization in silica sols. *The Journal of Physical Chemistry*, 94(13):5351–5356, June 1990.

[FHBS03] John L. Fulton, Steve M. Heald, Yaspal S. Badyal, and J. M. Simonson. Understanding the effects of concentration on the solvation structure of ca2+ in aqueous solution. i: The perspective on local structure from EXAFS and XANES. *The Journal of Physical Chemistry A*, 107(23):4688–4696, June 2003.

[FHC+07] C. L. Freeman, J. H. Harding, D. J. Cooke, J. A. Elliott, J. S. Lardge, and D. M. Duffy. New forcefields for modeling biomineralization processes. *Journal of Physical Chemistry C*, 111(32):11943–11951, 2007.

[FJWW97] Jan Forsman, Bo Jonsson, Clifford E. Woodward, and Hakan Wennerstrom. Attractive surface forces due to liquid density depression. *The Journal of Physical Chemistry B*, 101(21):4253–4259, May 1997.

[Fre04] D. Frenkel. Introduction to monte carlo methods. *Computational Soft Matter: From Synthetic Polymers to Proteins*, 2004.

[FS70] R. F. Feldman and P. J. Sereda. A new model for hydrated portland cement and its practical implications. *Engineering Journal*, 53(8/9):53–59, 1970.

[Gal09] M Galassi. *GNU Scientific Library Reference Manual*. 3rd edition, January 2009.

[Gar97] Ellis M. Gartner. A proposed mechanism for the growth of c—s—h during the hydration of tricalcium silicate. *Cement and Concrete Research*, 27(5):665–672, May 1997.

[GDC+02] Rodorico Giorgi, Luigi Dei, Massimo Ceccato, Claudius Schettino, and Piero Baglioni. Nanotechnologies for conservation of cultural heritage: Paper and canvas deacidification. *Langmuir*, 18(21):8198–8203, September 2002.

[GGGTCP09] G. Iván Guerrero-García, Enrique González-Tovar, and Martín Chávez-Páez. Simulational and theoretical study of the spherical electrical double layer for a size-asymmetric electrolyte: The case of big coions. *Physical Review E*, 80(2):021501, August 2009.

[GGLM08] A. Ghoufi, F. Goujon, V. Lachet, and P. Malfreyt. Surface tension of water and acid gases from monte carlo simulations. *The Journal of Chemical Physics*, 128(15):154716, 2008.

[GGN99] S Garrault-Gauffinet and A Nonat. Experimental investigation of calcium silicate hydrate (c-s-h) nucleation. *Journal of Crystal Growth*, 200(3–4):565–574, April 1999.

[GKM00] E. M. Gartner, K. E. Kurtis, and P. J. M. Monteiro. Proposed mechanism of c-s-h growth tested by soft x-ray microscopy. *Cement and Concrete Research*, 30(5):817–822, May 2000.

[Gla01] F. P. Glasser. The role of ca (OH) 2 in portland cement concretes. *Materials Science of Concrete, Special Volume: Calcium Hydroxide in Concrete*, 6:11–36, 2001.

[GMB+98] R. F. P. Grimbergen, H. Meekes, P. Bennema, C. S. Strom, and L. J. P. Vogels. On the prediction of crystal morphology. i. the Hartman–Perdok theory revisited. *Acta Crystallographica Section A Foundations of Crystallography*, 54(4):491–500, July 1998.

[GMS10] E. Gallucci, P. Mathur, and K. Scrivener. Microstructural development of early age hydration shells around cement grains. *Cement and Concrete Research*, 40(1):4–13, January 2010.

[Gou10] M. Gouy. Sur la constitution de la charge electrique a la surface d'un electrolyte. *J. Phys. Theor. Appl.*, 9(1):457–468, 1910.

[Gra47] David C. Grahame. The electrical double layer and the theory of electrocapillarity. *Chemical Reviews*, 41(3):441–501, December 1947.

[Gra90] Adrian Charles Gray. Crystal morphology and surface reactivity studies of calcium hydroxide. 1990.

[Gro81] G.W. Groves. Microcrystalline calcium hydroxide in portland cement pastes of low water/cement ratio. *Cement and Concrete Research*, 11(5-6):713–718, 1981.

[Gru84] Ake Grudemo. Variation with solid-phase concentration of composition, structure and strength of cement pastes at high age. *Cement and Concrete Research*, 14(1):123–132, January 1984.

[Gru99] M. W. Grutzeck. A new model for the formation of calcium silicate hydrate (CSH). *Materials Research Innovations*, 3(3):160–170, 1999.

[GS07] E. Gallucci and K. Scrivener. Crystallisation of calcium hydroxide in early age model and ordinary cementitious systems. *Cement and Concrete Research*, 37(4):492–501, April 2007.

[GSB+07] Krassimir Garbev, Peter Stemmermann, Leon Black, Chris Breen, Jack Yarwood, and Biliana Gasharova. Structural features of c-s-h(i) and its carbonation in air - a raman spectroscopic study. part i: Fresh phases. *Journal of the American Ceramic Society*, 90(3):900–907, 2007.

[GZPVD04] A. Gmira, M. Zabat, R. J.M Pellenq, and H. Van Damme. Microscopic physical basis of the poromechanical behavior of cement-based materials. *Materials and Structures*, 37(1):3–14, 2004.

[Ham37] H. C. Hamaker. The london–van der waals attraction between spherical particles. *physica*, 4(10):1058–1072, 1937.

[Ham81] S. A. Hamid. The crystal structure of the 11 a natural tobermorite. *Zeitschrift für Kristallographie*, 154:189–198, 1981.

[HAM+03] Valeri S. Harutyunyan, Eduward S. Abovyan, Paulo J. M. Monteiro, Vahram P. Mkrtchyan, Minas K. Balyan, and Ashoi P. Aivazyan. X-ray diffraction investigations of microstructure of calcium hydroxide crystallites in the interfacial transition zone of concrete. *Journal of the American Ceramic Society*, 86(12):2162–2166, 2003.

[Har12] V.S. Harutyunyan. Adsorption energy of stoichiometric molecules and surface energy at morphologically important facets of a ca(OH)2 crystal. *Materials Chemistry and Physics*, 134(1):200–213, May 2012.

[HBC+02] Wolfgang Hummel, Urs Berner, Enzo Curti, F. J. Pearson, and Tres Thoenen. *Nagra/Psi Chemical Thermodynamic Data Base 01/01*. Universal-Publishers, August 2002.

[HDLP02] F. M. Higgins, N. H. De Leeuw, and S. C. Parker. Modelling the effect of water on cation exchange in zeolite a. *Journal of Materials Chemistry*, 12(1):124–131, December 2002.

[Hel79] H. Helmholtz. Studien über electrische grenzschichten. *Annalen der Physik*, 243(7):337–382, 1879.

[HHF66] R. Hogg, T. W. Healy, and D. W. Fuerstenau. Mutual coagulation of colloidal dispersions. *Transactions of the Faraday Society*, 62:1638, 1966.

[HKM+09] V. Harutyunyan, A. Kirchheim, P. Monteiro, A. Aivazyan, and P. Fischer. Investigation of early growth of calcium hydroxide crystals in cement solution by soft x-ray transmission microscopy. *Journal of Materials Science*, 44(4):962–969, February 2009.

[Hoo85] William G. Hoover. Canonical dynamics: Equilibrium phase-space distributions. *Physical Review A*, 31(3):1695–1697, March 1985.

[HS52] M.R. Hestenes and E. Stiefel. Methods of conjugate gradients for solving linear systems. *Journal of Research of the National Bureau of Standards*, 49(6):409, December 1952.

[HS04] Hendrik Heinz and Ulrich W. Suter. Atomic charges for classical simulations of polar systems. *The Journal of Physical Chemistry B*, 108(47):18341–18352, November 2004.

[HTG94] Thomas Huber, Andrew E. Torda, and Wilfred F. Gunsteren. Local elevation: A method for improving the searching properties of molecular dynamics simulation. *Journal of Computer-Aided Molecular Design*, 8(6):695–708, 1994.

[HW78] Thomas W. Healy and Lee R. White. Ionizable surface group models of aqueous interfaces. *Advances in Colloid and Interface Science*, 9(4):303–345, June 1978.

[HZ85] John D. Head and Michael C. Zerner. A broyden-fletcher-goldfarb-shanno optimization procedure for molecular geometries. *Chemical Physics Letters*, 122(3):264–270, December 1985.

[JA12] Felipe Jimenez-Angeles. Effects of mixed discrete surface charges on the electrical double layer. *Physical Review E*, 86(2):021601, August 2012.

[Jen00] H. M Jennings. A model for the microstructure of calcium silicate hydrate in cement paste. *Cement and Concrete Research*, 30(1):101–116, 2000.

[JGFS10] P. Juilland, E. Gallucci, R. Flatt, and K. Scrivener. Dissolution theory applied to the induction period in alite hydration. *Cement and Concrete Research*, 2010.

[JLM+03] M. C. G. Juenger, V. H. R. Lamour, P. J. M. Monteiro, E. M. Gartner, and G. P. Denbeaux. Direct observation of cement hydration by soft x-ray transmission microscopy. *Journal of Materials Science Letters*, 22(19):1335–1337, 2003.

[JNL+05] Bo Jönsson, A. Nonat, C. Labbez, B. Cabane, and H. Wennerström. Controlling the cohesion of cement paste. *Langmuir*, 21(20):9211–9221, October 2005.

[Jur54] G Jura. Surface chemistry and catalysis. *Annual Review of Physical Chemistry*, 5(1):375–384, 1954.

[Kal11] A. Kalinichev. Computational molecular modeling of the multi-scale dynamics of water and ions at cement interfaces. 2011.

[KCMP05] Sebastien Kerisit, David J. Cooke, Arnaud Marmier, and Stephen C. Parker. Atomistic simulation of charged iron oxyhydroxide surfaces in contact with aqueous solution. *Chemical Communications*, (24):3027, 2005.

[KCSP05] S. Kerisit, D. J. Cooke, D. Spagnoli, and S. C. Parker. Molecular dynamics simulations of the interactions between water and inorganic solids. *Journal of Materials Chemistry*, 15(14):1454–1462, 2005.

[KDS+06] R. N. Kelly, K. J. DiSante, E. Stranzl, J. A. Kazanjian, P. Bowen, T. Matsuyama, and N. Gabas. Graphical comparison of image analysis and laser diffraction particle size analysis data obtained from the measurements of nonspherical particle systems. *AAPS PharmSciTech*, 7(3):93–106, 2006.

[KJ04] K. O Kjellsen and H. Justnes. Revisiting the microstructure of hydrated tricalcium silicate—-a comparison to portland cement. *Cement and Concrete Composites*, 26(8):947–956, 2004.

[KJB+00] I. Klur, J.-F. Jacquinot, F. Brunet, T. Charpentier, J. Virlet, C. Schneider, and P. Tekely. NMR cross-polarization when TIS>T1rho; examples from silica gel and calcium silicate hydrates. *The Journal of Physical Chemistry B*, 104(44):10162–10167, November 2000.

[KK01] Dmitrii A. Kulik and Michael Kersten. Aqueous solubility diagrams for cementitious waste stabilization systems: II, end-member stoichiometries of ideal calcium silicate hydrate solid solutions. *Journal of the American Ceramic Society*, 84(12):3017–3026, 2001.

[KK02] A. G Kalinichev and R. J Kirkpatrick. Molecular dynamics modeling of chloride binding to the surfaces of calcium hydroxide, hydrated calcium aluminate, and calcium silicate phases. *Chemistry of materials*, 14(8):3539–3549, 2002.

[KKY01] R. J. Kirkpatrick, A. Kalinichev, and P. Yu. Chloride binding to cement phases: exchange isotherm, exp 35 cl NMR and molecular dynamics modeling studies. *Materials Science of Concrete Special Volume: Calcium Hydroxide in Concrete(USA)*, 2001.

[KMM+07] J.-P. Korb, P.J. McDonald, L. Monteilhet, A.G. Kalinichev, and R.J. Kirkpatrick. Comparison of proton field-cycling relaxometry and molecular dynamics

simulations for proton-water surface dynamics in cement-based materials. *Cement and Concrete Research*, 37(3):348–350, March 2007.

[KP04] Sebastien Kerisit and Stephen C. Parker. Free energy of adsorption of water and metal ions on the {101-4} calcite surface. *Journal of the American Chemical Society*, 126(32):10152–10161, August 2004.

[KPH03] Sebastien Kerisit, Stephen C. Parker, and John H. Harding. Atomistic simulation of the dissociative adsorption of water on calcite surfaces. *The Journal of Physical Chemistry B*, 107(31):7676–7682, 2003.

[KRFK87] S. Komarneni, D.M. Roy, C.A. Fyfe, and G.J. Kennedy. Naturally occurring 1.4 nm tobermorite and synthetic jennite: Characterization by 27Al and 29Si MASNMR spectroscopy and cation exchange properties. *Cement and Concrete Research*, 17(6):891–895, November 1987.

[KS68] David H. Klein and Mblvin D. Smith. Homogeneous nucleation of calcium hydroxide. *Talanta*, 15(2):229–231, February 1968.

[KW09] Dmitrii A. Kulik and Thomas Wagner. GEM-Selektor version 2 - PSI, 2009.

[KWD+12] Dmitrii A. Kulik, Thomas Wagner, Svitlana V. Dmytrieva, Georg Kosakowski, Ferdinand F. Hingerl, Konstantin V. Chudnenko, and Urs R. Berner. GEM-Selektor geochemical modeling package: revised algorithm and GEMS3K numerical kernel for coupled simulation codes. *Computational Geosciences*, pages 1–24, August 2012.

[KWK07] Andrey G. Kalinichev, Jianwei Wang, and R. James Kirkpatrick. Molecular dynamics modeling of the structure, dynamics and energetics of mineral-water interfaces: Application to cement materials. *Cement and Concrete Research*, 37(3):337–347, March 2007.

[KYM+97] R. James Kirkpatrick, J.L. Yarger, Paul F. McMillan, Yu Ping, and Xiandong Cong. Raman spectroscopy of c-s-h, tobermorite, and jennite. *Advanced Cement Based Materials*, 5(3-4):93–99, 1997.

[LC85] G. V. Lewis and C. R. A. Catlow. Potential models for ionic oxides. *Journal of Physics C: Solid State Physics*, 18:1149–1161, 1985.

[LCL98] Philippe Leture, Jacques Chappuis, and Bruno Latrasse. Setting and hardening accelerating agent for siliceous hydraulic binders, January 1998. U.S. Classification: 106/713 International Classification: C04B 2200.

[LG01] D. A Litton and S. H Garofalini. Modeling of hydrophilic wafer bonding by molecular dynamics simulations. *Journal of Applied Physics*, 89:6013, 2001.

[LG08] Alessandro Laio and Francesco L Gervasio. Metadynamics: a method to simulate rare events and reconstruct the free energy in biophysics, chemistry and material science. *Reports on Progress in Physics*, 71(12):126601, December 2008.

[LGARH07] J.J. López-García, M.J. Aranda-Rascón, and J. Horno. Electrical double layer around a spherical colloid particle: The excluded volume effect. *Journal of Colloid and Interface Science*, 316(1):196–201, December 2007.

[LJP+06] Christophe Labbez, Bo Jönsson, Isabelle Pochard, André Nonat, and Bernard Cabane. Surface charge density and electrokinetic potential of highly charged minerals: Experiments and monte carlo simulations on calcium silicate hydrate. *The Journal of Physical Chemistry B*, 110(18):9219–9230, May 2006.

[LMMG08] Barbara Lothenbach, Thomas Matschei, Göril Möschner, and Fred P. Glasser. Thermodynamic modelling of the effect of temperature on the hydration and porosity of portland cement. *Cement and Concrete Research*, 38(1):1–18, January 2008.

[LOB81] Samuel Levine, Christopher W. Outhwaite, and Lutful B. Bhuiyan. Statistical mechanical theories of the electric double layer. *Journal of Electroanalytical Chemistry and Interfacial Electrochemistry*, 123(1):105–119, June 1981.

[LOWK61] A. L. Loeb, J. T. G. Overbeek, P. H. Wiersema, and C. V. King. The electrical double layer around a spherical colloid particle. *Journal of The Electrochemical Society*, 108(12):269C–269C, 1961.

[LPJN11] Christophe Labbez, Isabelle Pochard, Bo Jönsson, and André Nonat. C-s-h/solution interface: Experimental and monte carlo studies. *Cement and Concrete Research*, 41(2):161–168, February 2011.

[LPW80] L. Levien, C. T. Prewitt, and D. J. Weidner. Structure and elastic properties of quartz at pressure. *American Mineralogist*, 65(9-10):920–930, 1980.

[LS71] S. Levine and A. L. Smith. Theory of the differential capacity of the oxide/aqueous electrolyte interface. *Discussions of the Faraday Society*, 52(0):290–301, January 1971.

[LSF82] J. Lewis, D. Schwarzenbach, and H. D. Flack. Electric field gradients and charge density in corundum, alpha-Al2O3. *Acta Crystallographica Section A*, 38(5):733–739, September 1982.

[LVD96] George A Lager and Robert B Von Dreele. Neutron powder diffraction study of hydrogarnet to 9.0 GPa. *American Mineralogist*, 81(9-10):1097–1104, October 1996.

[LW06] Barbara Lothenbach and Frank Winnefeld. Thermodynamic modelling of the hydration of portland cement. *Cement and Concrete Research*, 36(2):209–226, February 2006.

[MAD07] H. Manzano, A. Ayuela, and J. S Dolado. On the formation of cementitious C–S–H nanoparticles. *Journal of Computer-Aided Materials Design*, 14(1):45–51, 2007.

[MBA99] S. Merlino, E. Bonaccorsi, and T. Armbruster. Tobermorites: Their real structure and order-disorder (OD) character. *American Mineralogist*, 84:1613–1621, 1999.

[MBA01] S. Merlino, E. Bonaccorsi, and T. Armbruster. The real structure of tobermorite 11A: normal and anomalous forms, OD character and polytypic modifications. *European Journal of Mineralogy*, 13(3):577, 2001.

[MBM11] Cagla Meral, C.J. Benmore, and Paulo J.M. Monteiro. The study of disorder and nanocrystallinity in C–S–H, supplementary cementitious materials and geopolymers using pair distribution function analysis. *Cement and Concrete Research*, 41(7):696–710, July 2011.

[MC95] P. J.M Monteiro and C. T. Chang. The elastic moduli of calcium hydroxide. *Cement and Concrete Research*, 25(8):1605–1609, 1995.

[MC08] Jon M. Makar and Gordon W. Chan. End of the induction period in ordinary portland cement as examined by high-resolution scanning electron microscopy. *Journal of the American Ceramic Society*, 91(4):1292–1299, 2008.

[MCLH93] Simone Melchionna, Giovanni Ciccotti, and Brad Lee Holian. Hoover NPT dynamics for systems varying in shape and size. *Molecular Physics*, 78(3):533–544, 1993.

[MDBD87] W.C. Mackrodt, R.J. Davey, S.N. Black, and R. Docherty. The morphology of alpha-Al2O3 and alpha-Fe2O3: the importance of surface relaxation. *Journal of Crystal Growth*, 80(2):441–446, February 1987.

[MDGP+12] E. Masoero, E. Del Gado, R. J.-M. Pellenq, F.-J. Ulm, and S. Yip. Nanostructure and nanomechanics of cement: Polydisperse colloidal packing. *Physical Review Letters*, 109(15):155503, October 2012.

[MHE+96] Viktor Moravetski, Jörg-R. Hill, Uwe Eichler, Anthony K. Cheetham, and Joachim Sauer. 29Si NMR chemical shifts of silicate species: Ab initio study of environment and structure effects. *Journal of the American Chemical Society*, 118(51):13015–13020, January 1996.

[Min01] S. Mindess. The strength and fracture of concrete: the role of the calcium hydroxide. *Materials Science of Concrete Special*, page 143–154, 2001.

[MJ75] P. Mondal and J. W. Jeffery. The crystal structure of tricalcium aluminate, Ca3Al2O6. *Acta Crystallographica Section B Structural Crystallography and Crystal Chemistry*, 31(3):689–697, March 1975.

[MMM+12] Hegoi Manzano, Sina Moeini, Francis Marinelli, Adri C. T. van Duin, Franz-Josef Ulm, and Roland J.-M. Pellenq. Confined water dissociation in microporous defective silicates: Mechanism, dipole distribution, and impact on substrate properties. *Journal of the American Chemical Society*, 134(4):2208–2215, February 2012.

[MN01] P. Mark and L. Nilsson. Structure and dynamics of the TIP3P, SPC, and SPC/E water models at 298 k. *The Journal of Physical Chemistry A*, 105(43):9954–9960, 2001.

[MNSM03] Takayuki Maeshima, Hiroaki Noma, Masato Sakiyama, and Takeshi Mitsuda. Natural 1.1 and 1.4 nm tobermorites from fuka, okayama, japan: Chemical analysis, cell dimensions, 29Si NMR and thermal behavior. *Cement and Concrete Research*, 33(10):1515–1523, October 2003.

[MP04] A. Marmier and S. C Parker. Ab initio morphology and surface thermodynamics of a-Al2O3. *Phys. Rev. B*, 69:115409, 2004.

[MRA10] Francesco Roberto Massaro, Marco Rubbo, and Dino Aquilano. Theoretical equilibrium morphology of gypsum (CaSO4·2H2O). 1. a syncretic strategy to calculate the morphology of crystals. *Crystal Growth & Design*, 10(7):2870–2878, 2010.

[MSGM13] Arnaud C. A. Muller, Karen L. Scrivener, Agata M. Gajewicz, and Peter J. McDonald. Densification of C–S–H measured by 1H NMR relaxometry. *The Journal of Physical Chemistry C*, 117(1):403–412, January 2013.

[MT82] K. Mohan and H.F.W. Taylor. A trimethylsilylation study of tricalcium silicate pastes. *Cement and Concrete Research*, 12(1):25–31, January 1982.

[MT89] William C. Mackrodt and Phillip W. Tasker. Segregation isotherms at the surfaces of oxides. *Journal of the American Ceramic Society*, 72(9):1576–1583, 1989.

[MU49] Nicholas Metropolis and S. Ulam. The monte carlo method. *Journal of the American Statistical Association*, 44(247):335–341, 1949.

[Mul55] R. S. Mulliken. Electronic population analysis on LCAO[Single Bond]MO molecular wave functions. II. overlap populations, bond orders, and covalent bond energies. *The Journal of Chemical Physics*, 23(10):1841–1846, October 1955.

[MWKA07] Makoto Matsumoto, Isaku Wada, Ai Kuramoto, and Hyo Ashihara. Common defects in initialization of pseudorandom number generators. *ACM Trans. Model. Comput. Simul.*, 17(4):15, 2007.

[Mye05] Allan S. Myerson. *Molecular Modeling Applications in Crystallization*. Cambridge University Press, September 2005.

[NA03] Roland R. Netz and David Andelman. Neutral and charged polymers at interfaces. *Physics Reports*, 380(1–2):1–95, June 2003.

[New14] I. Newton. *Philosophiae naturalis principia mathematica*. sumptibus Societatis, 1714.

[Nic11] Luc Nicoleau. Accelerated growth of calcium silicate hydrates: Experiments and simulations. *Cement and Concrete Research*, 41(12):1339–1348, December 2011.

[NM65] J. A. Nelder and R. Mead. A simplex method for function minimization. *The Computer Journal*, 7(4):308 –313, January 1965.

[Non04] A. Nonat. The structure and stoichiometry of CSH. *Cement and Concrete Research*, 34(9):1521–1528, 2004.

[OBL80] Christopher W. Outhwaite, Lutful B. Bhuiyan, and Samuel Levine. Theory of the electric double layer using a modified poisson-boltzmann equation. *Journal of the Chemical Society, Faraday Transactions 2*, 76:1388, 1980.

[OD79] I. Odler and H. Dörr. Early hydration of tricalcium silicate II. the induction period. *Cement and Concrete Research*, 9(3):277–284, May 1979.

[OHW82] Hiroyuki Ohshima, Thomas W Healy, and Lee R White. Accurate analytic expressions for the surface charge density/surface potential relationship and double-layer potential distribution for a spherical colloidal particle. *Journal of Colloid and Interface Science*, 90(1):17–26, November 1982.

[OMB95] J.P. Ollivier, J.C. Maso, and B. Bourdette. Interfacial transition zone in concrete. *Advanced Cement Based Materials*, 2(1):30–38, January 1995.

[PA99] D. L. Parkhurst and C. A. J. Appelo. User's guide to PHREEQC (version 2): A computer program for speciation, batch-reaction, one-dimensional transport, and inverse geochemical calculations. 1999.

[PCPJ92] A. Pavese, M. Catti, G. D. Price, and R. A. Jackson. Interatomic potentials for CaCO 3 polymorphs (calcite and aragonite), fitted to elastic and vibrational data. *Physics and Chemistry of Minerals*, 19(2):80–87, 1992.

[PCPW96] A. Pavese, M. Catti, S. C. Parker, and A. Wall. Modelling of the thermal dependence of structural and elastic properties of calcite, CaCO 3. *Physics and Chemistry of Minerals*, 23(2):89–93, 1996.

[Pet61] H. E. Petch. The hydrogen positions in portlandite, ca(OH)2, as indicated by the electron distribution. *Acta Crystallographica*, 14(9):950–957, September 1961.

[PKS+09] R. J.M Pellenq, A. Kushima, R. Shahsavari, K. J Van Vliet, M. J Buehler, S. Yip, and F. J Ulm. A realistic molecular model of cement hydrates. *Proceedings of the National Academy of Sciences*, 2009.

[PKW48] William Primak, Herman Kaufman, and Roland Ward. X-ray diffraction studies of systems involved in the preparation of alkaline earth sulfide and selenide phosphors1. *Journal of the American Chemical Society*, 70(6):2043–2046, June 1948.

[Pli95] S. Plimpton. Fast parallel algorithms for short-range molecular dynamics. *Journal of Computational Physics*, 117(1):1–19, 1995.

[PLVD08] R. J.M Pellenq, N. Lequeux, and H. Van Damme. Engineering the bonding scheme in C–S–H: the iono-covalent framework. *Cement and Concrete Research*, 38(2):159–174, 2008.

[PMB10] Maria Porus, Plinio Maroni, and Michal Borkovec. Highly-sensitive reflectometry setup capable of probing the electrical double layer on silica. *Sensors and Actuators B: Chemical*, 151(1):250–255, November 2010.

[PR81] M. Parrinello and A. Rahman. Polymorphic transitions in single crystals: A new molecular dynamics method. *Journal of Applied physics*, 52(12):7182–7190, 1981.

[PRM+06] Ingmar Pointeau, Pascal Reiller, Nathalie Macé, Catherine Landesman, and Nathalie Coreau. Measurement and modeling of the surface potential evolution of hydrated cement pastes as a function of degradation. *Journal of Colloid and Interface Science*, 300(1):33–44, August 2006.

[PXW10] Tongyan Pan, Kaiming Xia, and Linbing Wang. Chloride binding to calcium silicate hydrates (c-s-h) in cement paste: a molecular dynamics analysis. *International Journal of Pavement Engineering*, 11(5):367–379, 2010.

[QPMMHA04] M. Quesada-Perez, A. Martin-Molina, and R. Hidalgo-Alvarez. Simulation of electric double layers with multivalent counterions: Ion size effect. *The Journal of Chemical Physics*, 121(17):8618, November 2004.

[RBA10] Nicolas Ruffray, Paul Bowen, and Anne Aimable. Influence of different ionic species on the morphology of growing portlandite crystals. Technical report, EPFL, June 2010.

[RDSA12] Pawel Rejmak, Jorge S. Dolado, Malcolm J. Stott, and Andrés Ayuela. 29Si NMR in cement: A theoretical study on calcium silicate hydrates. *The Journal of Physical Chemistry C*, 116(17):9755–9761, May 2012.

[RG93] I. G. Richardson and G. W. Groves. Microstructure and microanalysis of hardened ordinary portland cement pastes. *Journal of Materials Science*, 28(1):265–277, January 1993.

[Ric04] I. G. Richardson. Tobermorite/jennite- and tobermorite/calcium hydroxide-based models for the structure of c-s-h: applicability to hardened pastes of tricalcium silicate, [beta]-dicalcium silicate, portland cement, and blends of portland cement with blast-furnace slag, metakaolin, or silica fume. *Cement and Concrete Research*, 34(9):1733–1777, September 2004.

[Ric08] I. G. Richardson. The calcium silicate hydrates. *Cement and Concrete Research*, 38(2):137–158, 2008.

[Ric09] I. G. Richardson. Problems with a 'realistic' model for the binding phase in concrete, 2009.

[RMC98] Andrew R. Roosen, Ryan P. McCormack, and W. Craig Carter. Wulffman: A tool for the calculation and display of crystal shapes. *Computational Materials Science*, 11(1):16–26, March 1998.

[RNRAOHH05] C. Rodriguez-Navarro, E. Ruiz-Agudo, M. Ortega-Huertas, and E. Hansen. Nanostructure and irreversible colloidal behavior of ca(OH)2: implications in cultural heritage conservation. *Langmuir*, 21(24):10948–10957, November 2005.

[Roh03] Andrew L. Rohl. Computer prediction of crystal morphology. *Current Opinion in Solid State and Materials Science*, 7(1):21–26, February 2003.

[RRL+09a] G. Renaudin, J. Russias, F. Leroux, C. Cau-dit Coumes, and F. Frizon. Structural characterization of CSH and CASH samples–Part II: local environment investigated by spectroscopic analyses. *Journal of Solid State Chemistry*, 182(12):3320–3329, 2009.

[RRL+09b] G. Renaudin, J. Russias, F. Leroux, F. Frizon, and C. Cau-dit Coumes. Structural characterization of CSH and CASH samples–Part i: Long-range order investigated by rietveld analyses. *Journal of Solid State Chemistry*, 182(12):3312–3319, 2009.

[RSS+13] Maria Ricci, Peter Spijker, Francesco Stellacci, Jean-Francois Molinari, and Kislon Voïtchovsky. Direct visualization of single ions in the stern layer of calcite. *Langmuir*, 29(7):2207–2216, February 2013.

[RZTHG93] R. Rassem, H. Zanni-Théveneau, D. Heidemann, and A.R. Grimmer. Proton high resolution solid state NMR study of C3S hydration. *Cement and Concrete Research*, 23(1):169–176, January 1993.

[SB98] Lev N Shchur and Paolo Butera. The RANLUX generator: resonances in a random walk test. *hep-lat/9805017*, May 1998. Int.J.Mod.Phys. C9 (1998) 607-624.

[SBP08] Dino Spagnoli, Jillian F. Banfield, and Stephen C. Parker. Free energy change of aggregation of nanoparticles. *The Journal of Physical Chemistry C*, 112(38):14731–14736, 2008.

[SBPU09] Rouzbeh Shahsavari, Markus J. Buehler, Roland J.-M. Pellenq, and Franz-Josef Ulm. First-principles study of elastic constants and interlayer interactions of complex hydrated oxides: Case study of tobermorite and jennite. *Journal of the American Ceramic Society*, 92(10):2323–2330, October 2009.

[SCB+10] L. B. Skinner, S. R. Chae, C. J. Benmore, H. R. Wenk, and P. J. M. Monteiro. Nanostructure of calcium silicate hydrates in cements. *Physical Review Letters*, 104(19):195502, May 2010.

[SCGT07] James L. Suter, Peter V. Coveney, H. Chris Greenwell, and Mary-Ann Thyveetil. Large-scale molecular dynamics study of montmorillonite clay: Emergence of undulatory fluctuations and determination of material properties. *The Journal of Physical Chemistry C*, 111(23):8248–8259, June 2007.

[SCKP06] D. Spagnoli, D. J. Cooke, S. Kerisit, and S. C. Parker. Molecular dynamics simulations of the interaction between the surfaces of polar solids and aqueous solutions. *Journal of Materials Chemistry*, 16(20):1997–2006, 2006.

[Scr04] Karen L. Scrivener. Backscattered electron imaging of cementitious microstructures: understanding and quantification. *Cement and Concrete Composites*, 26(8):935–945, November 2004.

[SDMW02] Dean C. Sayle, James A. Doig, S. Andrada Maicaneanu, and Graeme W. Watson. Atomistic structure of oxide nanoparticles supported on an oxide substrate. *Physical Review B*, 65(24):245414, June 2002. Copyright (C) 2009 The American Physical Society; Please report any problems to prola@aps.org.

[SF96] W. Smith and T. R. Forester. DL_POLY_2.0: a general-purpose parallel molecular dynamics simulation package. *Journal of Molecular Graphics*, 14(3):136–141, June 1996.

[SFM01] J. Stark, U. Frohburg, and B. Moser. Investigations by environmental SEM: ca (OH)2 during hydration and during carbonation. *Materials Science of Concrete Special*, page 167–189, 2001.

[SG00] Varghese Swamy and Julian D. Gale. Transferable variable-charge interatomic potential for atomistic simulation of titanium oxides. *Physical Review B*, 62(9):5406–5412, September 2000.

[SH08] J. Skibsted and C. Hall. Characterization of cement minerals, cements and their reaction products at the atomic and nano scale. *Cement and Concrete Research*, 38(2):205–225, 2008.

[Smi12] W. Smith. STFC computational science and engineering department - molecular simulation. http://www.ccp5.ac.uk/DL_POLY_CLASSIC/, 2012.

[Smo03] M. Smoluchowski. Contribution to the theory of electro-osmosis and related phenomena. *Bull Intern. Acad. Sci. Cracovie*, page 184–199, 1903.

[SMW02] J. Stark, B. Moser, and G. Weimar. Nano and microstructure of portland cement paste. *Frost resistance of concrete: from nano-structure and pore solution to macroscopic behaviour and testing, Essen, Germany, 18-19 April 2002*, page 15, 2002.

[SN11] Karen L. Scrivener and André Nonat. Hydration of cementitious materials, present and future. *Cement and Concrete Research*, 41(7):651–665, July 2011.

[Son96] Jürgen Sonnefeld. Determination of surface charge density constants for spherical silica particles using a linear transformation. *Journal of Colloid and Interface Science*, 183(2):597–599, November 1996.

[Sop00] A. K. Soper. The radial distribution functions of water and ice from 220 to 673 k and at pressures up to 400 MPa. *Chemical Physics*, 258(2-3):121–137, August 2000.

[SR78] F. H. Stillinger and A. Rahman. Revised central force potentials for water. *The Journal of Chemical Physics*, 68(2):666–670, January 1978.

[SS74] Peter H. Santschi and Paul W. Schindler. Complex formation in the ternary systems ca II-H4SiO4-H2O and mg II-H4SiO4-H2O. *Journal of the Chemical Society, Dalton Transactions*, (2):181, 1974.

[SSL+92] Klaus-Peter Schröder, Joachim Sauer, Maurice Leslie, C. Richard A. Catlow, and John M. Thomas. Bridging hydroxyl groups in zeolitic catalysts: a computer simulation of their structure, vibrational properties and acidity in protonated faujasites (h-y zeolites). *Chemical Physics Letters*, 188(3–4):320–325, January 1992.

[Ste24] O. Stern. Zur theorie der elektrolytischen doppelschicht. *Z. Elektrochem*, 30(21/22):508–516, 1924.

[Sto81] A. M. Stoneham. Ceramic surfaces: Theoretical studies. *Journal of the American Ceramic Society*, 64(1):54–60, 1981.

[Str01] C.S. Strom. Validity of Hartman–Perdok PBC theory in prediction of crystal morphology from solution and surface x-ray diffraction of potassium dihydrogen phosphate (KDP). *Journal of Crystal Growth*, 222(1–2):298–310, January 2001.

[SUCB+12] Sezen Soyer-Uzun, Sejung Rosie Chae, Chris J. Benmore, Hans-Rudolf Wenk, and Paulo J. M. Monteiro. Compositional evolution of calcium silicate hydrate (C–S–H) structures by total x-ray scattering. *Journal of the American Ceramic Society*, 95(2):793–798, 2012.

[SW74] H. Saalfeld and M. Wedde. Refinement of the crystal structure of gibbsite, al (OH) 3. *Zeitschrift für Kristallographie*, 139(1-2):129–135, 1974.

[Tay86] H. F.W Taylor. Proposed structure for calcium silicate hydrate gel. *Journal of the American Ceramic Society*, 69(6):464–467, 1986.

[TCAJ04] Jeffrey J. Thomas, Jeffrey J. Chen, Andrew J. Allen, and Hamlin M. Jennings. Effects of decalcification on the microstructure and surface area of cement and tricalcium silicate pastes. *Cement and Concrete Research*, 34(12):2297–2307, December 2004.

[TCJN03] Jeffrey J. Thomas, Jeffrey J. Chen, Hamlin M. Jennings, and Dan A. Neumann. Ca-OH bonding in the c-s-h gel phase of tricalcium silicate and white portland cement pastes measured by inelastic neutron scattering. *Chemistry of Materials*, 15(20):3813–3817, October 2003.

[Tea10] R. Development Core Team. *R: A Language and Environment for Statistical Computing*. Vienna, Austria, 2010. ISBN 3-900051-07-0.

[TGSB12] Abhishek Tewari, Sandra Galmarini, Michael Stuer, and Paul Bowen. Atomistic modeling of the effect of codoping on the atomistic structure of interfaces in alpha-alumina. *Journal of the European Ceramic Society*, 32(11):2935–2948, August 2012.

[TJE87] Olle Teleman, Bo Jönsson, and Sven Engström. A molecular dynamics simulation of a water model with intramolecular degrees of freedom. *Molecular Physics*, 60:193–203, 1987.

[TSB+99] M. B. Taylor, C. E. Sims, G. D. Barrera, N. L. Allan, and W. C. Mackrodt. Quasi-harmonic free energy and derivatives for slabs: Oxide surfaces at elevated temperatures. *Physical Review B*, 59(10):6742–6751, March 1999.

[TSK76] M. E. Tadros, Jan Skalny, and R. S. Kalyoncu. Early hydration of tricalcium silicate. *Journal of the American Ceramic Society*, 59(7-8):344–347, 1976.

[TT00] Miho Tanaka and Kazuya Takahashi. The identification and characterization of silicate complexes in calcium chloride solution using fast atom bombardment mass spectrometry. *Analytica Chimica Acta*, 411(1–2):109–119, May 2000.

[TT02] Miho Tanaka and Kazuya Takahashi. Characterization of silicate monomer with sodium, calcium and strontium but not with lithium and magnesium ions by fast atom bombardment mass spectrometry. *Journal of Mass Spectrometry*, 37(6):623–630, 2002.

[TV80] G. M. Torrie and J. P. Valleau. Electrical double layers. i. monte carlo study of a uniformly charged surface. *The Journal of Chemical Physics*, 73(11):5807, 1980.

[TV82] G. M. Torrie and J. P. Valleau. Electrical double layers. 4. limitations of the gouy-chapman theory. *The Journal of Physical Chemistry*, 86(16):3251–3257, 1982.

[UZWTC09] Piero Ugliengo, Claudio M. Zicovich-Wilson, Sergio Tosoni, and Bartolomeo Civalleri. Role of dispersive interactions in layered materials: a periodic B3LYP and B3LYP-D* study of mg(OH)2, ca(OH)2 and kaolinite. *Journal of Materials Chemistry*, 19(17):2564–2572, April 2009.

[vdV90] E. van der Voort. The role of solvent interaction with crystalline surfaces in crystal growth. *Geologica Ultraiectina*, 68:1–101, October 1990.

[Vin57] George H. Vineyard. Frequency factors and isotope effects in solid state rate processes. *Journal of Physics and Chemistry of Solids*, 3(1–2):121–127, 1957.

[VO99] Evert Johannes Willem Verwey and J. Th G. Overbeek. *Theory of the Stability of Lyophobic Colloids*. Courier Dover Publications, 1999.

[Vot07] A. F Voter. Introduction to the kinetic monte carlo method. *Radiation Effects in Solids*, 235:1568–2609, 2007.

[VTGN09] Markus Valtiner, Mira Todorova, Guido Grundmeier, and Jörg Neugebauer. Temperature stabilized surface reconstructions at polar ZnO(0001). *Physical Review Letters*, 103(6), August 2009.

[VVPB+12] Krystyn Van Vliet, Roland Pellenq, Markus J. Buehler, Jeffrey C. Grossman, Hamlin Jennings, Franz-Josef Ulm, and Sidney Yip. Set in stone? a perspective on the concrete sustainability challenge. *MRS Bulletin*, 37(04):395–402, 2012.

[WKdL+96] Graeme W. Watson, E. Toby Kelsey, Nora H. de Leeuw, Duncan J. Harris, and Stephen C. Parker. Atomistic simulation of dislocations, surfaces and interfaces in MgO. *Journal of the Chemical Society, Faraday Transactions*, 92(3):433, 1996.

[WKHD12] Thomas Wagner, Dmitrii A. Kulik, Ferdinand F. Hingerl, and Svitlana V. Dmytrieva. GEM-Selektor geochemical modeling package: TSolMod library and data interface for multicomponent phase models. *The Canadian Mineralogist*, 50(5):1173–1195, October 2012.

[WLO66] P. H. Wiersema, A. L. Loeb, and J. Th G. Overbeek. Calculation of the electrophoretic mobility of a spherical colloid particle. *Journal of Colloid and Interface Science*, 22(1):78–99, 1966.

[WR09] Matt Wand and Brian Ripley. *KernSmooth: Functions for kernel smoothing for Wand & Jones (1995)*. 2009. R package version 2.23-3.

[Wul01] G. Wulff. Zur frage der geschwindigkeit des wachstums und der auflösung der kristallflächen. *Z. kristallogr*, 34:449–530, 1901.

[WY84] Zhao-Qi Wu and J. Francis Young. Formation of calcium hydroxide from aqueous suspensions of tricalcium silicate. *Journal of the American Ceramic Society*, 67(1):48–51, 1984.

[YKP+99] P. Yu, R. J Kirkpatrick, B. Poe, P. F McMillan, and X. Cong. Structure of calcium silicate hydrate (CSH): near-, mid-, and far-infrared spectroscopy. *J. Am. Ceram. Soc.*, 82(3):742–748, 1999.

[Ypm95] Tjalling J. Ypma. Historical development of the Newton–Raphson method. *SIAM Review*, 37(4):531–551, December 1995.

[YTB77] J. F. Young, H. S. Tong, and R. L. Berger. Compositions of solutions in contact with hydrating tricalcium silicate pastes. *Journal of the American Ceramic Society*, 60(5-6):193–198, 1977.

[ZKR10] Piotr Zarzycki, Sebastien Kerisit, and Kevin M. Rosso. Molecular dynamics study of the electrical double layer at silver chloride-electrolyte interfaces. *The Journal of Physical Chemistry C*, 114(19):8905–8916, May 2010.

Curriculum Vitae

Sandra Caroline Galmarini

sandra@galmarini.ch

Date of Birth:	December 12th, 1981
Nationality:	Swiss

Education

2009–2013	**PhD Thesis in Materials Science: Atomistic Simulation of Cementitious Systems**, Laboratoire de Technologie des Poudres, Ecole Polytechnique Fédérale de Lausanne, Switzerland
2006–2008	MSc in Computational Science and Engineering, Eidgenössische Technische Hochschule Zürich, Switzerland.
2001–2006	MSc in Materials Science and Engineering, Ecole Polytechnique Fédérale de Lausanne, Switzerland.
2001	Federal Maturity type D: languages with Spanish, French and English.
1997–1998	Exchange year in Norway, certificate of Norwegian as a second language.

Professional Experience

2008–today	Assistant position at the Laboratoire de Technologie des Poudres, Ecole Polytechnique Fédérale de Lausanne, Switzerland.
	Supervision and co-supervision of several student semester projects, teaching experience in both practical work and preparation of a two hour lecture.
2004	Internship (6 weeks) at the NRC Research Facility in Ottawa Canada
	Work on fire resistance of reinforced concrete.
1999–2010	Part time development and maintenance of the company information system of Walt + Galmarini AG, Zürich.
	FileMaker database programming.

Languages

German	Mother tongue
English	Fluent
French	Fluent
Norwegian	Fluent
Spanish	Fair

Distinctions

2010	Best Student Oral Presentation
	Molecular Modelling Conference 2010, Melbourne Australia
2006	SVMT prize for best master thesis in materials science at EPFL

Publications

2013	S. Galmarini, S.C. Parker, and P. Bowen. Atomistic simulations to identify stable bulk defects in 14 a tobermorite - towards a realistic c-s-h model. *in prep.*, 2013
	S. Galmarini and P. Bowen. Atomistic simulation of the adsorption of calcium and hydroxide ions onto portlandite surfaces. *in prep.*, 2013
	S. Galmarini and P. Bowen. Atomistic simulation of silicate species interaction with portlandite surfaces. *in prep.*, 2013
2012	Abhishek Tewari, Sandra Galmarini, Michael Stuer, and Paul Bowen. Atomistic modeling of the effect of codoping on the atomistic structure of interfaces in alpha-alumina. *Journal of the European Ceramic Society*, 32(11):2935–2948, August 2012
2011	S. Galmarini, U. Aschauer, A. Tewari, Y. Aman, C. Van Gestel, and P. Bowen. Atomistic modeling of dopant segregation in [alpha]-alumina ceramics: Coverage dependent energy of segregation and nominal dopant solubility. *Journal of the European Ceramic Society*, 2011
	Sandra Galmarini, Anne Aimable, Nicolas Ruffray, and Paul Bowen. Changes in portlandite morphology with solvent composition: Atomistic simulations and experiment. *Cement and Concrete Research*, 41(12):1330–1338, December 2011
2008	S. Galmarini, U. Aschauer, P. Bowen, and S. C Parker. Atomistic simulation of y-doped a-alumina interfaces. *J. Am. Ceram. Soc*, 91(11):3643–3651, 2008